HARVARD UNIVERSITY

Graduate School of Arts and Sciences

DISSERTATION ACCEPTANCE CERTIFICATE

The undersigned, appointed by the

Harvard John A. Paulson School of Engineering and Applied Sciences
have examined a dissertation entitled:

"Hydrodynamics and Viscous Flow in Graphene Measured with Johnson Noise Thermometry"

presented by: Artem Vladimirovich Talanov

Signature _____

Typed name: Professor Philip Kim

Signature _____

Typed name: Professor Robert Westervelt

Signature _____

Typed name: Professor Amir Yacoby

Signature _____

Typed name: Professor Donhee Ham

October 23, 2023

Hydrodynamics and Viscous Flow in Graphene Measured with Johnson Noise Thermometry

A DISSERTATION PRESENTED
BY
ARTEM VLADIMIROVICH TALANOV
TO
THE SCHOOL OF ENGINEERING AND APPLIED SCIENCES

IN PARTIAL FULFILLMENT OF THE REQUIREMENTS
FOR THE DEGREE OF
DOCTOR OF PHILOSOPHY
IN THE SUBJECT OF
APPLIED PHYSICS

HARVARD UNIVERSITY
CAMBRIDGE, MASSACHUSETTS

OCTOBER 2023

Dissertation Advisor: Professor Philip Kim Artem Vladimirovich Talanov

Hydrodynamics and Viscous Flow in Graphene Measured with Johnson Noise Thermometry

Abstract

In this dissertation, we investigate thermal transport phenomena in 2-dimensional monolayer and bilayer graphene, both of which are candidates for strongly interacting, correlated electronic systems. The interactions between electrons in solid-state materials give rise to novel states of matter, leading to new theoretical developments and device applications. Measurement of thermal transport in such systems can reveal exotic physics in these new states that may be elusive to electrical transport, such as charge-neutral transport modes or collective behavior. One particular emergent phenomenon that has recently attracted significant attention is the viscous hydrodynamic transport regime, where particles' behavior is best collectively described as a viscous fluid rather than as individual particles. The recent discovery of this regime in graphene has driven new devices and insights about other materials as well.

Accordingly, several strongly-interacting electronic systems in addition to graphene have recently been both predicted and shown experimentally to exhibit a ratio of thermal conductivity to electrical conductivity that deviates from the near-universal Wiedemann-Franz law. Monolayer and bilayer graphene both present a strong opportunity for using thermal transport to study the interplay of quantum criticality and hydrodynamics due to a combination of intrinsic material properties and recent advances

in low-disorder sample preparation. However, despite previous experimental work, the Lorenz ratio suppression in doped graphene remains largely experimentally unstudied, and the viscous analogue of Joule heating remains entirely unexplored, limiting the real-life applications of electron hydrodynamics in devices.

To perform the thermal transport measurements, we have developed a Johnson noise thermometry measurement technique applicable to mesoscopic devices with variable source impedance with high bandwidth for fast data acquisition. We thoroughly discuss the details of the technique, including differential noise measurements, two-stage impedance matching, cryogenic circuitry components, calibration, and measurement. Most importantly, we have discovered and studied several parasitic effects in the noise measurement technique that could significantly reduce the measurement accuracy, and we discuss our novel methods to quantify and mitigate them. As a demonstration, we measure thermal conductivity on a bilayer graphene sample spanning the metallic and semiconducting regimes over a wide resistance range.

We use our advanced Johnson noise techniques to study hydrodynamics in monolayer and bilayer graphene, both at charge neutrality and in the doped regime, by searching for breakdowns of the Wiedemann-Franz law. We find that while both systems show some evidence of Lorenz ratio enhancement at charge neutrality and suppression at small doping, the evidence varies significantly from device to device due to the prevailing contact resistance, ballistic transport, and phonon-cooling, requiring careful consideration for quantitative analysis. We provide a systematic diagnosis and potential remedies for these technical challenges.

To explore viscous hydrodynamics further from a novel perspective, we use a combination of electrical and noise-based thermal magneto-transport measurements in the Corbino geometry to study viscosity directly. We find a new experimental signature of

viscous heating leading to magnetically-induced redistribution of temperature, an effect that is coincident in temperature and density with the aforementioned Lorenz ratio suppression. These two effects thus provide robust qualitative signatures of hydrodynamics, despite arising from two distinct aspects of this regime: microscopic momentum conservation due to electron-electron scattering, and geometry-dependent viscous dissipation. Our results mark the first observation of viscous electronic heating in an electron fluid, which may influence the design of hydrodynamic devices and offers a new methodology to identify hydrodynamic states in other systems.

Contents

Author List

The following authors contributed to Chapter 1: Artem Talanov.
The following authors contributed to Chapter 2: Artem Talanov, Aaron Hui, Jonah Waissman, Philip Kim.
The following authors contributed to Chapter 3: Artem Talanov, Aaron Hui.
The following authors contributed to Chapter 4: Artem Talanov, Jonah Waissman, Philip Kim.
The following authors contributed to Chapter 5: Artem Talanov, Jonah Waissman, Aaron Hui, Philip Kim.
The following authors contributed to Chapter 6: Artem Talanov, Jonah Waissman, Aaron Hui, Brian Skinner, Philip Kim.
The following authors contributed to Chapter 7: Artem Talanov, Jonah Waissman, Philip Kim.

Listing of figures

List of Tables

Listing of Acronyms

2D 2-dimensional

AC Alternating current

ACF Auto-Correlation Function

AdS Anti-de Sitter

ALD Atomic Layer Deposition

BLG Bilayer Graphene

BG Bloch-Grüneisen

BC Boundary Condition

BSCCO Bismuth Strontium Calcium Copper Oxide

CFT Conformal Field Theory

COTS Commercial Off-The-Shelf

CMRR Common mode rejection ratio

CNP Charge Neutrality Point

CPU Central Processing Unit

DC Direct current

EBL Electron-Beam Lithography

ESD Electrostatic Discharge

e-e electron-electron

EMI Electromagnetic Interference

ENBW Effective Noise Bandwidth

FET Field-effect transistor

FFT Fast Fourier transform

FWHM full width at half maximum

GM Gifford-McMahon

HAMR Heat-Assisted Magnetic Recording

HEMT High-Electron-Mobility Transistor

HF High Frequency

HF Hydrogen Fluoride, or Hydrofluoric Acid

h-BN Hexagonal Boron Nitride

HSQ Hydrogen Silsesquioxane

JNT Johnson noise thermometry

JK Joule Heating

JPA Josephson parametric amplifier

LC Inductor-capacitor

LL Landau Level

LNA Low noise amplifier

LTCC Low-temperature co-fired ceramic

MATBG Magic-Angle Twisted Bilayer Graphene

MC Matching circuit

MLG Monolayer Graphene

MOSFET metal-oxide-semiconductor field-effect transistor

MR Magneto-resistance

NIMS National Institute for Materials Science

NFL Non-Fermi Liquid

NV Nitrogen Vacancy

PC Poly(Bisphenol A carbonate)

PCM Phase Change Memory

PCB Printed circuit board

PDMS Polydimethylsiloxane

PID Proportional-Integral-Derivative

PMMA Poly(methyl methacrylate)

PTFE Polytetrafluoroethylene

RF Radio frequency

RIE Reactive Ion Etching

rms root-mean-square

SET Single Electron Transistor

SMD Surface-mounted device

SRS Stanford Research Systems

TLM Transfer-Length Method

TDBG Twisted Double Bilayer Graphene

TWPA Traveling Wave Parametric Amplifier

ULDFG Ultra-Low Distortion Function Generator

vdW van der Waals

VTI Variable temperature insert

WF Wiedemann-Franz

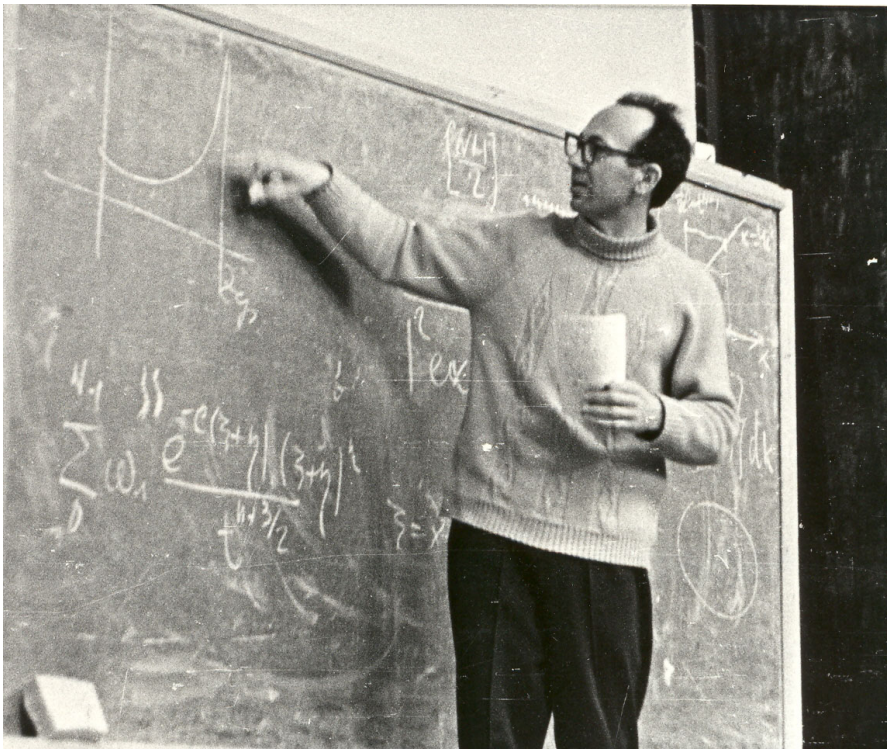

Dedicated to my late grandfather Vladimir Il'ich Talanov

Acknowledgments

My journey on this PhD and in writing this dissertation has been a long one, and it would have been impossible without help along the way from so many different people. Science is a collaborative field, and alone, no single scientist could realize discoveries without learning from and building upon the work of others. At the start of my PhD, I came to the field of graphene, mesoscopic physics, and nanoscale electronics without any direct experience in the field and had a lot to learn, including both research techniques and the intricacies of the field. The Kim group has always been large, around 20-25 people, and along with that comes deep institutional knowledge passed down from generation to generation of graduate students and post-docs. I have learned so much from everyone in our group, including new physics, laboratory techniques, data analysis and plotting, and critical analysis in analyzing my own science. While it's impossible to detail everyone's contributions here, I specially thank all group members, both the more senior, same-year, and more junior members, for all the helpful discussions we have had.

I started my noise measurement projects under the direct mentorship of Jesse Crossno, who taught me everything he knew about graphene devices, noise measurements, and radio frequency techniques. This included wiring up cryostats with RF cables, loading ESD-sensitive graphene devices, noise measurements with LNAs and calibration, impedance matching, and graphene hydrodynamic physics. Jesse was always very excited and passionate about our project, showing enthusiasm for anything cool that he or I would discover, and he passed that enthusiasm down to me. He also got me started with using MATLAB to run our experiments and data analysis, showing me how to communicate with GPIB instruments and how to plot lots of data. Due to the more complicated nature of our noise measurement algorithms, our noise group had to write our own measurement software in MATLAB, instead of using the more commonly accepted Special Measure software, to perform the measurement scans.

I also have to thank Kin Chung Fong and Keith Schwab, who first invented this self-heating noise measurement technique as a way to study electronic thermal conductance in mesoscale graphene back in 2012.

We had a few undergraduates and visiting interns contribute to our graphene noise

project. Kemen Linsuain worked very closely with me for the first few years, helping me set up various cryostat parts, devices for experiments, and running some of the experiments. During my first March Meeting conference when I was collecting data last minute, he was helping me set up and run some experiments in the lab when I was already at the meeting venue. Hugo Bartolomei made some graphene stacks and wired up with a matching circuit one of the first graphene devices that I measured for shot noise. Marine Arino developed a baseline nanofabrication process for dual-graphite-gated graphene devices that I used as a starting point and continued to improve upon.

Many people in the Kim group helped me learn how to do nanofabrication for graphene devices. Frank Zhao helped me learn how to use AutoCAD for designing devices, as well as using the Raith-150 e-beam system for lithography. Andy Joe, as well as a few others, taught me how to use the Elionix F-125 e-beam system. Austin Cheng also helped me figure out many of the details for designing graphene devices and using the Raith-150 for lithography. It is impossible to mention every contribution, but every Kim group member has in some way helped me learn something new about nanofabrication.

The single person that I worked most closely with overall during my PhD was the post-doc working on a closely related noise project, Jonah Waissman. We discussed many experimental details together, from temperature-feedback algorithms for time-efficient data collection and how to thermally isolate cryostat components, to understanding weird experimental results and how thick to spin PMMA for nanofabrication. With our combined effort across many experimental and theoretical fronts, we were able to produce the experimental results of Chapter 6, the simultaneous electrical and thermal magnetoresistance measurements in a graphene Corbino device in search for hydrodynamic signatures. We first saw the negative thermal magnetoresistance in our experiments in December 2018, more than 4 years before we were able to figure out the mechanism behind it thanks to our theory collaborators. Initially we had thought it maybe was a signature of phonon cooling, and we spent years brainstorming back and forth as to how hydrodynamic graphene could cause such an effect with electron-hole scattering.

Jonah often had a very different way of looking at problems and interpreting solutions than I did, and as a result, we had many productive scientific debates and discussions to make sure we were solving the problem correctly and not missing anything. I remember one time, we were debating how to write the noise correlation bandwidth Eq. 4.50, which was unclear since we had three different sources of noise, each with a different frequency dependence; neither of us had the correct answer at the start, and only after much debate and encouragement from Jonah to think outside of the box, did I come up with Eq. 4.51, writing the correlation bandwidths separately and adding the uncertainties in quadrature, which convinced us both this was the correct answer. Thanks to Jonah I learned to be self-critical of my work and to think beyond my own reasoning, in order to anticipate questions or concerns that audience members or reviewers might ask

about weak or missing parts in our scientific logic. I also learned to be very welcoming of criticism from my colleagues of my own work, as ultimately it was a way to make sure we had the soundest scientific solutions and arguments and didn't miss or forget anything.

Together, Jonah and I developed and troubleshot many of the techniques and tricks for RF noise thermometry measurements that I present in Chapter 4 of this dissertation; without these techniques, like thermometry filtering and outer DC-block thermal isolation, a lot of the measurements in this dissertation would have been impossible to perform. I am deeply indebted to Jonah for his extensive wisdom, perspective, and technical contributions that made the science I present here a reality.

Continuing on this noise project in our group are Terry Phang and Zhongying Yan. It has been exciting working with both of them, and their enthusiasm and commitment helped me stay motivated and focused on my project during the final few years. Terry only overlapped with me during my final year, but he paid very close attention to everything I taught him. I used some of the very first few stacks that he made under my guidance to fabricate very important devices in this thesis (MLG2 and BLG4), for realizing my simultaneous dual-channel experiment to measure contact resistance effects. I want to thank them for all the exciting technical questions and discussions we've had, and for the opportunity to collaborate together; it has helped me grow as both a scientist and mentor. I also wish to thank them for continuing on this noise-based research project; it's exciting and meaningful to be a part of this big multi-generation research, and I look forward to seeing in the future where it goes. A large part of this thesis, especially Chapter 4, I wrote with the intention of Terry and Zhongying using it as a reference for their continuation of our noise project. As such, I finally wish to thank them for reading it through, offering suggestions, and finding mistakes so I could fix them!

Rebecca Engelke and Laurel Anderson were both graduate students that started during my year, and we went through a lot of classes and the same learning experiences together. We had many fun and deep discussions, some about outrageous problem sets, some about scientific things such as hypothetical wormholes or Möbius strips made of graphene, and others about unrelated stuff including life, sports, hobbies, and hiking. It was a wonderful pleasure to be able to go through so many years of graduate school together with Rebecca and Laurel, and it definitely gave me a very unique experience thanks to the diverse thoughts and ideas that they contributed.

I also want to express deep gratitude to my advisor Philip Kim for giving me the opportunity to research a problem that was exciting on so many different levels, both technically and scientifically. He was such a kind advisor and supported me throughout all the various scientific and personal life difficulties I encountered during graduate school, while at the same time encouraging me to be the best scientist I could be. His broad knowledge of graphene physics as well as various technical lab suggestions, and his ability to secure excellent funding, really allowed this project to move forward

during some difficult setbacks. At some point before the final measurements presented in Chapter 6 were completed, the price of liquid helium skyrocketed, making many experiments on non-closed-system cryostats difficult to perform. The Janis cryostat we used for many of these measurements is a liquid-cryogen fuelled system, and re-building our low-loss noise measurement setup into a dry cryostat with magnetic field would have taken prohibitively long. It was also exciting being able to write and publish Philip's first paper in Review of Scientific Instruments, showcasing our lab's collective deep ingenuity at developing new scientific measurement techniques to unlock experiments that were previously impossible. Additionally, Philip read this thesis very thoroughly and offered many insightful and helpful editing suggestions. Philip also hosted a summer and winter group party every year, and it was fun being able to hang out with our labmates outside of a work environment and further build our friendships.

I have to thank Orso Mario Corbino, who invented the famous annular Corbino sample geometry in 1911, as a contrast to the Hall geometry. The magnetic field experiments in this thesis would not have been possible in a rectangular or Hall bar geometry due to the lack of rotational symmetry, and thus it was only possible to realize them in the Corbino geometry.

I also have many of our theorist friends to thank, most importantly Brian Skinner and Aaron Hui. Brian Skinner developed some of the early theoretical framework for verifying that our self-heating measurement works in a generic 2-terminal geometry not limited to the rectangle (such as a wedge), allowing us to pursue the measurements in a Corbino geometry. Aaron Hui, with contributions from Brian, led the development of the theory for the results of Chapter 6, showing how the negative thermal magnetoresistance is a clear signature of viscous heating in a Corbino device. Aaron and I went back and forth through many emails ironing out the details of how to understand the experiment in the context of the theory, and he performed the extensive numerical calculations of the $f(B)$ scale function, finally allowing us to extract an electron viscosity from our measurements. The relation between hydrodynamics and viscous transport in graphene is rather complicated, and as our experiments were focused primarily on hydrodynamic thermal transport and Lorenz ratio, and not on any viscous effects, we weren't experts on fluid mechanics parts; in particular, Aaron helped us better understand the fluid mechanics relevant to our experiments, including the scaling of viscosity and Gurzhi length with temperature. I also want to express thanks to my roommate Ophelia Sommer, who helped me figure out a few additional fluid mechanics concepts relevant to this work and even prepared me for a difficult question from the audience I received during my defense.

I must also thank ChatGPT 4 for valuable assistance in crafting this thesis. While it did not (and could not, as it's not the world's leading expert on this subject) write any of the text in this thesis, it did help me learn and troubleshoot various LaTeX syntax issues much faster than I could have with Google search. It also helped me very quickly learn a few tips, tricks, and functions for very nice formatting of figures in MATLAB, such as

arrows, text, axis overlaying, labeling, etc, and it helped me find some obscure scientific citations from the early and mid 20th century. Finally, ChatGPT 4 and DALL · E 3 have drawn the artwork used for the title pages of the chapters.

Of course, I couldn't have gotten to where I am now without the opportunities given to me by my parents. We moved from Russia to the USA in 1997 for my dad to do a physics post-doc at the University of Maryland. Rather than returning to Russia after the post-doc, we stayed in the USA due the much better science and general career opportunities available here. My parents always had the best academic opportunities for me in their vision, and as we moved around a few times they always made sure to prioritize a location with a top tier public school system. They also supported me going to Cornell for my undergraduate studies, which presented a lot of exciting learning and research opportunities, allowing me to showcase my abilities set the stage for success later on in my PhD. Even during my PhD, my dad and I had extensive technical conversations on the phone; he was always interested in how my research was progressing and often contributed his experience in RF to help us develop tricks for our measurement, such as the balanced differential noise measurement setup.

I have dedicated this thesis to my late grandfather, Vladimir Il'ich Talanov, a distinguished physicist, professor, and academic in the Soviet Union and later Russia. I am proud to continue his legacy of physics in our family for the third generation in a row. He was a large motivation for my father to pursue physics, and thus indirectly for me as well, and I thankful for that.

The important thing in science is not so much to obtain new facts as to discover new ways of thinking about them.

William Lawrence Bragg

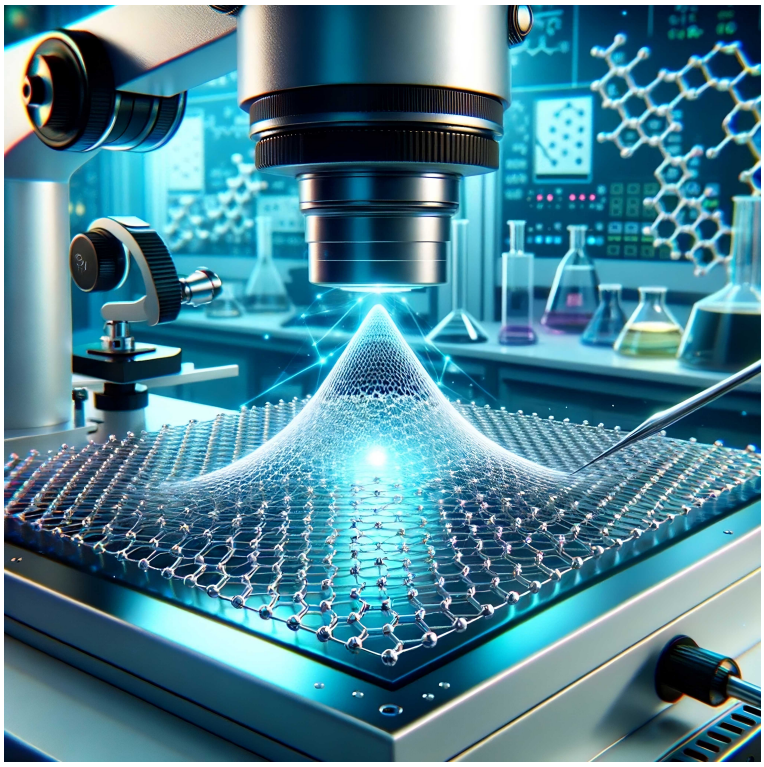

1 Introduction

Starting with the discovery of graphene in 2004[4], 2-dimensional (2D) van der Waals (vdW) materials have opened many remarkable new research directions in solid state physics, chemistry, and nanoelectronics[5–12]. Graphene is an isolated single

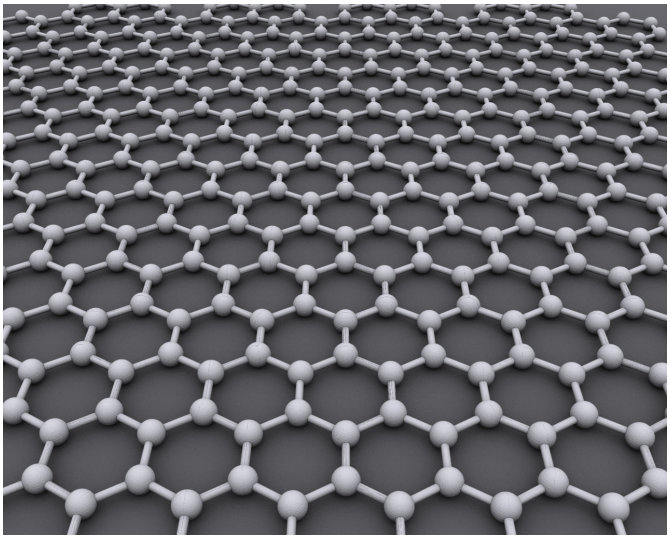

Figure 1.1: Schematic representation of the honeycomb lattice of monolayer graphene. Image from 13.

atomic layer of graphite, consisting of carbon atoms arranged in a honeycomb lattice, with each atom bonded to three other carbon atoms, as shown in Fig. 1.1. Owing to the strong nature of C-C bonds, it exhibits extremely high tensile strength, similar to carbon nanotubes and carbon fiber, while still being extremely flexible and highly conductive.

The quantum mechanical confinement of electrons to a pristine atomically thin layer mediates the dynamics in a truly 2D space. Electronically, graphene exhibits unique properties compared to conventional metals or semiconductors due to the geometry of the honeycomb lattice, which is crystallogaphically a 2-atom basis placed on a hexagonal Bravais lattice. Differing significantly from that of bulk graphite, the band structure of graphene has two linearly dispersing Dirac cones touching at a single Dirac point (Fig 1.2), with electrons and holes behaving as effectively massless relativistic particles all moving at the same effective speed of light equal to $\sim c/300$, analogously to how

photons move through vacuum at the real speed of light c. With this band structure, we can describe graphene as a zero-bandgap massless semiconductor, in contrast to conventional semiconductors which have an energy bandgap and a nonzero effective mass (Fig 1.2).

Unlike a bulk 3D material such as silicon that must be chemically doped, the density of electrons or holes in graphene, defined by the Fermi level, can be continuously tuned *in-situ* by a field effect gate, acting as a capacitor together with the graphene. Starting from a Fermi dot at charge neutrality, gated (or doped) graphene has a small Fermi surface, disallowing the electron-electron Umklapp scattering present in conventional metals and Fermi liquids that causes T^2 resistivity due to non-conservation of crystal momentum when scattering out of the first Brillouin zone. Additionally, electrons in graphene exhibit a sublattice-based pseudospin spinor that locks with the momentum direction, further suppressing backscattering by quantum mechanical destructive interference of time-reversed backscattering paths. Due to the hexagonal Bravais lattice, graphene has a hexagonal Brillouin zone with a distinct K and K' point, where at each point there is a copy of the electron and hole Dirac cone shown in Fig. 1.2.

Graphene by itself has a physical consistency, on an atomic scale, similar to cling wrap; it will readily fold, wrinkle, and stick to itself, destroying its exotic electronic properties that depend on the lattice symmetries. To solve this problem, since about 2010, hexagonal boron nitride (h-BN), a multi-layered 2D material related to graphene, has been used as both a substrate and dielectric layer for graphene to both provide an atomically flat encapsulating sandwich and to shield it from external charged impurities[14–17]. This encapsulation technology further progressed around 2016, using graphite top and bottom gates[18–21] in addition to the h-BN to provide a spatially uniform work function, strongly suppressing any disorder potential fluctuations and scattering impu-

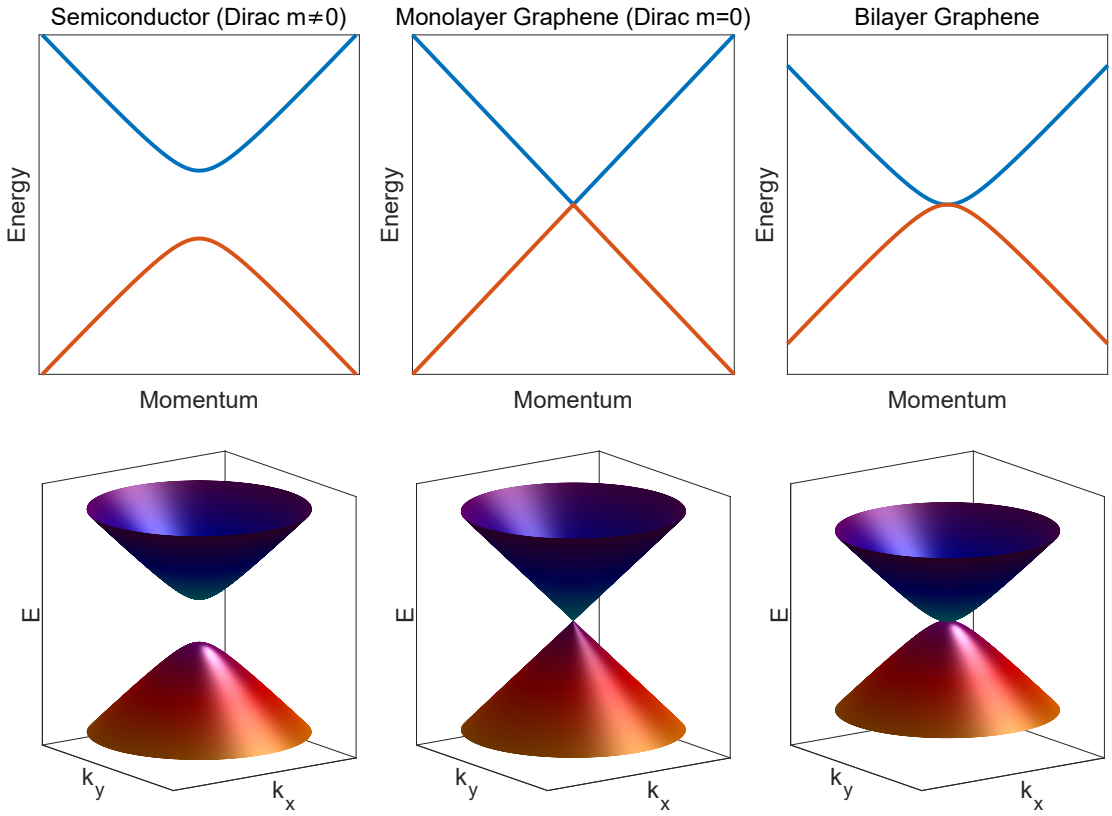

Figure 1.2: **Left:** Band structure of a conventional semiconductor with nonzero effective mass. The mass term is responsible for creating a gap and the curvature in the solution of the Dirac equation. Top panel shows a 1D linecut of the dispersion, and bottom panel shows the 2D dispersion. The top band (blue-themed) corresponds to electrons, or matter; the bottom band (red-themed) corresponds to holes (anti-matter). **Middle:** Band structure for monolayer graphene, which is the solution to the Dirac equation with $m = 0$. **Right:** Band structure for bilayer graphene, which does not follow the Dirac equation.

rities that affect the graphene and screening any external charged impurities.

Heterostructures made from bulk materials via techniques like epitaxial chemical vapor deposition, etching, or physical vapor deposition can have danging bonds, surface charges, and disorder at the interfaces, leading to undesired effects like Fermi level pinning and Schottky barriers. In contrast, low-dimensional heterostructures made from vdW materials have atomically pristine and flat interfaces with no dangling bonds, leading to the potential of significantly improved electronic devices. However, interfacial issues such as contact resistance still exist when making electrical connections to vdW materials[15,22].

The electronic properties of graphene, combined with the right substrates and superstrates, have led to graphene becoming a superior electronic conductor, with mobilities approaching $1 \times 10^6\,\mathrm{cm}^2/\mathrm{Vs}$ for low-disorder samples[23–27].

Bilayer graphene (BLG) is another variant of monolayer graphene (MLG) with a different bandstructure. Both monolayer graphene and conventional semiconductors have low-energy bandstructures that are qualitative solutions of the Dirac equation, where the presence (absence) of a mass term creates both the bandgap (absence of bandgap) and the curvature of the band leading to an effective mass (linear band and zero effective mass). However, BLG is unique in this regard as it has both a nonzero effective mass and a zero-gap bandstructure, having two parabolic bands that touch at a single point. Fig 1.2 illustrates this comparison. Furthermore, a bandgap can be induced in BLG by breaking the layer symmetry with an applied electric displacement field, distorting the bands away from each other and creating a tunable semiconductor[28,29].

1.1 Applications of Graphene

Due to its unique properties as a 2D tunable semiconductor, graphene has been considered in many applications for both fundamental science and nanoelectronics.

The immediate application that scientists first considered was as a replacement for silicon in CMOS logic. Unfortunately, MLG is not well-suited for this task because its electron density cannot be depleted due to the absence of a bandgap; similarly, BLG will also fail because its maximum induced bandgap of $\sim 250\,\mathrm{meV}$[28,30] is still too low of an energy scale for room temperature. Logic transistors made from these materials exhibit high leakage current and poor on/off ratios[31,32]. Nonetheless, the flexible and transparent nature of graphene makes it very conducive for integration into common flexible electronics for non-logic-based roles such as conductive inks, transparent films, touch screens, supercapacitors, and heat management.

Graphene also has applications in more exotic electronics. It can be useful in extremely high speed electronics such as radio frequency (RF) transistors[32–34] and electro-optical modulators[35–37] due to its ultrafast electron-electron interactions and thermalization[38]. Additionally, quantum dot spin qubits made from BLG for quantum computing is a growing research field that has potential to challenge more well-established technologies based on Si/SiGe quantum dots[39–44]. Due to its near transparency at a single atomic layer thickness, it is also useful in various types of optical devices, where an optically active element can be buried below the conductive graphene.

From a fundamental science perspective, MLG, BLG, and related materials offer a rich playground for condensed matter physics to study exotic phenomena such as the fractional quantum Hall effect and Moiré-based superconductivity. Beyond condensed matter physics, the strongly interacting Dirac plasma in MLG provides a physical system

that can be mapped to a 3-dimensional gravitational theory in AdS space based on the holographic principle of AdS/CFT correspondence, potentially helping to understand the large open problem of quantum gravity and general relativity[45,46]. More specifically, certain properties of graphene including electrical and thermal conductivity can be directly related to the properties of black holes in AdS space, and studying them in the lab can lead to inferences about cosmic-scale quantum gravity phenomena[47–51].

1.2 Solid State Physics and the Problem of Many Interacting Particles

Recent experimental efforts in solid state physics have shifted towards understanding the dynamics of systems with strongly correlated and interacting particles. The behaviors of such systems are often characterized by emergent phenomena that arise collectively as a result of the interaction dynamics but would not be present for a single unit of the system. Common examples of such phenomena include conventional and high-temperature superconductivity, Mott insulators, strange metals, fractional quantum Hall effect, viscous transport, and electron hydrodynamics. Graphene-based structures have been able to exhibit all of these phenomena, but the exact mechanisms are often still poorly understood.

In classical physics, a system as simple as three interacting bodies already does not have a closed form general-case solution. Solving for the quantum mechanical behavior of a large number of interacting particles becomes impossible, and theorists have devised many approximations for solutions, such as the Hartree-Fock method or mean-field theory.

The Fermi liquid is an important concept to be understood as background for the

work presented in this dissertation. For systems with weakly interacting electrons (or any fermions), such as most conventional metals, the electron-electron interactions can be "swept under the rug" by a careful consideration of adiabatic continuity first proposed by Landau[52]. In essence, if we begin with a system of non-interacting electrons, and we adiabatically turn on the interaction strength, the electron states of the non-interacting system will adiabatically evolve into quasiparticle states of the interacting electron system. The quasiparticles maintain the basic properties of electrons like charge and spin, but other properties like the effective mass become renormalized. The quasiparticle states still maintain some residual interactions that limit their lifetime, but for practical purposes the low-temperature excitations near the Fermi surface are long-lived and effectively non-interacting. The Fermi liquid picture will break down if the the adiabatic transformation undergoes or is nearby a quantum phase transition, such as charge neutrality for graphene, or if the interactions are so strong as to disallow long lived quasiparticles.

Another perspective on the relevance of interactions in quantum solid state systems is comparison of the typical potential energy scale of Coulomb interactions to the typical kinetic energy of particles. In particular, we consider the ratio[53]

$$\alpha = \frac{\text{typical potential energy}}{\text{typical kinetic energy}} = \frac{\frac{e^2}{4\pi\epsilon r}}{\frac{\hbar v_F}{r}} = \frac{e^2}{4\pi\epsilon\hbar v_F} = \frac{1}{137} \times \frac{c}{v_F} \times \frac{\epsilon_0}{\epsilon}. \tag{1.1}$$

In graphene, this ratio is close to 1, indicating that interactions may not simply be a small perturbation to the kinetic energy states of non-interacting electrons.

1.3 Emergent Hydrodynamics from Strongly Interacting Electrons

All the emergent phenomena listed in the previous section, except viscous transport and hydrodynamics, are outside the scope of this thesis. With high temperatures to wash out quantum coherence and to increase particle-particle interactions, most strongly interacting particle systems will trend towards the hydrodynamic limit. As temperature increases, electron-electron or electron-hole interaction rates in graphene grow as T^2 (doped graphene) or T (charge neutral graphene) due to the available phase space for scattering (i.e. a reduction of Pauli blocking by a completely filled band). Hydrodynamics occurs when the electron-electron (e-e) scattering rate dominates all other scattering rates in the system and thus dominates the particle kinetics.

A quantum and truly microscopic treatment of the particle dynamics involves a calculation of the multi-particle Hamiltonian $\hat{\mathcal{H}}$ and the corresponding eigenstates for every particle, or approximations thereof. Often, these fine details are unimportant, and transport properties can be computed semi-classically by averaging out over individual particles using the occupation/distribution function $f(\vec{k})$ via the kinetic Boltzmann equation approach; however, the notion of collisions is still retained, and every point in space has a particular distribution of occupied momentum states[54–56]. In this way, the Boltzmann equation can interpolate between ballistic transport, where particles are scattered only by the walls of their container, and viscous or hydrodynamic transport.

In the hydrodynamic framework, the behavior of the particles is described collectively as that of a classical fluid, even if the interactions between particles are quantum in nature. This description is only valid on length and time scales much larger than the electron-electron collision mean free path or time, effectively averaging out and further coarse-graining the quantum distributions into classical macroscopic variables including

energy, temperature, and velocity. The collisions from the kinetic Boltzmann approach are now absorbed into classical macroscopic fluid properties such as viscosity, diffusivity, and flow dampening. The Knudsen number Kn, the ratio of mean free path l_{mfp} to fluid container dimensions L, must be small ($l_{mfp}/L \ll 1$) to use this description, to avoid the ballistic or molecular flow regimes.

The viscous properties of electron liquids can be described by the Navier-Stokes equations with extra terms added to account for the Lorentz force on charged particles. For completeness, here we show the relevant Navier-Stokes-Ohm equation[57–59], which in the simplest description is Ohm's law with an added viscosity term:

$$\partial_t \vec{\mathbf{v}} + \nu \vec{\nabla}^2 \vec{\mathbf{v}} = -\gamma \vec{\mathbf{v}} + \frac{e}{m}\left(\vec{\mathbf{E}} + \vec{\mathbf{v}} \times \vec{\mathbf{B}}\right), \tag{1.2}$$

where $\vec{\mathbf{v}}$ is the fluid flow velocity, ν is the kinematic viscosity, and $\gamma = \dfrac{ne^2}{m\sigma_0}$ is the Ohmic momentum relaxation rate. We have neglected the convective acceleration term $\vec{\mathbf{v}}\cdot\vec{\nabla}\vec{\mathbf{v}}$ due to the low Reynolds number in typical near-equilibrium experiments involving degenerate electron liquids. In pure hydrodynamic systems without impurity or phonon scattering, such as water, the Ohmic relaxation rate is zero. The viscosity term in Eq. 1.2 represents diffusion of momentum. Similar to how we are used to thinking of the diffusion of heat as a scalar equation, in a hydrodynamic system, the vector field of momentum follows the same diffusion dynamics. Two adjacent fluid elements, moving at different velocities, will viscously exchange momentum with each other due to the random diffusive movement of particles between the fluid elements. Collisions with impurities, phonons, or other particles will reduce the viscosity. Through momentum diffusion, the walls or boundaries of the fluid's container can exert non-local momentum relaxation on the fluid through the combination of no-slip boundary conditions and

viscosity.

It should be noted that the standard semiclassical or quantum Boltzmann equation, used very often to describe the kinetics of electrons in materials via their distribution function, can be used to derive the Navier-Stokes-Ohm equation (Eq. 1.2) by properly including an electron-electron scattering term in the collision kernel[53,57].

1.3.1 Viscous Transport vs Hydrodynamics

While it may be tempting to visualize viscous transport and hydrodynamics as the same regime, they are distinct phenomena and, perhaps counterintuitively, may even occur in opposite limits. Recent literature on the subject has often conflated the hydrodynamic regime and the viscous regime[60–62], citing electronic hydrodynamic fluids as having very high viscosity. While true, each regime can exist without the other. In quantum degenerate electronic fluids, the electron-electron scattering rate scales as $\propto T^2$, and the viscosity correspondingly scales as $\nu \propto T^{-2}$. Hydrodynamics, defined as the regime where the electron-electron scattering rate is dominant over all others, thus occurs at higher temperature; in contrast, electronic fluids have higher viscosity at lower temperature, so the viscous regime should occur at lower temperature. How do we understand this seemingly paradoxical situation?

First, we must understand that fluids without electron-electron scattering have high or diverging viscosity. The viscosity of a 2D electronic fluid can be approximately written as[63]

$$\nu = \frac{v_F^2/4}{\gamma_{ee} + \gamma_{mr}}, \tag{1.3}$$

where v_F is the Fermi velocity and γ_{ee}, γ_{mr} are the electron-electron scattering and

momentum relaxation rates. In a non- or weakly interacting high-mobility electron fluid, an electron will carry its momentum a large distance before scattering, allowing a very high diffusivity of momentum. In contrast, scattering by impurities, phonons, or other electrons will reduce its mean free path, thus limiting how far it can carry its momentum before it is randomized in a collision. Although total momentum is conserved in an electron-electron collision, this process does not facilitate diffusion of momentum but rather hinders it, with ν becoming small as γ_{ee} becomes large. In the limit of low temperature where viscosity grows, viscous flow from the Navier-Stokes-Ohm equation is not realized because the assumption of low Knudsen number breaks down, i.e. $l_{mfp} = v_F / (\gamma_{ee} + \gamma_{mr}) \gtrsim L$.

Viscous electronic flow in solid state materials was first proposed in 1962 by the Soviet theorist R. N. Gurzhi[64], with a predicted experimental signature of resistance decreasing with T (as compared to conventional metals, where it increaes with T), caused by viscosity decreasing with T and thus allowing easier viscous flow of the fluid. Here, the system was assumed to be in the limit of zero impurities and thus hydrodynamic, such that the electrons would exhibit collective flow.

Real electron systems always have some momentum relaxation from impurities and phonons and thus cannot be purely hydrodynamic. To understand these mixed systems, a new length scale known as the Gurzhi length can be introduced[53,65–67]:

$$l_G = \sqrt{\frac{\nu}{\gamma_{mr}}}, \tag{1.4}$$

where ν is the kinematic viscosity and γ_{mr} is the momentum relaxation rate. The Gurzhi length can be roughly envisioned as the distance over which the boundaries of the sample can viscously relax electron momentum; at distances larger than l_G away

from the sample boundary, momentum relaxation by impurities or phonons is stronger than that from the viscous forces originating from the no-slip boundaries, and locally the electron flow follows a more Ohmic-like behavior, since the viscous forces in the Navier-Stokes-Ohm equation vanish. Thus, we see that whether a real sample exhibits viscous flow is determined by the ratio between the size L and l_G. If the size is smaller than l_G, viscous forces dominate the entirety of the sample and lead to viscous flow; if the size is larger than l_G, then impurity or phonon scattering dominates, and the flow pattern is Ohmic.

The requirement of $l_G \gtrsim L$ for viscous flow requires sufficiently low γ_{mr}, such that in the limit of low temperature where electron-electron scattering is absent, the momentum relaxation length $l_{mr} = \dfrac{v_F}{\gamma_{mr}}$ must be larger or comparable to the the sample size. We can thus see that ballisticity at lower temperature is a requirement for the sample to produce viscous flow at higher temperature. A sample that is diffusive at low temperature cannot enter the viscous regime at any higher temperature, because the high momentum relaxation rate forces an upper bound on the Gurzhi length to be always significantly smaller than the sample size. There is a crossover regime, where samples can be quasi-ballistic at low temperature but still exhibit viscous effects at high temperature[61].

A phase diagram showing Ohmic, ballistic, and viscous transport regimes, along with the dividing line between hydrodynamics and non-hydrodynamics, is shown in Fig. 1.3. The phase diagram is a 3-dimensional space, depending on the momentum relaxation rate, electron-electron scattering rate, and sample length. We define the mean free path relative to all collisions, i.e. $l_{mfp} = \dfrac{v_F}{\gamma_{mr} + \gamma_{ee}}$. How the sample length compares to l_{mfp} and l_G determines what regime it is in, so we plot the surfaces for l_{mfp} (blue/green) and l_G (magenta/yellow) as a function of γ_{ee}, γ_{mr}. To help visualization, we show a gray plane for a fixed sample length and divide the regions into ballistic,

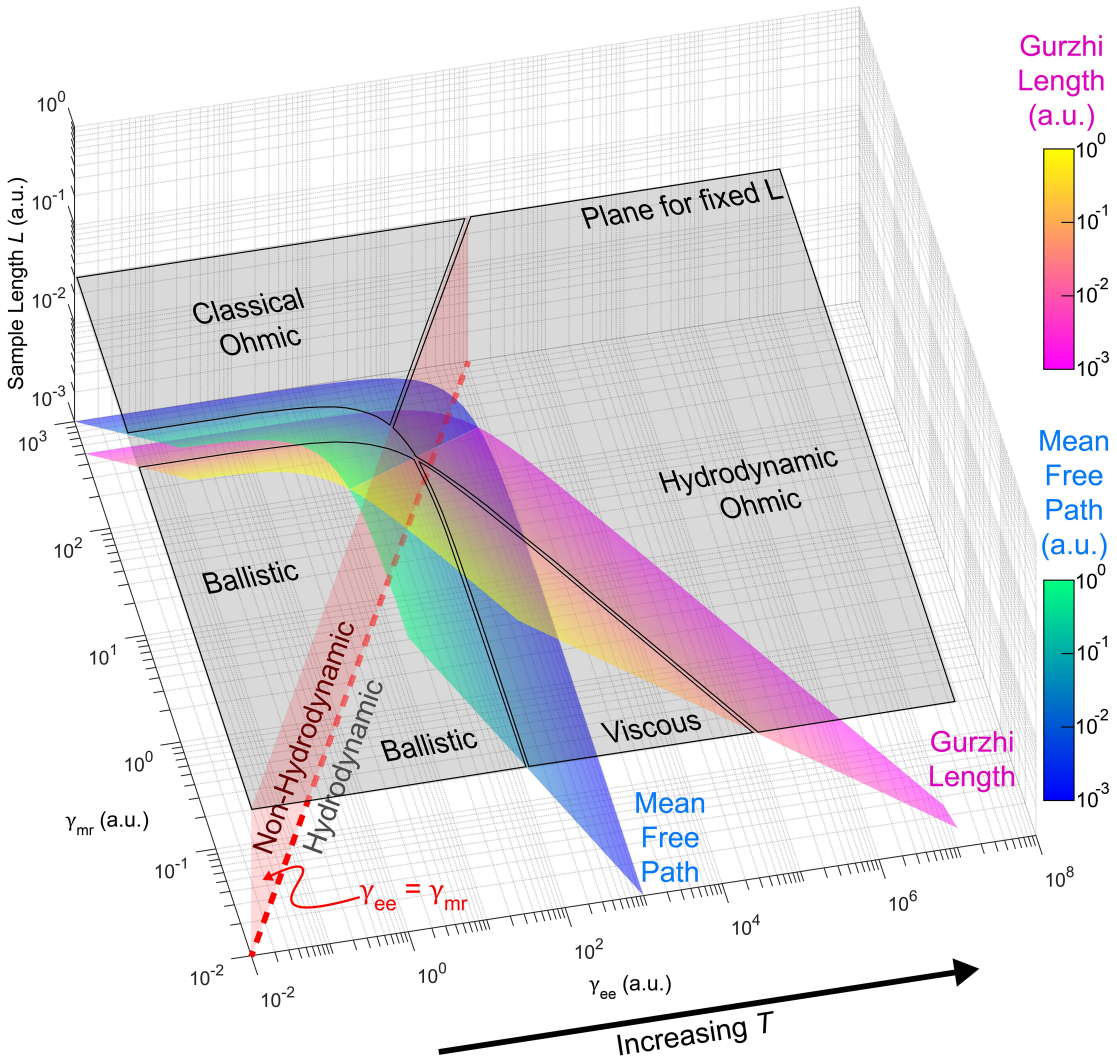

Figure 1.3: 3D phase diagram showing ballistic, viscous, and Ohmic transport regimes. The red plane divides hydrodynamics from non-hydrodynamics. The horizontal axes are the momentum relaxation rate γ_{mr} and the electron-electron scattering rate γ_{ee}. The vertical axis is the sample length. The mean free path is defined relative to all collisions, not just momentum-relaxing collisions. The sample length is to be compared to the Gurzhi length (blue-green surface) and the mean free path (magenta-yellow surface). The local color of the surface shows the corresponding length dimension, as indicated by the colorbars. A gray horizontal plane for a fixed arbitrary sample length $L = .03$ reduces the dimensionality of the phase diagram. The gray plane is divided into four transport regimes at the intersections with the Gurzhi length and mean free path surfaces. Each region is outlined with a thin black line and labeled with black text (ballistic, viscous, hydrodynamic Ohmic, and classical Ohmic). If the sample length were to change, the gray plane would shift vertically, and the borders of the regimes would move around accordingly as the intersections change but would keep their general qualitative shapes.

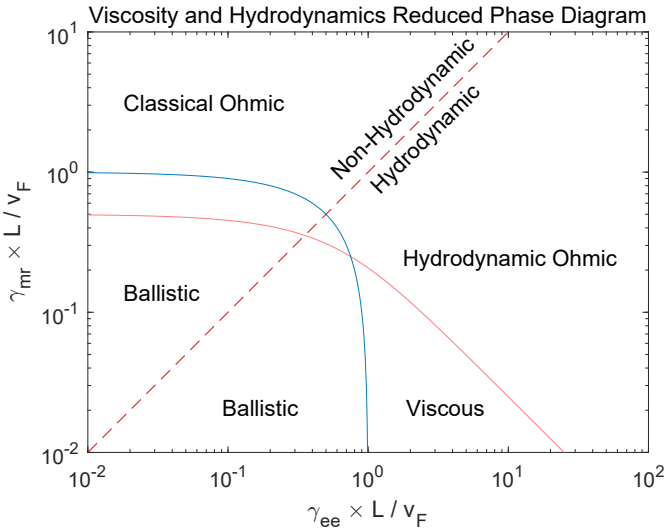

Figure 1.4: Reduced dimensionality phase diagram of ballistic, viscous, and Ohmic transport regimes. The sample length parameter is absorbed into the other axes. Red dashed line divides the hydrodynamic regime ($\gamma_{ee} > \gamma_{mr}$) from the non-hydrodynamic regime ($\gamma_{ee} < \gamma_{mr}$). The blue and pink curves correspond to the mean free path and Gurzhi length surfaces from Fig. 1.3 and delineate the phase boundaries.

viscous, hydrodynamic Ohmic, and classical Ohmic. In reality, the transitions across the boundaries are smooth and gradual. A vertical plane, shown in red, divides the hydrodynamic regime from the non-hydrodynamic regime.

Additionally, Fig. 1.4 shows a corresponding reduced dimensionality version phase diagram of Fig. 1.3, aligning with the gray plane for fixed sample length. Here, the momentum relaxation and e-e scattering rates are normalized to be unitless via L/v_F. The phases are still the same, but now the sample length parameter is absorbed into the other axes.

If γ_{mr} is fixed, such as the case with negligible phonon interactions, changing temperature amounts to moving along the γ_{ee} axis. We thus see that high temperature would always put the sample in the hydrodynamic-Ohmic regime, but to cross through the viscous regime while warming up, the sample must start out as ballistic at low tem-

perature. In the ballistic regime, analogously to how conductivity is not well defined, the viscosity is also not well defined due to absence of any scattering that would define γ_{ee} and γ_{mr}. Once the viscosity is well defined in the viscous regime, it decreases with temperature.

1.3.2 Requirements for Hydrodynamics

Why does not every electronic system exhibit hydrodynamics at high enough temperature? The first reason is due to the hydrodynamic temperature window created by different T-scaling power laws of various scattering processes. Typically, the electron-impurity scattering rate will be roughly independent of temperature, with slight dependencies due to electronic screening. The electron-electron scattering rate typically scales as $\sim T^2$, and the electron-phonon rate typically has a high power law, $\sim T^4$ or $\sim T^5$. Hydrodynamics will occur in the window, if it exists, where electron-electron scattering is the dominant rate. The phonon scattering rate and electron-electron scattering rate are mostly determined by intrinsic material properties and can't be engineered, but the impurity scattering rate has no theoretical lower bound, as materials could always theoretically have less disorder. Thus, engineering materials with low disorder and low impurity scattering rates is crucial to observing hydrodynamic effects. If the impurity scattering is too strong, the hydrodynamic window will close. In our previous discussion of Fig. 1.3, we ignored phonons in order to assume that γ_{mr} was temperature-independent; in reality, γ_{mr} will generally grow strongly with temperature due to increased phonon scattering.

In monolayer graphene, because of the small Fermi surface and the Bloch-Grüneisen effect[60,68], acoustic phonon scattering scales as $\propto T$, thus not generating a high-T cutoff for hydrodynamics; however, optical phonons still scale very quickly with T and

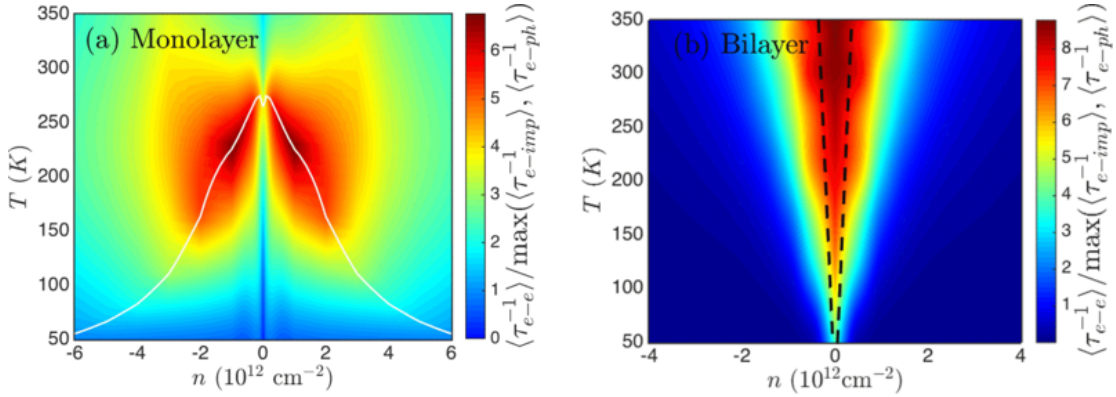

Figure 1.5: Theoretically calculated ratio of e-e scattering rate to either the e-impurity or e-phonon scattering for **(a)** MLG and **(b)** BLG. The higher the ratio is, the more hydrodynamic the system is. Figure from Ref. 69.

eventually overwhelm the electron-electron scattering rate, setting the upper bound to the hydrodynamic window.

The expected hydrodynamic window, for a range of densities, has been calculated for MLG and BLG[69] and is shown in Fig. 1.5. Monolayer graphene is most hydrodynamic near 200-250 K, with a lung-shaped hydrodynamic region. The charge neutrality point is less hydrodynamic than at small doping. The high-temperature cutoff is due to the transverse optical A_1' phonon mode[70]. In contrast, BLG has a V-shaped hydrodynamic region, with no such phonon cutoff below 350 K.

The second protagonist to hydrodynamics is Umklapp scattering, where an electron scatters to a different Brillouin zone via a collision with another electron. Outside of a crystal in a fluid such as water, momentum is always conserved; however, collisional kinematics in crystalline materials use crystal momentum rather than true momentum, as a consequence of Bloch waves and the Bloch theorem[54]. If an electron scatters across a Brillouin zone boundary, because the crystal momentum is only defined modulo a reciprocal lattice vector, the effective total momentum is not conserved, leading to

momentum and current relaxation. Umklapp scattering is the primary mechanism of resistance for Fermi liquids at low temperature, with a hallmark resistance scaling of $R \sim T^2$. In graphene, because the Fermi surface surface is so small, Umklapp scattering vanishes, allowing conservation of momentum and thus hydrodynamic flow.

1.3.3 Hydrodynamics in a Hall Bar Topology

There have so far been several electrical experiments observing hydrodynamic behaviors in MLG and BLG, enabled by the availability of low-disorder samples with h-BN encapsulation. This subsection, and the following one, present a non-exhaustive summary of the relevant experiments, setting the context for the results of this thesis work. This subsection describes experiments conducted using a Hall-bar type topology, as shown in Fig. 1.6(a), where electrodes are placed outside of the sample, and at least one sample edge connects the electrodes. In the next subsection, we will discuss experiments performed in devices in a different topology, without edges connecting the electrodes.

One of the first MLG hydrodynamic experiments measured negative vicinity resistance caused by viscous electron backflow[61]. Here, whirlpools of electron flow induced by viscosity reverse the electric field direction compared to the Ohmic case, showing up as a sign change from positive to negative for the vicinity resistance. However, ballistic effects in certain sample geometries can mimic this effect of a negative non-local resistance, creating a difficulty in distinguishing between the two regimes in graphene[57]. Further experiments and theory have clarified[60] that a subtlety in the temperature dependence of the negative vicinity resistance signals the onset of the viscous hydrodynamic regime from a quasi-ballistic regime, demonstrated in BLG[71]; specifically, the hydrodynamic regime is characterized by a decrease of viscosity with temperature and a corresponding decrease of the magnitude of the negative vicinity resistance.

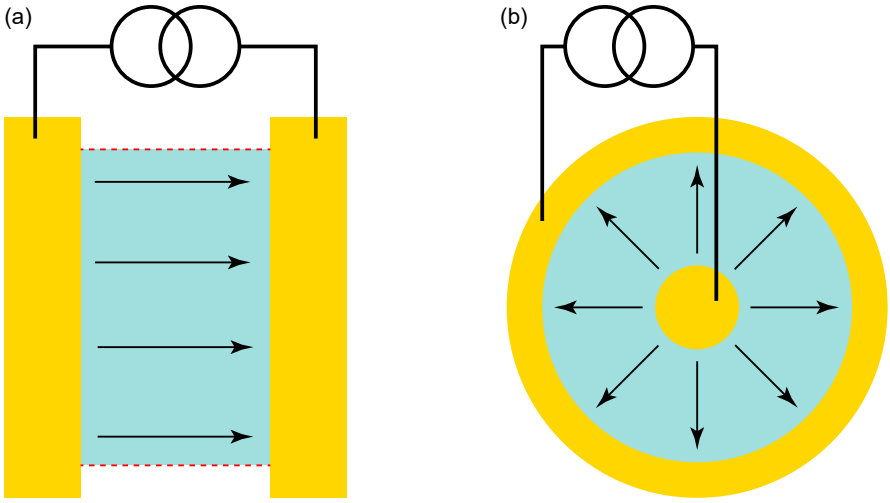

Figure 1.6: **(a)** Rectangle or Hall-bar topology for a mesoscopic sample. The sample is cyan, and the metal electrodes are gold. A current source is connected across the electrodes, and arrows indicate current flow direction. Sample edges, indicated by red dashed lines, connect the electrodes. **(b)** A Corbino topology, with concentric circular and annular electrodes. Arrows indicate radial current flow. No sample edges connect the electrodes.

A later experiment from the same group measured a Poiseuille flow effect through narrow constrictions in graphene. In Poiseuille flow, the velocity profile (or current density) across the channel is parabolic, being slowed down by the walls and thus flowing faster in the center. In this experiment, the presence of electron-electron interactions in the hydrodynamic regime increased the electrical conductance through the constriction above the ballistic transport limit, with the electrons near the boundary guiding other electrons towards the center of the constriction, helping them to avoid getting backscattered by the constriction walls[62].

A third experiment measured the Hall viscosity of graphene[72]. Similar to how the electrical conductivity tensor $\hat{\sigma}$ develops an off-diagonal non-dissipative component in a magnetic field termed the Hall conductivity, the viscosity $\hat{\eta}$ similarly becomes a tensor and develops an off-diagonal non-dissipative component, demonstrating a particular

geometry-based voltage signature.

Two separate experiments measured the crossover from ballistic flow to Poiseuille flow in a narrow graphene strip by using scanning probes (NV-center magnetometer, and a carbon nanotube SET) to map out the current density profile, showing evidence for viscous drag from the sample boundaries[73,74].

An experiment measuring four-probe electrical conductivity on single-gated suspended BLG, cleaned by current annealing, showed that the normalized conductivity curves as a function of density ($\sigma(n)/\sigma(0)$), at different temperatures, coincided near the charge neutrality point when plotted as a function of E_F/k_BT[75]. The authors explained this as stemming from a universal scaling behavior of transport limited by electron-hole collisions, using a simple formula to express Coulomb drag on both the electron and hole fluids. Later, a theorist[76] presented a simple correction to their formula, expressing the drag on each fluid as a mutual drag relative to the velocity of the other fluid. However, another theorist[77] suggested that a bandgap could be present in their BLG sample due to the single-sided gating.

A similar experiment[3] but now using dual-gated BLG studied electrical conductivity as a function of both density and induced gap, showing universal collapse as a function of a few different parameters indicating electron-hole collision dominated transport. However, we find a mistake in their work which affects the original interpretation, and we suggest a correction in Appendix E.

1.3.4 Hydrodynamics in a Corbino Topology

Very broadly, the application of classical hydrodynamics to systems with reduced dimensionality allows for novel effects not geometrically possible in 3D fluid systems. In particular, a fluid source can be embedded entirely within the fluid, with no edges of the

fluid chamber connecting the source to another sink. One realization of such a topology is the rotationally symmetric Corbino geometry[78], shown in Fig. 1.6(b), where an annular sample connects to an inner circular electrode and an outer annular electrode, all concentrically. In two dimensions, the fluid will flow radially between the electrodes.

In the fully hydrodynamic limit without any internal momentum relaxation, due to the absence of any sample boundaries, there will be no momentum relaxing force acting on the moving fluid. Consequently, in steady state flow no electric field is needed to drive the flow, and the electric field will thus be entirely expelled from the channel[58]. However, the system cannot have zero resistance, as there is viscous dissipation happening in the fluid elements as they are deformed in moving radially. Accordingly, a potential drop must exist somewhere to create global resistance and global "Joule" heating as I^2R. This potential drop occurs at the electrode-sample interfaces, and the total resistance of the sample results entirely from viscous dissipation. This viscous dissipation is a central element of the experiments described in Chapter 6.

Analogously to the superballistic transport through constrictions[62], the edgeless topology opens a new avenue for electronic conductance to exceed the ballistic limit. Non-hydrodynamic transport, including ballistic and Ohmic transport, will experience a Landauer-Sharvin contact resistance arising from equilibration in the contacts[79]. The edgeless Corbino geometry, which approximates one-half of the edgeless wormhole geometry, distributes the Landauer-Sharvin resistance from the larger contact into the bulk of the sample by squeezing out the number of available propagating modes and reflecting the terminated modes into their time-reversed conjugates[80]. In contrast to the ballistic regime, the hydrodynamic regime will eliminate this bulk Landauer-Sharvin resistance by facilitating the transfer of electrons from a terminated mode into a transmitted mode. Experimentally, this was confirmed in MLG using the same scanning

SET technique[81].

Additionally, the same Corbino experiment measured a viscous boundary-layer effect, where electrons injected radially into the channel from the inner contact acquire a Hall angle over the Gurzhi length scale, limited by viscosity[81].

A more thorough review of electron-hydrodynamic systems can be found in Refs.[53,57].

1.4 Thermal Conductivity and the Wiedemann-Franz Law

All of the previously mentioned experiments measuring electrical conductivity, in one way or another, rely mostly on some subtle signature of viscous hydrodynamics, such as the conductivity or resistance curves behaving in a very particular way, that aligns quantitatively with at least a moderately complicated hydrodynamic theory with several fitting parameters. The one exception may be the direct imaging of Poiseuille flow as a qualitative signature.

While subtle quantitative studies are useful for fine-tuning the theoretical understanding of hydrodynamics, they may sometimes be difficult to interpret or justify, especially against a ballistic transport picture. In the degenerately doped regime, hydrodynamics emerges from electron-electron collisions, which must conserve momentum and thus electrical current. Naturally, using only electrical transport to study an effect that conserves electrical current may lead to indirect evidence for hydrodynamics, such as in Poiseuille flow, where the momentum relaxation for the current arises nonlocally only from boundary drag. Nonetheless, it is rather remarkable that current-conserving collisions can still produce measurable effcts on the electrical resistance, including both 2-terminal resistance R_{2T}, R_{xx}, and R_{xy}.

In contrast, measuring thermal transport, including thermal conductance, thermal

conductivity, and heating effects, in conjunction with electrical transport, can provide a more encompassing picture of the dynamics of charge carriers in a material. In analogy to Ohm's law (Eq. 1.5) of electrical conduction, Fourier's law (Eq. 1.6) gives the heat current (or energy current) resulting from a temperature gradient via the thermal conductivity:

$$\vec{\mathbf{J}}_e = -\sigma\vec{\nabla}\phi \tag{1.5}$$

$$\vec{\mathbf{J}}_q = -\kappa\vec{\nabla}T, \tag{1.6}$$

where $\vec{\mathbf{J}}_e$, $\vec{\mathbf{J}}_q$ is the electrical or thermal current; σ, κ is the electrical or thermal conductivity; and ϕ, T is the electric potential or temperature.

Unlike electrical conductivity, which is directly tied to the momentum relaxation of charge carriers by phonons, impurities, or oppositely charged charge carriers, thermal conductivity is mostly unaffected by momentum relaxation, but a few exceptions do exist. These exceptions occur when the thermal current carries momentum,* which happens to a small extent from thermoelectric effects and can be significant in bipolar systems such as charge neutral graphene.

In a hydrodynamic system, unlike the electrical conductivity which becomes undefined or infinite due to the absence of momentum relaxation, thermal conductivity remains a well-defined quantity. Neglecting any convective effects, the thermal conductivity will be determined by the individual particle-particle interactions as they relax thermal currents. One might naively expect that strong particle-particle interactions will contribute to a fast diffusion of heat amongst the particles; conversely, and somewhat counterintu-

*This can be described formally through Boltzmann kinetic theory as a nonzero inner product between the thermal current and momentum mode of the distribution function's deviation from equilibrium[82,83].

itively, a high collision rate will relax thermal current very fast, since collisions between particles do not conserve the thermal current.

In a classical Ohmic, diffusive system, the thermal conductivity and electrical conductivity are both well-defined and closely related to each other due to the mechanics of non-interacting diffusion, where particles move around the material in a random-walk fashion with no correlations or interactions with other particles. This connection of the electrical and thermal conductivity is known as the Wiedemann-Franz (WF) law, and was empirically observed for metals in the mid 1800's[84], but its quantum mechanical, fermionic origin was not fully understood until nearly a century later[85]. The modern WF law relates κ and σ as[54]

$$\frac{\kappa}{\sigma T} = \frac{\pi^2}{3}\left(\frac{k_B}{e}\right)^2 \equiv \mathcal{L}_0 \approx 2.44 \times 10^{-8}\ \mathrm{V^2\,K^{-2}}, \tag{1.7}$$

where $\mathcal{L}_0$ is known as the Sommerfeld value for the Lorenz number.

The intuitive understanding behind the WF law is as follows: An electron traveling in a material at a velocity $\vec{\mathbf{v}}$ carries with it a unit of charge e and a unit of heat $\frac{\epsilon-\mu}{k_B T}$, corresponding to how much energy it has above the chemical potential μ relative to thermal excitations of energy $k_B T$. When this electron scatters (Fig. 1.7), and the particle velocity $\vec{\mathbf{v}}$ is either randomized or deflected, as long as the charge e and energy $\epsilon - \mu$ remain unchanged, the electrical and thermal currents carried by this electron will relax at the same rate. Naturally, the charge e is always conserved, but for the heat $\epsilon - \mu$ to be conserved, requires an elastic or quasi-elastic collision, where the energy lost $\Delta\epsilon$ is zero or small enough to satisfy $|\Delta\epsilon| \ll \epsilon - \mu$. This law is obeyed remarkably well in many materials, as well as in the theoretical Fermi liquid framework, under most conditions and temperatures. Accordingly, an experimental search for non-Fermi liquids

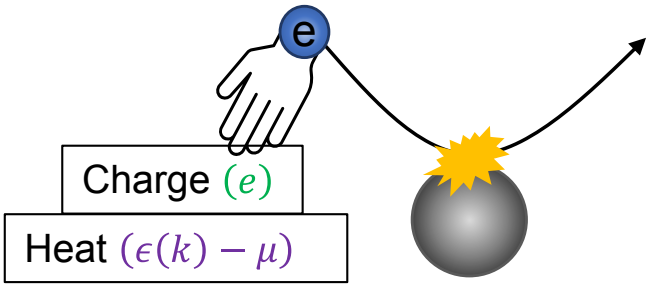

Figure 1.7: An electron traveling through a crystal carries charge e and heat $\epsilon - \mu$. If the scattering is elastic or quasi-elastic such that it conserves both of these quantities, the WF law holds.

may begin with checking the WF law in materials and excluding trivial, single-particle, non-interacting exceptions due to bipolar diffusion, inelastic phonon scattering, thermal Fermi surface smearing, and bandgap formation[86,87] (see Section 5.2).

Theoretical physicists have extensively studied and calculated the expected breakdowns of the WF law in hydrodynamic materials, especially in graphene[2,47,53,76,82,83,88–93]. However, due to the difficulty of measuring electronic thermal transport at the nanoscale, experimental studies on thermal conductivity in graphene are much more challenging[1,94–99], and of these, very few address the hydrodynamic regime.

The first electronic thermal conductance measurement of the hydrodynamic regime in encapsulated MLG was done in our group using Johnson noise thermometry[1], finding a 22-fold enhancement of the Lorenz ratio at charge neutrality, as shown in Fig. 1.8. However, as detailed in Sections 4.5.2, 4.9, and 5.3, this measurement was susceptible to unmeasured sample nonlinearities and associated parasitic noise modulations, effects which are relatively amplified for high Lorenz ratios and thus can significantly affect the measurement accuracy. These results have since stirred controversy in the theoretical community, with some theorists unable to reproduce the measured thermal conductivity with hydrodynamic models[87]. The experiment also measured a suppression of the

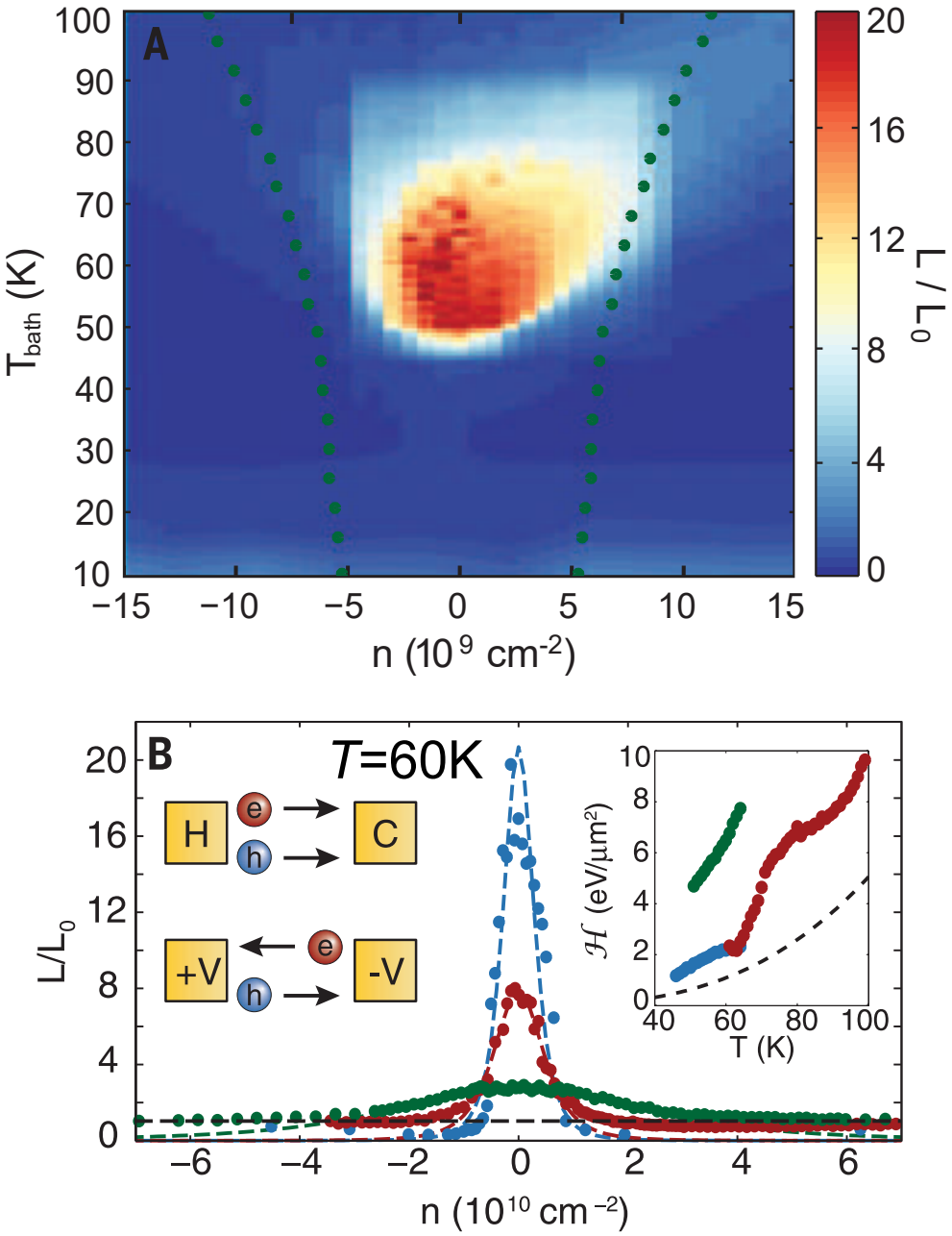

Figure 1.8: **(A)** Colormap of measured Lorenz ratio in MLG, showing an enhanced Lorenz ratio for n near 0 and from $45-80$K. **(B)** Linecuts of the Lorenz ratio from three devices; blue: least disordered; red: medium; green: most disordered. Left-side cartoon shows electron and hole movement under a temperature gradient and a potential gradient. Right-side inset shows the fitted enthalpy density. Figure from Ref. 1.

Lorenz ratio away from charge neutrality but focused little attention on this aspect.

A very recent experiment measured thermal conductance in suspended MLG, using a clever technique to subtract off the phonon contribution and calculate just the electronic component[99]. The authors found a 3-fold enhancement at charge neutrality and a slight suppression away from charge neutrality, qualitatively similar to Ref. 1. Here, they attribute the enhancement to likely bipolar diffusion, but consider two separate mechanisms for the suppression at different temperatures; a hydrodynamic suppression below 60 K, and a suppression induced by nonlinear acoustic flexural phonon (ZA-branch) above 60 K.

The two modes of WF breakdown in hydrodynamic materials, caused by particle-particle scattering, can be understood as follows:

1. In the bipolar regime near charge neutrality, both electrons and holes coexist due to thermal excitations. Under a potential gradient, they move in opposite directions (Fig. 1.8(b) left-side cartoon), exerting mutual friction on each other and thus limiting the electrical conductance. However, under a thermal gradient, electrons and holes both have a higher concentration in hotter regions from thermal excitation, and thus they diffuse together towards the cold side. Because they move in the same direction, they don't experience mutual friction and thus don't generate an impedance to thermal conductance. Together, this combination can lead to a significant enhancement of the thermal conductivity above the WF law.

2. In the monopolar, degenerate regime, only electrons exist, possibly with a small population of thermally excited holes. Considering only the electrons, electron-electron collisions will conserve electrical current due to momentum conservation, but there is no analogous conservation law for the thermal current, which will thus

be randomized and relaxed. Consequently, the thermal conductance is suppressed below the Lorenz ratio. This effect can persist in low-disorder samples even outside the degenerate regime with the presence of some holes, so long as there are excess electrons; here, the charge imbalance still allows for conserved momentum to be related to conserved electrical current[82,83].

In a perfectly disorder-free system, the thermal resistivity vanishes only at exactly charge neutrality, and any arbitrarily small doping away from charge neutrality sets only the electrical resistivity to zero[82,83]. However, the presence of momentum-relaxing disorder regularizes this singular behavior, and creates a narrow region around charge neutrality where the Lorenz ratio is enhanced, and suppressed outside of this region. This enhancement region was termed disorder-enabled hydrodynamics, because the disorder present is what causes the Lorenz ratio to rise above 1 in this entire region, rather than be equal to zero except at exactly charge neutrality[82,83].

1.5 Applications of Nanoscale Thermal Conductivity Measurements

In this thesis, we extensively develop techniques for using RF Johnson noise thermometry (JNT) to probe thermal effects in nanoscale structures and devices. Our primary goal in this work is to study the hydrodynamic regime in graphene, but the techniques are applicable to other nanoscale systems and structures as well, with potentially broad implications for nanotechnology advancement. Here we present a summary of more practical and technological applications of nanoscale thermometry.

Since approximately the mid 2000's, CPU manufacturers have faced a bottleneck for dissipating waste heat generated in the nanoscale structures on chip. This has limited the operating frequency to around 3 GHz, with little improvement in almost 2 decades,

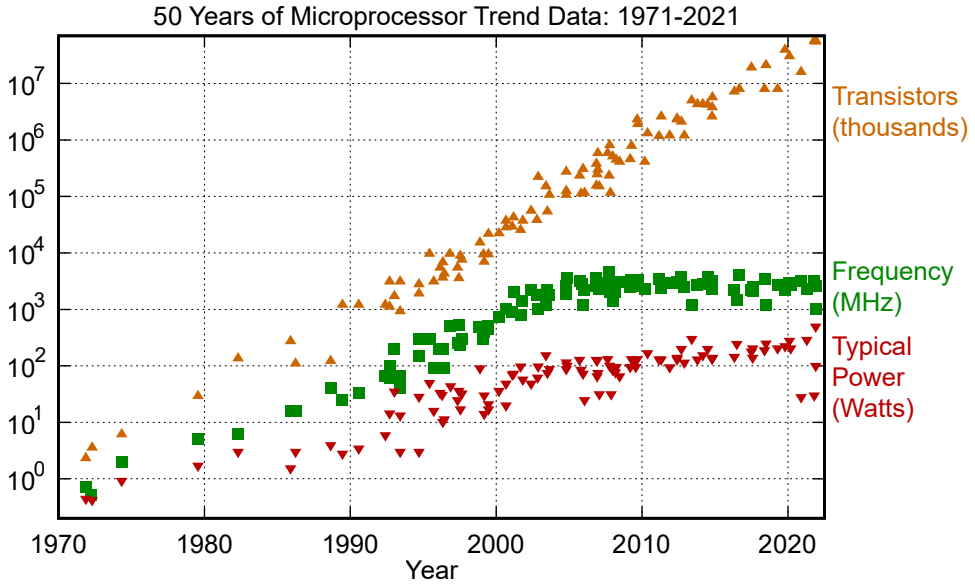

Figure 1.9: Microprocessor trend data from 1971-2021. Typical transistor count (orange), frequency (green), and power consumption (red) as a function of the year. While transistor counts continue to grow exponentially, the operating frequency and power consumption have plateaued since the year ∼2005. Adapted from Ref. 100.

as shown in Fig. 1.9. The waste heat comes from two primary contributions: leakage current in the off-state; and active/dynamic switching power, which requires a certain amount of capacitive charging energy[101]. Running the chip at higher speed is impossible, because the nanoscale components on the chip cannot cool down fast enough. Advancing technology past this bottleneck will require engineering more energy-efficient transistors, and/or more thermally conductive interconnects to help guide out the waste heat.

Due to the complicated multi-material heterostructures used in transistors, local heat dissipation and temperature profiles can become quite complicated, for example by concentrating heat in areas with high electric field when channel conductivity is non-uniform due to channel pinch-off. Different nanoscale transport regimes that may be used in future nanotechnology, including ballistic, diffusive, and hydrodynamic, will have inherently different spatial heat generation profiles, effects that we measure in

this dissertation. At the nanoscale, heat is generally first generated and thermalized in the electronic system, before being transferred to different phonon modes as additional cooling pathways; thus, understanding the different cooling pathways at the nanoscale can be of very practical use.

Modern CPU interconnects are primarily made of copper. With the technological discovery and development of new exotic materials, CPU manufacturers may start integrating very high thermal conductivity materials, such as graphene nanoribbons or carbon nanotubes[102–106], as replacements for interconnects. Measuring the thermal conductivity of these new materials, which will likely violate the WF law, will help select the most conductive ones for removal of waste heat.

For understanding time-dependent transient dynamics, which are important for understanding time-dependent equilibration in relation to high-speed transistor state switching, noise thermometry can also provide information on the heat capacity and thermal response time, using advanced techniques such as bolometric mixing[94].

While 3D bulk thermal dynamics are relatively well understood theoretically, the same equations cannot be blindly applied to accurately calculate thermal properties such as heating and thermal conductivity at the nanoscale or in reduced dimensionality, in part due to the increased influence of boundary effects. Classical and quantum contact resistances become more important as feature sizes are reduced, and their thermal behavior needs to be considered. Using the WF law to estimate the expected thermal conductivity or conductance of an exotic material or nanostructure is often doomed to fail; the hydrodynamic regime is a prime example, where the electrical resistance is an entirely boundary- and viscosity-dependent quantity, whereas the thermal conductance is related to the thermal conductivity through the bulk.

In addition to microprocessor heat management, with which many readers might

be familiar, there are other nanotechnological applications for nanoscale thermometry as well[107,108]. Phase change memory (PCM), which uses a transient burst of heat to warm up and then either quench or slowly recrystallize a memory bit, is a very recently emerging technology with potential applications including classical digital memory and neuromorphic computing[108]. Similarly, heat-assisted magnetic recording (HAMR) is a very recently commercialized technology using nanoscale heating to increase the density of data stored on magnetic media such as hard drives[108]. Medical applications involve implanting targeted nanoparticles into various tumors and then generating ultra-localized tissue damage by heating the nanoparticles with an external energy source[108]. Thermoelectric materials, especially in the context of nanoscale devices, are another exciting research direction that can enable higher device efficiency by extracting work from temperature differences[107,108].

The major attraction of JNT for the nanoscale is that it is a noninvasive probe that uses the sample itself as a primary thermometer, reducing the need for bulky external thermometers that might be poorly thermalized to the nanoscale sample in question. Moreover, JNT directly measures the electronic temperature, without relying on any phonon coupling to other thermometers. Noise thermometry is thus particularly well-suited to measuring thermal conductance of nanoscale structures. Chapter 2 provides a background overview of basic JNT properties and techniques, and Chapter 4 presents the novel RF JNT techniques developed in this work. In summary, JNT is particularly well-suited to studying a variety of thermal effects and properties in nanoscale structures.

1.6 Radio Frequency Techniques and Concepts

The main techniques used for Johnson noise thermometry (JNT) measurements in this dissertation operate at radio frequencies (RF). Chapter 2 provides an introductory overview to Johnson noise, not limited to only RF. In this section, we present some basic RF concepts to help the reader understand the basis for RF JNT techniques. For a thorough understanding of RF concepts for an experimentalist wishing to conduct similar experiments, the reader is referred to the excellent Refs. 109–112.

Low-frequency electronics typically measure either voltage or current. Voltage measurement devices, including amplifiers for voltage such as the very common Stanford Research Systems SR830 lock-in amplifier, typically have a high input impedance of 10 MΩ, ideally drawing negligible current from the circuit they are measuring. In an analogous way, current measuring devices ideally have very low input impedance, enough to not cause a significant voltage drop to affect the circuit.

Lumped-element electronic circuits take advantage of the very high speed of light c; in particular, they assume that for an AC signal, the phase is uniform across the entire circuit. At high frequencies (HF) or radio frequencies (RF), when the size or separation of components is no longer much smaller than the electromagnetic wavelength at the operating frequency, the constant-phase assumption breaks down, and lumped element circuits no longer behave as they do in the low-frequency limit. There will be a phase delay between different elements of the circuit, and it becomes appropriate to consider current and voltage transmission in the circuit in terms of travelling waves.

Rather than transmitting a current/voltage wave through a lone wire, it is best to do so through a coaxial cable (or more generally, a transmission line) in order for it behave with consistent and predictable properties. A coaxial cable can be thought

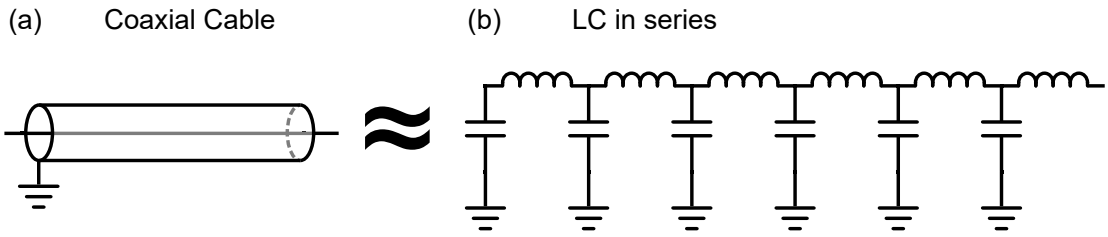

Figure 1.10: **(a)** A coaxial cable. **(b)** This is equivalent to a series of inductors and capacitors.

of as analogous to a fiber optic cable for carrying a wave or signal. A coaxial cable can be approximated as a continuous series of in-line inductors and shunt capacitors: The center conductor has a self-inductance, and the proximity to the outer conductor (which is typically "ground") through the insulating dielectric provides the capacitance. Fig. 1.10 demonstrates this analogy. Typically, we consider the LC model to have a certain inductance and capacitance per unit length. As a crude derivation, we can write the impedance of such an infinite LC series recursively:

$$Z = \frac{1}{i\omega C + \dfrac{1}{i\omega L + Z}}. \tag{1.8}$$

The solution is given by

$$Z(i\omega L + Z) = \frac{L}{C}. \tag{1.9}$$

In the limit of differentially small individual Ls and Cs, we have $Z \gg i\omega L$, giving us

$$Z^2 = \frac{L}{C} = \frac{\mathscr{L}}{\mathscr{C}} \tag{1.10}$$

$$Z = \sqrt{\frac{\mathscr{L}}{\mathscr{C}}}, \tag{1.11}$$

where we have now taken $\mathscr{L}, \mathscr{C}$ as the inductance and capacitance per unit length.

Here, Z is known as the characteristic impedance, usually written as Z_0 and defined as the ratio of voltage to current in a wave propagating along the transmission line. By adding resistive elements to Fig. 1.10, one can derive a coupled wave equation for I and V, known as the telegrapher's equation. This wave equation provides

$$v_{ph} = \frac{1}{\sqrt{\mathscr{L}\mathscr{C}}} \tag{1.12}$$

for the phase velocity of a wave. Due to historical reasons of choosing an optimal balance between attenuation and power handling, as well as consideration of the vacuum impedance $\sqrt{\frac{\mu_0}{\epsilon_0}} \approx 377\,\Omega$, a near-universal standard of Z_0 =50 Ω was chosen for coaxial cables. Typical propagation velocities are $\sim$ 66% the speed of light, dictated by the dielectric. With cable impedances at 50 Ω, we are no longer working in the "voltage" or "current" measurement system, but rather in the "power" measurement system. Note that a 50 Ω impedance appears equivalent to a resistive load due to its voltage-to-current ratio, but it is non-dissipative in nature; instead, the power supplied to a transmission line becomes a traveling wave, rather than dissipating as heat.

As the waves are associated with an impedance, there will be a particular reflection and transmission at the boundary between two impedances. A wave traveling along an impedance Z_0, seeing a load impedance or a change to impedance Z_L, will have a voltage wave reflection coefficient of

$$\Gamma = \frac{Z_L - Z_0}{Z_L + Z_0}. \tag{1.13}$$

Correspondingly, the reflected P_R/P_I and transmitted P_T/P_I wave power ratios to the

incident power are given by

$$\frac{P_R}{P_I} = \left|\frac{Z_L - Z_0}{Z_L + Z_0}\right|^2 \tag{1.14}$$

$$\frac{P_T}{P_I} = 1 - \left|\frac{Z_L - Z_0}{Z_L + Z_0}\right|^2. \tag{1.15}$$

For real impedances, Eq. 1.15 becomes

$$\frac{P_T}{P_I} = \frac{4ZZ_0}{(Z + Z_0)^2}, \tag{1.16}$$

a functional form that we will see come up again. We see that Eq. 1.16 is a simple representation of what fraction of power gets transferred to the load as a function of impedance mismatch. For full power transfer for real impedances, minimizing reflections, we must have the two impedances equal to each other in what is known as impedance matching.

In general, a transmission line terminated in anything other than a $50\,\Omega$ impedance (or resistance) will have an an input impedance that depends on the length, frequency, and termination of the line, due to the sum of the reflected waves, and can vary between $0\,\Omega$ and $\infty\ \Omega$.

One accurate measurement is worth a thousand expert opinions.

Grace Hopper

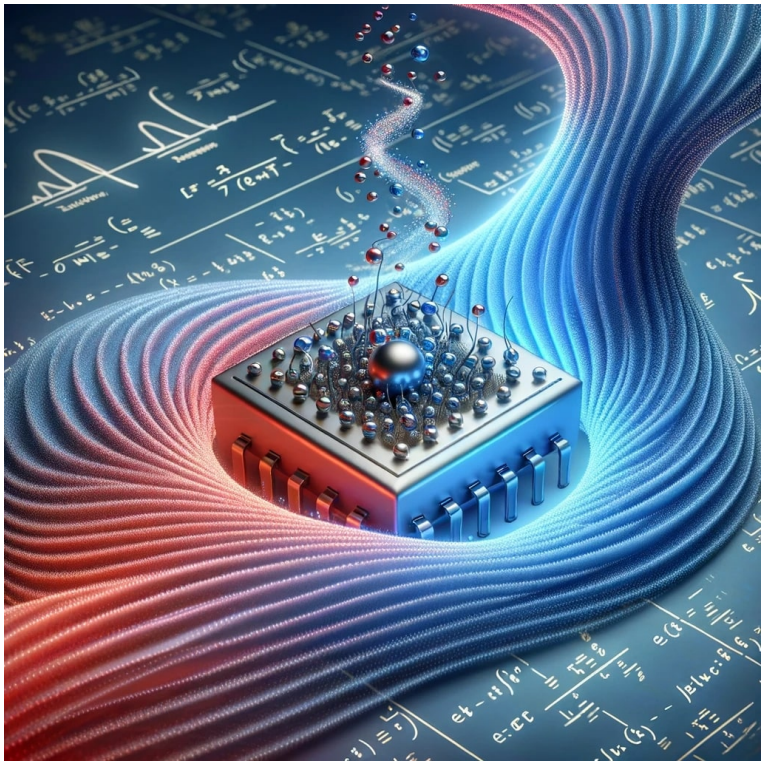

2

Johnson Noise Thermometry Overview

While most experimentalists endeavor to avoid noise, for us it forms the cornerstone of our thermometry technique. The thermal noise emitted from our graphene devices is itself the signal that we want to measure, as it contains valuable information about the temperature of the electrons. Unlike more conventional forms of thermome-

try, such as mercury thermometry or resistive thermometry, Johnson noise thermometry (JNT) is a primary thermometry technique, meaning it directly measures a universal thermodynamic property and can in principle be operated without calibration, using known fundamental constants. This contrasts with secondary thermometers, which measure the change of some arbitrary property that depends on temperature, such as the height of mercury in a thin column (via the thermal expansion of mercury), or the resistance of some electrical conductor or semiconductor that varies strongly with temperature (due to many different factors, including thermal carrier activation across a bandgap and temperature-dependent phonon scattering).

In principle, there is not a hard distinction between primary and secondary thermometers, as one could imagine measuring for example the thermal Fermi surface smearing, a universal thermodynamic property, via some contrived electro-resistive means. Even when measuring primary thermometers, often the measurement instruments needs to be calibrated themselves; for example, when measuring the volume or pressure of an ideal gas following the ideal gas law, the length gauge or barometer must be calibrated first. Typically for Johnson noise, as we will see, knowledge of the bandwidth and amplifier gains will be crucial calibration factors.

Johnson noise arises as a result of the fluctuation-dissipation theorem from statistical physics, which states that for any process that dissipates energy, there is a reverse process that generates corresponding thermal fluctuations. More specifically, consider a system with a generalized coordinate x and corresponding generalized force F, where the coordinate's response to the force is characterized by an AC susceptibility $\tilde{\chi}(\omega) = \dfrac{\tilde{x}(\omega)}{\tilde{F}(\omega)}$ that includes an imaginary dissipative component, where the tilde symbol indicates a Fourier transform in time. Then, there will be fluctuations in the generalized coordinate related to that dissipative component, with the power spectrum of the fluctuations in

the classical regime given by

$$S_x(\omega) = -\frac{2k_BT}{\omega}\mathrm{Im}\tilde{\chi}(\omega). \tag{2.1}$$

These thermal fluctuations are related to the equipartition theorem, which states that quadratic degrees of freedom, such as x, have an average energy of $\frac{1}{2}k_BT$ in thermal equilibrium. In the next subsection, we will discuss how a quantum mechanical description modified this equation.

Johnson noise thermometry has broad applications ranging from fundamental science[113], to use in harsh environments such as nuclear reactors[114–116], and commerce/industry[113,117,118]. JNT can function as a nanoscale probe to study thermal behavior in nanoscale devices and potentially help engineer more efficient cooling pathways to solve the growing problem of excess heat management in continuing miniaturization of electronics[119,120]. Fundamentally, JNT allows measurement of the cosmic microwave background[121–124], high-accuracy verification of the Boltzmann constant[125,126], and extension of the International Temperature Scale (ITS) down to 6 mK[127–129].

The advantages of JNT include (1) functionality as a primary thermometer, (2) dependence only on the sample resistance and not on any other microscopic or macroscopic system parameters or details, (3) a wide temperature range of application, and (4) the ability to non-invasively probe nanoscale conductors by directly measuring their fluctuations, without perturbing the system as would resistive or other types of thermometry.

This Chapter aims to give a broad and general introduction to Johnson noise, focusing on establishing the context for this work. The curious reader is referred to the excellent Refs. 113,130 for further review on experimental Johnson noise thermometry outside the scope of this thesis.

2.1 Thermal Radiation in the pre-Johnson-Nyquist Era

The reader may be familiar with free-space blackbody radiation via the Stefan-Boltzmann[131,132] law,

$$\mathcal{P} = \varepsilon \sigma_{SB} T^4, \tag{2.2}$$

where $\mathcal{P}$ is the radiated power density, $\varepsilon \leq 1$ is an emissivity factor, σ_{SB} is the Stefan-Boltzmann constant, and T is the blackbody temperature. This law describes how an object at a given temperature radiates wideband thermal electromagnetic radiation into free space. Planck's law[133,134] gives the spectral radiance of blackbody radiation:

$$B_\omega(\omega, T) = \frac{8\pi^2 \hbar \omega^3}{c^2} \frac{1}{\exp\left(\frac{\hbar\omega}{k_B T}\right) - 1}, \tag{2.3}$$

where ω is the angular frequency, $\hbar$ is Planck's constant, c is the speed of light, and k_B is Boltzmann's constant. Eq. 2.3 indicates an upper quantum frequency cutoff near $\hbar\omega = k_B T$, to avoid the ultraviolet catastrophe.

Blackbody radiation is often used as a thermometry technique in our everyday lives. Venturing outside on a sunny warm day, we are heated by the $\sim$5800 K blackbody radiation from the sun, or, going outside at night, we experience the frigidity of the 2.73 K cosmic microwave background in the night sky. More quantitatively, infrared blackbody thermometers are readily commercially available at hardware or home-improvement stores for home or industrial use.

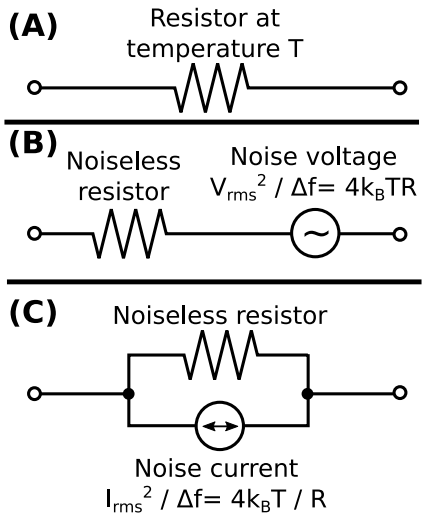

Figure 2.1: **(A)** A real resistor at a temperature T. **(B)** Equivalent circuit for voltage-based noise. **(C)** Equivalent circuit for current-based noise. Images from 137.

2.2 Johnson-Nyquist Noise

Johnson-Nyquist noise[135,136] is analogous to the Stefan-Boltzmann law, with an electrical resistor of resistance R radiating power into an electrical load (such as a coaxial cable, or another impedance) Z_L. Compared to the Stefan-Boltzmann law, the coaxial cable replaces three-dimensional free space, and this leads to the reduction of the power law in temperature. Johnson noise is a specific instance of the fluctuation-dissipation theorem, with the electrical resistance as the dissipative quantity.

Traditionally, the classical Johnson-Nyquist noise is written as the root-mean-square (rms) voltage fluctuations present on an open-circuit resistor. Electrically, this is equivalent to an ideal, noiseless resistor in series with an rms noise voltage source, as compared in Fig. 2.1 (A,B). The formula for the rms voltage fluctuations is famously given by

$$\langle V^2 \rangle = 4 k_B T R \, \Delta f, \tag{2.4}$$

where Δf is the measurement bandwidth. In practice, these fluctuations are measured by connecting a high-input-impedance low-noise amplifier (LNA) directly to the resistor, and then measuring the power of the amplified fluctuations.

How small are these voltage fluctuations? Suppose an experimentalist attempts to measure Johnson noise of a 1 kΩ room-temperature resistor using a lock-in amplifier set to a $\tau = 300$ ms time constant, parameters which are very commonly used in laboratories. The SR830 lock-in amplifier[138], using a 24 dB/oct slope, has a $5/(64\tau)$ effective noise bandwidth (ENBW), equal to 0.26 Hz (see also Appendix F). The resulting rms voltage fluctuations are 2.1 nV, a small signal but not impossibly so to measure.

Of course, the lock-in amplifier is the worst tool in the lab to measure Johnson noise, as it is designed specifically to have a very narrow bandwidth to avoid measuring noise at frequencies different from the signal in question. Eq. 2.4 tells us that a higher bandwidth will give us more Johnson noise, and in Section 2.5 we discuss in further detail the very important relevance of bandwidth for JNT, as a motivation for our RF-based JNT techniques.

2.3 Voltage, Current, and Power-Based Johnson Noise Thermometry

In addition to modeling Johnson noise as voltage fluctuations across an open-circuit resistor, we can also model it as current fluctuations through a short-circuited resistor,

as shown in Fig. 2.1(C). Here, the rms current fluctuations are given by a similar formula

$$\langle I^2 \rangle = 4k_B T/R \times \Delta f. \tag{2.5}$$

Both Eqs. 2.4 and 2.5 represent the Thevenin and Norton equivalent circuits for Johnson noise and are interchangeable and equivalent. For convenience, however, Eq. 2.4 is used for measuring Johnson noise with voltage amplifiers (high input impedance), and Eq. 2.5 is used for for measuring Johnson noise with current amplifiers (low input impedance).

There is yet another, power-based Johnson noise formula, that is more analogous to the Stefan-Boltzmann law and thus might be more fundamental. The resistor in Fig. 2.1(B) when short circuited, or in Fig. 2.1(C) when left in open-circuit, dissipates an internal power of

$$P_{JN}^{(int)} = 4k_B T \, \Delta f. \tag{2.6}$$

This equation conveniently sits between Eqs. 2.4 and 2.5 in a chain of division by R. With a connected load instead of a short or open circuit, the maximum available Johnson noise radiative power transmitted to the load happens when the load is impedance-matched to the source and is equal to

$$P_{JN}^{(matched\,load)} = k_B T \, \Delta f. \tag{2.7}$$

The vanishing of the factor of 4, as compared to Eqs. 2.4, 2.5, and 2.6, arises from the voltage drop being equally distributed between the source and the load. If, however, the load impedance R_L is fixed, and the source impedance R_S of the noise source is

varied, due to impedance mismatch (see Section 1.6 and Subsection 4.4.1), the actual power delivered to the load is given by

$$P_{JN}^{(non-matched\,load)} = \frac{4R_L R_S}{(R_L + R_S)^2} \times k_B T \Delta f, \tag{2.8}$$

where R_L is the load resistance, and R_S is the Johnson noise source resistance.

Voltage-based and current-based Johnson noise thermometry must operate at relatively low frequency, limited by the lumped-element circuit model. At high frequencies, the impedances of the connecting cables and other components, coupled with the high- or low-input impedance LNAs, will severely attenuate the signal. Conversely, power-based Johnson noise has no such limit to frequency, given that impedance matching is adequately satisfied (see Sections 1.6 and 4.4). The reason that large bandwidth in frequency is desirable is discussed in Section 2.5.

Fig. 2.2 demonstrates the comparison of the different types of noise in Eqs. 2.4, 2.5, and 2.8 as a function of source (sample) resistance. In all cases, the measured noise has a functional dependence on the source resistance, and therefore, to extract a meaningful temperature value, we must also measure the resistance.

There have been some clever work-around methods to bypass this restriction, e.g. measuring both $\langle I^2 \rangle$ and $\langle V^2 \rangle$ and then taking the product of the quantities[139]. Another example is using an inductor and capacitor to load the sensor such that the bandwidth is resistance-dependent in a way that the changes in R and Δf cancel out[140].

2.4 Quantum Johnson Noise

So far we have discussed classical Johnson noise, where we assumed a flat spectral density. In reality, analogously to Planck's law (Eq. 2.3), Johnson noise also has an

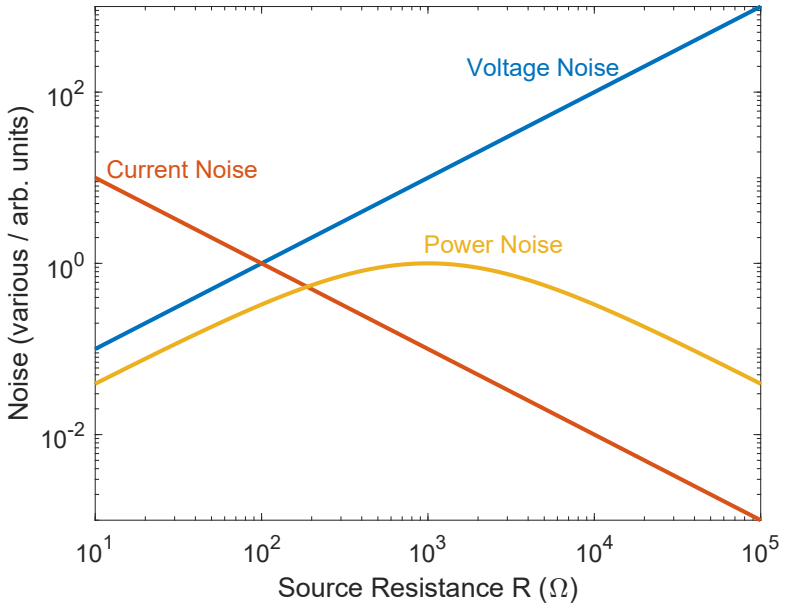

Figure 2.2: The scaling of voltage (blue), current (red), and power (yellow) noise as a function of source resistance. The power noise curve assumes a load resistance of 1 kΩ.

upper-frequency cutoff near $\hbar\omega = k_B T$. Accordingly, the full power spectral density of Johnson noise will be given by[113]*

$$S_V(\omega) = \frac{\hbar\omega}{e^{\hbar\omega/k_B T} - 1}. \tag{2.9}$$

Typically, this cutoff is important only at ultra-low temperatures, such as in a dilution refrigerator at GHz frequencies when working with qubits, for example. Below, Table 2.1 shows, for a given temperature, the corresponding frequency at which the Johnson noise spectral power decreases by 1% and 50% relative to its zero-frequency limit. If Johnson noise is measured at higher frequencies through the quantum roll-off, then the calibration must account for this.

*There is a controversial term representing the quantum mechanical zero point energy in Eq. 2.9, which we have omitted[113].

Quantum Johnson Noise					
T	10 mK	100 mK	1 K	10 K	300 K
99% remains at	4.2 MHz	42 MHz	420 MHz	4.2 GHz	125 GHz
50% remains at	262 MHz	2.6 GHz	26 GHz	260 GHz	7.9 THz

Table 2.1: The table lists at what frequency the spectral Johnson noise power is reduced to 99% and 50% of its zero-frequency limit.

2.5 Bandwidth

The bandwidth of a measurement of Johnson noise is an extremely important parameter. Since Johnson noise is effectively a measurement of the mean of random numbers, there is an intrinsic uncertainty to the measurement, as opposed to, for example, measuring an AC voltage signal with superimposed noise. In particular, JNT will measure the variance of the voltage, defined as

$$\mathrm{var}(V) = \int (V - \langle V \rangle)^2 f(V) dV \tag{2.10}$$

where $f(V)$ is the Gaussian distribution of V, and $\langle V \rangle$ is the DC bias on the device.

In practice, one single JNT measurement will only give an estimate of $\mathrm{var}(V)$, rather than the exact value. The variance of the JNT measurements will follow a chi-square distribution with k degrees of freedom, where $k = 2\tau\Delta f$ is the number of samples acquired in a measurement time τ over a bandwidth Δf, according to the Nyquist theorem.

Based on this principle, the Dicke radiometer formula gives the ideal measurement uncertainty for a temperature measurement[113,130,141,142]:

$$\sigma_T = \frac{T_{samp} + T_N}{\sqrt{\tau \Delta f_c}}, \tag{2.11}$$

where T_{samp} is the sample temperature, T_N is the effective temperature of additional (e.g. amplifier) background noise, and Δf_c is a correlation bandwidth, very similar to Δf, but defined specifically later in Chapter 4 (Eq. 4.50). The quantity under the square root is the effective number of samples $N \sim \frac{k}{2}$, and thus the uncertainty scales as $\sim \frac{1}{\sqrt{N}}$.

It is evident from Eq. 2.11, that for a given target uncertainty σ_T, a higher bandwidth Δf_c will require a significantly shorter measurement time τ than would a lower bandwidth. It is for precisely this reason that we perform JNT at RF frequencies, to be able to take advantage of 100s of MHz of bandwidth. Traditionally, and often still in modern times, noise measurements are performed using 10s - 100s of kHz or a few MHz of bandwidth[114,126,140,143–147]; our bandwidth is comparatively 100-10,000 times larger, allowing for significantly faster measurements.

Nonetheless, using higher bandwidth for JNT may also pose drawbacks in certain situations. If the gain and bandwidth of the LNAs are measured separately from the experiment, then a slight variation in gain over frequency might cause small systematic errors. Additionally, high-frequency measurements will inherently run into the Planck cutoff frequency (Eq. 2.9), potentially affecting high-accuracy measurements. However, in this dissertation, our goal is not to achieve extremely high accuracies as good as 1% or less; rather, we typically only need 5-15% accuracy at best to observe the needed hydrodynamic effects in mesoscopic systems.

If we knew what it was we were doing, it would not be called research, would it?

Albert Einstein

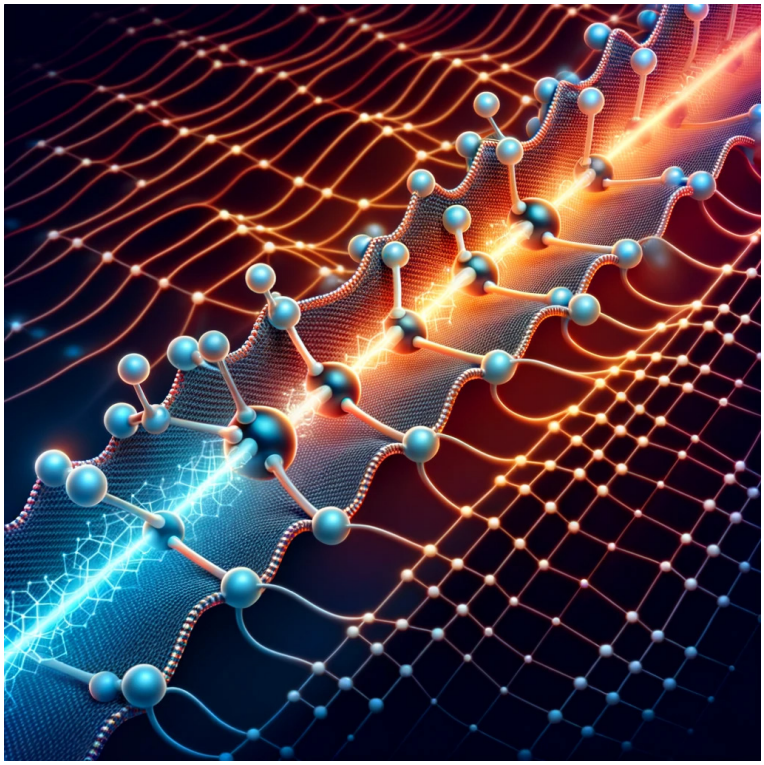

3

Measurement of Electronic Thermal Conductance at the Nanoscale

Thermal transport measurements are significantly more challenging than analogous electrical transport measurements. Electrical wires are especially good at

transporting charge to its destination without losing it along the way, and we readily have access to ammeters and voltmeters. In contrast, heat traveling along a "thermal" wire from a hot to a cold source will be lost along the way to either blackbody radiation or the environment directly outside the wire. An ideal "thermal" wire would need to exist in a pure vacuum and have blackbody emissivity of 0. Furthermore, measuring a temperature difference and especially a heat current, particularly at the nanoscale, are remarkably more difficult to do than their electrical counterparts.

For studying only the electron-electron (e-e) interactions in graphene, and not the phonons, we furthermore want to measure only the electrical component of the total thermal conductivity. This will involve heating the electrons, measuring their temperature, and measuring the thermal current, all without any interactions with the phonons. The lattice temperature must remain at the cryostat base temperature, while the electron temperature will decouple from the lattice. In principle, this is achievable at low enough temperatures and/or short enough device lengths, where the electron-phonon mean free path would be longer than the device length.

Alternately, it is possible to measure the total thermal conductivity, cleverly infer the phonon contribution, and then subtract it out to obtain only the electronic contribution[99], but this method still does not directly measure only the electronic contribution.

Here, we present methods and analysis for measuring the electronic thermal conductivity of encapsulated graphene devices using JNT in a self-heating configuration. We will also briefly introduce a non-local heating alternative configuration, but a detail discussion thereof is outside the scope of this dissertation. We discuss the requirements and limitations of the self-heating technique, as well as attempts to quantify and bypass the limitations. The two biggest thermal limitations to quantitative measurements are the effects of contact resistance and heat loss to phonons, which we have made signif-

icant progress in understanding during the course of this work. Additional limitations stemming from the JNT technique itself are discussed in Chapter 4.

3.1 Cooling Mechanisms in Graphene

In this section, we present some background on the different cooling mechanisms for electrons in graphene, although the same ideas will extend to many other experimental systems. Motivated by the weak electron-phonon coupling[53,68,96], we consider the electrons and phonons as separate subsystems in the sample, each at their own temperature.

The primary cooling mechanism we are interested in studying is electronic diffusion cooling. In most daily real life situations, we observe cooling or heating by three primary mechanisms: radiation, convection, and conduction. Conduction is the mode that obeys the diffusion equation; if we have a sample of a material and heat up one end of it, eventually that heat will diffuse and redistribute to other parts of the object, modulo losses to convection and radiation. However, in our everyday lives, we always feel a combined electron and phonon temperature, as the electron-phonon coupling on macroscopic scales at room temperature is strong enough such that the two temperatures are equilibrated.

3.1.1 Electronic Diffusion

As we consider the electron system only, we find it also to obey the diffusion heat equations, given by

$$\vec{J_Q} = -\kappa \vec{\nabla} T \tag{3.1}$$

$$\rho_m c \frac{\partial T}{\partial t} = \vec{\nabla} \cdot (\kappa \vec{\nabla} T) + \mathcal{P}. \tag{3.2}$$

Here, $\vec{J_Q}$ is the thermal current density; κ is the thermal conductivity; T is the temperature; ρ_m is the mass density; c is the specific heat capacity; and $\mathcal{P}$ is the rate of heat generation per unit area (2D) or volume (3D). Eq. 3.1, known as Fourier's law, is exactly analogous to the microscopic version of Ohm's law,

$$\vec{J} = -\sigma\vec{\nabla}\phi = \sigma\vec{E}, \tag{3.3}$$

where $\vec{J}$ is the electric current density, ϕ is the electric potential, and $\vec{E}$ is the electric field; Eq. 3.1 states that the flow of heat is proportional to the local temperature gradient, and the proportionality constant is the thermal conductivity. Eq. 3.2 is obtained from a spatial derivative of Fourier's law and the conversation of energy; it states that the change in temperature of a differential volume is related to the net heat current going into this volume, plus any internal heat generation. Under steady state conditions and assumption of a spatially homogeneous κ, Eq. 3.2 can be simplified to the more familiar form

$$\mathcal{P} = -\kappa\nabla^2 T. \tag{3.4}$$

Eq. 3.4 will be our starting point for future derivations. For diffusive cooling of electrons, we will need some sort of heat sink; often this will be a metal electrode that makes contact to the graphene, and we assume that the electrons in the metal are well-thermalized to the bath temperature. In this case, heat will diffuse from the hot electrons in the graphene to the colder electrons in the metal contact.

Generally, electronic diffusion cooling obeys the Wiedemann-Franz law as described in Chapter 1, with thermal conductivity proportional to temperature. However, we are

interested in studying hydrodynamic electrons, which will not obey the WF law.

3.1.2 Phonon Cooling

Another important mode of electron cooling in graphene is via heat loss to phonons. Very generally for most materials, the heat transfer between the electron and acoustic phonon subsystems is given by[148]

$$Q_{e-ac} = V_d \Sigma \left(T_e^{\delta} - T_{ac}^{\delta} \right), \tag{3.5}$$

where V_d is the d-dimensional volume, $T_{e/ac}$ is the temperature of the electron or phonon subsystem, Σ is a coupling constant, and δ is an exponent that depends on dimensionality. For 3D materials, it has been shown that $\delta = 5$[149,150]; this can be though of as analogous to the $\sim T^4$ Stefan-Boltzmann power law. In graphene, this formula applies with $\delta = 4$ for temperatures below the Bloch-Grüneisen (BG) temperature, but takes on a different limit above the BG temperature. The BG temperature is given by[68,148]

$$T_{BG} = 2\frac{v_s}{v_F}\frac{|\mu|}{k_B} = 2\frac{\hbar v_s k_F}{k_B}, \tag{3.6}$$

and represents the temperature scale at which phonon modes with a high-enough k become populated and able to scatter electrons fully across the small Fermi surface in graphene; $v_s \sim 2 \times 10^4$ m/s is the speed of sound, $v_F \sim 1 \times 10^6$ is the Fermi velocity, μ is the chemical potential, and k_F is the Fermi wavevector. For $T > T_{BG}$, the heat transfer is given by[148]

$$Q_{e-ac} = V_d \, g(\mu, T_e) \left(T_e - T_{ac} \right), \tag{3.7}$$

where $g(\mu, T_e)$ is a function given in Ref. 148. Acoustic phonon cooling in graphene has been previously measured using noise thermometry, with the ability to extract the coupling coefficient Σ and deformation potential D[94,95,151,152].

At even higher temperatures, optical phonons, both local in the graphene and remote in the substrate, start contributing significantly to cooling and eventually overpower the cooling from acoustic phonons[96]. The corresponding formulas are outside the scope of this thesis and are given in Ref. 148. Optical phonon cooling has also been measured, but due to the more complicated functional form and variability between substrates and samples, it is more difficult to extract meaningful parameters[153–156].

There is another form of phonon cooling involving supercollisions, occurring at higher temperatures. Here, a three-body collision between an electron, an impurity, and a phonon can cause rapid phonon cooling of the electrons at a rate higher than conventional phonon cooling. This has also been measured in graphene under high-T out-of-equilibrium conditions[157,158].

Importantly, the phonon cooling rates and coupling constants depend strongly on the substrate and will thus vary between suspended samples, samples on SiO_2, and samples encapsulated in h-BN. Suspended samples have flexural out-of-plane phonon modes that can interact strongly with the electrons[99,157].

3.1.3 Radiative Cooling

Finally, we have the radiative cooling modes. The first one is radiative emission into free space and can be calculated by the Stefan-Boltzmann law. Graphene on 285 nm SiO_2 has its highest optical absorption of about 7-8% in the green wavelengths, although this may change in encapsulated samples; this number could be used as a starting point for the emissivity in calculating the Stefan-Boltzmann law. However, depending on the

cryostat setup, the inner wall of the sample package enclosure would likely be at the same temperature as the sample, nulling out any cooling.

The second radiative cooling mode is precisely that which we measure in JNT; it is the radiation of microwave energy, for frequencies less than the Planck frequency given by $\hbar\omega = k_B T$, into electrically connected loads with an impedance, such as a resistor or a transmission line. The maximum available spectral power density to be radiated into a matched load is $S = k_B T$, but this is reduced by impedance mismatches. The total outbound radiated power would involve an integral over all frequencies less than the Planck frequency, involving the transmission coefficient. However, to calculate the net heat loss, we must also take into account the spectral power density of the noise radiated towards the sample from the LNA or other circuit elements, whose frequency dependence we will designate as $T_{N,in}(f)$, which could be higher or lower than the sample. The resulting cooling power then involves the difference between the sample temperature and $T_{N,in}$:

$$P = \int_0^\infty \left(1 - |\Gamma(f)|^2\right) k_B \left(\frac{T}{1 - \exp\left(-\frac{hf}{k_B T}\right)} - T_{N,in}(f) \right) df. \tag{3.8}$$

For typical experiments on conductive samples with high electronic diffusion thermal conductance, this contribution is usually negligible.

As an example, for a typical ideally-matched graphene sample at 1 kΩ with a, 80–260 MHz matching band, the radiative cooling power at 10 K with $T_{N,in} \sim 1.5$ K is $\sim 2 \times 10^{-14}$ W, which changes to $\sim 8 \times 10^{-16}$ W for a poorly-matched sample at 150 kΩ. Due to conservation of energy, and under the assumption that the other cooling mechanisms are negligible, the cooling power of the electronic diffusion cooling equals the self-heating Joule power (see Section 3.2), which, for sample warming of 200 mK,

typically ranges from $\sim 1 \times 10^{-9}\,\mathrm{W}$ at $1\,\mathrm{k}\Omega$ to $\sim 3 \times 10^{-11}\mathrm{W}$ at $1\,\mathrm{k}\Omega$[159]; see also Section 4.6. In all cases, cooling by Johnson noise emission is generally over 4 orders of magnitude smaller than the relevant electronic diffusion.

3.2 Self-Heating: Assumptions and Measurement Technique

A measurement of thermal conductance consists of two separate parts: (1) measuring the temperature difference across the sample, and (2) measuring the heat current through the sample. The thermal conductance can then be written as the ratio of the two.

Rather than performing a thermal conductance measurement in a traditional hot-side and cold-side configuration, we will use the self-heating configuration. Here, a rectangular sample of graphene is connected to two metal electrodes on each side, which act as heat sinks. In bulk metals at typical experimental temperatures, the electron-phonon coupling is much stronger than in graphene, and thus we can consider the metal electrodes as well thermalized to the bath temperature[96]. These metal electrodes at the bounadry of the graphene will serve as the cold side.

We generate the "hot side" of the measurement inside the channel of the device by flowing a current through the two metal terminals, generating Joule heating equal to $P_J = IV$. Due to conservation of energy, in steady state, all the Joule heat that is generated must also exit the sample to the two cold heat sinks. As a result of the particular balance between the Joule heating and the diffusion cooling, the sample acquires a particular temperature rise profile of $\Delta T(x, y)$ above the bath temperature, generally peaked near the center of the channel. Fig. 3.1 shows a schematic cartoon of a graphene device being heated, with the orange glow representing warming above the bath temperature. We use JNT to measure the average temperature rise, ΔT_{avg}. We

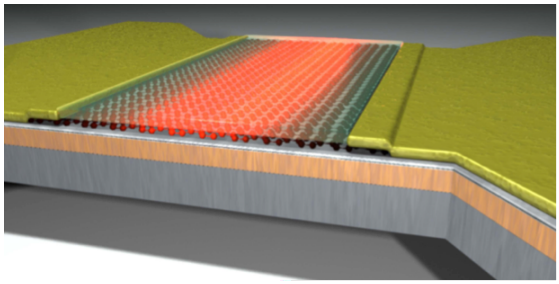

Figure 3.1: Schematic cartoon of a graphene device being Joule heated by current, with the orange glow near the center representing warming above the bath temperature. The yellow-colored parts are the metal leads, which act as heat sinks. Image from Ref. 151.

can thus define a generalized thermal conductance of the sample as the ratio of the heat flowing out of the sample to the average temperature rise:

$$G_{th,gen} = \frac{P_J}{\Delta T_{avg}}. \tag{3.9}$$

We emphasize the generality of this statement, as any more specific conclusions, such as the thermal conductivity value κ, will be related by situation-specific geometric factors.

We can get more useful information about the sample, in particular the thermal conductivity κ, if we make some assumptions. Let us assume that the flow of electrical current and the electrical conductivity are spatially homogeneous. Then, due to translational symmetry, we can solve the 1D heat equation to obtain the resulting spatial temperature profile $T(x)$ in the sample.

For simplicity, we will initially assume that the heating power is small, such that the temperature rise in the sample is much smaller than the bath temperature: $\Delta T(x) \ll T_0$. In this case, we are then justified in neglecting any temperature variation of κ throughout the channel, allowing us to use Eq. 3.4. If the sample has dimensions $L \times W$, then the

heat equation becomes

$$\frac{P_J}{LW} = -\kappa \frac{d^2T}{dx^2}. \tag{3.10}$$

With boundary conditions given by $T(x = 0) = T(x = L) = T_0$, the solution to this equation is given by

$$T(x) = T_0 + \frac{P}{2\kappa LW} x(L - x) \tag{3.11}$$

$$T(x) = T_0 + \frac{V^2}{2\mathcal{L}T_0\sigma} \frac{x}{L} \left(1 - \frac{x}{L}\right), \tag{3.12}$$

where in the last line, we have defined κ with a sample Lorenz number $\mathcal{L}$. We must figure out how the quantity ΔT_{avg} measured with JNT relates to $T(x)$.

To start, let us calculate the total sum Johnson noise from two series resistors of different resistances, R_1, R_2, which is more convenient to calculate with a voltage source model of Johnson noise. The rms voltage fluctuations for each resistor i are given by

$$\langle V_i^2 \rangle = 4k_B T_i R_i; \tag{3.13}$$

adding these together in quadrature, we get

$$\langle (V_1 + V_2)^2 \rangle = \langle V_1^2 \rangle + \langle V_2^2 \rangle = 4k_B \left(T_1 R_1 + T_2 R_2\right). \tag{3.14}$$

The total noise is the weighted sum of the individual temperatures, with the resistances as the weighting factors. Next, we shall calculate the total sum Johnson noise from two parallel resistors, which is more convenient to do with the current source model of

Johnson noise. If individually we have

$$\langle I_i^2 \rangle = 4k_B T_i / R_i, \tag{3.15}$$

the the sum is given by

$$\langle (I_1 + I_2)^2 \rangle = 4k_B \left(T_1/R_1 + T_2/R_2 \right). \tag{3.16}$$

Here, the weighting factor is the inverse resistance.

If we consider the sample as only uniform resistors in series, with a uniform 2D current density due to uniform resistivity, then ΔT_{avg} becomes simply a spatial average of the temperature:

$$\Delta T_{avg,JN} = \frac{P}{2\kappa LW} \frac{1}{L} \int_0^L x(L-x)dx \tag{3.17}$$

$$= \frac{PL}{12\kappa W}. \tag{3.18}$$

If we define a sample Lorenz number $\mathcal{L}$ via $\kappa = \mathcal{L} T_0 \sigma$, and rewrite in terms of the resistance R, we obtain

$$\Delta T_{avg,JN} = \frac{V^2}{12\mathcal{L}T_0}. \tag{3.19}$$

This gives us a convenient way to measure κ and compute the Lorenz number. We note that the factor of 12 in Eq. 3.19 has been well-known for decades[1,94–98,159–161].

We can define a thermal conductance specifically analogous to the 2-terminal electri-

cal conductance via

$$G_{th} = \frac{G_{th,gen}}{12} \tag{3.20}$$

that then allows us to write the Lorenz ratio as

$$\frac{\mathcal{L}}{\mathcal{L}_0} = \frac{1}{\mathcal{L}_0 T_0} \times \frac{G_{th}}{G_{el}} = \frac{1}{\mathcal{L}_0 T_0} \times \frac{\kappa}{\sigma}, \tag{3.21}$$

allowing us to express the Lorenz ratio as a ratio of the thermal to electrical conductances, or conductivities, in the same way.

We can see from Eq. 3.19 that the temperature rise of a sample can be related to just the voltage bias and Lorenz ratio, independent of the resistance. Thus, if we apply a constant fixed voltage bias V to a sample, then we can directly read off the Lorenz number $\mathcal{L}$ from the measured temperature rise, without needing to know what the current or resistance is.

Surprisingly, Eq. 3.19 applies to a much broader set of constraints than we originally described. More generally, for an arbitrary 2-terminal geometry, such as that shown in Fig. 3.2, the Johnson noise is related to the temperature $T(\vec{\mathbf{r}})$ via[162–165]

$$T_{avg,JN} = \frac{\int d^2\vec{\mathbf{r}}\, T(\vec{\mathbf{r}}) \vec{\nabla}\phi(\vec{\mathbf{r}}) \cdot \left[\hat{\sigma}\vec{\nabla}\phi(\vec{\mathbf{r}})\right]}{\int d^2\vec{\mathbf{r}}\, \vec{\nabla}\phi(\vec{\mathbf{r}}) \cdot \left[\hat{\sigma}\vec{\nabla}\phi(\vec{\mathbf{r}})\right]}, \tag{3.22}$$

where $\phi(\vec{\mathbf{r}})$ is a characteristic potential defined in Refs.[163,164]. In fact, as long as we have the thermal conductivity tensor proportional to the electrical conductivity tensor via $\hat{\kappa} = \mathcal{L}T_0\hat{\sigma}$, the temperature rise measured by Johnson noise for any arbitrary two

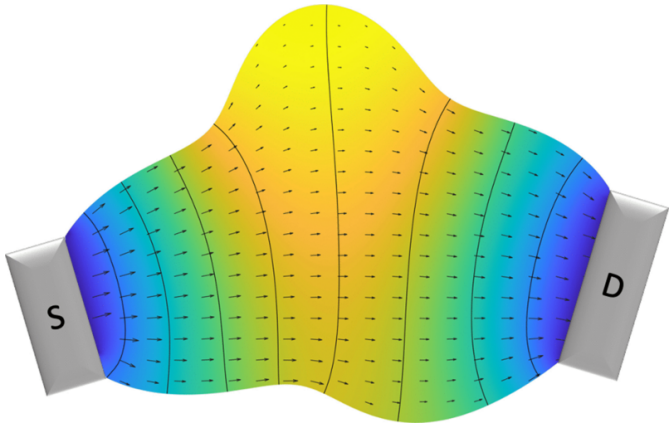

Figure 3.2: A schematic showing an arbitrary geometry for a conductive sample connected to two electrodes, source (S) and drain (D). The contour lines and arrows indicate equipotential surfaces and the gradient of the potential. The color represents an arbitrary temperature distribution. Image from Ref. 162.

terminal device in the weak self-heating limit is universally given by[162]

$$\Delta T_{avg,JN} = \frac{V^2}{12\mathcal{L}T_0}, \tag{3.23}$$

the same Eq. 3.19.

3.3 Self-Heating in a Magnetic Field

Upon application of a magnetic field, previously isotropic transport coefficients κ, σ become tensors. In practice, Eq. 3.23 breaks down in a magnetic field, as we can no longer relate $\hat{\kappa}$ and $\hat{\sigma}$ via a scalar C as $\hat{\kappa} = C\hat{\sigma}$[166]. If we wish to obtain a measurement of the longitudinal component κ_{xx}, then we must find some other symmetries by which to simplify the problem. Due to the rotational nature of the magnetic component of the Lorentz force on a moving charge, a natural geometry for symmetry is the Corbino geometry. The Corbino geometry[78], as shown in Fig. 3.3, places an annular sample

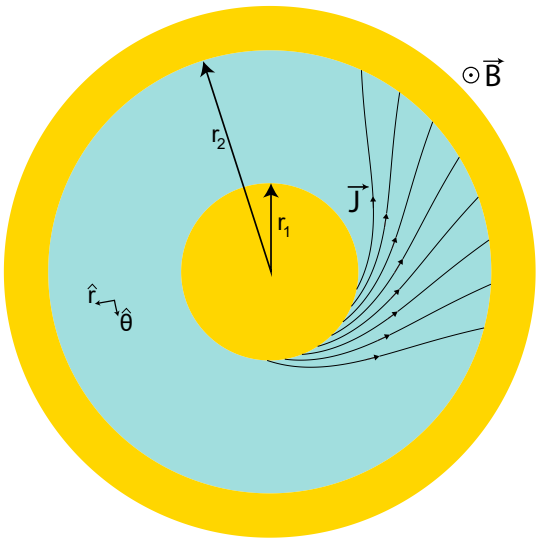

Figure 3.3: Schematic of a 2D Corbino device. The magnetic field points perpendicular the plane. The dark cyan is the sample (graphene). The gold color represents the metal contacts. Some of the current streamlines are shown with a $\vec{J}$. Inner and outer radii r_1, r_2 are marked. The polar coordinate system (r, θ) is also indicated.

concentrically between an inner circular electrode and an outer annular electrode, removing any sample boundaries connecting the two electrodes, and it allows current to flow radially between the two electrodes. In a magnetic field, the Lorentz force produces a rotational component of current, J_θ.

Electrically, a 2-terminal resistance measurement of an isotropic sample in the Corbino geometry provides a result for $\sigma_{xx} = \sigma_{rr}$, in contrast to a Hall bar geometry, which measures a combination of σ_{xx} and σ_{xy}. This can be seen by the following argument. In steady-state conditions and due to single-valuedness of the electric potential ϕ, the azimuthal component of the electric field E_θ must be zero. This immediately leads to the equation $J_r = \sigma_{rr} E_r$, and the rotational electrical current J_θ is irrelevant.

The 2-terminal resistance of a 2D Corbino device may be written as

$$R = \frac{1}{\sigma_{xx}} \int_{r_1}^{r_2} \frac{dr}{2\pi r} = \frac{1}{2\pi\sigma_{xx}} \ln \frac{r_2}{r_1}, \tag{3.24}$$

where r_1, r_2 are the inner and outer radii of the sample between the electrodes.

We now return to the heat equation for the Corbino geometry. The local Joule heating power will be of the form

$$\mathcal{P} = \vec{J} \cdot \vec{E} = J_r E_r \tag{3.25}$$

due to the absence of azimuthal electric field ($E_\theta = 0$). We note that the azimuthal component of the electrical current generates no Joule heating due to absence of azimuthal electric field. By current conservation, we must have $J_r = \dfrac{I}{2\pi r} = nq\vec{v}$ in relation to the total current I. The steady state equation of motion for a unit of current with charge q and mass m is given by

$$-\gamma\vec{v} = \frac{q}{m}(\vec{E} + \vec{v} \times \vec{B}), \tag{3.26}$$

where γ is a current relaxation rate and $\vec{v}$ is the velocity. We can write the $\hat{r}$ and $\hat{\theta}$ components of this equation as

$$(\hat{r}) \ : \ -\gamma v_r + \frac{q}{m}(E_r + v_\theta B_z) = 0 \tag{3.27}$$

$$(\hat{\theta}) \ : \ -\gamma v_\theta - v_r B_z = 0. \tag{3.28}$$

From this we obtain

$$v_\theta = -\frac{v_r B_z}{\gamma}. \tag{3.29}$$

If we define $\mu = e/(m\gamma)$ and $\sigma_0 = ne\mu$, then the solution to Eq. 3.26 becomes

$$E_r = \frac{1}{\sigma_0}\frac{I}{2\pi r}\left(1 + (\mu B)^2\right), \tag{3.30}$$

and we can express the local Joule heating power as

$$\mathcal{P} = \frac{1}{\sigma_0}\left(\frac{I}{2\pi r}\right)^2\left(1 + (\mu B)^2\right). \tag{3.31}$$

The potential drop across the electrodes is the integral of Eq. 3.30. From this, we explicitly calculate the resistance and the longitudinal conductivity:

$$R(B) = \frac{1}{2\pi\sigma_0}\ln\left(\frac{r_2}{r_1}\right)\left(1 + (\mu B)^2\right) \tag{3.32}$$

$$\sigma_{rr}(B) = \frac{1}{\sigma_0\left(1 + (\mu B)^2\right)}. \tag{3.33}$$

A geometrically intuitive explanation for the magnetoresistance is given in Appendix D.

Given the heating profile, we must now solve the heat equation. By rotational symmetry, there must be no thermal gradient in the azimuthal direction; we do not exclude a thermal current in the azimuthal direction, but it will be irrelevant for our calculations since it does not contribute to any temperature changes. We thus consider only the thermal current and temperature along the radial direction, reducing the problem

to 1D. The heat equation (Eq. 3.10), now in polar coordinates, becomes

$$\frac{1}{\sigma_{rr}}\left(\frac{I}{2\pi r}\right)^2 = -\kappa_{rr}\frac{d^2T}{dr^2} - \kappa_{rr}\frac{1}{r}\frac{dT}{dr}. \tag{3.34}$$

This solution is given by[59]

$$T - T_0 = \frac{1}{\kappa_{rr}}\frac{1}{\sigma_{rr}}\frac{I^2}{(2\pi)^2}\frac{1}{2}\ln\frac{r}{r_1}\ln\frac{r_2}{r}. \tag{3.35}$$

Written in this form, the boundary conditions of $T = T_0$ are easily seen to be satisfied at $r = r_1, r_2$. To find the measured Johnson noise temperature, we apply Eq. 3.22. The characteristic potential will be given by $\vec{\nabla}\phi(\vec{\mathbf{r}}) \propto 1/r$. Then Eq. 3.22 simplifies to

$$T_{avg,JN} = \frac{\int \frac{T(r)}{r}dr}{\int \frac{dr}{r}} = \frac{1}{\ln\frac{r_2}{r_1}}\int \frac{T(r)}{r}dr. \tag{3.36}$$

Upon integration, we get

$$T_{avg,JN} = \frac{V^2\sigma_{rr}}{12\kappa_{xx}} = \frac{V^2}{12\mathcal{L}_{rr}T_0}, \tag{3.37}$$

which is again Eq. 3.19.

To summarize, we have shown that in a Corbino geometry, even if the assumption $\hat{\kappa} = C\hat{\sigma}$ breaks down, due to symmetry, we are still able to measure κ_{rr}, σ_{rr}, and $\mathcal{L}_{rr}$, which would be impossible in a rectangle geometry due to the lack of proper symmetries.

3.4 Self-Heating: High-T limit

So far, we have been working in the low-heating limit such that $\Delta T \ll T_0$, which allows us to assume that κ is spatially homogeneous. However, we may consider the case where the heating is strong, and we have $\Delta T \sim T_0$ or even $\Delta T \gg T_0$. Since the thermal conductivity κ is generally proportional to temperature and will not be homogeneous, we must now use the full heat equation, Eq. 3.2, and we can not measure κ anymore, since it will take on a large range of values; the best we can do is measure $G_{th,gen}$.

We will not be able to compare the measured G_{th} with any particular value or compute any Lorenz ratio, since again these quantities only make sense for a single uniform temperature. In terms of analysis, it will be more instructive to examine ΔT as a function of the Joule power P. Furthermore, since we will be exiting the "linear" response heating regime, it will no longer make sense to perform the measurement in an AC-modulated fashion, so we must apply the Joule power P at DC and measure the noise also at DC. In doing this, we must also measure the differential resistance to correctly measure the impedance matching; see Section 4.9 for more details.

If we make the simple assumption that the thermal conductivity is proportional to the temperature, which is essentially a modified WF law with any allowed Lorenz number $\mathcal{L}$, then we can derive what we would expect to see for the T_{avg} vs P dependence. Let us then begin with Eq. 3.2 in the steady state:

$$0 = \mathcal{L}\sigma_0 \vec{\nabla} \cdot (T\vec{\nabla}T) + \mathcal{P}, \tag{3.38}$$

where, for simplicity, we have assumed the conductivity is a constant σ_0. Let us simplify

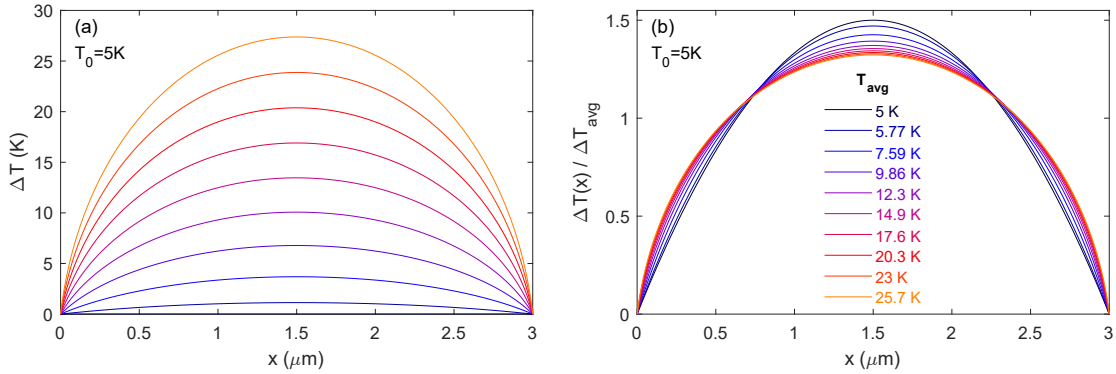

Figure 3.4: **(a)** Temperature rise profiles for a range of heating powers: low-power (dark blue) to high-power (orange), for a bath temperature of $T_0 = 5\,\mathrm{K}$. Legend is in panel (b). **(b)** Temperature profiles in (a), normalized by the average temperature rise ΔT_{avg}.

this equation to a 1D heat equation:

$$0 = \mathcal{L}\sigma_0 \frac{d}{dx}\left(T\frac{dT}{dx}\right) + \mathcal{P} \tag{3.39}$$

$$0 = \mathcal{L}\sigma_0 \left(\left(\frac{dT}{dx}\right)^2 + T\frac{d^2T}{dx^2}\right) + \mathcal{P}. \tag{3.40}$$

The exact solution is given by[167–169]

$$T(x) = \sqrt{T_0^2 + \frac{V^2}{\mathcal{L}}\frac{x}{L}\left(1 - \frac{x}{L}\right)}. \tag{3.41}$$

We verify by inspection that in the low-heating limit, Eq. 3.41 reduces to Eq. 3.12. The shape of Eq. 3.41 for low and high heating power is shown in Fig. 3.4. We can integrate Eq. 3.41 to obtain the average temperature measured by Johnson noise[168,170]:

$$T_{avg} = \frac{T_0}{2}\left[1 + \left(\frac{\sqrt{3}eV}{2\pi k_B T} + \frac{2\pi k_B T}{\sqrt{3}eV}\right)\cdot \arctan\left(\frac{\sqrt{3}eV}{2\pi k_B T}\right)\right], \tag{3.42}$$

which we plot in Fig. 3.5(a) as a function of applied bias, assuming $\mathcal{L} = \mathcal{L}_0$. At low

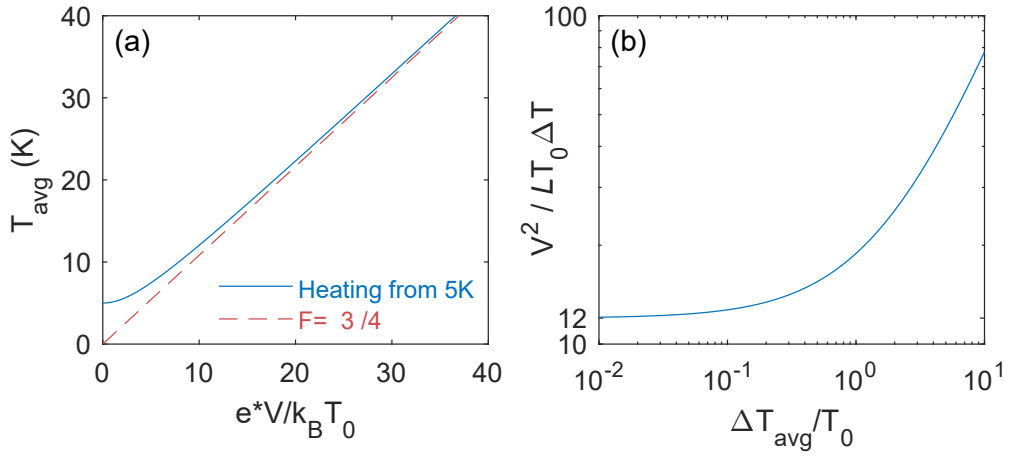

Figure 3.5: **(a)** Blue: Average electron temperature for self-heating from $T_0 = 5\,\mathrm{K}$ in the high-bias regime (Eq. 3.42). Red: Shot noise with Fano factor $F = \sqrt{3}/4$. **(b)** The evolution of the geometric ratio $V^2/\mathcal{L}T_0\Delta T$ from Eq. 3.19, as heating is increased past the low-heating limit.

bias, the temperature rise (blue) is quadratic, but at high bias, the temperature rise approaches the linear shot noise limit with Fano factor $F = \sqrt{3}/4$. We note that this is a significantly reduced Fano factor compared to $F = 1$ for a tunnel junction (see Subsection 4.5.1), but slightly larger than $F = 1/3$ for non-interacting diffusive transport[170,171]. In one sense, this noise is not real "shot" noise since it does not originate from stochastic Poissonian tunneling events; however, there is no true distinction between thermal noise and shot noise, as they are ultimately correlators of the fluctuations of a system under certain conditions[172].

It is enlightening to see the correspondence of $\mathcal{L} = \mathcal{L}_0 \iff F = \sqrt{3}/4$. A mesoscopic system that obeys the WF law for all temperatures, and has electrons with a well-defined temperature due to strong enough interactions, will exhibit a Fano factor of $F = \sqrt{3}/4$[170]. If, however, the system has a different Lorenz number, then it would deviate from $F = \sqrt{3}/4$, presenting another way of probing WF breakdowns outside of the weak-heating limit. In practice, for a hydrodynamic system, we would expect the

Lorenz number to have a temperature dependence, and thus such an experiment would likely not yield an exactly linear regime.

Fig. 3.5(b) shows the behavior of the geometric ratio $\frac{V^2}{\mathcal{L}T_0\Delta T}$ from Eq. 3.19, where it was equal to 12 in the low-heating limit, as a function of the average electron temperature normalized by the bath temperature. With increasing bias and heating, this factor grows very strongly, primarily because the T_0 used in Eq. 3.19 is no longer a good approximate representation of the average electron temperature to use for the WF law.

3.5 Effects of Phonons: Cooling and Scattering

In the simplest picture of electron-phonon scattering, the electron emits or absorbs a phonon, rather than interacting with a pre-existing phonon[54]. Thus, the primary mechanisms for both resistivity and heat loss to phonons arise from the same scattering process. In principle, if the deformation potential, temperature, and relevant kinetic constraints and dispersions are well known, a measurement of the electrical resistivity due to phonons could be related to the electron-phonon thermal coupling, and one could convert between the two quantities. In practice, these quantities must be empirically measured for each sample due to absence of accurate knowledge of the relevant constants and kinematic constraints.

In the absence of electronic diffusion cooling described in Section 3.2, but in the presence of phonon cooling, the sample will experience a uniform temperature rise upon Joule heating. This is a trivial limiting case, but can be useful in measuring the available electron-phonon cooling power[94–96,152] and calculating the electron-phonon coupling constants, helping to understand problems such as phonon-mediated superconductivity.

For the purposes of measurement electronic thermal conductivity, we are more interested in the parasitic effect that the additional phonon cooling channel will have on measuring the electronic thermal conductivity. In the simplest way, we could write the total cooling power of both the phonon cooling and electronic diffusion cooling as the arithmetic sum

$$G_{th,total} = G_{th,electronic} + G_{th,phonon}, \tag{3·43}$$

but this is not exact due to the different spatial profile temperatures of the two effects.

The exact solution would be a solution of the modified heat equation to include phonon cooling. For this, we work in the linearized regime of Eq. 3.5 for small temperature difference $\Delta T = T_e - T_{ac} << T_e$:

$$Q_{e-ac} \approx V_d \Sigma \delta \cdot \Delta T \cdot T_e^{\delta-1}. \equiv G_{e-ph} \Delta T \tag{3·44}$$

The heat equation becomes

$$\mathcal{P} = -\kappa \frac{d^2(\Delta T))}{dx^2} + G_{e-ph}\Delta T \tag{3·45}$$

and the temperature profile is

$$\Delta T(x) = P \frac{1 - \cosh\left[\sqrt{G_{e-ph}/\kappa} \cdot \frac{L-2x}{2}\right] \cdot \operatorname{sech}\left[\sqrt{G_{e-ph}/\kappa} \cdot \frac{L}{2}\right]}{G_{e-ph}}. \tag{3·46}$$

This temperature profile is plotted in Fig. 3.6. The resulting equation for the average

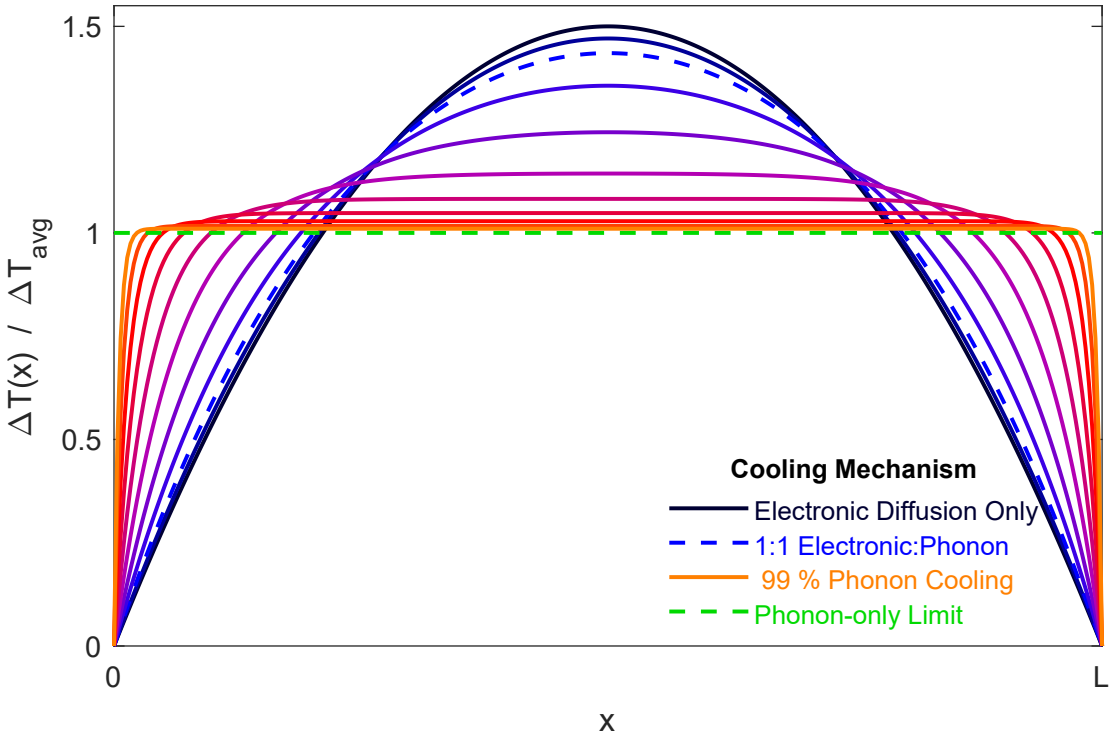

Figure 3.6: Temperature profile for the crossover between electronic cooling to phonon cooling, normalized by the average temperature rise. The fully electronic diffusion cooling power temperature profile is an exact parabola (solid dark blue). When the individual electronic and phonon contributions are equal, the result shape is also nearly a parabola (dashed blue line). When phonon cooling dominates (orange) the shape approaches a mesa (green dashed line).

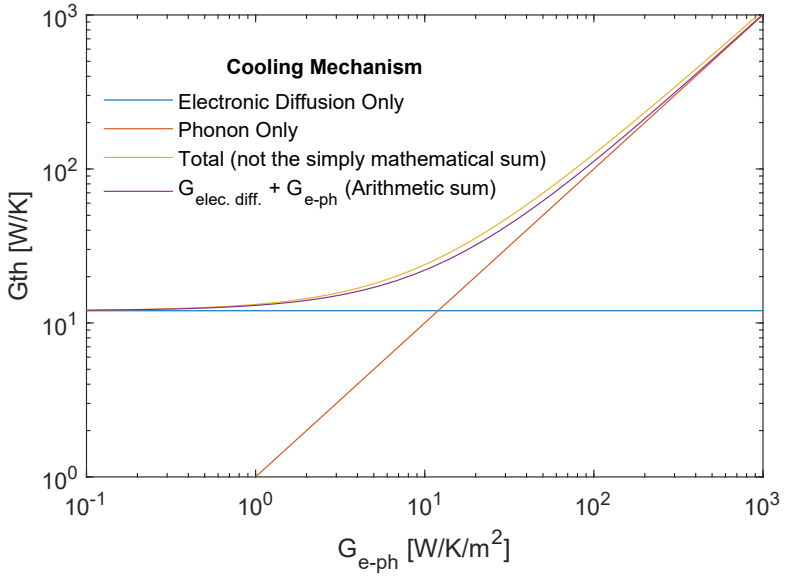

Figure 3.7: Blue: Constant electronic diffusion cooling. Red: Cooling power, if only the phonon contribution is present. Yellow: total cooling power, due to geometric combination of electronic and phonon (Eq. 3.48). Purple: arithmetic sum contribution of electronic and phonon cooling contributions (Eq. 3.43).

temperature rise is

$$\Delta T_{avg} = \frac{\mathcal{P}}{G_{e-ph}} - 2\mathcal{P}\sqrt{\kappa}\frac{\tanh\left[\sqrt{G_{e-ph}/\kappa}\cdot\frac{L}{2}\right]}{G_{e-ph}^{3/2}\cdot L}, \tag{3.47}$$

and the resulting total thermal conductance is

$$G_{th,total} = \frac{\mathcal{P}LW}{\Delta T_{avg}} = \left[\frac{1}{G_{e-ph}LW} - 2\sqrt{\kappa}\frac{\tanh\left[\sqrt{G_{e-ph}/\kappa}\cdot\frac{L}{2}\right]}{G_{e-ph}^{3/2}\cdot L^2 W}\right]^{-1}. \tag{3.48}$$

This formula for the total thermal conductance is plotted in Fig. 3.7 as the yellow curve. The purple curve indicates what we would get if we simply arithmetically added the individual electronic and phonon cooling contributions, but this does not quite match

Eq. 3.48. In the crossover regime, the total is slightly higher than the arithmetic sum; furthermore, even when phonon cooling strongly dominates, the electronic contribution slightly amplifiers the phonon cooling power. The blue dashed curve in Fig. 3.6 corresponds to the point in Fig. 3.7 where the blue and red curves (electronic only, and phonon only) contributions intersect.

Nonetheless, as seen from Fig. 3.7, Eq. 3.43 is a rather close approximation to Eq. 3.48, and can give us insight into the different cooling regimes. Let us rewrite Eq. 3.43 as a function of the sample parameters:

$$G_{th,total} \approx \frac{12\kappa W}{L} + G_{e-ph} \cdot LW. \tag{3.49}$$

We see that the electronic contribution to the thermal conductance scales as $\propto 1/L$, and the phonon cooling contribution scales as the sample area, so $\propto L$. We can immediately see that a shorter sample will have a stronger electronic contribution and a weaker phonon contribution compared to a longer sample, if all else is equal. Unfortunately, due to the dominance of contact resistance and ballistic effects (see Section 3.7) in short channels, we cannot make the channel length arbitrarily small, and thus we will likely always have a phonon crossover temperature.

3.6 Discerning Electronic Diffusion from Phonon Cooling

Experimentally with a single measurement of G_{th}, it is impossible to determine whether phonon cooling or electronic diffusion cooling dominates, since we do not know the exact temperature profile. To determine which regime are in, we need additional data.

One way to potentially understand which regime a particular sample is in, is to look at the power law scaling of G_{th} with T. In the WF regime at low-T, the scaling law will

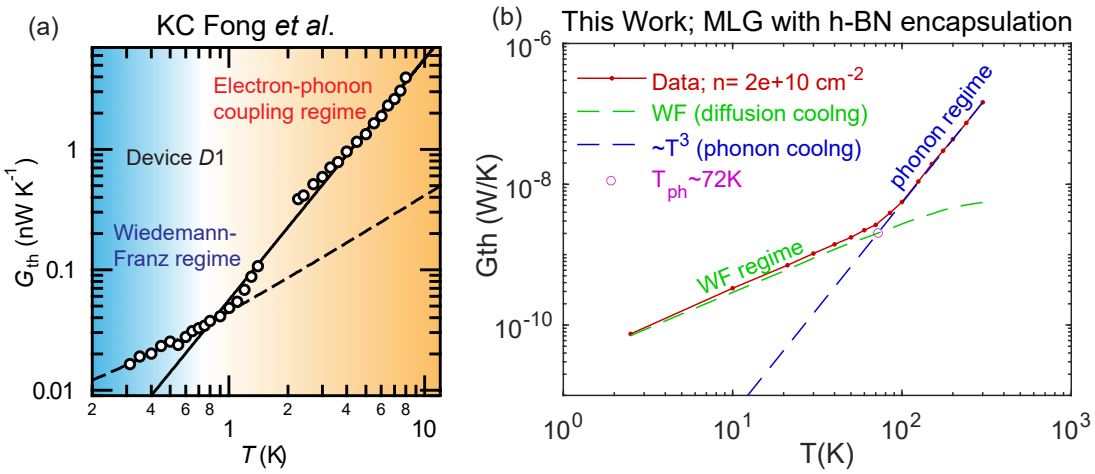

Figure 3.8: **(a)** Figure from Ref. 95. White circles are the data for G_{th}. They transision from $\propto T$ at low temperature, following the WF law, to a higher power scaling. The device is unencapsulated MLG with a channel length $L = 15\,\mu$m and has a low phonon crossover temperature of $\sim 9\,$K. **(b)** MLG encapsulated in h-BN device from this work, with a channel length of $L \sim 8\,\mu$m. Red dots (data) follow the WF regime (green dashed line) for low temperature, until around 72 K (magenta circle) they transition to an exact $\propto T^3$ power scaling law (blue dashed line).

be linear; at high-T where phonon cooling dominates, the scaling law will be higher, typically $\sim T^3$ or higher for a 2D system. Two examples of this are shown in Fig. 3.8. Panel (a) shows data on an unencapsulated MLG device with channel length $15\,\mu$m from Ref. 95, and panel (b) shows data from this thesis work, on an h-BN-encapsulated MLG device with channel length $8\,\mu$m. The longer device in panel (a) has a phonon crossover temperature of about 9 K corresponding to acoustic phonons, and the device from this work has a crossover of about 72 K, likely corresponding to optical phonons[96]. While not a direct comparison, in general the electron-phonon coupling seems to be weaker in encapsulated graphene than unencapsulated graphene.

A more advanced method we have developed during this work is a simultaneous multi-channel measurement of the thermal conductance, motivated by Eq. 3.49. If electronic diffusion cooling is the dominant mechanism in both samples, then the thermal

conductance should scale as $\propto 1/L$ among the two samples. Conversely, if phonon cooling is the dominant mechanism in both samples, then the thermal conductance should scale as $\propto L$ among the two samples. In an intermediate crossover regime where both cooling mechanisms are active, we will have approximately equal G_{th} in the two devices. In this way, we can determine which cooling regime we are in without having to study the T-scaling behavior.

Fig. 3.9 demonstrates this technique applied to an MLG sample (see also Subsection 5.5.3). We show the thermal conductance data for a short (solid line and dot) and long (dashed line) channel, keeping the width of the channels identical, on a log-log plot. For ease of viewing, we shift the different densities (colors) upwards, but for a given density, the short and long channel thermal conductances are directly comparable. At low temperatures where electronic diffusion dominates, we expect the short channel thermal conductance to be $L_{long}/L_{short} = 8/3 = 2.67$ times larger; in reality, it is approximately only a factor of 2 larger, possibly due to the different effects of contact resistance for the two channel lengths. As we increase temperature, for all densities, the long channel thermal conductance gets closer to the cold channel thermal conductance, and at some point becomes larger. The crossover point, which is the characteristic phonon crossover point, is marked with pink circles. At lower densities near charge neutrality, the crossover temperature is about 110–120 K, and at high densities the crossover temperature increases to about 250 K. At the crossover temperature, the diffusion cooling in the short channel is stronger than the phonon cooling, but in the long channel it is reversed. Thus, the thermal conductance data for the short channel is representative of the electronic contribution until approximately this crossover point, a certain point beyond which phonon cooling dominates in both channel lengths.

We can see that in the short channel at high density, we do not reach the high $\sim T^3$

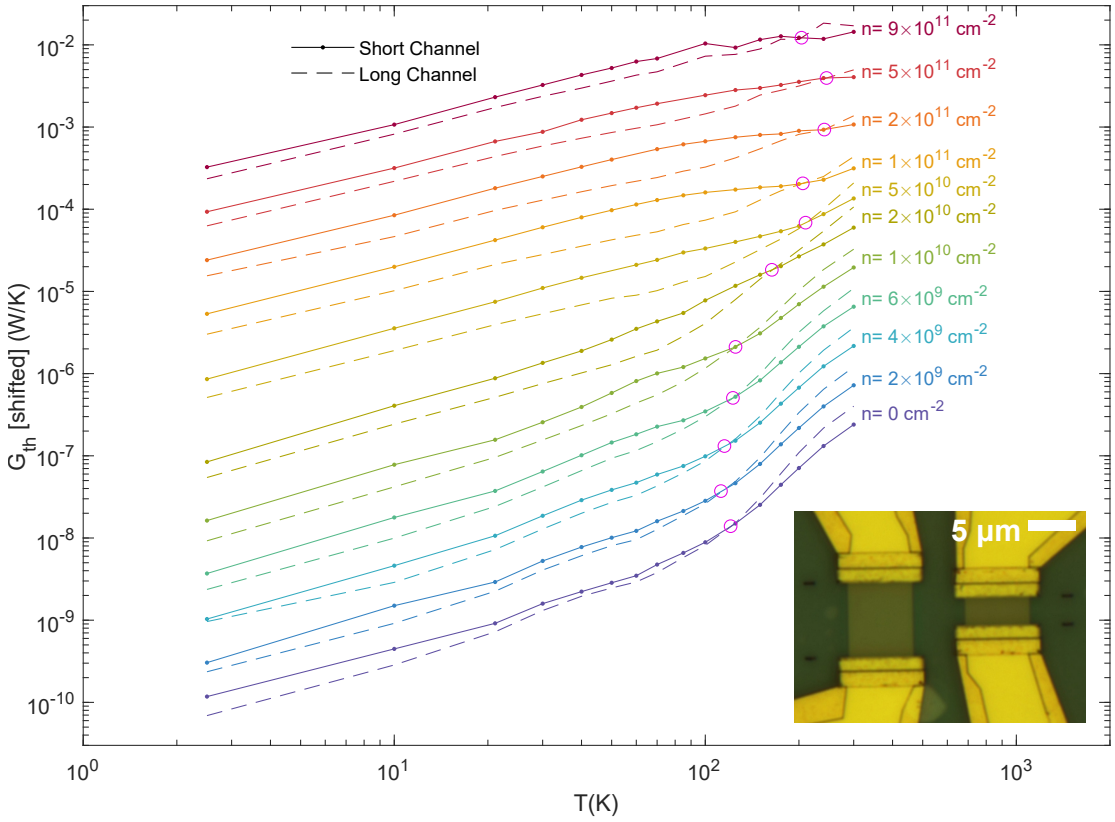

Figure 3.9: Comparison of short channel (dot and solid line) vs long channel (dashed line) G_{th} vs temperature, for a MLG sample. Different colors represent different electron densities, and for each density the data is shifted upwards on the vertical scale to offset them for visualization. For a given density, the thermal conductances are not shifted relative to each other and are directly comparable. Pink circles indicate where thermal conductance of the short channels equals that of the long channel. Inset: optical micrograph of the device; the two channel lengths are $3\,\mu$m and $8\,\mu$m. The channel width is $7\,\mu$m for both channels.

power law within the measured dataset up to 300 K. This is an indication that in monolayer graphene, especially at high density, the electron-phonon coupling is weak. This method extends the validity of the electronic thermal conductance measurement far above the 120 K limit measured in Ref. 96.

We can apply the same technique for BLG, for which we show data in Fig. 3.10 (see also Subsection 5.6.2), analogously to MLG. For BLG, we see that the phonon crossover temperature is significantly lower; approximately 7–10 K for low densities, and 10–20 K for high densities. For the highest three densities, the crossover points are not well-defined as the thermal conductances are nearly equal between the short and long channels for a wide range of temperature, and the circles thus mark approximately where they first become equal. Compared to the MLG sample, this BLG sample has slightly shorter channel lengths, which would cause a higher phonon crossover temperature, if all else is equal. There is an interesting feature in the data, where the low-T power law slows down around 40–80 K, and then resumes a higher power law above ~ 200 K. We will return to this feature in Chapter 5.

It is important for this method for the two devices to be fabricated out of the same vdW heterostructure, preferably as adjacent to each other as possible. Additionally, the contact resistance should be low (see the next Section); if the contact resistance significantly affects the measurement of G_{th}, then due to the different contact resistance fraction for each device, it will affect each device differently, corrupting the quantitative G_{th} scaling test. However, this multi-channel measurement provides the opportunity to calculate the contact resistance via a transfer-length method (TLM)[15,22,173].

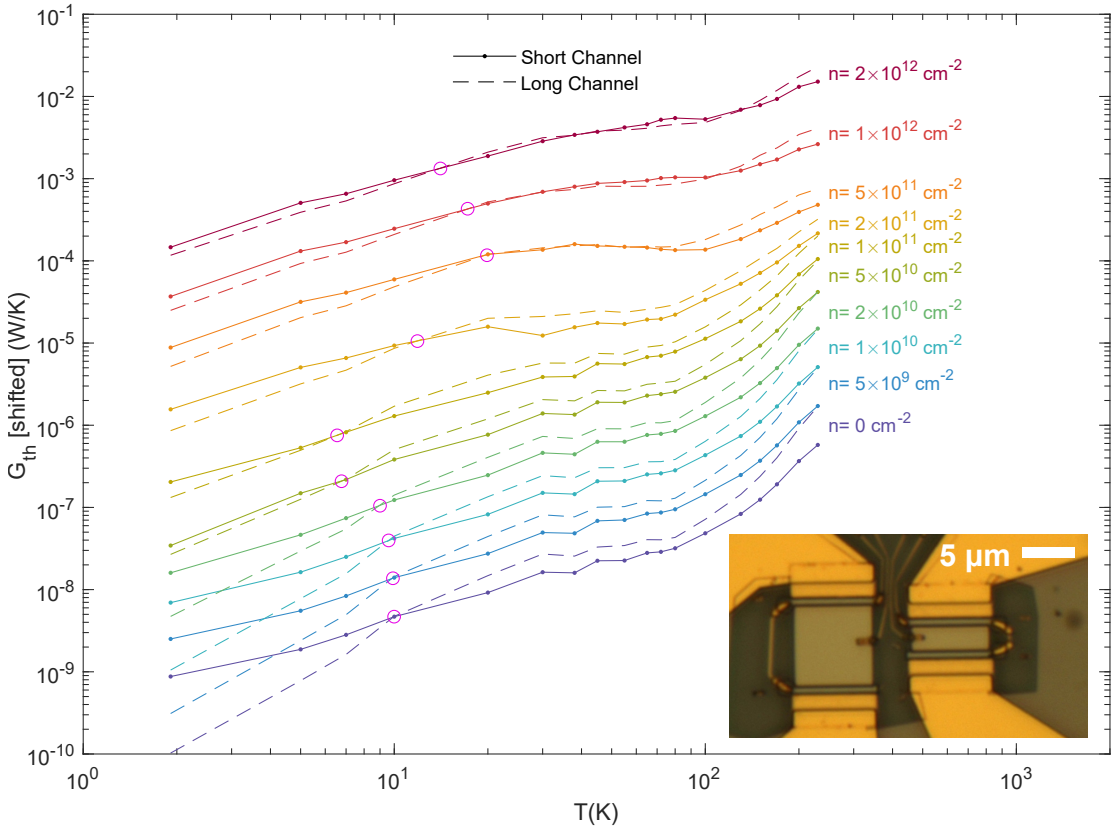

Figure 3.10: Comparison of short channel (dot and solid line) vs long channel (dashed line) G_{th} vs temperature, for a BLG sample. Different colors represent different electron densities, and for each density the data is shifted upwards on the vertical scale to offset them for visualization. For a given density, the thermal conductances are not shifted relative to each other and are directly comparable. Pink circles indicate where thermal conductance of the short channels equals that of the long channel; for the highest three densities, the thermal conductances are nearly equal for a wide temperature range, and the circles indicate the lowest temperature where they become equal. Inset: optical micrograph of the device; the two channel lengths are 2.5 μm and 7.5 μm. The channel width is 7 μm for both channels.

3.7 Effects of Contact Resistance

So far in our calculations, we have been assuming the contact resistance of samples is zero. In the case of superconducting contacts, this will be true; however, superconducting contacts will not provide an electronic heat sink to the electrons in the graphene, as superconductors have zero electronic thermal conductivity. In this case, all the heat generated in the sample by Joule heating will be transferred to the phonons. Moreover, superconducting contacts are typically not useful for studying the hydrodynamic regime, which occurs at temperatures far above the T_c of the superconductors used for contacts. Nonetheless, superconducting contacts may be useful in a nonlocal heating implementation[174] for measuring thermal conductance, a method that we propose in Subsection 7.2.6.

With realistic contacts to graphene made from Cr/Pd/Au, using CHF_3-based[15] or XeF_2+Si-based[22] etching chemistry, there is not an insignificant amount of contact resistance that we must consider. The simplest model of the effect of contact resistance on thermal conductivity measurements in the self-heating experiment was developed in Ref. 169, which we summarize here. The model assumes the channel of the graphene sample to be a resistor R_s and each contact to be a resistor R_c of spatial length l_c in series with the main channel, as shown in Fig. 3.11(a). When current flows through the sample, both the channel and the contact resistors experience Joule heating and temperature gradients. Fig. 3.11(b) shows the resulting temperature gradients for three different sample Lorenz ratios $\tilde{\mathcal{L}} = \mathcal{L}/\mathcal{L}_0$. As the Lorenz ratio increases above 1, most of the temperature rise in the channel happens due to the temperature drop across the contact resistors rather than the sample itself; in contrast, with no contact resistance, we expect the relative temperature rise in the sample to go to zero as the Lorenz

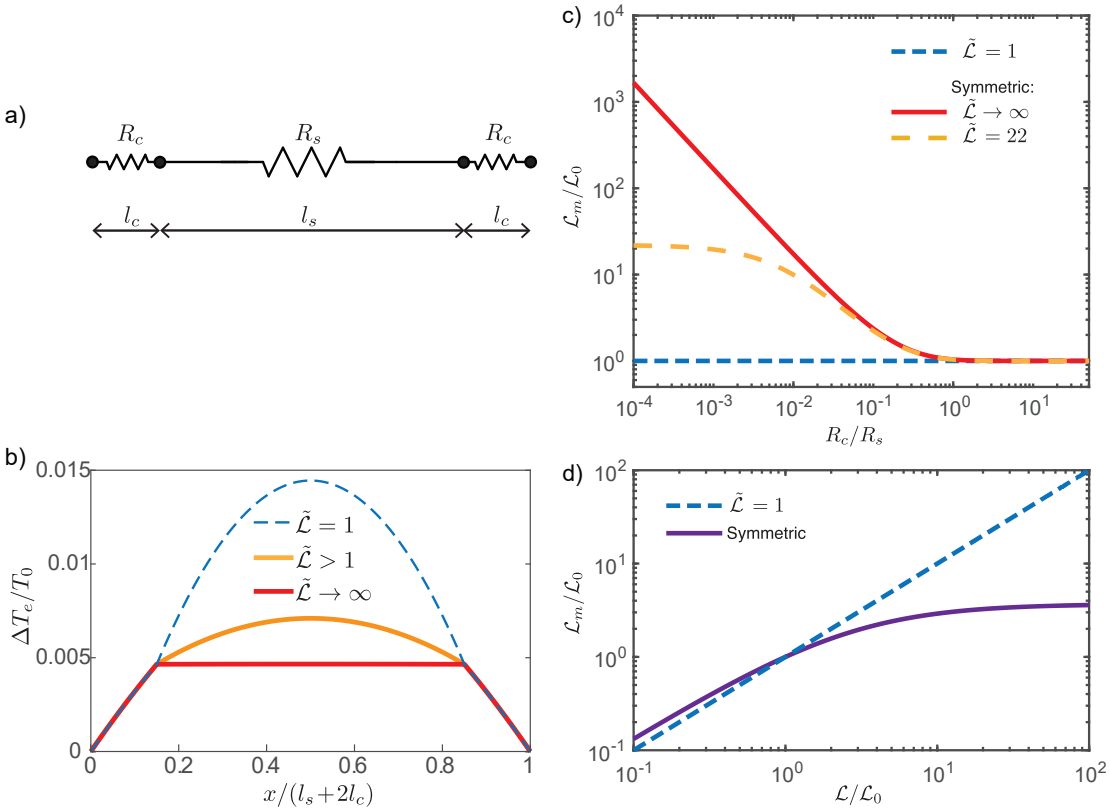

Figure 3.11: **(a)** Model of the contact resistance. R_s is the channel resistance of length l_s, and each contact resistance is modeled as a resistor R_c with spatial length l_c. The contact resistors follow the WF law. **(b)** Spatial temperature profile with contact resistances $R_c/R_s = 0.5$, for three different sample Lorenz ratios $\tilde{\mathcal{L}}$. **(c)** Measured Lorenz ratio as a function of $R_c/R_s = 0.5$, for three different sample Lorenz ratios. **(d)** Measured Lorenz ratio as a function of real sample Lorenz ratio, assuming $2R_c/(R_s + 2R_c) = 0.1$. Figure adapted from Ref. 169.

ratio goes to ∞. Thus, we will still measure an increase in noise, at a minimum of the temperature drop across the contact resistors, even for high thermal conductivity, experimentally limiting the highest measurable Lorenz ratio.

Fig. 3.11(c) shows the effect of the measured Lorenz ratio as the contact resistane fraction is varied, for three sample Lorenz ratios. For low contact resistance, the measured Lorenz ratio trends toward the true Lorenz ratio, and for high contact resistance, the measured Lorenz ratio trends towards 1. Panel (d) shows the measured Lorenz ratio, when the contact resistance is 10% of the measured resistance, as a function of the true Lorenz ratio. For true sample Lorenz ratios much below 1, most of the heating in the channel will happen as a temperature drop across the sample, and the contact resistors act as relatively good heat sinks for the boundaries of the sample, allowing a more accurate Lorenz ratio measurement than if the true sample Lorenz ratio is much larger than 1.

We can express the measured average temperature as a weighted sum of the average temperatures of the individual components:

$$T_{avg} = \frac{R_s T_{s,avg} + 2R_c T_{c,avg}}{R_s + 2R_c}, \tag{3.50}$$

where $T_{s,avg}$ and $T_{c,avg}$ are the spatially averaged temperatures of the contact resistances. Then, using a Joule power of $P = V^2/(R_s+2R_c)$, we can express the generalized thermal conductance as

$$G_{th,gen} = \frac{P}{\Delta T_{avg}} = \frac{V^2}{R_s \Delta T_{s,avg} + 2R_c \Delta T_{c,avg}}. \tag{3.51}$$

This model with spatially extended contact resistances, in the limit of $l_c \to 0$, is

equivalent to a point-like contact resistance with a discrete temperature drop ΔT_{cs} at the sample-metal interface, with the Joule power $I^2 R_c$ dissipated by the contact resistance being distributed equally on either side of the interface. The heat current flowing through the contact resistance is then $Q_c = \frac{1}{2} I^2 (R_s + R_c)$, and if we assume the contact resistance obeys the WF law, then the temperature drop across the sample-metal interface will be

$$\Delta T_{cs} = \frac{Q_c R_c}{\mathcal{L}_0 T_0}. \tag{3.52}$$

The effective bath temperature for the main channel now becomes $T_0 + \Delta T_{cs}$.

Experimentally, for devices that had significantly higher contact resistance due to a mistake in the fabrication process, we have observed both a strongly increased and a strongly suppressed Lorenz ratio, in contrast to the model above.

We thus conclude that the assumptions of the model above are incorrect, at least not for all types of contact resistances. One way we can improve the model is by relaxing the constraints of the contact resistors following the WF law, and/or the constraint that the Joule power dissipated in the point-like contact is equally distributed on each side of the interface. Mathematically, both of these assumptions only act to change ΔT_{cs}, although in slightly different ways. If we fix the contact Lorenz number and vary the distribution of the dissipated Joule power, this will lead to an upper bound of ΔT_{cs}; therefore, for more generality, we can assume that the dissipated Joule power is equally distributed on either side of the interface, but the Lorenz number of the contact $\mathcal{L}_c$ will no longer be fixed to $\mathcal{L}_0$.

With two unknown parameters, the Lorenz number of the sample $\mathcal{L}_s$ and the Lorenz number of the contact resistance $\mathcal{L}_c$, we need two independent measurements to gen-

erate two independent heating equations to solve for each unknown. We develop the mathematical procedure for this in Appendix C, and show applications and results of this technique in Chapter 5.

Another way to experimentally test the effect of contact resistance is with ballistic samples, where most or all of the measured resistance comes from the contact resistance. Graphene is easily made ballistic on a several-micron length scale at high density and low temperature, or in a quantum Hall regime with protected (ballistic) edge states connecting the two metal contacts. In both cases, experimentally we observe very high Lorenz ratios, meaning that for an applied Joule power, we see relatively very little heating of the device, consistent with measurements in Ref. 175.

This lack of heating is consistent with the mechanism for resistance in ballistic devices. In ballistic transport, electrons move through the sample channel without scattering, and they only scatter upon entering the metal contact. Thus, any dissipated Joule heat is located inside the metal contacts themselves, and not the sample channel. Because the metal is a very good heat sink with strong electron-phonon coupling (effectively $\mathcal{L}_c \to \infty$), the resulting temperature increase is very small.

3.8 Modifications for Viscous Heating Effects

In calculating the equations for self-heating, we have so far assumed uniform Joule heating in the sample due to locally Ohmic heating via $\mathcal{P} = \vec{J} \cdot \vec{E}$. However, in a hydrodynamic system, this changes, and the original equations are no longer valid.

In the absence of impurity or phonon scattering, momentum relaxation arises only from the edges of the sample or adjacent fluid elements with a differential velocity. In this way, the edges of a sample can non-locally relax the momentum of fluid elements

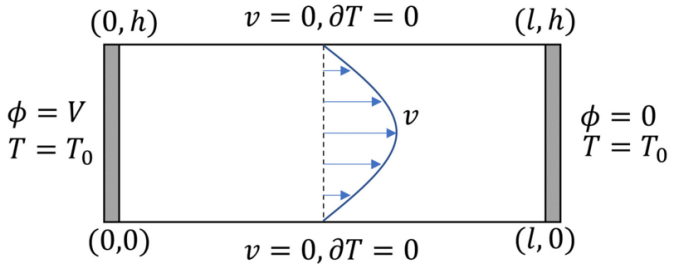

Figure 3.12: Viscous hydrodynamic flow through a sample. The white is the viscous sample, the gray rectangles at the left and right ends are the metal contacts, and the top and bottom is the sample edge. The flow velocity v profile, shown in blue, is parabolic. Image from Ref. 176.

far away in the interior via viscous drag through the intermediate fluid elements. The electrical transport becomes non-local, and the conductivity tensor $\hat{\sigma}$ is no longer well defined[176].

A simple hydrodynamic model of a fluid flowing through a pipe, or through a 2D rectangle, has no-slip boundary conditions along the edges, meaning the fluid elements directly adjacent to the edge have zero velocity, while fluid elements deeper in the sample can continue to flow. The resulting flow profile, known as Poiseuille flow, has a parabolic distribution for flow velocity across the sample[73,176,177] and is illustrated in Fig. 3.12.

Since the fluid at the edges is "stuck", it is not actively being scattered to generate heating, and instead local dissipation heating will arise from the viscous shearing of adjacent fluid elements.

The hydrodynamic stress tensor, which consists of gradients of velocities, will describe exactly the viscous heating profile. The stress tensor is given by

$$\sigma'_{i,j} = \eta \left(\partial_i v_j + \partial_j v_i \right) \tag{3.53}$$

for Cartesian coordinates, and by[59,178]

$$\sigma'_{rr} = 2\eta \partial_r v_r \tag{3.54}$$

$$\sigma'_{\theta\theta} = \frac{2\eta}{r}\left(\partial_\theta v_\theta + v_r\right) \tag{3.55}$$

$$\sigma'_{r\theta} = \eta\left(\frac{1}{r}\partial_\theta v_r + \partial_r v_\theta - \frac{v_\theta}{r}\right) \tag{3.56}$$

for polar coordinates. Here, η is the dynamic viscosity, and we can clearly see the action of velocity gradients. The corresponding dissipation heating power density is given by

$$\mathcal{P} = \sum_{i,j} \sigma'_{i,j} \partial_i v_j. \tag{3.57}$$

The larger velocity gradients near the edges of the sample will generate more viscous heating than the smaller gradients near the middle of the sample; thus, the heating is now concentrated along the edges rather than uniformly distributed as we have previously considered. Ref. 176 calculates this in detail along with the resulting temperature profiles and measured Johnson noise for a rectangular sample. In Chapter 6, we develop the analogous theory and experiment for a Corbino device, for which the origin of viscous dissipation is more subtle due to the absence of any boundaries. Here, we present a summary of the rectangular case.

For a square sample with a 1:1 aspect ratio, the heating is more concentrated along the edges. The thermal conductivity $\hat{\kappa}$ is still a well defined quantity, and thus the heat will diffuse locally throughout the sample. Heat dissipated by the edges of the sample will diffuse towards the middle of the channel, which is colder due to less local heat dissipation, and towards the metal contact heat sinks. As a result, the temperature profile now has a saddle shape, as shown in Fig. 3.13(a).

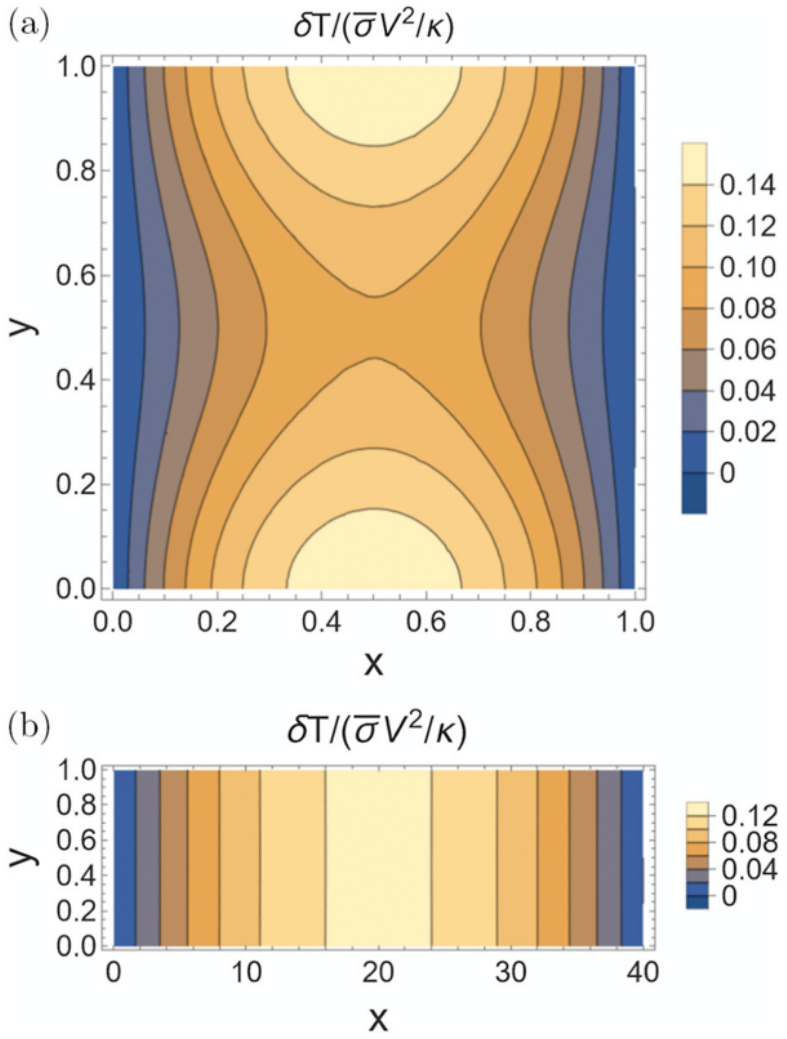

Figure 3.13: **(a)** Temperature profile for viscous heating in a square sample, with aspect ratio 1:1. The metal contacts are on the left and right boundaries of the sample. The resulting temperature profile has a saddle shape. **(b)** Temperature profile for a very low aspect ratio sample, that is much longer than it is wide. Heat diffuses much more quickly across the sample width that along to the contacts, and the temperature profile is nearly parabolic as in the non-viscous case. Image from Ref. 176.

Calculation of the Johnson noise temperature is not as straightforward anymore as applying Eq. 3.22, since the conductivity tensor is no longer well defined. The full mathematical formalism is complicated and developed in Ref. 176, based on the fluctuation-dissipation theorem and the Navier-Stokes equations. The results of the calculation show that due to the lower temperature in the center of the channel, the geometrical factor of 12 in Eq. 3.19 is modified, and the Lorenz number $\mathcal{L}$ becomes an effective Lorenz number defined only through the electrical conductance of the sample $G_{el} = 1/R$. For a square sample as in Fig. 3.13(a), the Johnson noise in self-heating is reduced by approximately 10%. For a high aspect ratio sample with a very short but wide channel, the maximum reduction in noise is approximately 40%, which would make the thermal conductivity appear 40% higher than the true value.

In the crossover regime between Ohmic and hydrodynamic flow where both are present, this correction factor now depends on l_G/h, where $l_G = \sqrt{\nu/\gamma}$ is a characteristic length scale[65–67,81,179], now known as the Gurzhi length, below which viscous effects are important; h is the width of the channel; γ is the dissipative Ohmic momentum relaxation rate; and ν is the kinematic viscosity. In a certain regime of $l_G/h \sim 0.1$, the correction can actually exceed 1 by a few percentage points. The Gurzhi length can be understood conceptually as follows: For a given γ, there is a distance far enough away from the sample boundary where the viscous forces acting on the fluid are weaker than the dissipative momentum relaxation forces, and the flow pattern follows an Ohmic flow, even though it may still be strongly hydrodynamic. As a concrete example, in the limit of a very wide rectangular sample with a flowing electron fluid, the flow velocity in the center will be limited by the weak Ohmic momentum relaxation, rather than viscous boundary effects, effectively flattening the parabolic velocity flow profile shown in Fig. 3.12.

In contrast, in the limit of a sample with a long and narrow channel, the factor of 12 is restored without any corrections. This can be seen from Fig. 3.13(b); here, the heat generated the boundaries diffuses much more easily across the sample due to the narrow width than it does along the length of the channel, effectively rendering the problem into solving the original 1D heat equation.

This analysis may suggest that for quantitative measurements of thermal conductivity in a quasi-hydrodynamic regime, where we don't know the ratio $\sqrt{\nu/\gamma}/h$, long and narrow devices might be more appropriate. However, it is unclear to what extent the boundaries of a narrow sample may change the measured thermal conductivity from the true bulk value, as is known to happen in thermal transport for nanoscale Ohmic conductors[101,107]. Boundary scattering will certainly play a role analogous to impurity scattering, but it will depend on the exact nature of the boundary, including for example any roughness effects that might effectively randomize particle velocity vs a low-disorder boundary that only produces specular reflection.

In computing the effective Lorenz ratio from such an experiment on a finite-sized sample, we would accurately measure the intensive quantity κ, but our measurement of the extensive quantity R necessarily will include viscous drag effects. To study hydrodynamics in a meaningful way, we would ultimate want the bulk Lorenz ratio in an infinite sample, computed from the measured κ and a hypothetical bulk σ calculated from the non-viscous momentum relaxation rate γ_{mr}. In Chapter 6, we present an experiment on a Corbino geometry where it is possible to compute both κ and γ_{mr} to obtain a hypothetical bulk Lorenz ratio.

3.9 Influence of Thermoelectric Effects

So far, we have only considered the case of thermal transport without regards to thermoelectric effects. Thermoelectric effects couple electrical currents to thermal gradients, and thermal currents to electrical gradients, primarily through the dependence of the chemical potential μ on temperature due the density of states $g(\epsilon)$ depending on energy[54]. The full thermoelectric transport matrix is given by

$$\begin{bmatrix} \vec{J}_e \\ \vec{J}_q \end{bmatrix} = \begin{bmatrix} \hat{\sigma} & \hat{\alpha} \\ T\hat{\alpha} & \hat{\bar{\kappa}} \end{bmatrix} \begin{bmatrix} -\vec{\nabla}\phi \\ -\vec{\nabla}T \end{bmatrix}, \tag{3.58}$$

where $\vec{J}_e$ is the electrical current, $\vec{J}_q$ is the thermal current, $\hat{\alpha}$ is the thermoelectric Seebeck coefficient, and $\hat{\bar{\kappa}}$ is the thermal conductivity under zero electric field. Traditionally, the more common thermal conductivity that is measured, and the one that we have discussed so far in this work, is the thermal conductivity $\hat{\kappa}$ measured under zero electric current. The two are related via

$$\hat{\kappa} = \hat{\bar{\kappa}} - T\hat{\alpha}\hat{\sigma}^{-1}\hat{\alpha}. \tag{3.59}$$

In the self-heating configuration described in Section 3.2, there is nonzero electric current flowing through the sample to generate Joule heating, and there is a nonzero electric field to drive this current. Thus, on a local scale, we are measuring neither $\hat{\kappa}$ nor $\hat{\bar{\kappa}}$, so it has been a longstanding question of which variant of thermal conductivity the self-heating method measures.

One qualitative description that we have put forth is the following. If we bend a rectangular sample into a U-shape, such that the two metal electrode heat sinks are

adjacent, then we have one hot side (the middle of the channel) and one cold side. Due to conservation of electrical current, the net current flowing from the hot side to the cold side is zero, and we would measure $\hat{\kappa}$. However, this description has remained unsatisfactory due to its qualitative nature.

Here, we derive an analytical proof that we are indeed conducting a global thermal conductance measurement that gives us the $\hat{\kappa}$ value, for thermal conductivity under zero electric current. Let us consider the 1D thermoelectric transport equations

$$I_e = -\sigma \frac{d\phi}{dx} - \alpha \frac{dT}{dx} \tag{3.60}$$

$$I_q = -\alpha T_0 \frac{d\phi}{dx} - \overline{\kappa} \frac{dT}{dx}. \tag{3.61}$$

From charge conservation, we must have that I_e is constant. The goal is to find the functions $\phi(x)$, $T(x)$, and $I_q(x)$. As there are three unknowns, we need another constraint equation, which is the local Joule heating equation:

$$\mathcal{P} = \frac{I_e^2}{\sigma}. \tag{3.62}$$

The thermal current continuity equation is

$$\frac{dI_q}{dx} = \mathcal{P} = \frac{I_e^2}{\sigma} = \frac{I_e^2 R}{L}. \tag{3.63}$$

Taking a derivative of Eq. 3.61 and setting it equal to the above,

$$\frac{dI_q}{dx} = -\alpha T_0 \frac{d^2\phi}{dx^2} - \overline{\kappa} \frac{d^2T}{dx^2} = I_e^2 \frac{R}{L}. \tag{3.64}$$

We can take the derivative of Eq. 3.60 and solve for d^2T/dx^2:

$$\frac{d^2T}{dx^2} = -\frac{\sigma}{\alpha}\frac{d^2\phi}{dx^2}, \tag{3.65}$$

And then substitute into Eq. 3.64:

$$-\alpha T_0 \frac{d^2\phi}{dx^2} + \overline{\kappa}\frac{\sigma}{\alpha}\frac{d^2\phi}{dx^2} = I_e^2\frac{R}{L} \tag{3.66}$$

$$\frac{d^2\phi}{dx^2}\left(\frac{\overline{\kappa}\sigma}{\alpha} - \alpha T_0\right) = I_e^2\frac{R}{L} \tag{3.67}$$

$$\frac{d^2\phi}{dx^2} = I_e^2\frac{R}{L}\left(\frac{\overline{\kappa}\sigma}{\alpha} - \alpha T_0\right)^{-1}. \tag{3.68}$$

We have a differential equation for $\phi(x)$, and we use the Ansatz $\phi(x) = Ax^2 + Bx + C$; where $\phi'(x) = 2Ax + B$ and $\phi''(x) = 2A$;

$$A = \frac{1}{2}I_e^2\frac{R}{L}\left(\frac{\overline{\kappa}\sigma}{\alpha} - \alpha T_0\right)^{-1}. \tag{3.69}$$

The constants B and C are obtained from boundary conditions (BCs) (total bias and symmetric bias).

$$\textbf{BCs:}\quad \phi(0) = -\phi(L)\,; \phi(L) - \phi(0) = V_{bias} \tag{3.70}$$

$$\phi(0) = C = -\left(AL^2 + BL + C\right) = -\phi(L) \tag{3.71}$$

$$0 = AL^2 + BL + 2C \tag{3.72}$$

$$\phi(L) - \phi(0) = V_{bias} = AL^2 + BL \tag{3.73}$$

$$B = \frac{V_{bias}}{L} - AL = \frac{I_e R}{L} - AL \tag{3.74}$$

$$C = -\frac{1}{2}\left(AL^2 + BL\right). \tag{3.75}$$

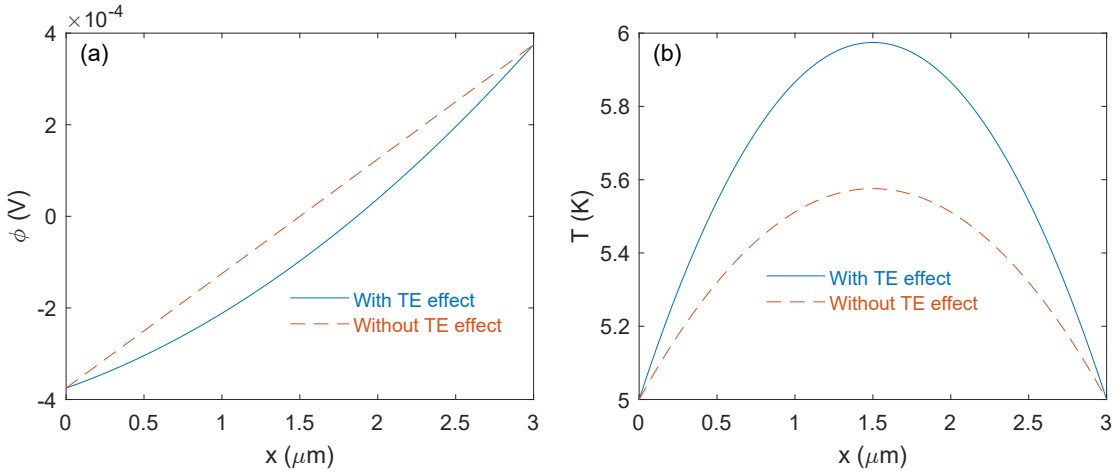

Figure 3.14: **(a)** Potential profile in the sample channel, with thermoelectric effects (blue) and without (red). Here, we use $\sigma = 1\,\mathrm{mS}$, $R = 375\,\Omega$, $I = 2\,\mathrm{mA}$, $T_0 = 5\,\mathrm{K}$, and $\bar{\kappa} = \mathcal{L}_0 T_0 \sigma$. $\bar{\kappa}$ is held constant, while α is chosen to be 0 (red) or $100\,\mathrm{nA/K}$ (blue). **(b)** Corresponding temperature profile in the sample channel.

Now for the thermal case, using Eqs. 3.65 and 3.68:

$$\frac{d^2T}{dx^2} = -\frac{\sigma}{\alpha}\frac{d^2\phi}{dx^2} = -\frac{\sigma}{\alpha} I_e^2 \frac{R}{L}\left(\frac{\bar{\kappa}\sigma}{\alpha} - \alpha T_0\right)^{-1} \tag{3.76}$$

$$= -I_e^2\left(\bar{\kappa}\sigma - \alpha^2 T_0\right)^{-1}. \tag{3.77}$$

We then solve for $T(x) = A'x^2 + B'x + C'$; where $T'(x) = 2A'x + B'$ and $T''(x) = 2A'$. Satisfying the boundary condition $T(0) = T(L) = T_0$, we obtain

$$\Delta T(x) = \frac{1}{2}\frac{I_e^2/\sigma}{\left(\bar{\kappa} - \frac{\alpha^2 T_0}{\sigma}\right)} x(L - x). \tag{3.78}$$

This is precisely Eq. 3.11 written in 1D units. ■

We have thus proven that we measure κ and not $\bar{\kappa}$. We plot the resulting potential $\phi(x)$ and temperature $T(x)$ in Fig. 3.14, for typical sample parameters, to observe the effect of thermoelectric terms on them. In both panels, the red dashed curves plot the

profiles for zero thermoelectric effect, i.e. $\alpha = 0$. The blue curves indicate the profiles with an arbitrarily chosen α for an exaggerated effect, keeping $\bar{\kappa}$ unchanged. After we add in thermoelectric effects, the potential profile becomes parabolically curved instead of linear, and the center of the channel is no longer at exactly zero potential under symmetric biasing. The temperature profile remains parabolic but becomes higher, due to the change of $\kappa = \bar{\kappa}$ (red) to $\kappa = \bar{\kappa} - \alpha^2 T_0/\sigma$ (blue).

3.10 Bipolar Diffusion

Bipolar is a phenomenon whereby an electronic system with two fluid components, especially oppositely charged with different thermoelectric coefficients, will produce a higher thermal conductivity κ than the sum of the individual thermal conductivities. We refer the reader to Ref. 180 for a more in-depth discussion of the bipolar diffusion effect in graphene, but here we provide short synopsis for completeness.

A measurement of κ, is performed under a condition of zero electric current, necessitating a potential to oppose any thermoelectrically induced electric currents from the thermal gradient. The thermoelectric transport matrix (Eq. 3.58) necessarily implies that this potential will oppose additional flow of thermal current. However, when two electronic fluids with opposite thermoelectric coefficients are present, the thermoelectrically induced electric currents will cancel out, removing the need for a thermal-current-opposing potential to null out the electric current. Thus, the thermal conductivity is enhanced about the sum of the individual fluid thermal conductivities. Additional quantitative calculations for this effect in graphene are performed in Ref. 87; see also Section 5.2.

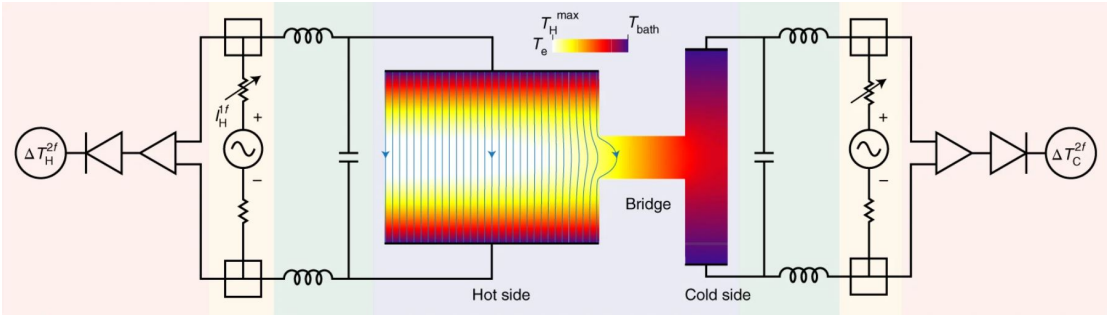

Figure 3.15: Nonlocal heating geometry and simplified measurement circuit schematic. The color gradient represents self-heating on the hot side, with heat flowing along the bridge to the cold side. A matching circuit and measurement circuit measures the Johnson noise on each of the hot and cold side separately. Image from Ref. 174.

3.11 Non-Local Noise Thermometry

In this dissertation, we focus primarily on measuring thermal conductivity using the self-heating technique. However, in a technique pioneered primarily by Jonah Waissman, we can connect two self-heating samples together at the centers with another sample as a bridge, with the goal of measuring the thermal conductance across the bridge, as shown in Fig. 3.15; see our publication Ref. 174 for an in-depth discussion of this technique. One self-heating side will act as the hot side, with temperature T_{hot}, and the other self-heating side as the cold side, with temperature T_{cold}. The bridge is then subject to a temperature difference $T_{hot} - T_{cold}$, causing a thermal current Q to flow across it. The cold side acts simultaneously as a thermometer and a heat current meter, in a thermal analog to an electrical voltage divider. The thermal conductance of the cold side must be measured separately in a self-heating experiment, and then that quantity used in the nonlocal heating experiment (with the heat coming from the hot side across the bridge) to measure the thermal current.

Disadvantages of the nonlocal heating setup are additional circuit complexity and

smaller signals, but the primary advantages are the ability to measure arbitrary samples without reliance on self-heating, for example electrical insulators with energy-based degrees of freedom for thermal transport.

The nonlocal geometry should also be less susceptible to nonlinearity effects in the channel to be described in Chapter 4; however, any temperature-dependence of the resistance will still modulate the resistance at $2f$ and generate $3f$ voltage harmonics.

3.12 Conclusion

In this Chapter, we have looked at various thermal effects in graphene samples that can contribute to and affect thermal conductance measurements. These effects are important to consider in interpreting results from measurements in studying electron hydrodynamics. However, there is a host of technical considerations as well on the Johnson noise thermometry methods, to which we now turn our attention in Chapter 4.

In physics, you don't have to go around making trouble for yourself - nature does it for you.

Frank Wilczek

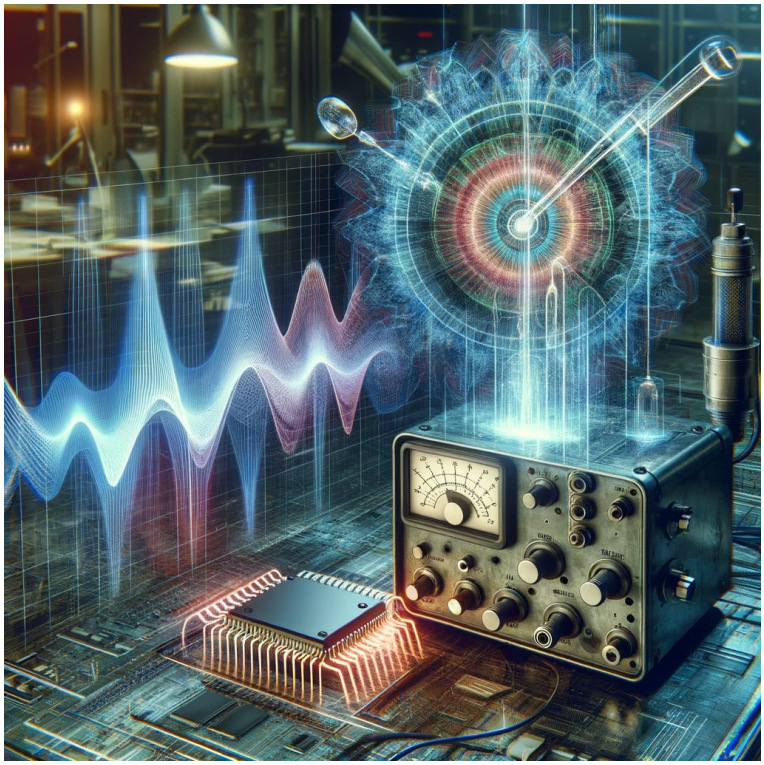

4

Advanced RF Johnson Noise Thermometry Techniques

Improving the signal to noise ratio is always a desired goal for any experimentalist or anyone performing a measurement. Often, the desired signal occupies a very narrow

frequency bandwidth, and noise corrupts the signal over a much larger bandwidth. In this situation, a lock-in amplifier working as an ultra-narrow bandpass filter performs extraordinarily well at improving the signal to noise ratio.

However, in the case of Johnson noise thermometry, the "signal" is wideband noise itself, occupying the same large bandwidth as the "noise", so we must now consider not the "signal" to "noise" ratio, but the ratio of useful noise (our "signal") to unwanted extrinsic noise. In principle, we would expect the two noises to be uncorrelated, and that their rms voltages would add in quadrature; alternately, that their powers add linearly. When ultimately measuring the noise, the unwanted noise will appear as a constant offset or additional term added to the desired noise.

This Chapter focuses on advanced techniques for measuring noise, especially applied to wideband RF Johnson noise thermometry. Many of the techniques are to boost the desired noise, weaken the unwanted noise, and improve the accuracy of the measurement. This Chapter builds upon the noise measurement methods previously developed in Refs. 96 and 175. All of the techniques presented in this Chapter were invented, developed, or improved here during the course of my PhD, most in close collaboration with Jonah Waissman. The reader of this Chapter is strongly encouraged to be familiar with the basic RF concepts from Refs. 109–112 as a prerequisite.

This Chapter is organized as follows. In Section 4.1, we outline the circuit and components used for JNT. Section 4.2 discusses filtering strategies for JNT. In Section 4.3 we discuss the differential-mode aspect of our JNT technique. Section 4.4 discusses various impedance matching strategies and intuition for matching variable-resistance samples to 50 Ω RF components. In Section 4.5, we discuss various calibration methods of our JNT, with a focus on variable-resistance gateable samples, and we discuss accuracy issues and parasitic effects that may arise during calibration. Section 4.6 briefly discusses

the inherent uncertainty present in noise measurements. Section 4.7 discusses methods to minimize attenuative loss in the JNT circuit to keep the background noise temperature as low as possible. Section 4.8 discusses thermal anchoring strategies to minimize the parasitic background gain from Section 4.5. The most important advancements in our JNT technique are presented in Sections 4.9 and 4.10, where we discuss a subtle non-linearity effect and another gate-line-noise effect that can significantly degrade the accuracy of our JNT technique, as well as methods to overcome them. Finally, Section 4.11 summarizes our technique and provides an outlook for the further advancement of RF JNT. Portions of this Chapter are reproduced from our original publication via AIP Publishing, Ref. 159.

4.1 Noise Measurement Circuit

In designing our noise measurement circuit, our main goals are to measure noise over a wide range of sample resistance, while still maintaining a low background noise temperature T_N and a wide bandwidth to facilitate faster measurements. We use commercially available components rather than custom ones wherever possible to simplify the design and to allow interchangeability and modifications. The matching circuit described below in Section 4.4 transforms a wide range of device impedance to closely match the $50\,\Omega$ RF components. The circuit also allows separate AC (quasi-DC) and RF measurements on the device. The total noise power N that we measure is the band-integrated quantity of the noise power spectral density S, with the high- and low-pass filters at $f_{1,2}$ determining the integration bounds:

$$N = \int_{f_1}^{f_2} S(f) df. \tag{4.1}$$

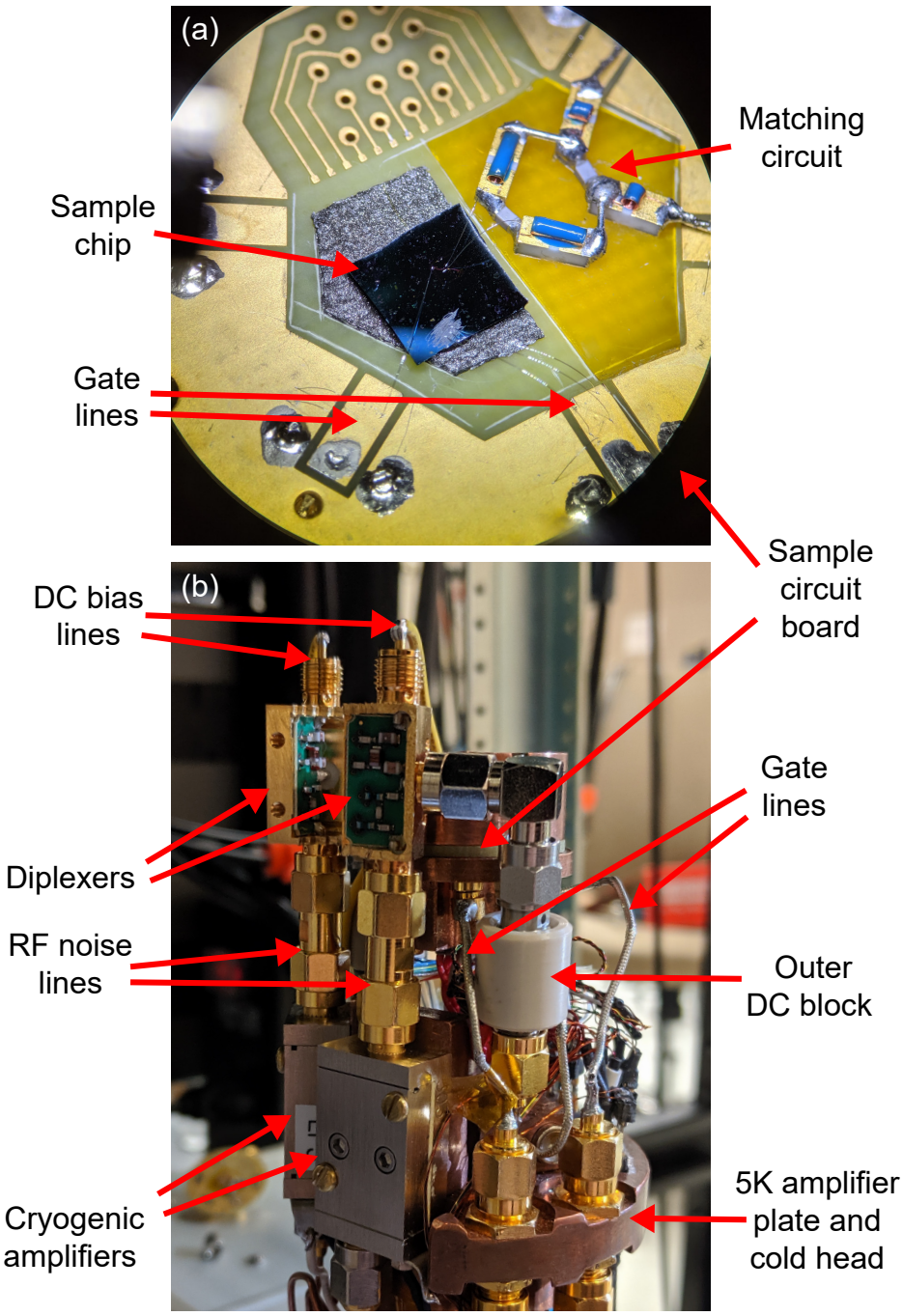

Figure 4.1: **(a)** Microscopic image of the circuit board with the sample chip and matching circuit. **(b)** The cryocooler cold head with LNA and other low temperature measurement components. The sample enclosure is weakly thermally anchored to the 5 K plate with an aluminum tube; it is heated separately from the 5 K plate.

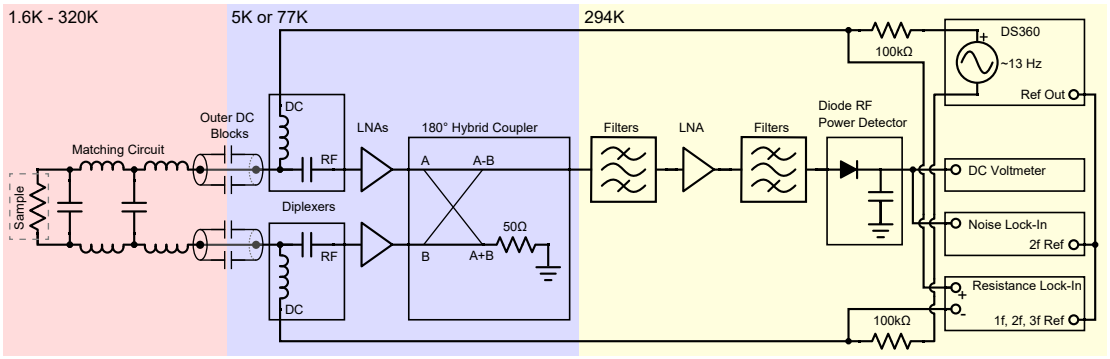

Figure 4.2: Schematic diagram of the circuit used for for Johnson noise thermometry. Light red area: Sample and matching circuit stage, controlled by a dedicated heater and thermometer. Temperature can be changed from cryostat base temperature to the maximum allowed by the cryostat. Outer DC blocks on the coaxial cables allow thermal isolation from the following stage. Light blue: First-stage readout electronics including LNAs sit at cryogenic temperature to minimize background thermal and amplifier noise. Light yellow: Room temperature electronics include a second-stage LNA, bandpass filters, power detection diode, and low-frequency measurement electronics.

Fig. 4.1 shows pictures of the thermometer components, and Fig. 4.2 shows the corresponding circuit diagram. The thermometer is demonstrated to operate on a bilayer graphene sample, sitting in a modified variable-temperature cryocooler (Janis SHI-4-5). The sample and matching circuit are on a separate custom-made printed circuit board (PCB) that is attached to the cryostat cold head via an aluminum tube, serving as a weak thermal link, allowing the sample to be heated independently of the cold head. We assemble the matching circuit using standard chip capacitors and air-core inductors (Piconics MC-series), to avoid temperature-dependence of solid-core inductors. We connect the matching circuit to the sample chip with Al wirebonds and keep the bonding pads small with lateral dimensions of 50 μm to minimize stray capacitance to the silicon back gate. Coaxial cables connect the rest of the circuit components outside the PCB. The two arms of the circuit correspond to the (+) and (−) arms of the differential-mode circuit, discussed further in Section 4.3.

On the cold head, diplexers (Mini-Circuits ZDPLX-2150-S+) separate the low-frequency band (0–10 MHz) from the RF band (> 50 MHz) for each arm of the circuit. Between the diplexers and hotter sample, we place outer DC blocks (Fairview Microwave SD3462) to improve thermal isolation. We use the low-frequency band for AC transport, measuring the resistance of and Joule-heating the device with a lock-in technique at a low frequency, typically ~ 17 Hz. The RF band goes into cryogenic standalone SiGe low noise amplifiers (LNA) (Cosmic Microwave Tech CITLF3) with ~ 35 dB gain and 4 K noise temperature. The diplexers and LNAs are held at a constant temperature around 5 K in the cold stage of the cryostat; the LNAs are tuned to have approximately the same gain.

Outside the cryostat at room temperature, a 180° hybrid coupler (Mini-Circuits ZFSCJ-series) combines the signals from the two arms into a single-ended signal corresponding to the difference of these two signals. Lumped LC filters (Mini-Circuits SHP-, SLP-, and VLFX- series) form an appropriate pass-band for the amplified noise, typically around 100–200 MHz. These filters reflect frequencies outside the matched band that contain mostly amplifier noise. A room-temperature LNA (Fairview Microwave SLNA-010-050-10-SMA) amplifies the signal by 50 dB to a level above the noise floor of the zero-bias Schottky diode RF power detector (Pasternack PE8000-50, or Herotek DHM124AAP). A second set of filters, typically identical to the first set, filters the signal again between the second LNA and the power detector. The power detector takes wide-spectrum RF power and produces a voltage at the output approximately proportional to the input RF power; this voltage is measured both at DC (Agilent 34401A) and at AC at twice the bias frequency, $f_2 = 2f_1 \sim 2 \times 17$ Hz (SR830 lock-in).

We calibrate out the nonlinearity of the power detector with an input of known power from an RF signal generator. Fig. 4.3 shows the calibration curves for the Herotek

DHM124AAP and Pasternack PE8000-50 diodes. The Herotek diode has a slightly better sensitivity of 1.2 mV/μW than the Pasternack's 0.8 mV/μW. The Herotek achieves excellent linearity over a wide input range of powers and has a lower noise floor, while the Pasternack only approaches linearity and has a higher noise floor. The Herotek diode has a 33.5 μV output offset. For making a look-up table for the calibration, we perform a 13th-order polynomial fit and then interpolate between those points, which we also use in calculating the AC conversion factor dP_{in}/dV_{out}. When building the JNT circuit, there should be enough total amplification to get above the noise floor and into the linear regime of the power diode, but not so much as to go into the high-power roll off. If there is too much gain from the LNAs, then an attenuator can be installed in front of the power diode.

4.2 Filtering

Many or all of the instruments typically used on a scientific rack, for example a Stanford Research Systems SR830 lock-in amplifier, produce a lot of RF noise that may enter into the JNT circuit either directly or indirectly. This can be easily seen by connecting a terminal of any instrument to a spectrum analyzer, or by connecting a pickup antenna loop to a spectrum analyzer and then placing the loop near an instrument.

To protect the quiet environment of the JNT measurement circuit, it is extremely important to filter out as much of this external instrument noise as possible. The filtering strategies will depend on the frequencies that the lines or cables must transmit. The proliferation of commercial off-the-shelf (COTS) RF components, especially filters, from companies such as MiniCircuits and Crystek, over the past few decades has significantly simplified the life of noise measurement experimentalists and unlocked many

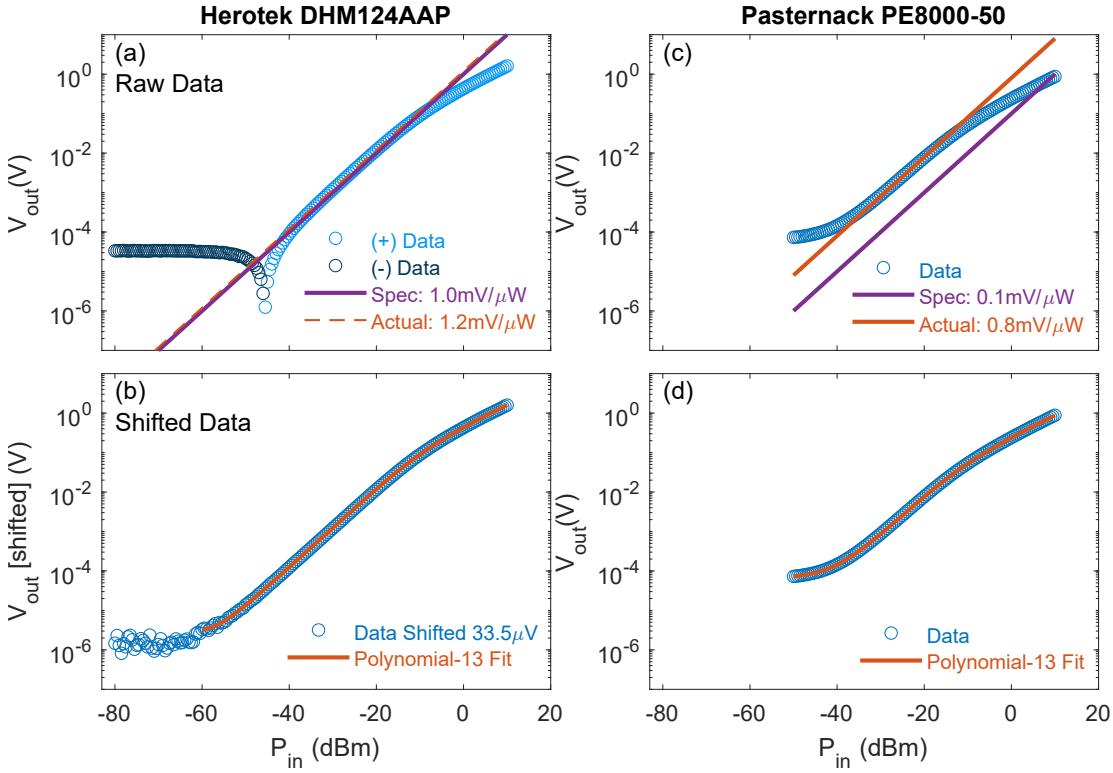

Figure 4.3: **(a)** Herotek power diode raw calibration data (blue circles), which has a 33.5 μV offset causing the output voltage to go negative (dark blue circles). Purple: sensitivity spec of the diode. Red: actual sensitivity. **(b)** Herotek diode shifted calibration data to account for the offset (blue circles). Red: 13^{th}-order polynomial fit. **(c)** Pasternack power diode raw calibration data (blue circles). Purple: sensitivity spec of the diode. Red: actual sensitivity. **(d)** Same data as in (c), showing the 13^{th}-order polynomial fit (red).

new experimental opportunities.

Typically, most lines will need to transmit a DC or quasi-DC ($\lesssim 40\,\mathrm{Hz}$) low frequency signal, and signals above that frequency will need to be filtered out. These lines include cryostat resistive thermometry lines, cryostat heater lines, gate lines, low-frequency sample bias lines, and amplifier power supply lines. A good set of filters will filter out to more than 40dB signals from $\sim 1\,\mathrm{MHz}$ to $\sim 20\,\mathrm{GHz}$; however, this often cannot be easily accomplished with one filter. The best strategy is to attach three filters in series: (1) a bias-tee such as a MiniCircuits ZFBT-4R2G+ used as a reflectionless DC filter with a $50\,\Omega$ terminator on the RF port, (2) a low-frequency filter such as MiniCircuits SLP-1.9 filter (which filters only up to a few GHz), and (3) a high-frequency filter such as a MiniCircuits VLFX-80 (the VLFX- series filters guarantee 40dB insertion loss up to 20 GHz).

In many cases this triple set of filters is sufficient overkill at removing unwanted noise to undetectable levels, but some rack instruments, in particular the Keithley 2400 SourceMeter, are particularly noisy and require the entire triple stack or sometimes additional filters.

In some situations, the proposed triple stack of filters will not work, in particular for lines harboring high voltage such as high-voltage gate lines, or for lines carrying high current such as cryostat heater lines. In the case of high-voltage gate lines, some filters will experience dielectric breakdown as they are driven far past their operating specs (e.g. 30V for the bias-tee); the rectification for this issue is to test filters individually for high-voltage breakdown, and connect many of the surviving ones in series. In the case of high-current lines (specifically cryostat heater lines, carrying up to $\sim$ 1A), more components are needed: Here, the high current overheats the filters and burns them out, creating an open circuit. The solution is to reduce the heating power, which scales as

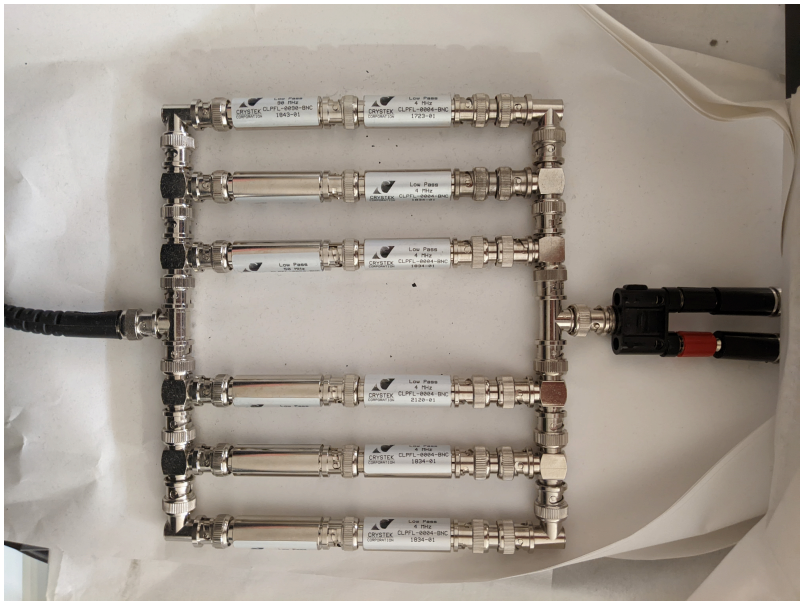

Figure 4.4: A filter bank of 6 series-pairs of Crystek low-pass RF filters used for filtering out RF noise for high-current heater lines for the cryostat. The 6 rows of filters are necessary to split the heating from the large DC current to avoid burning out the filters.

$\propto I^2$, through the filters by running several filter banks in parallel to share the current; MiniCircuits VLFX- style LTCC filters have a low current carrying capacity, so only BLP- style lumped element filters may be used, and as they are less effective at filtering high frequencies, more of them are needed in series. Fig. 4.4 illustrates a typical filter bank used for high-current applications.

One additional filter technique that we have used with limited success has been installing ferrite core beads onto wires. Ferrite cores attenuate high frequency signals on wires by capturing the energy from RF magnetic fields and transforming it into resistive losses. They are less effective on coaxial cables since the RF magnetic fields are inside the outer conductor and don't get captured by the ferrite; thus we typically use them on unshielded wires such as AC mains cables. One disadvantage of ferrite cores is they can easily induce quasi-DC transient voltages or currents on wires if there is any relative

motion involved; it might thus be unwise to install them on wires that may be subject to vibration, swaying, or any kind of motion.

In addition to installing filters on lines, we desire a methodology to verify the filtering system is functioning as intended, and that no extra noise is entering into the circuit. Generally, if a filter is absent or permits noise to pass through, the total DC noise measured on the JNT thermometer may fluctuate with time, show spikes, or be at a larger constant value than it would otherwise. In some cases, such as noise on a gate line, the extra noise will only appear upon biasing the sample (see Section 4.10).

An example of symptoms of incomplete filtering is demonstrated in Appendix A in Fig. A.4. This problem was later rectified with the method discussed in this section.

4.3 Differential Mode Measurement

The original implementation of RF wideband JNT was done via a single-ended unbalanced mode as shown in Fig. 4.5(a)[1,94–96]. In this method, one of the two terminals of the graphene device was wirebonded directly to the ground plane of the PCB, which sat at cryogenic temperatures. The other terminal was connected through a matching circuit and coaxial cable through to room temperature. There are a few disadvantages to implementing RF JNT in this way:

1. The high-impedance graphene must be matched to $50\,\Omega$ (instead of $100\,\Omega$ in differential mode). This higher impedance transformation ratio results in a narrower measurement bandwidth.

2. With the biased end of the graphene at room temperature, thermoelectric voltages or currents can build up on the bias line, introducing unwanted biasing of the sample.

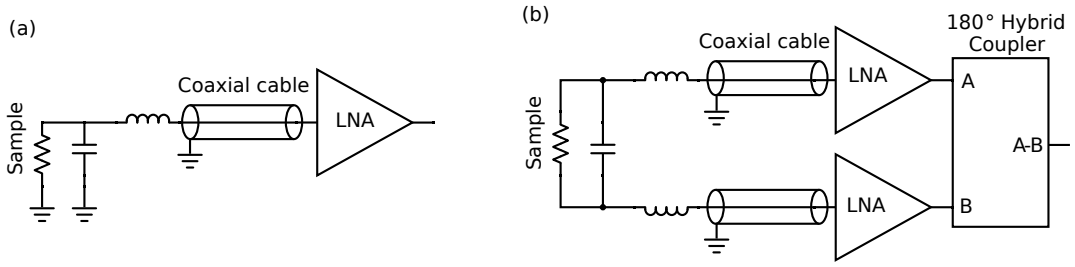

Figure 4.5: (a) Single-ended JNT with cold ground. **(b)** Differential JNT.

3. When the device is biased, it is subject to bias-gating: the average chemical potential or average gate voltage seen by the device will be modulated by the bias. This can cause serious issues via nonlinearity effects (see Section 4.9.)

4. There is no common mode noise rejection mechanism.

Our new differential method (illustrated in Fig. 4.5(b)) measures noise from the source and the drain of the sample in a differential mode. Our differential setup allows independent control of both source and drain contacts at room temperature, removing any thermoelectric effects by the symmetry of the measuring circuit, and allowing for balanced AC measurements or the possibility of DC-floating or DC-grounding any terminals. Antisymmetric biasing of the source and drain can minimize the bias-induced channel gating effect[181] to first order, which would be present in a single-ended setup.

The differential characteristic impedance of $50\,\Omega$ transmission lines (connected to LNAs) is $100\,\Omega$, which can be viewed as the series-connected input impedances of the two LNAs. This $100\,\Omega$ setup allows easier matches to high-impedance devices than does a single-ended $50\,\Omega$ setup.

The 180° hybrid coupler, sometimes known as a magic-T, combines the signals from the two arms A, B of the circuit 180° out of phase, effectively producing $A - B$. It typically has a high common mode rejection ratio (CMRR) that effectively attenuates

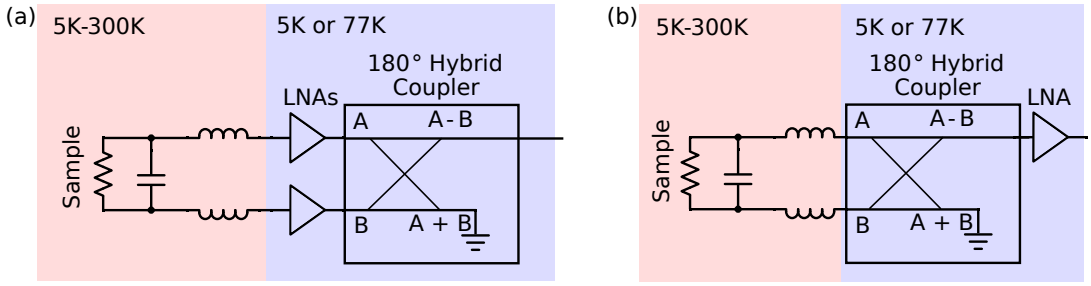

Figure 4.6: (a) Simplified circuit schematic with two cold LNAs; the hybrid comes after the LNAs. This variant achieves lower noise temperature. **(b)** Simplified circuit schematic with one cold LNA.

any common-mode noise that may have been symmetrically induced onto the two arms of the circuit. In particular, if the two arms before the hybrid are spatially adjacent and especially if they form a twisted pair, there is generally little differential mode noise picked up by them due to small loop area, but they may still pick up a common mode noise signal from external EMI; this common mode signal then gets exactly canceled out by the hybrid. This differential mode signal transmission can thus be a very powerful technique and can be useful in a scope beyond JNT[182].

The hybrid has an internal $50\,\Omega$ termination (sometimes external) for the common mode $A + B$ signal to avoid reflection. This termination generates its own Johnson noise (at the temperature of the terminator) that could contribute to the measured noise temperature but is suppressed by the gain of the upstream (first-stage) LNAs[172]. This differential mode circuit can alternately be implemented with just one first-stage LNA to reduce cost, as illustrated in Fig 4.6, with the hybrid placed before the LNA; in this case, the common mode thermal noise from the hybrid is directly incident on the sample, and it is wise to minimize it by placing the hybrid at a cryogenic temperature along with the first-stage LNAs.

When two cold LNAs are used in the differential setup, we must consider any vari-

ations between their gains. Any difference will appear as a common mode signal, as well as slightly unbalancing the differential mode signal. If a differential mode signal is not fully balanced, it may become more susceptible to external noise due to the loss of symmetry; thus, we attempt to match the two amplifier gains as closely as possible by tuning the individual supply voltages. Because the gain typically has a slightly frequency dependence which may vary between individual LNAs, we cannot in general match the gain over the entire frequency band; instead, we tune the gains to match at the center of the noise measurement band, effectively equating the band-integrated noise power for the two arms. To match the gains, we measure the gain of each LNA using a VNA connected across the LNA input and the hybrid output, adjusting the supply voltage until they match at the center of the noise band.

The development of differential mode measurement in RF JNT has been a revolutionary advancement, allowing us to realize a more complex graphene multi-terminal measurement for nonlocal noise thermometry that does not rely on self-heating for measuring thermal conductance[174].

4.4 Impedance Matching Optimization

As was discussed in Section 1.6, a high impedance mismatch will cause most the noise signal to be reflected, leading to poor JNT performance; thus, we implement impedance matching circuit to step down the impedance while minimizing reflections. Single-stage lumped-element LC matching circuits are a standard way to transform impedance, but they operate well for only a narrow frequency band. Ultimately, our goal with the impedance matching circuit is to allow a high efficiency transfer of Johnson noise power from a high-impedance sample to $50\,\Omega$ LNAs, necessarily integrated over a wide fre-

quency band. Achieving higher frequency bandwidths has been a standard procedure in electrical engineering with techniques extending far beyond component MCs[109]. Devices made from gateable two-dimensional (2D) materials such as BLG, however, require matching circuits that can cover changes in resistance of several orders of magnitude. We thus focus primarily on obtaining the widest resistance range with efficient coupling while maintaining a high frequency bandwidth.

Working at RF, we must be cautious in applying lumped-element circuit models to our analysis. At 200 MHz, the wavelength in a coaxial cable with $v \sim 0.7c$ is around 1 m. Our substrate chip is typically ~ 6 mm in size, the device leads are ~ 0.5 mm, the device itself is several μm, and the matching circuit is about 10 mm; all of these length scales are less than 1% of the wavelength of a 200 MHz electromagnetic wave, asserting our lumped element model.

4.4.1 No Matching Circuit

To understand impedance matching, let us first consider the impedance matching between a Johnson noise voltage source V_0 with an arbitrary (real) impedance Z and a fixed (real) impedance Z_0 representing the input impedance of the amplifier (in our differential mode measurement, $Z_0 = 100\,\Omega$), shown in Fig. 4.7(a). Because we are considering Johnson noise, as described in Chapter 1, the voltage from the source is proportional to $\sqrt{Z}$; we shall call the proportionality factor α for convenience. We shall ask the question, what is the power dissipated in the Z_0 impedance as a function of the Z impedance, relative to the maximum available power to be dissipated? Remember

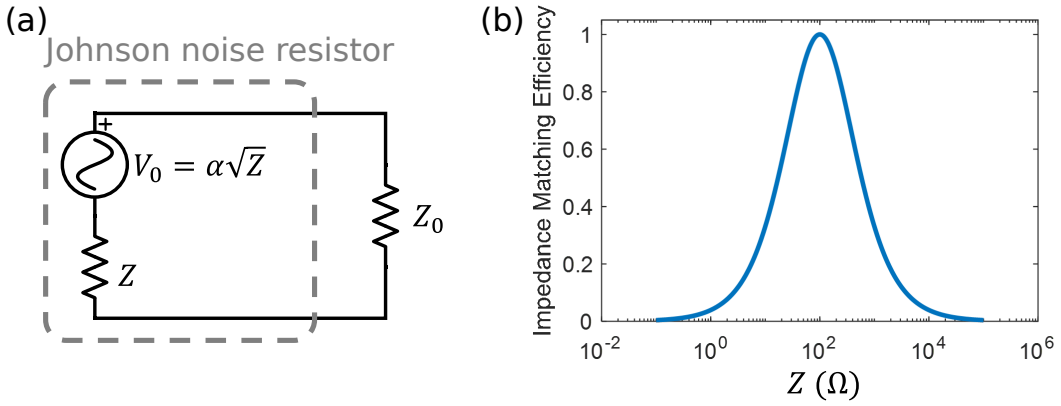

Figure 4.7: **(a)** A bare-bones Johnson noise power transfer circuit. The Johnson noise resistor is plotted as an ideal resistor Z in series with a voltage source. The impedance Z_0 =100 Ω represent the amplifier load. **(b)** Impedance matching efficiency as a function of source impedance Z. The shape is symmetric when plotted on a logarithmic scale.

that the source voltage here depends on Z. The power dissipated in Z_0 is

$$P_{Z_0} = I^2 Z_0 = \frac{\alpha^2 Z}{(Z + Z_0)^2} \times Z_0. \tag{4.2}$$

The maximum available power to be dissipated occurs when $Z = Z_0$ and is given by

$$\max(P_{Z_0}) = \alpha^2/4, \tag{4.3}$$

and thus, the power dissipated in Z_0 relative to the max power is given by

$$\frac{P_{Z_0}}{\max(P_{Z_0})} = \frac{4ZZ_0}{(Z + Z_0)^2}, \tag{4.4}$$

which is the impedance matching power efficiency transfer equation. This function is plotted in Fig. 4.7(b), and is symmetric about the point Z_0 when plotted on a logarithmic x-scale.

This functional form can also be easily derived by considering wave refection in transmission lines. If the wave reflection coefficient is given by

$$\Gamma = \frac{Z_0 - Z}{Z_0 + Z}, \tag{4.5}$$

then the matching efficiency is given by

$$1 - |\Gamma|^2 = 1 - \left|\frac{Z_0 - Z}{Z_0 + Z}\right|^2 = \frac{4ZZ_0}{(Z + Z_0)^2}. \tag{4.6}$$

This impedance matching occurs for all frequencies since there are no reactive matching circuit component used.

4.4.2 Single Stage Matching Circuit

The simplest type of MC is a single-stage component matching circuit, shown in Fig. 4.8(a), consisting of two inductors with identical inductance L and a bridging capacitor with capacitance C. Here, full power transfer happens at only one point in the resistance-frequency (R, f)-plane. At angular frequency ω, the impedance Z of the sample seen by the LNAs through the MC is given by

$$Z = 2i\omega L + \left(R^{-1} + i\omega C\right)^{-1}. \tag{4.7}$$

To match at a target angular frequency ω_0 and target sample resistance R_0 we equate this impedance to $Z_0 = 100\,\Omega$. This results in MC component values of $C = \sqrt{m-1}/\left(\omega_0 R_0\right)$ and $2L = \sqrt{m-1}\,Z_0/\omega_0$, where $m \equiv R_0/Z_0$ is the impedance step ratio.

Using the matched impedance Z, the matching efficiency can be expressed as $1-|\Gamma|^2 =$

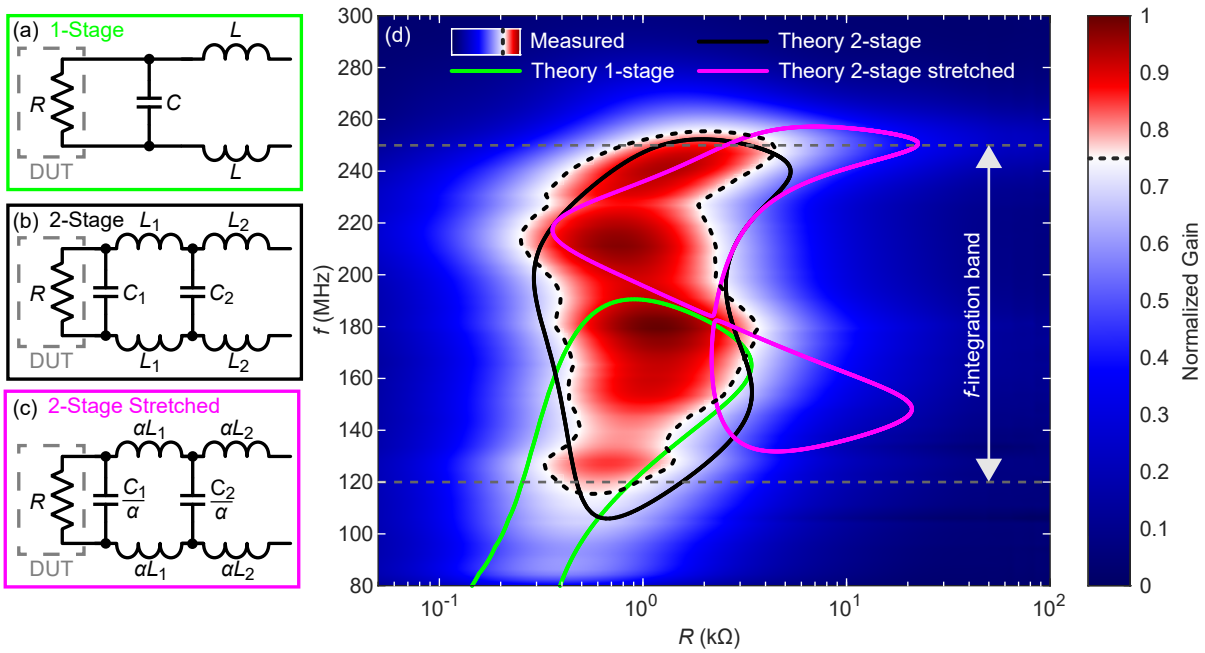

Figure 4.8: **(a)** Standard 1-stage impedance matching. **(b)** Standard 2-stage impedance matching. **(c)** Standard 2-stage impedance matching that has been stretched. **(d)** Measured normalized gain using standard 2-stage matching, as a function of sample resistance and measuring frequency, compared to modeled matching circuits. Colorplot is the measured normalized gain, with white corresponding to 0.75. Drawn contours are corresponding 0.75 coupling efficiency for the measured normalized gain (dotted line), as well as for the three matching circuits in (a)-(c).

$1 - |(Z_0 - Z)/(Z_0 + Z)|^2$. As a function of sample resistance R and frequency f, this is given by

$$\frac{4m\rho}{(1+m\rho)^2 + [m-1-(2m^2-3m+1)\rho^2]\Omega^2 + (m-1)^2\rho^2\Omega^4} \tag{4.8}$$

in terms of the normalized parameters $\rho = R/R_0$ and $\Omega = 2\pi f/\omega_0$.

A good match is achieved for R and f in a range close to R_0 and f_0, as shown in Fig. 4.8(d) by the green 75% matching efficiency contour. The full width at half maximum (FWHM) of the matching surface in R and f is

$$\Delta R = 4\sqrt{2}R_0 \quad \text{at } \omega = \omega_0 \tag{4.9}$$

$$\Delta f \approx \frac{2}{\sqrt{m}} f_0 \quad \text{at } R = R_0 \quad \text{for } m \gg 1. \tag{4.10}$$

These relations show that matching to a higher frequency enhances the frequency bandwidth, while matching to higher resistance enhances the resistance range at the cost of decreasing the frequency bandwidth. We define separate Q-factors for frequency and resistance using the width of matched regions Δf and ΔR, relative to the peak values f_0 and R_0:

$$Q_f^{-1} = \frac{\Delta f}{f_0} \approx \frac{2}{\sqrt{m}}; \quad Q_R^{-1} = \frac{\Delta R}{R_0} = 4\sqrt{2}. \tag{4.11}$$

4.4.3 Dual Stage Matching Circuit

The standard single-stage MC can be further extended to a two-stage MC by adding an additional LC-stage, as shown in Fig. 4.8(b). Compared to a single-stage MC, a

two-stage MC allows power transfer over a wider resistance range for a given fixed wide frequency band. The two-stage MC sets the first stage impedance equal to $R_1 = \sqrt{R_0 Z_0}$ via the following component values:

$$C_1 = \sqrt{\sqrt{m}-1}/(\omega_0 R_0), \quad 2L_1 = \sqrt{\sqrt{m}-1}\, R_1/\omega_0 \tag{4.12}$$

$$C_2 = \sqrt{\sqrt{m}-1}/(\omega_0 R_1); \quad 2L_2 = \sqrt{\sqrt{m}-1}\, Z_0/\omega_0 \tag{4.13}$$

The matching efficiency function is given exactly by

$$1 - |\Gamma|^2 = \frac{4m\rho}{A + B\Omega^2 + C\Omega^4 + D\Omega^6 + E\Omega^8} \tag{4.14}$$

where the coefficients in the denominator are given by

$$A = (1+m\rho)^2 \tag{4.15}$$

$$B = -\left(\sqrt{m}-1\right)\left(1 - 2\sqrt{m} - m + \left(4m^{3/2} + m - 2\sqrt{m} - 1\right)\rho^2\right) \tag{4.16}$$

$$C = \left(\sqrt{m}-1\right)^2\left(6m\rho^2 - \rho^2 - 1 + 2\sqrt{m}\left(\rho^2 - 1\right)\right) \tag{4.17}$$

$$D = -\left(\sqrt{m}-1\right)^3\left(\left(4\sqrt{m}+1\right)\rho^2 - 1\right) \tag{4.18}$$

$$E = \left(\sqrt{m}-1\right)^4 \rho^2. \tag{4.19}$$

In addition to a perfect-matching solution at R_0 and ω_0, we obtain another degenerate perfect-matching solution at R_0 and $\omega_1 = \omega_0 \times \sqrt{\sqrt{m}+1}/\sqrt{\sqrt{m}-1}$. The 75% matching efficiency is shown in Fig. 4.8(d) by the black contour line, and FWHMs and

Q-factors are

$$\Delta R = 4\sqrt{2}R_0 \quad \text{at } \omega = \omega_0,\, \omega_1 \tag{4.20}$$

$$\Delta f \approx \frac{\sqrt{2}}{\sqrt[4]{m}} f_0 \quad \text{at } R = R_0 \quad \text{for } m \gg 1 \tag{4.21}$$

$$Q_R^{-1} = 4\sqrt{2} \quad \text{at } \omega = \omega_0,\, \omega_1 \tag{4.22}$$

$$Q_f^{-1} \approx \frac{\sqrt{2}}{\sqrt[4]{m}} \quad \text{at } R = R_0 \quad \text{for } m \gg 1. \tag{4.23}$$

Like the single-stage case, frequency bandwidth is proportional to the match frequency, resistance range is proportional to the match resistance, and higher match resistance reduces frequency bandwidth. We find that the additional LC stage does not change Q_R^{-1}, but increases Q_f^{-1} for the same m compared to that of a single stage (changing as $2/\sqrt{m} \to \sqrt{2/\sqrt{m}}$), indicating there is significant additional bandwidth. If such a large frequency bandwidth were used with the single-stage MC, the band-integrated resistance range would be much smaller.

The frequency bandwidth and resistance range can be increased further by introducing more stages to the matching circuit. However, additional stages decrease the first-stage capacitance and increase the first-stage inductance values. Mesoscopic devices typically possess stray capacitance due to the presence of heavily doped silicon substrates, sample enclosures and other factors that are difficult to eliminate entirely. With three stages, the first-stage capacitor needs to be smaller than the stray values in our circuits, typically 0.1–0.4 pF. Further stages demand more space for the additional circuitry and the increased inductance, reducing practicality for low temperature setups. For these reasons, we choose to utilize the two-stage circuit.

4.4.4 Parametrically Stretched Dual Stage Matching Circuit

Additional component combinations for 2-stage matching can be obtained by parametrically stretching the standard two-stage matching described in the previous subsection. It is possible to manipulate the perfect matching solution points in the (R, f)-plane by scaling the inductors and capacitors via

$$L_i \to \alpha L_i \tag{4.24}$$

$$C_i \to C_i/\alpha \tag{4.25}$$

as shown in Fig. 4.8(c), where α is a parameter with values typically around 2-4, limited by the stray capacitance at the first stage. The resulting effect is demonstrated in Fig. 4.8(d), transforming the black contour into the purple one. Two solutions are shifted to higher resistance ($R \to \alpha^2 R$) and spread out in frequency, while one is held fixed at the original match value. The frequency-band-integrated coupling will thus be enhanced at higher resistance but reduced near the original match. Compared to the standard two-stage match at a correspondingly larger resistance, the stretched match has its solutions spread out more in resistance and frequency and subsequently has a larger frequency-bandwidth, at the cost of reduced coupling near the best-match resistance due to the empty space in the center of the band ($\sim 200\,\mathrm{MHz}$ in Fig. 4.8(d)). In addition, the resistance derivatives of the coupling are reduced, reducing parasitic signals (see below). In principle, the coupling in this setup can be optimized to surpass the standard two-stage match by using advanced filtering strategies, such as a mixer with a tuned local oscillator frequency and tunable low-pass filter, multi-bandpass filtering, or digital signal acquisition for multiband filtering.

4.4.5 Visualizing Impedance Matching Space

The behavior and existence of the matching solutions moving around in the (R, f) plane in Fig. 4.8 can be more intuitively understood by considering the impedance that the sample sees when looking into the matching circuit terminated with the LNAs. For the 2-stage matching circuits in Fig. 4.8, the impedance seen by the sample is given by

$$Z = \left(i\omega C_1 + \left(2i\omega L_1 + \left(i\omega C_2 + (2i\omega L_2 + Z_0)^{-1} \right)^{-1} \right)^{-1} \right)^{-1} \tag{4.26}$$

where Z_0 =100 Ω is the differential amplifier input impedance. The resulting spectral impedance matching efficiency $1 - |\Gamma(R, f)|^2$ is plotted as colormaps in Fig. 4.9 for a 1-stage matching circuit, an idealized 2-stage matching circuit, and a stretched 2-stage matching circuit with $\alpha = 3$. The black curve represents the absolute value of the impedance $Z(f)$ seen by the sample, as a function of frequency. At any given frequency, the best-matched resistance equals $|Z(f)|$. The right-side panels show the phase of $Z(f)$ as a function of frequency. At whichever frequencies the phase θ of Z equals zero, the impedance seen by the sample is real, and a perfect match is achieved, i.e. $1 - |\Gamma(R, f)|^2 = 1$; this occurs at the discrete points marked by the red circles. Some solutions are doubly degenerate and are marked by two concentric red circles. The matching resistance for this perfect match is $|Z(f)|$. There is always a solution at $f = 0$, which corresponds to passing a DC current through the sample; however, the value R of this solution is meaningless, since at DC frequencies the sample sees the low-frequency biasing electronics rather than the 100 Ω LNA input.

Manipulating the impedance matching by tuning the individual reactive components amounts to changing the functional shape of $|Z(f)|$ and $\theta(f)$, and explain how the solutions for perfect matching move around in the (R, f) plane and how the two degenerate

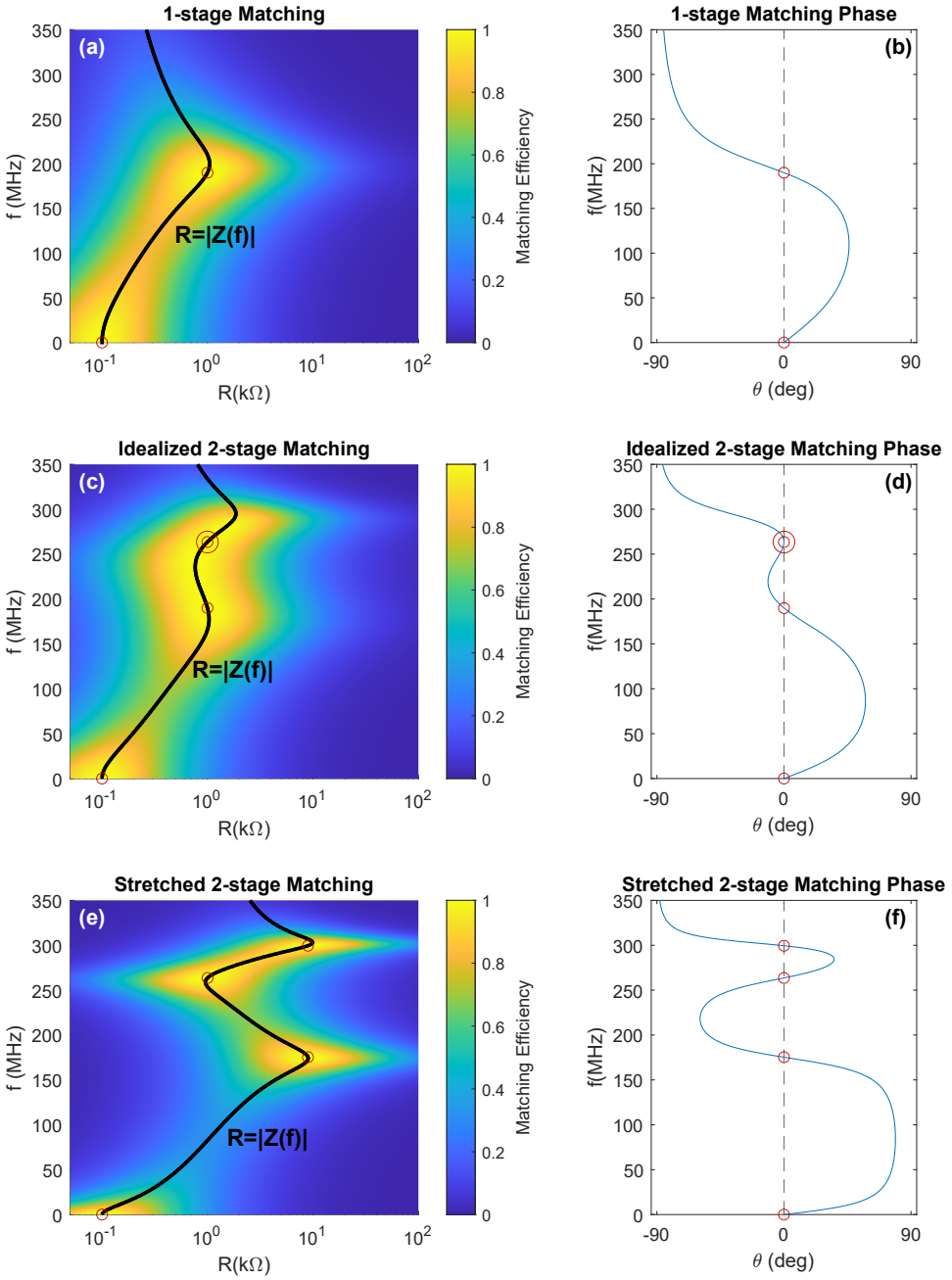

Figure 4.9: **(a,c,e)** Colormap: spectral impedance matching efficiency $1 - |\Gamma(R, f)|^2$ for (a) 1-stage matching circuit, (b) an idealized 2-stage matching circuit, (c) a stretched 2-stage matching circuit with $\alpha = 3$. The black curve is the absolute value of the impedance $Z(f)$ seen by the sample. Red circles represent points in the (R, f) with perfect matching; concentric circles represent a doubly-degenerate solution. **(b,d,f)** Phase plot vs f of the corresponding impedance Z in the left-side panels. Zeros are marked with a red circle, and doubly-degenerate zeros are marked with concentric circles.

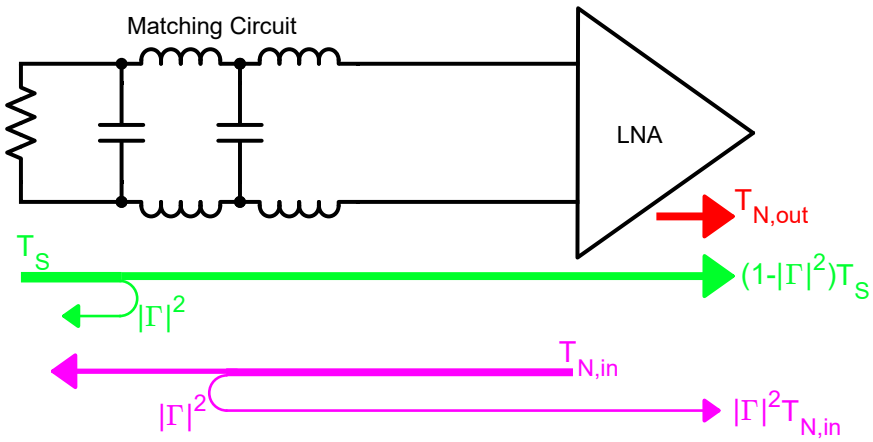

Figure 4.10: The three effective sources of noise in the circuit. Red: output-side amplifier noise. Green: sample Johnson noise. Magenta: input-side amplifier noise. Arrow directions and turnarounds indicate propagation and reflection of noise power. The difference between the sample Johnson noise and input-side amplifier noise, $T_S - T_{N,in}$, is what generates the parasitic noise modulation, as will be described in Section 4.9.

solutions can sometimes cancel each other out.

4.5 JNT Calibration

One of the most difficult parts in any noise measurement is performing an accurate calibration due to unknown exact values of amplifier gain, frequency bandwidth, and losses in the system. However, all these prefactors multiply together into one single total system gain, simplifying the calibration to just one number. We can obtain this total system gain by measuring the Johnson noise at several fixed cryostat temperatures, set by external precalibated thermometers. The calibration is performed *in situ* on the same sample on which actual thermometry measurements will be performed, eliminating any systematic errors due to sample differences such as varying stray capacitance. For our RF JNT thermometer, the gain is a function of the sample resistance only, as described in the following model. The noise going into the power detector in Fig. 4.2 consists of

the three separate noise channels shown in Fig. 4.10 added together: (1) the Johnson noise produced by the sample and then amplified; (2) the noise produced by the input-side of the LNA, reflected off the sample and matching circuit, and then amplified; and (3) the output-side noise produced by the amplifier (already amplified). Considering these three contributions, the total noise power N is given by

$$N = \int 4k_{\mathrm{B}}\tilde{G}_0 \left(\left(1 - |\Gamma|^2 \right) T_{\mathrm{samp}} + |\Gamma|^2 T_{\mathrm{N,in}} + T_{\mathrm{N,out}} \right) df \tag{4.27}$$

where $\tilde{G}_0 = \tilde{G}_0(f)$ is the frequency-resolved effective amplifier gain including the band-pass filters and any losses, $\Gamma = \Gamma(R, f)$ is the reflection coefficient of the sample with respect to the amplifier as defined in Sections 1.6 and 4.4, T_{samp} is the temperature of the sample, and $T_{\mathrm{N,in}}$ and $T_{\mathrm{N,out}}$ are the effective noise temperatures of the noise produced at the input and output terminals of the LNA, respectively. The input-terminal noise of the amplifier reflects off the sample and enters the amplifier, adding to the output noise temperature.

Integrating Eq. 4.27 over frequency, we can define a normalized gain $g = g(R)$, which we can also call a power-coupling coefficient, or band-integrated impedance matching efficiency, via

$$g = \int \left(1 - |\Gamma|^2 \right) df. \tag{4.28}$$

Then Eq. 4.27 can be rewritten as

$$N = 4k_B G_0 \left(gT_{samp} + (1-g)T_{N,in} + T_{N,out}\right) \tag{4.29}$$

$$n \equiv \frac{N}{4k_B G_0} = gT_{samp} + (1-g)T_{N,in} + T_{N,out} \tag{4.30}$$

$$n = g(T_{samp} - T_{N,in}) + T_{N,in} + T_{N,out} \tag{4.31}$$

where we have defined n as the normalized noise in units of K, and G_0 is the effective frequency-integrated amplifier gain. This paints a simplified picture of the three separate noise sources in Fig. 4.10, and will be a starting point for analysis in later subsections.

With integration, Eqs. 4.27 and 4.31 can be empirically simplified to

$$N = G\left(T_{\mathrm{samp}} + T_{\mathrm{N}}\right) \tag{4.32}$$

where $G = 4k_B G_0 g$ and $T_{\mathrm{N}} = \big((1-g)T_{N,in} + T_{N,out}\big)/g$ are the effective band-integrated gain and noise temperatures of the thermometer circuit, which depend only on the sample resistance R. We note that G is not a conventional amplifier gain, but rather a calibration factor for our thermometer; it includes the integrated matching circuit efficiency, amplifier gains, effective filter bandwidth, the Boltzmann constant, and any losses in the circuit. The gain G can be obtained by measuring the derivative dN/dT_{samp} by changing the cryostat temperature, as long as the sample resistance stays constant. However, in general the sample resistance also changes with temperature, for which we have developed our advanced calibration techniques described later in this section. From here on, we will generally drop the "samp" subscript and refer to the sample temperature as just T.

4.5.1 Tunnel Junction as a Calibration Test

The easiest calibration to perform is on a sample with constant resistance vs temperature. One such sample is a non-superconducting tunnel junction, which will exhibit constant resistance with temperature in certain regimes where thermally-assisted tunneling does not play a role. The samples for this experiment were aluminum tunnel junctions provided by K.C. Fong at BBN, and we operated them as normal-metal tunnel junctions above the $T_c = 1.2\,\mathrm{K}$ of aluminum. Tunnel junctions are especially useful for calibration testing of the JNT thermometer, because the calibration value can be verified by shot noise.

To perform the calibration, we vary the temperature of the cryostat and measure the total DC noise power from the amplifier for several temperatures, verifying that the sample resistance is constant. Typical data are shown in Fig. 4.11(a). This calibration was taken using an RF digitizer card and FFT algorithm in place of the analog power diode, but the principle is exactly the same.

The resulting noise vs temperature data is linear, and we perform a linear fit. The slope of the linear fit gives us the gain $G = 2.161 \times 10^{-9}\,\mathrm{W/K}$; here the units of Watts are somewhat arbitrary thermometer output units and arise from the digitizer and FFT. Similarly arbitrary units of Watts or Volts will arise when using a calibrated power diode. At $T = 0$, the extrapolated linear fit does not equal zero; the noise that would be seen at $T = 0$ is entirely background amplifier noise. This amplifier noise can be converted to effective amplifier noise temperature in units of Kelvin by dividing by the gain, or alternatively by taking the x-intercept value. The resulting noise temperature is 530 K. The noise temperature we obtain in this experiment is very large compared to the signal of interest (of order 5–50 K) because we did not using a cryogenic LNA for the

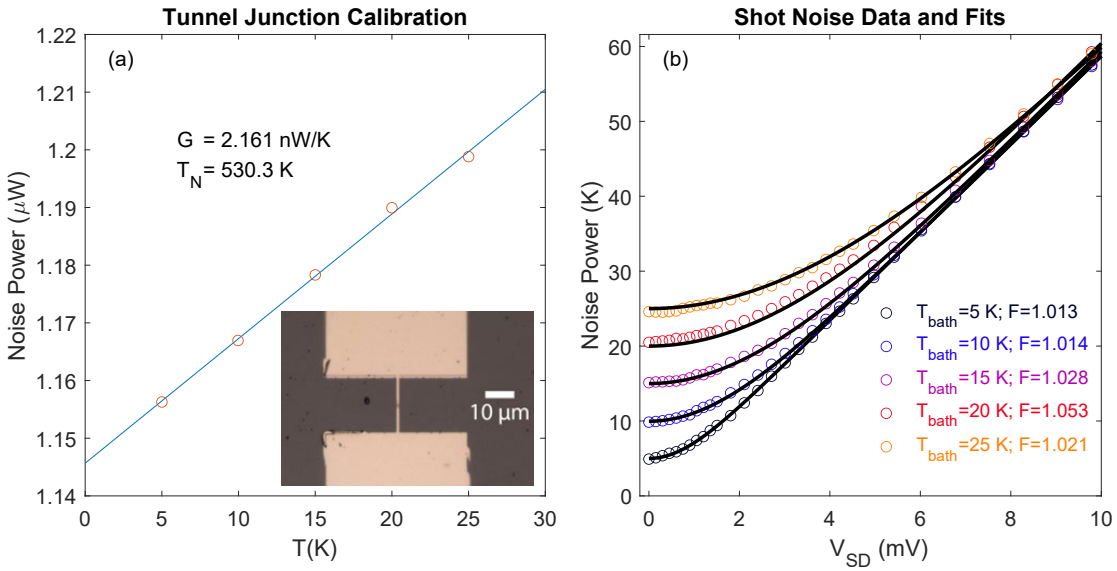

Figure 4.11: **(a)** Calibration of Johnson noise for the tunnel junction. Gain and noise temperature are obtained from the slope and extrapolated x-intercept. Inset: optical micrograph of the tunnel junction; scale bar is 10 μm. **(b)** Shot noise data, taken at several bath temperatures, plotted in units of Kelvin using the calibration. Solid lines are shot noise functional form fits, with the Fano factor F as a fitting parameter. The resulting fit parameter F is displayed in the legend entries.

first-stage amplification; nonetheless, we are able to obtain reasonably good accuracy and precision with long enough averaging; see also Section 4.6 for a discussion of the effect of background noise temperature on precision.

To verify the calibration, we measure and examine the shot noise of the tunnel junction in Fig. 4.11(b). To measure shot noise, we apply a DC bias voltage across the sample and measure the DC noise power from the amplifier, analogously to the initial calibration, as a function of the bias. Shot noise has a white spectrum for frequencies $\hbar\omega \ll k_B T$, and it comes from the quantization of charge and the granularity of individual random tunneling events of electrons. It has a spectral density of[170,171,183,184]

$$S = 2eV \coth\left(\frac{eV}{2k_B T}\right) \tag{4.33}$$

dependent on the sample bias V. At $V = 0$, this formula reduces to the Johnson noise limit $S = 4k_B T$, which we verify experimentally in Fig. 4.11(b) for 5 K to 25 K. In the limit of $eV \gg k_B T$, this is often written as $S = 2eVF$, where F is the Fano factor[185] and equals 1 for a tunnel junction. To include the Fano factor as a fitting parameter in Eq. 4.33, we can rewrite it via the Khlus formula as[154,186,187]

$$S = 2eVF \coth\left(\frac{eV}{2k_B T}\right) + 4k_B T \times (1 - F). \tag{4.34}$$

We can now use F as a fitting parameter for the data, at several different temperatures, to judge the accuracy of our calibration. The resulting fits are shown in Fig. 4.11(b) as the black lines, and the resulting Fano factors (in the legend) are very close to 1. We can thus conclude that our calibration is accurate to approximately 2%.

4.5.2 Gate-Voltage Calibration and the Differential Factor

In cases where the sample has a gate, the resistance can now be tuned arbitrarily within certain limits. The calibration method presented in the previous subsection needs to be generalized, so that it can be performed at every gate voltage or every resistance. This subsection describes a calibration technique where the tunnel junction method is applied for every gate voltage, but the constraint of T-independent resistance is relaxed. Initially, the relaxation of this constraint may seem beneficial, in fact, as now we don't have to worry at all about the sample resistance, and for each gate voltage we have a look-up table that allows us to convert between temperature and noise. This was the calibration technique used in Refs. 1,96. However, we will soon see that this method involves a subtle mistake with a factor of 3 that will yield inaccurate results for the self-heating method of measuring thermal conductivity.

A typical set of calibration data with this method is shown in Fig. 4.12. Due to the changing resistance vs temperature at a fixed gate voltage, the impedance matching conditions also change with temperature. Thus, the total noise power is affected not only by the temperature change but also by an impedance matching change. The resulting plots of noise power vs temperature are now nonlinear, and the gain is not well defined; however, the gain could still be defined locally as the slope of noise vs temperature.

Starting with Eq. 4.32, we can compute the slope of noise via chain rule:

$$\frac{dN}{dT} = G + \left(\frac{\partial G}{\partial R} (T + T_N) + G \frac{\partial T_N}{\partial R} \right) \frac{dR}{dT}. \tag{4.35}$$

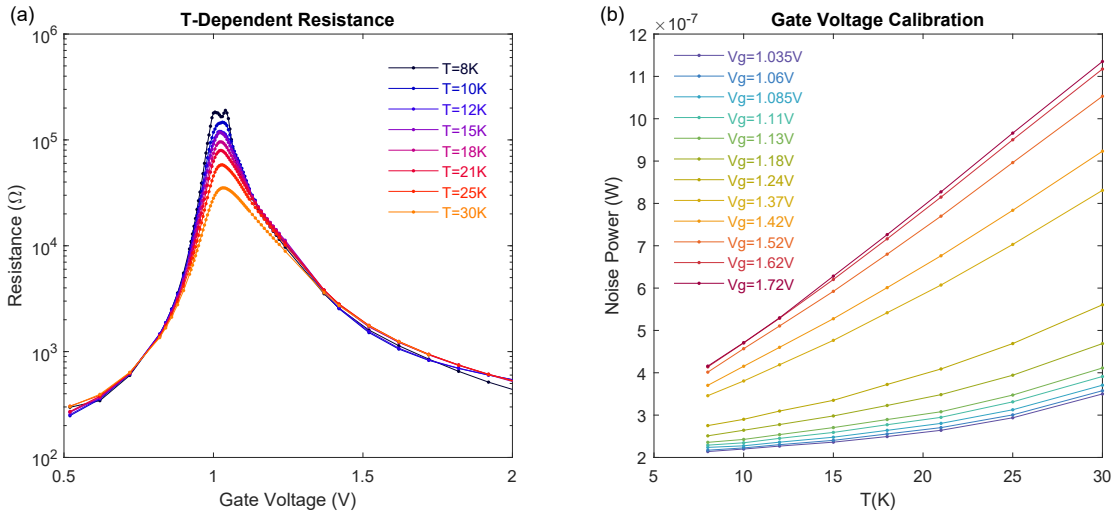

Figure 4.12: **(a)** Temperature-dependent resistance of a bilayer graphene sample. The high-resistance region is where a bandgap is opened up with displacement field. **(b)** Resulting traces of noise power vs temperature are nonlinear due to the changing resistance. This calibration data is the same data from our publication[159].

However, this can also be written in a simpler form starting from Eq. 4.31:

$$\frac{dn}{dT} = g + \frac{\partial g}{\partial R}\frac{\partial R}{\partial T}(T - T_{N,in}). \tag{4.36}$$

The apparent gain we measure is not equal to G (or g). Why is this gain number important here, if we are just using a nonlinear look-up table to convert between noise and temperature? It is because we perform a small-signal AC heating measurement; the temperature of the sample is modulated by a small amount ΔT, and we want to measure the corresponding Johnson noise modulation ΔN. The goal of the gain G here is to convert between them: $\Delta N = G\Delta T$, in the ideal case.

It is crucial to note that the R in Eqs. 4.36 and 4.35 is the instantaneous differential resistance of the sample, which differs from the DC resistance of the sample $R_{DC} = V/I$ if the sample is biased and has a nonlinear I-V curve. Fig. 4.13 illustrates the mechanism

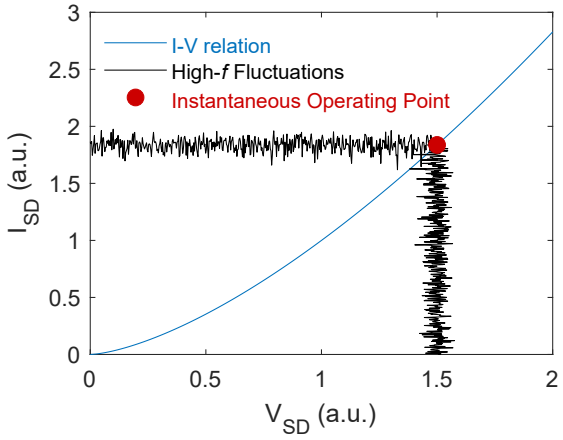

Figure 4.13: Under a DC bias of a sample with a nonlinear I-V curve, the small high-frequency fluctuations couple to the differential resistance dV/dI rather than the total DC resistance V/I.

for this. Under a DC or low-frequency bias, the small RF fluctuations have a voltage to current ratio given by the differential resistance dV/dI which is the quantity that affects the impedance matching mechanism. Importantly, the mechanism for nonlinearity must occur on a timescale faster than the relevant fluctuations. In graphene, local electron thermalization occurs on extremely fast timescales $<30\,\mathrm{fs}$[38,188–190]. Global sample-wide thermalization, which depends on ratio of graphene electronic heat capacity to thermal conductance, occurs on slower timescales, but is still measured to be faster than $\sim 2.3\,\mathrm{GHz}$ for $T > 5\,\mathrm{K}$ using bolometric mixing[94]. This implies that if the sample nonlinearity occurs from heating and temperature dependence of the resistance, that the voltage fluctuations, at a few hundred MHz that we typically use for JNT, will "see" this nonlinearity.

We will now see that the premise of this look-up table for converting ΔN to ΔT breaks down when it is used in a self-heating configuration. Expressing Eq. 4.36 for a finite change in noise, we get

$$\Delta N = G\Delta T_{\text{bath-heating}} + \frac{\partial G}{\partial R}(T - T_{N,in})\Delta R_{\text{bath-heating}} \tag{4.37}$$

where the subscripts indicate that $\Delta T, \Delta R$ arise from heating the cryostat bath temperature. For bath heating, the change in differential resistance will equal the change in total resistance.

If the device is instead Joule heated with a DC bias, the total resistance will correctly track the spatial average of the temperature:

$$\begin{aligned} R_{\text{total}} = \frac{V}{I} =& \frac{1}{W}\int_0^L \rho\left(T\left(x\right)\right) dx & (4.38)\\ =& \frac{1}{W}\int_0^L \left[\rho_0 + \frac{d\rho}{dT}\Delta T\left(x\right)\right] dx & (4.39)\\ =& R_0 + \frac{1}{W}\frac{d\rho}{dT}\int_0^L \Delta T\left(x\right) dx & (4.40)\\ =& R_0 + \frac{dR}{dT}\Delta T_{avg} & (4.41) \end{aligned}$$

where R_0, ρ_0 are the zero-bias resistance and resistivity at the bath (or reference) temperature, and $\rho(T)$ is the temperature-dependent resistivity. We can also rewrite Eq. 4.38 as a function of the applied bias current, using $\Delta T_{avg} = \frac{1}{2}\frac{d^2T}{dI^2}I^2$:

$$R_{\text{total}} = R_0 + \frac{dR}{dT}\Delta T_{avg} = R_0 + \frac{dR}{dT}\cdot\frac{1}{2}\frac{d^2T}{dI^2}I^2. \tag{4.42}$$

From Eq. 4.42, we can now easily calculate the total and differential resistance under

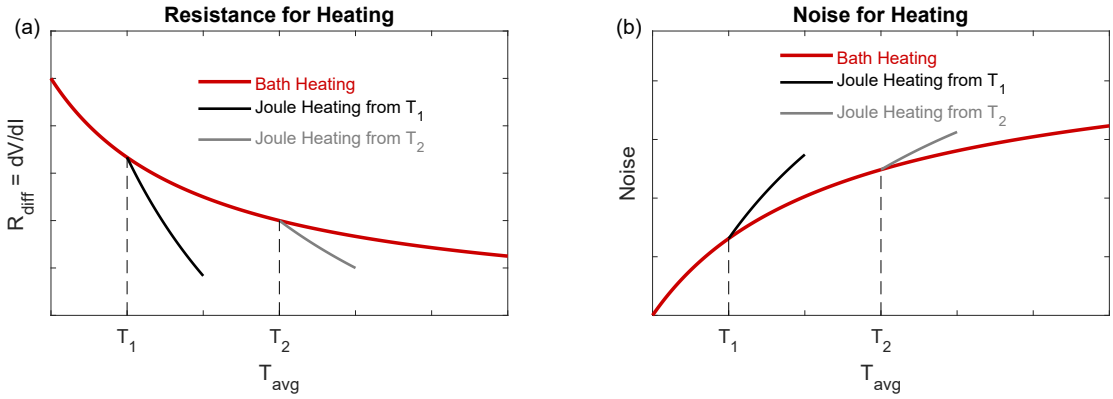

Figure 4.14: **(a)** Differential resistance as a function of temperature for a fixed gate voltage. Calibration under very low bias happens along the red curve, where the total and differential resistance are the same. If the bath temperature is fixed at T_1 (T_2) and the device is Joule-heated, the differential resistance follows the black (gray) curve while the total resistance follows the red curve. The change in the black (gray) curve is $3\times$ the change in the red curve. **(b)** The resulting noise change for different heating mechanisms. Starting from a temperature T_1 (T_2), bath heating will cause the noise to follow the red curve, but Joule heating will cause the noise the follow the black (gray) curve.

bias:

$$R_{\text{total}} = R_0 + \frac{1}{2}\frac{dR}{dT}\frac{d^2T}{dI^2}I^2 \implies \boxed{\Delta R_{\text{total}} = \frac{1}{2}\frac{dR}{dT}\frac{d^2T}{dI^2}I^2} \tag{4.43}$$

$$R_{\text{diff}} = \frac{dV}{dI} = \frac{d}{dI}\left(I \cdot R\left(I\right)\right) = \frac{d}{dI}\left(I \cdot \left(R_0 + \frac{dR}{dT}\frac{1}{2}\frac{d^2T}{dI^2}I^2\right)\right) = R_0 + \frac{3}{2}\frac{dR}{dT}\frac{d^2T}{dI^2}$$
$$\implies \boxed{\Delta R_{\text{diff}} = \frac{3}{2}\frac{dR}{dT}\frac{d^2T}{dI^2}I^2}$$

The change in differential resistance is three times that of the change in total resistance when Joule heating is used, $\Delta R_{\text{diff}} = 3\Delta R_{\text{total}}$, compared to bath-heating, where $\Delta R_{\text{diff}} = \Delta R_{\text{total}}$. This difference in differential resistance for bath-heating and Joule-heating is illustrated in Fig. 4.14(a). This factor of 3 difference, for which the sample thermalization rate must be faster than the voltage fluctuations, has been previously

explored in the context of 3ω resistance-based measurements of thermal conductivity[191,192].

The change in noise due to Joule heating (JH) is then

$$\Delta\ N_{JH} = G\Delta T_{JH} + \frac{\partial G}{\partial R}\left(T - T_{N,in}\right) \cdot 3\Delta R_{total} \tag{4.44}$$

which means that the original calibration curve cannot be used to get the device temperature from the noise, comparing with Eq. 4.37, since "the noise change due to differential resistance change" for Joule heating is different from "the noise change due to differential resistance change" during calibration bath heating, as shown in Fig. 4.14(b).

If we try to calculate the apparent temperature rise using the measured calibration gain slope $s = \Delta N/\Delta T$, we get

$$\Delta T_{\text{apparent}} = \frac{\Delta N_{JH}}{s} = \frac{G + \dfrac{\partial G}{\partial R}\left(T - T_{N,in}\right) \cdot 3\dfrac{dR}{dT}}{G + \dfrac{\partial G}{\partial R}\left(T - T_{N,in}\right) \cdot \dfrac{dR}{dT}} \times \Delta T_{JH}. \tag{4.45}$$

Depending on the exact ratio of the first to second terms in the numerator and denominator in the above equation, the apparent temperature rise can be made very different from the true temperature rise, including appearing much smaller. If the apparent temperature rise is much smaller than the true temperature rise, the Lorentz ratio will be grossly over-estimated.

By carefully measuring the temperature dependence of the resistance, and calculating the derivative $\partial G/\partial R$, we could correct for this error. However, as shown later, there are often other nonlinearities present in graphene beyond that of temperature-dependent resistance, and we present a different strategy to calculate and correct for the nonlinearity in Section 4.9.

4.5.3 Variable-R with Gating Calibration

We now present the correct technique to calibrate the JNT thermometer for a sample with a gate. Unlike the previous section, the calibration is now done for every resistance, rather than for every gate voltage value. The temperature dependence of resistance is effectively removed in this technique, allowing us to obtain the true thermometer gain G.

The key part of calibration is that the sample resistance R can be continuously varied by gate voltages (or magnetic fields) at several fixed temperatures T_{samp}, allowing us to determine G and T_{N} for any given R. Here, we use bilayer graphene (BLG) as the sample since it can be electrostatically tuned between a metal and a small-gap semiconductor[28,29,193–197]. The insets of Figs. 4.15(a) and Fig. 4.15(b) show a schematic diagram and optical image of the device. Tuning both the top gate voltage (V_{TG}) and back gate voltage (V_{BG}) to the same sign dopes the BLG channel, while applying gate voltages of opposite sign in the correct proportions opens a gap and places the chemical potential inside the gap. Indeed, Fig. 4.15(a) shows the sample's two-terminal resistance R change 30 kΩ–100 kΩ as we tune the chemical potential into the gap at 5 K, creating an ideal testing ground for our variable-resistance JNT.

Utilizing the continuously variable resistance, we calibrate our noise thermometer as follows: First, at a fixed cryostat temperature T_1, as we vary the top gate voltage V_{TG}, we simultaneously measure (1) the low-bias differential resistance $R(V_{\mathrm{TG}})$ of the channel using a lock-in technique and (2) the total noise power $N(V_{\mathrm{TG}})$, as shown in Fig. 4.15(b) and (c). The goal of this gate voltage sweep is to vary the resistance over as wide a range as possible, so we do it for several back gate voltages to get the full range. This process is repeated for several other temperatures $T_2, T_3, ...$

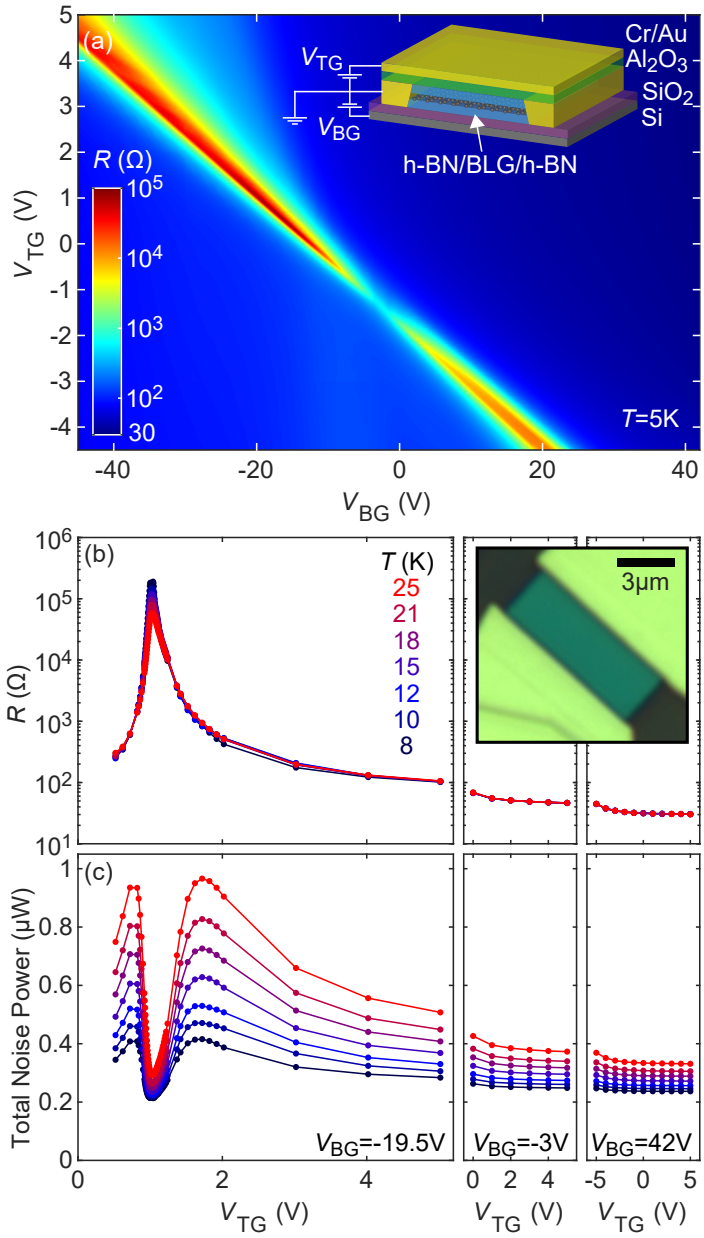

Figure 4.15: **(a)** The sample resistance measured at $T = 5\,\mathrm{K}$ vs top gate and back gate voltage $(V_{\mathrm{TG}}, V_{\mathrm{BG}})$. The inset shows a schematic for the device cross-section. **(b,c)** The top panel shows resistance as a function of V_{TG} at fixed temperatures, and the bottom panel shows total noise power measured from the sample as a function of V_{TG} at the corresponding temperatures. Each horizontal panel shows data from different fixed back gate voltage. To perform the calibration, we sweep the gates at fixed temperatures to vary the resistance and measure total noise power. Inset: an optical image of the device before top gate deposition.

Next, for each temperature T_i, the total noise is plotted against the resistance as in Fig. 4.16(a). Using interpolation or polynomial fits, we can then obtain a noise power vs temperature relation for any fixed resistance as shown in the inset of Fig. 4.16(a). We find the noise power to be linear in temperature with an offset, consistent with Eq. 4.32, for our entire range of measured resistances. For each resistance, we then perform a linear fit, obtaining the gain G as the slope and the noise temperature T_N as the horizontal offset. Fig. 4.16(b) shows the resulting G and T_N vs sample resistance R. We optimized the matching circuit for $R_0 = 1\,\mathrm{k}\Omega$, where it shows a peak of G and minimum of T_N. Away from this optimized R value, G decreases and T_N increases, reducing our thermometer's precision.

The long-term stability of the calibration is most affected by the gain stability of the LNAs as those are the only active elements in the circuit up to the lock-in amplifiers. The passive elements should remain relatively consistent under a constant laboratory temperature. We have found that, if we do not physically disturb the noise circuit, we typically achieve calibration stability to within a few percent over several weeks, which is sufficient for our measurements. The calibration stability can always be checked by converting the measured total noise to a temperature and comparing with the cryostat temperature.

To verify our understanding of the frequency integration in going from Eq. 4.27 to Eq. 4.32, we perform a different frequency-resolved version of the calibration just described. We modify the circuit in Fig. 4.2 by removing the band-defining filters and replacing the RF power detector diode with a spectrum analyzer. Instead of measuring the total noise power N, we now measure the frequency-resolved power spectrum S, which is the integrand of Eq. 4.27 without the filters. We then perform the previously-described calibration method for every $\sim 2\,\mathrm{MHz}$ frequency bin. The resulting quantity

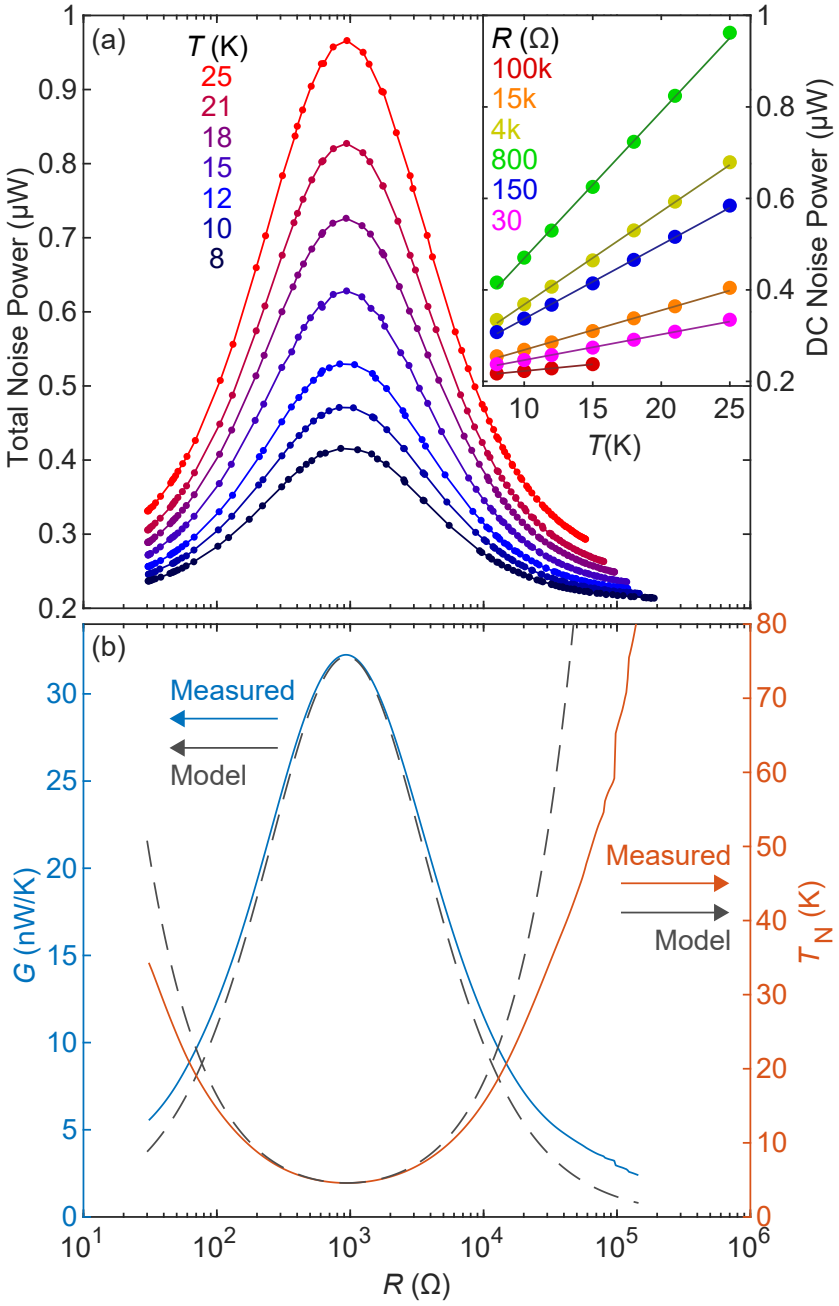

Figure 4.16: **(a)** Total noise power plotted vs sample resistance for the set of measured temperatures. Inset: For any resistance value, we construct a total noise vs temperature plot with the data measured in (a). The linear fit gives the gain and noise temperature. **(b)** The measured gain (blue) and noise temperature (red) as a function of sample resistance obtained from data in the inset of (a). The gray dashed curves are the scaled gain and noise temperature for the matching circuit model described in the text.

is $G_0(1-|\Gamma|^2)$ as a function of (R, f), which we have normalized to unity and plotted in Fig. 4.8(d) as the colormap with the dotted 0.75 contour. This contour approximately matches the solid black contour from the model for the ideal 2-stage matching circuit; the differences can be explained by a frequency-dependent LNA gain and circuit components whose values do not exactly match the idealized component values.

4.5.4 Background Gain

To estimate the relative accuracy of the calibration as a function of sample resistance, we compare the measured gain and noise temperature with our impedance matching model. We numerically integrate Eq. 4.27 with the calculated $1-|\Gamma|^2$ value over the measured frequency band and scale it to equate the peak heights. We use the actual matching circuit component values ($C_1 = C_{\text{stray}} + 0.9\,\text{pF}$, $L_1 = 240\,\text{nH}$, $C_2 = 4.3\,\text{pF}$, $L_2 = 76\,\text{nH}$) and use the stray capacitance as a fitting parameter to tune the horizontal position of the peak, with $C_{\text{stray}} = 0.12\,\text{pF}$. We use $T_{\text{N,out}} = 4.2\,\text{K}$ and $T_{\text{N,in}} = 1.5\,\text{K}$ as fitting parameters for the noise temperature. We have plotted this calibration model as the gray dashed curves in Fig. 4.16(b). The relative accuracy is approximately the fractional difference between the measured and model gain curves.

At the high and low ends of the sample resistance range, the measured gain deviates from our model, setting the working accurate resistance range for our thermometer. To investigate this deviation, we perform a dummy calibration on a similar matching circuit with no resistive sample connected, ideally expecting only T-independent amplifier noise ($G = 0$ and $T_{\text{N}} \to \infty$). However, this dummy calibration yields a background gain, with a noise vs T slope of $G = 1.6\,\text{nW/K}$ (about 5% of the peak gain) and $T_{\text{N}} = 122\,\text{K}$, accounting for most of the gain deviation at high and low R. To explain this artificial background gain without a sample, we propose two mechanisms:

1. The first is dissipation in non-ideal reactive circuit elements whose temperature follows that of the sample during calibration, including the Si substrate as part of the stray capacitance, the sample PCB, inductors, and sections of coaxial lines. In the limits of low coupling $R \to \infty$ or $R \to 0$ where the sample dissipation approaches zero, these dissipative elements still couple their own thermal noise into the LNA.

2. The second is the intrinsic temperature dependence of the reactive components or their dissipative losses, modulating the reflection coefficient of the circuit and thus the amount of LNA back-action reflected back towards the LNA. Due to these two effects, warming the sample stage during calibration increases the non-sample noise entering the LNA, thus artificially increasing the measured gain. This artificial increase in the slope of noise vs T far off-match (Fig. 4.16(a) inset) reduces the negative horizontal offset of the linear extrapolation, thus artificially reducing the measured noise temperature.

For these two reasons, we minimize losses (see Subsection 4.7) between the sample and LNA by using short coaxial cables, and we improve thermal isolation (see Subsection 4.8) between the sample and other circuit components by using outer DC blocks. This significantly helps bring the measured curve closer to the predicted model curve. If we want to measure a sample with a resistance where our thermometer has reduced accuracy due this background gain, it is more accurate to use the theoretical gain model. In this case, we fit the theoretical model to match the peak height and R-position of the gain curve, using the stray capacitance as a fitting parameter, and the typical $\pm 10\%$ uncertainty on the reactive matching circuit components as some additional wiggle room in fitting parameters.

4.5.5 Single-R Ungated Calibration

Some samples that are ungateable, such as 3-dimensional samples, exhibit a temperature-dependent resistance and it is thus impossible to perform the calibration at a constant resistance. In this case, a workaround using a functional fit is possible if the form of the impedance matching function is known. For this demonstration, we are showing a calibration on a 500 nm-thick BSCCO sample (Fig. 4.17), which is a high-temperature superconductor, provided by Frank Zhao. This particular sample is near optimally doped and exhibits a $T_c \sim 88\,\mathrm{K}$, and has about $2.9\,\Omega$ contact resistance, as seen in Fig. 4.17(a). The noise N vs temperature T trace is shown in Fig. 4.17(b) and is very nonlinear, especially as we approach T_c.

The noise can be written in the functional form

$$N = G\bigg(\Big(1 - |\Gamma|^2\Big)\,T + |\Gamma|^2\,T_{N,in} + T_{N,out}\bigg) \tag{4.46}$$

where we use G, $T_{N,in}$, and $T_{N,out}$ as fitting parameters. Γ is a function that is defined by the measured resistance trace in Fig. 4.17(a), with an extra fit parameter R_L for the lead resistance, given by

$$\Gamma = \frac{Z_0 - (R - R_L)}{Z_0 + (R - R_L)}. \tag{4.47}$$

All that is left to do is to fit the parameters in Eq. 4.46. The lead resistance R_L acts to offset the resistance in Fig. 4.17(a), and because it is physically located external to the sample and matching circuit, it must be subtracted off from the measured resistance in order to obtain the bare sample resistance. The resulting fit and fit parameters are shown in Fig. 4.17(b). The fit is excellent, and the 1-σ uncertainty bounds on the

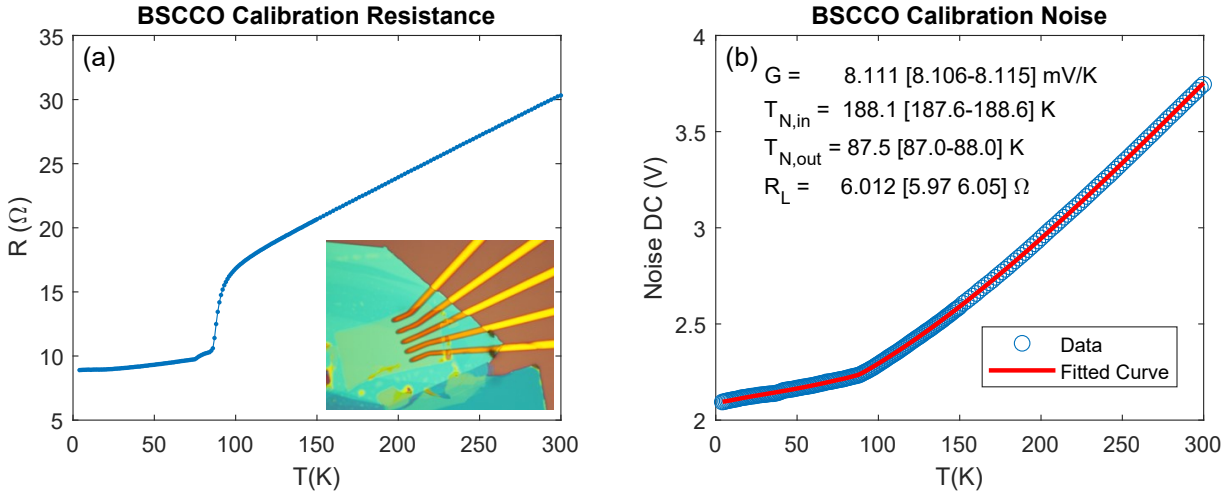

Figure 4.17: **(a)** BSCCO sample (500 nm thick), nearly optimally doped, resistance vs temperature. T_c ~88 K. Inset: optical micrograph of the device. **(b)** Noise power data (circles) and the fitted functional form of Eq. 4.46 (red). The resulting fit parameters with 68% confidence intervals are shown in the plot.

parameters are very small, allowing a highly accurate calibration on this device.

4.6 Measurement, Uncertainty, Dicke Formula, and Noise Channels

JNT directly probes the electron temperature of the sample. In graphene, at low enough temperature, the electron temperature can decouple from the lattice temperature, allowing the electrons to be heated to a temperature appreciably higher than that of the lattice[1,95–98]. If electron-electron scattering is strong enough to allow a well-defined electron temperature, electrons in mesoscopic graphene samples obey diffusive quasi-equilibrium transport. In this regime, cooling occurs by electronic diffusion to the bulk metal contacts, dominating cooling by direct heat exchange to phonons. These conditions allow us to use JNT to measure the electronic thermal conductivity (κ) of monolayer graphene[1,94–96].

In this section, we use our variable-resistance noise thermometry technique on a BLG sample to demonstrate κ measurements on a mesoscopic scale. We perform the measurements in the same cool-down on the same sample, with the same electrical configuration, as the calibration. No measurement configuration changes in the cryostat were made between calibration and measurement. We follow the same assumptions as for MLG, experimentally confirming that direct phonon cooling becomes appreciable only at higher temperatures. We measure κ as follows: we heat the electrons in the sample with a known amount of power via an AC current, typically at $1f \sim 17\,\mathrm{Hz}$. We measure the AC resistance using a lock-in amplifier at $1f$ and noise power modulation at the output of the power detector with a lock-in amplifier at $2f$. Using the calibrated value of the gain at the measured sample resistance, we convert the noise modulation amplitude to a temperature modulation ΔT. The ratio of applied Joule power to measured temperature rise then yields the generalized thermal conductance of the sample:

$$G_{\mathrm{th,gen}} = \frac{P_{\mathrm{Joule}}}{\Delta T}. \tag{4.48}$$

The effective thermal conductance is $G_{\mathrm{th}} = G_{\mathrm{th,gen}}/12$ with the factor of 12 arising from the spatial temperature distribution in channel self-heating[95–98,160,161]. We work in the low-heating limit $\Delta T \ll T_{\mathrm{bath}}$ relative to the bath temperature so that the factor of 12 remains valid. The thermal conductivity κ is then related by a geometrical aspect ratio. Measurement with this $2f$ modulation technique is advantageous over applying DC bias and measuring total noise due to reduced susceptibility to drifts of the gain and amplifier noise.

We quantify the back-action of the LNAs to ensure it does not corrupt our thermometry measurements. The SiGe LNAs use internal resistive feedback to achieve

good input impedance matching and high gain stability[198]. The back-action spectral power density incident on the sample is $S = k_B T_{N,in}$, where $T_{N,in} = 1.5\,\mathrm{K}$ from our calibration model, which provides photon-mediated cooling to the sample[199] which sits at a higher temperature of $T_{samp} = 10\,\mathrm{K}$. We estimate the cooling power by integrating $(1 - |\Gamma(R, f)|^2) k_B (T_{N,in} - T_{samp})$ over the working bandwidth of the RF diplexer channel (30 to 2150 MHz), where the factor $(1 - |\Gamma(R, f)|^2)$ accounts for the impedance mismatch. We find that the measured electronic diffusion cooling power, equal to the Joule power shown in Fig. 4.18(a), dominates the photon cooling power by over 4 orders of magnitude across the range of measured resistances. The remaining reflected back-action noise power contributes to the amplifier noise temperature T_N as in Eq. 4.32, but it is entirely considered in the calibration and does not influence the thermal conductivity measurement, except as discussed below in Section 4.9.

We perform AC-bias JNT on the device shown in Fig. 4.15(a) and measure G_{th} as described above. To achieve a large resistance range in a single gate-sweep, we hold the top gate voltage fixed at 1.0 V and sweep the silicon back gate voltage. The bath temperature is fixed at 10 K, and at each back gate voltage value, a feedback loop sets an AC bias ($1f$) to maintain a temperature modulation ($2f$) of 200 ± 5 mK rms.

Figs. 4.18(a) and (b) show the AC Joule power and measured temperature modulation as a function of sample resistance. We have computed statistical uncertainties in the measured temperature modulation and plotted those in Fig. 4.18(b) as error bars and in Fig. 4.18(c) explicitly as the blue data points.

As a reference, we compare with expected uncertainties from a balanced Dicke Ra-

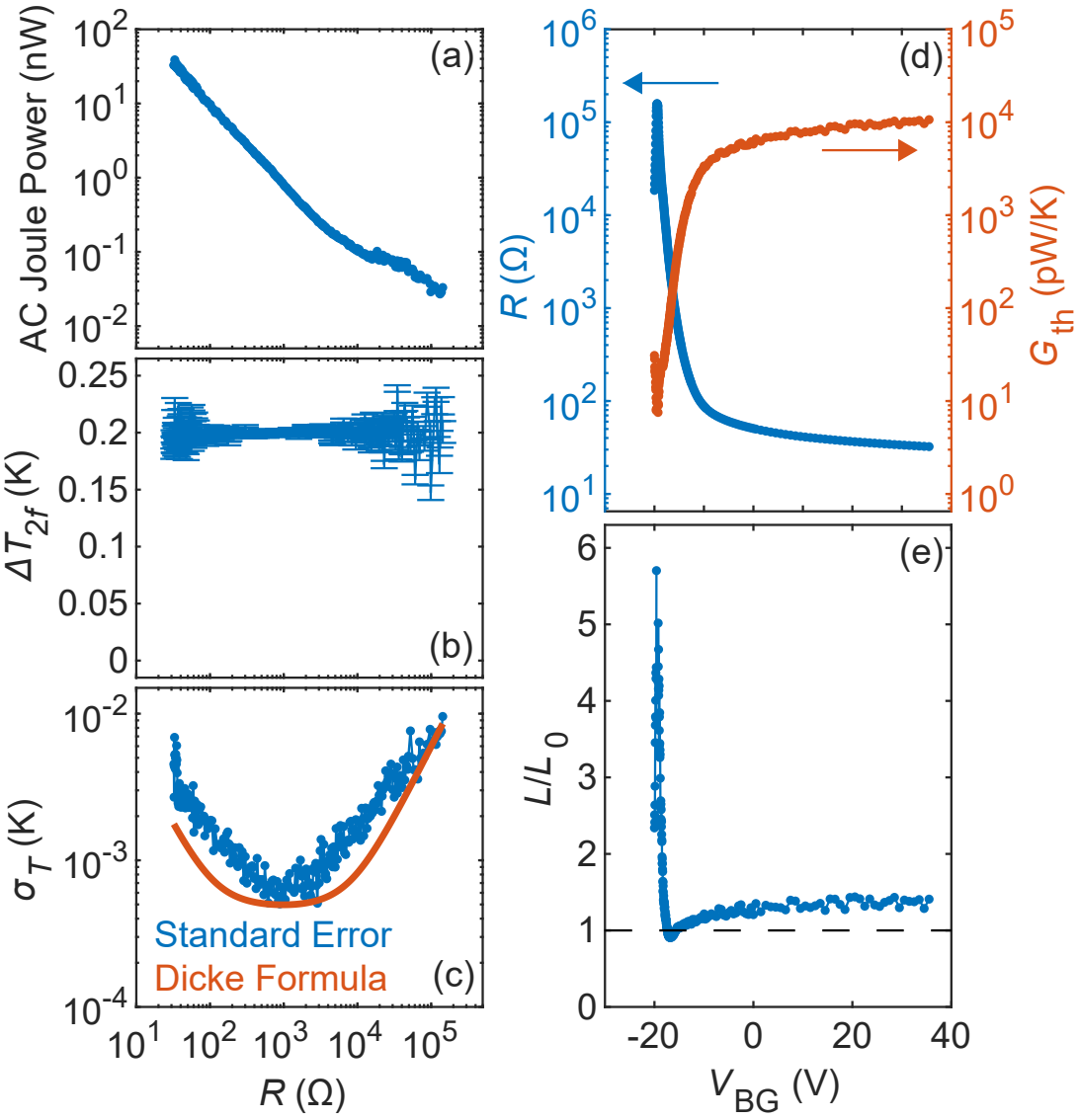

Figure 4.18: **(a)** The AC bias power applied to the sample as a function of resistance, controlled via a feedback loop to keep the temperature modulation at 200 mK. **(b)** The measured temperature modulation. The error bars are estimated from the standard deviation of the data before averaging. **(c)** The statistical uncertainty of measured temperature estimated in (b) is plotted as a function of sample resistance. It approximately follows the prediction from the Dicke radiometer formula (Eq. 4.49 in the text), using 130 MHz bandwidth. The variation as a function of resistance is due to the increasing effective amplifier noise temperature away from the optimally matched resistance. **(d)** The measured resistance and thermal conductance as a function of back gate-voltage, with top gate voltage at 1.0 V. **(e)** Lorenz ratio computed from the ratio of thermal conductivity to temperature and electrical conductivity. The black dashed line is the Wiedemann-Franz law.

diometer. From Eq. 2.11, the uncertainty is given by[142]

$$\sigma_T = \frac{F\left(T_{\text{samp}} + T_{\text{N}}\right)}{\sqrt{\tau \Delta f_{\text{c}}}} \tag{4.49}$$

with $F = 2\sqrt{2}$ for our sine-modulated and sine-correlated radiometer. The filters we select in our amplifier chain define a bandwidth that overlaps maximally with the high-coupling region of the matching circuit. For this device, this provides a bandwidth of ~ 130 MHz, from 120 MHz to 250 MHz, as shown in Fig. 4.8(a) by the gray dashed lines. However, the correlation bandwidth Δf_{c} is slightly smaller and given by[130,142,200–202]

$$\Delta f_{\text{c}} = \frac{\left[\int_0^\infty |G(f)|\, df\right]^2}{\int_0^\infty |G(f)|^2\, df} \tag{4.50}$$

where $G(f)$ is the frequency-dependent gain. Our total noise signal is the sum of the three effective noise channels shown in Fig. 4.10 and in Eq. 4.27. Although the input- and output-side amplifier noise may be correlated, we assume for simplicity they are uncorrelated, motivated by the presence of two separate gain stages in the cryogenic LNA. The uncertainty for each noise channel is given by the Dicke radiometer formula (Eqs. 2.11 and 4.49) with the appropriate F factors and the corresponding correlation bandwidth Δf_c (Eq. 4.50). Since we measure the sum noise power of these three channels, the individual uncertainties will add in quadrature to obtain the uncertainty for the total noise:

$$\sigma^2_{N_{total}} = \sigma^2_{N_{T_S}} + \sigma^2_{N_{T_{N,in}}} + \sigma^2_{N_{T_{N,out}}}. \tag{4.51}$$

The correlation bandwidths Δf_c of the channels vary depending on the sample resistance: for the sample noise it varies from 130 MHz on-match to 122 MHz far off-match;

for the amplifier input-side noise it varies from 44 MHz on-match to 130 MHz far off-match; and for the amplifier output-side noise it is constant at 130 MHz.

Our ∼130 MHz noise bandwidth is orders of magnitude larger than bandwidths used in low-frequency noise thermometry and allows significantly faster measurements. This is an improvement upon single-stage matching, which achieved a 20 MHz bandwidth centered at 100 MHz for measuring a monolayer graphene device[1]. As shown in Fig. 4.18, we achieve 650 μK uncertainty measuring a 200 mK temperature modulation on a 10 K background, equivalent to 65 ppm, with 30 s of averaging, for the best matched resistance around 1 kΩ. The precision is reduced at resistances further away from the best match; we achieve only 10 mK precision at a resistance of 150 kΩ.

For the entire resistance range measured, our radiometer shows standard errors no larger than about 3 times the predicted uncertainty. The excess standard error can arise from sources such as amplifier gain/noise drifts and additional noise at the input of the lock-in.

In Fig. 4.18, we plot in parallel the electrical resistance measured via a standard lock-in technique and the thermal conductance. As the electrical resistance exhibits a strong peak due to opening of the gap by applied gate voltage, the thermal conductance correspondingly falls very sharply. By taking the ratio of the thermal conductance to the electrical conductance ($= R^{-1}$) and the temperature T, we obtain the Lorenz number $L = G_{th}R/T$. In a degenerate Fermi liquid, L should be close to the Sommerfeld value $L_0 = \pi^2/3\,(k_\mathrm{B}/e)^2$. The Lorenz ratio $\mathcal{L}/\mathcal{L}_0$ then quantifies the degree to which the Wiedemann-Franz law is satisfied in our sample. In our high-resistance gapped BLG, the Lorenz ratio increases up to a maximum measured value of around 5–6; however, due to device nonlinearities in the gap, this value is possibly overestimated as we did not use a nonlinear correction here (see Section 4.9). As we move the chemical potential into

the valence band, graphene becomes more linear, and Fermi liquid behavior returns with the Lorenz ratio tending towards 1. Upon further gating, the experimentally measured Lorenz ratio is ∼1.3, slightly larger than the expected unity.

4.7 Loss Minimization

To optimize the performance of the JNT thermometer, we need to minimize the reflective and dissipative losses in the circuit between the sample and the LNA. For the dissipative losses, we can describe a simple model for the first mechanism (1) of background gain described in Subsection 4.5.4. Consider a sample at temperature T_s perfectly impedance-matched to a coaxial cable; in this case, we may write the noise power spectral density of the waves traveling along the coaxial cable away from the sample as $S = 4k_BT_s$. Suppose there is a dissipative attenuator at temperature T_A with attenuation (=absorptivity) α along this cable; then the signal traveling through the attenuator gets attenuated as

$$4k_BT_S \to 4k_BT_S(1-\alpha). \tag{4.52}$$

Due to the second law of thermodynamics and Kirchoff's law of thermal radiation, the attenuator must also emit thermal noise with emissivity equal to its absorptivity. Therefore, on the other side of the attenuator, we get

$$4k_BT_S \to 4k_BT_S(1-\alpha) + T_A\alpha. \tag{4.53}$$

If the sample is at cryogenic temperatures (e.g. 3 K), but the attenuator is at warm or room temperature (300 K), then even a small attenuation of 1% will emit thermal noise

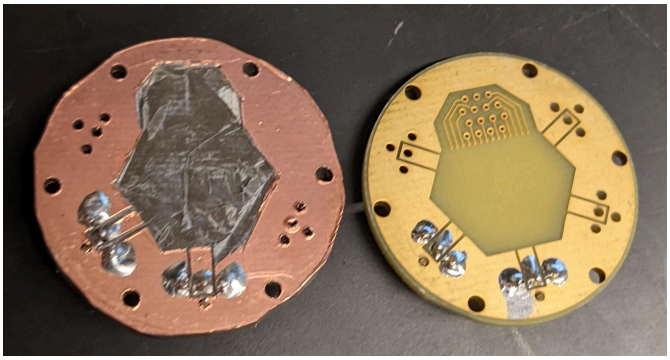

Figure 4.19: Left: Test PCB made from Rogers low-RF-loss dielectric. **Right:** Production PCB made from generic FR-4 dielectric.

at a spectral power of $1\% \times 300 k_B T = 3 k_B T$, equal to the already small thermal noise from the sample. However, this only increases the effective system noise temperature parameters T_N, $T_{N,in}$, and $T_{N,out}$.

For this effect to generate a background gain, the temperature of the attenuating element must at least partially follow the temperature of the sample during the calibration temperature sweeps. For example, the Ohmic losses in the matching circuit inductors and the dielectric losses in the sample PCB will directly follow the sample temperature during calibration and have a significant effect on the background gain. We characterized the effect of the dielectric losses in the PCB by comparing a hand-made PCB made of low-loss Rogers Duroid dielectric, against a standard non-RF-optimized PCB made with generic FR-4 dielectric, shown in Fig. 4.19. We performed the experiment by measuring the background gain of each PCB without a sample attached. We compare the background gain relative to the full-scale gain of a fully-matched $100\,\Omega$ resistor. The results are tabulated in Table 4.1.

Switching the dielectric from FR-4 to Rogers Duroid decreased the background gain by 4.5% of the fully-matched $100\,\Omega$ gain. In this particular setup, there still remained

PCB Dielectric Comparison: Background Gain		
PCB Type	Background Gain (W/K)	$T_N(K)$
Rogers Duroid	8.56×10^{-9}	105
FR-4	1.21×10^{-8}	76

Table 4.1: Comparison of background gain measured for two different types of PCB material, measured by performing a temperature-calibration with no sample connected to the PCB. A 100 Ω resistor gave a fully-matched gain of 7.86×10^{-8}W/K. Changing the PCB material decreased the background gain by 4.5% relative to the fully-matched gain. In this experiment, there is still a significant amount of background gain from other sources.

11% background gain even with the low-loss PCB, with most of it likely coming from other attenuative elements of the circuit that were not thermally anchored; in particular, the RF boards that will be shown in Fig. 4.20 were not yet anchored with copper braids and were later confirmed to be another significant contributor to the background gain. With the decrease of the background gain, we also observe an increase of the measured noise temperature $T_{N,in}$. A calibration with no sample (i.e. the limit of zero impedance matching) should, in the ideal case, produce zero background gain and infinite noise temperature; thus, the increase in noise temperature also indicates that some background gain was removed.

In the VTI implementation of the JNT circuit, there is about 2.5 m of coaxial cable and a diplexer between the sample and the first-stage cryogenic LNAs, which sit in a liquid nitrogen dewar external to the main cryostat. Over 2.5 m of coax, a significant part of which is at room temperature or significantly above the low sample temperature, a very significant amount of thermal background noise can end up being generated from the losses along the way. A typical thin 047 Ag/Cu coaxial cable has 1.31 dB/m (26% power/m) attenuation at room temperature at 1 GHz. Due to the skin depth effect in coaxial cables[109], there is more attenuation at higher frequencies, and thicker coaxial cables will have less attenuation. Thus, it is best to make JNT lines between the

sample and first-stage amplifier out of the thickest available coaxial cable with copper- or silver-clad conductors, and to consider the tradeoff of high vs low frequency. As described in Subsections 4.4.2 and 4.4.3, a higher matching center frequency will lead to a proportionately higher bandwidth; this will occur at the cost of more background thermal noise from the lines which raises the noise temperature. Both of these effects are easily captured by the Dicke formula in Eq. 2.11 or 4.49.

We typically place the center frequency somewhere between 150 and 700 MHz and have found this to work well for us; however, higher or lower center frequencies will also generally work. Finally, dielectric losses in the PTFE dielectric in coaxial cables can be slightly improved by using cables with low-loss porous PTFE dielectric. Similarly to the PCB, the coaxial cables connecting the sample PCB to the rest of the circuit also partially follow the sample temperature and can contribute to the background gain. To help mitigate this issue if the coaxial cable loss cannot be reduced any further, the solution is described in the next section.

It is also beneficial to make the attenuative components between the sample and first stage LNAs as cold as possible. In particular, placing the diplexers into the liquid nitrogen dewar next to the LNAs instead of keeping them at room temperature will help reduce their thermal noise contribution.

4.8 Thermal Anchoring and Thermal Isolation

Our primary goals with thermal isolation and anchoring are to minimize the background gain by minimizing the temperature swing of any attenuative components, and to mitigate the heat load on the cold sample stage. Typically, installation of coaxial cables into multi-stage cryogenic systems often uses strong attenuators and high-loss resis-

tive coaxial cable at each stage to help thermalize the coaxial cable to the cryogenic temperature and block high-temperature Johnson noise from reaching the sample. Sections 4.5.4 and 4.7 described how these techniques with attenuators are incompatible with Johnson noise thermometry, and how very low-loss coaxial cable is necessary. In dilution refrigerators, NbTi superconducting coaxial lines offer a convenient solution of ultra-low loss (dominated by dielectric loss) and zero electronic thermal conduction (phonon thermal conduction, while present, is extremely weak), but are unavailable at temperatures above 10 K.

However, we have invented other ways to connect low-loss coaxial cable across high thermal gradients to minimize heat leaks. By placing an outer DC block on the coaxial cable, we effectively stop electronic heat transport (following the Wiedemann-Franz law) along the outer conductor of the coaxial cable, using the phonon thermal transport across the DC block as the thermal bottleneck. Fig. 4.20 demonstrates some implementations of this outer DC block method. Panels (a,c) show standard outer DC blocks (green arrows) in a cryocooler and VTI setup. If the inner conductor is not used for DC biasing, an inner-outer DC block can be used in place of the aforementioned outer DC block to stop electronic heat transport along the inner conductor. However, on some coaxial cables the inner conductor has a steel core with a copper and silver cladding; the steel provides structural rigidity and less thermal conductance than full copper, but because of the skin depth effect the steel does not affect Ohmic losses in the line.

Sometimes outer DC blocks can be too large to comfortably fit into small cryostat spaces, such as the bore of a magnet. In this case, we have developed a technique to fabricate home-made outer DC blocks using a section of coaxial cable and a standard large-value SMD capacitor. The outer conductor along the entire circumference, for a short 1 mm span of cable, is removed from a braided tinned semi-rigid coaxial cable. A

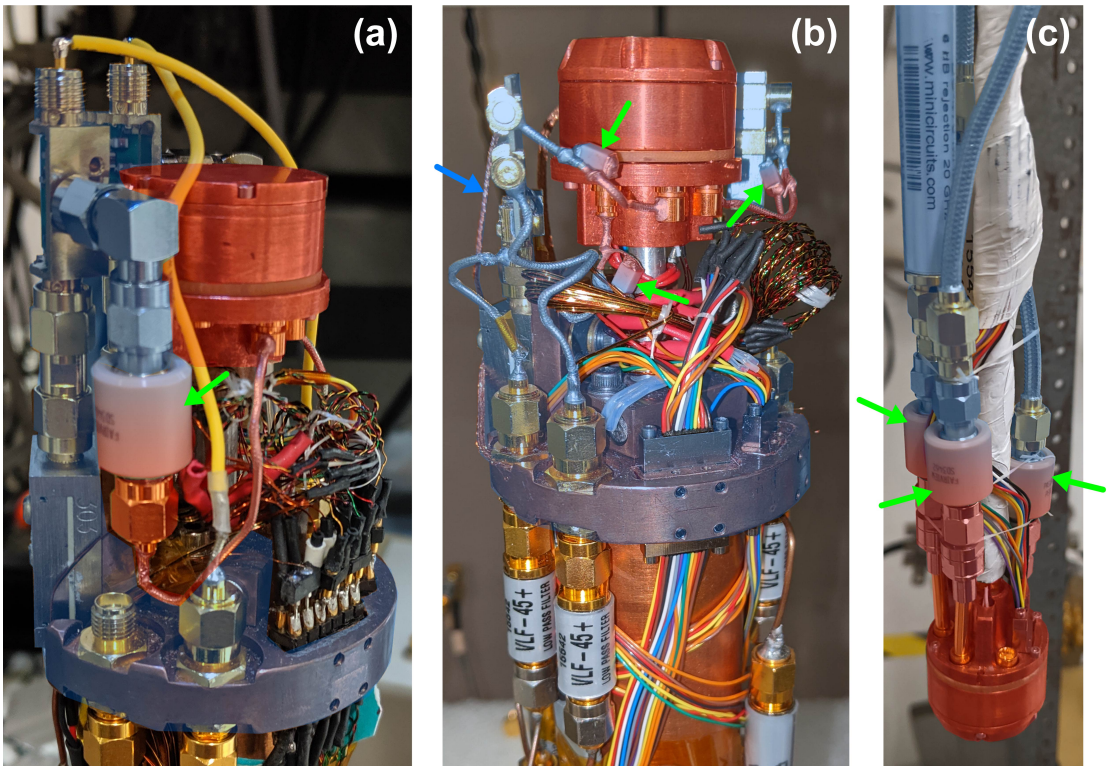

Figure 4.20: **(a)** Thermal isolation in a cryocooler. The hotter sample stage is overlaid in red, and the cooler amplifier stage at 5 K is overlaid in blue. Green arrow indicates the outer DC block. **(b)** Next generation cryocooler circuit, with thermal isolation provided by home-made outer DC blocks with SMD capacitors (green arrows). Copper braid (blue arrow) is used to help thermally anchor the RF PCB to the cold plate. **(c)** Thermal isolation on a probe for a VTI cryostat, following the same principles.

tinned copper wire is wound around and soldered to each remaining end of the outer conductor and bridged with a capacitor. Fig. 4.20(b) shows home-made outer DC blocks (green arrows) in a cryocooler.

For thermal anchoring, panel (b) shows the use of a copper braid (blue arrow) to help heatsink the RF PCBs to reduce background gain. In panel (c), thermal anchoring is provided by the vapor. Rather than the usual VTI procedure where the vapor is held at a temperature just below the sample temperature, we maintain the vapor at base temperature with a high rate of helium flow to help maintain a cold temperature for the main body of the probe, with only the copper sample package being heated.

Appendix H reviews in more detail the cryostats used in our measurements.

4.9 Sample-Nonlinearity-Induced Noise Modulation

As introduced in Subsection 4.5.2, the nonlinear I-V curve in a graphene device can introduce noise power modulations due to the modulation of the impedance matching, rather than just the modulation of the temperature, causing an incorrect measurement (Eq. 4.44). This can create hidden and serious inaccuracies in the measurements and must be strictly accounted for. An example of nonlinearity in a graphene sample is shown in Fig. 4.21. While this direct measurement of the nonlinearity during DC biasing was measured by a small AC bias superimposed on a large DC bias, we instead require a way to measure the nonlinearity under a large AC bias concurrently with the AC JNT measurement itself. In this section, we present a way to quantify the sample nonlinearities and their effects on the noise modulation.

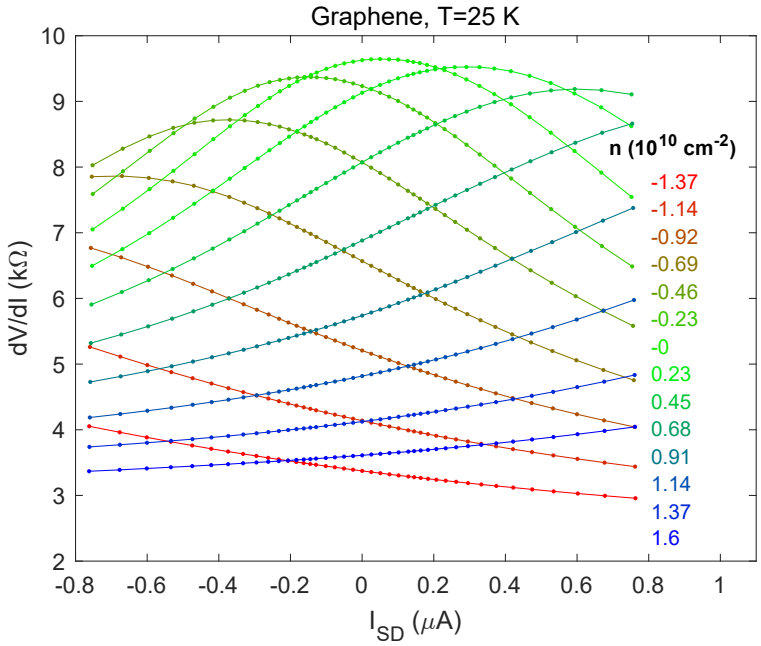

Figure 4.21: Differential resistance dV/dI for a graphene sample as a function of bias current at $T = 25\,\mathrm{K}$, for different electron densities.

4.9.1 Explanation and Measurement

We require an equation that describes how the noise is modulated with regards to the biasing current. Since the biasing current through the sample is modulated at $1f$, and we measure the temperature and noise modulation at $2f$, we effectively measure the second derivative of noise with respect to bias current. Starting with Eq. 4.31, we take consecutive derivatives of the noise and obtain the following equation:

$$\boxed{\left.\frac{d^2N}{dI^2}\right|_{I=0} = G\frac{d^2T}{dI^2} + \left(\frac{d^2G}{dR^2}\left(\frac{dR}{dI}\right)^2 + \frac{dG}{dR}\frac{d^2R}{dI^2}\right)(T_S - T_{N,in})}, \tag{4.54}$$

where we have dropped the subscript for the differential resistance R. This equation is the central result of the work on understanding the noise modulations induced by

sample nonlinearity. The steps of the derivation are left as a calculus exercise to the reader.

Here, we have assumed for simplicity that the apparent Johnson noise temperature of the sample is equal to its actual temperature. Johnson noise for nonlinear systems is not a deeply studied subject; however, Ref. 203 discusses corrections to the Johnson noise formula Eq. 2.4 that arise due to nonlinearity of the $I-V$ curve, which could potentially modify the apparent noise temperature of the sample and introduce additional terms in Eq. 4.54. In Subsection 7.2.3, we propose an experiment using the methods in this Chapter to directly measure the nonlinear corrections to the Johnson noise formula.

The d^2N/dI^2 term is the noise $2f$ modulation term that is measured on the lock-in amplifier. The first term on the r.h.s. corresponds to the thermal conductance of the sample, in particular how the temperature responds to an applied bias. The second term on the r.h.s. is the parasitic noise modulation term from sample nonlinearities. It involves derivatives of the gain G with respect to the sample resistance, the nonlinear resistive coefficients of the sample, and the $T_{N,in}$ noise parameter. All of these components can be separately measured or calculated in order to quantify this parasitic term.

First, we devise a method to characterize the sample nonlinearities via measurement of voltage harmonics on the sample. This methodology is closely related to measuring thermal conductance using non-RF methods via the 3ω-technique[191,192,204–210]; however, here we generalize to sample nonlinearities beyond temperature-dependence of resistance, including more intrinsic nonlinearities.

This technique is particularly difficult to implement because often the harmonic distortion is small and is comparable to the harmonic distortion of the instruments or tools used. For this reason, the harmonic distortion of all non-sample elements of the circuit

must be accounted for before making quantitative measurements of the sample. For this purpose, we use an ultra-low harmonic distortion function generator Model No. DS360 from Stanford Research Systems, and high-precision external bias resistors, typically 100 kΩ each.

To measure the harmonic distortion of the sample, we generate a low-distortion sinusoidal current through the sample. Under the condition that the external bias resistors are much larger than the sample resistance, $R_{ext} \gg R_{sample}$, the current through the sample is approximately a perfect sinusoid $I(t) = I_0 \sin(\omega t)$[192]. If we write the I-V curve of the sample as a Taylor expansion via

$$V = R_1 I + R_2 I^2 + R_3 I^3 + \ldots, \tag{4.55}$$

and we measure the voltage harmonics as

$$V(t) = V_{DC} + V_1 \sin(\omega t) + V_2 \cos(2\omega t) + V_3 \sin(3\omega t) \ldots, \tag{4.56}$$

then after substitution and grouping of harmonic terms, we obtain the following:

$$\begin{aligned}
V_{DC} &= \frac{1}{2}R_2 + \frac{3}{8}R_4 + \cdots && [\sin(\omega t)] \\
V_{1f} &= R_1 I_0 + \frac{3}{4}R_3 I_0^3 + \cdots && [\sin(\omega t)] \\
V_{2f} &= -\frac{1}{2}R_2 I_0^2 - \frac{1}{2}R_4 I_0^4 + \cdots && [\cos(2\omega t)] \\
V_{3f} &= -\frac{1}{4}R_3 I_0^3 - \frac{5}{16}R_5 I_0^5 + \cdots && [\sin(3\omega t)] \\
V_{4f} &= \frac{1}{8}R_4 I_0^4 + \cdots && [\cos(4\omega t)] \\
V_{5f} &= \frac{1}{16}R_5 I_0^5 + \cdots && [\sin(5\omega t)]
\end{aligned} \tag{4.57}$$

For simplicity, we limit ourselves to the R_3 term and the third harmonic. We need to ultimately calculate how the differential resistance R_{diff} changes with the sample bias, since the impedance matching depends on the differential resistance. From Eq. 4.55, we get

$$\left.\frac{dR_{diff}}{dI}\right|_{I=0} = 2R_2 = -4\frac{V_{2f}}{I_0^2} \tag{4.58}$$

$$\left.\frac{d^2R_{diff}}{dI^2}\right|_{I=0} = 6R_3 = -24\frac{V_{3f}}{I_0^3} \tag{4.59}$$

for the first- and second-order derivatives of the differential resistance with respect to bias.

Next, we describe how to calculate the dG/dR and d^2G/dR^2 terms. We can obtain the experimental calibration curve $G(R)$ as described in Section 4.5.3 and shown in Fig. 4.16(b); however, numerical differentiation of this curve may lead to pretty significant errors, especially if the curve isn't very smooth. Instead, to obtain more accurate

derivatives, we will numerically differentiate the theoretical model shown as the gray dashed curve shown in Fig. 4.16(b). The resulting derivatives, normalized by G, are plotted in Fig. 4.22.

Panel (a) shows the calibration data used in Subsection 4.5.3, and panels (b) and (c) show the first and second normalized derivatives taken from the model. Since the derivative changes sign, it is plotted in purple for positive and red for negative on a log-scale. The green dashed line is a guide to the eye that indicates the upper bound for the gain derivatives. The first derivative exhibits a dip at the peak-matched resistance, and the second derivative exhibits dips at the corresponding inflection points in the gain curve. At each dip, the corresponding term in Eq. 4.54 vanishes; however, we can never get both terms to vanish simultaneously at any given resistance. By tuning the matching resistance, we can shift the positions of the dips, and they will shift along the directions indicated by the gray arrows. We cannot lower the gain derivative curve below the green dashed line by tuning to a different resistance; it will always approach that fixed line asymptotically.

If the sample exhibits only one type of nonlinearity from Eq. 4.54, then the matching can be tuned to place a corresponding dip at the desired resistance measurement value; however, in general, samples will exhibit both types of nonlinearities.

The final ingredient to complete Eq. 4.54 is the determination of the $T_{N,in}$ parameter. We have already seen how to determine it for an ungated sample in Subsection 4.5.5; here we present a more robust method for a gated sample. From Eq. 4.46, we see that if $T = T_{N,in}$, changing the sample resistance and thus the refection coefficient Γ will not change the total measured noise power N, as the T- and $T_{N,in}$-contribution are equal, and the source of noise shifts proportionately between the two. Clearly in Fig. 4.16, this temperature occurs below 8 K and can be obtained via extrapolation.

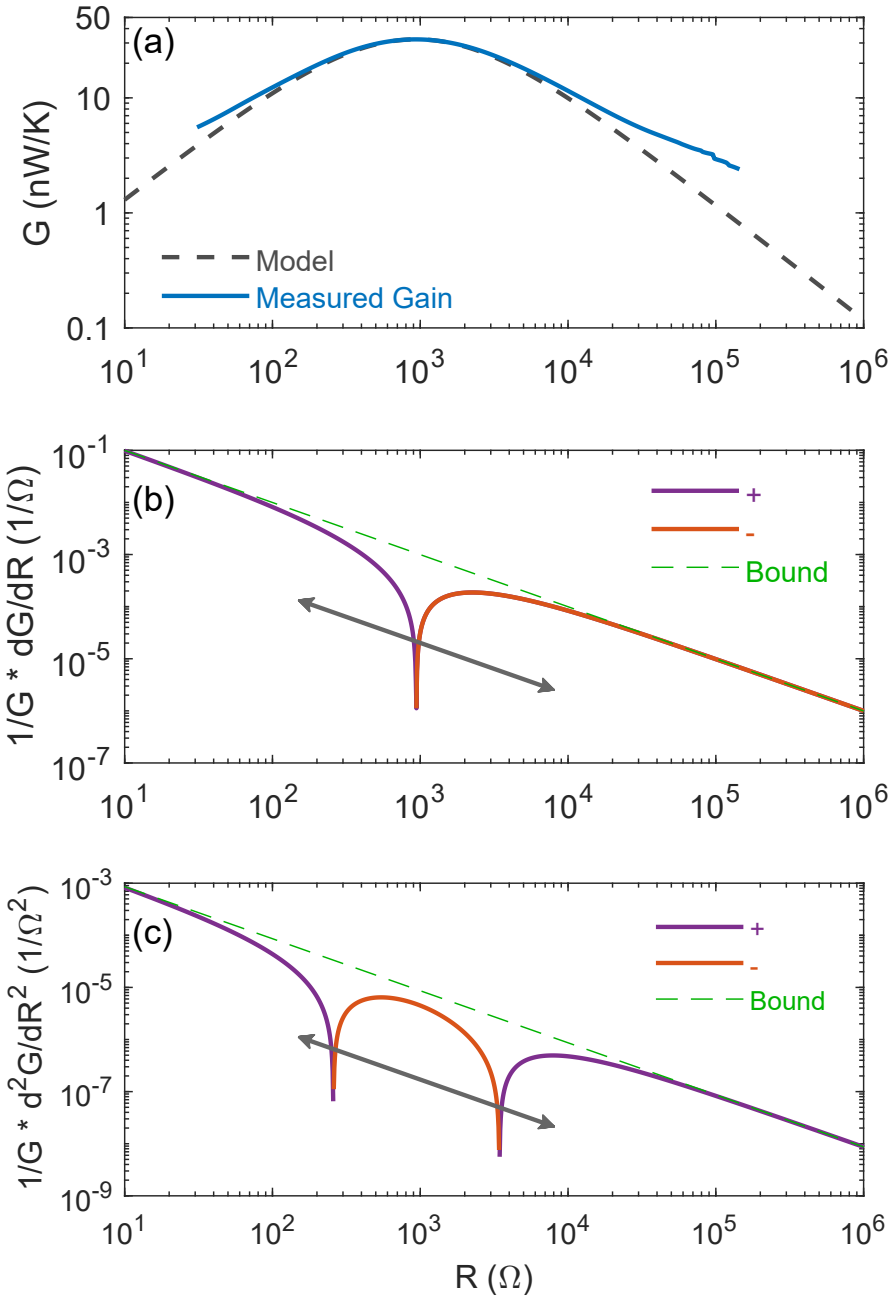

Figure 4.22: **(a)** Measured and theoretically predicted scaled gain, from Fig. 4.16. **(b)** Normalized first derivative of gain; positive (purple) and negative (red). There is a single dip at the peak matched resistance of 1 kΩ. **(c)** Normalized second derivative of gain; positive (purple) and negative (red). There are now two dips, each at an inflection point of the gain curve. In (b) and (c), the green dashed line is a guide to the eye of the fixed upper bound of the normalized gain derivative. Gray arrows indicate the shift direction of the dips when tuning the peak matching resistance.

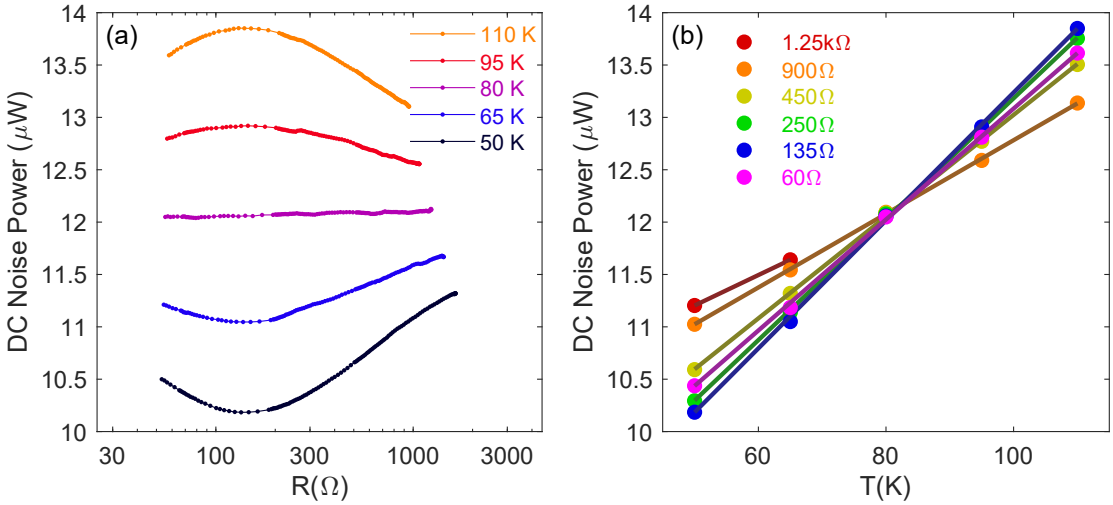

Figure 4.23: **(a)** Noise vs resistance for several temperatures during a calibration. The sample is monolayer graphene. **(b)** The resulting plots of noise vs temperature for a set of resistance values. The different lines intersect at $T_{N,in}$.

Here, we show an example calibration on monolayer graphene in Fig. 4.23 where this temperature is directly measured. In panel (a), the calibration is performed the same way as in Fig. 4.16(a). At $T = 80\,\mathrm{K}$, the noise has almost no dependence on the sample resistance, indicating this is very nearly the "magic" temperature. Fig. 4.23(b) confirms this, where all the linear fits of noise vs temperature intersect at the same point of 82 K. At this one magic temperature, in fact, the parasitic term in Eq. 4.54 vanishes, leaving just the true measurement of thermal conductance.

In an alternative setup in which a sinusoidal voltage bias is used[207] instead of a current bias, and current harmonics are measured, then the equations in this section undergo a transformation $R_i \leftrightarrow \mathfrak{G}_i; V \leftrightarrow I$, where $\mathfrak{G}$ represents the conductance and $\mathfrak{G}_i$ are the nonlinear Taylor expansion terms for $I(V)$ analogous to Eq. 4.55. Eq. 4.54

becomes

$$\boxed{\left.\frac{d^2N}{dV^2}\right|_{V=0} = G\frac{d^2T}{dV^2} + \left(\frac{d^2G}{d\mathfrak{G}^2}\left(\frac{d\mathfrak{G}}{dV}\right)^2 + \frac{dG}{d\mathfrak{G}}\frac{d^2\mathfrak{G}}{dV^2}\right)(T_S - T_{N,in})}. \tag{4.60}$$

Voltage or current biasing may be chosen depending on which Taylor expansion more closely represents the sample nonlinearity: current biasing if differential resistance increases with bias, and voltage biasing if differential conductance increases with bias. In practice, we have found that current biasing is technically easier, as voltage biasing introduces unintended heating of the sample at zero applied bias, and current harmonics are more difficult to measure. However, with improvements in measurement techniques, these limitations may be overcome in future experiments.

Due to the difficulty of measuring small higher-order harmonics, there exist clever measurement techniques that mask the primary harmonic, such as the Wheatstone bridge method[208,209].

4.9.2 Subtraction of the Parasitic Term

Once we know all the ingredients of Eq. 4.54 or 4.60, we can then either verify that the parasitic term is small relative to the thermal conductance term, or if we are confident in our assumptions, we may subtract the parasitic term from the measured noise modulation to obtain the true thermal conductance of the sample. To convert between Eq. 4.54 and the measured noise modulation, we use the simple relation

$$\frac{d^2N}{dI^2} = 4\sqrt{2}N_{rms}/I_0^2, \tag{4.61}$$

where N_{rms} is the rms component of the sinusoidal noise modulation (excluding DC component), and I_0 is the peak heating current through the sample.

By tuning the "magic" temperature as will be described in Subsection 4.9.4, we can test the accuracy of subtracting off the parasitic term. We conduct one measurement of thermal conductance at the magic temperature, where the parasitic term is zero. The magic temperature for this test is $T_{N,in}$ =82.8 K, but we conduct the test at 85 K, since the difference is small enough that the parasitic term is negligible. We then conduct a second measurement at the same sample temperature, now using a different circuit with a different magic temperature of $T_{N,in}$ =21.3 K, and then subtract the parasitic term to obtain the true thermal conductance.

We illustrate this procedure for a monolayer graphene sample. First, we measure the $2f$ and $3f$ voltage harmonics as shown in Fig. 4.24(a,b). We measure them for a few different excitation powers, with feedback at each datapoint to maintain a target temperature rise ΔT as a fraction of the bath temperature T. Comparing across several excitation powers to make sure the R_2, R_3 values are consistent and phase angles are consistent is a valuable safety check.

Fig. 4.24(c,d) ensures the measured harmonics are (mostly) above the harmonic distortion floor of the SR830 lock-in amplifier. Panels (e,f) confirm the measured phase angles match the expected values of $\pm 90^\circ$ for the $2f$ cosine term, and 0° or 180° for the $3f$ sine term. The panel (e) inset shows the measured resistance for the same density range shown in the other panels, for comparison.

Fig. 4.25 illustrates how the measured nonlinearities integrate into the parasitic correction. Panels (a,b) show the gain derivatives (red, purple) and the measured resistance curve (green curve and green region) in the same plot. For the $2f$ component, the steepest part of the resistance curve coincides with the dip in gain derivative, and combined

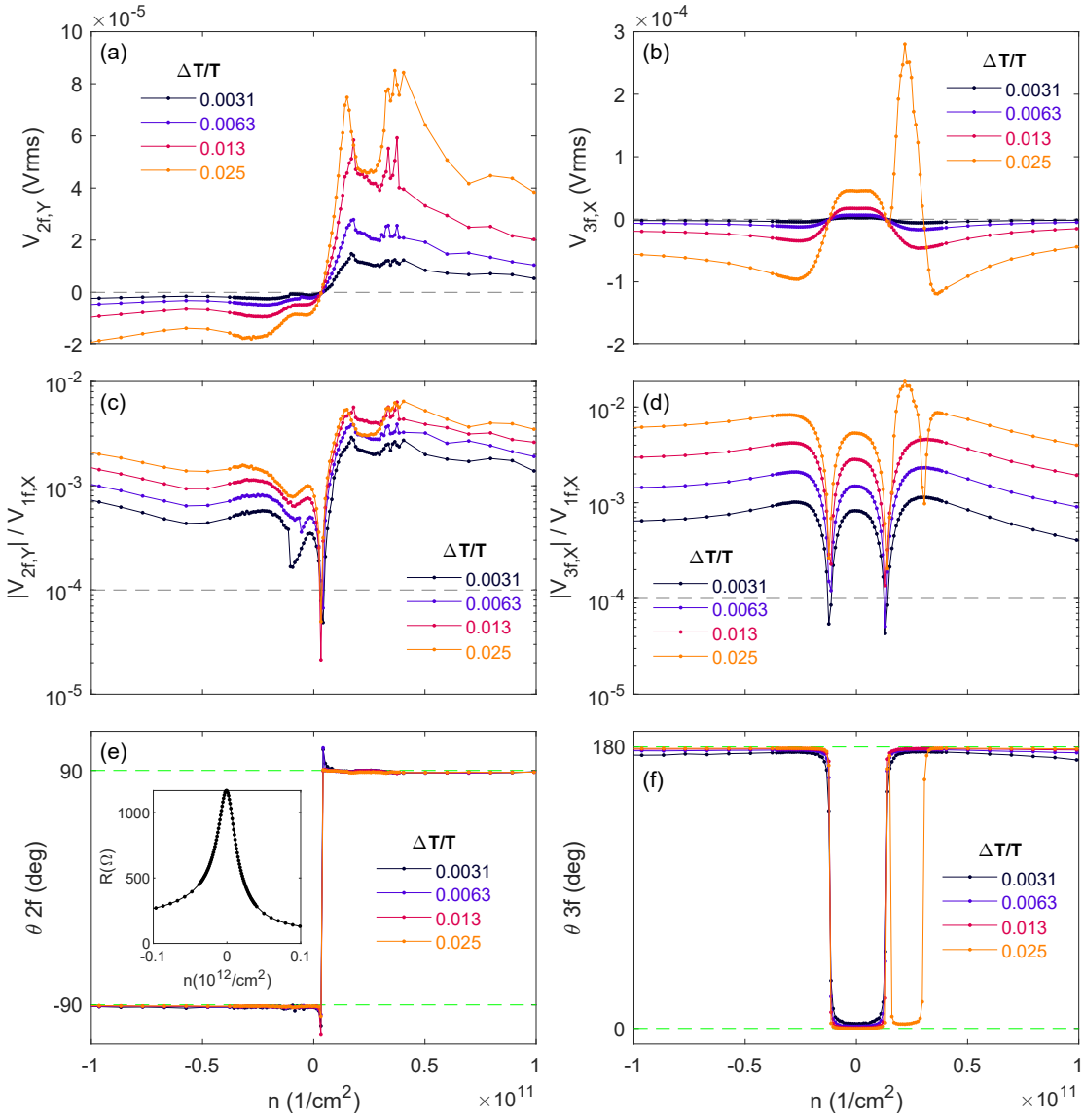

Figure 4.24: **(a)** Voltage harmonics for $2f$. Different colors indicate different excitation powers for different heating temperatures ΔT. **(b)** For $3f$. **(c)** Voltage harmonics for $2f$ normalized by the fundamental at $1f$. Gray dashed line shows the harmonic distortion floor of the SR830 lock-in amplifier. **(d)** For $3f$. **(e)** Measured phase angle of the $2f$ harmonic. Expected values at $\pm 90°$, indicated by green dashed lines. Inset: measured resistance for the same density range as in panels (a-f). **(f)** For $3f$, with expected values at $0°$ and $180°$.

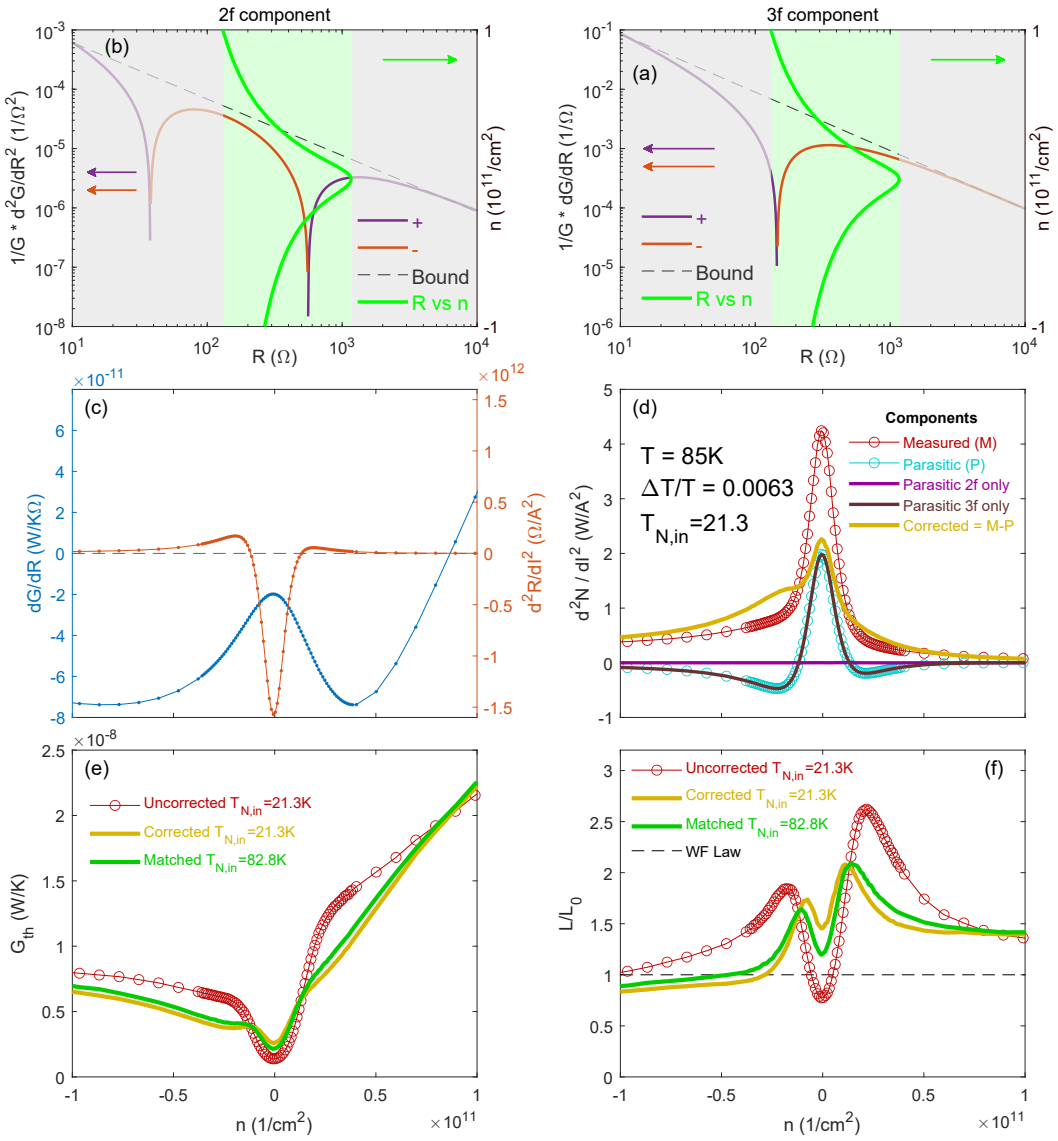

Figure 4.25: **(a)** Left axis: Gain derivative (red: negative; purple: positive) for the $2f$ component of the correction. The green region indicates the range of sample resistance. Gray dashed line is a guide to the eye for an upper bound. Right axis, green curve: Sample resistance plotted vs density. **(b)** Same for $3f$ component. **(c)** Components of the parasitic correction: gain derivative (blue, left axis) and $3f$ sample nonlinearity (red, right axis). $2f$ nonlinearity not shown here because it is negligible. **(d)** Components of the measured $2f$ noise modulation, in units of d^2N/dI^2, at $T = 85\,\mathrm{K}$ with a $0.63\,\%$ temperature modulation. Red: measured noise modulation. Cyan: calculated parasitic correction, consisting of the $2f$ term (magenta) and $3f$ term (dark brown). Yellow: corrected noise modulation, taken by subtracting the parasitic term from the measured term. **(e)** Uncorrected (red) and corrected (yellow) G_{th} from data with mismatched $T_{N,in}$. Green: Uncorrected G_{th} measured with matched $T_{N,in}$. **(f)** Same for Lorenz ratio. Black dashed line is WF law.

with a thick back-gate oxide of 1 µm, fortuitously sets the $2f$ correction to a negligible value (purple curve in panel (d); see also the next subsection for details). The components of the $3f$ correction term are plotted in panel (c), and do not cancel out as they do for the $2f$. Panel (d) shows the raw measured $2f$ noise modulation (red), demodulated into into units of d^2N/dI^2. The total parasitic contribution, calculated from Eq. 4.54, is plotted in cyan. Its $2f$ and $3f$ components are plotted in purple and dark brown; as the $2f$ component is negligible, the parasitic term consists entirely of the $3f$ component. After subtracting the parasitic term (cyan) from the measured data (red), we obtain the corrected value for d^2N/dI^2 (yellow).

From this corrected value, we compute the thermal conductance and Lorenz ratio, shown in panels (e) and (f). Here, we show the starting uncorrected raw data in red. To confirm the correction, we plot an accurate measurement of the two quantities in green, obtained by measuring with a circuit where the $T_{N,in}$ parameter closely matches the sample temperature. The yellow corrected curve closely, although not perfectly, coincides with the true green curve.

As shown in Fig. 4.25(e,f), we over-estimate the correction by a factor of approximately $\sqrt{2}$. We can verify this, by re-doing the correction but scaling it by $1/\sqrt{2}$; the result is shown in Fig. 4.26, where the corrected values now agree very well with the matched $T_{N,in}$ values. It is unclear whether this $1/\sqrt{2}$ is a coincidence. Nonetheless, we will mention that one possibly significant source of error here is higher harmonics. If the device resistance decreases with bias, corresponding to $R_3 < 0$ and $V_{3f} > 0$, then a Taylor expansion of V in powers of I will not be a good approximation of the $I-V$ curve without higher-order terms. This occurs near charge neutrality, as seen in Fig. 4.24. Away from charge neutrality, however, the resistance increases with bias and we expect the Taylor approximation to work better. This pattern of resistance increasing or de-

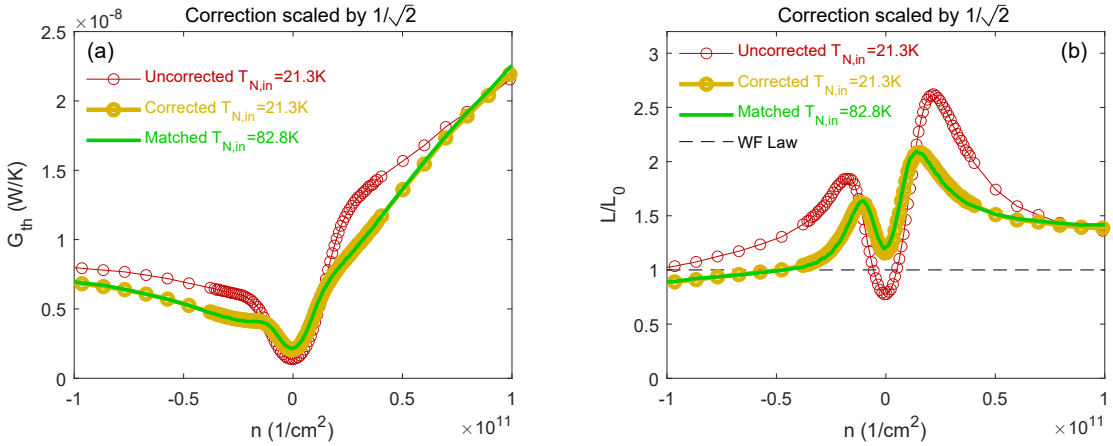

Figure 4.26: **(a)** Uncorrected (red) and corrected (yellow) G_{th} from data with mismatched $T_{N,in}$, with correction scaled by $1/\sqrt{2}$. Green: Uncorrected G_{th} measured with matched $T_{N,in}$. **(b)** Same for Lorenz ratio. Black dashed line is WF law.

creasing with bias near charge neutrality or in the doped regime is consistent with the resistance changing due to device heating. However, our correction is consistently too large by a factor of $\sqrt{2}$ and cannot be explained by poor polynomial fitting only near charge neutrality.

4.9.3 Reduction of Parasitic Nonlinear Effects by Balanced Biasing

As seen in the previous subsection, graphene devices can exhibit both I^2 and I^3 nonlinearities. From the 3ω-method, we saw that one of the sources of the I^3 nonlinearity arises from the temperature dependence of resistance. However, the I^2 nonlinearity is a more intrinsic type of nonlinearity, breaking the bias anti-symmetry analogously to a diode, or a MOSFET operating in the saturation or pinch-off regime. In fact, we can draw a rather close analogy between our 2-terminal graphene devices and a pinched-off MOSFET, as shown in Fig. 4.27. In both a graphene device and a MOSFET, the gate

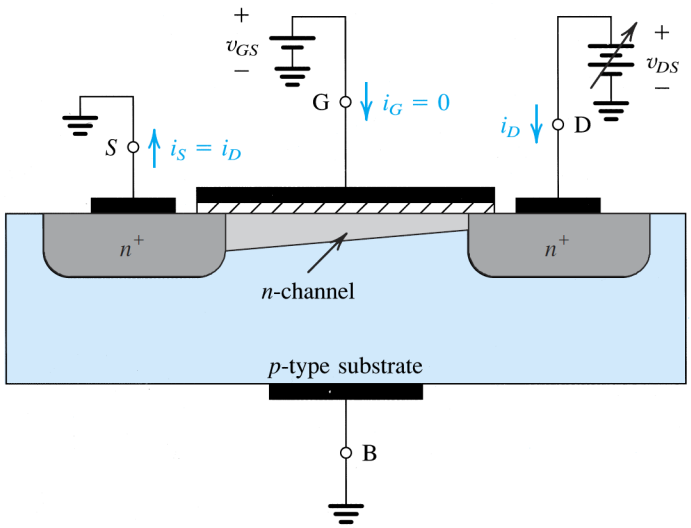

Figure 4.27: A MOSFET demonstrating the channel pinch-off due to the gate-field-effect varying along the channel length. Image from Ref. 211.

induces a density of electrons in the channel due to the electrostatic potential. Under a bias current, the potential is not uniform in the channel but rather has a slope. This causes the average gate potential seen by the channel to depend on the bias, a clear recipe for nonlinearity. One very simple mitigation for this effect is to use balanced biasing: instead of grounding one side of the device and applying a bias through the other side, one can apply opposite biases from each side, creating a virtual ground in the center of the device and forcing the average gate potential seen by the channel to be constant.

In this sense, this type of non-linearity is not "intrinsic" to the sample, since it depends on how the sample is biased. By using a balanced biasing scheme (Fig. 4.2) instead of grounding one side, we can mitigate this effect to first order, as shown in Fig. 4.28. This measurement is done with a fixed external voltage on the ultra-low-distortion function

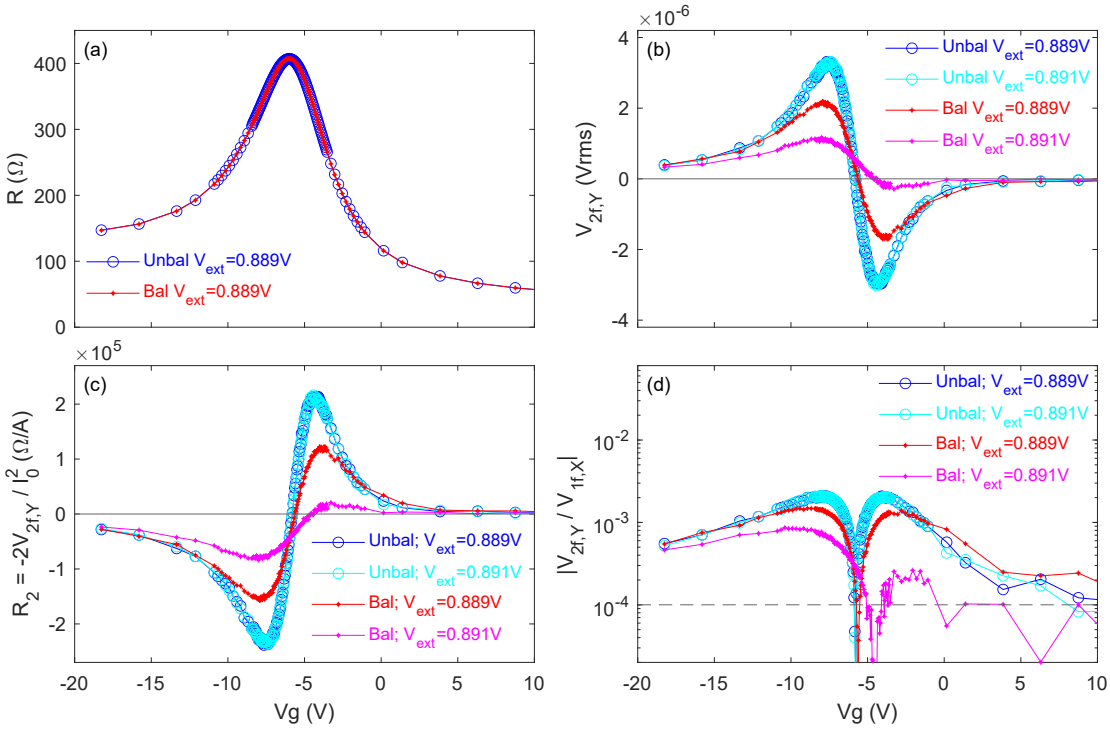

Figure 4.28: **(a)** Measuring resistance (R_1) vs gate voltage for a monolayer graphene sample, for unbalanced (blue) and balanced (red) excitation, at the same external source voltage on the ultra-low-distortion function generator (ULDFG). **(b)** Measured $2f$ voltage harmonic, for balanced and unbalanced excitations, comparing two different but nearly identical biasing voltages, between which the ULDFG switches ranges. **(c)** Corresponding R_2 nonlinear resistivity term. **(d)** Ratio of $2f$ harmonic voltage to the $1f$ fundamental. The gray dashed line at 1×10^{-4} indicates the harmonic distortion specification of the SR830 lock-in amplifier.

generator (ULDFG). Panel (a) shows that the measured resistances are identical for the balanced and unbalanced cases.

In panel (b), we also compare two different ranges of the ULDFG; 0.891 V is the lower bound of one range, and 0.889 V is the upper bound of the other range, the difference between which is 1/4 of a percentage point and makes no practical difference. Panel (b) shows that the two balanced excitations have significantly less harmonic distortion than the unbalanced ones. The unbalanced excitations have the same degree of harmonic distortion, since here the nonlinearity stems from the effect shown in Fig. 4.27.

However, in the balanced case, the excitations are unexpectedly different for different ranges on the ULDFG. These leftover harmonic distortions arise from an "interaction" between the sample and the ULDFG, as they vanish when the sample is replaced with an Ohmic resistor. We can explain them as an imbalance or offset on the (+) and (−) outputs on the ULDFG due to instrument imperfections, and these imbalances/offsets are different between different ranges as shown in Table 4.2, explaining the change in harmonic distortion as the range switches. At the 89.10 mVrms output level, the

Stanford Research Systems DS360 Specs: Residual Offset	
Residual Offset [(+) Output Only]	Source Output Range
25 mV	0.8910 < Vrms
2.5 mV	0.089 10 < Vrms < 0.8910

Table 4.2: Specifications of the Stanford Research Systems DS360 Ultra-Low-Distortion Function Generator, for the Residual Offset for the (+) output only. Source ranges have been converted from unbalanced Vpp in the manual to balanced Vrms shown here. Specifications from [212]

ULDFG switches between different specifications for the residual offset voltage, and an audible relay click is heard on the instrument during the switch.

To confirm this source of distortion, we expect the harmonic distortions to be proportional to dR/dV_g, the derivative of resistance with respect to gate voltage. Fig. 4.29 compares the distortion to the derivative (scaled), showing they are nearly equal, but there is still a small difference in shape. This suggests that most of the remaining distortion could be nulled out by manually correcting for the residual offset with a potentiometer, and there is likely a very small amount of intrinsic distortion that cannot be removed by properly balancing the bias.

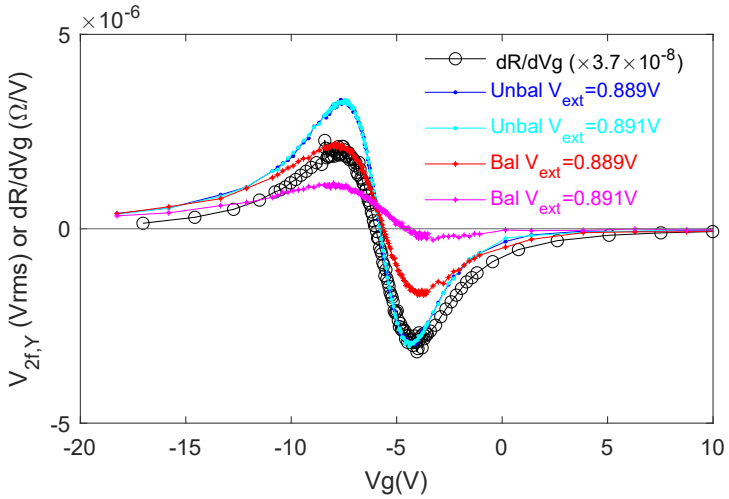

Figure 4.29: Harmonic distortions reproduced from Fig. 4.28, with scaled dR/dVg for comparison.

4.9.4 Reduction of Parasitic Nonlinear Effects by Noise-Temperature Matching

As hinted at in Subsection 4.9.2, we have some flexibility in tuning the $T_{N,in}$ parameter. While we cannot tune the input-side noise that the first-stage LNA produces without varying the temperature of the LNA, we can insert attenuators between the sample and the LNA that will produce their own thermal noise, both in the direction towards the sample and towards the LNA. Because the attenuators are a Π-circuit of resistors, they must be placed between the diplexer and the first-stage LNA; otherwise if they come before the diplexer, they will interfere with the low-frequency operation and measurement. This arrangement is illustrated in Fig. 4.30. Attenuators typically come in discrete steps of no smaller than 0.5 dB, thus not allowing us to continuously vary $T_{N,in}$ without implementing a controlled heating or cooling mechanism for the attenuators. To be able to switch the attenuators *in situ*, the coaxial cables transporting the Johnson

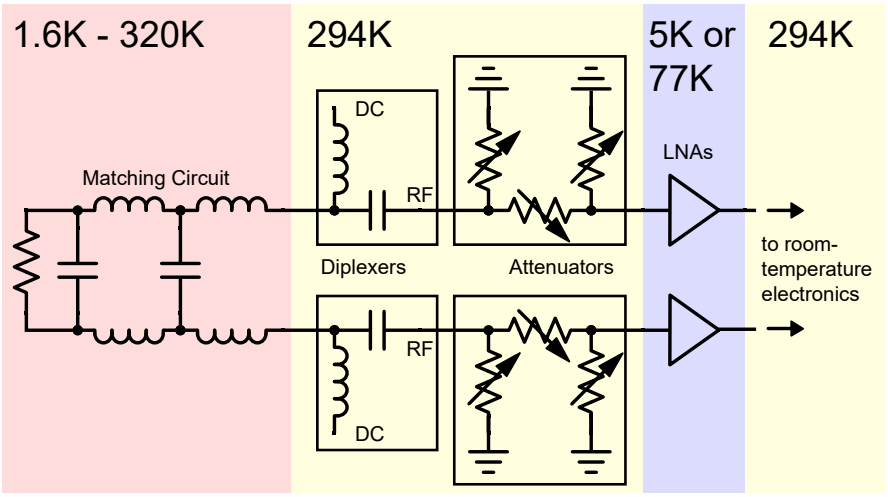

Figure 4.30: Circuit schematic of using attenuators to tune $T_{N,in}$.

noise from the sample to the cryogenic LNAs must exit the cryostat into ambient conditions; thus, the setup we have implemented with the VTI cryostat where the LNAs sit in an external nitrogen dewar is especially amenable to this, at the cost of a minimum bound of $T_{N,in} \sim 21\,\mathrm{K}$. Table 4.3 summarizes the approximate values $T_{N,in}$ achieves for various values of attenuators on the VTI cryostat.

Attenuators in VTI						
Attenuation (dB)	0	0.5	1	2	3	4
$T_{N,in}$ (approx.) (K)	22	45	80	125	160	185

Table 4.3: Comparison of $T_{N,in}$ values for different attenuation strengths.

4.10 Gate Line Noise Amplification

Section 4.2 summarized filtering strategies for reduction of noise from quasi-DC signals and methods to verify the filters are functioning as intended. However, there is a

very subtle method by which external noise may avoid detection by the experimentalist and corrupt the thermal conductance measurement. If there are voltage fluctuations present on the gate electrode of an unbiased two-terminal graphene device, they will induce fluctuations in the electron density of the graphene, which would propagate as a common-mode signal along the coaxial lines and be rejected by the hybrid coupler (alternately on a single-ended measurement, they would not propagate at all, generating no voltage drop across the device). They would not be measurable as spikes, jumps, or offsets in the DC noise.

However, with an applied biasing current across the channel, now these voltage fluctuations on the gate electrode will cause voltage fluctuations to develop across the channel by modulating the sample resistance, acting analogously to a MOSFET amplifier. This is illustrated in Fig. 4.31.

This effect causes the noise of the channel to increase with the bias current squared, which exactly resembles noise from heating, except the excess noise is amplified noise rather than intrinsic Johnson noise. It appears as though the channel is heated to a higher temperature than it is actually is, generating the illusion of reduced thermal conductance.

We demonstrate this effect using a graphene device with a bottom graphite gate, separated from the graphene channel by a 45 nm thick h-BN dielectric. To demonstrate how sensitive our measurement can be to noise on the graphite gate, we still use filters outside the cryostat for the main graphite gate line, and instead we remove filters from either the silicon gate line or the sample package heater lines, which run along the graphite gate line on the cryostat probe, and which capacitively or inductively couple their own noise into the graphite gate line. The silicon gates only the narrow strip of graphene between the graphite gate and the metal contacts and is separated by 1-micron

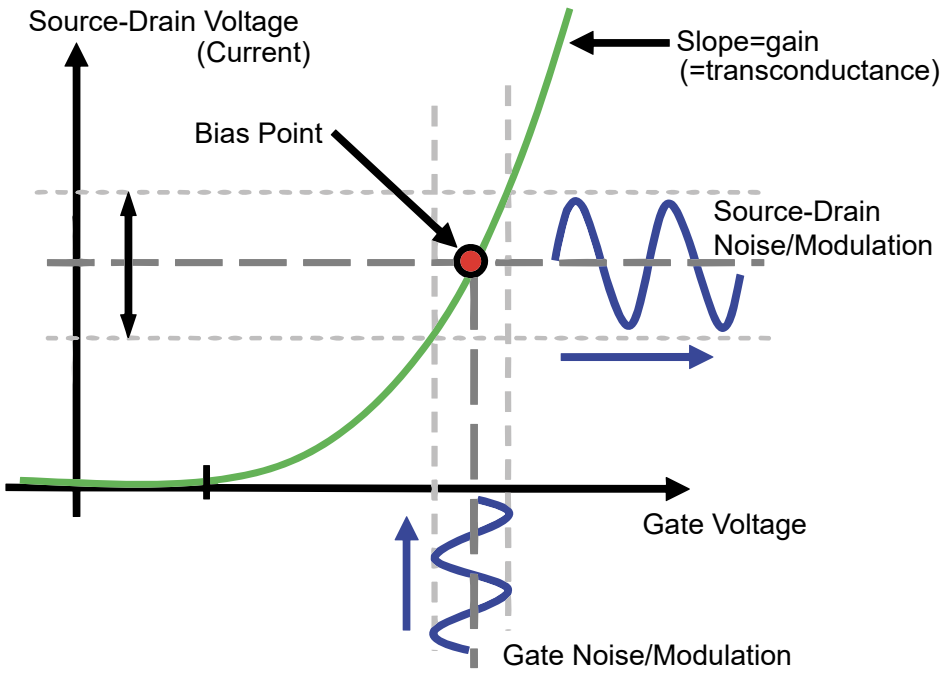

Figure 4.31: Bias-point for a FET amplifier. Under a constant applied bias current (voltage), changing the gate voltage changes the source-drain voltage (current). Small gate modulations can be transmitted or amplified into the channel voltage (current) modulations. Image adapted from Ref. 213.

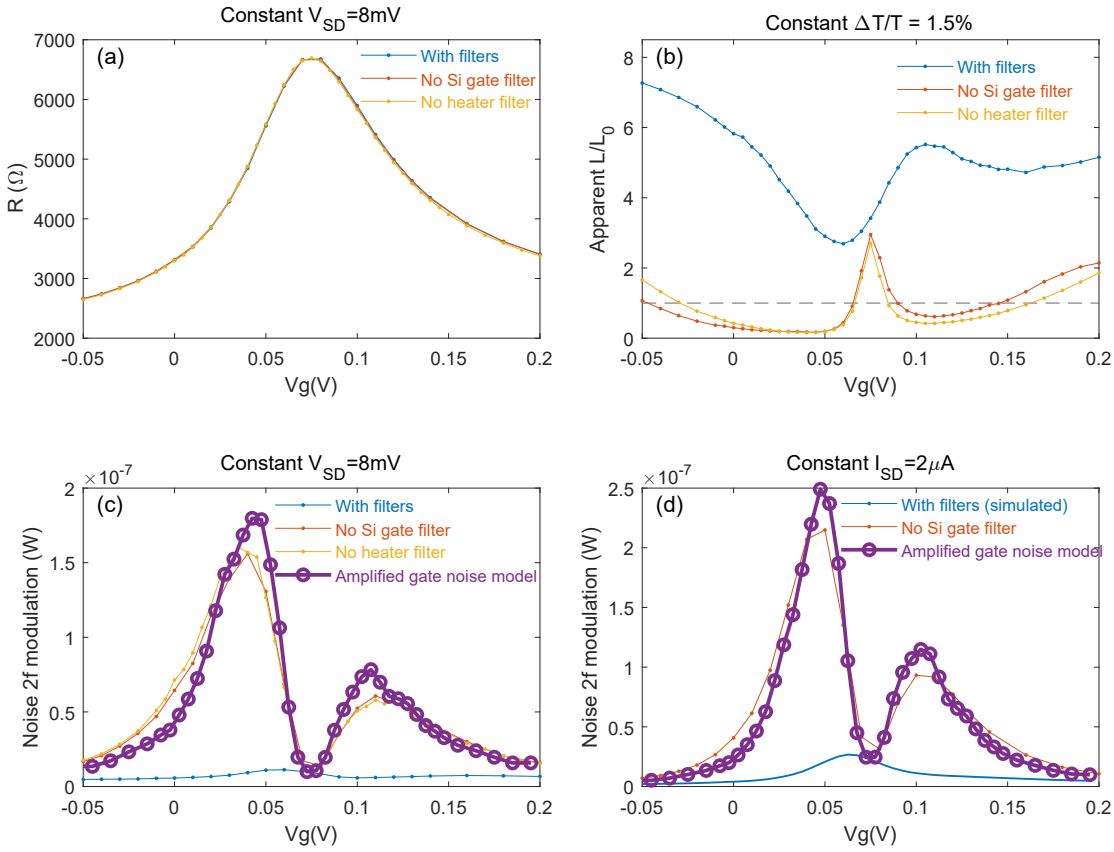

Figure 4.32: **(a)** Resistance vs gate voltage. **(b)** Apparent Lorenz ratio. With filters (blue) the Lorenz ratio is significantly above 1. Without filtering on lines (Si gate: red; heater: yellow) adjacent to the graphite gate, the apparent Lorenz ratio is suppressed. **(c)** Noise modulation at $2f$, for constant sample V_{SD} bias at $1f$. With filters (blue) the noise modulation is from heating. Without filters (red, yellow) on lines adjacent to th gate, the measured noise modulation includes amplified gate noise. Purple: amplified noise model described in the text. **(d)** Red: noise modulation at $2f$, for constant sample I_{SD} bias at $1f$, with filters (blue, simulated) and with no filter (red) on the the adjacent Si gate line. Purple: amplified noise model described in the text.

oxide; thus, any noise on it has very little direct effect on the JNT measurement.

Since we are using an AC-modulated biasing current, the excess amplified gate noise appears as an AC modulation of the total noise. Fig. 4.32(a) shows the measured resistance during this measurement. The resistance is almost unaffected as the filtered and unfiltered curves coincide. Panel (b) shows the apparent Lorenz ratio, both for fully filtered (blue) and a noisy (red, yellow) graphite gate line. The noisy gate line causes the apparent Lorenz ratio to become strongly suppressed due to the excess noise. Panel (c) shows the corresponding measured noise modulation for the filtered and unfiltered cases; here, the sample is current-biased with feedback to achieve a constant 8 mV voltage drop to allow a more direct comparison of amplified gate noise across the gate range. With filters, the noise modulation is small, consistent with the large apparent Lorenz ratio in panel (b). Conversely, without the filters, the noise modulation is significantly larger. Panel (d) is similar to panel (c), but shows the noise modulation for a constant bias current of $2\,\mu$A; here the noise modulation for the filtered case is simulated since the filtered variant was not measured for constant current biasing.

The voltage fluctuations from this amplification effect may be modeled in the following way. Consider the graphene device biased with I_{SD}; then the voltage across the electrodes is $V_{SD} = I_{SD} \times R(V_g)$ where $R(V_g)$ is the resistance as a function of gate. Taking the derivative and rearranging, we get

$$dV_{SD} = I_{SD} \times \frac{dR}{dV_g} \times dV_g. \tag{4.62}$$

The amplification factor of this transistor is $\mathbb{G} = I_{SD} \times dR/dV_g$ which achieves a maximum of about $\mathbb{G} = 0.15$ for the $2\,\mu$A bias used in Fig. 4.32(d). The noise power N generated in the channel by this effect is proportional to the square of the voltage

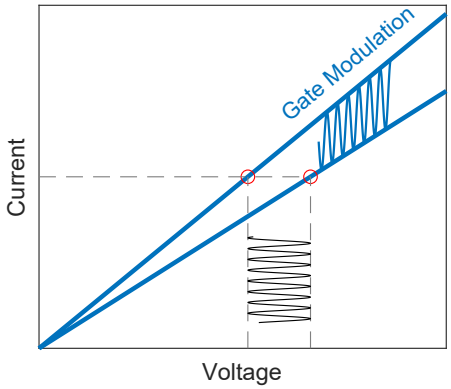

Figure 4.33: Simulation of $I-V$ curve for modulations of the gate voltage. If the current is held fixed (by e.g. an external current bias), the gate modulation causes voltage modulations.

fluctuations dV_{SD}; thus we get

$$N_{\text{amplified gate}} \propto \left(I_{SD} \times \frac{dR}{dV_g}\right)^2. \tag{4.63}$$

In this model, there are no current fluctuations as we are assuming the current is externally fixed (Fig. 4.33), but, if this were the case, these fluctuations would have infinite differential resistance and thus not be impedance matched to the JNT thermometer. In reality, there must still be some current fluctuations creating an effective finite impedance and thus coupling to the JNT thermometer. Without knowing the rms noise voltage on the gate, we cannot quantify the amplified current or voltage fluctuations. Here, the impedance matching is not determined by the conventional differential resistance so we also cannot estimate the coupling. Nonetheless, if we take this simple model and scale the noise power uniformly, we get a reasonable agreement with the data. The purple circles in Fig. 4.32(c,d) plot the results of this model. The slight disagreement with the data is possibly a result of this impedance matching being modulated with the gate voltage.

There is no way to distinguish this noise from heating noise, and thus there is no way to ascertain whether this effect has been fully mitigated. Even if every line is filtered at room temperature, the gate lines on the cryostat are typically made of resistive wire and thus may generate a non-insignificant amount of their own Johnson noise. Since this effect scales as $\propto (dR/dV_g)^2$, increasing the gate dielectric thickness very rapidly diminishes this effect. In cases where the gate dielectric cannot be made thick enough, such as with graphite gates separated by typical h-BN thicknesses of 30–60 nm, we can install cold low-pass filters on or directly next to the sample PCB, to filter out the Johnson noise from the span of gate line between room temperature and the sample. A demonstration of this is shown in Fig. 4.34, where two cold low-pass filters with a 15 MHz cutoff frequency (Coilcraft S3LP156L surface mount LC filters) are glued onto the sample PCB and wirebonded into the gate lines.

4.11 Outlook and Conclusion

In this Chapter, we have thoroughly covered the JNT techniques that developed during the work of this dissertation. The focus of the techniques was to reduce effective background noise that degrades precision, as well as finding and mitigating parasitic modulation effects that degrade accuracy. A significant effort went into discovering and understanding the details of many techniques in this Chapter; with this, we hope the hard work has been done, and the technique is now mature enough to produce accurate results. We hope that future noise experiments will take full advantage of the richness of the JNT techniques presented here

Of course, there is always room for improvement, and here we suggest some ways in which our RF JNT technique can be further improved:

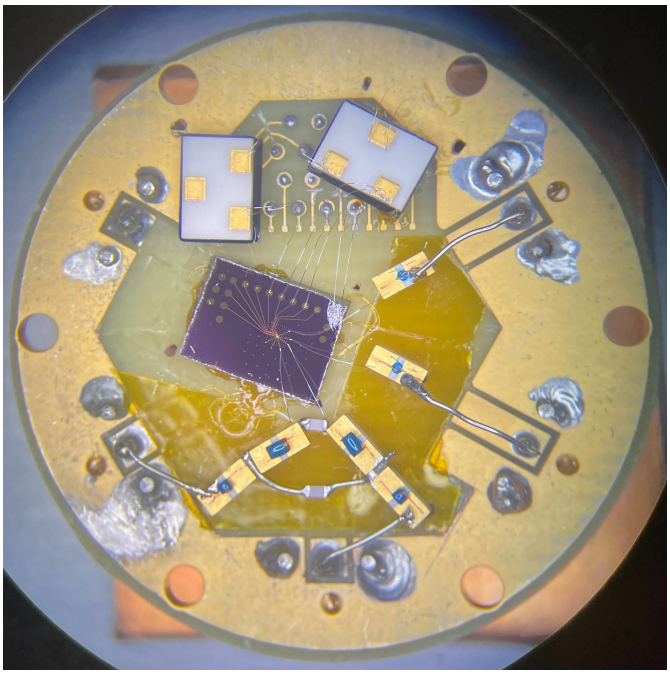

Figure 4.34: Optical micrograph showing two low-pass filters connected to the gate lines at the sample PCB, filtering out any Johnson noise from the gate line itself.

1. Traveling wave parametric amplifiers (TWPAs)[214–217] and the similar Josephon parametric amplifiers (JPAs)[218] are a new class of Josephson-junction-based RF amplifiers that can achieve quantum-limited noise temperatures of ∼500–600 mK, nearly an order of magnitude lower than conventional low-noise semiconductor HEMT amplifiers. Implementing these into the circuit can significantly reduce the noise temperature.

2. Ultra-low-loss coaxial cables made with porous PTFE dielectric, which also typically have a full copper inner conductor with silver plating, can further reduce attenuation on long cable runs between the sample and the LNAs, helping to reduce the effective $T_{N,in}$ parameter and thus the sample-nonlinearity-induced noise modulation.

3. PCBs made with Rogers Duroid or other low-loss dielectrics can help further reduce the background gain, allowing the JNT to operate at high accuracy over an even higher range of resistances.

4. The SR830 lock-in amplifier has a harmonic distortion of 1×10^{-4}, which can sometimes present a problem in quantifying the sample nonlinearities under AC bias when the bias must be small, such as at very low temperatures, in order to keep $\Delta T/T_0$ small. Perhaps some new instrument or method, such as a Wheatstone bridge configuration, may overcome this limitation.

5. Digital noise measurements have an advantage over analog power-detection noise measurements in that arbitrary noise measurement bands may be chosen. Using the parametrically stretched matching circuit described in Subsection 4.4.4, a digital noise measurement method can continuously switch between different

bands depending on the sample resistance and matching map in the (R, f) plane, or it can use several matching bands separated in frequency to surpass the resistance width of the nominal impedance matching functional form in Eqs. 1.16 and 4.6. The primary goals would be to either (1) switch between different impedance matching resistance points *in situ* with a single matching circuit, or (2) make the $G(R)$ function as flat as possible in order to reduce the derivatives dG/dR, d^2G/dR^2 that enter into the nonlinearity-induced noise modulation.

It is more important to have beauty in one's equations than to have them fit experiment.

Paul Dirac

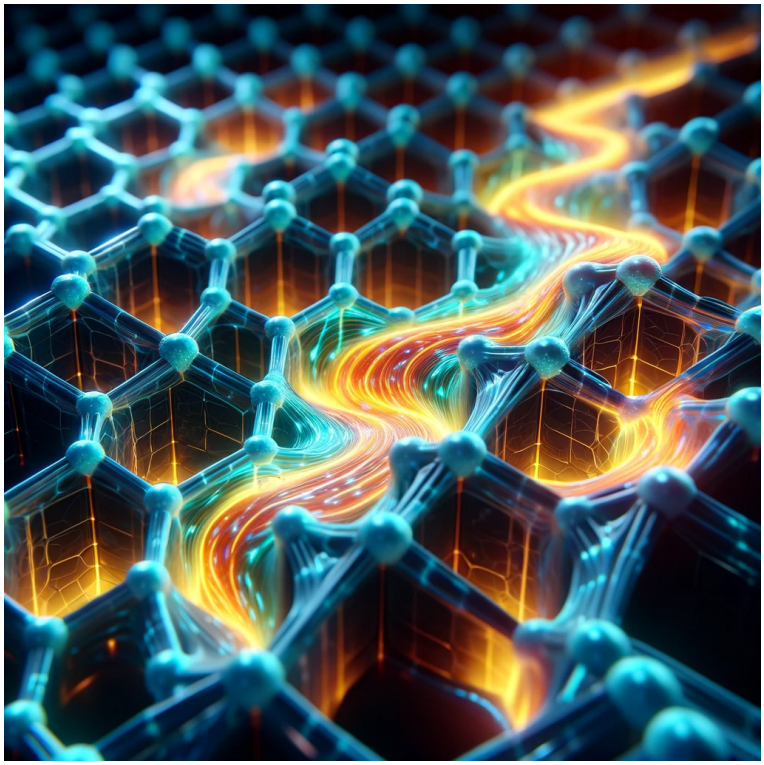

5

Hydrodynamic Thermal Conductivity

The kinematics of carrier-carrier collisions provides us a clear separation in behavior of momentum relaxation and energy current relaxation. With the small Fermi surface and thus absence of Umklapp scattering in graphene, carrier-carrier collisions conserve the total momentum of the system and do not generate resistivity in the cor-

responding transport sector. In contrast, because carriers will exchange energy during collisions with each other, the energy current will not be conserved, and thus carrier-carrier collisions increase the resistivity in this transport sector.

This behavior contrasts starkly with conventional Ohmic and ballistic transport, where in most cases, energy current and momentum is relaxed at the same rate via elastic collisions, leading to the Wiedemann-Franz (WF) law (see Section 1.4).

The clear separation of the energy and momentum transport sectors motivates us to use the power of thermal conductivity measurements to search for and study hydrodynamics. As we shall see in Chapter 6, our thermal conductance measurements led to the unexpected discovery of a novel thermal viscous effect never before observed in electronic liquids.

The terms momentum and energy current have been purposely chosen to be vague, as depending on which system in particular we are studying, they will correspond to different physical observables. In this Chapter, we summarize the extensive theoretical background about thermal conductivity and WF law breakdowns in graphene, discuss geometric effects on the WF law, and present and analyze the results that were obtained during this work. Finally, we offer an outlook for future experimental directions to continue further understanding the hydrodynamic regime.

5.1 Theoretical Background: Hydrodynamic Breakdown of Wiedemann-Franz

In a material with a single species of charge carriers that follow a quadratic dispersion (sometimes called a Galilean-invariant electron system with mass m), for example bilayer graphene (BLG) or a conventional semiconductor, where velocity is proportional to

momentum via $\vec{\mathbf{v}} \propto \vec{\mathbf{p}}$, the total electrical current is exactly directly proportional to the total momentum of the charged particles and is thus exactly conserved in a purely hydrodynamic picture (no impurity or phonon for momentum relaxation). This can be seen by defining the particle current $\vec{J_n}$ and similarly the charge current $\vec{J_e}$:

$$\vec{J_n} = \sum_i \vec{v_i} = \sum_i \frac{\vec{p_i}}{m} \tag{5.1}$$

$$\vec{J_e} = \sum_i e\vec{v_i} = \sum_i e\frac{\vec{p_i}}{m}, \tag{5.2}$$

where the sum is implicitly over occupied states i, with charge e.

Similarly, we can define an energy current

$$\vec{J_u} = \sum_i \varepsilon_i \vec{v_i} = \sum_i \frac{p_i^2}{2m}\frac{\vec{p_i}}{m}, \tag{5.3}$$

where $\varepsilon = p^2/2m$ is the band dispersion energy. However, the energy current is referenced to the bottom of the band, and is thus not necessarily a physical quantity; we want the thermal current for a physical observable, which tells us how energy is moved around relative to the chemical potential μ, and is the one that actually contributes to heating:

$$\begin{aligned}\vec{J_q} &= \sum_i (\varepsilon_i - \mu)\,\vec{v_i} = \sum_i \left(\frac{p_i^2}{2m} - \mu\right)\frac{\vec{p_i}}{m} \\ &= \vec{J_u} - \mu\vec{J_n}.\end{aligned} \tag{5.4}$$

In the last line we have expressed the thermal current mathematically in terms of the energy current and the particle current. Unlike the electrical current, there is no corresponding conservation law, and thus the total thermal current will get relaxed by

electron-electron interactions.

The observant reader might notice, however, that the $\vec{J}_n$ component of $\vec{J}_q$ is conserved. This is related to the thermoelectric effect. As discussed in Section 3.9, the thermal conductivity $\kappa = \bar{\kappa} - T\alpha^2/\sigma$ is defined under a thermal gradient with zero electric current (maintained by an applied electric field); thus, only the $\vec{J}_u$ component of $\vec{J}_q$ would be nonzero, and that component is fully subject to relaxation by carrier-carrier collisions. It is a rather subtle point that $\vec{J}_u$ is completely relaxed by collisions and does not have any overlap with conserved quantities; a solution of the Boltzmann equation is needed to see this[82,93].

So far we have only considered the case for one band, but BLG has both a parabolic hole and electron band that touch at charge neutrality (see Fig. 1.2). If the condition $T \ll T_F$ is not satisfied, then we must consider bipolar thermal excitations and accordingly sum over both bands $\gamma = \pm 1$ in each equation. Now, the total momentum and electric current are no longer equal:

$$\vec{J}_n = \sum_{i,\gamma} \vec{v}_i = \sum_{i,\gamma} \frac{\vec{p}_i}{m} \tag{5.5}$$

$$\vec{J}_e = \sum_{i,\gamma} q_\gamma \vec{v}_i = \sum_{i,+} e\frac{\vec{p}_i}{m} - \sum_{i,-} e\frac{\vec{p}_i}{m}. \tag{5.6}$$

Away from charge neutrality, the momentum contributions to $\vec{J}_e$ will be biased from one band; in other words, any electrical current will still have a nonzero total momentum. For any arbitrarily small doping, the $\vec{J}_n$ component of $\vec{J}_e$ will be conserved by collisions, leading to zero electrical resistivity[82] without any other momentum relaxation mechanisms such as impurity, phonon, or boundary scattering. The thermal current, whose equations we skip here due to complexity, again has no conservation laws and will relax

to zero.

Exactly at charge neutrality, the electrical current will be carried equally by holes and electrons with no net momentum; thus, carrier-carrier collisions can now relax the electrical current to zero since it is not protected by momentum conservation, giving nonzero electrical resistivity. In contrast, the thermal current is carried equally by thermally excited electrons and holes moving in the same direction; this transport mode has net momentum and thus overlaps with the conserved momentum mode, allowing zero thermal resistivity.

We now consider the case for a Dirac cone dispersion with strong doping, as in monolayer graphene (MLG). Here, the energy is given by $\varepsilon_{\vec{k}} = \pm\hbar v_F|\vec{k}| = \pm v_F|\vec{p}|$. The particle and charge currents are no longer defined with a mass. For a single band, we have

$$\vec{J}_n = \sum_i \vec{v}_i = v_F \sum_i \frac{\vec{p}_i}{|p_i|} \tag{5.7}$$

$$\vec{J}_e = \sum_i \vec{v}_i = e v_F \sum_i \frac{\vec{p}_i}{|p_i|}. \tag{5.8}$$

Surprisingly, we now find that these currents are no longer exactly conserved. However, the particle and electrical currents still have a strong overlap with momentum and thus have a large conserved component. If we assume a low temperature $T \ll T_F$ and Taylor expand $|\vec{p}_i| \approx \hbar k_F + \delta p_i$[93], we get

$$\vec{J}_{n(e)} = (e) v_F \sum_i \frac{\vec{p}_i}{|p_i|} \approx \frac{(e) v_F}{\hbar k_F} \sum_i \vec{p}_i (1 - \frac{\delta p_i}{\hbar k_F}). \tag{5.9}$$

We thus see that in the degenerate limit, we recover current conservation by momentum conservation; this results from the fact that for $T \ll T_F$, the curvature of a parabolic

band vs a linear Dirac band is negligible for the small window k_BT of energies that contribute to transport.

The energy and thermal currents are written as

$$\vec{J_u} = \sum_i \varepsilon_i \vec{v_i} = \sum_i v_F^2 |\vec{p_i}| \cdot \frac{\vec{p_i}}{|p_i|} = v_F^2 \sum_i \vec{p_i} \tag{5.10}$$

$$\vec{J_q} = \sum_i (\varepsilon_i - \mu)\, \vec{v_i} = v_F^2 \sum_i \vec{p_i} - \mu \vec{J_n}. \tag{5.11}$$

The energy current is directly proportional to momentum (even when summing over two bands). If we substitute Eq. 5.9 into 5.11 and neglect the difference between μ and ε_F,

$$\vec{J_q} = v_F^2 \sum_i \vec{p_i} - \mu \frac{e v_F}{\hbar k_F} \sum_i \vec{p_i}(1 - \frac{\delta p_i}{\hbar k_F}) = \frac{v_F^2}{k_F} \sum_i \vec{p_i} \delta p_i, \tag{5.12}$$

we find that the $\vec{J_u}$ part of $\vec{J_q}$ is exactly canceled by the conserved part of $\vec{J_n}$, leaving a small temperature-dependent portion that is now fully susceptible to relaxation, giving thermal resistivity when measuring $\bar{\kappa}$.

If we attempt to measure κ, however, we must set $\vec{J_e} \propto \vec{J_n} = 0$, which would seemingly cause the thermal current to be equal to $\vec{J_u}$ and thus be exactly conserved. However, to set $\vec{J_e} = 0$, we must apply an electric field to the sample, breaking the conservation of momentum and thus of the energy current.

If we consider non-degenerate graphene, but still not at exactly the charge neutrality point, the math is more complicated, but it can still be shown that the same results are obtained, namely, relaxation of thermal current (finite thermal resistivity) and conservation of electrical current (zero electrical resistivity)[83].

Finally, if we consider monolayer graphene at charge neutrality, we will now find that

the thermal current that is conserved and the electrical current is relaxed, analogously to bilayer graphene[83].

In real-life experiments, the presence of disorder in both types of graphene smears out the singular behavior at charge neutrality, thus creating two distinct hydrodynamic regimes. As a result, for a narrow region around charge neutrality, the Lorenz ratio will be enhanced due to near-conservation of thermal current; and for higher densities, the Lorenz ratio will be suppressed due to stronger relaxation of thermal current by e-e scattering.

5.2 Non-Hydrodynamic Breakdowns of Wiedemann-Franz

Although we have shown that the dominance of carrier-carrier collisions in hydrodynamics will lead to a breakdown of the WF law, conversely not all breakdowns indicate the hydrodynamic regime. The WF law is derived using the Sommerfeld expansion under the assumptions of elastic or quasi-elastic scattering and $T \ll T_F$, and consequently is an approximation with correction terms of order $\mathcal{O}(T/T_F)^2$[54]. Outside the degenerate regime $T \ll T_F$, we already expect the WF law to be unsatisfied due to considerations of bandstructure and scattering rate dependence on energy without invoking hydrodynamic carrier-carrier scattering. In this section, we briefly review some of the effects and mechanisms whereby this occurs, with the intent of ruling out these effects before ascribing WF breakdowns to hydrodynamic origins. Refs. 86,87 provide a detailed overview of these effects.

When both electrons and holes are simultaneously present in a system, their thermoelectric effects can cancel out, allowing a significantly higher total thermal conductivity κ_{tot} than just the arithmetic sum of the individual thermal conductivities κ_i. Mathe-

matically, this effect can be written as[180]

$$\kappa_{tot} = \kappa_1 + \kappa_2 + T\frac{\sigma_1\sigma_2}{\sigma_1+\sigma_2}(S_1 - S_2)^2 \tag{5.13}$$

where the subscripts 1,2 denote the properties of either the electron or hole system by itself, and $S = \alpha/\sigma$ is the thermopower. For a single charge carrier system, $\kappa < \bar{\kappa} = \kappa + T\alpha^2/\sigma$; in other words, an electrical potential gradient $\vec{\nabla}\phi$ applied to maintain zero electrical current for a κ measurement thermoelectrically always counteracts heat flow induced by a thermal gradient $\vec{\nabla}T$. For two species of charge carriers, the individual electrical currents induced by $\vec{\nabla}T$ cancel out, requiring less (or none if fully cancelled out) applied electric potential to maintain zero electrical current, thus increasing the total thermal conductivity.* The degree to which the Lorenz ratio is raised above the WF law depends wholly on the bandstructure, gap size, and energy dependence of the scattering rates; detailed calculations are given in Refs. 87,180.

At elevated temperatures, in particular $T \sim T_F$ or higher, the Sommerfeld expansion[54] no longer holds. The Fermi surface becomes strongly thermally smeared, causing the system to behave classically following the Boltzmann distribution, and lowering the Lorenz ratio to $\sim 6/\pi^2 \approx 0.6$[86].

The final effect to consider is that of inelastic phonon scattering[54,86]. At low temperature, impurity scattering is predominantly elastic, allowing the conservation of both energy and charge during scattering, thus relaxing thermal and electrical currents at the same rate and satisfying the WF law. At high temperatures, where electron thermal energies are significantly higher than the maximum phonon energy, phonon emission or absorption by an electron will change the electron's energy by an amount much smaller

*For exactly symmetric electron and hole bands, the thermoelectric effects cancel out, giving $\kappa_{tot} = \bar{\kappa}_{tot} = \bar{\kappa}_1 + \bar{\kappa}_2$.

than its typical thermal energy, thus effectively creating a quasi-elastic collision, and satisfying the WF law to a good approximation. It is at intermediate temperatures where phonon scattering becomes inelastic, significantly changing the electron's energy and thus relaxing thermal currents faster than electrical current. Here, the degree of Lorenz ratio suppression is ultimately determined by the balance of inelastic phonon scattering to impurity scattering, and the Lorenz ratio trends towards 0 or 1 in the limit of low-disorder or high-disorder samples, respectively. Experimentally, the characteristic crossover from inelastic to quasi-elastic phonon scattering typically occurs at around $1/10^{\text{th}}$ of the Bloch-Grüneisen or Debye temperature[68] (see also Subsection 3.1.2).

In interpreting any WF breakdowns as evidence for carrier-carrier scattering, we must carefully rule out bipolar diffusion, bandstructure, and Fermi surface smearing effects if we do not satisfy $T \ll T_F$. If we do satisfy $T \ll T_F$, then we must verify the temperature is above the Bloch-Grüneisen temperature.

5.3 The Crossno Experiment

In 2016, Crossno *et al.*[1] conducted an experiment measuring the thermal conductivity of three graphene samples, the cleanest with a low disorder of $n_{min} = 5 \times 10^9\,\text{cm}^{-2}$, as was introduced in Section 1.4 and shown again in Fig. 5.1. The work indicated that MLG entered into a hydrodynamic regime between 45 and 80 K, showing a strong Lorenz ratio enhancement at the charge neutrality point that became less pronounced for higher disorder samples. Additionally, the data showed a suppression of the Lorenz ratio down to ~ 0.4, but the authors did not discuss this in the context of hydrodynamics, instead focusing mostly on the enhancement.

In this dissertation, as will be discussed in Section 5.5, we have measured an even

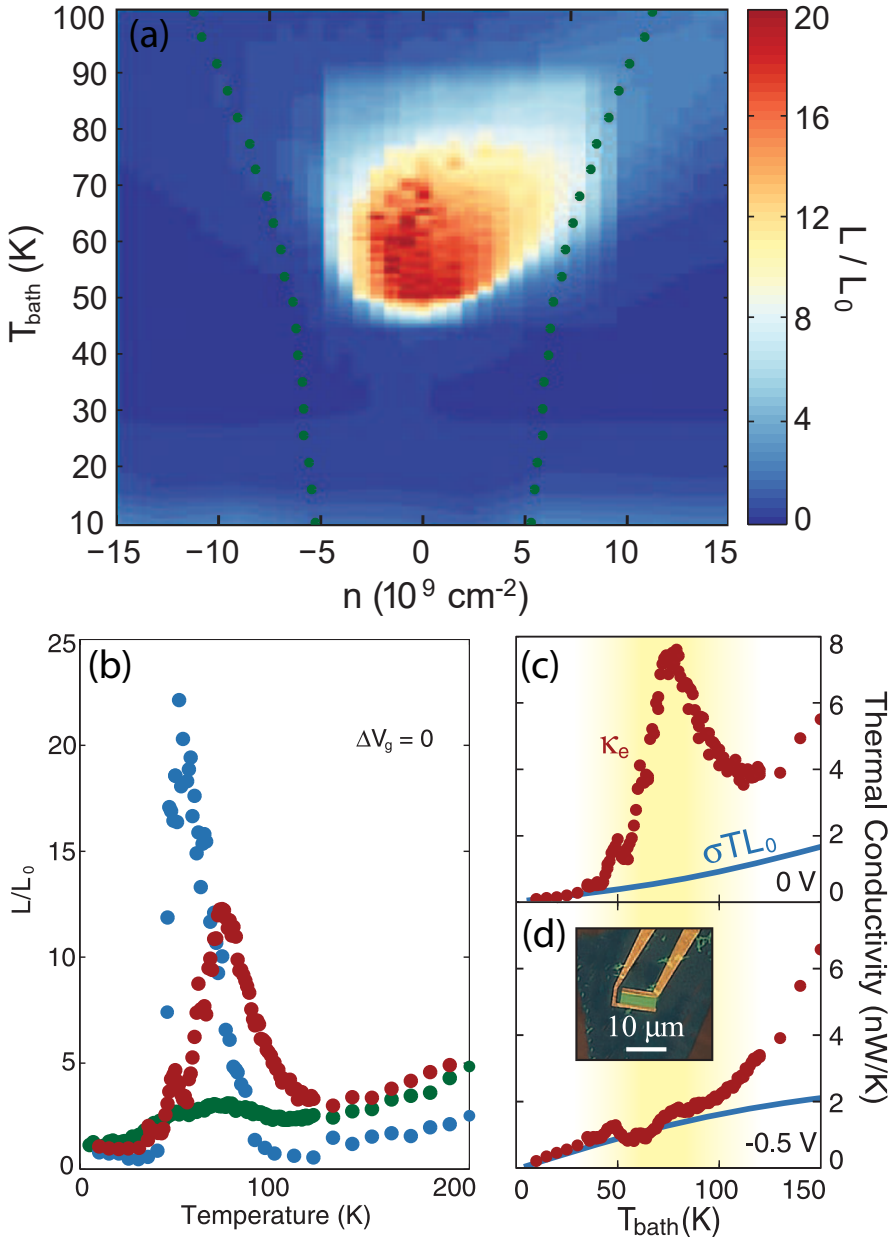

Figure 5.1: **(a)** Colormap of measured Lorenz ratio in MLG, showing an enhanced Lorenz ratio for n near 0 and from 45–80 K. **(b)** Linecuts of the Lorenz ratio vs temperature from three devices; blue: least disordered; red: medium; green: most disordered. The large enhancements have a sharp drop-off on both the high and low sides. **(c)** Thermal conductivity of the medium-disorder device vs temperature at charge neutrality, showing a non-monotonic behavior with peak. **(d)** Same as (c) but for small hole-doping; the peak is gone. Figure from Ref. 1.

cleaner MLG sample with a graphite gate, showing an arbitrarily large apparent enhancement of the Lorenz ratio. The differential noise upon heating decreased to zero, and then became negative, appearing as "negative" thermal conductance. This was unphysical and led to us eventually discovering the nonlinearity-induced noise modulation effect, as was described in Section 4.9.

The experiment by Crossno *et al.*[1] was unaware of the nonlinear effect directly, and they did not measure negative differential noise. However, we believe their device was also sensitive to this nonlinearity-induced noise modulation effect, although to a partially lesser extent than our graphite-gated device due to their much larger dielectric thickness to the silicon backgate. They also used single-ended biasing instead of symmetric biasing, likely increasing the effect of the nonlinear noise modulation (see Subsection 4.9.3). If a graphene device already has a relatively higher thermal conductivity, it will exhibit a relatively smaller noise heating signal; thus, any additional nonlinearity-induced noise modulation effects will become significantly more pronounced. For a 20-fold enhancement of the Lorenz ratio and a corresponding 20-fold decrease in the noise modulation due to heating, it is significantly easier for small nonlinearity-induced noise modulations to dominate the heating signal.

While some theorists[2,8,3] have qualitatively explained the very high Lorenz ratio in a hydrodynamic Dirac fluid in graphene, a later and more careful re-examination by other theorists[8,7] has brought into question the sharp temperature dependence of the Lorenz ratio (Fig. 5.1(b)), nominally understood as coming from the hydrodynamic window in temperature. In Crossno's experiment[1], the measured Lorenz ratio shows a sharp peak in temperature from 45–80 K, decreasing rapidly for temperatures outside the hydrodynamic window, due to dominance of impurity and phonon scattering at the lower and higher temperature bounds, respectively.

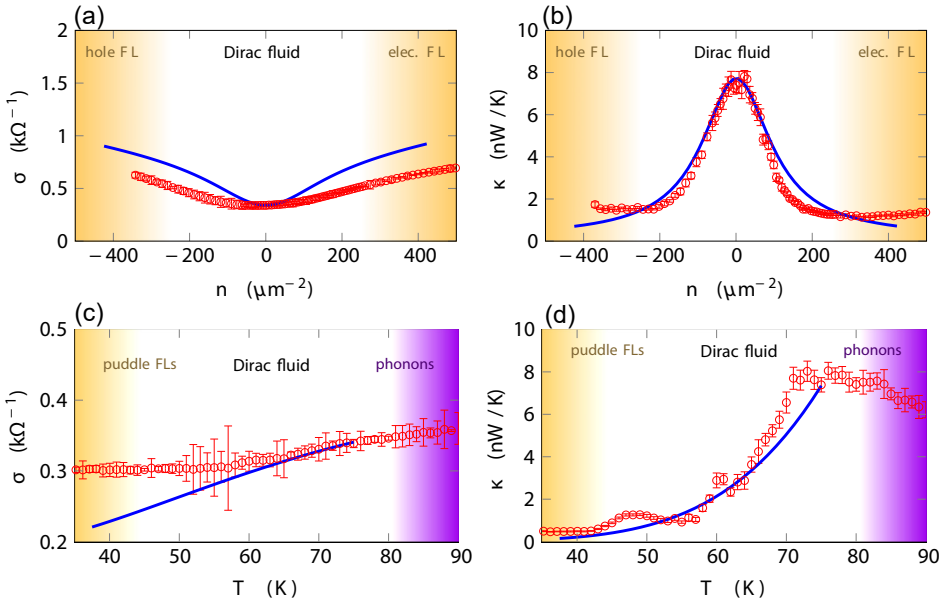

Figure 5.2: **(a,c)** Electrical and **(b,d)** thermal conductivity of the Dirac fluid in graphene, as a function of density (a,b) and temperature at $n = 0$ (c,d). Red circles are the data from Ref 1, and blue lines are the theory of Ref. 2. Figure from Ref. 2.

The authors of Ref. 87 state that the theory in Ref. 2 was not able to explain or fit the data despite having 6 free parameters in the theory, as shown in Fig. 5.2. However, the authors of Ref. 2 did not perform an exhaustive statistical fit to obtain the optimal values of their 6 parameters; instead they only showed that some choice of parameters close to the optimum provided excellent qualitative, and nearly quantitative, agreement with the experimental data. The authors of Ref. 2 non-perturbatively considered the role of inhomogeneity stemming from charge puddle disorder, citing it as critical to explaining the shape of the measured electrical conductivity vs density. Within the Dirac fluid regime, the thermal conductivity prediction matches the density and temperature dependence very well; however, the predicted dip in electrical conductivity is narrower than the experiment, and it does not predict the observed low-T disorder-limited saturation of σ at $0.3\,\mathrm{k\Omega}^{-1} \approx 7.7e^2/h$.

The authors of Ref. 2 also did not include the effects of phonons in their main hydrodynamic calculation, and thus their main theory does not address how the Lorenz ratio or thermal conductivity behaves as a function of temperature when phonon scattering enters at high-T. In other words, since their theory does not include phonons, it cannot predict the sharp decrease of the Lorenz ratio seen in Crossno's experiment[1] at $T = 80\,\mathrm{K}$. However, Ref. 2 does include a brief phonon calculation using a perturbative approach to the charge puddles, showing qualitatively that indeed, the thermal conductivity can behave non-monotonically with temperature, decreasing as the phonons start dominating.

Due to the presence of acoustic and optical phonons and their unknown exact deformation potentials and temperature power laws, an all-encompassing numerical theory that accurately considers impurity scattering, similar and dis-similar carrier scattering, and all the varieties of phonons at high-T is a significantly challenging task that has not yet been undertaken.

The authors of Ref. 87 started from the presumption that the Crossno graphene samples were not exhibiting Dirac fluid hydrodynamics, and only attempted to explain the data qualitatively via the presence of charge puddle disorder, impurity scattering, and a bandgap. The authors of Ref. 87 showed that a non-interacting zero-bandgap theory cannot explain the observed data in the Crossno experiment, but they also did not explicitly check whether adding electron-hole scattering, as would be present in the Dirac fluid, would change their predictions at zero gap to match the data. They further criticized the Dirac fluid interpretation of the Crossno data, noting that the measured minimum conductivity of $\approx 7.7e^2/h$ at the charge neutrality point is far higher than the theoretically predicted universal Dirac point quantum conductivity of $4e^2/\pi h \approx 1.27e^2/h$ at charge neutrality, citing the higher conductivity as a sign of

transport being dominated by electron-hole puddles rather than universal hydrodynamic scattering. However, Refs. 1,2 had already explicitly accounted for the charge puddles non-perturbatively, so the increased conductivity is already consistent with a charge-puddle-disordered Dirac fluid picture in their theory.

The inequality $T_{ph} \gg T \gg T_F \gg T_{puddle}$, where $T_{ph} \sim T_{BG}/5$ is the effective temperature where phonon scattering becomes significant, is given in Ref. 87 as a condition for the existence of the Dirac fluid. However, it is slightly incorrect in that the existence of the Dirac fluid should be measured at charge neutrality where $T_F \sim 0$; thus we do not require $T_F \gg T_{puddle}$ (in fact, this condition would create doped graphene), but instead we require both $T \gg T_F$ and $T \gg T_{puddle}$ to ensure strongly coexisting electrons and holes. These conditions are easier to achieve than the conditions suggested by Ref. 87. As additional concrete counterexamples, other electronic hydrodynamic experiments[61,62,71,73,74,81] as well as this dissertation show that hydrodynamic effects for doped graphene do indeed occur for $T > T_{ph}$.

We can investigate the data used in the Crossno experiment more closely. Fig. 5.3 shows the measured resistance vs density for the calibration measurement done under low bias power for minimal heating, and for the thermal conductivity self-heating experiment done under an especially high power to maintain a given fixed temperature rise, even in the case of high thermal conductivity. The resistance data shows the typical cat-ears pattern that we have observed on other devices. The resistance measured during the self-heating is strongly suppressed relative to the low-power data, especially at the charge neutrality point, indicative that the device was exhibiting very strong $I-V$ nonlinearity coming from the temperature dependence of the resistance. The contribution of the nonlinear terms to the measured resistance at $1f$ was shown in Eq. 4.57,

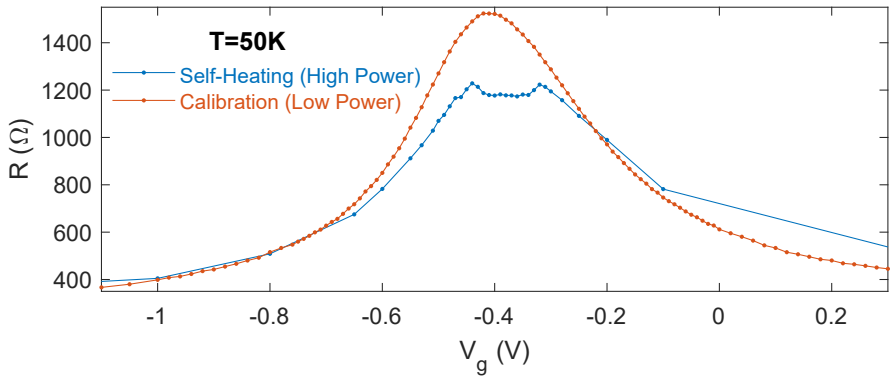

Figure 5.3: Measured resistance of the sample during the Crossno experiment. The red data indicates the resistance measured during the low-power calibration, and the blue data indicates the resistance measured during the high-power self-heating measurement.

reproduced here:

$$V_{1f} = R_1 I_0 + \frac{3}{4} R_3 I_0^3 + \cdots \qquad [\sin(\omega t)]. \tag{5.14}$$

The strong suppression of the the resistance stems from a large negative R_3 term. We can thus estimate that the peak value was about $R_3 \approx -1.58 \times 10^{12}\mathrm{V/A}^3$. Unfortunately, we cannot measure the $T_{N,in}$ value from the raw calibration data, because the apparent $T_{N,out}$ and/or $T_{N,in}$ values have a very strong resistance dependence, as shown in Fig. 5.4; however, based on other similar experiments we have done, we would estimate $T_{N,in} \gtrsim 100\,\mathrm{K}$. Importantly, we expect that because the apparent $T_{N,out}$ and/or $T_{N,in}$ vary so strongly with resistance, the change in noise measured during the Crossno gate-voltage calibration was also affected by this skewing the calibration even further, as indicated by the third term, where T_N is an effective combined amplifier noise temperature:

$$\Delta N = \left.\frac{\partial N}{\partial T}\right|_R \Delta T + \frac{\partial N}{\partial R}\frac{dR}{dT}\Delta T + \frac{\partial T_N}{\partial T}\frac{dR}{dT}\Delta T. \tag{5.15}$$

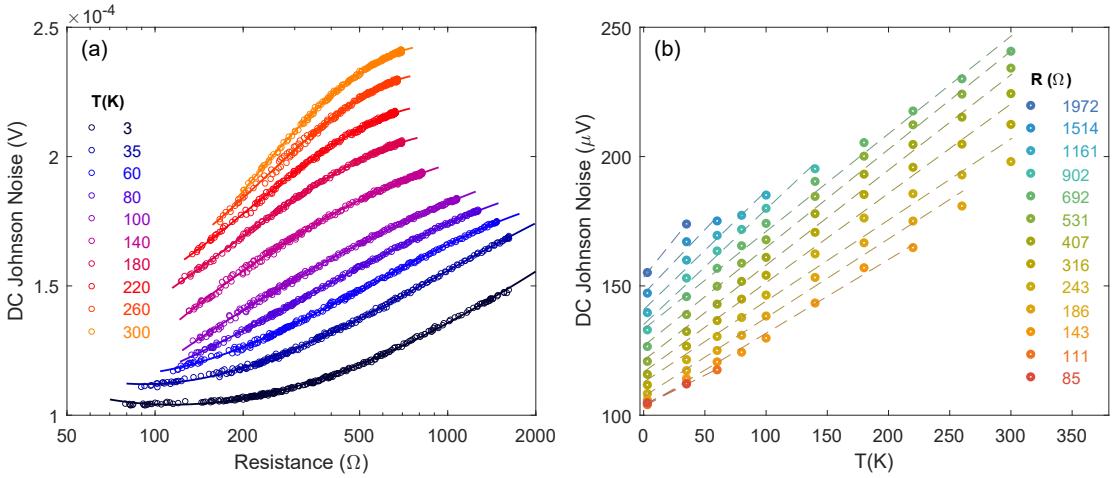

Figure 5.4: **(a)** DC noise vs resistance for the set of temperatures measured in the Crossno experiment calibration. **(b)** Corresponding linear fits of DC noise vs temperature for fixed resistance.

Fig. 5.4(b) shows that the linear fits do not have an apparent common intersection at any reasonable temperature, in contrast to Fig. 4.23.

Next, we can also examine the calibration data in the (T, V_g) space. The gain in the Crossno experiment was computed from $\frac{dN}{dT}$, as in Eq. 5.15, rather than $\left.\frac{\partial N}{\partial T}\right|_R$. Fig 5.5 shows the comparison of the constant-gate-voltage gain value used in the Crossno experiment in panel (c) (scaled by 2 to match the convention used in this dissertation), with the constant-resistance gain $\left.\frac{\partial N}{\partial T}\right|_R$ in panel (d). The ratio of panel (c) to panel (d) is shown in panel (f), and the two are only equal where $\frac{dR}{dT} \sim 0$ (panel (b)). Due to the very strong temperature dependence of the resistance, however, neither of these quantities correctly converts between the AC noise modulation and the AC sample temperature modulation (see Eqs. 4.45 and 4.54). Panel (a) shows the measured resistance, and panel (e) the reported Lorenz ratio, for reference to the other panels.

The difference between the $\frac{dN}{dT}$ calibration and the $\left.\frac{\partial N}{\partial T}\right|_R$ calibration indicates qualitatively how strong of an effect the temperature dependence of resistance, compared

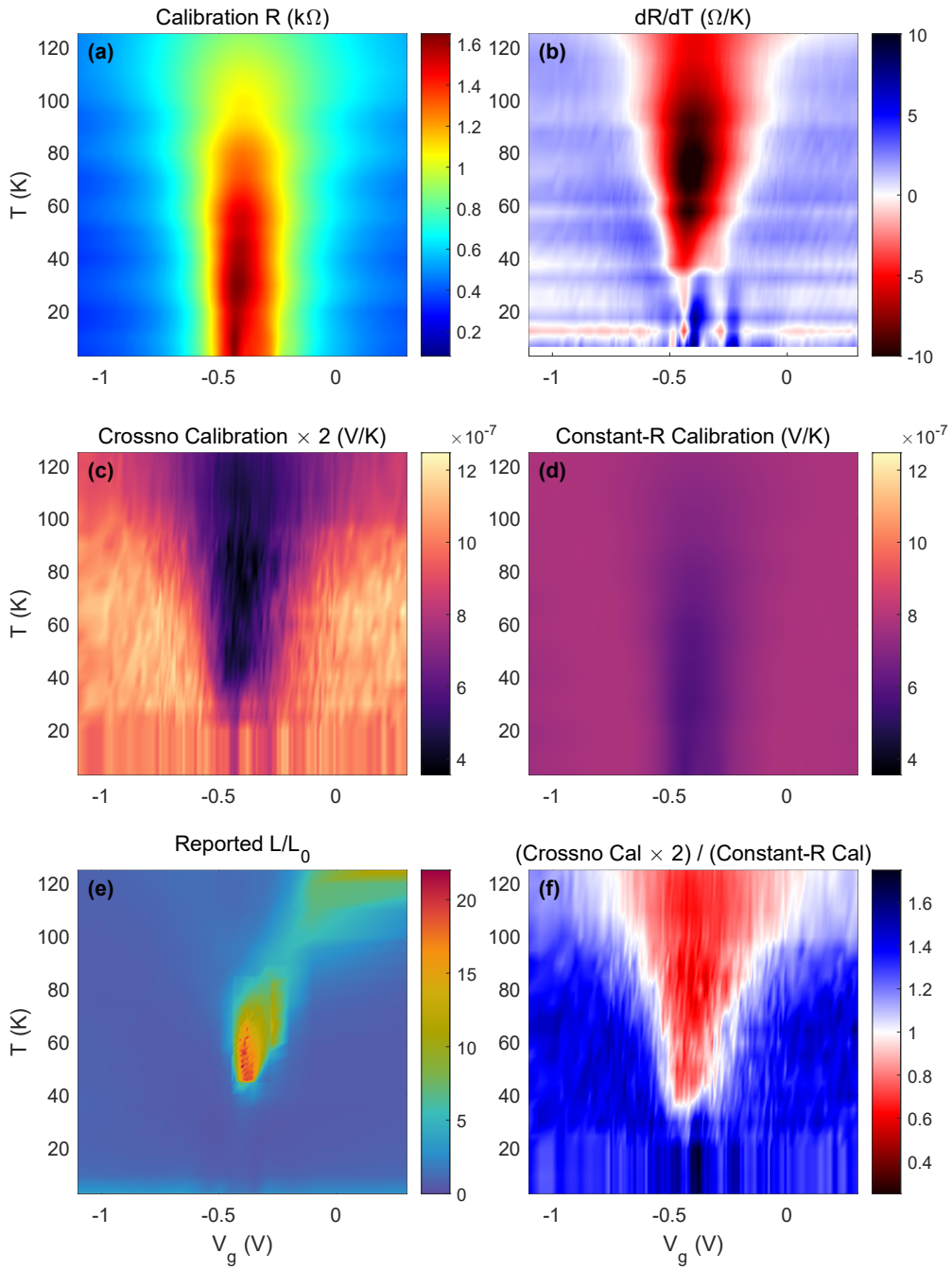

Figure 5.5: **(a)** Resistance measured during the calibration of the Crossno experiment, sample 1, plotted vs gate voltage and temperature. **(b)** Calculated dR/dT. **(c)** The calibration used in the Crossno experiment, dN/dT at constant V_g. **(d)** The true calibration, $\partial N/\partial T$ at constant R; same color scale as (c). **(e)** Reported $\mathcal{L}/\mathcal{L}_0$ in Ref. 1. **(f)** Ratio of the calibration used in the Crossno experiment (c) to the true calibration (d).

to the heating, will have on the noise modulation. Here, the temperature dependence of resistance increases $\frac{dN}{dT}$ by about 75% for the calibration, which theoretically has an even larger effect in self-heating (see Subsection 4.5.2 and Eq. 4.45).

To conclude and summarize this section, we have shown that the results from the Crossno experiment[1] for the Lorenz ratio are likely plagued by nonlinearity-induced noise modulation, and thus we should likely interpret the Lorenz ratio enhancement as qualitative rather than quantitative, with the true Lorenz ratio likely being significantly lower. This may bring into question the results of the Dirac fluid, as bipolar diffusion is predicted to be able to produce Lorenz ratio enhancement in graphene on the order of 2-4[87,180].

Additional experiments on ultraclean graphene devices are needed to confirm or rule out the presence of the Dirac fluid. However, these experiments are difficult to perform because clean graphene samples, especially those using graphite gates, have very strong nonlinearities that can modulate the noise; thus, extreme care must be taken in verifying the noise signal is unaffected by them. One potential workaround is to use non-local noise thermometry to measure thermal conductance[174].

5.4 Hydrodynamic Geometrical Effects

So far, we have been concerned with measuring the thermal and electrical conductivities of graphene as intensive, 2D "bulk" properties in order to compute the Lorenz ratio. However, due to the effects of viscosity, transport in hydrodynamics inherently becomes non-local, no longer obeying Ohm's law, as was described in Section 1.3. The conductivity σ is no longer defined, as the electrical conductance is a function of the boundary geometry rather than the bulk geometry.

Consider the flow of a fluid through a capillary or tube, as studied by Poiseuille[177]. There is no analog inside the tube of phonon scattering or impurity scattering as a mechanism of momentum relaxation; all the resistance to the fluid comes from the boundaries due to the no-slip boundary condition, and is transferred to all elements of the fluid through viscosity. In this case, the flow impedance for the fluid scales as $\propto \nu/r^4$, where ν is the viscosity and r is the tube radius. In a 2-dimensional electronic hydrodynamics analog, the electrical conductance of a rectangle, or a constriction, scales as $\propto w^2$, where w is the width, as has been verified experimentally[62]. This contrasts with Ohmic flow, where $G_{el} \propto w$.

However, when measuring the thermal conductance in a hydrodynamic material, specifically $G_{th,ex}$ for a rectangle between a hot (external heating) and a cold side (no self-heating), there is no no-slip condition on the thermal current at the boundary, and likewise there is no thermal viscosity, as thermal current is not a momentum current. The thermal current continues to follow Fourier's law $\vec{J}_q = -\vec{\nabla}T$, and the thermal conductance of a rectangle will scale as $\propto w$.

It is thus clear that for a perfectly hydrodynamic sample, the ratio of $G_{th,ex}$ to G_{el} could be made arbitrarily small or large by choosing an appropriately wide or narrow sample, respectively. This "experimentalist's Lorenz ratio" will then differ quite significantly, and might even be unrelated to, a "theorist's Lorenz ratio". Many theorists, when calculating the conductivities σ, κ of a hydrodynamic material, assume an infinite sample with no boundaries, and then they add in a small amount of momentum relaxation from impurity or phonon scattering to regularize the conductivity to a finite value[82,83].

In practice, no graphene samples are purely hydrodynamic. They will always exhibit some amount of impurity or phonon scattering and thus will have a finite bulk

conductivity. However, when measuring a sample in the lab, it is difficult to measure how much of the resistance comes from impurity/phonon momentum relaxation, and how much of it comes as viscous resistance through the no-slip boundary conditions. Starting with a perfectly Ohmic sample, we can imagine slowly turning on the hydrodynamics, and observing deviations of the Lorenz ratio from 1 that are indicative of the onset of hydrodynamics. However, because it is not an infinite sample, it is no longer clear whether the measured Lorenz ratio would increase or decrease as predicted for the infinite sample.

In this dissertation, however, we are primarily focused on measuring the thermal conductivity via self-heating rather than connecting the sample between a hot and cold reservoir. In self-heating, the question of what we measure becomes even more complicated, because of (1) the non-uniformity of viscous heat dissipation and (2) the modified weighting of the hydrodynamic Johnson noise temperature, as described in Section 3.8.

Nominally, the self-heating in a viscous rectangle produces a measurement of R and κ[176]:

$$\Delta T_{JN,hydro} = \frac{L}{W}\frac{V^2}{R}\frac{1}{12\kappa} \cdot f(L/W, \lambda/W), \tag{5.16}$$

where f is the viscous correction factor, with a minimum value of ~ 0.6 in the fully viscous regime[176]. In contrast, the external-heating setup measures R and $G_{th,ex}$. However, κ and $G_{th,ex}$ are related by the simple geometrical factor L/W; thus, aside from the correction factor f, the self-heating and external heating experiments ultimately provide the same information.

In a Corbino, the viscous resistance comes from fluid element reshaping and shear-

ing[58], rather than from viscous boundary drag as in the rectangle.

Although we know what the theorist's bulk Lorenz ratio should be for σ, κ in an infinite sample with nonzero momentum relaxation, there is yet no all-encompassing theoretical calculation that predicts how the Lorenz ratio behaves for finite-sized samples with mixed Ohmic-hydrodynamic transport. Such a calculation would involve several parts, each of which has been done individually:

1. Calculating the viscosity ν from the electron-electron interaction rates γ_{ee} and the bandstructure. This has been done recently for electrons in 2D[63,219].

2. Calculating the total sample resistance as a sum of viscous drag and momentum relaxation effects using the respective parameters ν and γ_{mr}. This has already been done recently for both the rectangle[65,220] and Corbino[59,220] geometry.

3. Calculating the value of the thermal conductivity based on the momentum relaxation rate and the electron-electron scattering rate. Such a calculation has been nominally already done in Ref. 89 for the ratio $\kappa/\sigma T$.

4. A calculation of the Johnson noise for the heated mixed Ohmic-hydrodynamic system, as a function of sample resistance R and thermal conductivity κ. This calculation has very recently been done in Ref. 176.

Until only very recently, we have generally interpreted our Lorenz ratio results in the context of the bulk or infinite-sized sample predictions. We do not yet know exactly how the Lorenz ratio is expected to behave in a finite-sized sample in the transition to hydrodynamics. Furthermore, it is likely that the Corbino and rectangle will produce different results for the hydrodynamic Lorenz ratio, as the electronic viscous resistance mechanism differs between the two geometries. It has been shown that for fully hydro-

dynamic flow, the viscous correction factors for heating and Johnson noise are different between the rectangle and Corbino geometries[59].

5.4.1 Behavior of the Experimentalist's Lorenz Ratio

Here, we perform a rough calculation to estimate the experimentalist's Lorenz ratio in a rectangle for a hydrodynamic electron liquid. Our goal is to determine how the combination of electrical geometric resistance being changed by viscous effects, and thermal conductance being decreased by electron-electron scattering, affects the Lorenz ratio as we transition from Ohmic to hydrodynamic flow.

The viscosity of electrons in 2D is given by[63]

$$\nu = \frac{1}{4} v_F^2 \left[\tau_{2,ee}^{-1} + \tau_{2,0}^{-1} \right]^{-1}, \tag{5.17}$$

where $\tau_{2,ee}^{-1}$ is the relaxation rate of the second moment of the electron distribution function due to only e-e scattering,[†] and $\tau_{2,0}^{-1}$ is the same rate due to only disorder scattering. The rates add, and thus, viscosity is determined by larger of the e-e or disorder relaxation rate. For simplicity, we consider that $\tau_{2,i} \sim \tau_i$, i.e. that the generic scattering rate is the same as the relaxation for the second moment; likewise $\tau_{2,0} \sim \tau_{mr}$.

The bulk electrical conductivity is $\sigma_0 = \dfrac{ne^2\tau_{mr}}{m}$, unaffected by momentum-conserving e-e scattering. The electrical resistance of a rectangular hydrodynamic sample, however,

[†]Relaxation rate of the second moment is defined as the relaxation rate of the $\sim e^{2i\phi}$ harmonics of the distribution function, where ϕ is the single electron velocity angle[63].

is given by[220]

$$R = \frac{L}{W}\frac{1}{\sigma_0}\frac{1}{1-\frac{2}{w}\tanh\frac{w}{2}} \tag{5.18}$$

$$w = \frac{d}{l_G}, \tag{5.19}$$

where d is the channel width and $l_G = \sqrt{\nu/\gamma_{mr}}$ is the Gurzhi length, and $\gamma_{mr} = 1/\tau_{mr}$.

Finally, the bulk thermal conductivity is given by[89]

$$\kappa = \sigma_0 T \frac{\pi^2}{3}\left(\frac{k_B}{e}\right)^2 \frac{\tau_{mr}^{-1}}{\tau_{ee}^{-1}+\tau_{mr}^{-1}}, \tag{5.20}$$

which scales geometrically to the bulk thermal conductance via W/L.

Finally, combining Eqs. 5.17, 5.18, and 5.20, we calculate the predicted measured Lorenz ratio:

$$\frac{\mathcal{L}}{\mathcal{L}_0} = \frac{\gamma_{mr}/\left(\gamma_{ee}+\gamma_{mr}\right)}{1-\left[\frac{d}{v_F}\sqrt{(\gamma_{ee}+\gamma_{mr})\gamma_{mr}}\right]^{-1}\times\tanh\left(\frac{d}{v_F}\sqrt{(\gamma_{ee}+\gamma_{mr})\gamma_{mr}}\right)}. \tag{5.21}$$

For simplicity, we ignore the viscous noise correction factor f from Eq. 5.16 as it is an $\mathcal{O}(1)$ correction. The numerator of Eq. 5.21 corresponds to the intrinsic reduction of thermal conductivity from e-e scattering, and the denominator corresponds to the increase of electrical resistance due to viscous drag at the boundary. In fact, the correction factor f from Eq. 5.16 will only be significant if the denominator of Eq. 5.21 differs strongly from 1, which would only happen when l_G is comparable to or larger than d. We plot Eq. 5.21 as a function of γ_{ee} for a typical set of experimental parameters, $\gamma_{mr} = 5\times10^{12}\,\text{Hz}$ and $d = 5\,\mu\text{m}$, as the red curve in Fig. 5.6. We also a plot a blue curve with more extreme parameters, $\gamma_{mr} = 2\times10^{12}\,\text{Hz}$ and $d = 1.5\,\mu\text{m}$, as a

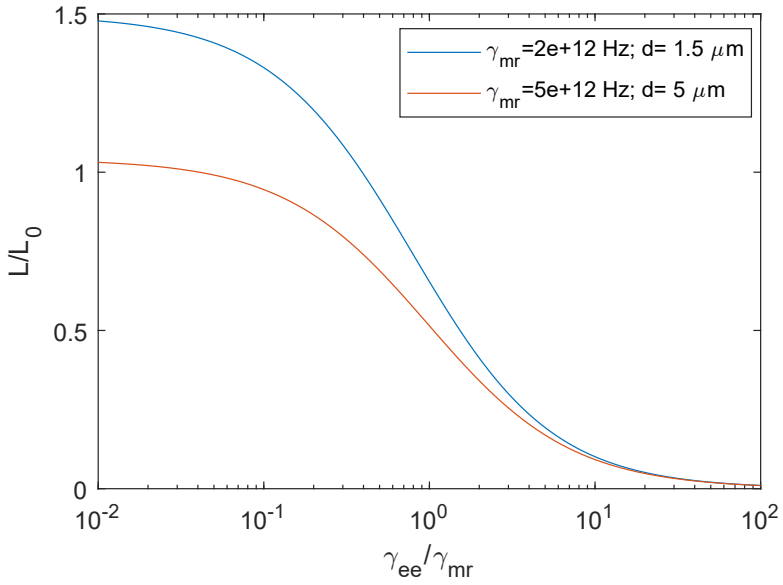

Figure 5.6: Theoretically calculated experimentalist's Lorenz ratio, from Eq. 5.21, using the parameters shown in the legend for each curve.

comparison. For the red curve, the denominator has a small correction from 1 for low γ_{ee}, giving $\mathcal{L}/\mathcal{L}_0 \to 1.04$, and it trends closer to 1 as γ_{ee} increases. In contrast, for the blue curve, the denominator is significantly affected by the extra viscous drag, increasing the electrical resistance by up to $\sim 50\%$. In both cases, however, the behavior of the function is significantly dominated by the numerator, corresponding to the intrinsic reduction of thermal conductivity from e-e scattering and giving a Lorenz ratio strongly suppressed below 1. We conclude that for reasonable experimental parameters, we may see a slight increase of the Lorenz ratio above 1 at low-T, but the onset of strong e-e scattering at higher-T will diminish the viscous drag effect (by shrinking the Gurzhi length) and significantly reduce the measured Lorenz ratio, indicating that we should be able to observe a hydrodynamic Lorenz ratio suppression experimentally.

In the next section, we present experimental results measuring the Lorenz ratio in monolayer graphene to see if we can observe the aforementioned suppression.

5.5 Monolayer Graphene: The Inconsistent Picture

We have measured the Lorenz ratio in monolayer graphene in several devices over several generations of noise measurement techniques. All measurements were performed with constant-R calibration, but the early measurements did not take into account the nonlinearity-induced noise modulations or the gate-line-noise-amplification effect. We will present data from both Corbino geometry and rectangle geometry.

To perform the thermal conductance measurements, we generally use a feedback algorithm on the measured AC temperature rise ΔT in order to maintain a constant $\Delta T/T_0$ ratio, typically about $\sim 1-2\%$.

5.5.1 Disorder Characterization

Because we expect the degree of disorder to affect the low-T bound of the hydrodynamic window, we wish to characterize device disorder in a consistent way between devices. One method to do this is by extrapolating the first linear regime on a log-log plot of σ vs n to the minimum conductivity[1,221], which estimates the width of the Dirac peak. Fig. 5.7(a) shows an example of this residual density fitting analysis. The residual density indicates how much charge is present when the device is doped to average or global charge neutrality. There will be contributions both from charge puddles[16,17,222–224] and from thermally excited carriers. Upon lowering temperature, the number of thermally excited carriers is reduced until the charge puddle carrier density dominates, at which point the residual density approximately saturates for further decreases in temperature.

This method of calculating disorder with the charge puddles describes the electric potential inhomogeneity in the sample and is directly related to long-range Coulomb scattering. However, the presence of uncharged crystal defects, such as substitutions or

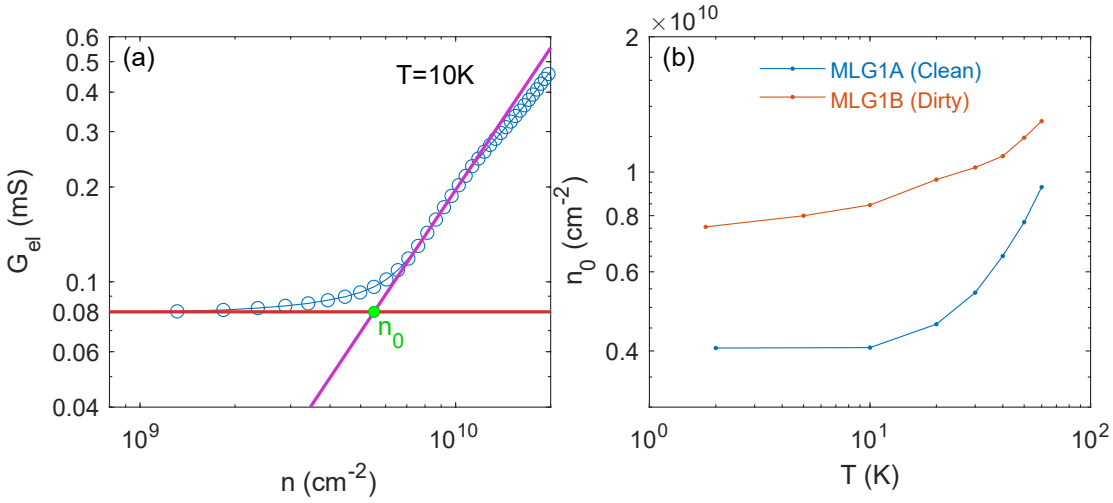

Figure 5.7: **(a)** Log-log plot of conductivity vs density (circles). The red line is $n = 0$ value, and the purples line is the extrapolation of the linear regime in log-log. The intersection of the two lines indicates the knee position at n_0 (green dot). **(b)** Residual density vs temperature for MLG1A (clean), and MLG1B (dirty), after it was removed and re-inserted into the cryostat.

lattice imperfections, creates short-range impurity scattering that is not characterized by the charge-puddle method. Measuring short-range scattering is harder, as it will affect only the mobility of the sample, which is also affected by charge puddles.

Nonetheless, the mobility is a good general characterization of sample disorder, but it must be measured in a 4-terminal setup to avoid contact resistance effects. However, we can still estimate it by techniques such as TLM[15,22,173] for rectangle-shaped samples, or magneto-resistance for Corbino samples. For a single rectangle device without TLM, we can only provide a lower bound for the mobility due to the contact resistance.

5.5.2 Ultra-Clean Graphene without Dirac Fluid

We will first present the data for our cleanest graphite-gated device (MLG1). This device was initially low-disorder (MLG1A) with $n_{0,min} = 4 \times 10^9\,\mathrm{cm}^{-2}$, but became disordered upon removal and re-insertion into the cryostat (MLG1B) with $n_{0,min} \sim 8 \times 10^9\,\mathrm{cm}^{-2}$

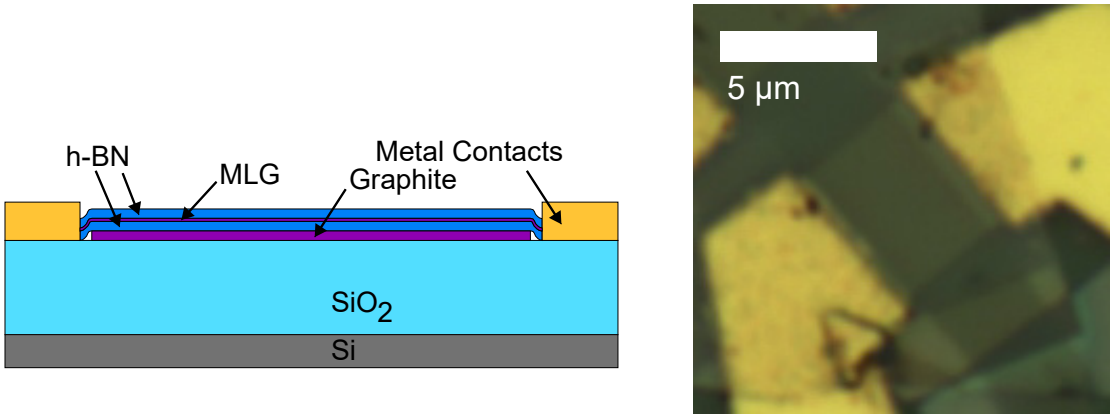

Figure 5.8: Left: Cross-sectional schematic of the MLG1 device, not to scale. **Right:** Optical micrograph.

in the second thermal cycling, as shown in Fig. 5.7(b). The two different disorder levels allow measuring the effect of disorder on the same exact device.

This device has a strip graphite back gate, with a h-BN/MLG/h-BN heterostructure on top and sloping down off the graphite past the edges onto the SiO_2 substrate. A cross-sectional schematic and an optical micrograph are shown in Fig. 5.8. We used the Si gate to set the regions not over the graphite gate to a high electron density ($n \sim 1.7 \times 10^{12}\,\mathrm{cm}^{-2}$) in order to minimize contact resistance. Fig 5.9 shows the resistance vs the graphite gate voltage, for a high positive and negative Si gate voltage. We can identify a pattern in the contact resistance values at high density. We propose there is a small region of the graphene immediately next to the metal contacts that is n-doped by the metal; the other regions are the graphite-gated regions and the Si-gated regions. The contact resistance is lowest when all regions have the same doping, n-n-n-n-n. Introducing pn junctions, via an n-p-p-p-n or an n-n-p-n-n configuration, increases the contact resistance. Finally, having four pn junctions in an n-p-n-p-n configuration produces the highest contact resistance. For the measurements presented here, we

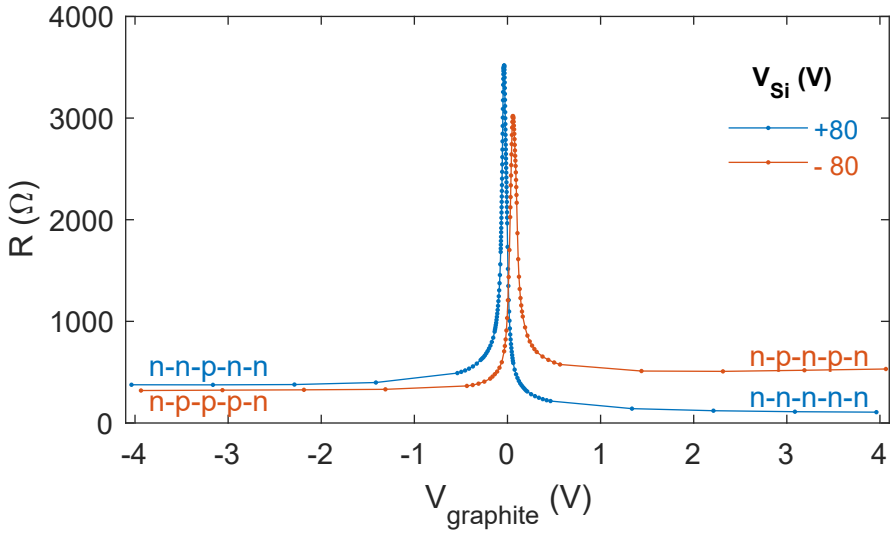

Figure 5.9: Graphene pn junctions forming at the contact interfaces due to gate doping polarity, for two values of the Si gate. The labels represent the doping polarity in regions of the device: (adjacent to metal contact)-(gated by Si)-(gated by graphite)-(gated by Si)-(adjacent to metal contact). Data from device MLG1B at $T = 10\,\mathrm{K}$.

operate in the n-n-n-n-n regime to achieve lowest contact resistance on the electron-doping side. Additionally, the Dirac peak in graphite gate voltage shifts with the Si gate, corresponding to about 2% Si-gate electric field penetration through the graphite due to incomplete screening.

During the original measurement of this device, we observed significant nonlinearity-induced noise modulations as shown in Fig. 5.10. Panel (a) shows the measured zero-bias resistance, at different temperatures, during a low-power calibration measurement. Panel (b) shows the resistance during the self-heating experiment, subject to whatever heating power necessary to maintain the target $\Delta T/T_0$. As the apparent Lorenz ratio increases, indicating apparent high thermal conductance, the applied power increases; the result is that the measured resistance decreases strongly due to heating and non-linearity effects. It is impossible to tell what the relative contributions to the change

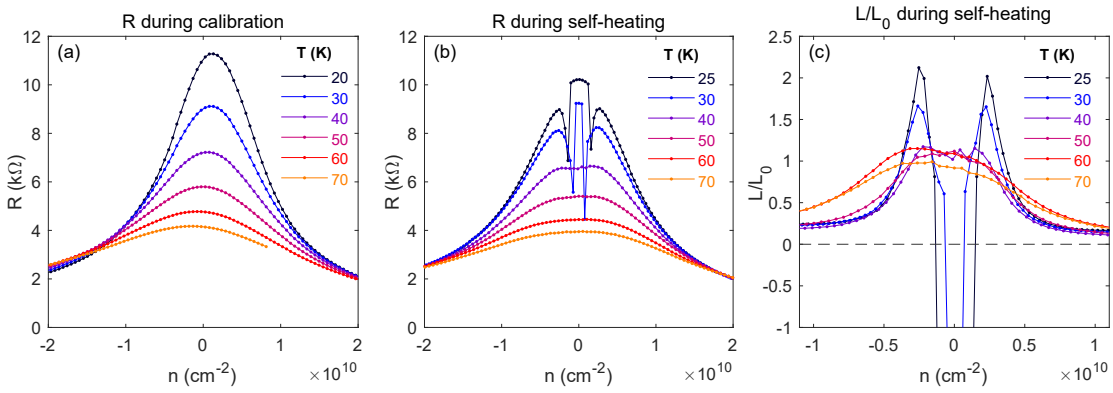

Figure 5.10: **(a)** Resistance during low-power calibration. **(b)** Resistance during self-heating, where higher power is used as necessary to maintain a target $\Delta T/T_0$. **(c)** Resulting apparent Lorenz ratio.

in measured resistance are without an accurate measurement of the actual temperature rise, which is degraded by the nonlinearity-induced noise modulation effect. Where the measured heating signal was negative, the feedback look reduced the power, normalizing the resistance again.

Panel (c) shows the apparent measured Lorenz ratio. For 25 and 30 K, the measured noise modulation goes towards zero (indicating a high thermal conductivity and Lorenz ratio) before becoming negative, indicated an unphysical negative thermal conductance. It is clear that a measured negative noise modulation must arise from the nonlinearity effect, rather than true sample heating.

This device has the noise parameter $T_{N,in} = 55$ K. Thus, without measuring the nonlinearity of the device, we can still trust the measurement around this temperature due to the vanishing of the nonlinearity effect, as shown in Eq. 4.54.

In Fig. 5.11, we compare the resistance and Lorenz ratio for MLG1A and MLG1B at 50 K, a temperature close enough to $T_{N,in}$ where the nonlinearity effects are insignificant. Upon introduction of disorder, the peak in resistance decreased at 50 K. In MLG1A,

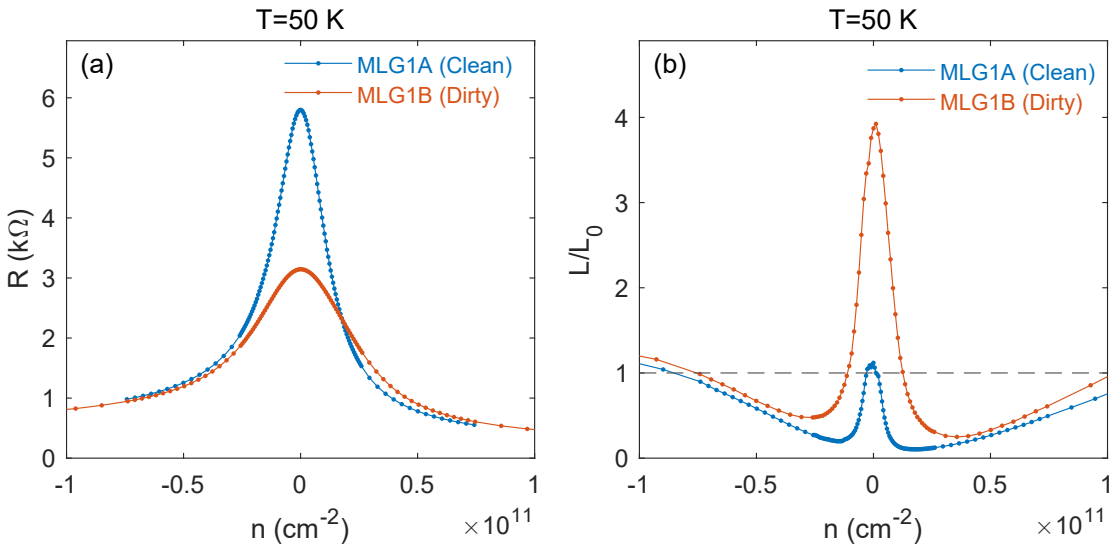

Figure 5.11: **(a)** Resistance for the clean and dirty versions of MLG1 at 50 K. **(b)** Corresponding Lorenz ratios at 50 K, where the nonlinearity-induced noise modulation is insignificant.

the peak resistance of 12.7 kΩ was at 2 K, corresponding to $\sigma \approx 1.39e^2/h$ (ignoring contact resistance), very close to the ideal $4e^2/\pi h \approx 1.27e^2/h$[87]; however, by 50 K the conductivity approximately doubles to $\sigma \approx 3.05e^2/h$.

In the clean version, surprisingly, the Lorenz ratio peak at charge neutrality is almost exactly 1. Upon introduction of disorder, the peak in Lorenz ratio increases to 4. Most of these behaviors are unexpected in the hydrodynamics context; both the value of the Lorenz ratio at 50 K and the dependence on disorder are completely opposite to the results of the Crossno experiment[1].

The treatment of acoustic phonons in Ref. 2 suggests that cleaner samples have a lower phonon cutoff temperature for hydrodynamics; while this may suggest that our sample MLG1A was already above the phonon cutoff temperature at 50 K, we find this unlikely given the similar residual density to the Crossno experiment.

Unfortunately, the data at other temperatures for this device is unreliable due to

corruption by the non-linearity effect, and thus we cannot investigate the temperature dependence of the peak or absence thereof.

While there is a measured suppression of the Lorenz ratio for densities away from charge neutrality, we cannot for certain ascribe this entirely to hydrodynamics, as we cannot entirely rule out the effect of gate-line noise amplification except at $n = 0$ where $dR/dV_g = 0$, since this particular measurement did not yet use the cold-ground filter for the gate line (see Section 4.10).

5.5.3 Correcting for Contact Resistance Effects via Dual-Channel Measurement

In Section 3.7, we introduced the complicated effects of contact resistance on the thermal conductance measurement, as well as a method to separately measure the contact effective Lorenz ratio and the sample Lorenz ratio. The method involves using 2 devices of different channel length to have different ratios of contact resistance to total resistance,[‡] and using the two obtained Lorenz numbers to calculate the Lorenz numbers of the contact and graphene individually. The contacts and channel must be be as similar to each other as possible, and so must be made at the same time from the same graphene heterostructure. The mathematics of this procedure are described in Appendix C, and here we show the results applied to sample MLG2. We denote the short and long channel devices in this sample as MLG2S and MLG2L. The thermal conductance data and optical micrographs for this sample was shown previously in Fig. 3.9, indicating at which temperatures phonon cooling begins to dominate electronic diffusion cooling.

Fig. 5.12(a,b) shows the resistances of the short and long channels. Using the TLM

[‡]In this method, we assume the contacts are Ohmic barriers rather than non-linear Schottky barriers, i.e. the electron side of the devices discussed herein.

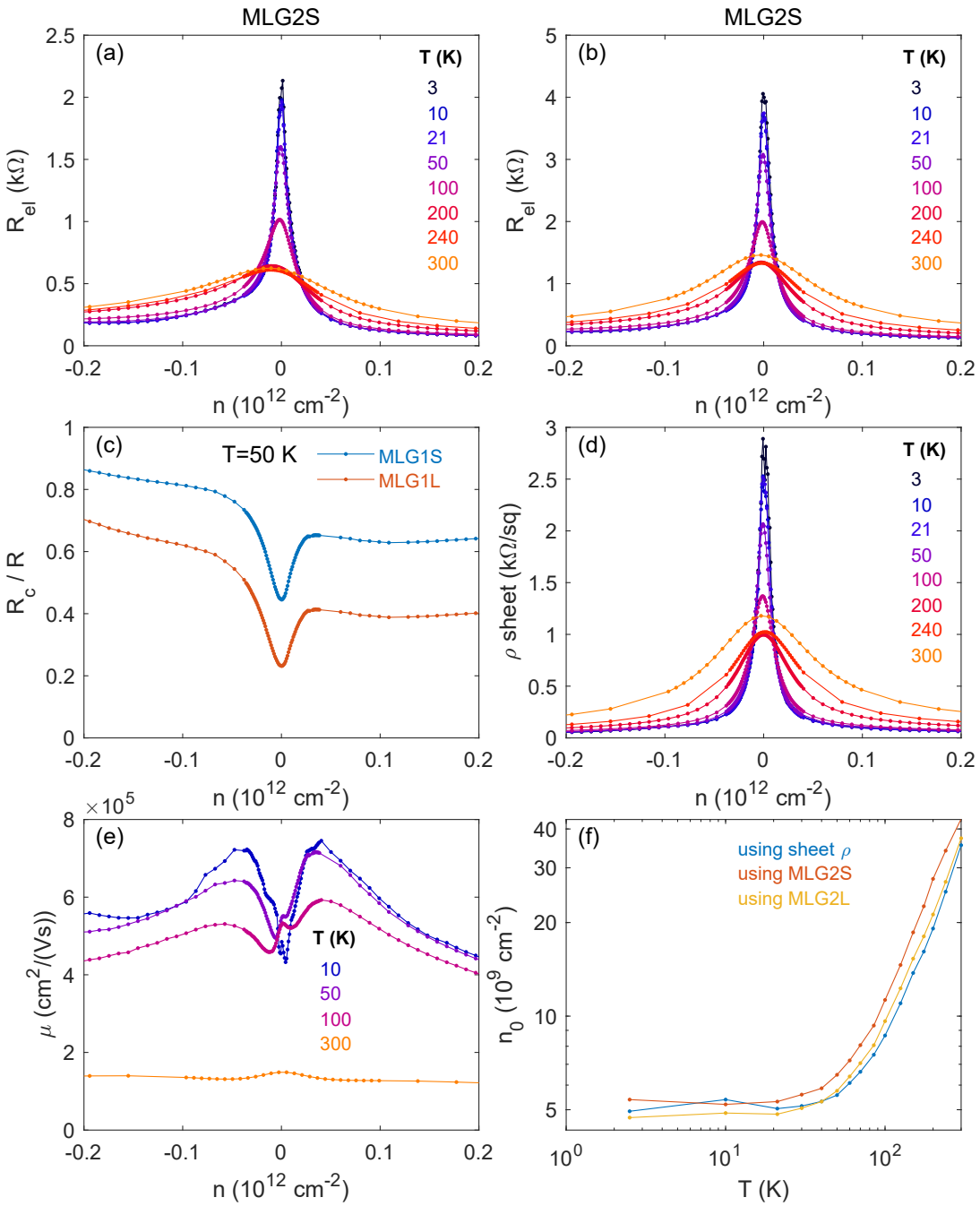

Figure 5.12: **(a)** Electrical resistance for MLG2S (3 μm channel length). **(b)** Electrical resistance for MLG2L (8 μm channel length). **(c)** Contact resistance fraction, for MLG2S (blue) and MLG2L (red), calculated via TLM. **(d)** Sheet resistivity calculated via TLM. **(e)** Mobility calculated using sheet resistivity and $n_{tot}^2 = n_0^2 + n^2(V_g)$. **(f)** Residual density vs temperature for sheet resistivity and for each device.

method, we can further estimate the contact resistance fraction and sheet resistivity of the devices, shown in panels (c) and (d). We find the contact resistance to be a significant portion of the total resistance, indicating our approximation of $R_c \ll R_{tot}$ may not be valid. Further, we see that the higher resistance on the hole side arises entirely from contact resistance and p-n junctions, as the sheet resistivity is symmetric for electrons and holes. Due to local inhomogeneity and the effect on transport, the TLM method with only two points is not an extremely accurate measurement of the contact resistance, but nonetheless it is likely to give us a reliable estimate.

From the electrical data, we obtain a low-temperature residual density of $\sim 5 \times 10^9\,\mathrm{cm}^{-2}$ (Fig. 5.12(f)), the same value as the Crossno experiment. We estimate the mobility using $\sigma = n_{tot} e \mu$, where $n_{tot}^2 = n_0^2 + n^2(V_g)$, with $n_0(T)$ being the residual density and $n(V_g)$ is the net density induced by the gate. The mobility is shown in panel (e), reaching an excellent high value $\sim 750,000\,\mathrm{cm}^2/\mathrm{Vs}$ at low temperature.

Having established the disorder level via the electrical data, we move onto the thermal sector. In Fig 5.13(a,b) we show the measured Lorenz ratio of the two individual devices, limiting the data to 100 K, as above that temperature, phonon cooling begins to dominate for some densities (Fig. 3.9). Neither the short nor the long channel exhibit any significant Lorenz ratio suppression; the exception is the hole-side on the short channel at 100 K, but we believe this may be a contact resistance effect. There is a weak central peak in the Lorenz ratio that grows with temperature; however, it is not strong enough to rule out bipolar diffusion. It is also possible the peak is caused by a phonon-cooling contribution; as seen in Fig. 3.9, the short and long channel thermal conductances are very close to each other above 40 K, suggesting the phonon bath may already be playing a significant role in thermalizing the electrons in the long channel. Additionally, the peak splits into two peaks above 60 K. This may be suggestive of a

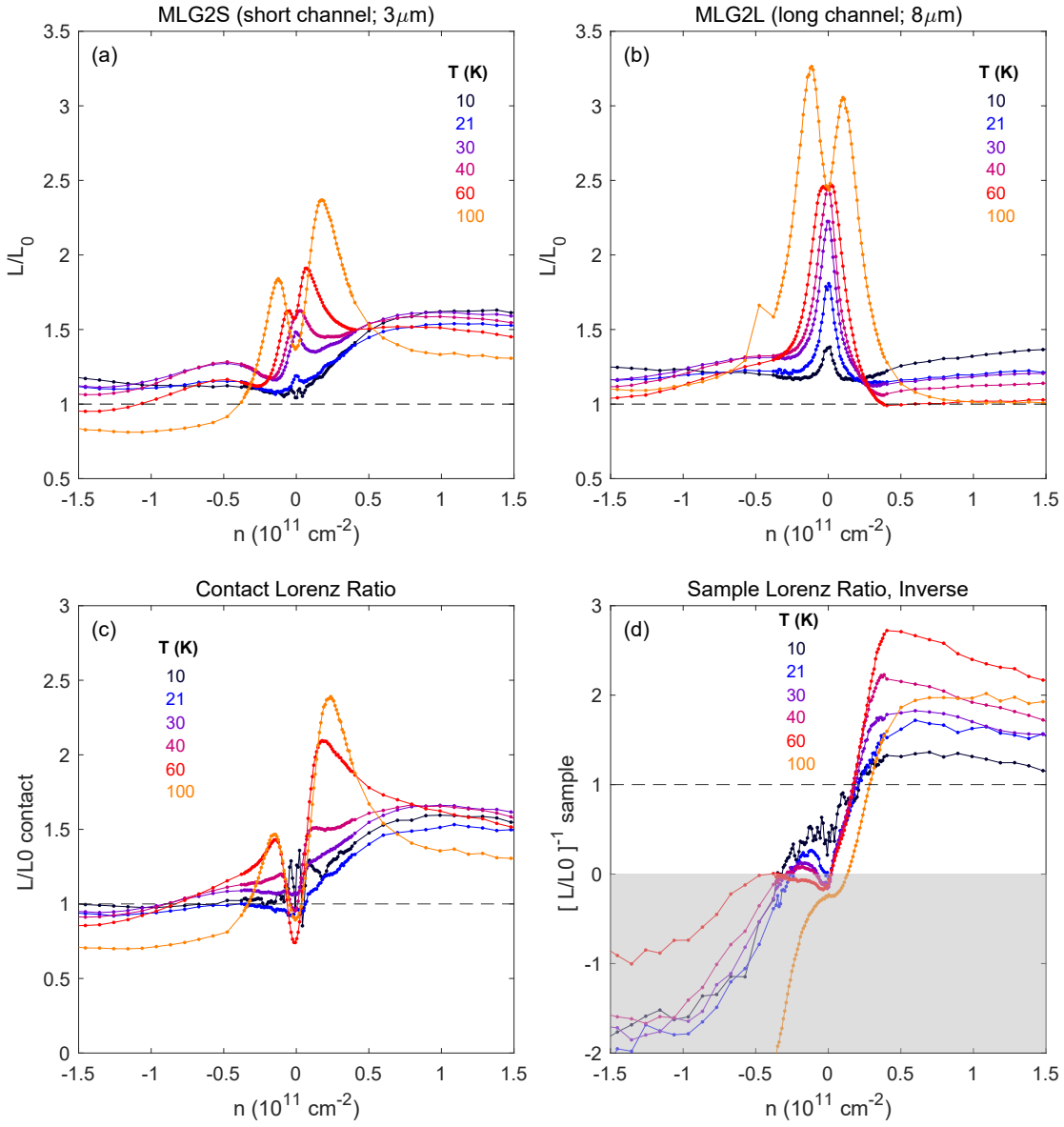

Figure 5.13: **(a)** Measured total Lorenz ratio for the short channel sample MLG2S. **(b)** Measured total Lorenz ratio for the long channel sample MLG2L. **(c)** Using the contact-resistance model, we calculate the Lorenz ratio of the contact. **(d)** The Lorenz ratio of the sample, plotted as the inverse Lorenz ratio $[\mathcal{L}/\mathcal{L}_0]^{-1}$ which is proportional to the temperature rise. The gray region marks $\mathcal{L} < 0$ and is unphysical.

bandgap; however, the electrical resistance data indicates the absence of any significant bandgap, especially comparable to a 60 K energy scale.

We now apply the method described in Section 3.7 and Appendix C to calculate the sample and contact Lorenz ratios, assuming a value of $\alpha = 0.5$. The results of the calculation are shown in Fig. 5.13(c,d). Panel (c) indicates the Lorenz ratio of the contact resistance; it is close to 1, but surprisingly has a temperature dependence at small density ($n \sim 2 \times 10^{10}\,\mathrm{cm}^{-2}$) . Interestingly, the effective Lorenz ratio of the contacts is higher than 1 at higher density, consistent with a ballistic transport picture where contact resistance thermalization happens inside the metal contacts and does not contribute to a temperature rise.

Panel (d) shows the resultant sample Lorenz ratio from the calculation, plotted as the inverse Lorenz ratio $[\mathcal{L}/\mathcal{L}_0]^{-1}$. Despite panels (a) and (b) not indicating any suppression in the sample, this calculation indicates a Lorenz ratio suppression for electron-doping, strongest at $T \sim 60\,\mathrm{K}$ and $n \sim 4 \times 10^{10}\,\mathrm{cm}^{-2}$. The inverse Lorenz ratio reaches a maximum value of ~ 2.7, which is a Lorenz ratio of 0.37. The apparently increased Lorenz ratio of the contact resistance appears to balance out the suppressed Lorenz ratio in the sample for an overall measured Lorenz ratio close to 1.

Near charge neutrality, panel (d) indicates that with increasing temperature, the sample Lorenz ratio trends toward infinity, indicating the increase in noise from the sample trends towards zero. Beyond $\sim 20\,\mathrm{K}$, the calculation shows a negative noise from the sample, which is unphysical; it possible that the influence of minor phonon cooling affects the calculation. If we choose $\alpha = 0$ in the model, the issue of negative noise is mostly reduced, and below 100 K, the inverse Lorenz ratio trends towards zero but remains positive (see Appendix A). The difference between a small negative and a small positive Lorenz ratio is in a sense a rather insignificant, as we can interpret it as

a small error in the model.

Finally, for the hole side, the model calculates a negative inverse Lorenz ratio that is not close to zero. In this regime, the model fails spectacularly, likely due the p-n junction nature of the contact resistance. In a p-n junction, the I-V behavior is inherently non-Ohmic, leading to a breakdown of our resistive mode based on Ref. 169. One such failure mechanism can be that when the sample is current-biased, one of the contact resistances has a much larger effective resistance than the other due to being reverse-biased; this can make the temperature profile across the sample tilted with a curve, rather than symmetrically peaked in the center. However, upon choosing $\alpha = 0$ in the model, the negative Lorenz ratio becomes positive and approximately 1 (see Appendix A).

It is unclear why the MLG1 device showed a total Lorenz ratio suppression, but in MLG2 the contact resistance appeared to mask it. MLG1 had a low-temperature resistance at $n = 1 \times 10^{12}\,\mathrm{cm}^{-2}$ of $700\,\Omega$ normalized to a $1\,\mu$m width, and for MLG2 the value is $370\,\Omega$. MLG2 thus likely has lower contact resistance, but it is possible the Lorenz ratio of the contacts is inconsistent between devices.

More experiments are needed to verify the plausibility of this model, ideally with three or more devices with different channel lengths. However, the calculation for the sample Lorenz ratio in the model qualitatively agrees with what we expect for hydrodynamics: a suppression of $\mathcal{L}/\mathcal{L}_0$ for small doping, and an enhancement of $\mathcal{L}/\mathcal{L}_0$ at charge neutrality.

5.5.4 Thermal Conductance in the Corbino Geometry

We now turn our attention to thermal conductance measurements in the Corbino geometry. Interestingly, in the Corbino geometry, the potential drop associated with the quantum Landauer-Sharvin contact resistance of the outer electrode is distributed through the bulk of the sample[58,80] due to propagating modes that are squeezed out and

reflected into their time-reversed states. Counterintuitively, any heat dissipation from this bulk-distributed contact resistance should still appear inside the metal contact, as that is where the momentum of the squeezed-out electrons is ultimately randomized. Unlike the rectangle geometry, the Corbino allows the measurement of thermal conductivity under an applied magnetic field due to the rotational symmetry. In Chapter 6, we explore the measurement of thermal conductance as a function of magnetic field in the context of a search for hydrodynamic effects in these Corbino devices.

Fig. 5.14 shows the data for two Corbino devices, MLG3 and MLG4. Panels (a) and (d) show optical micrographs of the devices; the red arrow in (d) indicates which Corbino was measured for the data shown here. In both devices, the bridge connecting to the inner contact was insulated from the outer contact using HSQ dielectric. In MLG3, the dielectric and bridge was deposited over the entire area of the channel to improve homogeneity; the left optical micrograph shows the device before deposition of the central contact bridge, and the right optical micrograph shows afterwards. Panels (b) and (e) show the resistance vs density at several temperatures. Device MLG3 achieves a minimum of residual density at $T \sim 90$ K with a value of $\sim 4.5 \times 10^{10}\,\mathrm{cm}^{-2}$, and MLG4 at $\sim 3.0 \times 10^{10}\,\mathrm{cm}^{-2}$.

Fig. 5.14(c) and (f) show the measured Lorenz ratio for each device. In both devices, the Lorenz ratio at low temperature is close to 1, with the exception of the common high-density low-temperature enhancement that likely arises from ballistic effects. In Chapter 6, we show via magnetoresistance that the device indeed is ballistic at high-density and low-temperature. As temperature increases to around 90 K, for both devices, the Lorenz ratio vs density develops a peak at charge neutrality, and a relative dip at a small density of approximately $1.1 \times 10^{11}\,\mathrm{cm}^{-2}$. However, at progressively higher temperatures, the behavior of the two devices diverges.

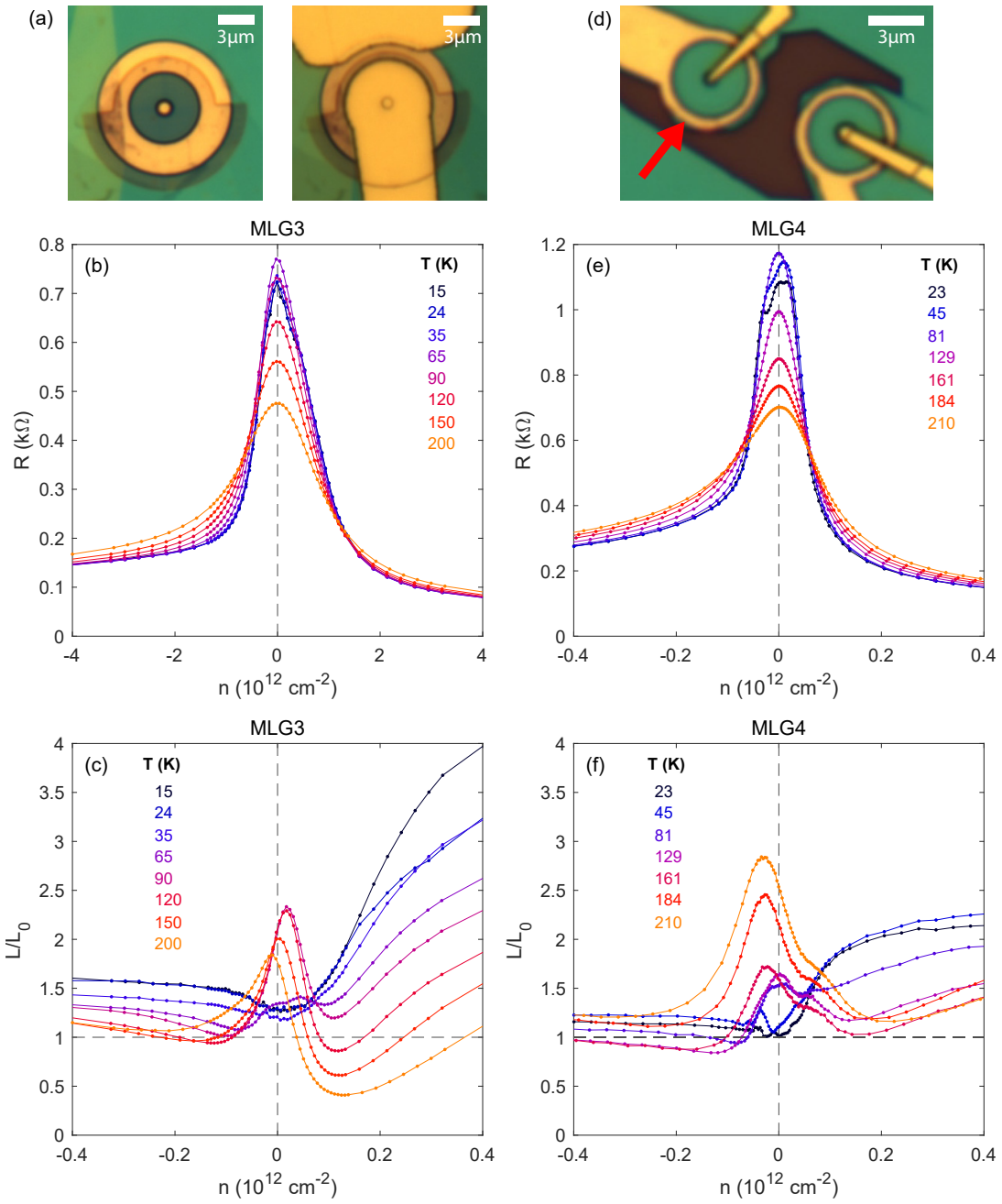

Figure 5.14: **(a)** Optical micrograph of the MLG3 Corbino device. Left: the device just before the final central contact deposition step; the dark region is the HSQ insulator. Right: after central contact deposition, covering the entire channel. **(b)** MLG3 resistance vs density curves for different temperatures. **(c)** MLG3 Lorenz ratio vs density curves for different temperatures. **(d)** Optical micrograph of the MLG4 Corbino device; the red arrow indicates the device that was studied. **(e)** Same as (b) for MLG4. **(f)** Same as (c) for MLG4.

The peak of $\mathcal{L}/\mathcal{L}_0$ at charge neutrality in MLG3 begins to decrease above 120 K, suggestive of the upper-temperature bound of the hydrodynamic window at charge neutrality as discussed in Ref. 1. However, the local minimum of $\mathcal{L}/\mathcal{L}_0$ away from charge neutrality concurrently develops into a suppression below 1, still becoming stronger at 200 K, strongly suggestive of hydrodynamic behavior in a temperature window consistent with previous experiments and theory[61,62,69,72]. Based on the data from device MLG2 in Fig. 3.9, at a density of $1 - 1.5 \times 10^{11}\,\mathrm{cm}^2$, the electronic cooling still dominates for a channel length of $3\,\mu$m; the Corbino MLG3 has a channel length of $2.35\,\mu$m and thus should have even more dominant electronic cooling, which is consistent with a suppressed measured Lorenz ratio rather than an artificially enhanced Lorenz ratio from thermalization to the phonon bath.

In MLG4, the central peak in the Lorenz ratio continues to grow to the highest measured temperature of 210 K without an indication of reaching a high-T hydrodynamic boundary, suggesting the phonon bath may be playing a significant role in electron thermalization. The dip never develops into a full suppression on the electron side, reaching a minimum of 1.0 at 161 K and then turning upwards again at higher temperature.

Out of the entire MLG data from devices MLG1 to MLG4, the only commonality is the relative peak at charge neutrality, with a relative dip at small doping. Otherwise, the temperature dependence of the peak between MLG2, MLG3, and MLG4 is significantly different between all the devices, with MLG2 showing a double-peak structure. At small doping away from charge neutrality, MLG4 is similar to MLG2, but neither show a clear monotonic temperature dependence of the Lorenz ratio suppression like MLG3 does. Given the strong disparity in disorder and residual density between MLG2 and MLG3/4, we wouldn't expect the thermal conductance behavior to be consistent between the two. However, we would expect the cleaner device to exhibit stronger signs

of hydrodynamics, but if we ignore the contact resistance for each device, there is no clear trend of hydrodynamics vs device disorder.

Despite not having the dual-channel configuration to measure the contact resistance as we did in Subsection 5.5.3, we are nonetheless able to use a trick involving the Drude formula and the magnetic field to calculate the contact resistance. The Drude formula gives us the electrical conductivity in magnetic field as

$$\sigma_{xx}(B) = \frac{\sigma_{xx}(B=0)}{1+(\mu B)^2}, \tag{5.22}$$

where μ is the mobility in units of $\mathrm{T}^{-1} = \mathrm{m}^2/\mathrm{Vs}$. At $B = 0$ the mobility formula is

$$\sigma_{xx}(B=0) = \frac{ne^2\tau}{m} = ne\mu. \tag{5.23}$$

Combining these two equations, we get

$$\sigma_{xx}(B) = \frac{ne\mu}{1+(\mu B)^2}, \tag{5.24}$$

Written with contact resistance, the total resistance measured in a Corbino would be

$$R_{2T}(B) = R_c + \frac{\ln\frac{r_o}{r_i}}{2\pi\sigma_{xx}(B)} \tag{5.25}$$

$$= R_c + \frac{\ln\frac{r_o}{r_i}}{2\pi}\cdot\frac{1+(\mu B)^2}{ne\mu} \tag{5.26}$$

$$= R_c + \frac{\ln\frac{r_o}{r_i}}{2\pi}\cdot\frac{1}{ne\mu} + \frac{\ln\frac{r_o}{r_i}}{2\pi}\cdot\frac{\mu B^2}{ne}. \tag{5.27}$$

From this last equation, we can then determine μ without knowing $\sigma_{xx}(B=0)$. Similar to Fig. 5.12, we use $n^2 = n_{tot}^2 = n_0^2 + n^2(V_g)$ to calculate the density in Eq. 5.27. In

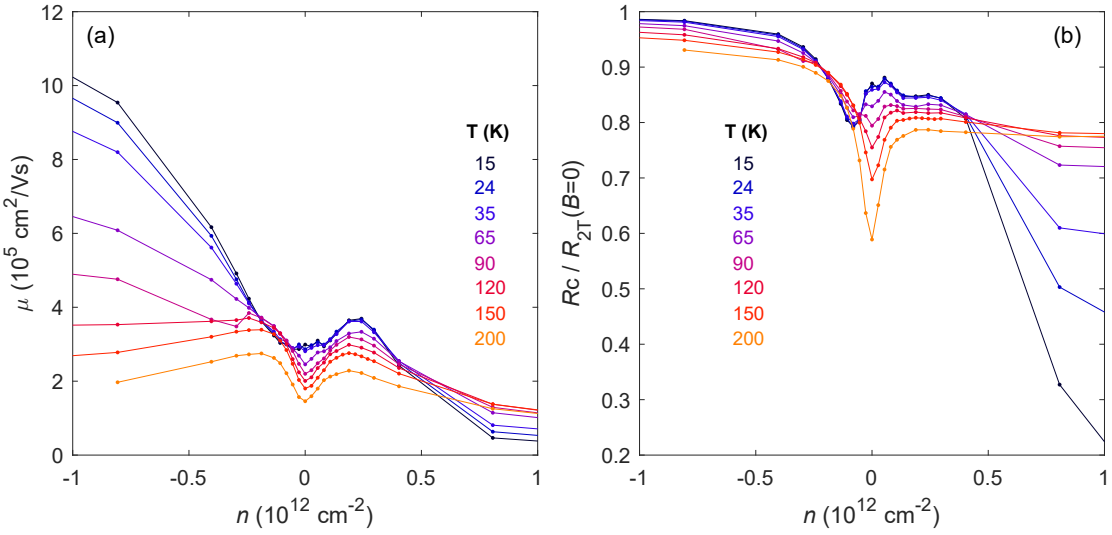

Figure 5.15: **(a)** Mobility of MLG3 computed via magnetoresistance and geometrical factors, assume diffusive Drude transport theory. **(b)** The resulting contact resistance as a fraction of the total 2-terminal resistance.

reality, the mechanism for magneto-resistance is significantly more complicated than the Drude model for a single kinematic velocity $\vec{v}_{avg}$ [55], especially for a quantum system like graphene, so we cannot expect this method to necessarily give us accurate results. Moreover, the Drude model predicts the opposite result for ballistic transport in a Corbino device (see Chapter 6). Nonetheless, we use it to estimate the mobility and contact resistance of the Corbino samples, and we show the results in Fig. 5.15 for MLG3. The results for MLG4 are qualitatively very similar.

We ignore the hole-side due to p-n junction effects, which invalidate the simple Drude model. The highest electron mobility we observe is about $400,000\,\mathrm{cm}^2/\mathrm{Vs}$, also excellent but not quite as high as for MLG2. The contact resistance is calculated to be very significant, as much as $80-90\%$ of the total measured resistance; however, because we observe rather significant hydrodynamic effects including the Lorenz ratio suppression down to 0.45, we suppose that this method may significantly over-estimate the contact

resistance, and the actual value may be in the $20 - 60\%$ range.

5.5.5 Conclusion on Monolayer Graphene

We have shown thermal conductivity data for several MLG devices; however, the data is somewhat inconsistent and does not always agree between devices. The cleanest device, with a bottom graphite gate, showed a strong Lorenz ratio suppression at small density at 50 K, but the Lorenz ratio peak at charge neutrality was equal to 1, rather than being enhanced above the WF law. Introducing disorder to this device did not affect the suppression significantly, but it did change the charge neutrality Lorenz ratio from 1 to 4, surprisingly. The unavailability of data at other temperature makes further analysis difficult, but at the least this striking behavior at charge neutrality is unexpected and likely inconsistent with hydrodynamic theories.

We observed a Lorenz ratio suppression outright in device MLG3, and in sample MLG2 using the dual-channel technique. We plot colormaps of the resulting dataset in Fig. 5.16, for comparison, showing the Lorenz ratio suppression in red. Here, the Bloch-Grüneisen temperature is marked with a green dashed line, and the Fermi Temperature is marked with a gray dashed line. The suppression in both samples clearly happens significantly below the Fermi temperature and (mostly) above the Bloch-Grüneisen temperature, ruling out non-interacting effects[86]. Despite the similarity of MLG4 to MLG3, it did not show such a suppression.

The general region of the suppression in density and temperature agrees roughly with theoretical predictions of where MLG should be most hydrodynamic[69], as was shown in Fig. 1.5. By themselves, the results in this Chapter do not form conclusive evidence for the hydrodynamic regime in low-density MLG, but they provide reasonably secure evidence for some devices. In Chapter 6, we will demonstrate an additional independent

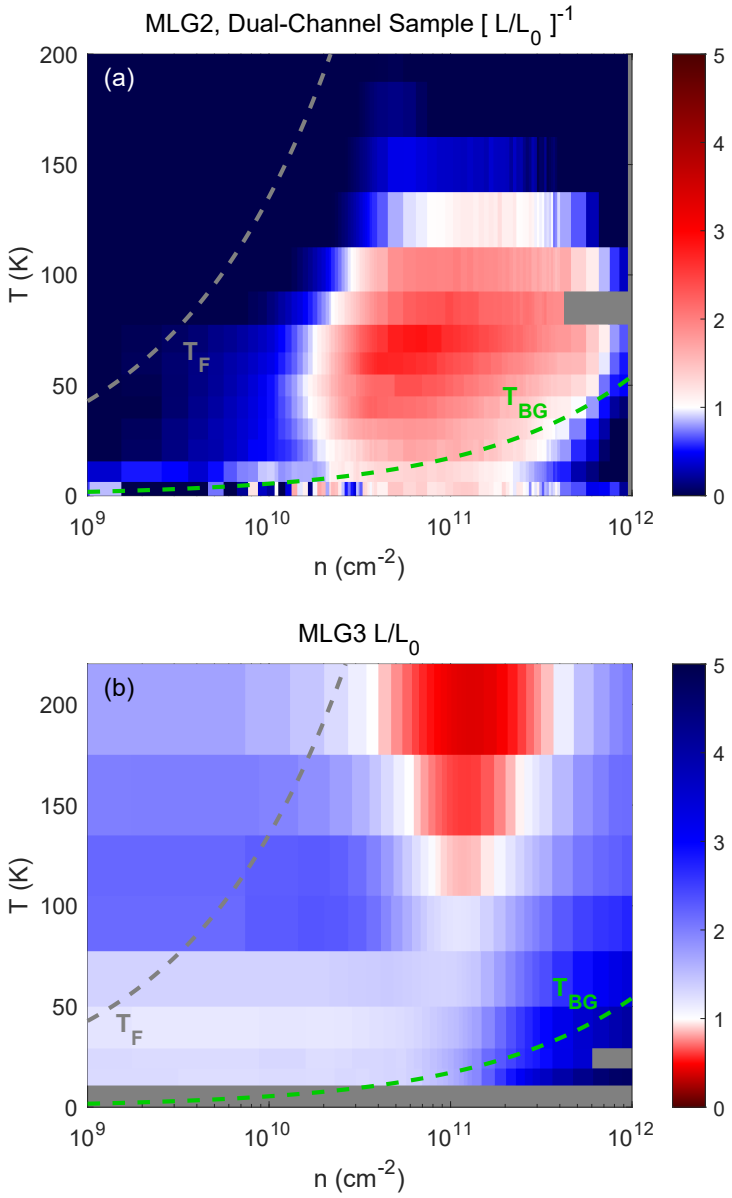

Figure 5.16: **(a)** Lorenz ratio colormap for MLG2, calculated via the dual-channel method described in the text. The inverse Lorenz ratio is plotted, and red indicates a suppression of the Lorenz ratio (enhancement of the inverse Lorenz ratio) to match the colors in (b). **(b)** Lorenz ratio colormap for MLG3. In (a) and (b), the gray dashed line indicates the Fermi temperature, and the green dashed line indicates the BG temperature; the suppression lies mostly above the BG temperature and below the Fermi temperature, excluding non-hydrodynamic suppressions of the Lorenz ratio[86].

thermal signature of viscous hydrodynamics, coincident with the suppressions we saw in this Chapter, as significantly more robust evidence for hydrodynamics in MLG.

Most of the devices measured in this Chapter did not use graphite gates due to fabrication and measurement challenges. However, the advancement of JNT techniques (Chapter 4) and fabrication methods (Appendix B) would allow an experimentalist to more easily conduct these measurements. As shown by device MLG1, ultraclean graphite-gated MLG has some very unexpected behavior in the thermal conductance, completely contradicting the existence of the Dirac fluid with a positive breakdown of the WF law, and even contradicting the predictions of a bipolar diffusion thermal conductivity enhancement. Further experiments on graphite-gated MLG are encouraged; however, the experimentalist must be very cautious with the nonlinearity-induced noise modulations and gate noise amplification effects, as ultra-clean MLG with thin h-BN dielectrics is extremely susceptible to these parasitic effects.

5.6 Bilayer Graphene: Lorenz Ratio Suppression Masked by Phonon Cooling?

Bilayer graphene (BLG), due to its different bandstructure, is expected to be hydrodynamic to lower temperatures than monolayer graphene (MLG). For a nominally charge neutral sample with a fixed degree of charge puddles due to extrinsic charged impurities and corresponding fixed densities of electrons or holes in those puddles, BLG will exhibit significantly lower corresponding chemical potential fluctuations to accommodate the excess carriers than will MLG, due to its higher density of states. This ultimately means that the low-temperature cutoff for electron-hole-plasma hydrodynamics can be much lower in BLG than in MLG, if it is not limited by impurity scattering. In other

words, at a given temperature and for the same degree of charge puddle electron density, MLG could exhibit the monopolar charge puddle regime, while BLG could exhibit thermally excited coexisting electrons and holes despite the charge puddles. Motivated by the Dirac fluid in the Crossno experiment[1], or its absence as seen in device MLG1A, we study thermal conductance in bilayer graphene to search for hydrodynamic effects at low temperatures.

BLG has two touching approximately parabolic bands (Fig. 1.2); however, an applied perpendicular opens a bandgap, creating a system which is expected to be more hydrodynamic. We explore this system experimentally in Subsection 5.6.3.

5.6.1 Disordered Bilayer Graphene

First, we present data on a relatively disordered bilayer graphene sample BLG2. This sample still has the BLG encapsulated in h-BN, but there is an additional 20 nm of Al_2O_3 oxide on top of the h-BN separating the metal top-gate, deposited via an ALD process. This oxide layer and the SiO_2 substrate are both amorphous and can thus introduce additional charge puddles into the sample. The BLG2 device has a residual density n_0 that slowly saturates below 50 K, trending asymptotically towards $\sim 9 \times 10^{10}\,\mathrm{cm}^{-2}$ (Fig. 5.17(a) inset).

The resistance vs density for several temperatures for device BLG2 is shown in Fig. 5.17(a). Compared to MLG, the resistance peak in BLG does not saturate abruptly upon entering the charge puddle regime at low-T, but the peak in resistance also does not grow to such large values as in MLG because of the larger density of states in BLG and correspondingly more thermally excited carriers at low-T. In this sense, our BLG samples do not enter the fully-saturated charge puddle regime at the measured temperatures like our MLG samples do, and the BLG samples continue to display some

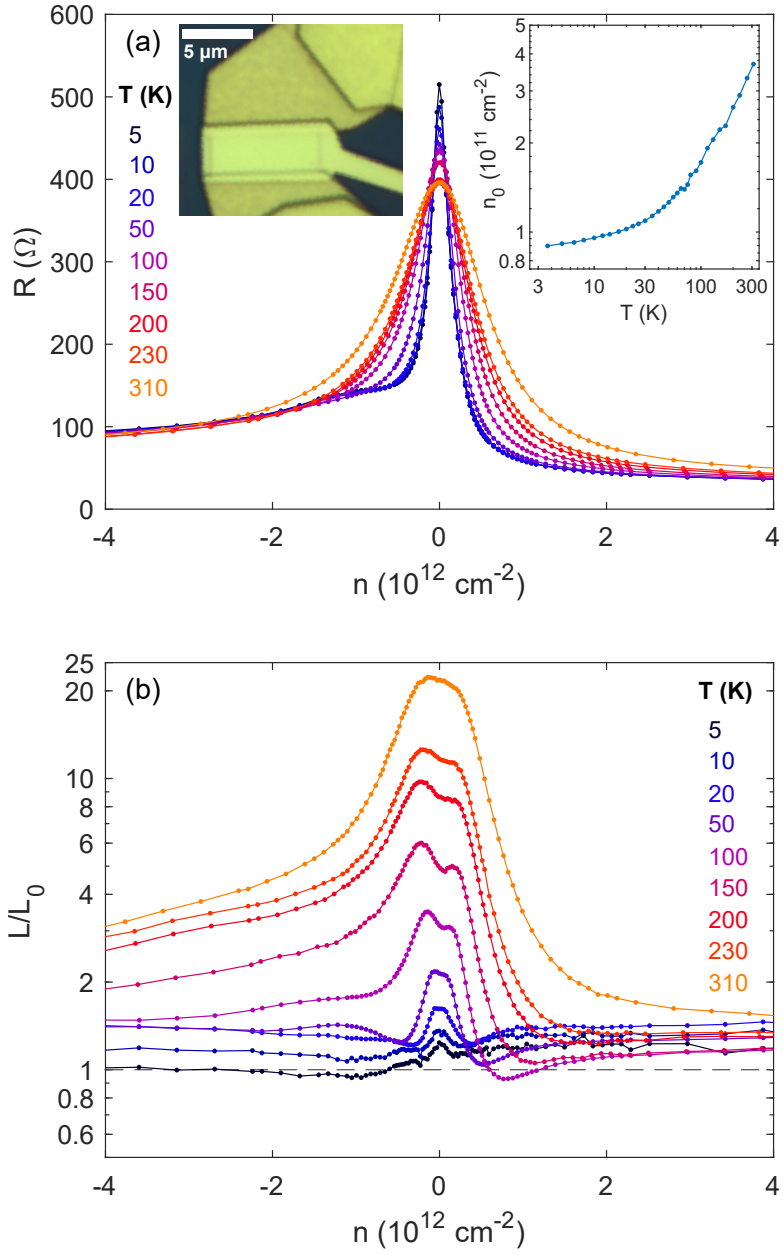

Figure 5.17: **(a)** Resistance vs density curves for BLG2. Top-left inset: Optical micrograph of the device. Top-right inset: Residual density vs temperature, approaching a limiting value of $\sim 9 \times 10^{10}\,\mathrm{cm}^{-2}$ at low temperature. **(b)** Lorenz ratio vs density for BLG2. The central peak, especially at high temperatures, is likely mostly phonon cooling, rather than a hydrodynamic enhancement.

thermally excited electron-hole coexistence at charge neutrality even at 4 K. A shoulder in resistance on the hole side at low doping, and the higher resistance at high-doping on the hole side, are very likely coming from pn-junction effects near the contacts.

Fig. 5.17(b) shows the measured Lorenz ratio for BLG2. At low temperature, the Lorenz ratio is nearly uniformly 1 for all the measured densities. Upon raising temperature, a peak develops at charge neutrality that continues to grow until the highest measured temperature of 310 K. At higher density, there is no significant suppression below 1, and the highest density Lorenz ratio stays very close to 1. Oddly, even through the device is likely limited by the $\sim$30 Ω contact resistance at high density, we do not observe the typical low-T, high-n ballistic enhancement commonly seen in other devices. It is possible that the transport in this regime is limited by long-range scattering through the charge puddles, but it is impossible to tell from a single channel length. At densities larger than $\sim 5 \times 10^{11}\,\mathrm{cm}^{-2}$, the Lorenz ratio takes a slight downturn with increasing temperature around 100 K, before turning back upwards.

The peak in the Lorenz ratio at charge neutrality suggests a hydrodynamic origin; however, there is no way to distinguish it from strong thermalization to the phonon bath. Fig. 5.18(a) shows the temperature scaling behavior of the thermal conductance at different densities, and the curves for densities around charge neutrality have a rather unremarkable transition from $\propto T$ at low temperature to $\propto T^3$ at high temperature. At the highest densities for $n \gtrsim 2 \times 10^{12}\,\mathrm{cm}^{-2}$, the thermal conductance scales linearly in temperature for the entire temperature range, consistent with WF-type electronic diffusion cooling.

At intermediate densities of $2\times10^{11}\,\mathrm{cm}^{-2} < n < 2\times10^{12}\,\mathrm{cm}^{-2}$, we observe a sublinear-in-temperature scaling of the thermal conductance, commensurate with a slight decrease of the Lorenz ratio with increasing temperature, as shown in Fig. 5.18(b). The sublinear

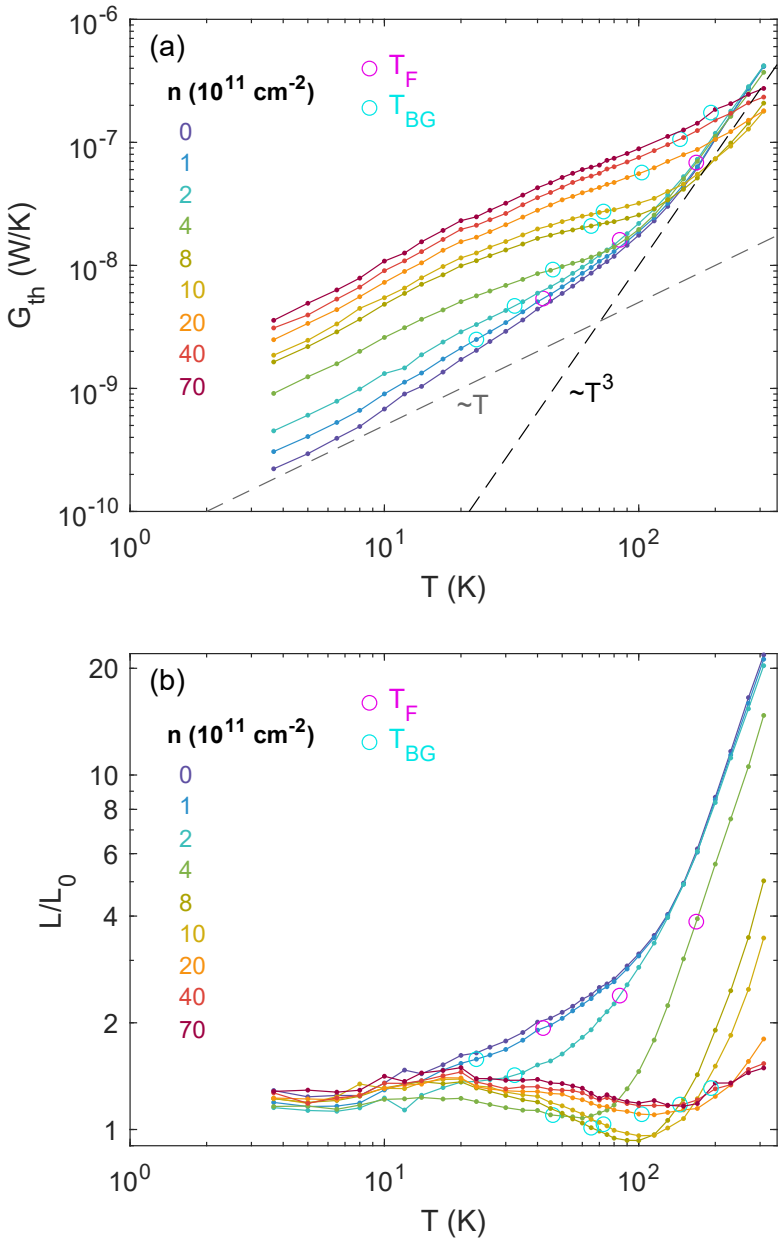

Figure 5.18: **(a)** Thermal conductance of BLG2 vs temperature on a log-log scale. Gray dashed lines indicate $\sim T$ and $\sim T^3$ power laws vs temperature. The scaling at charge neutrality transitions from a $\sim T$ power law at low T to a $\sim T^3$ power law at high T. Magenta and cyan circles mark, for the density curves, the locations of the Fermi and BG temperatures; if the temperature falls outside the measured range, it is not marked. **(b)** Lorenz ratio vs temperature of BLG2 on a log-log scale. Circles are the same as (a).

scaling in temperature occurs between approximately 50 K and 150 K, before transitioning to a superlinear scaling in temperature.

While not an outright suppression of the Lorenz ratio significantly below 1, this sublinear feature suggests the beginning of a thermal conductance suppression, just before it is masked by phonon cooling, which follows a superlinear-in-T scaling law. Relative to the low temperature value, the Lorenz ratio is suppressed by about 32% in this feature; while the absolute value of the Lorenz ratio might be scaled by contact resistance effects, the relative changes are more qualitatively reliable.

For each density in Fig. 5.18, the corresponding Fermi temperature T_F and Bloch-Grüneisen temperature T_{BG} are indicated with circles along the data curve if they fall within the measured temperature range. The aforementioned sublinear scaling of G_{th} occurs just above T_{BG}, and significantly below T_F, ruling out any single-particle effects that can suppress thermal conductance below the WF value[86].

The hydrodynamic suppression is the only remaining mechanism that can cause a reduction of thermal conductance, and we thus conclude that this subtle feature may be evidence of hydrodynamic effects, although it is strongly masked by a significant phonon cooling background. Unlike MLG, BLG will cross over from diffusion cooling to phonon cooling at significantly lower temperatures, as seen by comparing Figs. 3.9 and 3.10, and explained in the next subsection. While we cannot conclude that our BLG2 sample is hydrodynamic, there is evidence that the e-e scattering is lightly suppressing the thermal conductivity below the non-interacting value. In the next subsection, we revisit this feature using the dual-channel-length method to better understand the diffusion to phonon cooling crossover.

5.6.2 Dual-Channel Measurement

In this subsection, we present the results of sample BLG4, which has a short and a long channel device BLG4S and BLG4L respectively; this sample was previewed previously in Fig. 3.10. The channel lengths, defined by the topgate size, are 2.5 and 7.5 μm. Unlike BLG2, to reduce the disorder of this device, the topgate was deposited as Cr/PdAu directly on top of the h-BN, avoiding any disorder from an oxide grown by ALD process. Because the topgate is not insulated from the source/drain electrodes by ALD, a gap of $\sim 350\,\text{nm}$ was left between the topgate and contacts, covered by an HSQ insulator after topgate deposition, and then gated to a high density by a separate gate called the U-gate, acting similarly to the Si gate for device MLG1 (see Appendix B).

For now, we focus on measurements conducted at zero displacement field, when the BLG is not gapped, and sweeping density. In BLG4, the gate voltage values for charge neutrality and zero gap are slightly misaligned between the two devices, necessitating separate scans for each device to measure the zero-gap behavior. The resistance curves are shown in Fig. 5.19.

The slight density-shift in the resistance peak with increasing temperature is mostly due to the thermal smearing of the hole-side contact resistance; we can see the density-shift is much smaller for BLG4L, which has a weaker relative contact resistance contribution. We confirm this by using the TLM method to eliminate the contact resistance and calculate the sheet resistivity, shown in Fig. 5.20(a). We see that the resistivity peak is mostly unshifted due to temperature.

At low temperatures, the inhomogeneities between the two devices are different, causing the low-temperature resistance curves to have different shapes, as shown in Fig. 5.19(a,b) and Fig. 5.20(a) inset. At $T = 1.9\,\text{K}$, the resistances have a narrow peak

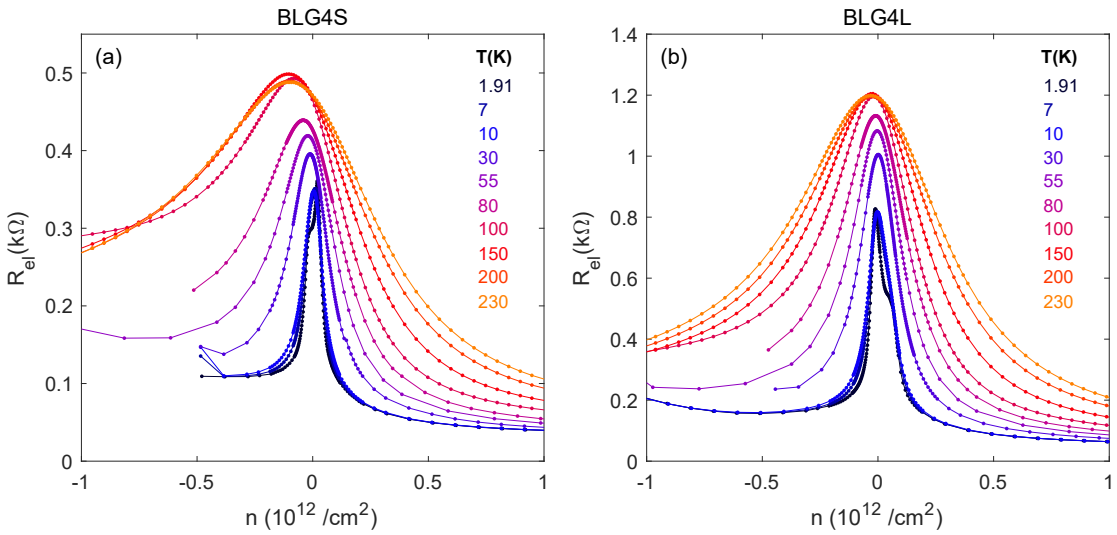

Figure 5.19: **(a)** Resistance vs density for BLG4S. **(b)** Same for BLG4L.

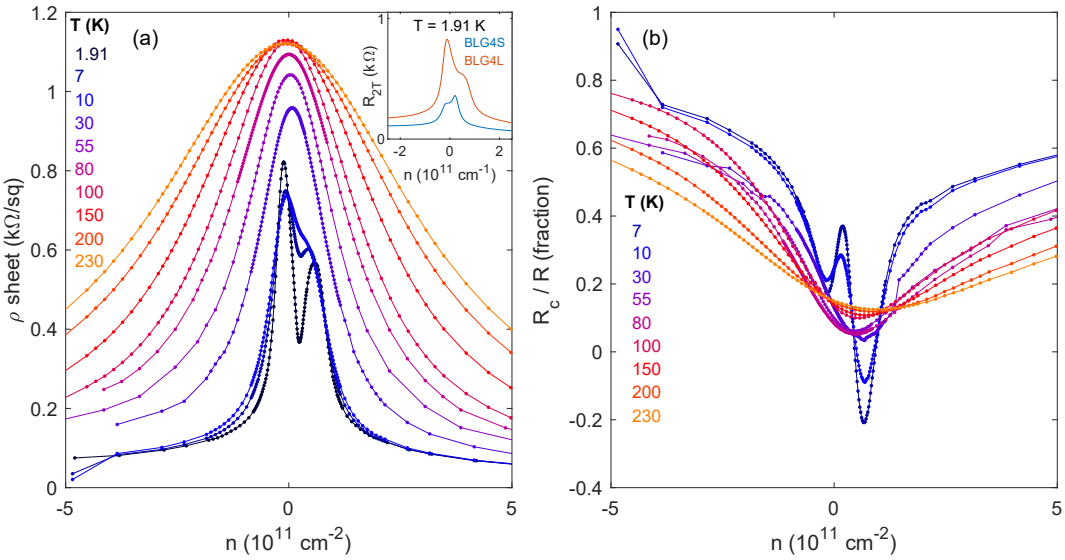

Figure 5.20: **(a)** Sheet resistivity computed for BLG4 via TLM. Inset: 1.91 K 2-terminal resistance traces for the short and long channels, showing universal conductance fluctuations or inhomogeneity inconsistent between the two devices, leading to a distortion of the low-T calculated sheet resistivity. **(b)** The resulting calculated contact resistance as a fraction of the total resistance. The low-T values are distorted for the same reason as in (a).

and a shoulder, but the relative positions do not match. The resulting sheet resistivity, contact resistance fraction, and residual density calculations are thus adversely affected, and the numbers below 10 K are not necessarily a good representation of the true values. At high temperature, the thermal broadening overpowers the small-scale charge puddle inhomogeneities and makes the two devices more similar to each other, allowing a more accurate TLM measurement of resistivity. Fig. 5.20(a) shows the sheet resistivity calculated for the range of measured temperatures. From 20 K to 130 K, the charge neutrality resistivity grows slowly from 0.83 kΩ/sq to 1.13 kΩ/sq, above which it is nearly constant with temperature. This value is consistent with the expected hydrodynamic universal BLG charge neutrality conductivity $1/\sigma_0 \sim 1\,\mathrm{k\Omega} \sim [25e^2/h]^{-1}$, both experimentally and theoretically[3,75,76]. This contrasts with MLG, where experiments have been unable to obtain the theoretical hydrodynamic conductivity at charge neutrality.

Fig. 5.20(b) shows the resulting contact resistance fraction for the short channel BLG4S. The double-peak feature in the resistivity at low-T, and the corresponding double-dip feature in the contact resistance fraction, are artifacts of the different shapes of the resistance curves. Clearly, the negative values of the contact resistance fraction are unphysical and are explained by this mechanism. With enough thermal smearing by 30 K, we see the contact resistance fraction starts to normalize around ~ 0.1 at the charge neutrality point, and remains relatively low for a reasonably-sized window around charge neutrality. This contrasts with MLG2S, which had a higher contact resistance fraction for all densities.

The residual density, calculated from the resistivity is shown in Fig. 5.21(a), and it reaches a minimum value of $\sim 5.6 \times 10^{10}\,\mathrm{cm}^{-2}$ at a temperature of 20 K, indicating slightly less disorder than BLG2.

The mobility, calculated from the sheet resistivity, is shown in Fig. 5.21(b), calcu-

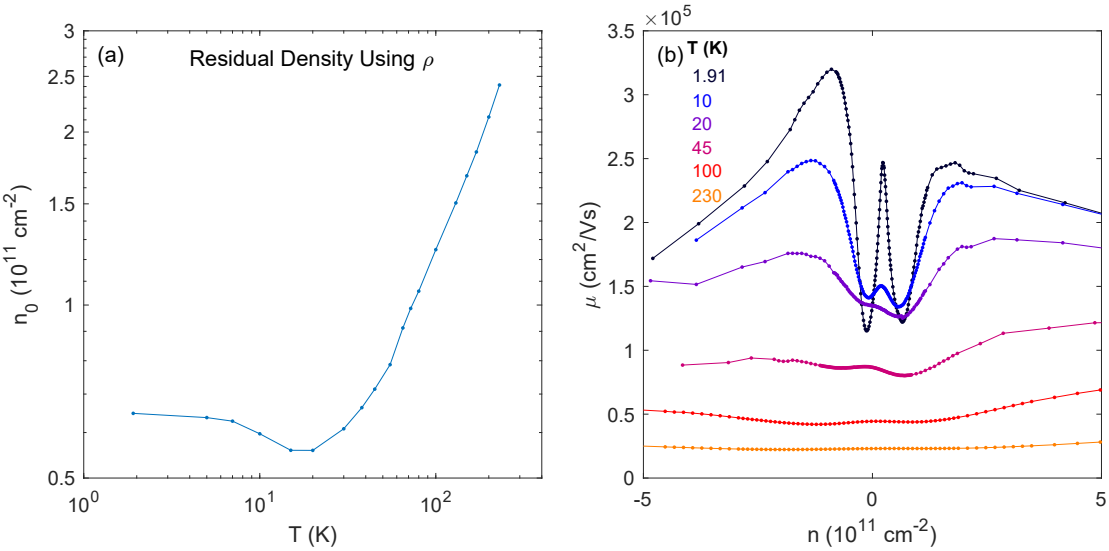

Figure 5.21: **(a)** Residual density for BLG_4 vs temperature. **(b)** Calculated mobility vs density for BLG_4, for different temperatures. The low-T values are distorted due to differences between the two devices.

lated via $\mu = 1/(ne\rho)$, where $n = \sqrt{n_0^2 + n(V_g)^2}$ is approximately the total charge density. Disregarding the 1.91 K data, the sample mobility reaches an excellent value of $\sim 230,000\,\mathrm{cm}^2/\mathrm{Vs}$.

We now examine the Lorenz ratio, shown for each device in Fig. 5.22. While the 1.9 K data is noisy due to universal conductance fluctuations and small signals, by 5–7 K the Lorenz ratio shows a small but clear relative peak at charge neutrality and a suppression at small doping, although like in BLG2, there is no significant suppression below 1. As temperature is increased, by 10 K the general shape stays the same, but the overall values generally increase. Near 10 K, the Lorenz ratio for the long channel starts increasing much more suddenly with temperature than in the short channel, or than in BLG2. This sudden increase likely comes from the onset of thermalization to the phonon bath dominating over the diffusion cooling, and it is further evidenced by the data previously shown in Fig. 3.10, where the long-channel thermal conductance

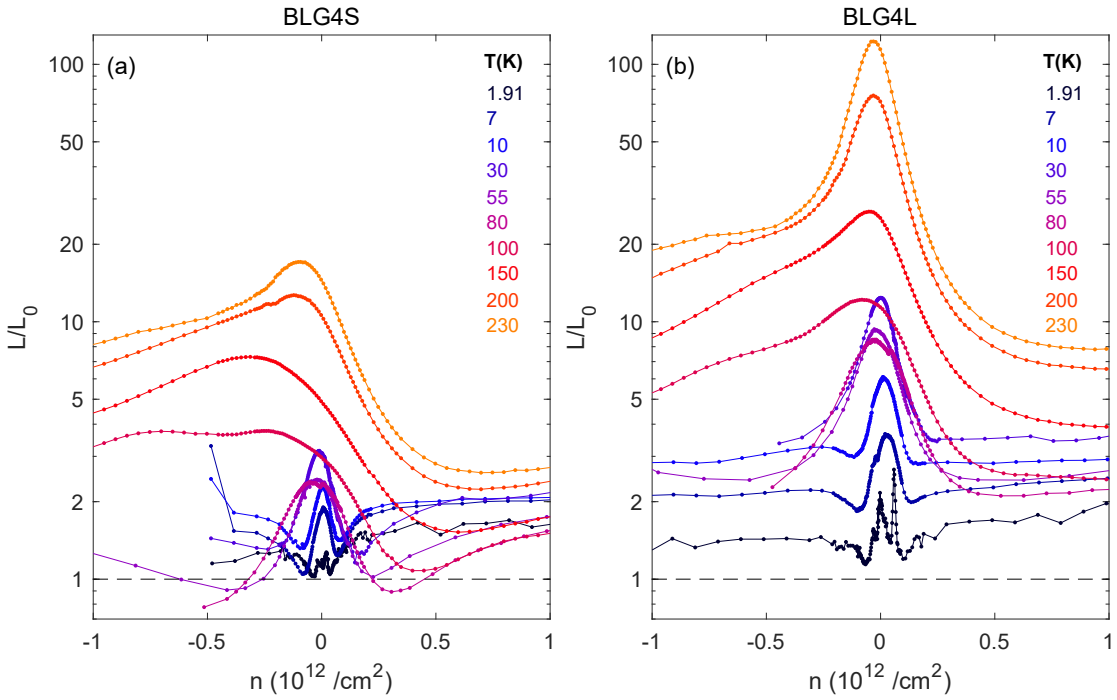

Figure 5.22: **(a)** Lorenz ratio for BLG$_4$S vs density. **(b)** Lorenz ratio for BLG$_4$L vs density.

becomes higher than that of the short channel by around 6–20 K, depending on the exact density. Thus, the data above 10 K is likely unreliable in a quantitative sense, but we may still hope to extract something useful from the qualitative aspect.

We observe that both for the short and long channels, there are regions in density where the Lorenz ratio decreases with increasing temperature, similar to what we saw in BLG2, although here the decrease is more significant. Fig 5.23 plots the thermal conductance G_{th} and Lorenz ratio vs temperature for BLG4S, along with circles marking T_{BG} and T_F if they occur inside the measured temperature range.

We see the regions with Lorenz ratio decreasing with temperature correspond to the regions where G_{th} is either slightly decreasing with T or near constant with T, and this behavior happens above T_{BG} and below T_F. This is the same effect we observe in BLG2, although here it is more pronounced, as would be expected in a cleaner, more hydrodynamic device. We again propose that this effect is indirect evidence for hydrodynamic in bilayer graphene, as we are unable to measure the thermal conductance from diffusion cooling due to the much stronger phonon cooling pathways.

We can apply the same calculation as in Subsection 5.5.3 to estimate the contact and sample Lorenz ratios. Due to the clear onset of thermalization to the phonon bath by 20 K, we limit our analysis here only to temperatures up to 20 K; however, due to the inhomogeneity differences between the devices, the low-temperature calculations still fail to produce an accurate result near charge neutrality. Nonetheless, we show the calculated contact and sample Lorenz ratios in Fig 5.24(a,b). The calculated Lorenz ratio of the contact has very strong dips and peaks at low-T due to the inhomogeneity differences between the samples. As temperature smears out the inhomogeneities, the contact Lorenz ratio trends towards an asymptotic curve; the values are approximately 1 at charge neutrality, a deep dip towards ~ 0 for a small density of $\sim 7 \times 10^{10}\,\mathrm{cm}^{-2}$,

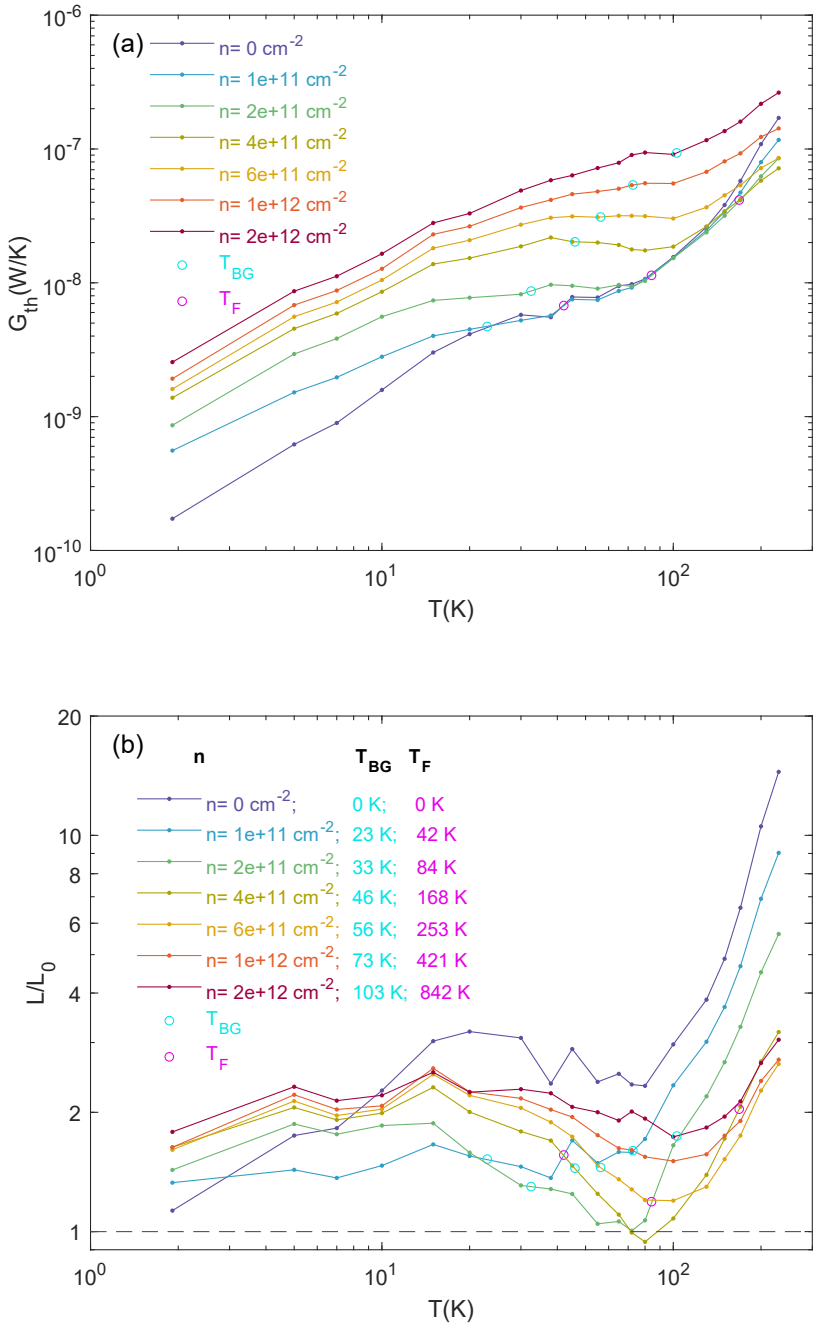

Figure 5.23: **(a)** Thermal conductance vs temperature for BLG4S on a log-log scale. Magenta and cyan circles mark, for the density curves, the locations of the Fermi and BG temperatures; if the temperature falls outside the measured range, it is not marked. **(b)** Lorenz ratio vs temperature scaling for BLG4 on a log-log scale. Circles are the same as in (a). In the legend, the BG and Fermi temperatures are also listed for each density.

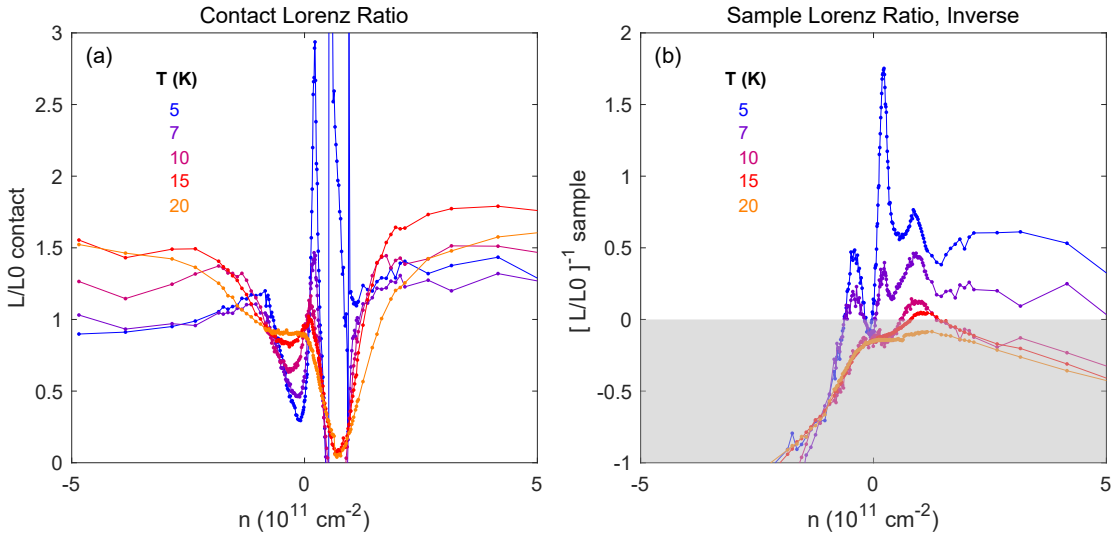

Figure 5.24: **(a)** Lorenz ratio of the contact resistance for BLG_4, calculated via the dual-channel method. The low-temperature values are distorted due to differences between the devices, and the higher temperature values (approaching 20K) are distorted due to the presence of phonon cooling. **(b)** Inverse Lorenz ratio of the channel for BLG_4, calculated via the dual-channel method. The same distortions apply. The gray region region marks unphysical negative Lorenz ratios. The data trends towards the unphysical region at higher temperatures likely due to the presence of phonon cooling.

and finally an increase towards 1.3-1.8 at higher density.

The behavior of the sample Lorenz ratio differs from that of the contact. Similarly to MLG2, the hole-side sample Lorenz ratio is calculated to be negative, an unphysical value likely caused by the p-n junction effects at the contacts. Near neutrality and electron doping, the low-T curves again have strong hills and valleys due to the same effects. Warming to 10 K and beyond, where phonons start to dominate entirely, the effective sample Lorenz ratio becomes negative. This means the temperature profile in the sample is now calculated to be parabolic-up, instead of the usual parabolic-down. This change is consistent with heat loss to the phonon bath exceeding the Joule heat generated in the sample channel, and the channel itself now acts as a phonon-mediated heat sink for the heat generated at the contact resistances, which now flows inwards towards the sample center rather than outwards towards the contacts, creating the parabolic-up shape.

This is only a rough qualitative description, of course, as the assumptions for calculating the sample Lorenz ratio (see Appendix C) assume the same effective thermal conductivity and no phonon cooling, and at these temperatures the phonon cooling contribution is significantly different between the two devices (see Fig. 3.10 and the corresponding discussion in Chapter 3). Unfortunately, the phonon cooling mechanism foils our plan for quantitatively extracting the contact and sample Lorenz ratio in the expected hydrodynamic regime around $T \gtrsim 100$ K. It may be possible to perform this experiment with a less disordered dual-channel sample, using graphite gates, to ensure homogeneity/similarity between the two devices below 5 K so that the TLM technique works.

One additional analysis technique we can perform is to plot the measured transport quantities as a function of μ/k_BT rather than n, as was done in Refs. 3,75. In the case

of a universal hydrodynamic conductor with no impurity or phonon scattering, μ/k_BT becomes the only relevant quantity for determining the transport properties, as they are self-similar at different temperatures for appropriately scaled densities. Fig. 5.25 plots the sheet conductivity, as well as the individually measured Lorenz ratios, for different temperature, vs μ/k_BT. The conductivity does not collapse onto a uniform curve like in Ref. 75, but obtains very similar behavior and numbers as Ref. 3, indicating there is still some amount of disorder scattering present on top of electron-hole hydrodynamic scattering. However, by 150 K, the curves do just begin to reach an asymptotic collapse, and the 200 and 230 K curves lie directly on top of each other.

The curves for the Lorenz ratio also do not coincide, but interestingly for BLG$_4$S, for $T \gtrsim 50$ K, the dip in the Lorenz ratio remains around $\mu/k_BT \sim 1.3$ to 1.6 up to 230 K. While the dip at higher temperatures is strongly dominated by phonon cooling, its shape and position may still qualitatively indicate a hydrodynamic suppression of thermal conductance that is strongest around $\mu/k_BT \sim 1.5$.

BLG$_4$L indicates a similar effect, where the Lorenz ratio plateaus at approximately the same value of μ/k_BT, but here the phonon cooling is even more strongly dominant.

5.6.3 Thermal Conductance in Gapped Bilayer Graphene

Application of a perpendicular electric field in BLG breaks the layer potential symmetry and induces a small bandgap, as described in the Subsection 4.5.3 with experimental data in Fig. 4.15(a).

Fig. 5.26 demonstrates the shape of the bands as the gap is opened. The quadratic bands are distorted, first into a flattened shape, and the further into a "Mexican-hat" shape for higher layer asymmetry. The flat band edge quenches the kinetic energy and increases the relevant importance of the Coulomb interaction energy to the carrier

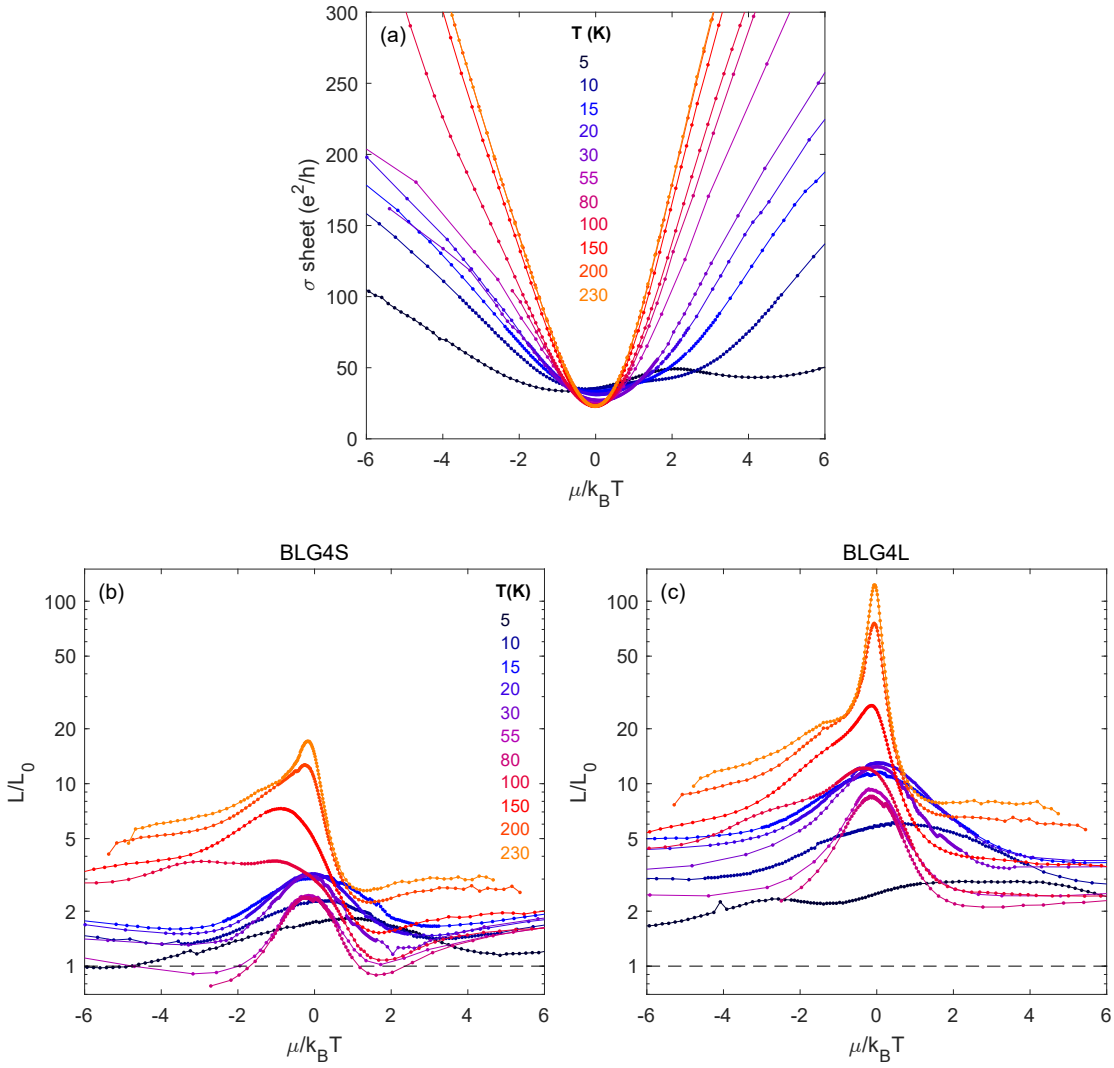

Figure 5.25: **(a)** Sheet conductivity of BLG_4, computed via TLM, vs μ/k_BT. **(b,c)** Measured Lorenz ratio for BLG_4S and BLG_4L, vs μ/k_BT.

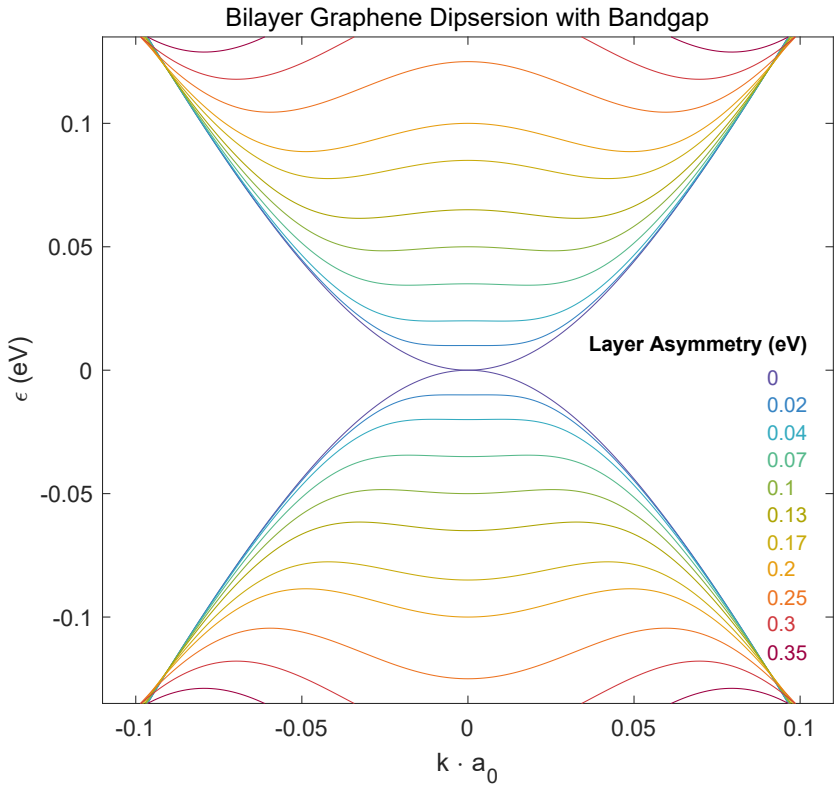

Figure 5.26: Low-energy dispersion of gapped bilayer graphene, showing the evolution of the bandstructure as a gap is opened due to layer potential asymmetry. The x-axis is in units of the wavevector k times the lattice constant a_0. The equations and parameters for this plot are from Ref. 29.

dynamics. It is thus possible that gapped BLG could be more hydrodynamic at the van Hove singularity than ungapped BLG. While it is difficult to directly measure the gap, with different techniques yielding conlicting values[29], we can instead describe a polarization parameter p, and analogous to the electron density n, using a combination of gate voltages:

$$ne = c_t V_t + c_b V_b \tag{5.28}$$

$$pe = c_t V_t - c_b V_b, \tag{5.29}$$

where $c_{t/b}$ is the capacitance per unit area to the top or bottom gate, and $V_{t/b}$ is the corresponding gate voltage. The polarization is roughly proportional to the layer asymmetry and experimentally a much easier parameter to define than the actual induced bandgap. We will vary the polarization p and study the resulting effects on thermal transport.

Due to the nonlinearity-induced noise modulation effect, we must be very careful in interpreting any data from this measurement, as gapped samples will exhibit significantly stronger I-V nonlinearities than will ungapped samples. We thus perform the experiment at a temperature equal to $T_{N,in} = 22.8$ K in order to remove the parasitic signal. Unfortunately, at this temperature phonons are still a significant contribution to the cooling power, and thus the measured Lorenz ratios are significantly higher than the true values, and we can only attempt to interpret the data qualitatively.

The measured electrical and thermal conductances, for gapped BLG4S, are plotted in Fig. 5.27. As the polarization is increased, the electrical conductance decreases as expected due to having fewer excited carriers. The thermal conductance follows a similar behavior, although there is some non-monotonicity at densities above $6 \times 10^{10}\,\mathrm{cm}^{-2}$, and

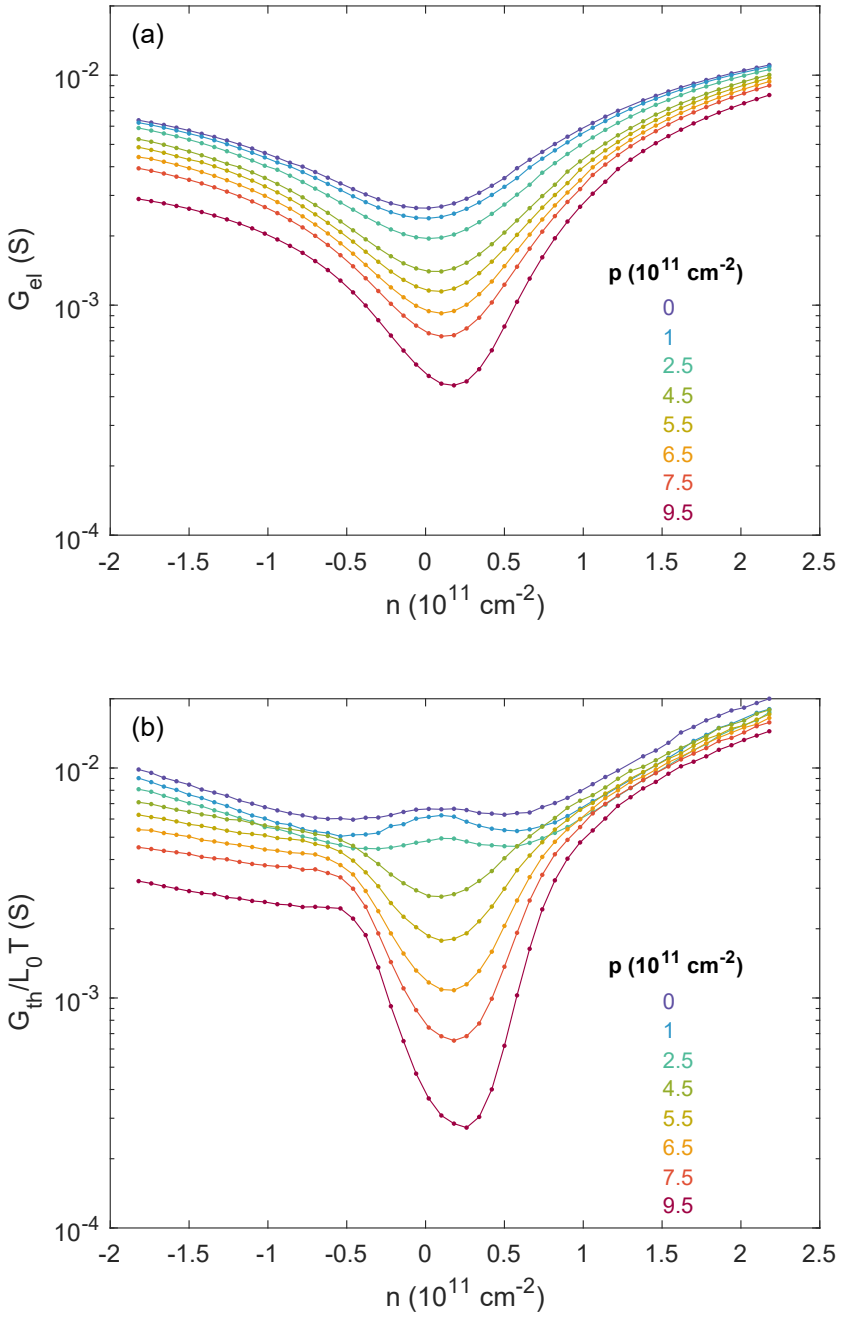

Figure 5.27: **(a)** BLG$_4$S electrical conductance vs density for several different values of polarization p. The polarization is proportional to the bandgap; the gapped system has lower conductance. **(b)** Same for thermal conductance.

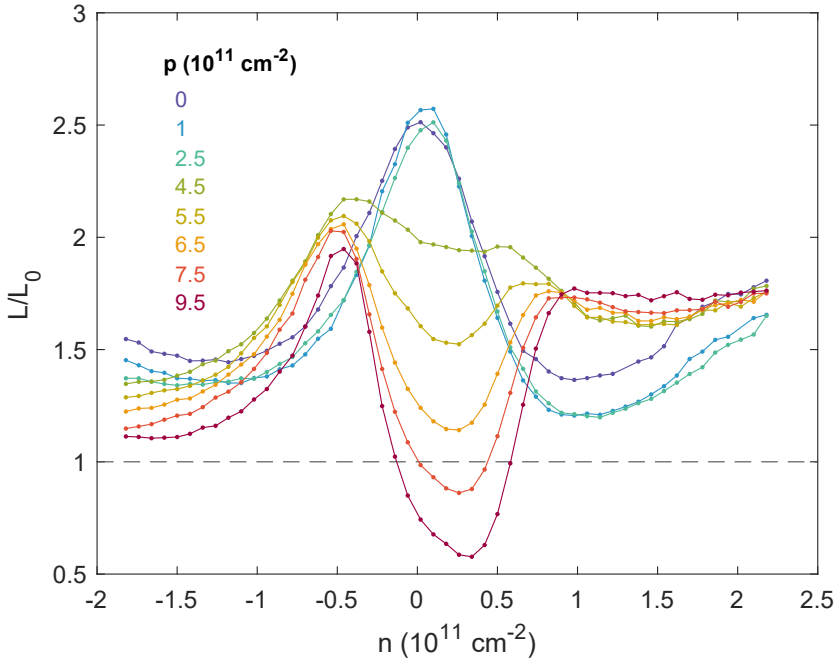

Figure 5.28: BLG$_4$S Lorenz ratio vs density, for several different values of polarization, corresponding to the opening of a bandgap.

the decrease in the thermal condutance at zero density is stronger than in the electrical conductance.

Fig. 5.28 shows the resulting measured Lorenz ratio. For small polarizations, the Lorenz ratio dip decreases from 1.37 to 1.21, while the peak remains unchanged. This may be suggestive of a stronger hydrodynamic regime due to flatter bands; however, the contact resistance fraction of the channel is also changing, and it is impossible to disentangle the two effects.

Near a polarization value of $\sim 4.5 \times 10^{11}$ cm^{-2}, the behavior drastically and suddenly changes. The peak at charge neutrality transitions into a dip, and the dip at small doping becomes increased to a near-constant flatline of ~ 1.75. At the highest polarization measured, the dip at charge neutrality acquires a value of 0.58. This is surprising

behavior, given the presence of both phonon cooling and bipolar diffusion at charge neutrality, which should only act to increase the Lorenz ratio. Theoretical calculations for the Lorenz ratio in gapped bilayer graphene, without any carrier-carrier scattering, have found that the Lorenz ratio is always larger than 1 at charge neutrality due to the effects of bipolar diffusion[87], in contrast with our measured data. We do not show data for higher polarization values, because the sample resistance becomes very large and far from the ideal operating point of the matching circuit, and because of the possibility of increased gate-induced noise due to larger dR/dV_g values.

It is unclear what would be the expected Lorenz ratio in a gapped 2D semiconductor with electron-hole scattering, although we suppose that such scattering would only act to increase the Lorenz ratio at charge neutrality due to electron-hole friction. It is possible that the device is extremely non-linear and this affects the JNT techniques beyond what is discussed in Chapter 4. It is also possible that the central dip is caused by inelastic phonon scattering at charge neutrality, since the maximum energy of electrons is lowered due to the bandgap opening; however, it is unclear what role the Bloch-Grüneisen temperature plays in a 2D low-density gapped electronic system.

Ultimately, the mystery of the suppression remains unexplained, as it does not follow the usual expectations, and only some exotic explanations may account for it.

5.6.4 Conclusion on Bilayer Graphene

We have presented thermal conductivity data on two bilayer graphene samples. Data for two additional samples are shown in Appendix A; however, the data from those samples is likely unreliable due to fabrication and/or measurement issues.

From the two devices in this Chapter, we have not seen any clear signatures of hydrodynamics, such as a direct Lorenz ratio suppression below 1 for small density, or a strong

enhancement above bipolar diffusion (and not caused by phonons) at charge neutrality. Both devices showed quantitatively similar behavior, with a small relative "dip" in the Lorenz ratio at small doping which did not go significantly below 1, and a moderate enhancement at charge neutrality that grew with temperature. Most importantly, there is a range of densities at small doping where the Lorenz ratio decreased with temperature, while concurrently the thermal conductance either scaled sub-linearly with temperature or actually decreased with temperature. However, phonon cooling dominated at the temperatures where this occurred, obscuring the true value of the Lorenz ratio. We can thus only take this behavior as indirect evidence of hydrodynamic thermal conductance, as it is only a relatively small charge on a large phonon background.

The dual-channel method, unlike for MLG, failed for BLG due to the very low phonon-cooling crossover temperature, as well as differences in sample inhomogeneity. Future experiments, with more uniform samples, such as by using graphite gates, may be able to resolve this issue.

Gapped BLG did not show any clearly expected signatures of stronger hydrodynamics due to the flat bands; however, it did provide a new mystery of the strongly suppressed Lorenz ratio in the gap, despite already-strong thermalization to the phonon bath at 22.8 K.

Further experiments, using bilayer graphene with graphite gates and lower contact resistance, are strongly encouraged to future experimentalists. In the work of this thesis, several graphite-gated bilayer devices were attempted, but all failed to produce useful experimental data due to various reasons (see Appendices A and B). With the improved JNT techniques in Chapter 4, the dual-channel method discussed in this Chapter, and better understood fabrication methods for graphite-gated devices as discussed in Appendix B, such experiments will be considerably easier to undertake.

However, due to the strong phonon cooling compared to MLG, it is possible that BLG will always obscure the hydrodynamic thermal conductance suppression with strong phonon cooling. In this case, other signatures might be necessary to observe hydrodynamic transport, such as electrical-only signatures[3,71,75], or the methods discussed in Chapter 6.

5.7 Outlook on Hydrodynamic Thermal Conductivity

We have presented a study of thermal conductivity in monolayer graphene and bilayer graphene, focusing on deviations from the WF law as a signature of hydrodynamics. While we have found some evidence in both MLG and BLG, the data for MLG is more extensive and has shown clear suppressions of the Lorenz ratio below 1. However, not all MLG devices showed this suppression, and there is no clear trend or pattern with regards to residual density or disorder that may explain the discrepancies. It is possible that the variability in contact resistance, including the effective Lorenz ratio of the contacts, may play a role in sometimes masking the Lorenz ratio suppression.

Due to the effects of viscosity on electrical resistance, but the absence thereof on thermal resistance, Lorenz ratio measurements in finite-sized laboratory samples can depend non-trivially on the sample geometry. Potentially, viscous finite-size effects may thus also explain the variability and inconsistency in our measured Lorenz ratios. On the theoretical front, there is more work to be done in understanding our experimentally measured Lorenz ratios. Theorists have generally considered Lorenz ratios in infinitely sized sample, but in such calculations, they miss viscous finite-size effects that may renormalize the values. Individually, the ingredients for a grandmaster theory or calculation are mostly present, and it may be relatively easy to perform it.

Advancements in reduction of contact resistance, perhaps below the quantum level via adiabatic contact, or via multi-terminal self-heating geometries, may improve the measurement. Further and more systematic studies using the current state of the art XeF_2 contacts for MLG are needed to understand the data variability.

Graphite gates are an easy way to reduce disorder in the samples; however, they make nanofabrication significantly more challenging, especially with the constraints imposed upon the device for noise measurements (see Appendix B), and they can make measurements also more difficult due to the higher nonlinearity and gate-line-noise effects. Several graphite-gated devices were attempted in the work of this thesis, but almost every attempt failed due to either fabrication or measurement problems. However, we have learned from these mistakes, both fabrication and measurement, describing the difficulties and solutions in Chapter 4 and Appendix , and hope that subsequent work will build upon this knowledge. Experiments comparing graphite- and non-graphite-gated devices, ideally in the same monolithic heterostructure, can reveal the role that disorder plays in hydrodynamic thermal conductivity.

Nonlocal noise thermometry[174] is an alternative method we have developed to local self-heating for measuring thermal conductance. While it relies on local self-heating for thermometer calibration, the measurement of the sample is done non-locally. This technique is more involved than the basic self-heating configuration, as there are now three noise measurements that need to be done, rather than just one, but it offers potential advantage of working around some of the contact resistance issues. Ultimately, hydrodynamic breakdowns of the WF law could be confirmed more conclusively if measurements using both techniques agree with each other. This a currently ongoing research direction in our group.

It is a profound and necessary truth that the deep things in science are not found because they are useful; they are found because it was possible to find them.

J. Robert Oppenheimer

6

Electronic Viscous Dissipation in Graphene Magneto-thermal Transport

Measurement of thermal transport in strongly interacting and correlated electronic systems can reveal exotic new physics that may be elusive to electrical trans-

port, such as neutral modes or emergent collective behavior. Graphene can host both a strongly interacting quantum-critical Dirac fluid and a degenerate viscous hydrodynamic electron liquid, where the thermal conductivity can deviate from the Wiedemann-Franz law. In Chapter 5, we examined graphene thermal conductance at zero magnetic field in this context.

In this Chapter, we extend our noise thermometry techniques to now measure thermal magneto-resistance in graphene. Application of a magnetic field in these exotic regimes can further enrich the thermal transport, as thermally drifting electron and hole motions differ from each other, and the magnetic field can introduce rotational flow into the system.

Studying magneto-resistance in a rectangular geometry for observation of viscous hydrodynamics involves a lot of competing variables at play, including influence from the Lorentz force, momentum and energy relaxation, viscous friction, and edge effects. Furthermore, the rectangular self-heating method does not work in a magnetic field due to hot spot formation near the contacts[175]. However, in a Corbino geometry, the rotational symmetry allows measurement of the radial component of electrical and thermal conductivity even under a magnetic field.

In Chapters 3 and 5, we focused on measuring the thermal conductivity κ and the Lorenz number $\mathcal{L}$ as a signature of hydrodynamic transport. As we discussed in Subsection 1.3.1, viscous transport and hydrodynamics are related but do not describe the same phenomena. In this Chapter, we now turn our attention more towards viscous transport and its relation to hydrodynamics, building upon the results from Chapter 5.

This Chapter is organized as follows. In Section 6.1 we motivate thermal transport for studying viscous hydrodynamics in the context of previous experiments. In Section 6.2, we describe the self-heating technique for measuring thermal conductance using Johnson

noise thermometry. In Section 6.3, we review the thermal conductance measurements in zero magnetic field from Subsection 5.5.4 showing a hydrodynamic suppression of the Lorenz ratio, as they will tie in closely to the magnetotransport results. In Section 6.4, we present and discuss the negative thermal magneto-resistance as correlated with the Lorenz ratio suppression. In Section 6.5, we discuss the negative thermal magneto-resistance as a qualitative signature of viscous heating. In Section 6.6, we present a simplified calculation to extract a limiting case for viscosity from the negative thermal magneto-resistance. In Section 6.7, we calculate the viscosity from the combined measured electrical and thermal magneto-resistance, using a more advanced model than the foregoing section. Section 6.8 presents additional data to support our conclusion. In Section 6.9, we discuss the quantitative analytic methods for interpreting the electrical and thermal magneto-transport data to better understand our results in the presence of momentum relaxation and viscosity. Finally, in Section 6.10, we conclude and analyze this work in the broader context of hydrodynamic electron liquids.

6.1 Electrical and Thermal Transport for Studying Viscous Flow

Experimental evidence for viscous hydrodynamics in graphene has recently grown, with experiments in the degenerately doped regime showing viscous backflow[71], Poiseuille flow[73,74], superballistic flow[62], Hall viscosity[72], and vanishing of the Landauer-Sharvin resistance[81]. These experiments have focused on electrical transport and, so far, have not studied how hydrodynamic electrons dissipate heat.

Furthermore, many of the observed electrical effects are subtle and can be difficult to discern from ballistic transport[57,61] because e-e collisions conserve momentum and thus do not relax total electrical current. Conversely, thermal signatures have the potential

to be stronger indicators of hydrodynamics due to the separation of charge and energy currents due to e-e scattering.

However, thermal transport is less experimentally studied due to the challenge of measuring nanoscale thermal effects in low-dimensional systems. A recent experiment found that in charge neutral graphene, the thermal conductivity can become much higher than expected from the WF law[1,2], as was described in Chapter 5. Another recent experiment[99] found a suppressed Lorenz ratio in the degenerate regime from 30–300 K, but attributed the high-T (> 120 K) suppression to inelastic phonon scattering rather than hydrodynamics; however, their conclusion does not agree with the theoretical estimation in Ref.[86], according to which any suppression from inelastic phonon scattering should only appear for $T < T_{BG} \sim 70$ K for the density of 1.6×10^{12} cm^{-2} considered in the paper. To date, no study has conclusively demonstrated a clear thermal signature of the degenerate hydrodynamic electron fluid in the temperature range seen by electrical-only experiments.

Here, we use Johnson noise thermometry and energy loss measurement to find two thermal signatures of a degenerate hydrodynamic liquid: first, the predicted suppression of the thermal conductivity below the WF law[2,49,53,82,83,89–93,225]; second, viscous heating as a source of dissipation proportional to particle current, as opposed to Ohmic Joule heating proportional to charge current[176].

6.2 Measuring Thermal Conductance

Using RF Johnson noise techniques, we measure the spatially averaged temperature rise ΔT_{avg} of the electron system in a 2-terminal (2T) graphene sample when it is heated by a quasi-DC current I. The temperature rise is related to the thermal conductivity

of the electrons through a generalized thermal conductance of the entire sample

$$G_{th,gen} = \frac{I^2 R}{\Delta T_{avg}}, \tag{6.1}$$

where I^2R is the total Joule heat generated in the sample with resistance R. The temperature profile is generally peaked near the center of the channel and decreases towards the contacts, which act as heat sinks at the bath temperature T_0. Under assumptions of zero contact resistance, Ohmic heating, cooling by electronic diffusion only, and uniform electrical and thermal conductivities σ and κ,* we can obtain the sample Lorenz ratio $\mathcal{L}/\mathcal{L}_0$ and thermal conductivity for an arbitrarily shaped 2-terminal sample via a universal geometrical factor of 12[162] from Eq. 6.1 as

$$\frac{\mathcal{L}}{\mathcal{L}_0} = \frac{1}{\mathcal{L}_0 T_0} \times \frac{\kappa}{\sigma} = \frac{1}{\mathcal{L}_0 T_0} \times \frac{G_{th,gen}}{12 G_{el}}, \tag{6.2}$$

where $\mathcal{L}_0$ is the WF or Sommerfeld value of the Lorenz number.

Eq. 6.2 fails for a rectangular geometry in a magnetic field due to sample edges breaking the transverse translational symmetry, which affects electron flow under a magnetic field and causes the Hall angle to break certain symmetries[175]. In contrast, Eq. 6.2 holds for a Corbino geometry both at zero and nonzero magnetic field due to the interplay of rotational symmetry and electron flow under a magnetic field (see Section 3.3). We will, however, see that this equation fails in the Corbino geometry for non-Ohmic viscous heating, which we use as the basis for detecting viscous flow.

The inset in Fig. 6.1(a) shows the 2-terminal Corbino geometry we use for this exper-

*In particular, the requirement is that $\hat{\kappa} \propto \hat{\sigma}$, i.e. the thermal conductivity tensor is proportional to the electrical conductivity tensor (constant Lorenz number $\mathcal{L}$ for the sample). See Ref 162 for details.

iment. We measure the thermal conductance and Lorenz ratio of two graphene Corbino devices as a function of temperature, electron density, and magnetic field to examine the interplay of WF law breakdowns at zero magnetic field with the electrical and thermal magneto-resistance (MR) in the context of hydrodynamics.

6.3 Thermal Conductivity in Zero Magnetic Field

We first characterize the electrical and thermal properties of the MLG3 Corbino device, first introduced in Section 5.5.4, under zero magnetic field. Fig. 6.1 (a) shows the measured two-terminal electrical resistance vs electron density n for three representative temperatures: 24, 90, and 200 K which we will find correspond respectively to diffusive/quasi-ballistic/ballistic, crossover, and hydrodynamic viscous regimes. The resistance is higher on the hole side (negative n) due to p-n junction formation causing higher contact resistance, which we have verified with similarly made rectangular devices utilizing the transfer-length method (TLM)[15,22,226]. The width and height of the Dirac peak characterize the total residual charge density due to a combination of thermal carrier excitation and electron-hole puddle disorder[1,221]. In this device, for $T \lesssim 90\,\mathrm{K}$ the residual density becomes disorder-limited and saturates at a minimum of $\sim 4.5 \times 10^{10}$ cm^{-2} , calculated by the knee position on a log-log plot of conductivity vs density (see Subsection 6.8.1).

Fig. 6.1(b) shows the measured thermal resistance of the device. The right-side vertical axis indicates the generalized thermal resistance $R_{th,gen} = 1/G_{th,gen} = \Delta T_{avg}/I^2R$ which we normalize by $1/T_0$. For the left-side axis, we convert this quantity to units of Ω by multiplying by $\mathcal{L}_0/12$, allowing direct comparison with electrical resistance in Fig. 6.1(a). At 24 K, the thermal resistance qualitatively matches the electrical resis-

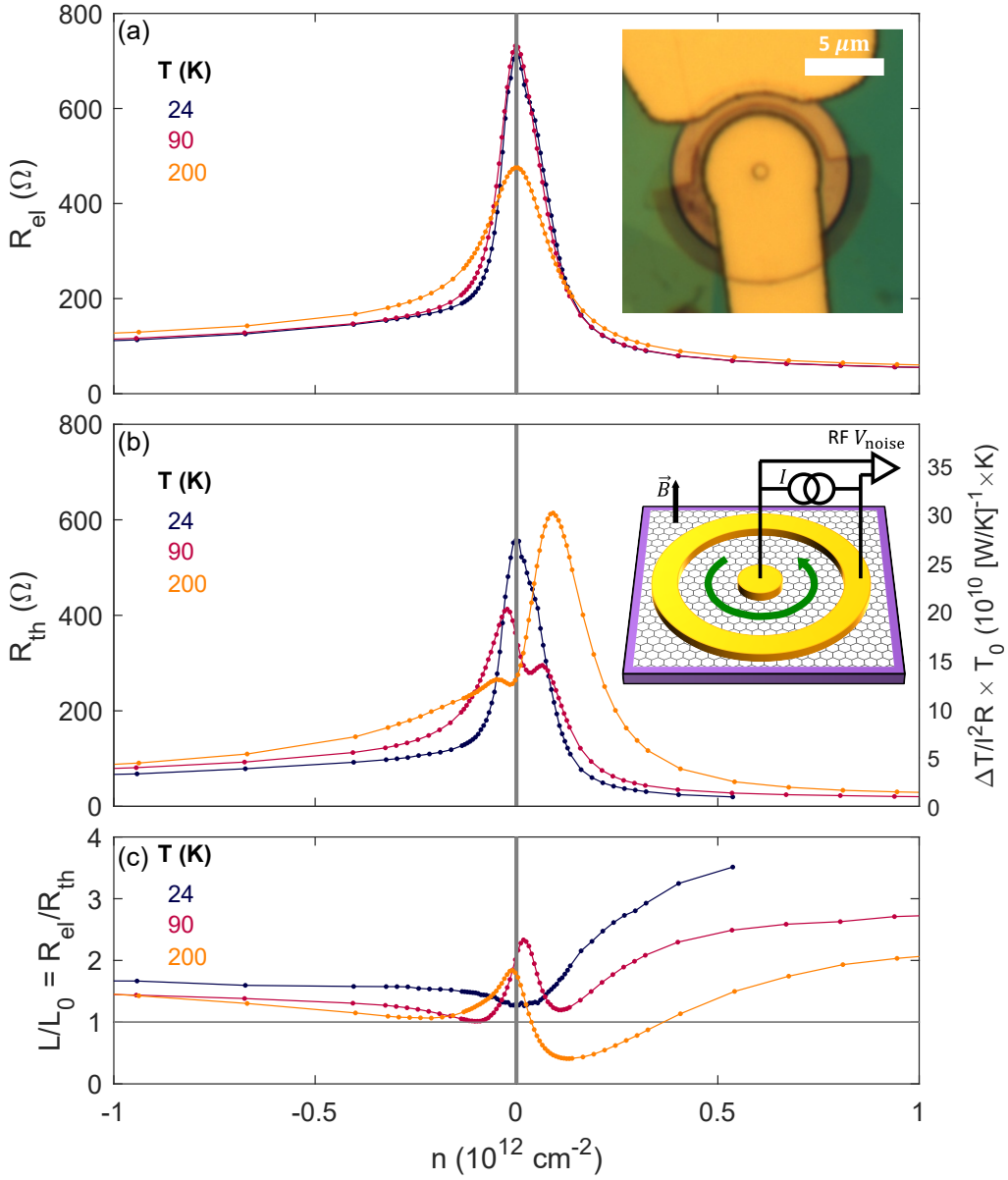

Figure 6.1: **(a)** 2-terminal DC electrical resistance at three representative temperatures. Inset: optical micrograph of typical Corbino device showing center contact covering entire channel for homogeneity. **(b)** Thermal resistance of the device, plotted in raw units $(\mathrm{W/K})^{-1}$ scaled by the bath temperature (right axis), and in Ohm units for comparison to electrical resistance (left axis). At higher temperature, the shape qualitatively deviates from the electrical resistance. Inset: Simplified schematic diagram of Corbino device and measurement circuit showing DC bias current and RF noise voltage measurement. Magnetic field is applied perpendicular to the plane. **(c)** Lorenz ratio of the device obtained from the ratio of electrical to thermal resistance. At higher temperatures, a peak appears at $n = 0$ and a suppression appears away from charge neutrality.

tance. As temperature is increased to 90 K and then 200 K, the thermal resistance develops a dip near $n = 0$ and one peak on each side of charge neutrality, features which are absent in the electrical resistance.

To compare the electrical and thermal resistance directly, we compute the Lorenz ratio via

$$\frac{\mathcal{L}}{\mathcal{L}_0} = \frac{R_{el}[\Omega]}{R_{th}[\Omega]}, \tag{6.3}$$

shown in Fig. 6.1(c). The WF law corresponds to $\mathcal{L}/\mathcal{L}_0 = 1$. At low temperature, the Lorenz ratio is close to 1 at charge neutrality, indicative of typical disorder-limited diffusive Fermi liquid transport due to charge puddles; at higher density, especially on the electron side, the measured Lorenz ratio increases strongly above 1, indicating charge transport transitions from diffusive to ballistic (see Section 3.7; also see 6.9.3 for additional discussion specifically on this device).

As temperature is increased, by 90 K there develops a small peak at charge neutrality in the measured Lorenz ratio, decreasing to a slightly smaller value by 200 K. The magnitude of the peak is consistent with both a weak hydrodynamic enhancement [2,49,83,89,91,92,225] and a bipolar diffusion enhancement [87,180], but our experiment cannot measure their relative contributions. Typically, bipolar diffusion effects grow with temperature, but this peak weakens from 90 K to 200 K, consistent with a hydrodynamic enhancement at 90 K getting suppressed by additional phonon scattering at higher temperatures. This behavior is qualitatively consistent with the large Lorenz ratio enhancement seen in Ref. 1, but the enhancement here is much smaller and occurs at a different temperature. However, this discrepancy could be explained by this device's disorder being about 10 times larger than the cleanest device in Ref. 1, which

would reduce the effects of hydrodynamics seen here and move the low-T hydrodynamic bound upwards in T.

As the neutrality peak develops around 90 K, a relative suppression in the Lorenz ratio develops at a density of about $n = \pm 1.1 \times 10^{11}\,\mathrm{cm}^{-2}$, and by 200 K this suppression goes below 1, with the lowest measured Lorenz ratio of about 0.45. The only single-particle effects that may cause such a suppression are inelastic phonon scattering (for $T \lesssim T_{BG} \sim 18$ K at this density) or thermal smearing of the Fermi surface (for $T \gtrsim T_F \sim 450$ K at this density), but these temperature ranges do not coincide with that of the measured suppression (90–200 K) (see Section 5.2). Additionally, we can rule out the gate noise amplification effect (Section 4.10) since this device has a thick 285 nm dielectric and from the temperature dependence.[†] Hydrodynamic relaxation of thermal current via electron-electron collisions is the only mechanism that can explain this suppression in this temperature range. Furthermore, it occurs in a temperature and density range consistent with those measured in other electrical-only hydrodynamic experiments[61,62,81]. In the second Corbino device MLG4 (see Section 6.8), we measure only a relative suppression; we speculate that there, the absolute suppression does not go below 1 due to the stronger influence of ballistic effects on the self-heating measurement, as that device has a shorter channel length.

6.4 Magneto-Resistance

Having established the hydrodynamic Lorenz ratio suppression at zero magnetic field, we now examine how the thermal and electrical resistances vary with magnetic field. The

[†]The derivative dR/dV_g decreases in magnitude as temperature is increased, but the suppression gets stronger. Gate noise amplification scales as $\propto (dR/dV_g)^2$, and thus an apparent suppression caused by gate noise would become weaker with increasing temperature.

diffusive Drude model predicts that the electrical conductivity decreases in magnetic field as

$$\sigma_{xx}(B) = \frac{\sigma(0)}{1 + (\mu B)^2}, \tag{6.4}$$

where $\sigma(0) = ne^2/(m\gamma_{mr})$ is the conductivity at zero magnetic field[54] with γ_{mr} the momentum relaxation rate, and $\mu = \mu(n) = e/(m\gamma_{mr})$ is the electrical mobility. The two-terminal resistance that we measure can be related geometrically via

$$R_{el}(B) = R_c + \frac{1}{\sigma_{xx}(B)} \frac{\ln(r_o/r_i)}{2\pi}, \tag{6.5}$$

where R_c is the contact resistance that we presume to be independent of magnetic field[227], and r_o, r_i are the outer and inner contact radii, respectively. We could extract γ_{mr} and R_c directly from the magneto-resistance (MR) $\Delta R_{el} = R_{el}(B) - R_{el}(0)$ in a diffusive sample (see Subsection 5.5.4); however, in ballistic and viscous samples this method will not work. Ballistic Corbino disks will exhibit significantly reduced MR relative to Eq 6.5 due to geometrical effects (see Subsection 6.9.3), causing γ_{mr} to be over-estimated. In viscous systems, the resistance has additional non-local viscous contributions[220], rendering $\sigma_{xx}(B)$ ill-defined. The relative MR $\Delta R_{el}/R_{el}(0)$ is affected by the density-dependent contact resistance[15,22] and thus fails to quantify the bulk properties[227]. Thus, we examine the total MR ΔR_{el}, which, for a known geometry, can be well-defined even for mixed Ohmic/viscous transport[220].

Fig. 6.2(a,c,e) shows the ΔR_{el} for three different electron densities for measured temperatures of 15–200 K. For a direct comparison with the electrical MR, we consider the thermal MR $\Delta R_{th} = R_{th}(B) - R_{th}(0)$, shown in Fig. 6.2(b,d,f) for the same three

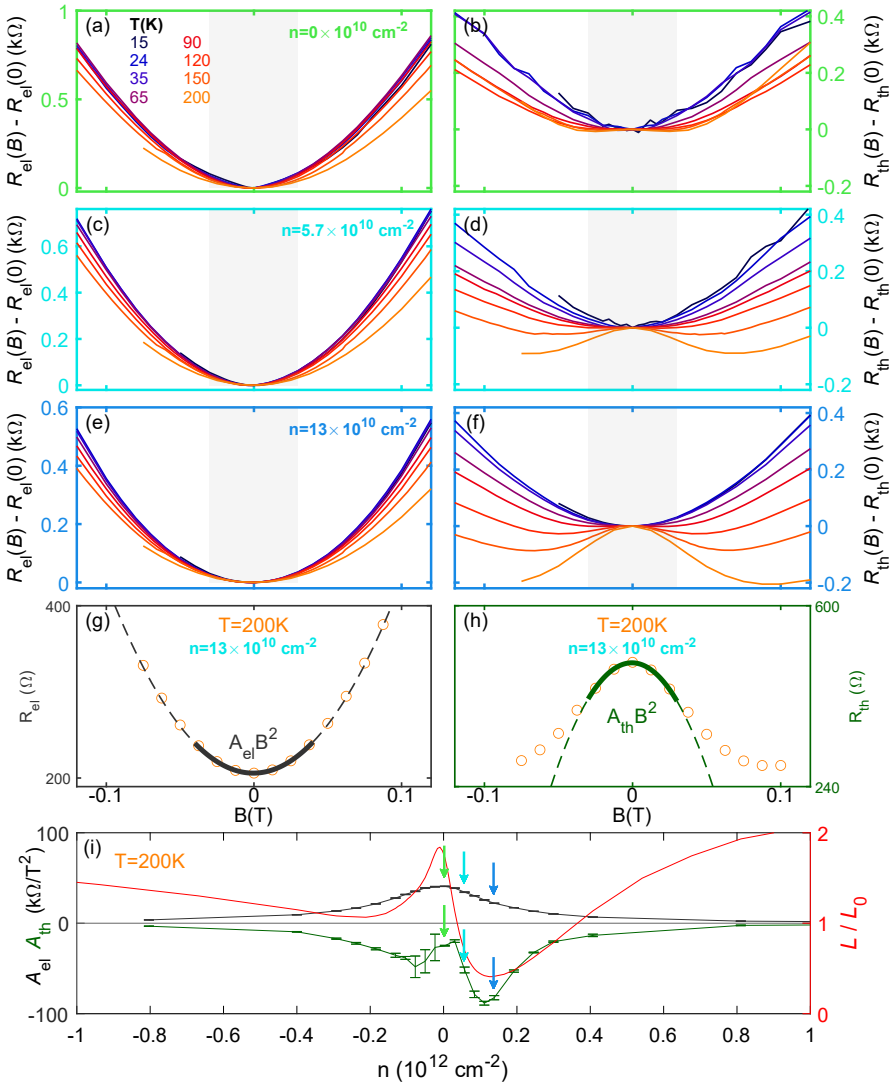

Figure 6.2: **(a,b)** Electrical and thermal MR for $15 - 200\,\mathrm{K}$ for $n = 0$. Gray shaded boxes indicate $|B| < 30\,\mathrm{mT}$ fitting range for parabolas. **(c,d)** For $n = 5.7 \times 10^{10}\ \mathrm{cm}^{-2}$. **(e,f)** For $n = 1.3 \times 10^{11}\ \mathrm{cm}^{-2}$. At high temperatures, the electrical MR remains positive and parabolic while the thermal MR becomes negative before increasing again. **(g)** Representative electrical MR parabolic fit for 200 K to extract A_{el}. Circles represent the data, solid curve represents the parabola in the fitted region, and dashed curve represents the extrapolated parabola. The data continues to follow a parabolic trend up to the measured $B = 200\,\mathrm{mT}$. **(h)** Thermal MR fit to extract A_{th}, analogous to (g). The data deviates from parabolic behavior beyond $B \sim 30\,\mathrm{mT}$. **(i)** Comparison of electrical (black) and thermal (dark green) MR coefficients at 200 K obtained from parabolic fits as in (g,h) (left axis). Error bars indicate statistical 1σ uncertainty from fitting. Colored arrows (light green, cyan, light blue) match the corresponding densities plotted in (a-f). Overlaid (red) is the Lorenz ratio at $B = 0$ (right axis). The Lorenz ratio suppression below 1 occurs at approximately the same density as the most negative A_{th} coefficient.

densities.

The electrical MR is always positive, and, except for lower temperatures where Landau quantization or ballistic effects play a role, is nearly parabolic upwards in the measured magnetic field range of $\pm 200\,\mathrm{mT}$. In contrast, the thermal MR changes sign from positive to negative as a function of temperature, density, and magnetic field. At low temperatures of 15 and 24 K, the thermal MR very closely and nearly quantitatively resembles the electrical MR, as expected for the WF law in a magnetic field[89]. At a temperature of 90 K, where hydrodynamic effects begin to appear, the low-B thermal MR is nearly zero and then turns upwards, for n away from the charge neutrality point. As the temperature is raised further to 200 K, where the hydrodynamic effects are strongest as seen in the $B = 0$ Lorenz ratio, the thermal MR becomes strongly negative for low magnetic field and then reverses direction. Even at charge neutrality, we now see a slightly negative thermal MR at 150K and 200 K.

We quantitatively characterize the low-B electrical and thermal MR by performing phenomenological parabolic fits to the data via $\Delta R_{el,th} = A_{el,th} B^2$, limited to $\sim 30\,\mathrm{mT}$ to remain in the parabolic regime, away from Landau quantization (see below) or higher-order effects. The 30 mT fitting window is indicated in Fig. 6.2(a-f) by the gray shaded region.

Fig. 6.2(g,h) shows typical 30 mT parabolic fits at 200 K indicated with a solid thick line, and it shows extrapolating the parabola past 30 mT with a dashed line. The resulting MR fit coefficients A_{el} (black) and A_{th} (dark green) are plotted in Fig. 6.2(i) for 200 K (left-hand axis), in parallel with the measured Lorenz ratio (red, right-hand axis) at $B = 0$, reproduced from Fig. 6.1(c). In the same style as Fig. 6.2(i), Fig. 6.3 shows linecuts of A_{el} and A_{th}, in parallel with the Lorenz ratio, for all measured temperatures. The Lorenz ratio suppression and negative thermal MR appear gradually at the same

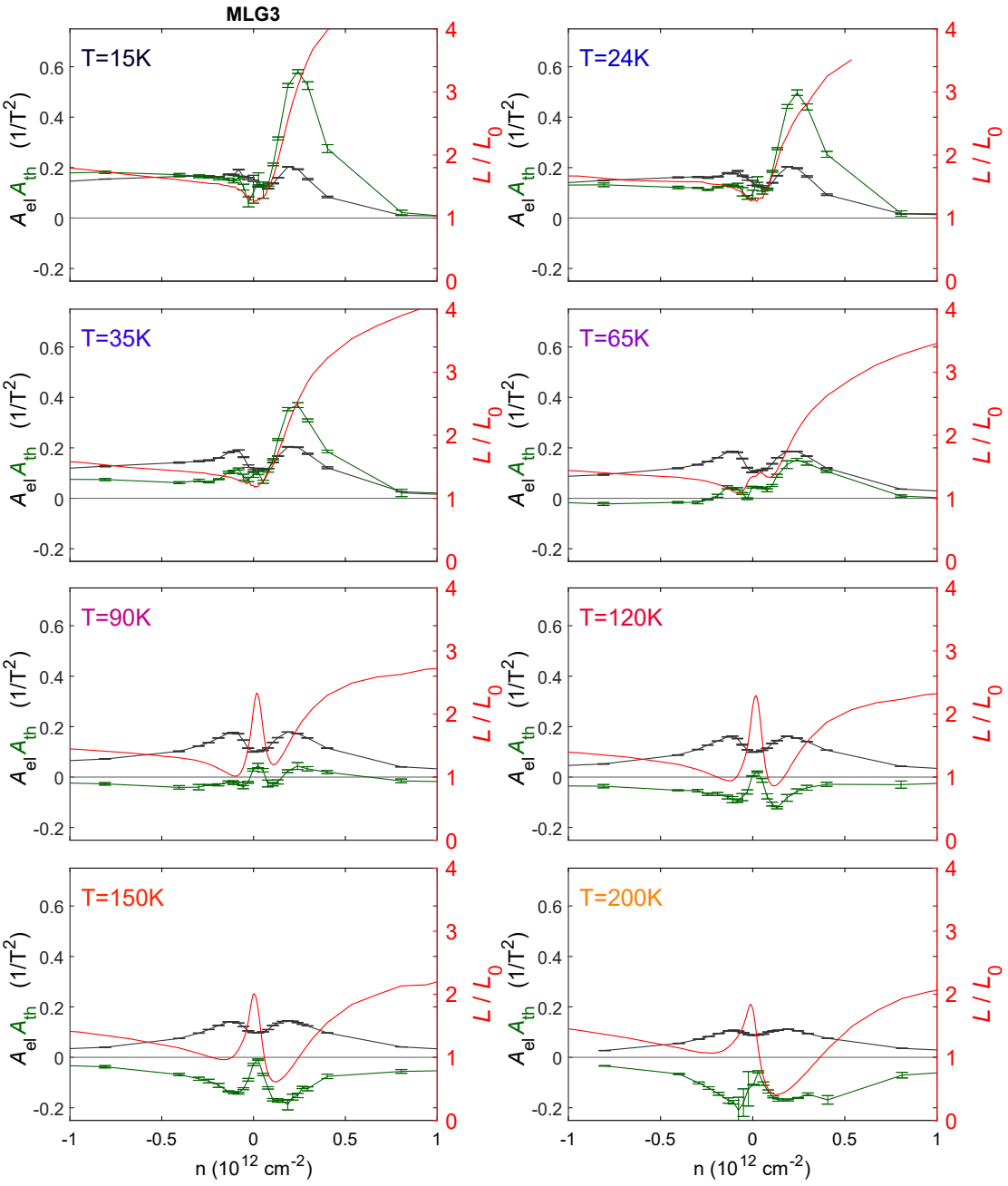

Figure 6.3: For MLG3, linecuts of the thermal MR coefficient A_{th} (green) and the electrical MR coefficient A_{el} (black), plotted on the left-hand axes, vs density, for the set of measured temperatures 15–200 K. The corresponding Lorenz ratio at $B = 0$ is plotted on the right-hand axes.

density as temperature is increased. At 200 K, the thermal MR coefficient is negative for the entire range of densities measured, and attains the most negative value at a density of $n = 1.3 \times 10^{11}$ cm^{-2}, closely corresponding to the density where the Lorenz ratio is most strongly suppressed to 0.45, suggesting a correlation between these two effects.

To confirm the correlation between the negative thermal MR and the Lorenz ratio suppression, we show colormaps of the Lorenz ratio and of the A_{th}/A_{el} ratio in Fig. 6.4 (a,b). We consider the ratio A_{th}/A_{el} instead of the bare A_{th} since we expect $A_{th}/A_{el} \to 1$ for diffusive and ballistic behavior following the WF law. Now, any deviation from 1, and especially a negative value, may indicate non-diffusive and non-ballistic transport. We emphasize that while this ratio appears analogous to the $B = 0$ Lorenz ratio, it entirely independent of the absolute value of the Lorenz ratio, and it results only from the relative changes of R_{th}, R_{el} vs B. Indeed, the negative A_{th}/A_{el} ratio region (shown in green) corresponds very closely to the suppressed Lorenz ratio region (shown in red), suggesting the two independent effects are of the same origin. At 200 K, the A_{th}/A_{el} ratio is negative for all densities measured, even though the measured Lorenz ratio is enhanced for low and high n.

In Fig. 6.4, we also plot the Fermi temperature, the Bloch-Grüneisen temperature[68], and the temperature corresponding to the energy separation of Landau levels given by $k_B T = \hbar\omega_c$ for $B = 30$ mT. The Lorenz ratio suppression and the negative thermal MR both occur significantly above T_{BG}, ruling out inelastic phonon sacttering, and significantly below T_F, ruling out Fermi surface thermal smearing[86] (see Section 5.2).

Furthermore, Landau quantization of electrons in a magnetic field can also disrupt the Lorenz ratio. The Lorenz ratio suppression and the negative thermal MR both occur at a temperature far above the Landau level energy splitting for our 30 mT fit

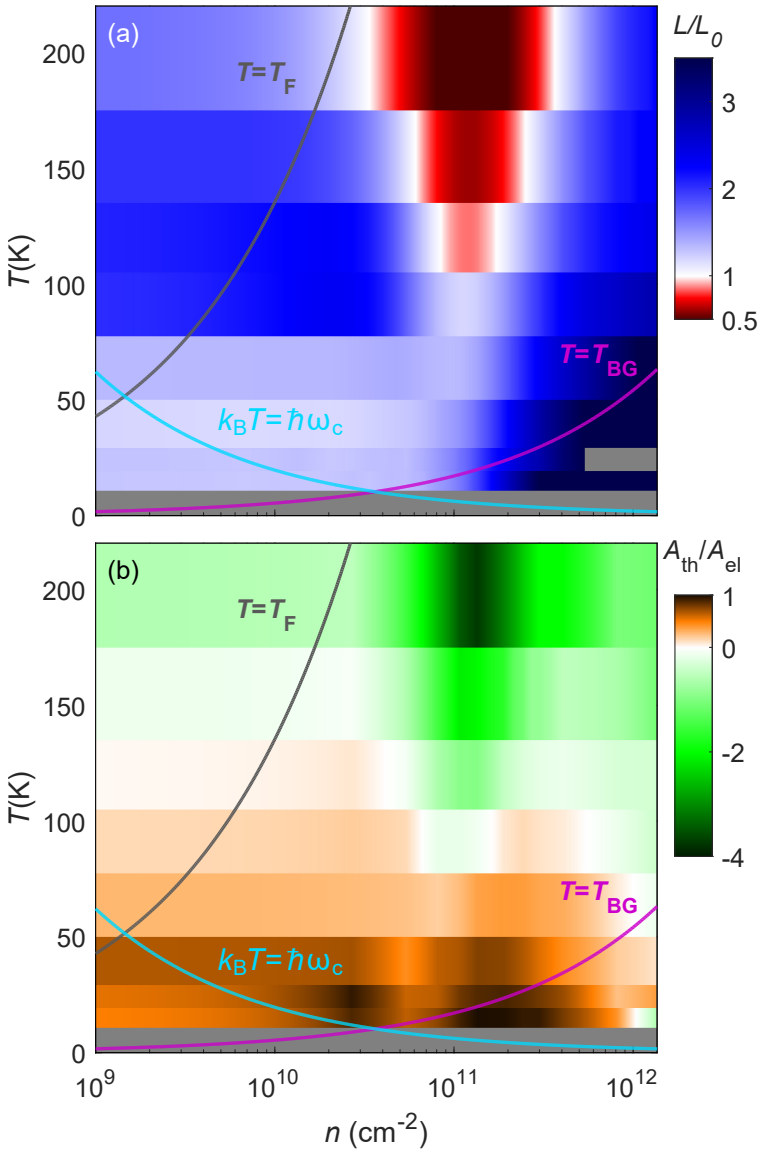

Figure 6.4: **(a)** Colormap of the Lorenz ratio measured at $B = 0$. White corresponds to $\mathcal{L}/\mathcal{L}_0 = 1$. The hole side is not shown due to higher contact resistance. The Lorenz ratio is suppressed below 1 around $n = 1.3\times10^{11}$ cm^{-2} at higher temperatures. The low-temperature ballistic enhancement at higher density is likely a measurement artifact from ballistic transport dominated by contact resistance. For small densities near charge neutrality ($|n| \lesssim 4 \times 10^{10}$ cm^{-2}), a weak enhancement to ~ 3 exists near 90–150 K. **(b)** Colormap of the ratio of thermal to electrical magneto-resistance coefficients, A_{th}/A_{el} as defined in the text and in Fig. 6.2. White corresponds to $A_{th}/A_{el} = 1$. The intensity and location of the negative A_{th}/A_{el} correlates very closely with the suppressed Lorenz ratio in (a). Gray curves: Fermi temperature $T = T_F$. Cyan curves: temperature scale for Landau level spacing $k_BT = \hbar\omega_c$. Purple curves: Bloch-Grüneisen temperature T_{BG}.

field limit, verifying that quantization effects are irrelevant to these phenomena.

In the next section, we explain how the negative thermal MR arises from viscous fluid effects and how it relates to hydrodynamics.

6.5 Viscous Heating and Noise in Hydrodynamics

The negative thermal MR can be explained by the combination of two distinct effects arising in viscous transport: (1) a magnetic-field-dependent viscous heating effect of the electron fluid and thus a breakdown of the assumptions for Eq. 6.2; and (2) a viscous weighting of the Johnson noise (see Appendix G for mathematical details). The weighting is a reflection of how local noise sources in the sample bulk are ultimately collected at the contacts, which is determined by the equation of motion governing transport. Because viscous transport proceeds by a different mechanism, this leads to a qualitatively distinct weighting for Johnson noise in the viscous regime (see also Ref. 176).

Fig. 6.5 contrasts theoretical dissipation heating profiles, fluid flow streamlines, and resulting temperature profiles between the Ohmic and the viscous cases, at zero and nonzero magnetic field, for the Corbino geometry measured here. Our device also exhibits ballistic and quasi-ballistic transport at lower temperature, where the heating is concentrated at the contact resistance, and there is not a well-defined streamline for current or a well-defined local temperature. A theory for the Johnson noise due to self-heating in a magnetic field in this regime would depend very sensitively on the contact resistance and how that contact resistance is thermalized (see the discussion in Section 3.7). While there is a theory and an experiment that describes the crossover from ballistic to viscous transport in the electrical sector with a focus on contact re-

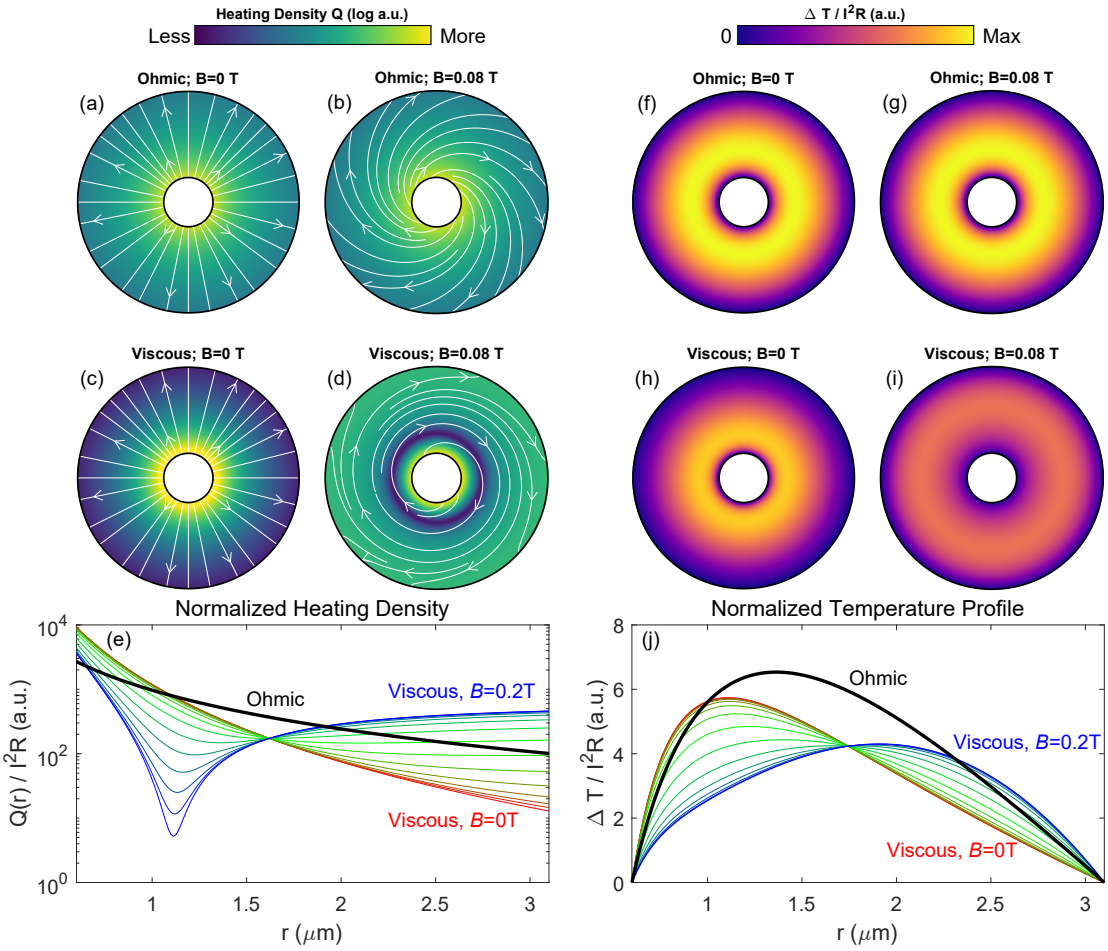

Figure 6.5: **(a-d)** Ohmic and viscous flow heating density Q, normalized by the total Joule power, plotted on a logarithmic color scale, for $B = 0$ and 80 mT, and constant κ_{xx}. White streamlines indicate flow velocity. Ohmic heating profile is independent of magnetic field. In viscous regime under magnetic field, flow enters/exits electrodes at a right angle and transitions to rotational velocity over the Gurzhi length scale. A higher velocity gradient from the transition generates additional heating near the inner and outer contact. **(e)** Linecuts of the data in (a-d); normalized heating density as a function of radius for Ohmic flow (black) and viscous flow as a function of magnetic field (red: 0 mT → blue: 200 mT). With increasing magnetic field, viscous heating develops a minimum near the middle of the channel. **(f-i)** Resulting Ohmic and viscous flow temperature rise profile ΔT, normalized by the total Joule power, for $B = 0$ and 80 mT, and constant κ_{xx}. Ohmic temperature profile is independent of magnetic field. In viscous regime, temperature profile differs that of Ohmic and varies with magnetic field. **(j)** Linecuts of the data in (f-i); normalized temperature rise profile as a function of radius for Ohmic flow (black) and viscous flow as a function of magnetic field (red: 0 mT → blue: 200 mT). With increasing magnetic field, viscous temperature profile flattens and shifts its peak to higher radius. Johnson noise thermometry will measure the spatially averaged temperature rise.

sistance[80,81], there is no corresponding theory for Johnson noise in the thermal sector. However, we observe and explain that the heating in such a (quasi-)ballistic regime will not cause a negative thermal MR (see Subsection 6.9.3). We thus use the diffusive Ohmic case as a point of comparison for the viscous case in Fig. 6.5, remembering that our device also displays (quasi-)ballistic effects whose MR qualitatively resembles that of the diffusive/Ohmic regime.

We first discuss the non-viscous Ohmic regime. Here, the heating of the electrons arises from Joule dissipation via impurity or phonon scattering, with a 2D power density p given by

$$\mathcal{P} = \vec{J} \cdot \vec{E} \tag{6.6}$$

where $\vec{J}$ is the electrical current density and $\vec{E}$ is the electric field. Both components scale as $\propto 1/r$, giving a $\propto 1/r^2$ power dissipation profile, independent of magnetic field, and the resulting temperature profile is also magnetic-field-independent. Thus, the generalized thermal resistance

$$R_{th} \equiv \Delta T_{JN}/P = \frac{1}{12\kappa_{xx}} \cdot \frac{\ln(r_o/r_i)}{2\pi} \tag{6.7}$$

changes with magnetic field only through $1/\kappa_{xx}$ (see Section 3.3 for a more detailed derivation).

In the viscous regime with the absence of impurity or phonon scattering, the heat dissipation now comes from viscous shearing and deformation of fluid elements caused by velocity gradients. In a Corbino geometry at $B = 0$, hydrodynamic electron flow

has zero electric field inside the channel, as there is no boundary scattering to relax momentum, and fluid elements experience zero net viscous force[58,81]. This contrasts with the more common Poiseuille flow in a pipe, where momentum relaxation comes from no-slip boundary conditions along the walls, and fluid elements do experience a net viscous force with a non-vanishing electric field. The Corbino viscous flow is in a way analogous to Couette flow, where a constant velocity gradient imposes no net force on any fluid element (divergence of the stress tensor is zero) but still generates viscous heating (nonzero stress tensor).

Although the velocity vector field at $B = 0$ is the same $\propto 1/r$ as in the Ohmic case, now the dissipation heating scales as $\propto 1/r^4$ from the viscous stress tensor (see Appendix G), as shown theoretically in Fig. 6.5(a,c,e). The viscous temperature profile is thus also different from the Ohmic case, as demonstrated in Fig. 6.5(f,h,j), with the peak in temperature lower and closer to the inner electrode, since the heating is relatively more concentrated towards the inner electrode.

For Ohmic flow, a JNT measurement takes a spatial average of the temperature profile weighted by the electric potential[162,164]; however, in the viscous case, the potential weighting factor is replaced by a linear operator which depends on the details of viscous transport in this geometry (see Appendix G). The combination of viscous heating and noise results in a scaling factor $f(B, \nu)$ to T_{JN} in Eq. 6.7, such that the generalized thermal resistance takes the modified geometric form

$$R_{th} = \frac{1}{12\kappa_{xx}} \frac{\ln(r_o/r_i)}{2\pi} \times f(B, \nu). \tag{6.8}$$

We emphasize that $f(B, \nu)$ arises from both a spatial temperature profile redistribution and a different temperature-weighting factor for viscous flow. In the viscous regime, σ

is no longer well defined due to viscous non-locality, and the function $f(B, \nu)$ thus also accounts for how viscosity affects the resistance and total Joule power $I^2 R_{el}$. In a mixed Ohmic and viscous case, the scaling factor becomes $f(B, \nu, \gamma_{mr})$, acquiring a dependence on the momentum relaxation rate γ_{mr}, and must be computed numerically[59].

Upon application of an external magnetic field, the electron fluid traversing the channel of a Corbino geometry will acquire a rotational velocity due to the Lorentz force, both in the Ohmic and viscous regimes, as shown in Fig. 6.5 (b,d). Due to no-slip viscous boundary conditions at the electrodes[58,220], the fluid transitions to mixed radial-rotational velocity in the channel over the Gurzhi length scale $l_G = \sqrt{\frac{\nu}{\gamma_{mr}}}$ [65–67,81,179]. In the Ohmic regime, however, due to the absence of viscosity, this transition happens over an infinitesimally small Gurzhi length scale and is thus not visible in Fig. 6.5(b).

The additional rotational velocity adds to the $1/r$ radial component and modifies the velocity gradients, the viscous stress tensor, and the heating profile. Larger gradients from the varying rotational component are present near the inner and outer electrodes, generating additional heating near the contacts, leaving an area near the middle of the channel with relatively less heating (Fig. 6.5(d)). However, normalized by the total Joule power, the heating near the inner electrode decreases and the heating near the outer electrode increases, as shown in Fig. 6.5(e).

The resulting viscous temperature profile thus acquires a magnetic field dependence, as shown in Fig. 6.5(h,i,j). The temperature peak near the inner contact decreases and shifts outwards towards a more uniform temperature distribution with increasing B. This reshaping of the temperature profile, in conjunction with the viscous Johnson noise weighting, acts to decrease R_{th} for a given fixed $\kappa_{xx}(B)$.

The magnetic field dependence of the purely viscous (i.e. with zero momentum relaxation) scaling factor $f(B)$, introduced in Eq. 6.8, is plotted in Fig. 6.6, both in absolute

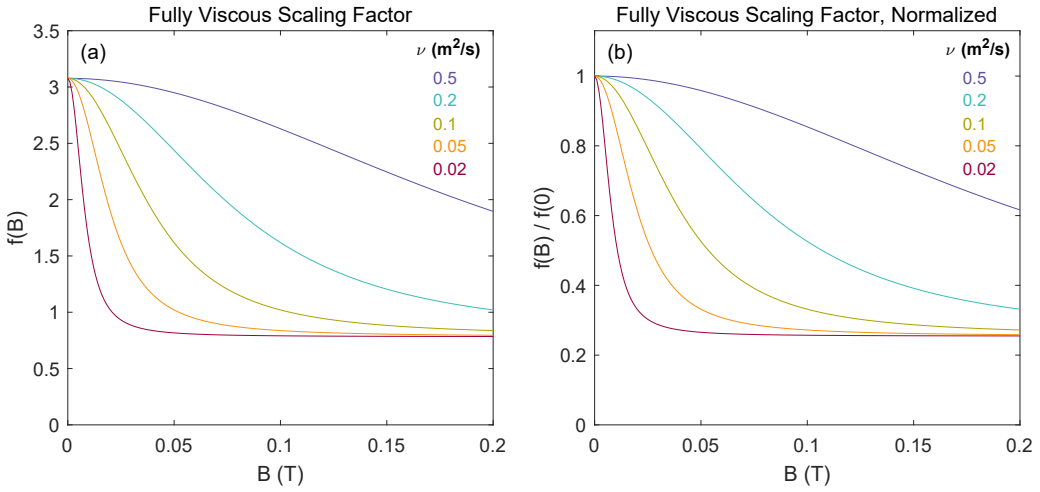

Figure 6.6: **(a)** Absolute self-heating Johnson noise scaling factor for fully viscous transport (zero momentum relaxation) for the Corbino geometry of MLG3. Mathematical details are given in Appendix G. Different colors indicate different viscosity values, which affect only the horizontal rescaling of the function. The shape of the function in general depends on the sample aspect ratio r_o/r_i. **(b)** The same function from (a) plotted relative to its value at $B = 0$. It approaches an asymptotic limit of $\dfrac{f(B \to \infty)}{f(0)} \approx 0.25$ for the Corbino geometry of MLG3.

value and relative to its value at $B = 0$. In general, the function $f(B)$ depends on the aspect ratio of the Corbino geometry, and it is shown in Fig. 6.6 specific to the MLG3 sample. In the purely viscous case, the effect of changing viscosity is only to rescale the function horizontally in magnetic field. At zero magnetic field $f(0) \approx 3.1$, and for high magnetic field this function approaches an asymptotic value of $f(B \to \infty) \approx 0.25 \times f(0)$.

Let us emphasize the meaning of the scaling factor $f(B)$ in comparing diffusive and viscous transport. The electrical resistance R_{el}, in each case, is caused by either momentum relaxation or by fluid viscosity; for the same given R_{el} and κ_{xx}, the factor $f(B)$ then tells us how much more Johnson noise self-heating will produce in the viscous case relative to the diffusive case, for the same total Joule power $I^2 R_{el}$. In the diffusive case, the ratio of electrical resistance to thermal resistance (Eq. 6.7) will give us information

about the Lorenz ratio, which is proportional to $\frac{\kappa_{xx}}{\sigma_{xx}}$. It may appear that for a purely viscous system, when $f(B) > 0$, it will reduce the measured Lorenz ratio relative to a diffusive system; however, the ratio $\frac{\kappa_{xx}}{\sigma_{xx}}$ is not well-defined in a purely viscous system since $\gamma_{mr} \to 0$ implies $\sigma_{xx} \to \infty$. Interpreting the measurements becomes a question of understanding the difference between the experimentalist's and the theorist's Lorenz ratio, as was discussed in Section 5.4. Thus, an experimentally measured Lorenz ratio cannot be converted to $\frac{\kappa_{xx}}{\mathcal{L}_0 T \sigma_{xx}}$ via the scaling factor $f(B)$.

The behavior of the $f(B, \nu, \gamma_{mr})$ function, now taking into account both viscosity and momentum relaxation, is shown in Fig. 6.7. Here, the function of three variables $f(B, \nu, \gamma_{mr})$ depends on ν and γ_{mr} only through the ratio $\lambda \equiv \frac{\sqrt{\nu/\gamma_{mr}}}{r_i} = \frac{l_G}{r_i}$; thus, λ is a convenient parameter for plotting the family of curves. The horizontal scale in Fig. 6.7 is set only by the momentum relaxation rate via $B_0 = m\gamma_{mr}/e$. The curve for the value of $\lambda = 5$ approaches the purely viscous limit shown in Fig. 6.6; however, in the limit of zero disorder via $\gamma_{mr} \to 0; \lambda \to \infty$, the horizontal scale $B_0 = m\gamma_{mr}/e$ of Fig. 6.7 becomes ill defined and thus a different scale is needed (see Appendix G and Fig. G.1, where the scale of $B_0 = (\gamma_{mr} + \nu/r_i^2) \times m/e$ is used). In the weakly viscous regime of $\lambda \lesssim 0.45$, $f(B)$ increases with B due to additional perturbative viscous heating in the bulk of the channel while maintaining a nearly Ohmic $\approx 1/r^2$ heating profile (see also Appendix G). In contrast, in the more viscous regime of $\lambda \gtrsim 0.45$, $f(B)$ decreases with B, as discussed above.

The measured thermal magneto-resistance $R_{th}(B)$ will have contributions from both a changing $\kappa_{xx}(B)$ and the B-dependence of $f(B, \nu, \gamma_{mr})$, resulting in a relative scaling

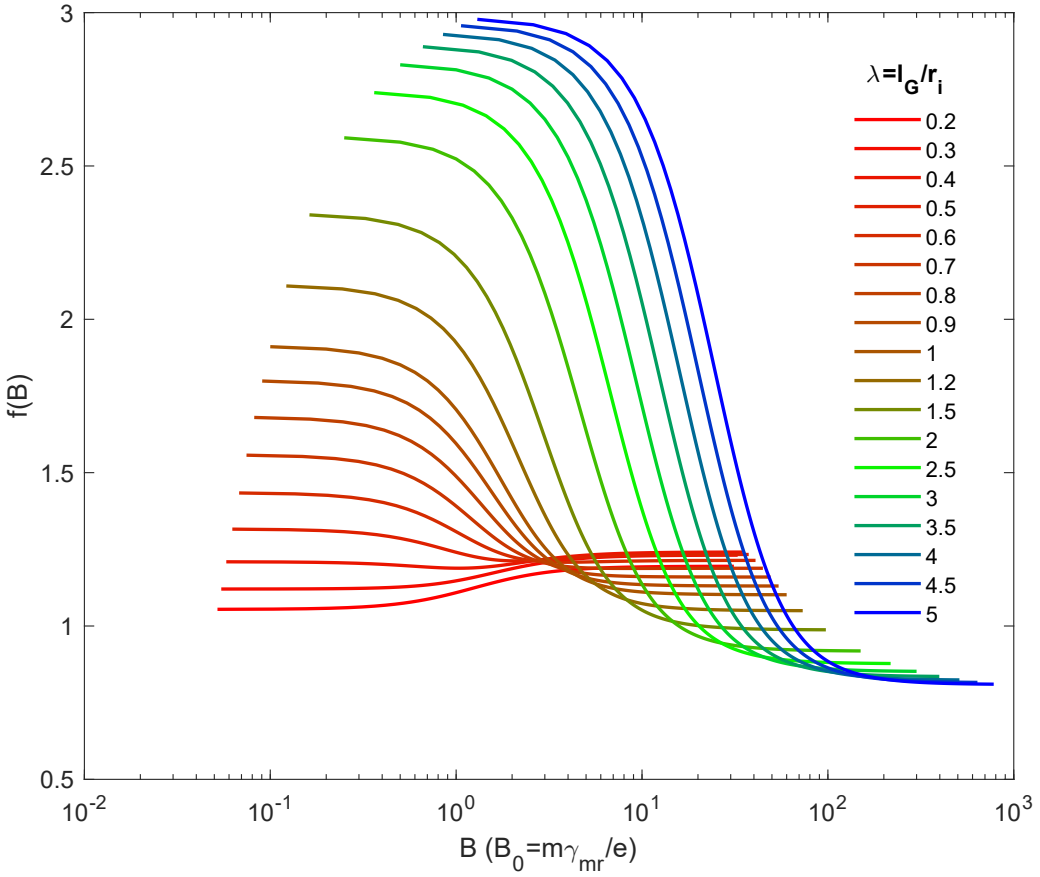

Figure 6.7: Self-heating Johnson noise scaling factor for mixed diffusive-viscous transport for the Corbino geometry of MLG3, as a function of magnetic field. Mathematical details are given in Appendix G. Different colors indicate different $\lambda \equiv \frac{\sqrt{nu/\gamma_m r}}{r_i} = \frac{l_G}{r_i}$ values, indicating how diffusive or viscous the transport is. Low λ trends towards the diffusive regime, and high λ towards the viscous regime. The function is scaled horizontally in magnetic field in units of $B_0 = m\gamma_{mr}/e$. Only a few widely spaced values of λ are shown for ease of viewing, and the full computational dataset has a denser spacing of λ. Calculations were directly performed and provided by Ref. 59.

of R_{th} given by

$$\frac{R_{th}(B)}{R_{th}(0)} = \left[\frac{\kappa_{xx}(B)}{\kappa_{xx}(0)}\right]^{-1} \times \frac{f(B)}{f(0)}. \tag{6.9}$$

The $\left[\frac{\kappa_{xx}(B)}{\kappa_{xx}(0)}\right]^{-1}$ factor is expected to only increase with magnetic field[89,228], but the $\frac{f(B)}{f(0)}$ factor can decrease with magnetic field if viscous heating from velocity gradients is strong enough relative to Ohmic heating from velocity magnitude (see Fig. 6.7, and Appendix G for more details). The functional form of the $\frac{f(B)}{f(0)}$ factor is shown in Fig. 6.8, as a renormalized version of the calculation in Fig. 6.7.

The behavior of the measured $\frac{R_{th}(B)}{R_{th}(0)}$ is shown for three different densities in Fig. 6.9(a-c), for a range of temperatures 24–200 K. The green and magenta dashed lines correspond to the limiting behavior expected for respective purely diffusive and purely viscous hydrodynamic transport, computed with momentum relaxation rates and viscosities at 200 K obtained with the method described later in this Chapter. At charge neutrality (Fig. 6.9(a)), the fluid has zero collective mass and thus kinematic viscosity is not well-defined, so we do not show the viscous limit as our theory will not apply.

In the fully viscous and hydrodynamic limit (magenta curve), $\frac{R_{th}(B)}{R_{th}(0)}$ would directly follow the $\frac{f(B,\nu)}{f(0,\nu)}$ viscous scaling factor in Eq. 6.9, as the $\kappa_{xx}(B)$ factor is predicted to be constant in this limit[89]. To attain this limit, the e-e scattering rate γ_{ee} and the momentum relaxation rate γ_{mr} must satisfy two conditions: (1) $\gamma_{ee} \gg \gamma_{mr}$ and (2) $l_G \approx \frac{v_F^2}{4\gamma_{ee}\gamma_{mr}} \gg r_i^2$ (see Section 1.3).

In the diffusive limit (green curve) where the WF law is expected to hold, the thermal conductivity would scale with B in the same way as the electrical conductivity. The green-to-magenta gradient indicates the transition of thermal MR from the diffusive

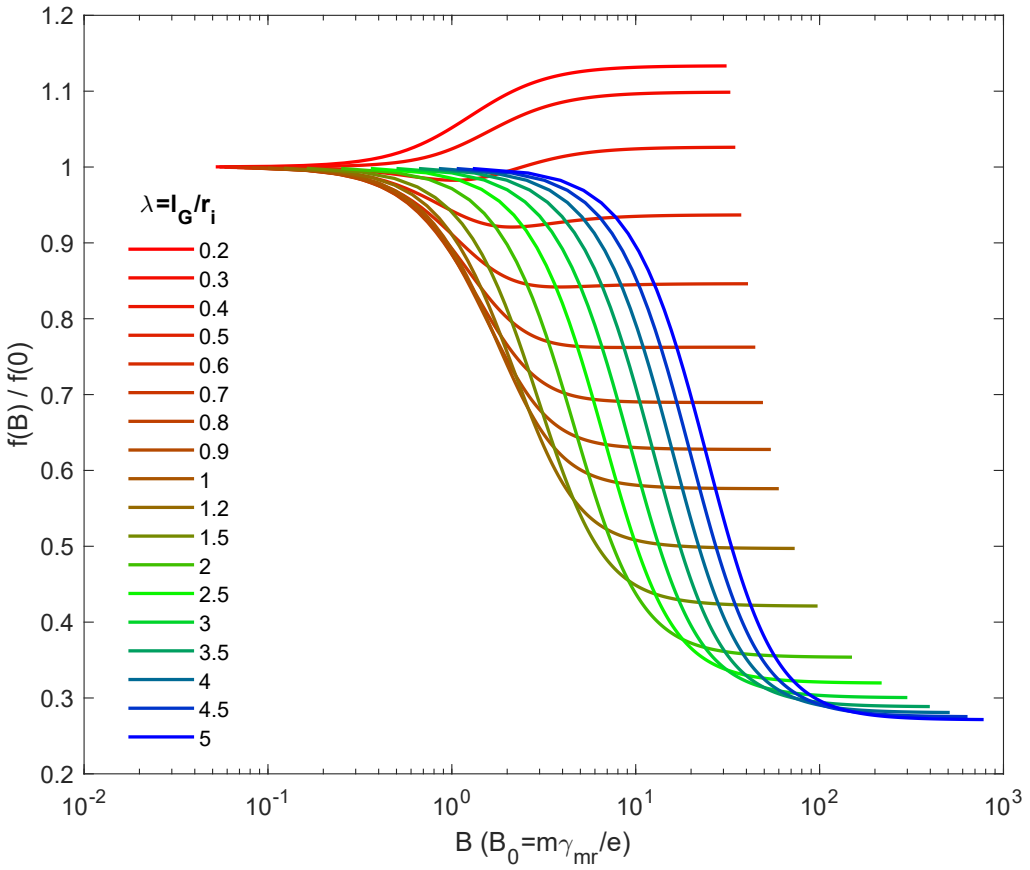

Figure 6.8: Self-heating Johnson noise scaling factor for mixed diffusive-viscous transport for the Corbino geometry of MLG3, as a function of magnetic field, normalized by the value at $B = 0$. Mathematical details are given in Appendix G. Different colors indicate different $\lambda \equiv \dfrac{\sqrt{nu/\gamma_m r}}{r_i} = \dfrac{l_G}{r_i}$ values, indicating how diffusive or viscous the transport is. Low λ trends towards the diffusive regime, and high λ towards the viscous regime. The function is scaled horizontally in magnetic field in units of $B_0 = m\gamma_{mr}/e$. Only a few widely spaced values of λ are shown for ease of viewing, and the full computational dataset has a denser spacing of λ. Calculations were directly performed and provided by Ref. 59.

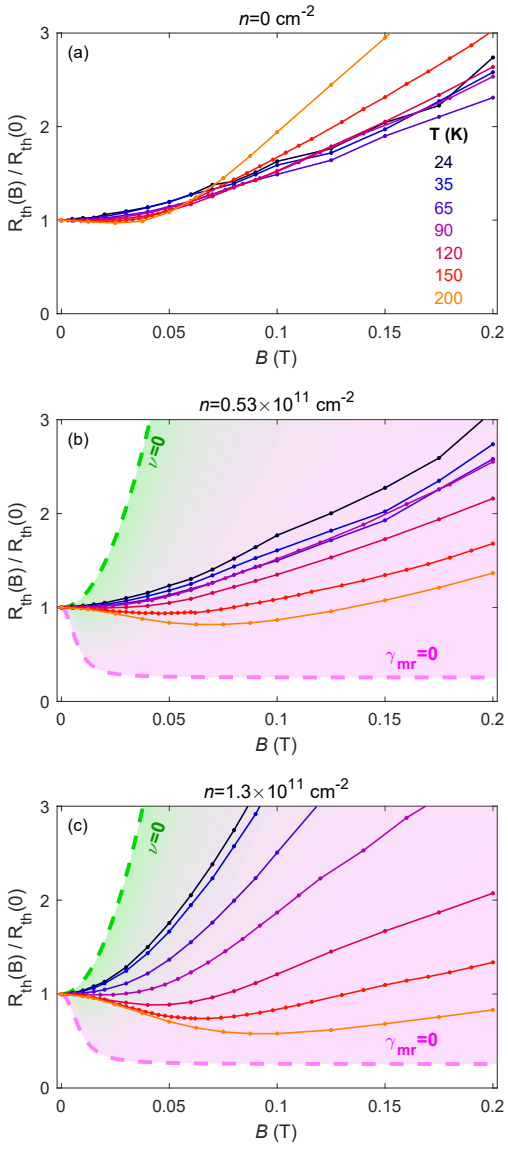

Figure 6.9: **(a-c)** Measured normalized thermal magneto-resistance (MR) $R_{th}(B)/R_{th}(0)$, vs magnetic field for three different electron densities. Black to orange colors indicate different temperatures. The magenta dashed curve indicates the geometric scaling factor $f(B)/f(0)$ for a fully-viscous and hydrodynamic sample ($\gamma_{mr} \to 0$; $\kappa_{xx}(B) = \text{const}$), using the viscosity obtained at 200 K. The green dashed curve shows the expected behavior for a diffusive semiclassical Drude model using the momentum relaxation rate obtained at 200 K, with the thermal conductivity scaling vs B the same as the electrical conductivity. The shaded gradient indicates the transition between these two regimes. At lower temperatures, the thermal MR always increases with magnetic field. At higher temperatures, the thermal MR first decreases with magnetic field due to the $f(B)$ behavior, as a clear sign of viscous heating; and then at larger magnetic field it turns upwards when the behavior is dominated by $\kappa_{xx}(B)$ changing.

limit to the viscous limit. For the nonzero densities, the thermal MR curves for all temperatures fall between the viscous and diffusive limits, showing a strong temperature dependence but not reaching either limit.

At low temperature away from charge neutrality, where the sample is (quasi-)ballistic, R_{th} increases with B due to a gradual transition from the (quasi-)ballistic to the diffusive regime caused by increased effective channel length, as supported by the magneto-Lorenz-ratio data (see Subsection 6.9.3). In this (quasi-)ballistic regime, our theory with a mixed diffusive and viscous $f(B, \nu, \gamma_{mr})$ will break down, and thus we must be careful in interpreting any resulting extracted quantites as quantitative.

As temperature increases, $R_{th}(B)$ gradually changes its shape to decrease with B at low field and nearly flatten out at high field, approaching the viscous limit. We conclude that this negative thermal MR is caused by the viscous scaling factor $f(B)$, as the $\left[\frac{\kappa_{xx}(B)}{\kappa_{xx}(0)}\right]^{-1}$ factor can only increase with B[89,228].

As our sample never attains the fully viscous and hydrodynamic limit, whether R_{th} increases or decreases with B for low B depends on the balance between the two factors in Eq. 6.9. In the regime where we measure a suppression of $\frac{\mathcal{L}}{\mathcal{L}_0}$ below 1, the graphene sample trends towards the degenerate hydrodynamic limit, and thus the $\left[\frac{\kappa_{xx}(B)}{\kappa_{xx}(0)}\right]^{-1}$ factor is expected to change more slowly, and the behavior of $R_{th}(B)$ becomes dominated by $f(B)$, allowing us to observe the negative thermal MR concurrently with the hydrodynamic suppression of $\frac{\mathcal{L}}{\mathcal{L}_0}$.

Interestingly, even at 90 K, where the thermal MR is approximately zero for low magnetic field, the increasing $\left[\frac{\kappa_{xx}(B)}{\kappa_{xx}(0)}\right]^{-1}$ factor approximately cancels the decreasing $\frac{f(B)}{f(0)}$ factor, indicating the transport is still viscous even without a negative thermal MR.

6.6 Investigating Limiting Behavior

While we cannot independently separate the cancelling quadratic contributions at low field of the factors containing $\kappa_{xx}(B)$ and $f(B)$ in Eq. 6.9, the decrease of R_{th} with B nonetheless sets a lower bound on the magnitude of the change of $\frac{f(B)}{f(0)}$. If we assume, for simplicity, that the change in $\left[\frac{\kappa_{xx}(B)}{\kappa_{xx}(0)}\right]^{-1}$ is negligible, then we can match the decrease in $\frac{R_{th}(B)}{R_{th}(0)}$ with the decrease in $\frac{f(B)}{f(0)}$. The degree to which the $\frac{f(B)}{f(0)}$ function drops is dependent on l_G and the specific geometry of the sample (Fig. 6.7). By comparing the minimum of $\frac{R_{th}(B)}{R_{th}(0)}$ and the dependence of $\frac{f(\infty)}{f(0)}$ on l_G, we can obtain a lower bound on l_G, although not yet on the viscosity directly. Here, $f(\infty)$ is the asymptotic value of $f(B)$ in the limit $B \to \infty$. In reality, due to an increase of $\left[\frac{\kappa_{xx}(B)}{\kappa_{xx}(0)}\right]^{-1}$ with magnetic field, the actual $\frac{f(B)}{f(0)}$ will decrease more than we estimate here, corresponding to a larger l_G, as we will see in Section 6.7.

The numerically calculated $\frac{f(\infty)}{f(0)}$ used in this computation[59] is shown in Fig. 6.10, and the resulting lower bound for l_G at 200 K is shown in Fig. 6.11. Additionally, Fig. 6.11 compares l_G with the inner radius r_i of the Corbino, shown as a dashed line. This visualization of the data is the clearest indication of geometry-dependent viscous behavior in our device. Indeed, near the most viscous density of $n = 1.3 \times 10^{11}\,\mathrm{cm}^{-2}$, the Gurzhi length closely approaches the size of the inner radius, indicating a strongly viscous flow pattern. Nearing charge neutrality, the Gurzhi length decreases as the sample transitions away from the degenerate hydrodynamic regime to the bipolar electron-hole regime. At charge neutrality, the theory with kinematic viscosity approaches a singularity as the fluid mass goes to zero; however, we can still calculate an effective Gurzhi length of nearly half the inner radius due to the presence negative thermal MR, which

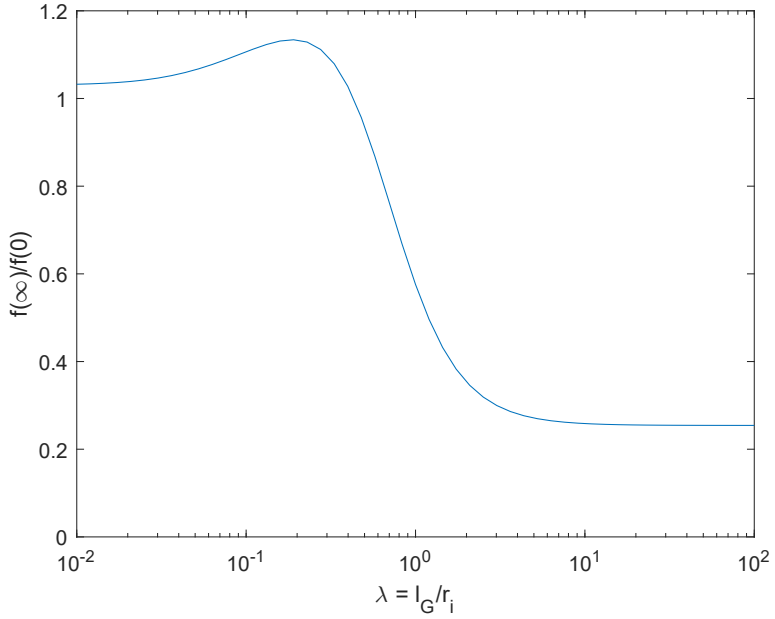

Figure 6.10: The functional form of $f(\infty)/f(0)$ used in the calculation of the Gurzhi length lower bound, plotted as a function of the ratio $\lambda = l_G/r_i$, where r_i is the radius of the inner contact. Calculation provided by 59.

may suggest weakly viscous flow at charge neutrality, which was previously not able to be measured in any other electrical-only experiments[61,62,71,74,81]. The presence of charge puddle disorder may complicate this interpretation, however. At high density, the Gurzhi length decreases as electronic screening reduces the e-e scattering rate.

We only show the Gurzhi length lower bound at 200 K because our mixed Ohmic and viscous model is less accurate at lower temperatures where the sample becomes (quasi-) ballistic. As temperature decreases, viscosity should increase and the momentum relaxation rate should decrease, which should cause the Gurzhi length to increase; however, at lower temperatures, $\frac{R_{th}(B)}{R_{th}(0)}$ does not drop as strongly as it does at 200 K (Fig. 6.9), so the calculated Gurzhi length lower bound would decrease instead of increasing. Our model would incorrectly explain this behavior as the sample becoming more diffusive/Ohmic rather than ballistic.

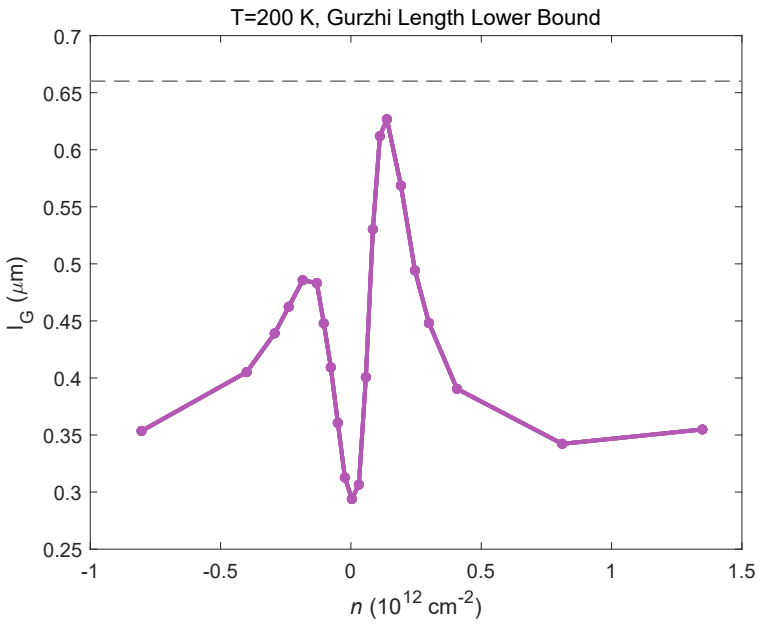

Figure 6.11: Purple: lower bound on the Gurzhi length l_G, computed by matching the minimum of $R_{th}(B)/R_{th}(0)$ to the value of l_G that sets $f(\infty)/f(0)$ equal to this minimum. The gray dashed line indicates the inner radius of the device.

After computing the lower bound for l_G at 200 K, the remaining fit parameter for the $\frac{f(B)}{f(0)}$ function is the momentum relaxation rate γ_{mr}, which enters simply as a scaling in magnetic field via the characteristic magnetic field field value $B_0 = m\gamma_{mr}/e$[59]. An appropriate scaling fit to the data, truncated up to the local minimum in R_{th}, provides a value for γ_{mr}, allowing calculation of ν from the l_G lower bound. We note that because γ_{mr} calculated in this way is not a lower bound, the resultant obtained values for the viscosity, $\nu = l_G^2\gamma_{mr}$, are only a quasi-lower bound rather than a robust lower-bound like those for l_G.[‡]

Fig. 6.12(a,b) shows the normalized thermal MR data for two densities at 200 K in orange, and the corresponding fits, using the single fit parameter γ_{mr}, of the numerically

[‡]However, we will find that these values of viscosity are indeed significantly lower than those calculated in Section 6.7 using a more complete model.

calculated[59] function $f(B, l_G, \gamma_{mr})$ in gray. The resulting γ_{mr} and ν values are plotted in Fig. 6.12(c,d). The functional fits of $f(B, l_G, \gamma_{mr})$ to the R_{th} data do not match very well; in particular, the R_{th} data attains a minimum and starts increasing again (at approximately 60–90 mT, depending on the density), before the $f(B)$ function begins to saturate, especially for the most viscous density of $1.3 \times 10^{11}\,\mathrm{cm}^{-2}$. We can explain this incongruence between the model and the data as stemming from our oversimplified assumption that $\kappa_{xx}(B)$ is constant, which, in the next section, we will relax to obtain a more complete model.

Nonetheless, this simple analysis yields a robust lower bound on the Gurzhi length, and order of magnitude estimates for the viscosity and momentum relaxation rate. Moreover, the values obtained for viscosity are comparable to those in the literature obtained using electrical-only measurements[62,73].

Finally, in Fig. 6.12(a,b), we compare the model and data with the purely viscous/hydrodynamic and purely Ohmic limits, in the same manner as in Fig. 6.9. Here, the values of viscosity and momentum relaxation rate for the magenta and green curves are taken from this simplified limiting-case fit, yielding qualitatively similar behavior as that shown in Fig. 6.9, where the values are taken from the more advanced fit discussed in the next section.

6.7 Calculating Viscosity, Momentum Relaxation, and Thermal Magneto-conductivity from Viscous Heating

Having seen the failure of the simplified model of $\kappa_{xx} = \text{const}$ in the previous section, we now relax this assumption for a more complete model. Motivated by the parabolicity of $R_{el}(B)$ at 200 K (Fig. 6.2), we assume the thermal inverse magneto-conductivity is

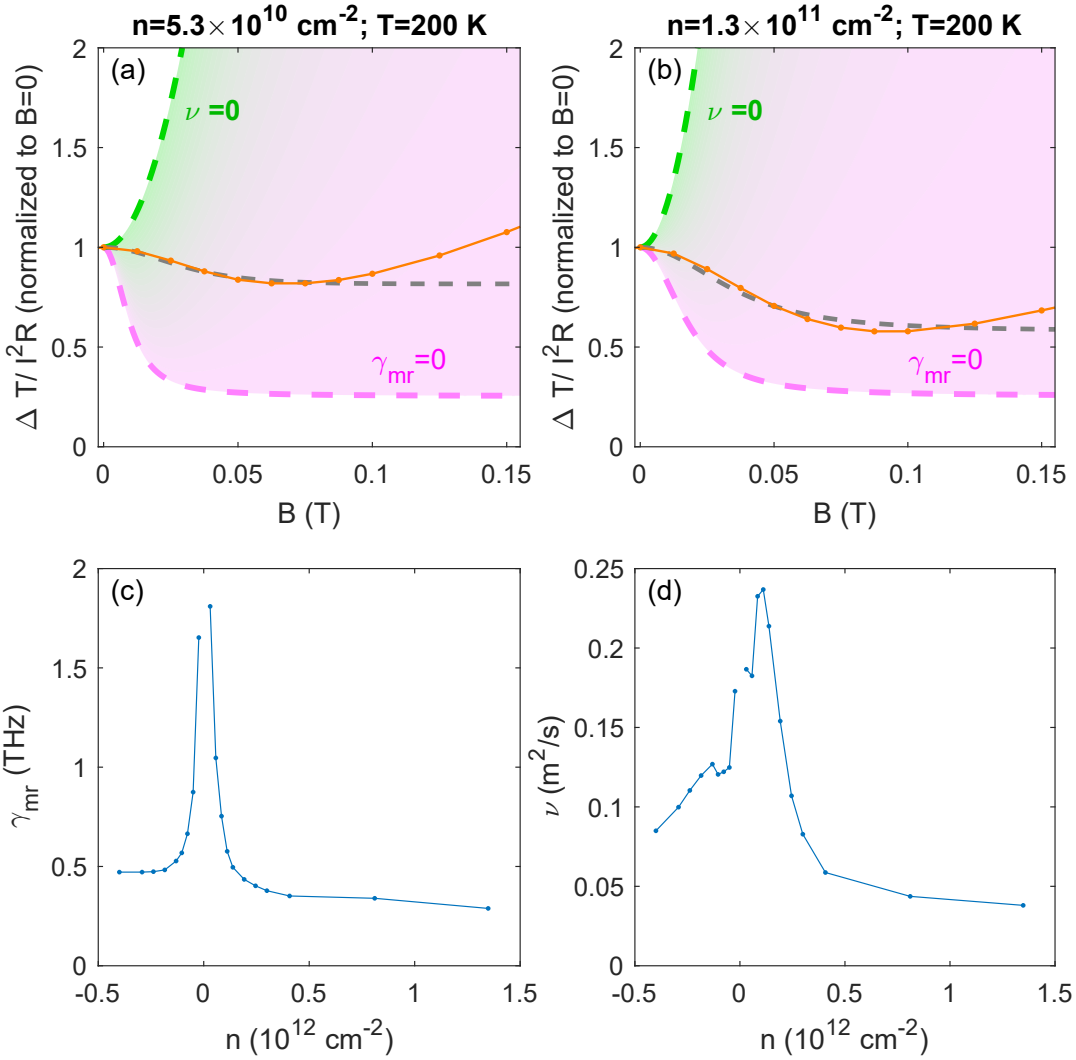

Figure 6.12: **(a,b)** Orange: measured thermal magneto-resistance (MR) $R_{th} = \Delta T/I^2R$, normalized by the value at $B = 0$, vs magnetic field for two different electron densities at 200 K. Gray: fit of the viscous function $f(B, \nu, \gamma_{mr})$ obtained by fixing the l_G value to the lower bound via the minimum of R_{th} with γ_{mr} as the only fit parameter, while assuming $\kappa_{xx}(B)$ is constant, as described in the text. The agreement with the data is not excellent; the data reaches the local minimum at significantly lower magnetic fields than when the model for $f(B)$ begins to saturate at its minimum. The magenta dashed curved indicates the fully viscous and hydrodynamic scaling factor $f(B)/f(0)$ using the viscosity obtained from the fit; the data would follow this curve if $l_G \gg r_i$ and $\kappa_{xx}(B) = \text{const}$. The green dashed curve shows the expected behavior for a diffusive semiclassical Drude model using the momentum relaxation rate obtained from the fit, with the thermal conductivity scaling vs B the same as the electrical conductivity. The shaded magenta-green gradient indicates the transition between these two regimes. **(c)** Calculated momentum relaxation rate γ_{mr} using this simplified model fit. **(d)** Calculated viscosity ν using this simplified model fit.

parabolic as $\left[\frac{\kappa_{xx}(B)}{\kappa_{xx}(0)}\right]^{-1} = 1 + (\alpha_{th}B)^2$, where α_{th} is functionally analogous to the electrical mobility μ, as in Eq. 6.4.

Thus, we rewrite Eq. 6.9 as

$$\frac{R_{th}(B)}{R_{th}(0)} = \left[1 + (\alpha_{th}B)^2\right] \times \frac{f(B;\lambda,\gamma_{mr})}{f(0;\lambda,\gamma_{mr})} \tag{6.10}$$

in order to fit this model to the data. Here, B is the independent variable, and α_{th}, $\lambda = l_G/r_i$, and γ_{mr} are the three fitting parameters in the model. We have parameterized $f(B)$ via λ instead of ν, as this significantly simplifies the numerical computations of $f(B)$. The numerically computed $f(B)$ that is used in this fit, for an experimentally relevant range of λ, was shown in Fig. 6.8; these computations were kindly provided by 59.

We have found that the model in Eq. 6.10, with three fit parameters, is able to fit the data extremely well for $|B| \lesssim 0.13\,\mathrm{T}$, above which the R_{th} transitions to a linear-in-B behavior. However, due to the excessive number of parameters in the model, the fit is poorly conditioned and a large range of parameters can correspond to nearly the exact same curve to fit to the data, giving broad confidence intervals for the parameters. We thus require another constraint during the fitting to obtain more reliable fit parameters with narrower confidence intervals.

We use the electrical magneto-resistance data, which is measured concurrently with the thermal magneto-resistance, as another fitting constraint. To avoid the effects of contact resistance, we consider only the change in absolute resistance ΔR_{el}, rather then the relative electrical magneto-resistance $\frac{R_{el}(B)}{R_{el}(0)}$. The theory for electrical magneto-resistance in a mixed Ohmic-viscous Corbino device is developed in Ref. 220, the results

of which we summarize here. The field dependent part of the resistance is given by[220]

$$\Delta R_{el}(B) = \frac{B^2 \ln(r_o/r_i)}{2\pi\rho_0(ne)^2} \times \left[1 - \frac{1}{\ln a}\left\{\frac{[\mathrm{I}_0(b) - \mathrm{I}_0(b/a)]\,[(a/b)\mathrm{K}_1(b) - (1/b)\mathrm{K}_1(b/a)]}{\mathrm{I}_1(b/a)\mathrm{K}_1(b) - \mathrm{I}_1(b)\mathrm{K}_1(b/a)} + \frac{[\mathrm{K}_0(b) - \mathrm{K}_0(b/a)]\,[(a/b)\mathrm{I}_1(b) - (1/b)\mathrm{I}_1(b/a)]}{\mathrm{I}_1(b/a)\mathrm{K}_1(b) - \mathrm{I}_1(b)\mathrm{K}_1(b/a)}\right\}\right], \quad (6.11)$$

where ρ_0 is the non-viscous resistivity from momentum relaxation, $a \equiv r_o/r_i$, $b \equiv r_o/l_G$, and $\mathrm{K}_0, \mathrm{K}_1, \mathrm{I}_0, \mathrm{I}_1$ are Bessel functions.[§]

As a mathematical trick for fitting Eqs. 6.10 and 6.11 simultaneously, we use the electrical magneto-resistance for negative B and thermal magneto-resistance for positive B. Fig. 6.13 demonstrates these simultaneous fits to the electrical and thermal MR data for two densities at 200 K, at which temperature we expect our model to be most physically representative of the viscous transport

In performing the fits, in order to equalize the residuals between the absolute electrical and relative thermal MR data, we have scaled down both the electrical data and model for Eq. 6.11 by $C \times R_{el}(0)$, and plotted it relative to the value of 1. Here, $C = 3$ is a relative weight parameter we have chosen so that the fit to the thermal data carries 3 times as much weight in the residuals compared to the electrical data; however, for plotting the data and the fit, we have used $C = 1$ so that both the electrical and thermal sides show $\dfrac{R(B)}{R(0)}$.

To avoid fitting the parabolic $1 + (\alpha_{th}B)^2$ factor to the linear part of the data for $|B| \gtrsim 0.12\,\mathrm{T}$, we fit to only a truncated part of the data, indicated by the red circles. The gray circles indicate the measured data that was excluded from the fit, as a point of comparison. The electrical part from Eq. 6.11 is shown with a thick black curve,

[§]Due to the nature of the modified Bessel functions here, we perform the computations using variable-precision arithmetic in MATLAB.

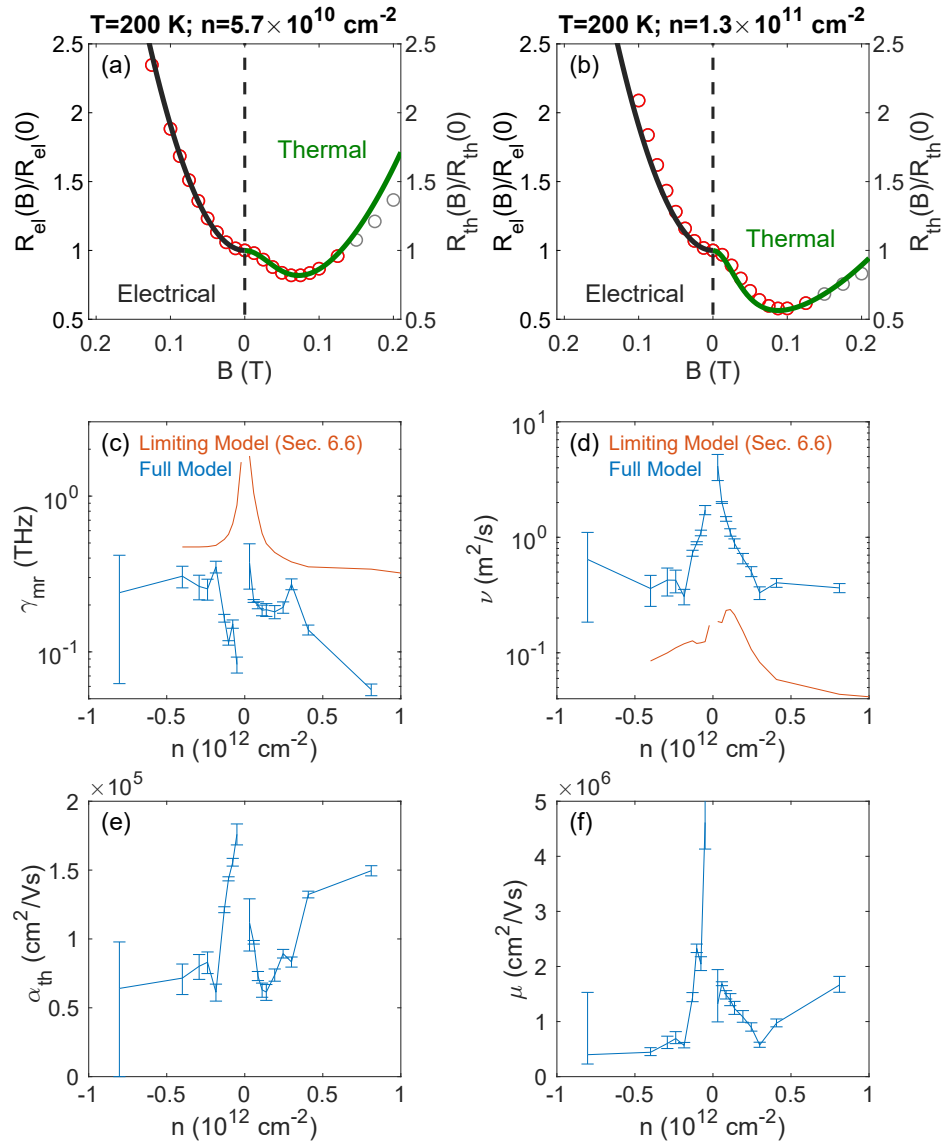

Figure 6.13: **(a,b)** Fits, as described in the text, of simultaneous Eq. 6.10 and 6.11 to the thermal and electrical MR data for two densities and at $T = 200\,\mathrm{K}$. The left side of each panel indicates the electrical MR, and the right side indicates thermal MR. Black and green curves ares the electrical and thermal fits, respectively. Red circles indicate data used in the fitting, and gray circles are the data excluded from the fits due to the linear-in-B behavior of thermal MR. Magenta dashed curve indicates the behavior of the thermal conductivity factor, and blue dashed curve indicates the behavior of the $f(B)$ factor, vs magnetic field, as described in the text. **(c)** Blue: Momentum relaxation rate fit parameter resulting from the fits of Eq. 6.10 in panels (a,b), with 1σ error bars (68% confidence intervals). Red: from the limiting model in Section 6.6. **(d)** Same as (c), for the viscosity. **(e)** Thermal mobility coefficient fit parameter only. **(f)** Electrical mobility calculated from (c).

and the thermal part from Eq. 6.10 is shown with a thick green curve. The dashed magenta curve indicates the $\left[\frac{\kappa_{xx}(B)}{\kappa_{xx}(0)}\right]^{-1}$ factor, and the dashed blue curve indicates the $\frac{f(B;\lambda,\gamma_{mr})}{f(0;\lambda,\gamma_{mr})}$ factor, both of which multiply together to obtain the green curve. We can thus see how the B-dependencies of the individual factors in Eq. 6.10 contribute to the overall measured thermal MR. For low B, the decrease of the $\frac{f(B)}{f(0)}$ factor dominates the behavior of $R_{th}(B)$ until it begins saturating; for higher B, the increase of the $\left[\frac{\kappa_{xx}(B)}{\kappa_{xx}(0)}\right]^{-1}$ factor causes the thermal resistance to start increasing with B again.

The fits are not a perfect match to the data even when it is truncated, as visible in Fig. 6.13(b), which introduces additional statistical fitting uncertainty to the extracted parameters. Fig. 6.13(c-f) shows the 1σ error bars (68% confidence intervals) for the extracted parameters γ_{mr}, ν, and α_{th}, as well as the electrical mobility computed from γ_{mr}, for $T = 200\,\mathrm{K}$. Especially on the hole side, the error bars indicate this method of calculating the transport parameters is not very quantitatively accurate, in part due to the imperfect agreement of the model with the data at some densities.

We also compute the Gurzhi length at $200\,\mathrm{K}$ from the fits in Fig. 6.13(a,b) and plot it in Fig. 6.14 with comparison to the lower bound computed in Section 6.6. The new model in this section provides a much larger Gurzhi length than our previously calculated lower bound. We compare this Gurzhi length with the channel length of the device $r_o - r_i$, and we see that it is comparable to and sometimes longer than the channel length, indicating strongly viscous flow and heating in our device.

The model we use only accounts for a crossover between the diffusive and viscous transport regimes, whereas our device is in a quasi-ballistic transport regime at low temperature. If momentum relaxation does not increase enough with temperature, then it may still not be strong or uniform enough at $200\,\mathrm{K}$ to completely justify the mixed

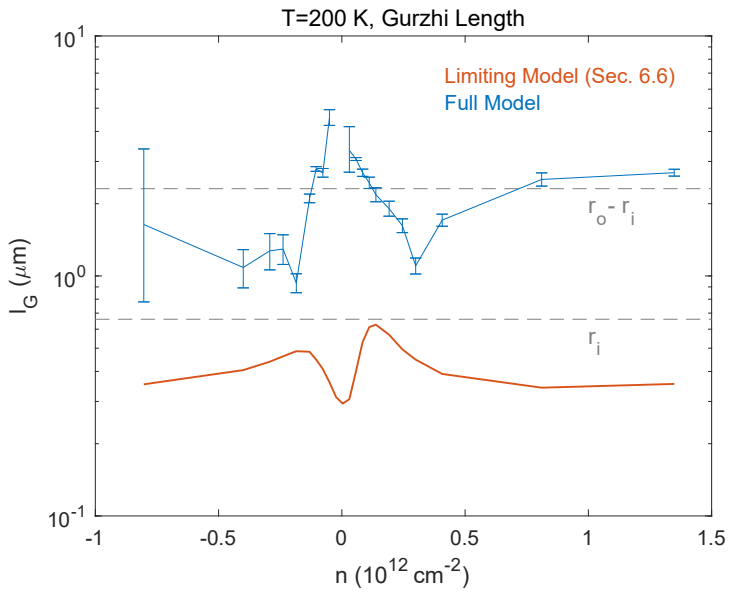

Figure 6.14: Blue: Gurzhi length computed from the fits and parameters in Fig. 6.13, with 1σ error bars (68% confidence intervals). Red: Gurzhi length from the limiting model from Section 6.6, replotted from Fig. 6.11. Gray dashed lines indicated the inner radius r_i and the channel length $r_o - r_i$, for comparison to the Gurzhi length.

diffusive and viscous transport picture used in the model. The diffusive Drude transport model for magnetoresistance is grossly incorrect in the high-mobility, ballistic limit, as it predicts the opposite result from semi-classical ballistic transport (see Subsections 6.9.1 and 6.9.3), so analogously we cannot necessarily expect the diffusive aspect of our mixed model to give quantitative predictions for magneto-resistance in a mixed quasi-ballistic and viscous transport regime. Furthermore, the viscosity is expected to have a dependence on the magnetic field[63], so it might be expected that the functional form may be more complicated in the higher magnetic field regime.

Although we expect the model to be a progressively poorer description of the inherent physics at lower temperatures, we nonetheless, for completeness, perform the same electrical/thermal fits down to 90 K, the lowest temperature where there is any evidence of viscous heating by negative thermal MR. The fits for these lower temperatures are

shown in Fig. 6.15, in the same manner as Fig. 6.13(a,b). At these temperatures, the viscous drop in $R_{th}(B)$ is weaker due to the sample trending towards (quasi-) ballistic transport. While the fit reflects this in the much weaker magnetic field dependence of the $f(B)$ factor (blue dashed curve), the fit trends towards entirely diffusive transport with an insignificant temperature dependence of the $\left[\frac{\kappa_{xx}(B)}{\kappa_{xx}(0)}\right]^{-1}$ factor, whereas the device in reality enters a quasi-ballistic regime that our model cannot capture. Thus, the parameters extracted from these fits are progressively less reliable as the temperature is lowered.

For completeness, we show in Fig. 6.16 the evolution of the 3 fit parameters and the mobility over the four highest temperatures measured, as was shown in Fig. 6.13(c-f) for 200 K. The general trend for the momentum relaxation rate, especially at lower temperatures, is to increase near charge neutrality, which can be understood from reduced screening of charged impurities due to low electron density. The temperatures of 150 and 200 K do not follow this trend as clearly, which is likely a failure of our model to capture the exact behavior of the device as described previously.

The calculated viscosity follows a trend of increasing with temperature, which is opposite of the effect predicted for the hydrodynamic regime, where increasing e-e interactions with temperature should decrease viscosity (see Subsection 1.3.1). However, at low temperature in the quasi-ballistic regime, we expect that viscosity will not be well defined due to an insufficient rate of electron collisions, and that our model cannot quantitatively describe this quasi-ballistic regime.

On the electron side, we find that the calculated thermal mobility α_{th} generally decreases with temperature, consistent with a suppression of thermal conductivity and Lorenz ratio due to increasing hydrodynamic e-e scattering. Additionally, the thermal mobility is approximately an order of magnitude lower than the electrical mobility, also

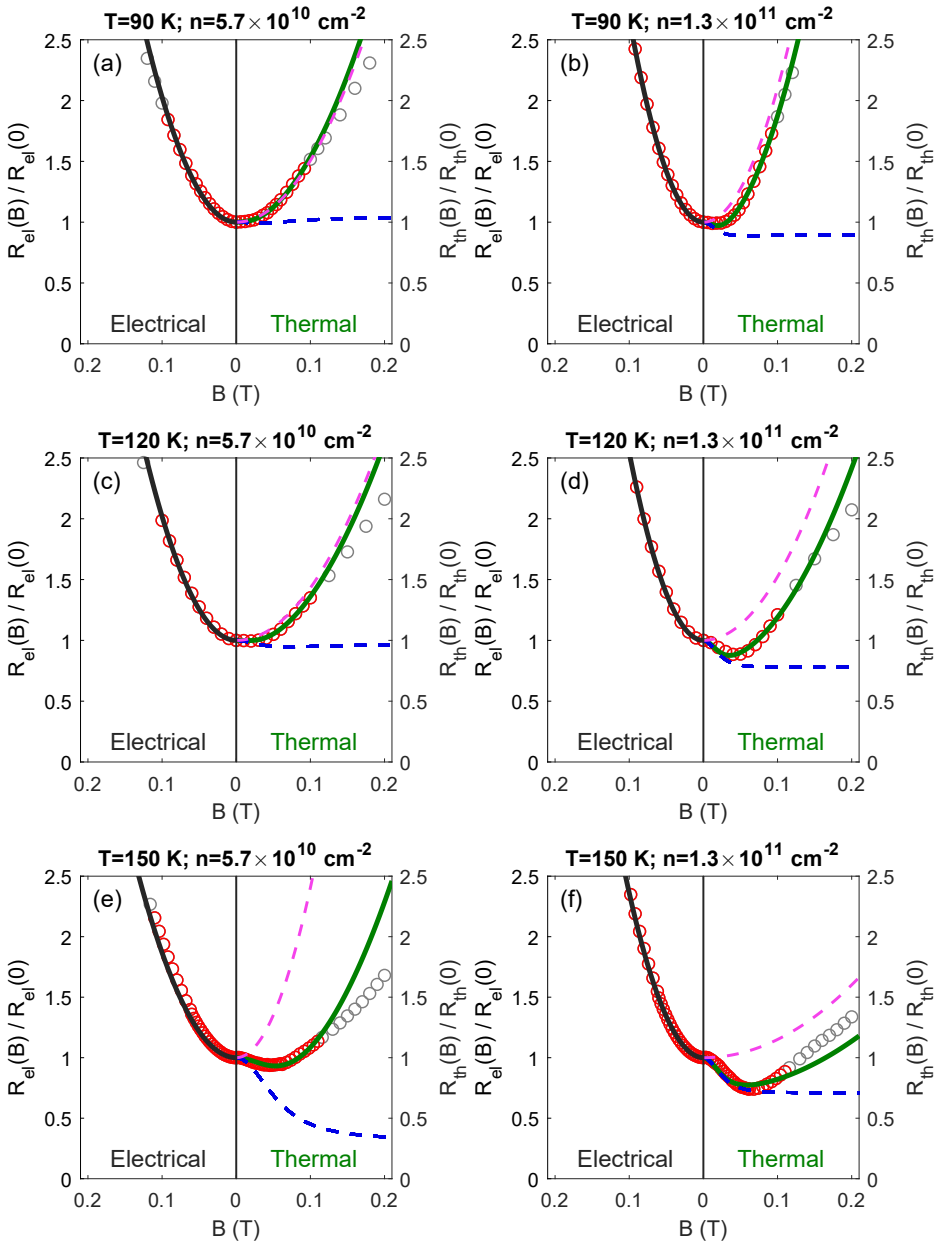

Figure 6.15: **(a-f)** Fits, as described in the text, of simultaneous Eq. 6.10 and 6.11 to the thermal and electrical MR data for two densities at lower temperatures. The left side of each panel indicates the electrical MR, and the right side indicates thermal MR. Black and green curves ares the electrical and thermal fits, respectively. Red circles indicate data used in the fitting, and gray circles are the data excluded from the fits due to the linear-in-B behavior of thermal MR. Magenta dashed curve indicates the behavior of the thermal conductivity factor, and blue dashed curve indicates the behavior of the $f(B)$ factor, vs magnetic field, as described in the text.

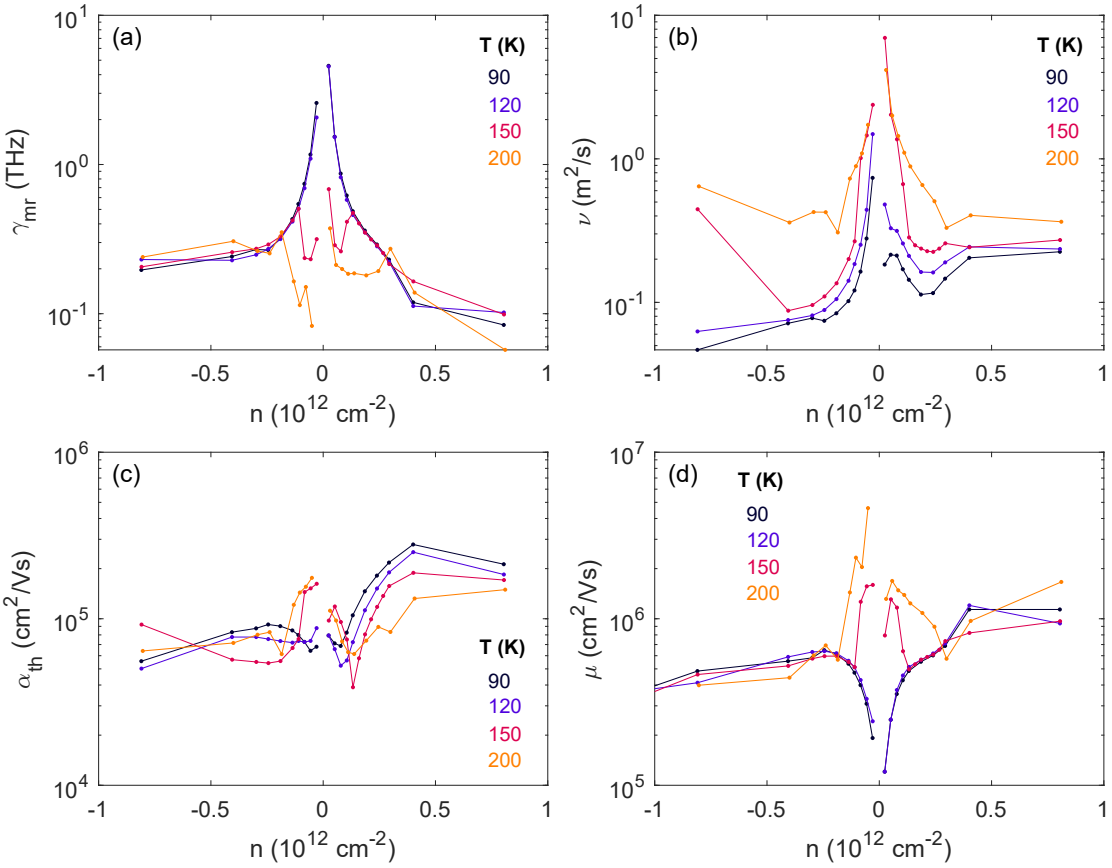

Figure 6.16: (a-d) The evolution of the fit parameters γ_{mr}, ν, and α_{th}, as well as the electrical mobility computed from γ_{mr}, from 90 K to 200 K.

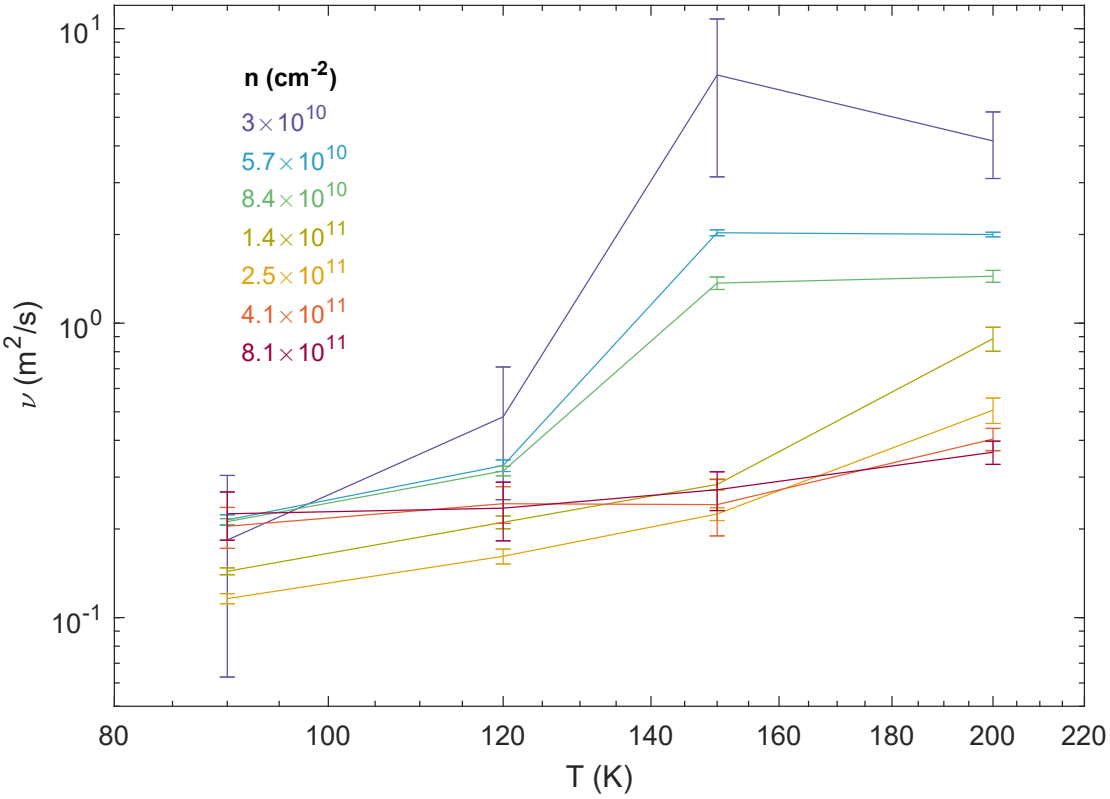

Figure 6.17: Effective viscosity parameter from the full model fit as a function of temperature. The temperature dependence is opposite to what we expect, and we attribute it to the model failing progressively more at lower temperature as the device becomes (quasi-)ballistic, which our model does not capture.

consistent with a suppressed Lorenz ratio.

Finally, we also present the viscosity parameter extracted from the fit, for the electron side, plotted vs temperature to show its dependence in Fig. 6.17(b). It should not come as a surprise that the apparent viscosity decreases as temperature is lowered. We already saw this in the raw data in Fig. 6.2, and in the low-B thermal MR coefficients in Fig. 6.4: the negative thermal MR viscous signature goes away at low temperature.

The effect we see here is analogous to the temperature dependence of the vicinity resistance in previous viscous graphene experiments[61,71]. There, the magnitude

of the negative vicinity resistance, which should be proportional to viscosity, first increased with temperature before decreasing; the authors concluded that the former regime corresponded to the quasi-ballistic regime with viscous effects, and the latter regime corresponded to the true hydrodynamic regime. In our experiment, the Lorenz ratio at $B = 0$ offers another perspective into whether our sample is hydrodynamic; the decrease of it that happens concurrently with the negative thermal MR indicates the sample approaches or begins to enter the hydrodynamic regime, even if it is not strongly hydrodynamic. In a strongly hydrodynamic regime, the Lorenz ratio should be much smaller than 1, where we only observe it decrease to ~ 0.45.

We remark that our model of Eqs. 6.10 and 6.11 can describe the data semi-quantitatively. The significance of our results lies not in measuring the exact viscosity, but in observing a qualitative effect of viscous heating through the thermal magnetoresistance.

6.8 Additional Data from Another Device

In this section, we present additional data for the Corbino devices in this Chapter to further support our results. First, we show the residual density data of both Corbino devices. Then, we show the thermal MR data for MLG4 in the same style as previously shown for MLG3.

6.8.1 Residual Density

The residual charge density corresponds approximately to how many charges remain when the gate sets the chemical potential to charge neutrality; these remaining charges are a result of both chemical potential disorder fluctuations (charge puddles)[16,17,222–224],

as well as thermal excitation. At high temperatures where thermal excitation dominates, the residual charge density represents coexisting electrons and holes, roughly in an equal ratio. In this regime, the residual density increases with temperature. At low temperatures, the thermal excitation becomes negligible and all remaining charges are those from the charge puddles, and lowering temperature further will not reduce the residual density. The residual density will roughly correspond to the width in n of the Dirac peak.

Fig. 6.18 shows the residual density vs temperature for both devices, and indicates that the residual density for Device 1 saturates at a temperature of $\sim 80\,\mathrm{K}$ with a minimum value of approximately $4.5 \times 10^{10}\,\mathrm{cm}^{-2}$. In both devices at lower temperatures, the residual density deviates from saturation, but this is an artifact of universal conductance fluctuations appearing at charge neutrality and distorting the smooth peak in the $R_{2T}(n)$ data on the log-log plot.

Fig. 6.18 shows the residual density for both of the devices used in this work.

6.8.2 Results for Second Corbino Device MLG4

We present additional data for a second, similar Corbino device, MLG4. First, we show the individual linecuts of the electrical and thermal MR coefficients plotted in parallel with the Lorenz ratio in Fig. 6.19.

Fig. 6.20 shows the matched colormaps of Lorenz ratio and thermal MR coefficient. Here, the measured Lorenz ratio does not show an absolute suppression, but it nonetheless shows a relative suppression qualitatively consistent with the device shown in the main text. If we take the low-T value of the Lorenz ratio as a baseline, the higher-T relative suppression of the Lorenz ratio still coincides closely with the negative thermal MR. This device has a shorter channel length of $\sim 1.64\ \mu$m, and thus it will be

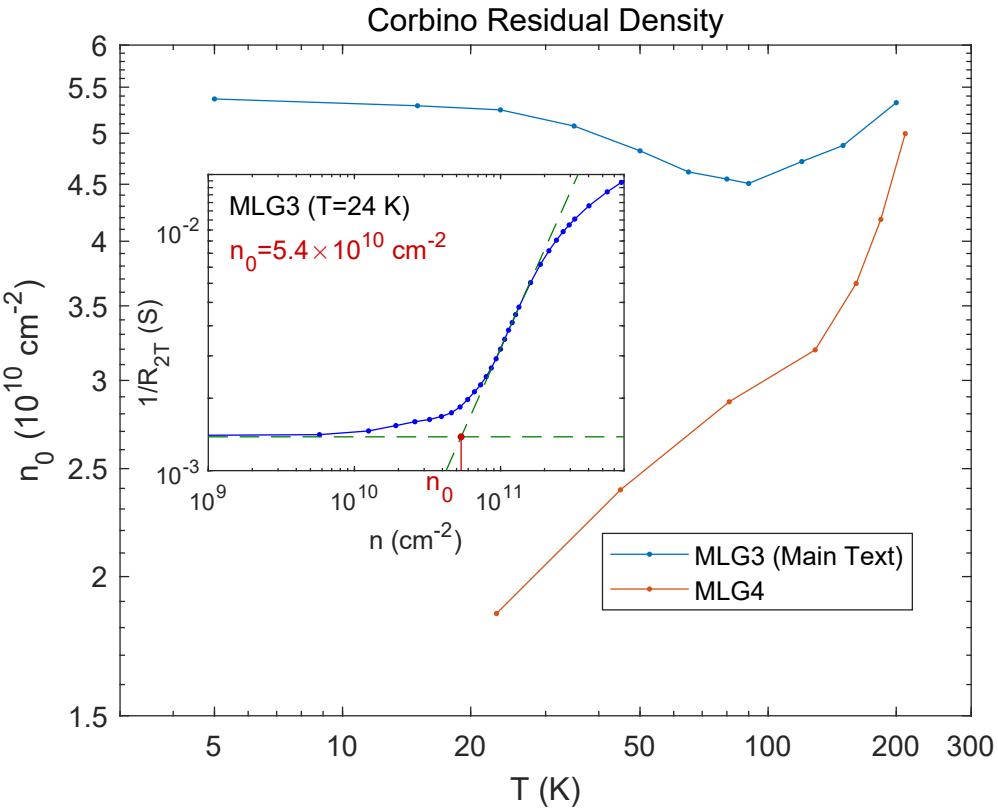

Figure 6.18: Main panel: Residual density of both devices in this work. Inset: log-log plot of electrical conductance vs n (blue). Extrapolations to the linear and flat parts are indicated by the green dashed lines. Red indicates the intersection of these, which is the residual density n_0.

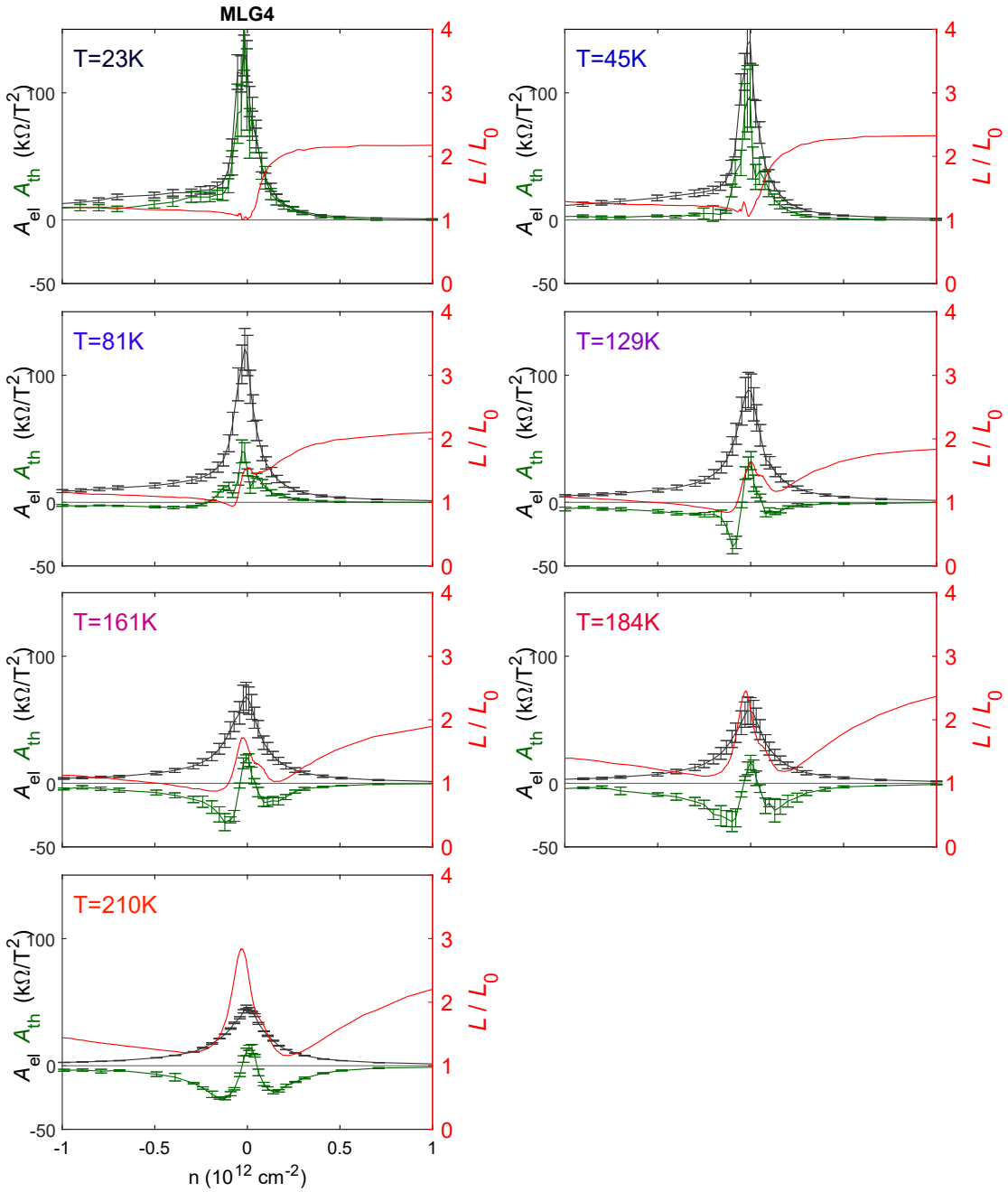

Figure 6.19: For MLG4, linecuts of the thermal MR Coefficient A_{th} (green) and the electrical MR coefficient A_{el} (black), plotted on the left-hand axes, vs density, for the set of measured temperatures 23–210 K. The corresponding Lorenz ratio at $B = 0$ is plotted on the right-hand axes.

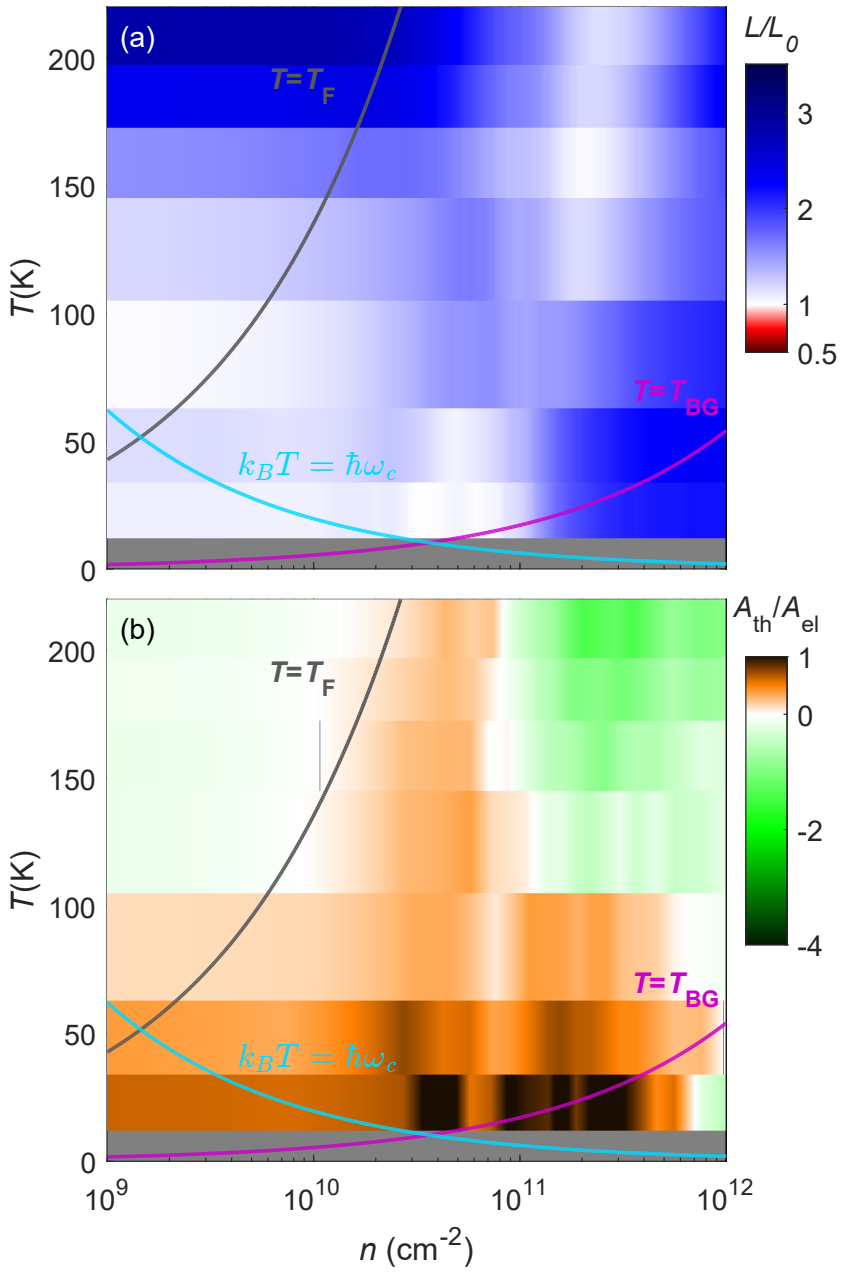

Figure 6.20: Correlation of **(a)** zero-field Lorenz ratio suppression and **(b)** negative thermal magneto-resistance for MLG_4, plotted in the same style as Fig. 6.4.

more ballistic at low-temperature than the device shown in the main text, for the same approximate disorder level, and would thus be expected to produce higher measured Lorenz ratios. Furthermore, the shorter channel length and smaller radii make it easier for this device to enter the viscous flow regime, as it is easier to make these dimensions smaller than the Gurzhi length l_G.

Qualitatively, the data is consistent with MLG3, also showing viscous transport correlating with the relative Lorenz ratio suppression.

6.9 Special Methods for Viscous Magneto-Transport

In this section, we refine and develop additional special methods for analyzing and interpreting the viscous magneto-transport data.

6.9.1 Calculation of Contact Resistance and Momentum-Relaxing Mean Free Path

In the previous Chapter in Subsection 5.5.4, we derived a formula for calculating the contact resistance and momentum relaxation rate of a diffusive Corbino device based on the geometry and the electrical magneto-resistance within the Drude model, and presented the calculated results for MLG3. However, as will be described further in Section 6.9.3, these diffusive methods fail to correctly describe the true ballistic limit, so they cannot correctly estimate the contact resistance or the momentum relaxation rate. Additionally, this method breaks down at higher temperature when the transport becomes viscous and has another mechanism for magneto-resistance[220]. Nonetheless, for a complete analysis we show the momentum-relaxing mean free path via this calculation in Fig. 6.21(a), referenced to Section 5.5.4. For comparison, we also show the

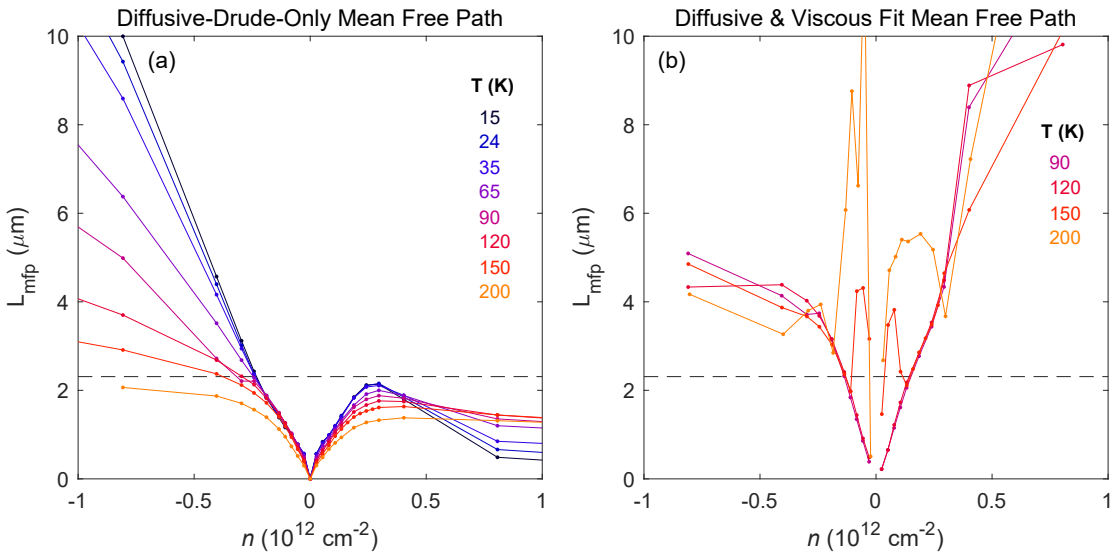

Figure 6.21: (a) Mean free path, for several temperatures, calculated using only the parabolic electrical magnetoresistance, as described in Section 5.5.4, with the diffusive Drude model. Gray dashed line indicates the channel length, i.e. $r_o - r_i = 2.3\,\mu$m. **(b)** Mean free path, for several temperatures, calculated using the γ_{mr} from Section 6.7. Gray dashed line indicates the channel length.

momentum-relaxing mean free path calculated via the γ_{mr} parameter from the functional fits in Section 6.7, using the combined diffusive and viscous model, in panel (b). While the resulting parameter is not at clearly defined as from the diffusive-only model, we can see the general trend is that the mean free path is even larger in this model, since we are now assigning part of the magnetoresistance to viscous effects via Eq. 6.11. We take the computed large mean free paths as a strong suggestion that our device is in the ballistic or quasi-ballistic regime at low-T.

Moreover, we remark that the mean free path calculated by the diffusive-Drude-only model in Fig. 6.21(a) necessarily underestimates the true ballistic mean free path. From

Eq. 5.27, the Drude model electrical magneto-resistance is given by

$$\Delta R_{2T}(B) = \frac{\ln \frac{r_o}{r_i}}{2\pi} \cdot \frac{\mu B^2}{ne}. \tag{6.12}$$

As will be discussed further in Section 6.9.3, this model over-estimates the measured electrical magneto-resistance for a given true mobility when the sample is ballistic. Alternately, for a given true magneto-resistance, it will under-estimate the mobility, thus under-estimating the mean free path. We can robustly conclude that the true mean free path is larger than shown in Fig. 6.21(a), both due to the Drude-model under-estimation as well as ignoring that a fraction of the electrical magneto-resistance comes from viscous effects via Eq. 6.11.

6.9.2 Artificially Enhanced Lorenz Ratio in the Ballistic Regime at $B = 0$ of Corbino Devices

In the ballistic regime, our self-heating Johnson noise thermometry measurement technique produces artificially enhanced Lorenz ratios, as was discussed in Section 3.7.

Generalized Model of Contact Resistance

Taking Eq. C.11 from Appendix C, we can set the parameter $\alpha \to 0$ for the ballistic limit, corresponding to dissipating all the heat from the contact resistance in the metal heat sink contacts. Microscopically, this corresponds to electrons scattering and randomizing their momenta only once in the large reservoirs (corresponding to the metal contacts in our device) of the ballistic wire model. Applying this limit and, we find the measured

Lorenz ratio becomes

$$\mathcal{L}_m = \mathcal{L}_s \frac{(R_s + 2R_c)^3}{R_s^3 + 6R_c R_s (R_s + R_c) \dfrac{\mathcal{L}_s}{\mathcal{L}_c}}. \tag{6.13}$$

Expanding Eq. 6.13 in $\dfrac{R_s}{R_c} \to 0$ (as occurs in a quasi-ballistic or ballistic system), we obtain to the lowest two orders

$$\mathcal{L}_m \approx \mathcal{L}_c \cdot \frac{4}{3}\frac{R_c}{R_s}\left(1 + \frac{1}{2}\frac{R_s}{R_c}\right), \tag{6.14}$$

showing explicitly how the measured Lorenz ratio will become large in ballistic samples.

We note that even in the case of the distribution of the Landauer-Sharvin contact resistance into the channel bulk for a ballistic Corbino device[80,81], we still expect all corresponding Joule heating to happen within the contacts, as the back-reflection of the ballistic modes due to their termination will not generate any random scattering that can lead to heating.

Absence of Heating

The strongly enhanced measured Lorenz ratio corresponds to measuring less noise from a sample for a given bias. Experimentally, we observe such an absence of noise from self-heating in most of our devices when measured at low temperature and high density. In the extreme limit of ballisticity of a quantum hall edge state protected from any backscattering, Lorenz ratios of order 100–1000 have been measured with this self-heating Johnson noise method[175].

Our model assumes the metal contacts are perfect heat sinks fixed at the bath temperature T_0. In reality, they are not perfect, but they still have strong electron-phonon

coupling at our experimental temperatures to produce negligible heating from the ballistic dissipation.

As seen in the main text in Fig. 6.1(c), the upwards trends of the measured Lorenz ratio at $T = 24$ K as the density is increased is evidence for the device transitioning to the ballistic regime.

6.9.3 Ballistic Effects: Electrical and Thermal Magnetoresistance

In a 2-terminal electrical resistivity measurement, when the sample enters the ballistic transport regime the resistance will not go to zero due to contact resistance effects, making it difficult to ascertain when the sample becomes ballistic. In the Corbino geometry, a sample will have a characteristic signature of ballisticity in the electrical magneto-resistance. A non-ballistic sample with finite local conductivity $\sigma_{xx}(B = 0)$ will exhibit a Drude-type electrical MR as in Eqs. 5.27 and 6.4. However, a ballistic sample will exhibit zero electrical MR up to a critical magnetic field, since all electrons exiting one electrode will arrive at the other electrode until their cyclotron radius becomes small enough to divert them[229].

In our sample, we observe such an effect at the highest measured densities at the lowest temperature. Concurrently with the zero electrical MR, the sample exhibits a strongly enhanced apparent Lorenz ratio at $B = 0$ that is consistent with ballistic transport (see Section 3.7). In the ballistic regime, we furthermore measure the thermal magneto-resistance to also be zero for low magnetic fields. We take this as empirical evidence that in the fully ballistic regime, the generalized thermal magneto-resistance is not negative, as it is for the viscous case.

In this Subsection, we analyze the effects of ballistic transport on electrical and

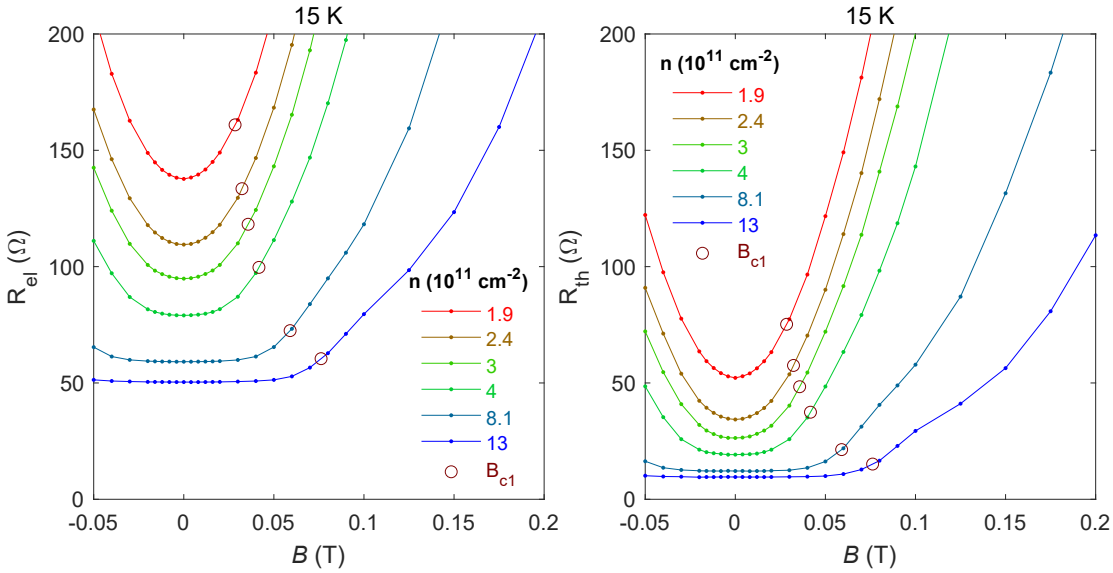

Figure 6.22: (Left) Electrical MR and **(Right)** thermal MR for MLG3, for several of the highest electron densities at 15 K. The brown circles labeled B_{c1}, marked on the curves, indicate where the resistance would begin to increase due to ballistic cyclotron orbit trajectories missing the opposite contact. The upturn of resistance before reaching the critical field suggests the device being behaving quasi-ballistically.

thermal MR, as well as the measured Lorenz ratio. Figs. 6.22 and 6.23 demonstrate the nearly flat electrical MR and thermal MR at high densities at 15 K, corresponding to the strongest low-T contact-induced measured Lorenz ratio enhancement discussed above. Similarly, Fig. 6.24 shows the measured Lorenz ratio vs B, which also exhibits analogous plateaus at low-B.

Electrical Ballistic MR Effects

The absence of electrical MR (the plateau at low-B) signifies ballistic transport, where increasing the length of the ballistic electron trajectory via path bending due to cyclotron radius will not cause the resistance to increase[229]. This occurs until a certain critical field B_{c1}, which corresponds to the cyclotron radius where electron orbits begin to miss

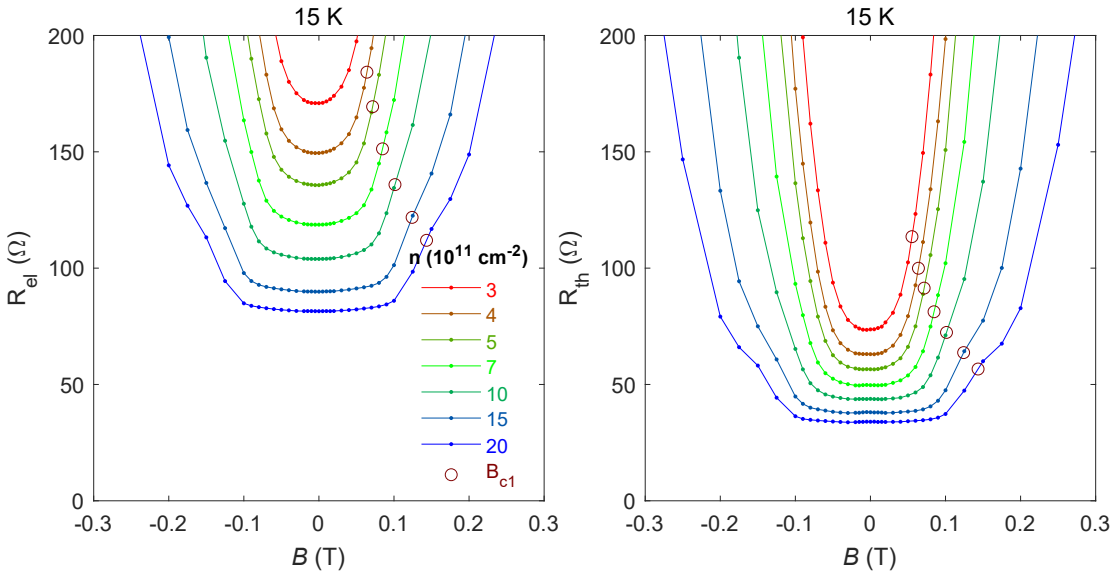

Figure 6.23: MLG_4 electrical and thermal MR, plotted in the same was as Fig. 6.22.

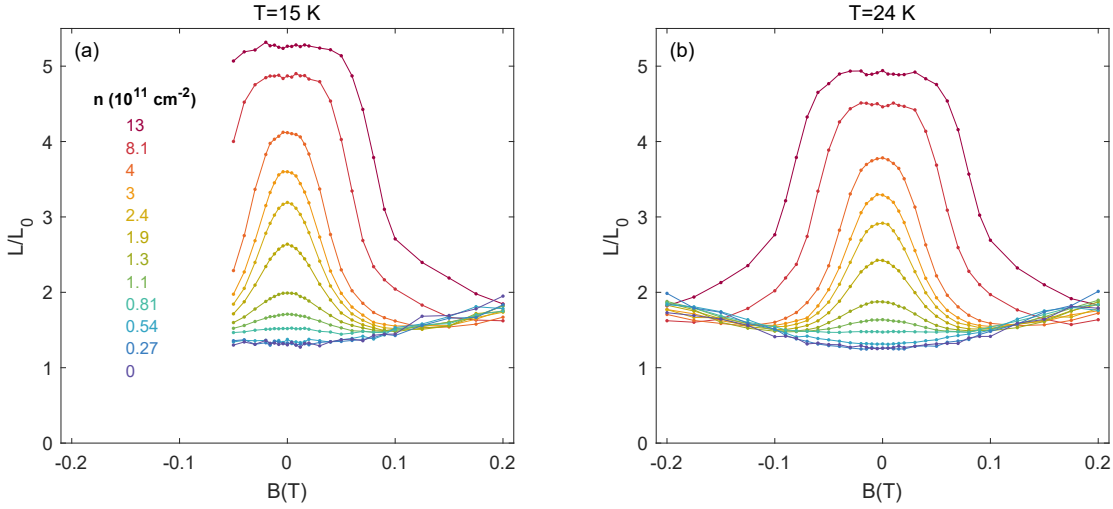

Figure 6.24: **(a,b)** MLG_3 Lorenz ratio vs magnetic field, for several densities, shown for 15 and 24 K. Only the data for the electron side is shown. in the flat plateaus with elevated Lorenz ratios, the device continues to behave ballistic. When the elevated Lorenz ratio begins to decrease with B, this is a signature of the device transitioning through the quasi-ballistic regime and becoming more diffusive. For densities below $8.1 \times 10^{11}\,\mathrm{cm}^{-2}$, the device already starts in the quasi-ballistic regime at $B = 0$.

the opposite contact, given by $r_c = (r_i + r_o)/2$ with $r_{i,o}$ the inner and outer contacts. Dark red circles in Fig. 6.22 indicate this critical field.

Our measured magneto-resistance starts to increase before reaching this critical field, for which we propose the following quasi-ballistic explanation: As the magnetic field increases, the arc length along the cyclotron orbit that that electrons take to reach the other contact increases. In a purely ballistic device, this process will get cut off when the cyclotron orbit radius reaches a critical value at B_{c1}. In a nearly-ballistic or quasi-ballistic device with a small amount of impurity scattering or momentum relaxation, the arc length may reach the momentum-relaxing mean free path first, before reaching the critical arc length πr_c at B_{c1}. Then, diffusive/Ohmic resistance starts being generated in the sample, causing the magneto-resistance to increase. This is supported by the ballistic Lorenz ratio behavior as a function of B, as explained further below.

For MLG3, both the thermal and electrical magneto-resistances (Fig. 6.22) are flat for the highest two densities of $n = 8.1,\ 13 \times 10^{11}\text{cm}^{-2}$; and for lower densities of $n = 3,\ 4 \times 10^{11}\text{cm}^{-2}$, the MR is starting to flatten out as the ballistic regime is approached.

The Drude model for electrical MR (Eq. 5.27) predicts the wrong behavior (strongly increasing electrical MR) for the limit mobility $\mu \to \infty$ because it assumes uniformly diffusive transport (corresponding to the quantum mechanical formation of non-conductive bulk Landau levels at arbitrarily small B). The equation does not capture the correct semi-classical description of mesoscopic ballistic transport, and thus the methods of Subsections 5.5.4 and 6.9.1 cannot be used to truly ascertain where the device transitions to ballistic transport.

Empirical Thermal Ballistic MR Effects I

We take the flat thermal MR in Fig. 6.22, coincident with the flat electrical MR, as empirical evidence that ballistic transport in the self-heating Johnson noise thermometry measurement setup will not produce negative thermal MR. Interpolated through the transition to diffusive transport (and corresponding positive thermal MR as described earlier in this Chapter) that occurs at charge neutrality, there are no non-viscous effects that can cause negative thermal magneto-resistance. After discussing the behavior of the measured Lorenz ratio vs magnetic field, we return to the thermal magneto-resistance for additional analysis.

Lorenz Ratio when Exiting the Ballistic Regime due to Applied Magnetic Field

As the magnetic field applied in the ballistic regime is increased, we have proposed that our sample starts behaving quasi-ballistically or quasi-diffusively before reaching B_{c1}, the critical transition field between the flat and increasing MR. The Lorenz ratio data to support this shown in Fig. 6.22. At the highest densities, the ballistically-enhanced Lorenz ratio exhibits a plateau vs magnetic field (due to the plateau in both R_{th} and R_{el}) until the device starts transitioning to diffusive transport just before B_{c1}, at which point the measured Lorenz ratio starts decreasing with B towards the diffusive WF value of 1. We take the decreasing of $\mathcal{L}/\mathcal{L}_0$ with B as a signature of the device transitioning from ballistic transport to quasi-ballistic/diffusive. The Lorenz ratio plateaus are additional evidence that the device is nearly fully ballistic for the highest two densities measured ($n = 8.1,\ 13 \times 10^{11}\text{cm}^{-2}$). The other densities are only quasi-ballistic, as the Lorenz ratio starts decreasing with B nearly immediately. For

densities below approximately $n \lesssim 0.81 \times 10^{11}\text{cm}^{-2}$, the decreasing of $\mathcal{L}/\mathcal{L}_0$ with B stops, indicating fully diffusive transport, concurrent with Lorenz ratios very close to the WF value of 1. Correspondingly, these lower densities with fully diffusive transport show only very weak viscous heating effects at higher temperature, as expected.

Thus, only for densities where our sample is ballistic or quasi-ballistic at low-T are we able to observe viscous heating at higher temperatures, consistent with previous electrical-only experiments on viscous graphene[61,62,71,74,81]. Moreover, the physics governing hydrodynamics and viscous flow in the Dirac fluid near charge neutrality is more complicated and very different from that in degenerate hydrodynamic metals[2,53,89,91,225,230].

Empirical Thermal Ballistic MR Effects II

Given that the measured Lorenz ratio is enhanced in ballistic or quasi-ballistic graphene due to contact resistance effects as described in Subsection 6.9.2, and that it decreases with magnetic field due to the sample becoming less ballistic, we can show that the measured thermal MR must be positive in this regime, in contrast to the negative thermal MR for the viscous regime.

The Lorenz ratio as a function of magnetic field, to order B^2, can be expressed as

$$\frac{\mathcal{L}}{\mathcal{L}_0} = \frac{1}{12\mathcal{L}_0 T_0} \times \frac{R_{el}(B)}{R_{th}(B)} = \frac{1}{12\mathcal{L}_0 T_0} \times \frac{R_{el}(0)(1+\alpha_{el}B^2)}{R_{th}(0)(1+\alpha_{el}B^2)} \tag{6.15}$$

$$\approx \frac{1}{12\mathcal{L}_0 T_0} \times \frac{R_{el}(0)}{R_{th}(0)} \times \left[1 + (\alpha_{el} - \alpha_{th})B^2\right]. \tag{6.16}$$

Because the measured Lorenz ratio must decrease with B, and the electrical MR increases ($\alpha_{el} > 0$), we must have that $\alpha_{th} > \alpha_{el}$, and thus the relative thermal MR must be positive. This applies both within the plateau for small magnetic field $B < B_{c1}$, as

the sample is marginally perturbed out of the ballistic regime, as well as beyond the plateau for $B > B_{c1}$ where the sample exits the ballistic regime. This excludes the ballistic or quasi-ballistic regime from exhibiting negative thermal MR.

6.9.4 Explanation of Requirement for Ballistic Transport at low-T for in Order to Be Viscous at High-T

In this section, we derive the approximate result that a device must be ballistic at low-T in order to see viscous transport at intermediate-T.

The viscosity for an electronic system can be written as[67]

$$\nu = \frac{v_F^2/4}{\gamma_{ee} + \gamma_{mr}}, \tag{6.17}$$

where γ_{ee}, γ_{mr} are the e-e scattering and momentum relaxation rates. The Gurzhi length is written as

$$l_G = \sqrt{\frac{\nu}{\gamma_{mr}}} = \sqrt{\frac{v_F^2/4}{\gamma_{mr}(\gamma_{mr} + \gamma_{ee})}}. \tag{6.18}$$

The Gurzhi length decreases with T due to the increased e-e scattering rate. The system will be most viscous at the lowest temperature where viscosity is still well defined. At low temperature, $\gamma_{ee} \to 0$, so the Gurzhi length asymptotes to the upper bound of

$$l_G \to \sqrt{\frac{v_F^2/4}{\gamma_{mr}^2}} = \frac{v_F}{4\gamma_{mr}}. \tag{6.19}$$

If we take the condition that $l_G \gtrsim L/4$, where L is a sample dimension, as an approximate requirement for seeing viscous effects, and use $v_F = l_{mr}\gamma_{mr}$, where l_{mr} is the

momentum relaxation length, we obtain

$$l_{mr} \gtrsim L. \tag{6.20}$$

Note that Eq. 6.19 is an upper bound for l_G, and adding in e-e scattering will only decrease l_G and make the flow less viscous.

6.10 Conclusion

We demonstrated in a monolayer graphene Corbino device, the hydrodynamic suppression of the Lorenz ratio coincides closely with a negative thermal magneto-resistance , when using Johnson noise in the self-heating configuration to measure thermal magneto-resistance. The decrease in thermal resistance with B arises from a combination of (1) redistribution of the viscous spatial heating and thus spatial temperature profiles with B due to additional velocity gradients, and (2) a different viscous weighting function for the average temperature measured by Johnson noise.

This negative thermal magneto-resistance is a "smoking gun" signature for observing viscous flow in a low-dimensional electron-hydrodynamic system. Additionally, even a plateau in the thermal MR, but not in the electrical MR, still indicates viscous heating, as the relative changes in $f(B)$ and $1/\kappa_{xx}(B)$ cancel out. In contrast to other electrical-only viscosity experiments, which often rely on quantitative measurements of electrical resistance over different temperatures and sample geometries to confirm viscous flow, our method for detecting viscous transport provides a distinctive sign change of the thermal MR, thus being relatively insensitive to the detailed parameters in the theoretical model. Moreover, it is a global measurement of the device and does not rely on strategic placement of local voltage or scanning probes.

While the Lorenz ratio suppression is a more quantitative measurement for hydrodynamics, we emphasize that this suppression is distinct and broader in scope than viscous transport. Viscous flow will have a relatively low upper temperature cutoff due to the decreasing viscosity and Gurzhi length with T, but the Lorenz ratio would continue getting further suppressed with T, mediated by the ratios of the microscopic e-e scattering rate to the impurity/phonon scattering rate. However, eventually at higher temperature, optical phonon scattering would both close the hydrodynamic window[69] and overpower the electronic diffusion cooling in our experiment[96].

In addition to the qualitative aspect of detecting viscous flow, we are able to calculate the Ohmic and viscous dissipation constants γ_{mr} and ν, showing that both play important roles in determining the dissipative device properties. Devices with lower disorder and lower γ_{mr} than ours would likely be more dominated by the viscous term.

Our method could be easily generalized to other materials, including bilayer graphene and twisted graphene systems, in the search for hydrodynamics and other strongly correlated regimes. It could also potentially apply even in the presence of more moderate electron-phonon coupling, as the phonon cooling power would not depend on applied magnetic field, but the heating profile could still acquire such a dependence due to viscous heating. In this regard, our method could potentially be applied to more general systems beyond graphene, including bulk 3D materials.

Science cannot solve the ultimate mystery of nature. And that is because, in the last analysis, we ourselves are a part of the mystery that we are trying to solve.

Max Planck

7

Conclusion: Future Work and Outlook

We thank the reader for making it this far. As we have now seen, experiments with Johnson noise thermometry are extremely delicate, and the results are often difficult to interpret in the context of many confounding variables that are difficult to

quantify. In this dissertation, we have focused on RF JNT due to its advantages over traditional low-frequency JNT, in particular the significantly faster measurement times. We have explored many of the technical intricacies of measurement techniques, both for measuring the noise and for interpreting it in the context of thermal conductance measurements.

In the author's personal opinion, the most significant technical contribution has been characterizing the nonlinearity-induced noise modulation effect, as described in Section 4.9 and described in Eq. 4.54. This newfound understanding allowed us to critique the results of the Crossno experiment[1], which has been the central experimental motivator for the work in this thesis. As we saw, the case of the Dirac fluid in graphene is not fully settled, and future experiments on this platform are warranted to gain a deeper understanding.

Measuring the nonlinearity of graphene devices is a difficult process due to the small signals and harmonic distortion effects, but when done carefully, it enables us to verify or correct our JNT measurements. As was shown in Fig. 4.26, there is still a mysterious, perhaps missing, factor of $\sqrt{2}$ that is unexplained in the nonlinearity correction, and the reader of this thesis is invited to perform their own studies of the nonlinearity effects to hunt it down.

Chapter 4 has aimed to explain all the JNT techniques that we developed during the course of this thesis, so that future experimentalists can harness their power and continue or build further upon the projects described in this work.

7.1 Summary of Experimental Results

Experimentally, we have focused on two main effects related to graphene hydrodynamics. The first effect was discussed in Chapter 5, and is the suppression or enhancement of the Lorenz ratio, deviating away from the WF law, when electron-electron or electron-hole scattering becomes comparable or dominant to impurity or phonon scattering. Generally, electron-hole scattering near charge neutrality will increase the Lorenz ratio, and electron-electron scattering away from charge neutrality will suppress the Lorenz ratio.

In monolayer graphene, most devices have shown both of these effects. However, the data from device MLG1A shows that in the limit of clean graphene, the enhancement at charge neutrality may not be present, for reasons that we do not yet understand. The suppression away from charge neutrality may sometimes be hidden by contact resistance effects, as for devices MLG2S / MLG2L.

For bilayer graphene, the strong apparent enhancement at charge neutrality appears to be caused by phonon cooling, and we cannot measure the true electronic thermal conductivity. There is evidence that there is some suppression of the thermal conductance at higher temperatures away from neutrality, based on the temperature scaling of the thermal conductance, but this is not directly measurable and is only a perturbation on a large phonon cooling background. Overall, BLG appears to have stronger electron-phonon coupling than MLG and a lower temperature crossover point from electronic diffusion cooling to phonon cooling.

The second effect is the signature of viscous electronic heating, as opposed to Ohmic heating, and was discussed in Chapter 6. Most importantly, we have shown that for monolayer graphene, the region of the Lorenz ratio suppression, whether absolutely

below 1 or just relative to the low-T value, occurs in the same region of (n, T)-space as viscous heating, detectable as a negative generalized thermal magnetoresistance. The coincidence of these effects serves as empirical evidence of their mutual origin in viscous graphene hydrodynamics.

7.2 Ongoing and Proposed Future Experiments

During the course of this work, we have started some Johnson noise thermometry experiments that will need additional work to complete, as well as conceived other novel related experimental ideas. In this section, we describe some of the ongoing experiments and show their preliminary results, motivating further work on the subjects.

7.2.1 Thermal Conductivity in Quantum Hall Landau Levels

In a quantizing magnetic field, electrons in 2 dimensions form flat bands called Landau levels (LLs) in the bulk of a material[231,232]. Due to the strongly quenched kinetic energy, even nominally weak Coulomb interactions between electrons can become relevant and lead to strongly correlated dynamics, exhibiting phenomena like the fractional quantum Hall effect in fractionally-filled LLs[233]. In particular, graphene has exhibited a rich variety of physics in the fractional quantum Hall effect and drawn much experimental and theoretical attention, but not everything is yet well understood[18,234,235].

One additional tool to probing interactions in the quantum Hall or fractional quantum Hall effect would be through thermal transport. Some work has already been done in studying thermal conductance of edge states[143,175,236–239]. A very recent experiment has measured the bulk thermal conductance by subtracting away the edge state thermal conductance[240], but to our knowledge no one has yet directly measured the bulk thermal

condutance in a quantum Hall state.

The bulk electrical condutance of a quantum Hall state will depend on the level filling number N; it will be very low in the plateau regions where the bulk is gapped ($N \sim$ integer), and higher in transition regions where the chemical potential is inside of a LL. The thermal conductance would likely trend with the electrical conductance, being low in the gapped regions and higher inside the LLs themselves. Some lower-numbered degenerate LLs begin splitting into non-degenerate integer levels, and then further into fractional levels, as the magnetic field is increased. Studying thermal conductance at these filling levels that correspond to splittings can reveal more details about the exotic interactions and behavior.

During the course of this thesis, we have performed some preliminary measurements of the bulk thermal conductance and Lorenz ratio of degenerate LLs at intermediate magnetic fields, and we have set the stage for future experiments to complete a more accurate and thorough study.

To completely avoid the effects of edge states and to probe only the bulk, we utilize the Corbino geometry on devices MLG3 and MLG4, whose data at zero and low magnetic field was shown in Chapters 5 and 6, respectively. The primary challenge of this thermal conductance measurement is the strong I-V nonlinearity due to the alternately compressible and incompressible Landau level structure, causing nonlinearity-induced noise modulations that must be measured and subtracted out. The quantum Hall effect in graphene is best observed at the lowest temperatures possible, and in the VTI cryostat used for this study, the sample sits at $1.5 - 1.7$ K while the lowest attainable $T_{N,in}$ parameter is about 21 K. So far, we have not yet been able to tune this parameter lower to match the sample temperature in order to cancel out the parasitic effect.

Fig. 7.1(a) shows the 2-terminal Corbino resistance measured for the $N = -1, 0, 1, 2, 3$

LLs (located between filling numbers $\nu = -6, -2, 2, 6, 10, 14$) at $T = 1.8$ K; $B = 1$ T. The resistance is measured for several different biases, and the spread of resistance for different biases is related to I-V nonlinearity at that point, in part from the temperature dependence of the resistance. Because the resistance is significantly higher than the values at $B = 0$, and the contact resistance is not expected to change significantly with magnetic field, our device is likely in the regime of ultra-low contact resistance relative to the channel resistance, providing significantly improved accuracy of the thermal conductivity measurements. Additionally, at this low temperature, we do not have to consider phonon cooling.

Fig. 7.1(b) shows the temperature rise for heating with a ~ 250 μV bias. The red curve shows the measured heating, computed directly from the noise modulation. The green curve shows the corrected heating, using the nonlinearity correction presented in Chapter 4. The light blue shaded region shows the difference between the measured and corrected temperature rise. Near full LL fillings, when the resistance is large and the Fermi level is in the gap, the corrections to the measured temperature rise are large and likely untrustworthy, possibly due to higher-order $4f, 5f$ nonlinearity modulations.

The black curve indicates what the temperature rise would be if the Lorenz ratio of the sample was 1. This curve is not flat due to the measurement algorithm that sets the bias; the bias voltage is nominally set to a constant value via feedback for the highest measured bias (here, 2mV), and then the applied current is scaled down for other bias points, under the assumption of constant resistance. In reality, the measured AC resistance has a bias dependence, so with appropriate scaling down of the current, the bias voltage does not get scaled down evenly.

We shall limit our discussion only to the measured temperature rise near the center of the LLs, where the resistance is at a local minimum and the bulk is compressible. Here,

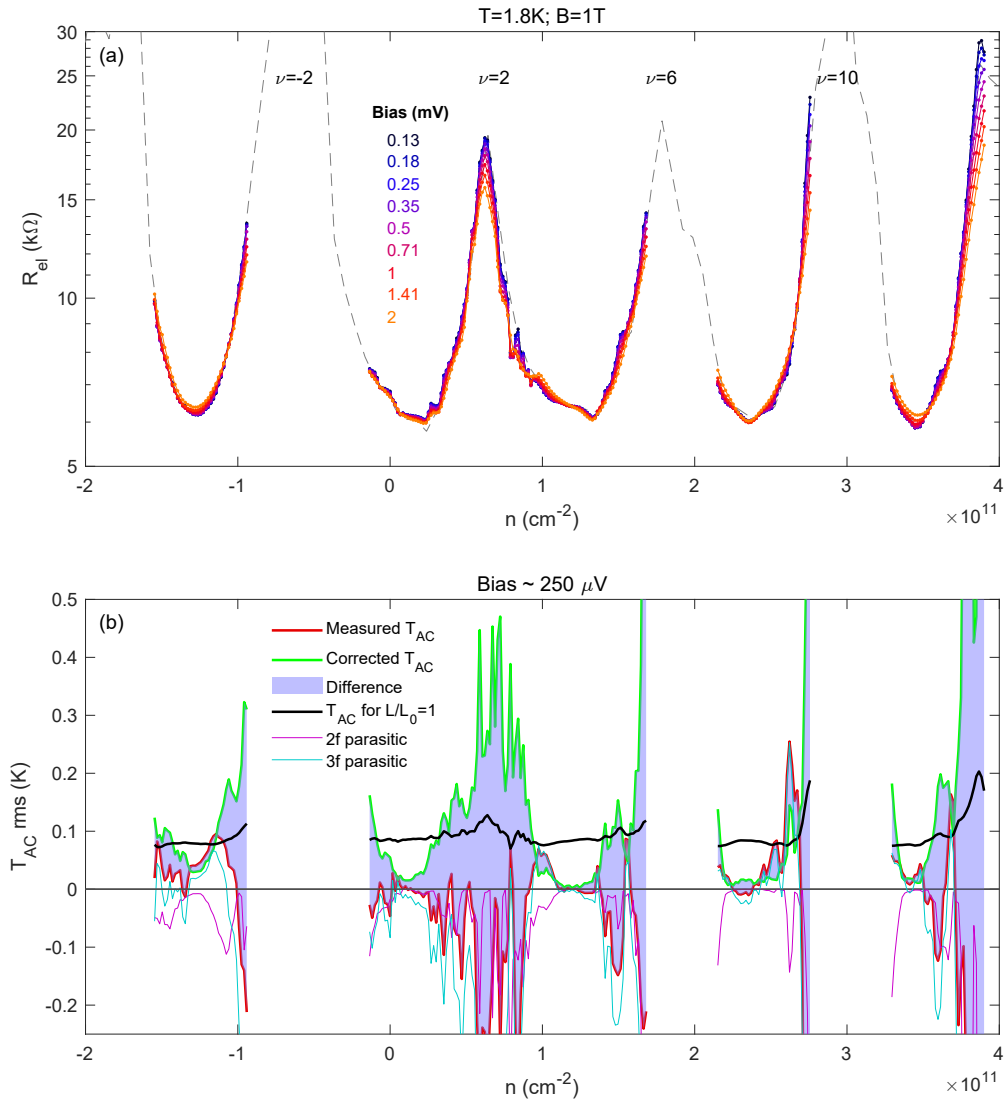

Figure 7.1: **(a)** Measured resistance of MLG5 in quantum Hall at $T = 1.8\,\mathrm{K}$, $B = 1\,\mathrm{T}$ vs density, for different AC excitation biases. The filling numbers ν are labeled at the resistance peaks, which correspond to points when the Fermi level is in the gaps. The resistance peaks were not measured for all of the biases shown, and the gray dashed curve indicated the approximate shape from another scan. **(b)** Measured temperature rise under a $\sim 250\,\mu\mathrm{V}$ bias, corresponding to the Landau levels shown in (a). Red: raw measured temperature rise. Green: Temperature rise after correcting for the nonlinearity modulation effect. Blue shading: indicates the difference between the green and the red. Black curve: The expected temperature rise for $\mathcal{L}/\mathcal{L}_0 = 1$ at this bias. Violet curve: the $2f$ parasitic component of the nonlinearity modulation effect. Cyan curve: the $3f$ parasitic component of the nonlinearity modulation effect.

the measured temperature rise is significantly lower than that for a Lorenz ratio of 1, indicating a highly enhanced Lorenz ratio above the WF law. The individual $2f$ and $3f$ components to the correction are plotted in magenta and cyan, respectively; we can thus verify that the individual components of the correction are not just cancelling each other out. Near the centers of the LLs, the correction takes on very small absolute values, especially between $\nu = 2$ and $\nu = 6$. Without being certain of the exact accuracy of the correction, we can nonetheless confidently conclude that the measured temperature rise is significantly reduced relative to the WF law.

However, relative to the actual value of the temperature rise, the correction is still large. The Lorenz ratio is enhanced significantly above 1, but we are not able to accurately quantify it; it may be anywhere from ~ 5 to ∞. Additional data from this experiment is presented in Appendix A.

We propose that the enhanced Lorenz ratio may be a result of strongly interacting and correlated electron dynamics, enabled by the kinetic energy quenching of the flat bands. Aside from the very recent work in Ref. 240, which even then only considers Coulomb interactions between localized bulk states in the quantum Hall plateaus, to our knowledge there is no theoretical work in understanding bulk thermal conductance within LLs. We thus encourage the theoretical community to explore this avenue as another perspective on partially filled LLs.

Further experiments on this project should attempt to optimize the matching circuit so that the points of low or minimum nonlinear effects (i.e. $\frac{dg}{dR}$ or $\frac{d^2g}{dR^2}$), would coincide with the measured sample resistances, as was demonstrated in Figs. 4.22 and 4.25(a,b). This would involve building an impedance matching circuit centered likely somewhere around $5 - 20\text{k}\Omega$, depending on how high of a magnetic is desirable.

7.2.2 Bilayer Graphene: Shot Noise as a Way to Study Hydrodynamics

We have previously discussed the high-T limit of Johnson noise under DC bias as that of the interacting hot-electron shot noise in Section 3.4. In this case, the Fano factor is $F = \sqrt{3}/4 \approx 0.433$[170], which corresponds to $\mathcal{L}/\mathcal{L}_0 = 1$. We have measured the shot noise of bilayer graphene, at a base temperature of $T_0 = 4.5$ K, and plot the results in Fig. 7.2. We find that the Fano factor over the densities shown varies between 0.29 and 0.34, rather far from the expected value of 0.433 for the interacting hot electrons obeying WF cooling. As a reference, we plot the expected shot noise for non-interacting, diffusive hot electrons as the black dashed lines, which have a Fano factor of 1/3.

Interestingly, the shot noise for many densities follows approximately along the 1/3 curve before deviating away from it at higher temperature. The presence of phonon cooling would lower the temperature and thus cause the shot noise to go below the dashes lines. However, for some densities, including $n = 3,\ 6 \times 10^{11}$ cm^{-2}, the shot noise goes above the dashed lines. This indicates a reduction in cooling power at higher temperatures.

It is unclear why even at low electron temperatures, there is an apparent deviation below the WF law of about $\sim 20\%$. It is possible that it stems from contact resistance affecting the noise measurement. At higher temperatures, the conditions could become highly non-equilibrium, making experimental interpretation difficult.

We propose this shot noise method as a potential alternative method to studying electron hydrodynamics in BLG without the involvement of phonon cooling. The electrons can be heated to extremely high temperatures of several hundred K without significantly heating the phonons, which likely remain close to the bath temperature. Hotter

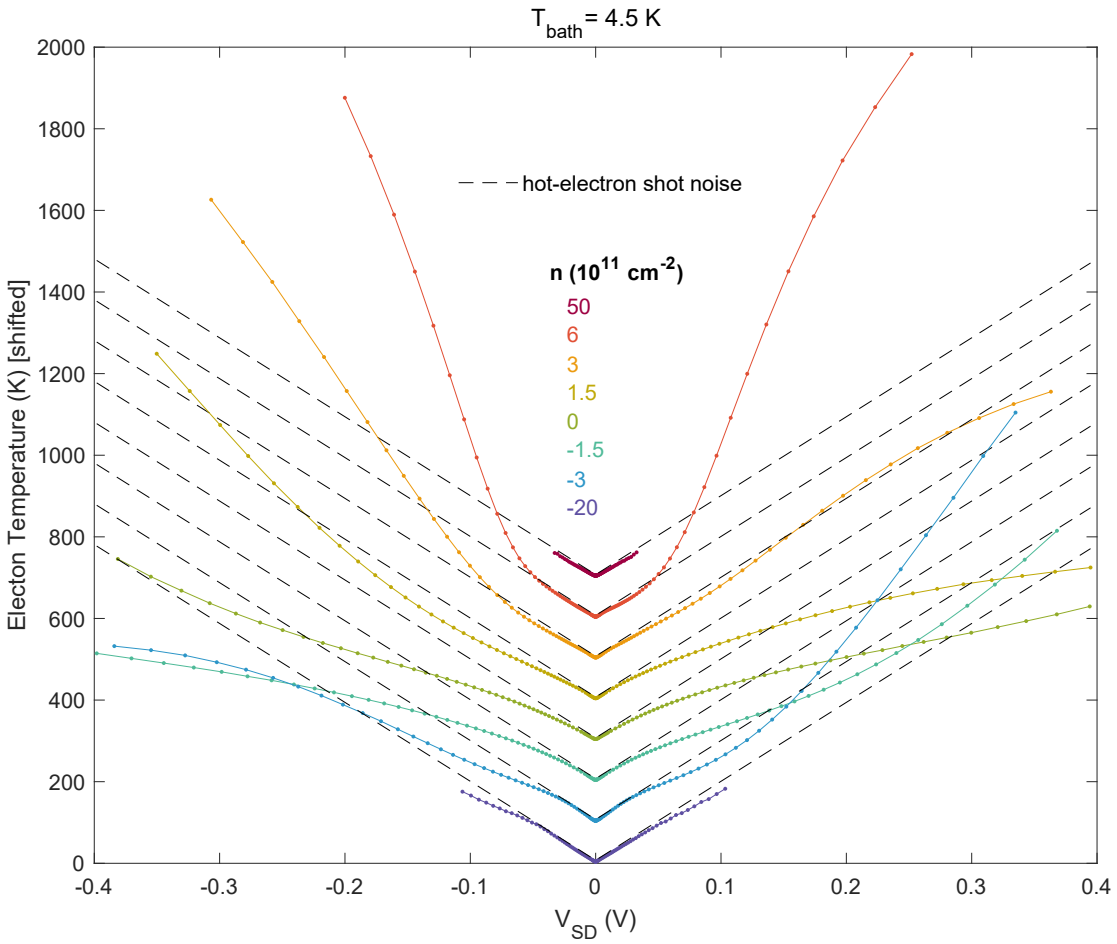

Figure 7.2: Shot noise measurements of BLG2, for different densities, shifted vertically for easier viewing. Black dashed lines are the exptected non-interacting hot electron shot noise, with Fano factor $F = 1/3$[170].

electrons will likely be more hydrodynamic and can thus show deviations from the WF law. However, care must be taken to understand the highly non-equilibrium situations at high bias.

7.2.3 Exploring Nonlinear Johnson Noise

So far in this work, we have assumed that the effective Johnson noise temperature of a nonlinear graphene sample under bias is equal to its true temperature. However, Ref. 203 considers a specific set of assumptions for a nonlinear resistor and calculates the apparent Johnson noise temperature, show that it can be higher or lower than the actual temperature, allowing for example the possibility of the sample to act as a refrigerator.

In this subsection, we propose a method to directly measure such a temperature deviation of a nonlinear graphene sample. Using the convention defined in Eq. 4.55, we can write the first and second order differential conductances as

$$\frac{dI}{dV} = \frac{1}{R_1 + 2R_2 I + 3R_3 I^2} \tag{7.1}$$

$$\frac{d^2 I}{dV^2} = -\frac{2R_2 + 6R_3 I}{(R_1 + 2R_2 I + 3R_3 I^2)^2}. \tag{7.2}$$

The term β characterizing the device nonlinearity defined in Eq. 22 of Ref. 203 is then

$$\beta = -\frac{1}{2} \cdot \frac{2R_2 + 6R_3 I}{R_1 + 2R_2 I + 3R_3 I^2}. \tag{7.3}$$

The apparent temperature t_n of the device, relative to the actual temperature T, is then

$$t_n = T \cdot (1 + R_2 I + 3R_3 I^2). \tag{7.4}$$

The I^2 term (measured as the $2f$ noise modulation) would be indistinguishable from the I^2 Joule heating, and if present, would affect the accuracy of our thermal conductance measurements. However, there should be no $\propto I$ term from Joule heating, and thus any apparent temperature modulation at $1f$ would come from this nonlinear term. We explicitly note that this nonlinear term directly describes the inherent nonlinear noise in the device; this contrasts with the extrinsic noise modulations induced by impedance matching modulations as described in Chapter 4.

With impedance matching g, if the normalized noise n is given as a function of I by

$$\begin{aligned} n(I) =& g t_n(I) + (1 - g(I))T_{N,in} + T_{N,out} && (7.5)\\ =& g\left(T \cdot (1 + R_2 I + 3R_3 I^2)\right) + (1-g)T_{N,in} + T_{N,out}, && (7.6) \end{aligned}$$

then the measured $1f$ noise modulation will be given by

$$\begin{aligned} \frac{dn}{dI} &= g\frac{dt_n}{dI} + \frac{dg}{dR}\frac{dR}{dI}\left(t_n - T_{N,in}\right) && (7.7)\\ \frac{dn}{dI}\Big|_{I=0} &= gR_2T + 2\frac{dg}{dR}R_2\left(T - T_{N,in}\right). && (7.8) \end{aligned}$$

In Eq. 7.8, the first term corresponds to the intrinsic nonlinearity described in Ref. 203, and the second term corresponds to the noise modulation by impedance matching modulation. The second term can be nulled by working at a sample temperature equal to $T_{N,in}$, (and further nulled by tuning the gate so that $\frac{dg}{dR} = 0$), thus isolating the first term with the possibility to directly measure it, along with its expected value from the measured R_2 value. Such an experiment would be relatively straightforward to perform with the techniques described in Chapter 4.

7.2.4 Thermal Conductivity in Moiré systems

In 2018, superconductivity was discovered in magic-angle twisted bilayer graphene[241,242] (MATBG) with a phase diagram closely resembling that of the high-T_c cuprates, showing many different correlated phases. The correlations arise from flat band physics, where the twisting of the two layers relative to each other creates a Moiré pattern that hybridizes the band structure of both layers in a particularly sensitive way to create a flat band for a certain narrow range of twist angles. In the following years, interest in Moiré materials grew exponentially, and many other Moiré systems were also shown to host a rich variety of correlated phases[243–247], including, for examples twisted double bilayer graphene[248,249] (TDBG).

Given that the Johnson noise techniques presented in this thesis have been developed on graphene, extension of these experiments to MATBG and TDBG would be a rather straightforward exercise, although caution always needs to be taken with regards to contact resistance and phonon cooling modes. The correlated insulating phases can be studied using nonlocal noise thermometry[174].

7.2.5 Nonlocal Noise Thermometry to Escape Contact Resistance Effects

As was described in Chapter 5, contact resistance can play a significant hindering role in the self-heating JNT setup for measuring thermal conductance. Electrically, the contact resistance simply adds to the total resistance, but in the thermal self-heating setup it has a more complicated role.

Using the geometry of the nonlocal noise thermometry[174] for measuring thermal conductance, the contact resistance between the sample under study (the bridge region)

and the two side thermometers becomes additive to both the electrical and thermal resistances of the bridge. In this way, the effect of the contact resistance on Lorenz number measurements is significantly simplified, in comparison to Eq. 3.51 and the discussion in Appendix C. However, the contact resistance in the self-heating configuration for the hot- and cold-side thermometers will still play the same significant role, and can thus affect the accuracy of the measurement, although now indirectly.

Furthermore, the effects of contact resistances could potentially be completely subtracted out by implementing a thermal analog to the electrical TLM method, with several nonlocal "H" devices with bridges of varying lengths fabricated from the same heterostructure. However, such an implementation requires many additional RF lines and LNAs.

7.2.6 Nonlocal Noise Thermometry with Superconducting Contacts

The nonlocal noise thermometry technique[174] could also be modified slightly by using superconducting contacts on the hot-side thermometer. Changing the normal metal contacts for superconducting contacts would change the temperature profile from parabolic to nearly flat, since in the absence of electronic diffusion cooling to the contacts, phonon cooling would dominate. Additionally, the lack of contact resistance on the hot-side thermometer would improve the measurement accuracy of the peak temperature.

7.3 Closing Remarks

Viscous hydrodynamics continues to be an exciting research field in graphene, albeit with very difficult experiments. The hydrodynamic regime is difficult to access in

graphene, especially given that the presence of graphite gates tends to complicate RF JNT measurements due to the thinner h-BN dielectrics involved. Nonetheless, we hope that future experiments on ultraclean, graphite-gated devices will provide more insights into this exciting regime in graphene, as well as open up new opportunities for device applications. Moreover, we hope that the techniques and insights gained during the course of this dissertation will be applied to other exotic materials, especially Moiré-based superconductors. With the atomic precision available to vdW-based materials and devices, the possibilities of atomic-scale device perfection are limitless.

There is nothing new to be discovered in physics now. All that remains is more and more precise measurement.

William Thomson, Lord Kelvin

A

Supplementary Data

In this Appendix, we present additional data to supplement that shown in the main text. We include some calibration profiles of various devices and matching circuit parameters to showcase examples of typical calibrations, as well as those with some technical

issues. For completeness, we also show data for two additional BLG devices, which, however, had some flaws in the fabrication or measurement technique. We will also show the raw thermal conductance data for several devices, as in the main text we have mostly examined only the electrical resistance and Lorenz ratios.

A.1 Dual-Graphite Gated BLG: Gate-Line Noise

Here we show thermal conductivity data for BLG3, a dual-graphite gated BLG device. In this device, the bottom h-BN was 140 nm and the top h-BN was 7.5 nm. This large difference in thicknesses was intentionally chosen so that the CHF3/O2/Ar etch for the contacts (see Appendix B) was easy to do without shorting to the global bottom graphite gate. However, one unintentional side-effect of the very thin top BN was to make the device very sensitive to gate-line noise amplification (see Section 4.10). Moreover, the cryostat for this device had been recently reconfigured before the measurement, and the noise filtering strategies on the thermometer and heater lines had not yet been optimized. We were not aware of this gate-line noise effect at the time, but in retrospect, we believe this effect artifically caused the Lorenz ratio to be significantly suppressed at all temperatures. The trends in this device are inconsistent with BLG2 and BLG4 presented in Chapter 5, so we thus believe the data to be incorrect. Nonetheless, we still present the data for completeness, shown in Fig. A.1.

Additionally, we show the behavior of σ and $\mathcal{L}/\mathcal{L}_0$ vs μ/k_BT in Fig. A.2. The conductivity σ is calculated using the 2-terminal resistance and the sample aspect ratio, and includes the effects of the contact resistance. The true sheet conductivity would be significantly higher. Curiously, for all temperatures above 20 K, the Lorenz ratio collapses onto a universal curve for a large range of μ/k_BT. Initially, we though this

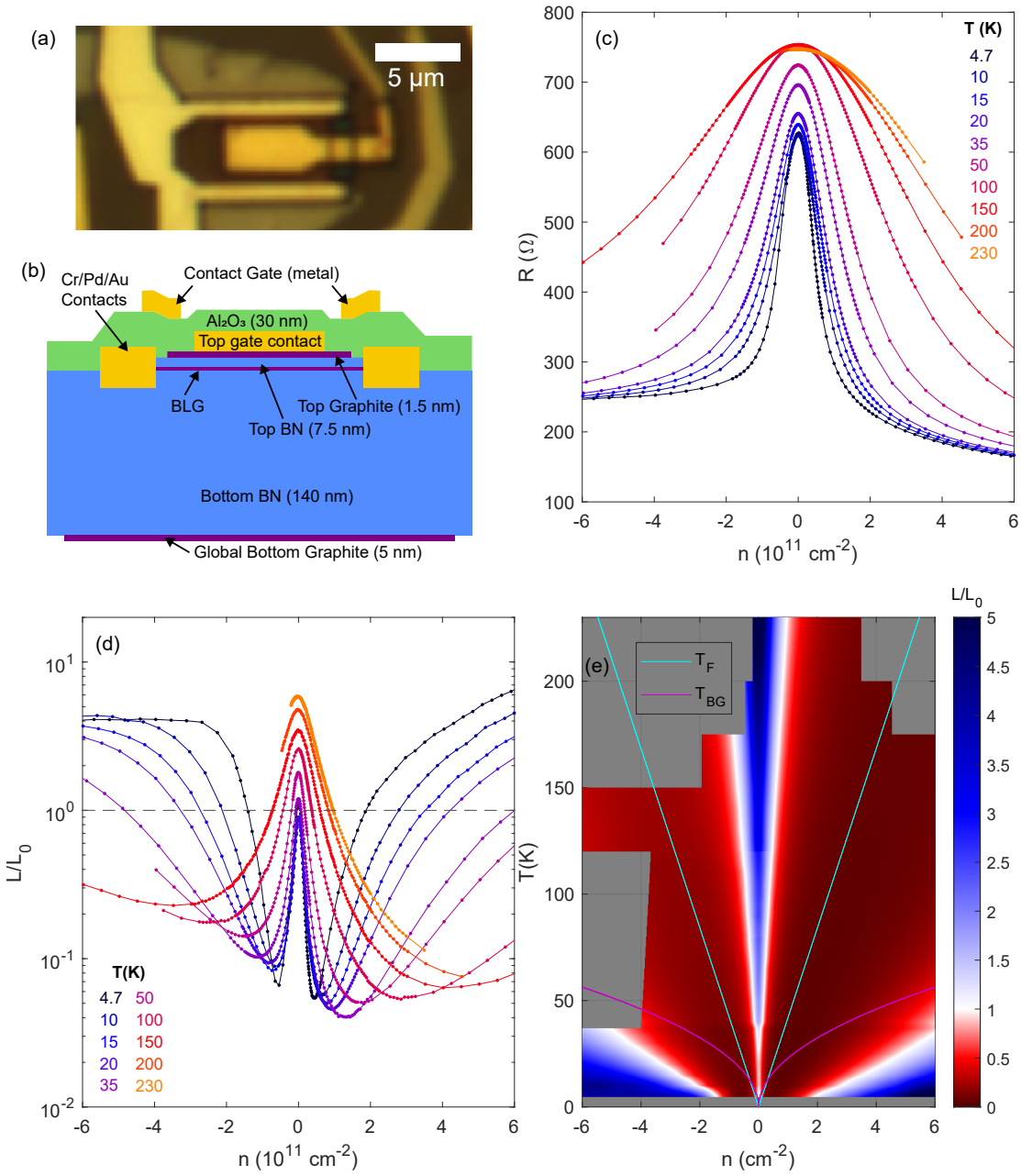

Figure A.1: **(a)** Optical micrograph of the BLG3 device. The central metal panel connects to the top graphite gate, and the U-shaped metal gates the graphene between the metal contacts and the top graphite gate. **(b)** Schematic cross-sectional diagram of the device (not to scale). **(c)** Resistance traces vs density for all measured temperatures. **(d)** Measured Lorenz ratio linecuts vs density for all measured temperatures. The suppression of the Lorenz ratio very likely is caused by the gate line noise amplification effect. **(e)** Colormap of the Lorenz ratio data from (d).

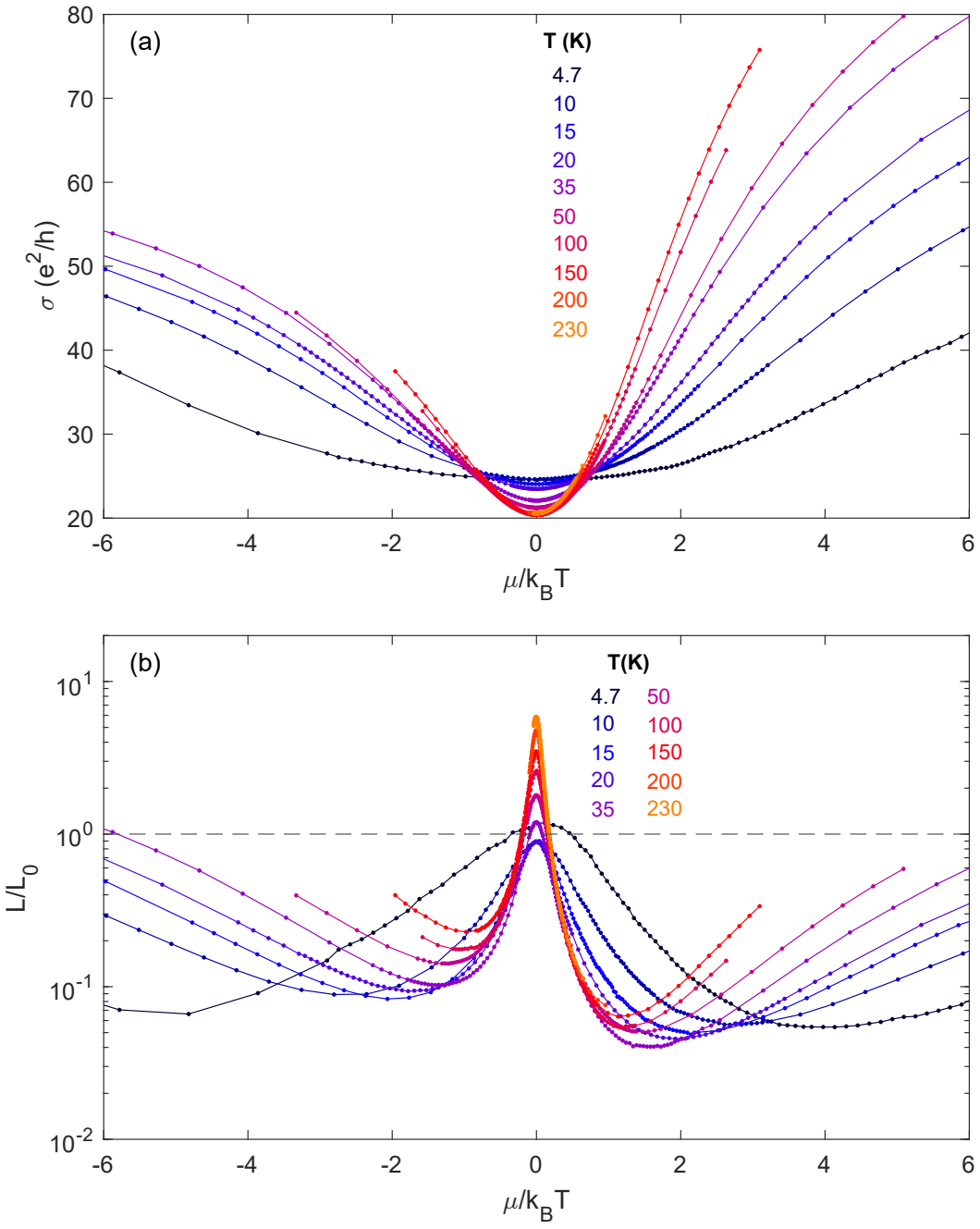

Figure A.2: **(a)** BLG3 conductivity traces for different temperatures, plotted vs μ/k_BT. **(b)** Lorenz ratio traces for different temperatures, plotted vs μ/k_BT. Interestingly, the Lorenz ratios appear to collapse onto a single curve for the suppressed regime, but this may be just a coincidence from the gate-line noise amplification effect.

universal collapse was a signature of hydrodynamic suppression; however, it seems to be caused by the temperature-dependent width of the resistance peak vs gate voltage, combined with the gate-noise-amplification effect.

A.2 Landau Levels

Here, we show additional data for LL thermal conductivity in the quantum Hall regime, in the same manner as Subsection 7.2.1. This data is for MLG5, the other Corbino on the same chip as MLG4 (See Fig. 5.14(d).). Fig. A.3 shows LL data at $T = 5\,\mathrm{K}$ and $B = 1\,\mathrm{T}$, for $-50 < \nu < 54$. In panel (a), the resistance oscillates as the Fermi level moves in out of LLs. Curiously, the electron-side resistance oscillation is much lower than that of the hole-side resistance; this is possibly related to the electron-side contact resistance being lower, but we do not understand the direct connection. Panel (b) shows the measured temperature rise in red and the corrected temperature rise in green. These are to be compared with the black curve, showing the expected temperature rise if the Lorenz ratio were equal to 1. Again, in the incompressible regions, the device nonlinearities are higher and the correction is less trustworthy. Similar to what we saw in Subsection 7.2.1, the Lorenz ratio inside the LLs appears to be enhanced above 1 to varying degrees.

For the lower LLs, between $\nu = -2$ and $\nu = 6$, the temperature rise is again very low and with low values for the correction, with some uncertainty around zero, suggesting highly-elevated but not exactly quantifiable elevated Lorenz ratio.

For higher LLs, on both the electron and the hole sides, the meausured temperature rise is above that for $\mathcal{L}/\mathcal{L}_0$; however, the correction moves it back down below, indicating that the Lorenz ratio is somewhere between about 1.5 and 2. At higher temperatures and higher filling fractions, the energy spacing between the LLs can become comparable

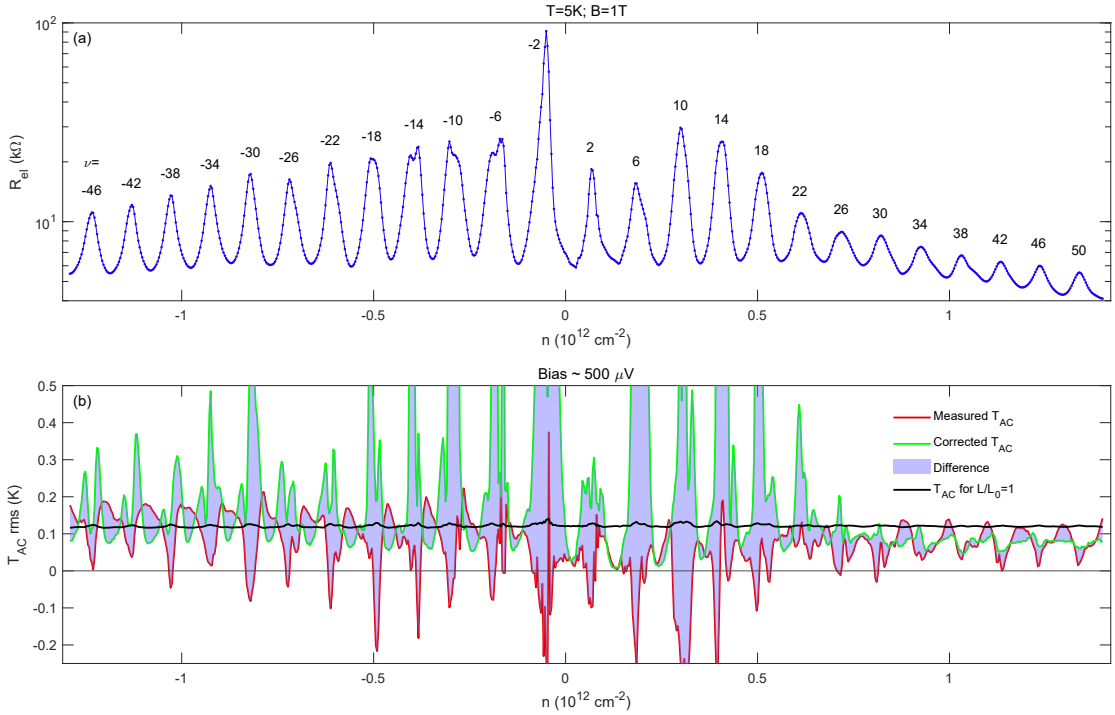

Figure A.3: **(a)** Measured resistance of MLG5 in quantum Hall at $T = 5\,\mathrm{K}$, $B = 1\,\mathrm{T}$ vs density. The filling numbers ν are labeled at the resistance peaks, which correspond to points when the Fermi level is in the gaps. **(b)** Measured temperature rise under a $\sim 500\,\mu\mathrm{V}$ bias. Red: raw measured temperature rise. Green: Temperature rise after correcting for the nonlinearity modulation effect. Blue shading: indicates the difference between the green and the red. Black line: The expected temperature rise for $\mathcal{L}/\mathcal{L}_0 = 1$ at this bias.

to the thermal energy; in this regime, the behavior of a single LL is not completely isolated, and it is complemented by "classical" or sparse thermal occupation of the LLs above and below, which may distort the measured Lorenz ratio. In this context, this distortion appears the shift the highly enhanced Lorenz ratio back closer to 1, something we would expect as we move towards a more classical, continuous-band system.

A.3 Calibrations

We begin with the calibration for device BLG3 (see Section A.1. Here, we suspect the experimental setup was strongly susceptible to the gate line noise amplification effect. In the calibration, shown in Fig. A.4, we can see some indications for this. The DC Johnson noise vs R traces in panel (a) have a looping behavior at high R, which occurs in the gap region as the gates are swept. We later determined in subsequent experiments that this looping behavior stems from noise in the cryostat gate line, especially when driven by a Keithley 2400 DC voltage source, still passing through the gate line low pass filters. The amount of noise from the DC voltage source depends on the value of the voltage it is outputting, creating the illusion that the DC Johnson noise depends on a parameter other than just temperature and sample resistance. Moreover, similar to the Crossno experiment, we see that the $T_{N,in}$ and/or $T_{N,out}$ parameters appear to depend on resistance through its dependence on the gate voltage. In particular, the DC Johnson noise vs R curves are strongly asymmetric (on a log-x scale) about the point of maximum gain ($\sim 582\ \Omega$). This is more clearly visible in panel (c), where the peak in the gain ($\sim 582\ \Omega$) is strongly offset from the minimum in the noise temperature ($\sim 300\ \Omega$), when they should coincide.

For device MLG4, we performed calibrations for several different values of attenua-

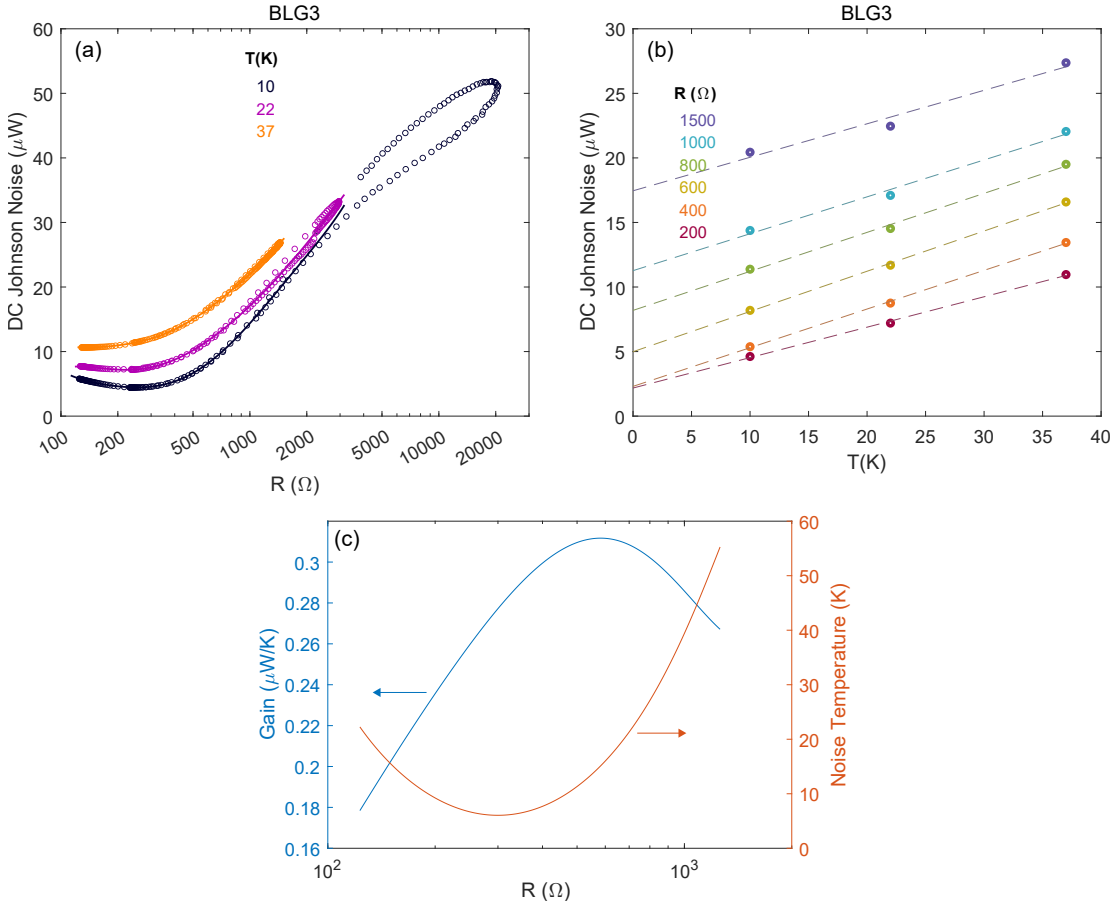

Figure A.4: **(a)** BLG3 calibration traces for three temperatures, showing the DC Johnson noise vs resistance. For a given temperature, the noise is not symmetric about the best-matched resistance ($\sim 550\,\Omega$), and at high-R values, the out-and-back trace does not collapse in on itself. Both of these effects are indicators that noise from the gate voltage source is leaking past a filter and entering into the measured DC noise. **(b)** Corresponding linear fits of DC noise vs temperature, indicating no clear intersection for $T_{N,in}$. **(c)** Computer gain (blue) and noise temperature (red) from this calibration. The mismatch between the peak gain and the minimum noise temperature is again a sign of noise from the gate voltage source leaking past a filter.

tors, in order to obtain several different values of $T_{N,in}$. The raw calibration data for 0 dB and 4 dB attenuation is shown in Fig. A.5. We expect the gain to decrease accordingly with the attenuation. In Fig. A.6, we plot these calibration curves along with the expected matched theoretical gain curves. The inset shows how the measured peak gain depends on the attenuation value, as well as the expected behavior. The values of 0.5 dB and 4dB lie significantly off the expectation curve, but 0, 1, and 2 dB align very well with it. It is possible that those calibration runs were affected by a DC drift of the noise, or that the attenuators do not offer the exact attenuation value specified.

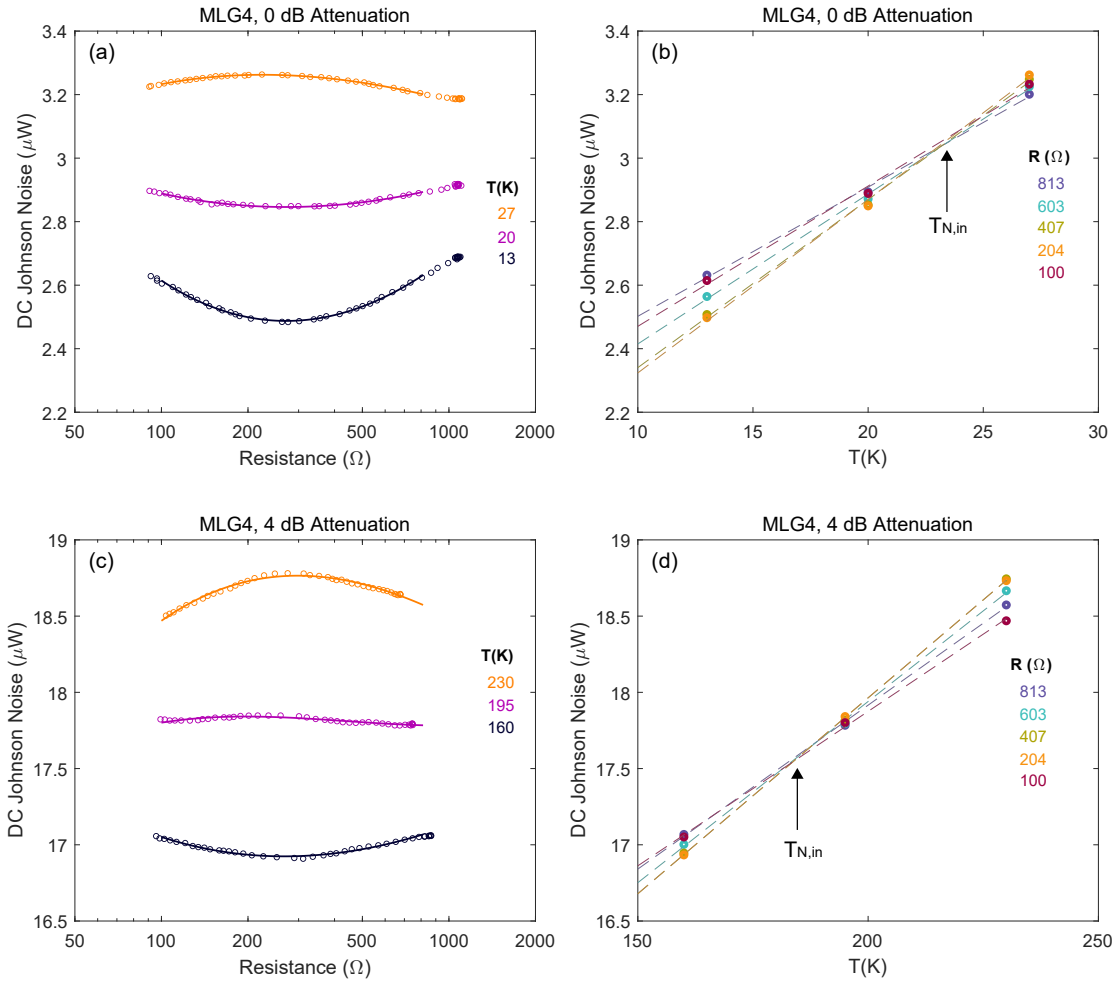

Figure A.5: Comparison of MLG4 calibration with 0 db attenuators **(a,b)** and 4 dB attenuators **(c,d)**. Panels **(a,c)** show the DC Johnson noise vs resistance traces for three temperatures, with the $T_{N,in}$ temperature near the middle temperature for both cases. Panels **(b,d)** show the linear fits of DC noise vs temperature for a few different resistance values, showing the intersection of the best-fit lines occurring at the $T_{N,in}$ values marked by the black arrows.

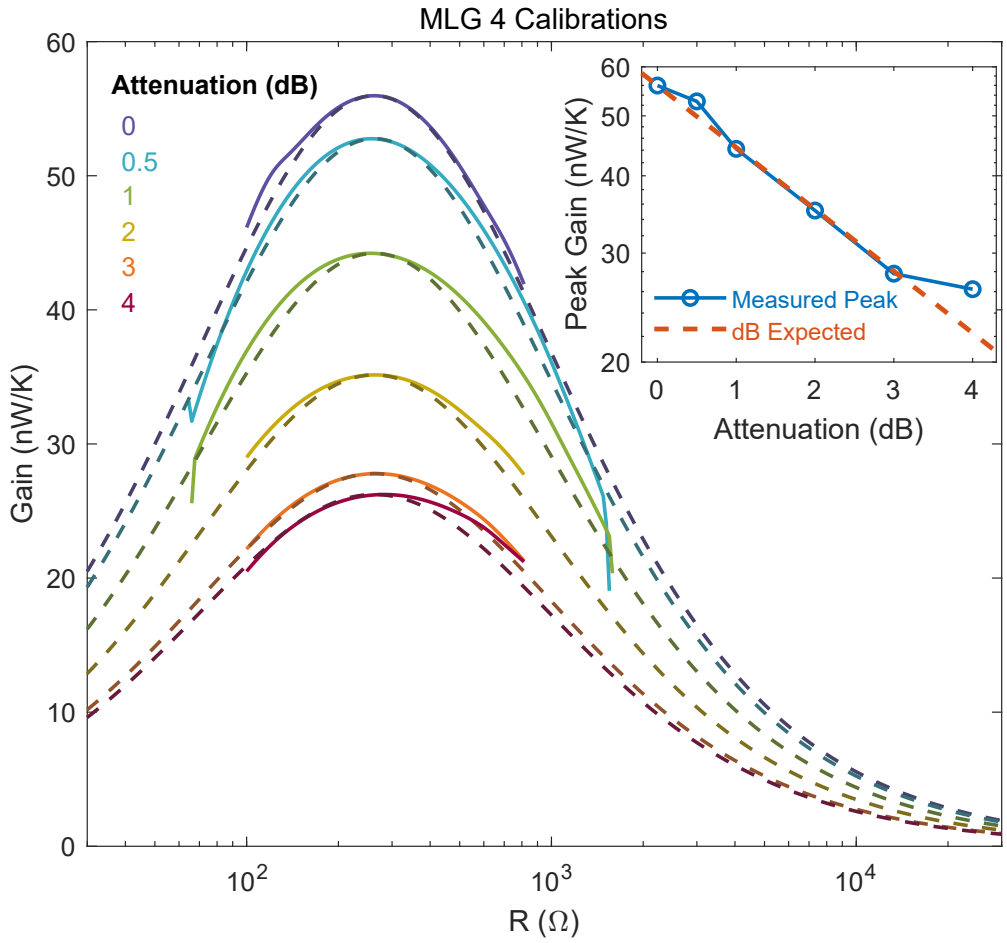

Figure A.6: Calibration data for the Corbino device MLG4 from Chapters 5 and 6. Solid lines are the measured experimental gain, and the dashed lines are the corresponding theoretical gain model. Colors represent the different attenuations used between the sample and LNA. Inset: Blue circles show the peak of the gain, at $R \sim 260;\Omega$, vs the attenuation value. Red dashed line is the expected power decay with attenuation value A_{dB}, $P \propto 10^{-A_{dB}/10}$.

Water is fluid, soft, and yielding. But water will wear away rock, which is rigid and cannot yield.

Lao Tzu

B

Device Fabrication

Fabrication of van der Waals heterostructures is a complicated process involving several distinct steps, and is still an active area of research. A full review and walkthrough of all the techniques used in this work is outside the scope of this thesis. We will provide a brief, non-exhaustive overview of the general steps and fabrication processes, with

appropriate references, to manufacture van der Waals graphene devices.

Due to the certain constraints needed on devices for Johnson noise thermometry, we have modified or developed a certain subset of techniques to better suit our needs. In this Appendix, we will cover these methods in detail for experimental reproduction. Finally, we will cover any additional unique fabrication methods that were developed during the course of this work, that are not limited to just devices for JNT.

B.1 Overview

B.1.1 vdW Heterostructure Assembly

Fabrication of vdW devices first begins with obtaining the raw materials for the heterostructure. In this work, we have used only h-BN and graphite as the raw building blocks. Graphite was obtained from a variety of sources at the discretion of the lab manager based on convenience, including but not limited to kish graphite. Extremely high-quality h-BN crystals were obtained from our collaborators Takashi Taniguchi and Kenji Watanabe at the National Institute for Materials Science (NIMS) in Namiki, Tsukuba, Japan.

The raw materials consist of flakes on or the order of $\sim 10^4$–10^6 vdW layers. The layers are separated repeatedly using the tape method[250], and then transferred to a Si/SiO_2 substrate via the tape. The SiO_2 must be 285 nm for the best optical contrast with graphene. The tape is peeled back, and a small fraction of the flakes or layers remain stuck to the SiO_2.

The substrate is then manually raster scanned under an optical microscope under 10x magnification, while visually observing for flakes. Graphene monolayers have a 7-8% contrast in the green spectrum on 285 nm SiO_2, bilayers have approximately 14-16%

contrast, trilayers have 21-24% contrast, and thicker multi-layers of graphene begin to deviate from this pattern. The 285 nm substrate appears as violet under the microscope, graphene flakes appear as slightly darker violet, and thicker graphite reflects the yellow light from the microscope bulb.

To ease optical strain, and simplify the optical searching process, we implemented using a pure green filter to remove all other colors. Green is chosen because that wavelength has the highest optical contrast for graphene. Visually analyzing a single color channel, green, for contrast differences is less exhaustive than examining the full color gamut for hue and contrast, allowing extensive continual scanning for several hours nonstop.

In contrast to graphene, h-BN flakes display a wide variety of colors depending on their thicknesses. Additionally, the colors change as the objective lens magnification is changed, due to differing numerical apertures. To aid in gauging their approximate thickness from the colors, we have compiled an h-BN color chart, tuned to most closely visually resemble the 10x magnification seen with the naked eye under the microscope, as shown in Fig. B.1.

After the flakes are visually identified and catalogued, they may be scanned with an AFM to confirm thickness and cleanliness.

Next, the vdW heterostructure assembly begins, using a computer-assisted motor-controlled 3-axis micropositioner to pick up, move, and transfer the flakes. The flakes are picked up with a sticky polymer, typically a thin film of PC (poly(bisphenol A carbonate)), mounted on top of a thick ($\sim$ 0.5–1 mm) block of polydimethylsiloxane (PDMS), which is mounted onto a standard microscope glass slide. The slide/polymer assembly must be transparent in order to see the flakes through it using a microscope.

The micropositioner is the main part of the transfer station, the primary tool used in

Thickness (nm)	Image (10x)
6	
10	
21	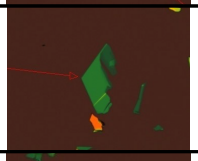
36	
44	
47	
56	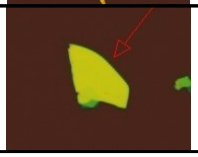

Thickness (nm)	Image (10x)
79	
89	
98	
113	
124	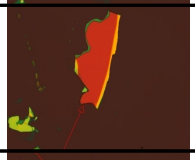
138	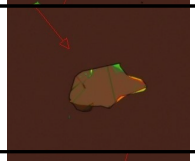
155	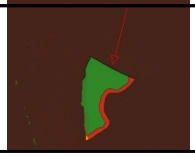

Figure B.1: Color thickness chart for approximately gauging BN thickness. Calibrated colors are for 10x magnification, to match what is visually seen through our microscope. Calibration settings are as follows. RGB white balance = 1 1 2; Exposure = 4 ms; Gamma = 1; Light setting = third tick; Gain = 1; Light source type = Halogen.

the Assembly of these heterostructures. The transfer station has a main temperature-controlled stage for holding the substrate, a micropositioner that holds the slide directly above the stage, and an optical microscope directly above the glass slide. The entire tool sits on a floating air table to minimize vibrations as the atomically-thin layers are handled. One variant of the transfer station is a modified probe station, using a micropositioner modified to hold a slide instead of a probe tip.

The vdW heterostructure is assembled starting from the top layer. If the heterostructure is to have a top graphite gate, then the top layer is either a h-BN flake used to pick up and encapsulate the top graphite, or the top graphite itself. Assembly is usually easier when using an h-BN flake (called the cover BN) to pick up the top graphite, than picking up the top graphite itself, because the top graphite is typically thin (a few nm) whereas the cover BN is thicker (typically 25–50 nm), which provides more structural integrity.

To pick up the top layer, the flake is positioned under the microscope, and the PC polymer (on the transfer slide) is brought into gentle contact with the substrate nearby the flake. By a combination of lowering the transfer slide closer to the substrate, and heating to make the polymer expand, the polymer is made to entirely cover the flake. The polymer should be heated to around 60-80°C and then cooled to about 30-40°C, which allows the polymer to stick to the flake, but unstick enough from the substrate to allow pickup. The transfer slide is then raised, either as the temperature is lowered to $\sim$30°, or mechanically, picking up the flake from the substrate.

The subsequent flake is then positioned under the picked up flake. If picked up flake is h-BN, then the subsequent flake (usually graphene, or top graphite) should be picked up using the h-BN assist technique. In this method, the h-BN is lowered over the next flake from one side, completely covering the flake, but with part of the h-

BN still not touching the substrate. The flake to be picked up should not be in direct contact with the polymer. At this point, the h-BN on the PC is raised upwards, and the vdW attractive forces between the graphene/graphite and the h-BN cause them to stick together, lifting up the flake from the substrate. In this way, the interface between the flakes is never directly exposed to the polymer, allowing exceptionally clean, atomically precise interfaces.

However, when sitting in ambient conditions, the flakes will naturally attract a thin, usually uniform, layer of hydrocarbons on their surfaces that will not usually be visible on a topographical AFM scan of the flake. When the flakes are engaged together during the assembly process, the surface hydrocarbons are usually mobile and will thus get pushed around by the contact interface, often conglomerating into optically visible bubbles. Generally, the hydrocarbons and bubbles are more mobile at higher temperature.

Further flakes are picked up in similar ways, until the entire heterostructure is fully assembled on the transfer slide. Finally, the stack must be lowered onto its final substrate. In this step, a much higher temperature of 180-220°C is used, both to make the bubbles more mobile to push them out of the active area of the stack, and to increase polymer stickiness. The substrate is heated up to this temperature, and then the stack is gently lowered onto it, being careful to push the bubbles in a "clothes-ironing" manner using the contact interface. It is possible to move the interface back and forth repeatedly a few times, by moving the transfer slide up and down, to further push out the bubbles. Finally, the stack is completely lowered onto the substrate, with the polymer contacting the substrate far beyond the boundaries of the stack. The high temperature makes the polymer stick exceptionally well to the substrate. The transfer slide is then lifted, and the PC polymer delaminates from the PDMS, dropping on the stack onto the substrate. A subsequent chloroform and IPA wash will remove the polymer. Optionally, the stack

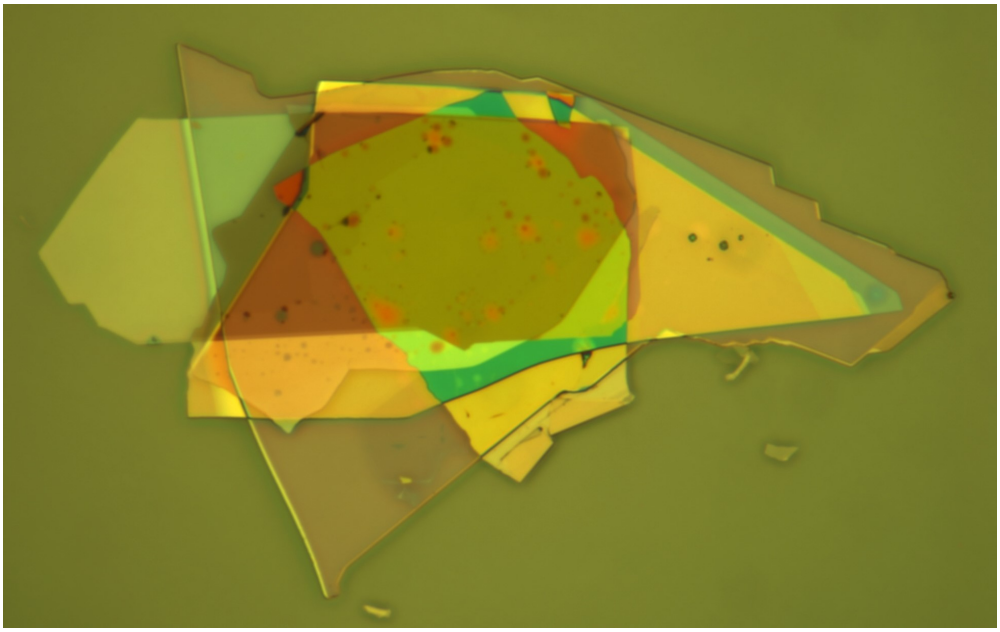

Figure B.2: Optical micrograph showing a completed vdW stack with 6 layers. Bubbles are seen trapped in between layers.

may be vacuum annealed at 350°C to burn off any additional residue (although PC residue requires a higher temperature) and to relieve any possible internal stresses in the assembly.

An image of a completed stack is shown in Fig. B.2. The bubbles in this stack have mostly been pushed out of the active area of the device and pinned to flake edges, but some bubbles have remained in the center.

B.1.2 Nanofabrication of vdW Devices

Next, the stack must be fabricated into a useful electronic device using standard clean-room nanofabrication techniques. Due to the size and precision needed for our features, we use almost exclusively electron beam lithography with PMMA resist to define masks for processing steps. The fabrication process for each device is different, and more steps

are added as needed, but generally, the process will involve the following steps:

1. Alignment marks are defined in the PMMA and then deposited used evaporation and a liftoff technique.

2. The top graphite, if present, is etched into the shape of the top gate via a PMMA/HSQ bilayer mask and an O_2 plasma etch. A $CHF_3/O_2/Ar$ etch is used to etch the cover BN between the PMMA and top graphite. Alternately, the topgate may be created be evaporating metal.

3. Contacts to the device are made by first defining the mask in PMMA; then etching away the BN/Gr/BN using a $CHF_3/O_2/Ar$ RIE plasma etch, or etching the BN selectively up to the graphene using a XeF_2 gas etch (for which a silicon chip must be present in the chamber for the correct chemistry); then finally using 15°angled rotating evaporation (Cr/Pd/Au) and liftoff.

4. The edges of the device are defined via a PMMA mask and a $CHF_3/O_2/Ar$ etch.

5. HSQ as a bridge for gate lines, or as an insulator for gates, is defined.

6. Any thin gates, such as contact gates, are deposited on top of the HSQ

7. Leads and bond pads are created via PMMA mask, metal deposition, and liftoff.

Additional steps are added to define more gates or insulating dielectrics as needed.

B.2 Device Constraints for Noise Thermometry

For performing self-heating JNT, there are several device constraints that must be satisfied in order to get a quantitative measurement of thermal conductance:

1. The device must be spatially homogeneous, in order for the resistivity and thus the Joule power per unit $\mathcal{P}$ area to be constant. Although for the Corbino the Joule power per unit area is not constant, the resistivity must still be constant to get a correct measurement. With this constraint, the goal is to obtain the effectively 1D temperature profile in Eq.3.12. Thus, we must avoid spatially extensive regions between the main gated channel, and the metal contacts. In practice, this means the contacts should be placed as close as possible to the top gate or bottom gate, ideally 150 nm or less.

2. The contact resistance must be low, relative to the channel resistance, as described in Section 3.7.

3. The stray capacitance of the bond pads must be small. In practice, this would mean using an insulating Si substrate, a sapphire substrate, or small bond pads with 50 μm diameter. Additionally, we typically use a Si substrate with a 1 μm wet oxide to reduce the stray capacitance of the bond pads to the Si.

4. The channel length L must be short enough that electronic diffusion cooling $\propto 1/L$ dominates the phonon cooling $\propto L$, but not so short as to make the device ballistic. The ideal length depends on density, temperature, BLG vs MLG, and is still an active area of research. Typically, we use 2.5–3.5 μm as a starting point.

5. We want the h-BN dielectrics to be as thick as possible, in order to minimize the gate-voltage derivative of the device resistance dR/dV_g, to reduce the nonlinear effects and gate-line noise amplification as much as possible.

In satisfying these constraints, we become limited significantly by many of the conventional vdW fabrication techniques used for low-frequency devices and measurements.

For example, a typical multi-terminal Hall bar uses a 4-point method to measure resistance, which eliminates the contact resistance and is unavailable to us. Additionally, the Hall bar, if using a graphite bottom gate, will use a narrow strip-like bottom graphite gate, and have an extensive graphene overhang region, gated by the Si gate or a top gate, connecting the main area of the device to the contact.

In fabricating our devices, we have often tried to use a "global" bottom graphite gate, under the entire h-BN substrate, so that the entire area of the graphene between the metal contacts is gated by this graphite. This method creates significant fabrication challenges, as the metal Cr/Pd/Au contacts to the graphene must be deposited above the graphite into partially etched h-BN, which often has pinholes or spots weakened by the etching that allows the metal contacts to short to the graphite. Later in this Chapter, we describe some of the approaches we have tried to mitigate this issue.

The wet-grown oxide that we use on the Si substrate is more disordered than standard dry-grown oxide, thus having a lower breakdown electric field and not allowing us to gate our devices as strongly as we could on dry-grown oxide.

B.3 Stacking

We have described the general stacking procedure above. In this section, we describe techniques and methods specifically tailored to making devices for self-heating JNT.

One important aspect of devices for JNT is thicker h-BN dielectrics than typically used in other vdW experiments. Typical h-BN thicknesses used in non-JNT experiments are 15–35 nm; however, for JNT experiments, we ideally use 60 nm or thicker, ideally over 100 nm. Such thick h-BN flakes can be more difficult to assemble using the previously described polymer technique.

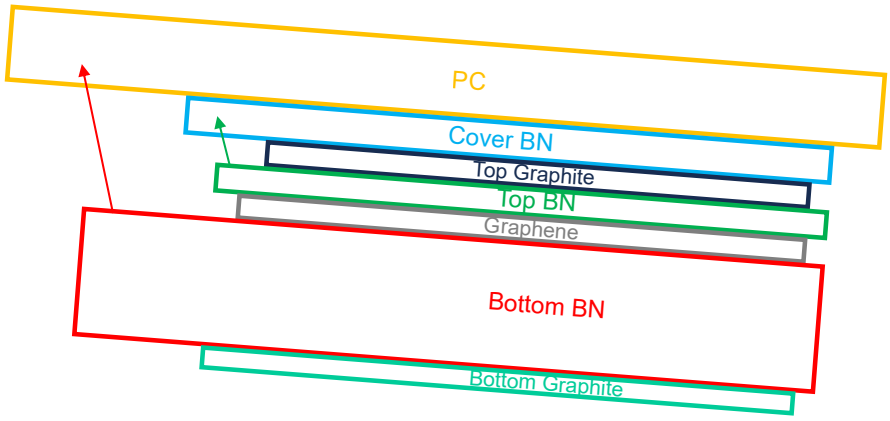

Figure B.3: Arrangement for pickup of thick h-BN flakes via polymer assist rather than h-BN assist.

In particular, if we are using a global bottom graphite gate, and the etch for the contacts will have to partially etch into the bottom h-BN, then thickness of this h-BN needs to be maximized to minimize the risk of shorting to the bottom graphite. A good starting thickness for this h-BN would be 150 nm, although going even higher up to 300 nm can help further reduce the risk.

To pick up such thick h-BN flakes, the h-BN assist method will not work reliably. Instead, when picking up the very thick h-BN, it should extend beyond any h-BNs that will be on top it, so that it makes direct contact with the polymer and is then picked up with the polymer stickiness. A 60–80 nm thick h-BN flake, for top BN, can usually be reliably picked up using the cover BN as an h-BN assist. This arrangement is demonstrated in Fig. B.3.

Additionally, using thicker flakes for the heterostructure results in an overall thicker stack. If the PC film used in the stacking process is too thin, then the stack will embed itself into the PDMS, and upon final dropdown, it will come up with the PDMS instead of getting left behind on the substrate. The process for making PC films is not very

well controlled for thickness, but this issue can be mitigated by using a higher PC concentration in the initial solution, or using more solution on the glass slides when making the film so that it does not spread out as thinly.

B.4 Lithography and Design Techniques

B.4.1 Stack Anchoring

When depositing contacts on Corbino devices, there is a piece of metal inside the ring, unattached to the main outer metal, that must be lifted off. Because it does not attach to the main piece, it often won't lift off by itself and will require ultrasonic agitation in acetone. However, ultrasonic agitation can also cause the vdW stack to become detached from the substrate and completely float away, leaving the experimentalist without any sample. To combat this problem, we have developed a technique for anchoring the stack down to the SiO_2 substrate so that it can survive extended times in high-power sonication baths.

To anchor the stack down, first, thick metal anchors are evaporated sparsely at various places along the sample edge. Ideally, the cover BN is one of the largest flakes, and if the anchors are placed at the edge of the cover BN, then they will be able to hold down the entire stack. Then, the entire perimeter of the stack is sealing with an HSQ layer; however, before this step, the metal leads must first be evaporated so that they do not have to climb over a tall HSQ barrier.

During sonication, it is likely that if a small region of the stack becomes detached from the substrate, then that provides a good anchor point for the ultrasonic waves to remove the entire stack. It is analogous to manually peeling a tape away from a surface: if the tape has any loose edges, it is very easy to peel it off, compared to if the tape is

flat and attached everywhere to the surface. In a similar manor, the HSQ seal around the perimeter of the stack bonds the potentially loose edges of the vdW flakes to the SiO_2 substrate, so that they cannot start peeling off. An example of this metal anchor and HSQ sealant is shown in Fig. B.4.

B.4.2 Evaporation of Metal Topgates onto h-BN

If a metal is evaporated directly onto an un-etched h-BN surface, especially Cr/Au metal, sometimes it does not stick reliably and will come off the surface in subsequent etching steps. This is possibly due to the lack of dangling bonds at the h-BN surface, not allowing the metal to chemically anchor to anything. The stickiness can be improved by going a gentle etching, such as a gentle O_2 etch, to remove any PMMA residue on the BN as well as roughen up the surface a bit to give the metal more chemical bonds to stick to.

Sometimes, a metal topgate must be evaporated directly onto h-BN. Generally, this will produce less disorder than using an oxide grown via an ALD process underneath the metal. The disorder introduced by the metal will be determined by the metal grain size, work function difference between different crystallographic faces of the metal, and any atomic-scale kinetic damage induced to the BN during the evaporation process. Additionally, if Cr is used as a thin sticking layer, it may form into clumps rather spread uniformly along the surface. For this reason, monocrystalline graphite gates tend to produce significantly less disorder than analogous metal topgates.

The common generational knowledge from our research group is the following: the recommended metal to use for topgate evaporation is Cr or Pd as a sticking layer, and then a PdAu alloy for the main deposition of the gate due to its smaller grain sizes. Pd appears to stick better to pristine BN than does Cr, and it may also be used for the

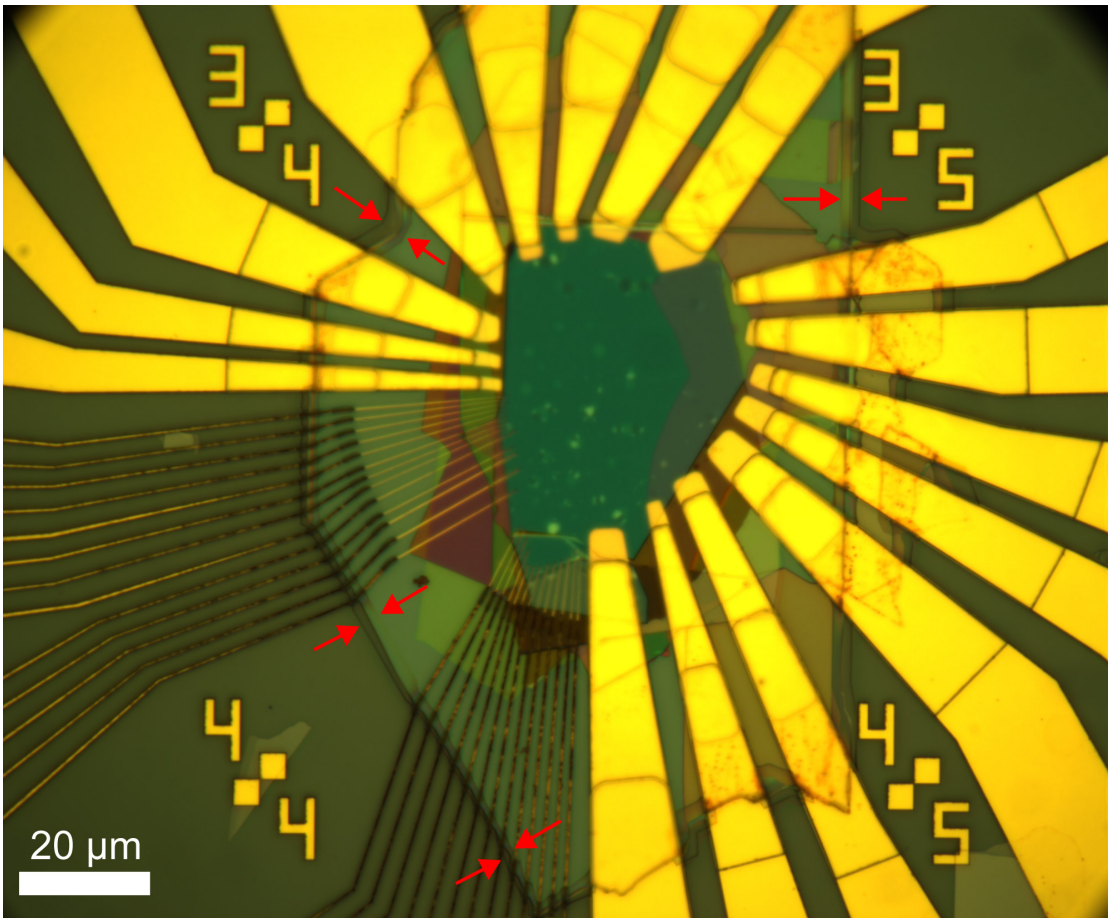

Figure B.4: Optical micrograph of a sample partway through the nanofabrication process. The leads and stack anchors (yellow/gold) have been deposited as thick metal layers, and the HSQ sealant, marked as in between the red arrows in a few places, has been created around the perimeter of the stack.

entire gate deposition.

B.4.3 Contact Gates

When using a metal or graphite topgate, there will inherently be an ungated section of graphene between the contact and the topgate. Ideally, this section of graphene is as narrow as possible, but in practical design, we need to allow for feature size increasing during fabrication, as well as misalignment errors. State of the art e-beam machines typically achieve an alignment tolerance of under 20 nm; however, between different steps, this may become maximized at 40 nm. Feature size growing during e-beam exposure due to proximity effect may cause features to swell by up to around 50 nm, sometimes more, depending on feature size, acceleration voltage, and dose. Such parameters may be tested on an e-beam machine dose dose-testing. Thus, the minimum design gap accounting for all these effects should be at least ~ 150 nm. Generally, 250–300 nm gaps between the topgate and contact features in the design will allow for safe, non-shorted resulting devices.

If the top graphite gate etch mask is defined via a PMMA mask, rather than an HSQ mask, then the gap could be smaller, as the positive-tone PMMA resist will cause the topgate feature to shrink.

The ungated regions must be then be gated, to achieve low series resistance and low contact resistance. If the region is gated to very high density, then the contact resistance at the graphene-metal interface will become very low[15], but unfortunately, there will still be an interfacial resistance between the highly-gated contact region and the less-so gated main channel region.

One method to gate this region is to use an oxide grown via ALD process to insulate the metal contact and topgate from the to-be evaporated contact gate (also known as

a U-gate, due to its shape). However, the drawback to ALD here is that a very thick layer is needed to achieve a high density in the contact region; a thin layer of ALD will allow dielectric breakdown between the contact gate and the top gate or contacts well before a high density is achieved in the contact region. Nonetheless, one benefit of ALD is conformal coverage of any bunny-ear features that may be present in the contacts or top gate.

The alternative method for this region is to make the dielectric selectively from HSQ, a negative tone e-beam resist. Despite being a rather disordered oxide, HSQ can still achieve moderate breakdown voltages, although we have not directly measured this in the lab. The benefit of HSQ is that one can deposit it selectively in only certain regions, easily with thicknesses in the 100–150 nm range. The drawback, is that any bunny ear features in the contacts or topgate will not get conformally covered and will be the weak points for dielectric breakdown. For this reason, we discuss techniques to minimize bunny ears in the next subsection.

B.4.4 The Problem of Bunny Ears, and How to Avoid Them

When performing a PMMA liftoff process, the metal deposited along the sidewalls of the resist can be left behind, causing tall tower-like points along the edges of features, often called bunny ears, as shown in Fig. B.5. This effect is amplified when using angled evaporation for e.g. contacts, as the sidewalls get more coverage.

Using a bilayer PMMA resist, with the bottom layer more sensitive to dose, will create an undercut and help to reduce some of the bunny ears. Furthermore, intentionally over-dosing the features in the e-beam will further increase the undercut and reduce bunny ears, as seen in Fig. B.6.

One must be cautious with using large undercuts for contact deposition. If the etching

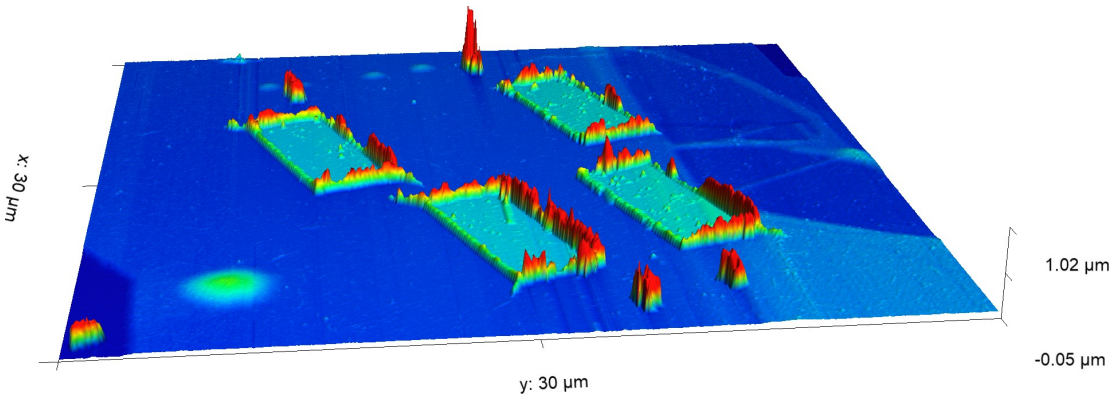

Figure B.5: AFM topography scan showing the bunny ear effect after a metal liftoff process for contact deposition, using 15° angled metal evaporation. The bunny ears appear as the neon green, yellow, and red borders along the contact, which are the cyan rectangular mesas.

process for the contacts is more isotropic, rather than directional, it can etch away the BN even further under the undercut, and then during the directional evaporation of contacts, the metal may fail to make adequate contact to the graphene, leading to higher contact resistance. This is less of an issue with a $CHF_3/O_2/Ar$ etch in an RIE plasma etcher, but could potentially lead to problems in a gas-phase XeF_2 etcher, although this has not been experimentally tested.

B.5 Etching

Etching is the most difficult part of vdW device nanofabrication. In most other processes, the rates, doses, parameters, etc are well-controlled and generally reproducible. However, the etch rate in an RIE machine that is used for different etching chemistries by different users might be affected by residual chemicals from previous etches, as well as rate sensitivities to RF power fluctuations. The powers typically used for etching vdW materials are far towards the low end of the range of available power, and thus may be as stable over time.

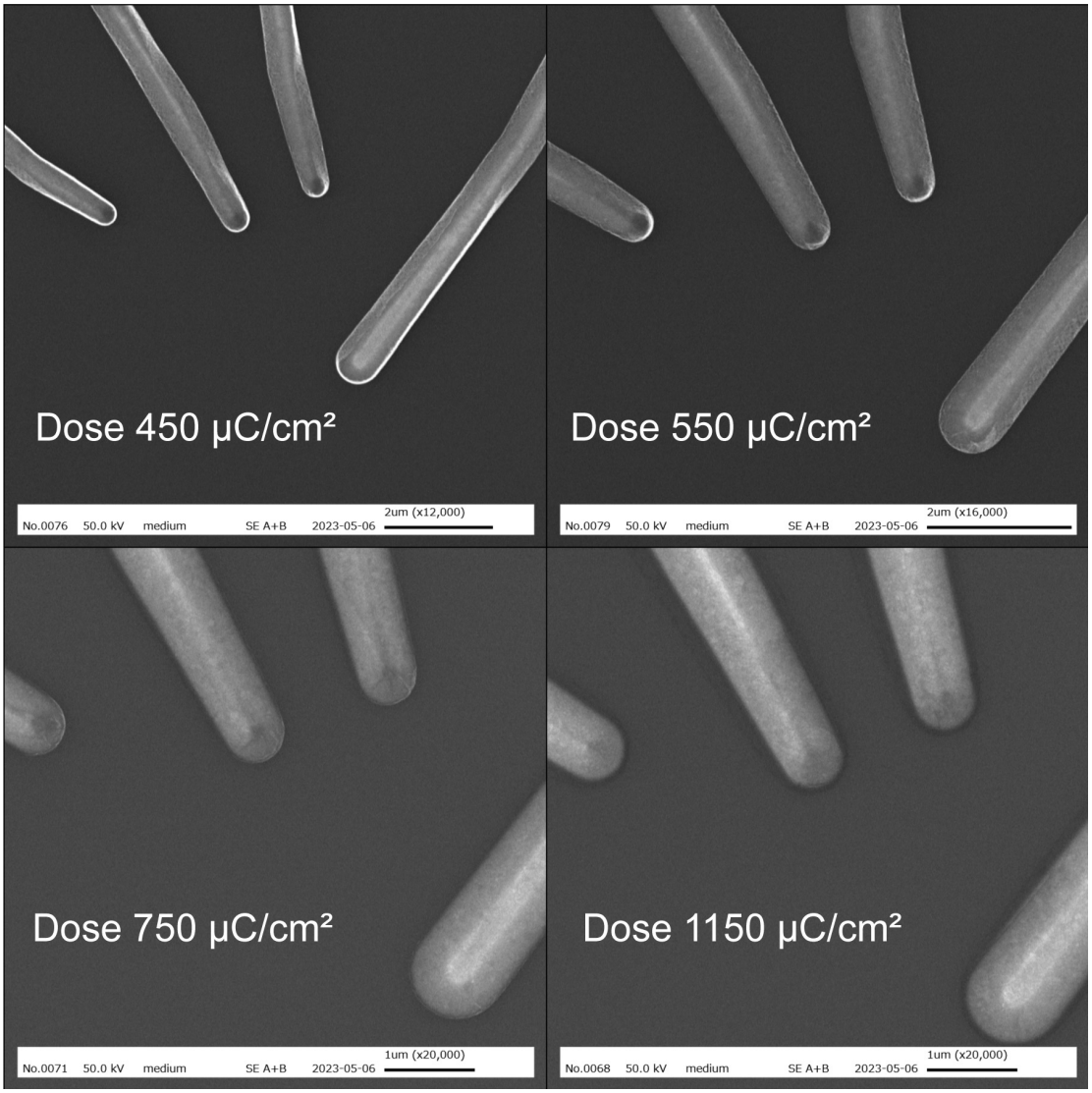

Figure B.6: SEM micrographs, showing the comparison of EBL exposure dose at 50 kV on the ELS-HS50 machine. Doses were 450, 550, 750, and 1150, as labeled in the images. Metal was evaporated using a rotator set to 15°. The bunny ears are seen as bright white outlines on the features. The "standard" dose on this machine is 750, which still has some small residual bunny ears. The over-exposed dose of 1150 entirely gets rid of the bunny ears.

Moreover, etching is an inherently stochastic process, where individual radicals collide with the sample at random times and locations, producing an atomically rough etched surface if there is no chemical etch stop. Any additional residue on the sample surface may also delay or stop the etching in that location, adding in extra non-uniformities.

In particular, the SF_6-only etch recipe, which selectively etched BN but not graphene, is extremely sensitive to PMMA residue, and will not at all etch if there is even a thin layer of residue left. For this reason, a 25-30 s gentle O_2 descumming etch must be done after development whenever using SF_6-only etching chemistry. This procedure is also helpful for other etches, including the $CHF_3/O_2/Ar$, which is slowed down by PMMA residue, generating additional surface non-uniformity.

B.5.1 Etch Stops

Due to the variable etch rates and spatial non-uniformity, it is extremely difficult to etch to a certain precise depth in the sample. Often, etches are done in short 30-60 s runs, with the sample checked after each run to verify whether the correct amount has been etched.

Verifying whether an etch has reached a certain depth, or completed, is a difficult task. Because the etching is not uniform, the end condition is not well defined. Parts may have etched to the desired depth, and other may have not yet etched.

The most reliable method for an etch stop is using chemical selectivity. O_2-only etches are very selective to graphene, and will etch BN at a negligible rate. Similarly, XeF_2, and SF_6-only (when the plasma power is tuned appropriately), etches will etch BN but not graphene due to chemical selectivity. Relying on a chemical selectivity etch stop, one must be careful to avoid exposing unintended regions of the sample that may not have the chemical etch stop present, as well as pinholes/tears in graphene.

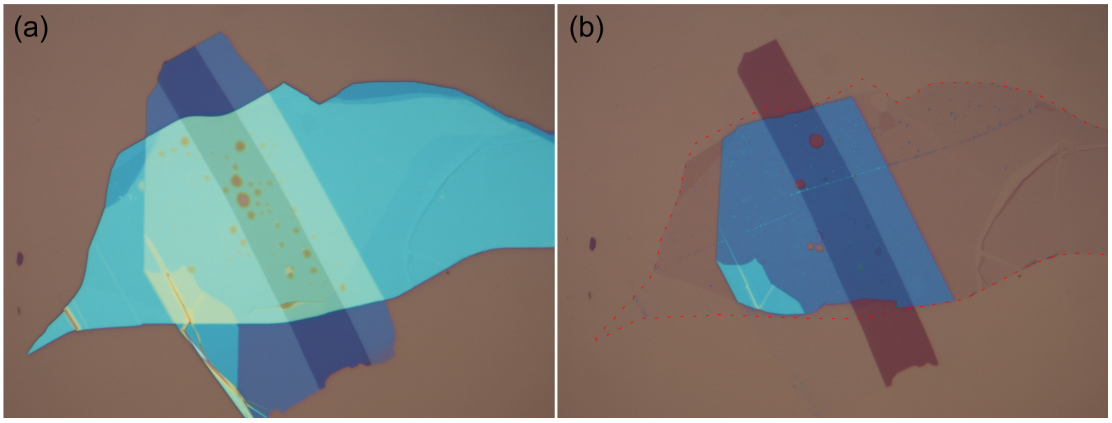

Figure B.7: **(a)** Optical micrograph of a stack after an O_2 etch to strip any exposed graphite, leaving only layers covered by h-BN. The remaining stack is a BN-Gr-BN stack with a strip bottom graphite gate. **(b)** Optical micrograph of the same stack after a plate-power-only RIE SF_6 etch for 60 s at 50 W. Any exposed BN, including the BN that was on top of the graphene, is entirely etched away, leaving graphene or graphite on bare SiO_2 (darker purple), as well as on top of the BN (blue). The red dashed line indicates the outline of the top BN from (a), which extended past the graphene in some areas. Also visible are pinholes in the BN, which were caused by bubble-related pinholes in the graphene.

Sometimes, graphene stacked in h-BN may develop small holes or tears from the stress of the bubbles, and this will cause the chemically-selective etch to etch deeper into the hole. See Fig. B.7 for an example of this pinhole effect.

The next reliable method is to use an electrical etch stop test. Here, electrical contact is made to a piece of graphene or graphite, and usually either an O_2 etch for etching the graphite, or a $CHF_3/O_2/Ar$ etch for etching h-BN and graphene, is used to etch the graphite or the graphene. After 30-60 s etch increments, the electrical resistance through the graphene or graphite can be probed; once the resistance is an open circuit, the graphene or graphite has been fully etched away.

Optical etch stops, by optically examining the color of flakes, are very unreliable. First, the SiO_2 substrate is often used as a reference color; however, some etches will slowly etch this away, changing the color; the result is that some thicker flakes will leave

a "shadow" in the SiO_2 color, even if the flake has been entirely etched. Furthermore, we have extensively observed that even when a flake optically looks completely etched, an AFM scan will still show a nonzero flake thickness with a lot of roughness, typically 10–30 nm thick. We believe this may be caused by a spare amount of small residue chunks left behind, causing the AFM tip to be overly sensitive but contributing negligible optical contrast.

One can also attempt a reference-based etch stop. Several reference chips, containing the same flakes as to be etched on the sample and a pattern of circles or lines exposing the flakes, is loaded into the etcher concurrently with the sample. After each 30-60 s etch run, the resist on one of the reference chips is dissolved, and the etch depth is measured with an AFM.

In a similar manner, an etch rate chart can be constructed, by etching several chips individually for varying amounts of time. If a time-based etch stop is used, the etch rate measurement should be done as close as possible to immediately before the sample etch.

One technique we have invented to make 1D side-contacts to graphene, using an effective etch stop to avoid shorting to the bottom graphite gate, is the following. Write the windows in PMMA for the contacts, but slightly smaller ($\sim$ 50–80/,nm smaller) than the final desired size. Etch the BN up to the graphene using the directional and selective SF_6 etch. Remove the fluorinated resist film using a gentle 25-30 s O_2 etch, and wash away the resist. Re-spin new resist, and now write the full-size windows in the PMMA for the contacts. Perform a short $CHF_3/O_2/Ar$ etch, typically 30–40/,s, to expose a fresh edge of graphene for contacts, and then evaporate the contacts using the standard method. In this way, the $CHF_3/O_2/Ar$ etch has very little time to etch deeply into the bottom BN and cause shorts to the bottom graphite, but still provides

a fresh graphene edge for high-quality contacts. We have found that SF_6-only contacts form poor, unreliable contacts to graphene with several kΩ of contact resistance.

B.5.2 Etching h-BN with XeF_2

XeF_2 is primarily designed to be a fast gas-based Si etcher. A solid chunk of XeF_2 as the source is heated to vaporize it, and the resulting vapor, typically at a pressure of 3 mTorr or less, is then transferred to the sample chamber for etching for a pulse of typical duration 20-60 s. Usually, deep features in Si are etched with this technique via many cycles.

Coincidentally, XeF_2 also etches BN very selectively, and will not etch graphene. Most importantly, monolayer graphene contacts using the XeF_2 etching chemistry have achieved near quantum-limited contact resistance[22], the best options available outside of using superconducting contacts. However, the etching chemistry is not well understood. The authors of Ref. 22 originally proposed a chemical reaction where the XeF_2 directly reacts with the BN, but they later determined that BN only gets etched if there is bare Si present in the chamber, implying some chemical product of Si and XeF_2 causes the BN to get etched.

However, we expect that XeF_2 will not make quantum-limited contacts to bilayer graphene, as it will only make contact to the top layer of the two layers. Instead, we expect that the standard $CHF_3/O_2/Ar$ 1D contacts[15] will provide lower contact resistance.

The XeF_2 etch rate on BN is very poorly controlled. One of our late lab members, Antti Laitinen, discovered that XeF_2 reacts readily with water, and even a small amount of water vapor present in the chamber will react with the XeF_2 first, leaving the BN unetched. One workaround is to do perform several cycles of XeF_2, but this can over-etch

the BN with significant undercuts. Another workout that he discovered is to pump and flush with N2 gas repeatedly several times to bring the water vapor to a controllable level, and then perform a single XeF_2 pulse at 3 mTorr and 60 s, which will often reliably etch up to around 200 nm of BN.

B.5.3 HSQ Etch Masks

Unlike PMMA, which is a "soft" polymer-based etch mask, HSQ is a hard SiO_2-based etch mask that will not dissolve in resists. HSQ is a silicon polymer-based negative-tone resist that transforms to a disordered, spare SiO_2 matrix after exposure to e-beam. For etching graphite with O_2, HSQ is preferentially used due to its resistance to oxygen plasma, compared to PMMA which etches very fast in O_2.

A typical process for using an HSQ etch mask for etching graphite top gates is to first spin an underlayer of PMMA, typically 950 A2, and then spin a thin layer of HSQ 6% on top. The region where the graphite is to be kept is exposed, and then the HSQ is developed in Microposit MF CD-26 developer (Caution: 2.5% TMAH is toxic!). The PMMA, where it is not shielded by the HSQ, is then etched away in an RIE etcher using an O_2 etch. After the device topgate has been etched as needed, the HSQ is removed by dissolving the PMMA underlayer in acetone.

An alternate, newly developed process for using HSQ is to spin the HSQ directly onto the cover BN. In this way, the HSQ acts as an etch mask for both the top gate etch and a subsequent device etch, allowing perfect alignment of the graphene edge with the graphite edge. HSQ, while somewhat resistant to $CHF_3/O_2/Ar$ plasma, does get etched away at a faster rate than dry- or wet-grown SiO_2. The remaining thickness and etch rate should be verified by the experimentalist. In this method, the HSQ can be left behind on the device, or, if needed, it can be removed via an HF or buffered HF etch

(Caution: extremely toxic!), using a window in PMMA resist to protect the remainder of the sample.

When performing the top gate etch on a dual-graphite gated device with a cover BN, one should be careful and aware of device regions where there is bottom graphite, but no top graphite. In these regions, when the cover BN is etched during the top gate etch step, the top BN and bottom BN will also be etched as there is no top graphite to stop the etch. During subsequent etches and deposition, the BN in these regions may become thin enough to cause shorting to the back graphite. One way to avoid this issue is to use an HSQ shield for these regions, or to evaporate the leads first, before doing the topgate etch.

B.6 HSQ Bridges and Dielectrics

In addition to being used as an etch mask, HSQ is also usable as an insulator or dielectric due to its ease of selective deposition.

When the top gate edge aligns with the graphene edge, rather than extending past it, simply making an electrical connection to the top gate would short the graphene. To work around this issue, we have developed a technique using HSQ bridges to insulate the edge of the graphene. An HSQ bridge is deposited in a small area, typically $\sim 1 \times 3\,\mu$m, on the edge of the device, and a metal connection to the top gate is then deposited over the bridge.

Additionally, we have used HSQ as bridges for Corbino devices, in order to insulate the connection to the central contact or top gate from the outer contact. In the case of the MLG3 device (Subsection 5.5.4), HSQ covered the entire channel, with a hole for the central contact; the connecting lead for the central contact then also covered the

entire channel for homogeneity.

As discussed previously, HSQ is also used as an insulator/dielectric for contact gates. We have also used it for local top gates, for example for the hot/cold side gates in the non-local H-device setup.

B.7 Corbino Fabrication Processes

Here, we describe a typical nanofabrication process for a dual-graphite gated BLG Corbino device with a global bottom graphite. The process can be simplified as needed when there is no bottom graphite gate, or the top graphite gate etch could be replaced with a metal gate evaporation step.

1. Alignment marks. EBL and evaporate.

2. Top gate contact using vias through the cover BN. Etch and evaporate small circles. EBL, etch, evaporate.

3. Thin leads on top of the stack and substrate, to avoid evaporating thin leads onto thick metal in later steps, as well as to avoid shorting to bottom graphite in regions with no top graphite. EBL and evaporate.

4. Thick metal stack anchors, as well as thick metal to help the leads make electrical connection over thick flake steps.

5. HSQ sealant along the stack boundaries. EBL and develop.

6. Topgate etch mask 1 with HSQ rings. Define the topgate boundary with HSQ directly on top of the cover BN. EBL and develop.

7. Topgate etch final mask with PMMA/HSQ. Use PMMA/HSQ to cover the inside of the HSQ rings from previous step, and let the previous step define the actual etch mask. EBL and etch. Use $CHF_3/O_2/Ar$ selectivity to stop the BN etch, and O_2 selectivity to stop the graphite etch.

8. Contacts etch 1: SF_6 selective etch to the graphene. EBL and etch.

9. Contacts etch 2: $CHF_3/O_2/Ar$ short etch (into slightly larger windows than previous step), and contacts evaporation. EBL, etch, and evaporate.

10. Bottom graphite gate contact. EBL, etch, and evaporate.

11. Device etch, using SF_6 for BN and O_2 for the graphene. EBL and etch.

12. HSQ for the contact gates (inner and outer), as well as insulating bridge over the outer contact. EBL and develop.

13. Contact gates (O-shape) evaporation. EBL and evaporate.

14. HSQ bridge over the O-shaped contact gates, for both the topgate lines and the central contact. EBL and develop.

15. Final evaporation to connect everything, including central contact, outer contact, topgate, and contact gates, using a thick ($\sim 200\,\text{nm}$) rotating evaporation. EBL and evaporate.

If the device is a MLG device, steps 8 and 9 can be combined into a single step using XeF_2 contacts. Between many steps, especially before and after the HSQ bridge steps, the device should be AFMed in order to verify the absence of bunny ears pre-HSQ, and the thickness of HSQ after development. Several devices have inadvertently

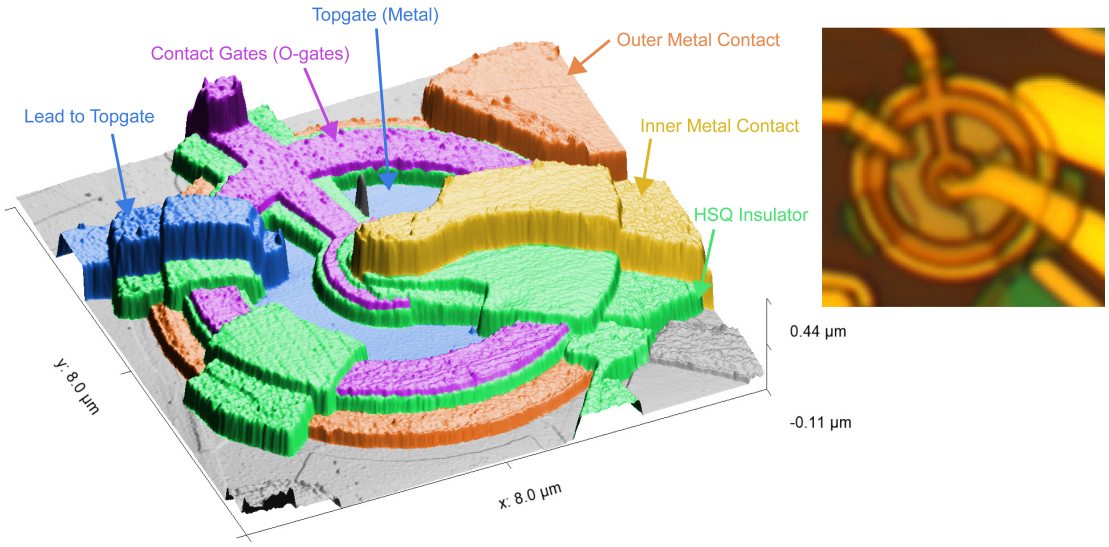

Figure B.8: **Left:** False color AFM micrograph showing the topology of a dual-gated BLG Corbino device, where the gate shorted, likely due to the HSQ dielectric insulator being too thin. **Right:** Optical micrograph of the same device.

had gates shorts due to the HSQ being too thin, or bunny ears protruding into the HSQ and effectively causing it to be too thin. Fig. B.8 shows a false color AFM 3D topographical micrograph of an example of such a Corbino device, which, unfortunately, had the gates shorted. Hopefully, the reader of this section will have better luck in their own fabrication by carefully following the tips presented here, learned from mistakes. A false color SEM of another example of such a Corbino device is shown in Fig. B.9.

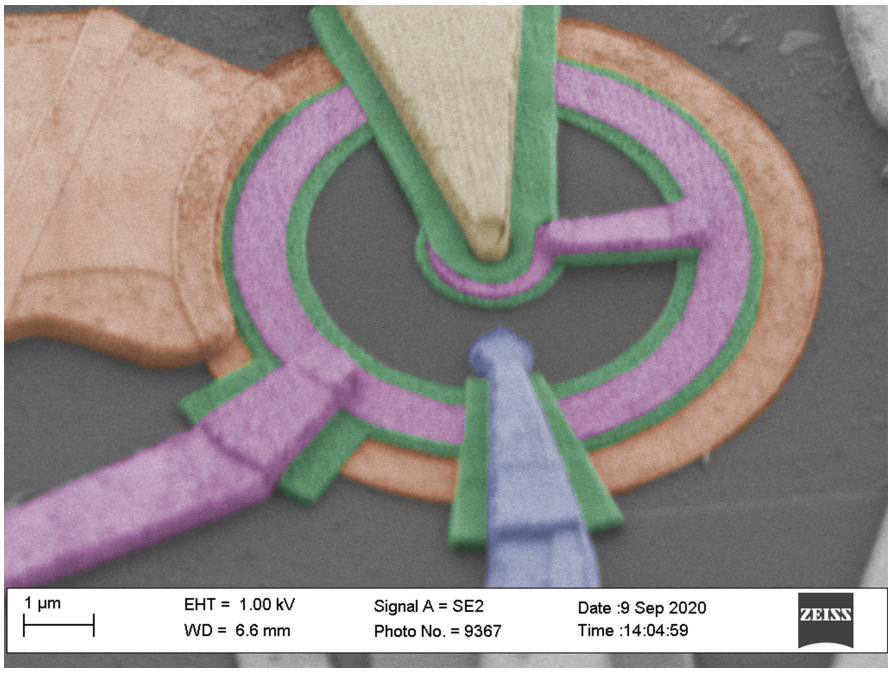

Figure B.9: False color SEM micrograph of another Corbino device where the gates were shorted. Orange indicates the metal outer contact. Yellow indicates the inner metal contact. Green indicates the HSQ dielectric insulator. Pink indicates the inner and outer contact gates (O-gates). Blue indicates the connection to the top graphite gate through the via. The top graphite gate (not visible) is buried under the cover BN (annular gray region).

All science is either physics or stamp collecting.

Ernest Rutherford

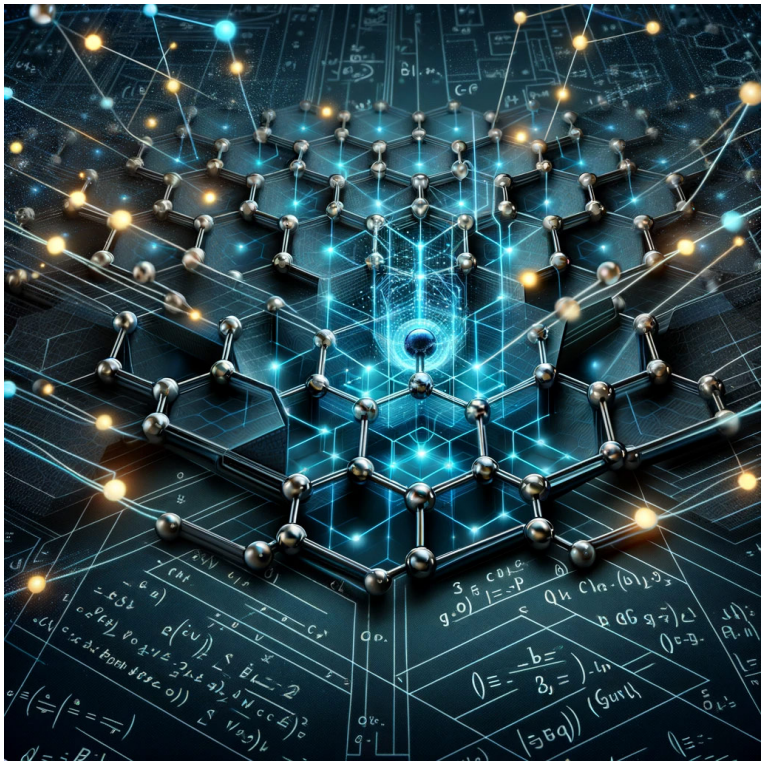

Sample and Contact Resistance Lorenz Numbers from Multi-Channel Measurements

Here, we present a calculation for extracting the sample Lorenz ratio in a 2-device configuration with contact resistance. We follow the general principles of the model of Ref. 169 but we relax some constraints for a more general case.

The total sample resistance is $R_s + 2R_c$, where R_s is the main channel resistance and R_c is each contact resistance. For simplicity, we assume that each contact resistance is point-like, and thus there is no temperature gradient in the contact. We use T_0 to denote the bath temperature.

We wish to obtain a formula that gives us the measured Lorenz number $\mathcal{L}_m$ as a function of the sample Lorenz number $\mathcal{L}_s$ and the contact resistance Lorenz number $\mathcal{L}_c$, as well as other fixed or known parameters in the system including resistance. Most generally, we can write the generalized thermal conductance of the sample (see Eq. 3.9), using the total Joule power P and the average Johnson noise temperature rise $\overline{\Delta T}$, as

$$G_{th,gen} = P/\overline{\Delta T} = \frac{I^2 \left(R_s + 2R_c\right)^2}{R_s \overline{\Delta T_s} + 2R_c \overline{\Delta T_c}}, \tag{C.1}$$

where $\overline{\Delta T_s}$ and $\overline{\Delta T_c}$ are respective average Johnson noise temperature rises of the sample channel and contact above T_0.

We define the contact resistance R_c to have a thermal resistance $R_{c,th} = 1/G_{th,c}$ such that the temperature drop ΔT_{cs} across the contact resistance is related to the heat Q_c that flows through it via

$$\Delta T_{cs} = \frac{Q_c}{G_{th,c}}, \tag{C.2}$$

and we can likewise define a contact Lorenz number as

$$\mathcal{L}_c = \frac{G_{th,c} R_c}{T_0}. \tag{C.3}$$

We will assume, without rigorous justification, that the average Johnson noise temperature of the contact resistance is one half of ΔT_{cs}. This would certainly be the case for a spatially extended uniformly resistive contact resistance, and as in Ref. 169, we use the same model for a point-like contact resistance.

Ref. 169 assumed that the Joule heat generated at each contact is distributed equally on each side of the contact resistance; the half that goes into the metal contact is immediately thermalized to bath temperature, and the half that goes into the graphene channel flows through the contact resistor and causes a temperature rise. Here, instead of assuming that the contact resistance Joule power is equally distributed on each side, we will instead suppose that a fraction α is distributed to the graphene side, and $1 - \alpha$ is distributed towards the metal contact. In the case of a ballistic device, we typically expect $\alpha \to 0$ because the dissipation happens inside the metal contact (reservoir) itself after the electrons leave the sample.

We will write $\overline{\Delta T_c} = \frac{1}{2}\Delta T_{cs}$ in terms of the total electrical current and the contact Lorenz number. The heat current Q_c flowing through each contact resistance is then half of the heat generated in the channel R_s added to the fraction α of heat generated in the contact resistance R_c:

$$Q_c = \frac{1}{2} I^2 R_s + \alpha I^2 R_c. \tag{C.4}$$

We then obtain

$$\overline{\Delta T_c} = \frac{1}{2}\Delta T_{cs} = \frac{1}{2}\frac{Q_c}{G_{th,c}} = \frac{1}{2}\frac{\frac{1}{2}I^2R_s + \alpha I^2 R_c}{\mathcal{L}_c T_0/R_c} \tag{C.5}$$

$$\Delta T_{cs} = \frac{1}{2}I^2\frac{R_c}{\mathcal{L}_c T_0}\left(R_s + 2\alpha R_c\right). \tag{C.6}$$

The effective bath temperature for the channel becomes $T_0 + \Delta T_{cs}$. We can define an effective self-heating average Johnson noise temperature rise for just the channel, above the effective bath temperature, as

$$\widetilde{\Delta T_s} = \overline{\Delta T_s} - \Delta T_{cs} = \frac{I^2R_s}{G_{th,gen,s}} = \frac{I^2R_s}{12T_0\mathcal{L}_s/R_s} \tag{C.7}$$

where $G_{th,gen,s}$ is the generalized thermal conductance of the sample channel only, using the sample Lorenz ratio $\mathcal{L}_s = \dfrac{G_{th,gen,s}R_s}{12T_0}$. This allows us to write

$$\overline{\Delta T_s} = \Delta T_{cs} + \frac{I^2R_s^2}{12T_0\mathcal{L}_s}. \tag{C.8}$$

Substituting Eqs. C.6 into C.8 and into C.5, and the results into Eq. C.1, and re-arranging, we obtain

$$G_{th,gen} = \frac{\left(R_s + 2R_c\right)^2}{\dfrac{R_s^3}{12T_0}\dfrac{1}{\mathcal{L}_s} + \dfrac{R_c}{2T_0}\left(R_s + 2\alpha R_c\right)\left(R_s + R_c\right)\dfrac{1}{\mathcal{L}_c}}. \tag{C.9}$$

Finally, relating $G_{th,gen}$ to the measured Lorenz ratio as

$$G_{th,gen} = \frac{12T_0\mathcal{L}_m}{R_s + 2R_c}, \tag{C.10}$$

we can write Eq. C.9 as

$$\mathcal{L}_m = \frac{(R_s + 2R_c)^3}{\dfrac{R_s^3}{\mathcal{L}_s} + \dfrac{6R_c\,(R_s + 2\alpha R_c)\,(R_s + R_c)}{\mathcal{L}_c}}. \tag{C.11}$$

If we now have measurements of two different channel lengths with different resistances R_s but the same contact resistances R_c, and they have different measured Lorenz ratios $\mathcal{L}_m$, we can solve two copies of Eq. C.11 to obtain $\mathcal{L}_s$ and $\mathcal{L}_s$. This is done as follows: Define

$$A \equiv (R_s + 2R_c)^3 \tag{C.12}$$

$$B \equiv 6R_c\,(R_s + 2\alpha R_c)\,(R_s + R_c) \tag{C.13}$$

$$C \equiv R_s^3. \tag{C.14}$$

Then Eq. C.11 can be written as

$$\mathcal{L}_{m,i} = \frac{A_i}{\dfrac{C_i}{\mathcal{L}_s} + \dfrac{B_i}{\mathcal{L}_c}}, \tag{C.15}$$

where the subscript $i = 1, 2$ refers to one of the two different channel lengths. These

two equations are then solved as

$$\mathcal{L}_c = \frac{\dfrac{B_1}{C_1} - \dfrac{B_2}{C_2}}{\dfrac{A_1}{\mathcal{L}_{m,1}C_1} - \dfrac{A_2}{\mathcal{L}_{m,2}C_2}} \tag{C.16}$$

$$\mathcal{L}_s = \frac{\dfrac{C_1}{B_1} - \dfrac{C_2}{B_2}}{\dfrac{A_1}{\mathcal{L}_{m,1}B_1} - \dfrac{A_2}{\mathcal{L}_{m,2}B_2}}. \tag{C.17}$$

We can thus obtain the sample and contact resistance Lorenz ratios from a measurement of the two channels, under the assumption of a known α. *A priori*, α is unknown and may depend on the density; to extract a value for α we would need a third channel length for a third copy of Eq. C.11 to solve for the third unknown.

The scientist is not a person who gives the right answers, he is one who asks the right questions.

Claude Levi-Strauss

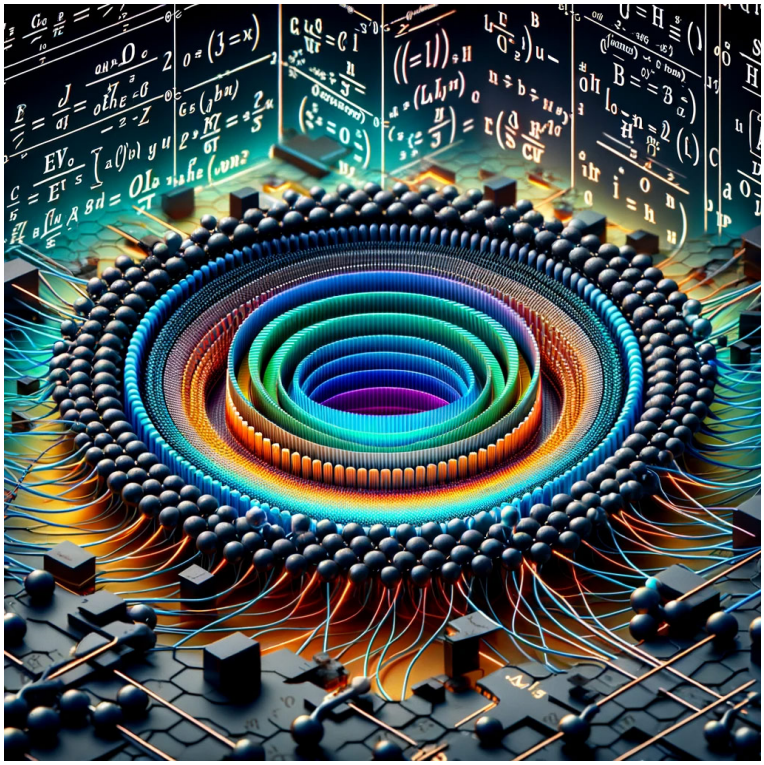

D

Corbino Geometric Magnetoresistance

We wish to obtain an intuitive understanding of the electrical magnetoresistance of a Corbino geometry, described in Section 3.3. The magnetoresistance of a Corbino device in the diffusive Drude theory is nonzero, in stark contrast to that of a Hall bar or rectangular sample, where the same theory predicts zero magnetoresistance[55] contrary

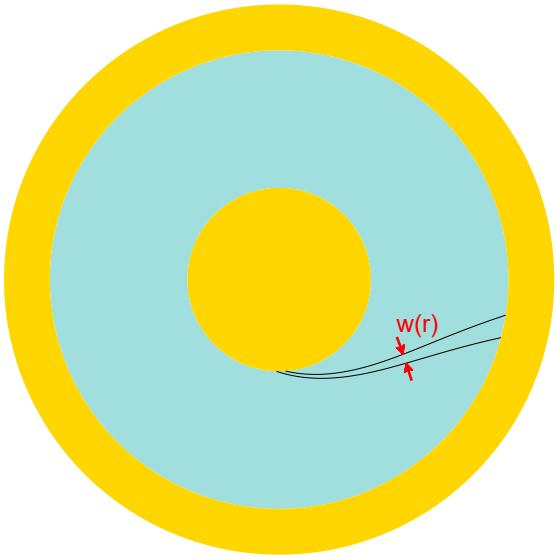

Figure D.1: A Corbino disk where the two black lines indicate current streamlines. We will consider current flowing through this narrow sliver defined by the black lines, with a width $w(r)$.

to nearly all experiments. For the Corbino, let us consider the current flow streamlines under a low magnetic field as shown in Fig. D.1. These are modified from the usual radially pointing current flows in zero magnetic field. To begin, we can calculate the distance L a current element travels while traversing the channel from inner to outer electrode. From Section 3.3, we can write the radial velocity as

$$v_r = \frac{C}{r} = \frac{dr}{dt}, \tag{D.1}$$

where C is a constant and we have defined a differential equation. The solution to this is

$$v_r(t) = \sqrt{\frac{C}{2t}} \tag{D.2}$$

$$v_\theta(t) = -\mu B\sqrt{\frac{C}{2t}}. \tag{D.3}$$

We can defines times t_1, t_2 when the current element is at the inner or outer edges of the sample:

$$t_1 = \frac{r_1^2}{2C} \tag{D.4}$$

$$t_2 = \frac{r_2^2}{2C} \tag{D.5}$$

We then integrate the velocity parametrically via t from inner to outer radius:

$$L = \int_{t_1}^{t_2} |v(t)| dt \tag{D.6}$$

$$L = \int_{t_1}^{t_2} \sqrt{v_\theta^2 + v_r^2}\, dt \tag{D.7}$$

$$L = \int_{t_1}^{t_2} \sqrt{\frac{C}{2t} + \mu^2 B^2 \frac{C}{2t}}\, dt \tag{D.8}$$

$$L = \sqrt{1 + (\mu B)^2} \int_{t_1}^{t_2} \sqrt{\frac{C}{2t}}\, dt \tag{D.9}$$

$$L = \sqrt{1 + (\mu B)^2}\, (r_2 - r_1) \tag{D.10}$$

We see that the increase in path length for the current is not enough to explain the full increase in resistance! We must consider the sliver of sample between the two black lines, and calculate the resistance of this sliver, of angular width $\delta\theta$, assuming the current flows along the sliver. Let the effective flow width of the sliver be $w(r)$.

We can determine that

$$w(r) = \delta\theta \cdot r \cos\theta_H \tag{D.11}$$

where θ_H is the Hall angle, given by

$$\tan\theta_H = \frac{v_\theta}{v_r} = -\mu B. \tag{D.12}$$

If we define ds to be along the sliver, then the resistance is

$$R_{\delta\theta} = \frac{1}{\sigma_0}\int_0^L \frac{ds}{w}. \tag{D.13}$$

Based on Eq. D.10, we can write

$$s(r) = \int_{t_1}^{t_r} |v| dt = \sqrt{1+(\mu B)^2}(r - r_1) \tag{D.14}$$

$$ds = \sqrt{1+(\mu B)^2}\, dr. \tag{D.15}$$

Then the resistance is

$$R_{\delta\theta} = \frac{1}{\sigma_0}\int_{r_1}^{r_2} \frac{\sqrt{1+(\mu B)^2}\, dr}{\delta\theta \cdot r\cos\theta_H} \tag{D.16}$$

$$R_{\delta\theta} = \frac{1}{\sigma_0}\frac{1}{\delta\theta}\frac{\sqrt{1+(\mu B)^2}}{\cos\theta_H}\int_{r_1}^{r_2}\frac{dr}{r} \tag{D.17}$$

$$R_{\delta\theta} = \frac{1}{\sigma_0}\frac{1}{\delta\theta}\frac{\sqrt{1+(\mu B)^2}}{\left[\sqrt{1+(\mu B)^2}\right]^{-1}}\ln\frac{r2}{r1} \tag{D.18}$$

$$R_{\delta\theta} = \frac{1+(\mu B)^2}{\sigma_0}\frac{1}{\delta\theta}\ln\frac{r2}{r1}. \tag{D.19}$$

For the total resistance, we must add the conductances together of these strips, of which there are $2\pi/\delta\theta$. Thus the total resistance becomes

$$R_{tot} = \frac{1+(\mu B)^2}{\sigma_0}\frac{1}{2\pi}\ln\frac{r2}{r1}, \tag{D.20}$$

which is the correct resistance from Eq. 3.32. We can see the magnetoresistance comes from both the lengthening of the path the current takes, plus the "squeezing" of the current into narrower slivers.

An expert is a person who has made all the mistakes that can be made in a very narrow field.

Niels Bohr

E

Correction to the Bilayer Graphene Hydrodynamic Formula

In Ref. 3, the authors propose a conductivity formula for hydrodynamic bilayer graphene of

$$\sigma = \frac{4n_e n_h}{(n_e + n_h)} \frac{e^2}{m} \tau_0 + \frac{(n_e - n_h)^2}{(n_e + n_h)} \frac{e^2}{m} \tau_{dis} \tag{E.1}$$

in the limit of $\tau_0 \ll \tau_{dis}$, where τ_0 is the electron-hole scattering relaxation time, τ_{dis} is the dissipative relaxation time, $n_{e/h}$ is the density of electrons/holes, and m is the effective mass. The non-intuitive part of this equation was that the individual conductivities, rather resistivities as in Matthiesen's rule, add together. This allowed the authors to interpret the conductivity as a sum of relative motion and center of mass motion.

In this Appendix, we propose an alternative derivation of the author's formula, keeping more careful track of small terms in the Taylor expansions as needed. The authors performed a zeroth order Taylor expansion in τ_0/τ_{dis}.

Here, we assume for simplicity that $\tau_{dis,e} = \tau_{dis,h} = \tau_{dis}$. Beginning with Eq. S11 in the supplement, and defining $\tilde{\sigma} = \sigma \frac{m}{e^2}$, we get

$$\tilde{\sigma} = \frac{4n_e n_h \tau_0 \tau_{dis} + (n_e - n_h)^2 (\tau_0 + \tau_{dis}) \tau_{dis}}{(n_e + n_h)(\tau_0 + \tau_{dis})}. \tag{E.2}$$

We perform some algebra:

$$\tilde{\sigma} = \tau_{dis} \frac{4n_e n_h \tau_0 + (n_e - n_h)^2 (\tau_0 + \tau_{dis})}{(n_e + n_h)(\tau_0 + \tau_{dis})} \tag{E.3}$$

$$= \tau_{dis} \frac{4n_e n_h \tau_0 + (n_e - n_h)^2 \tau_0 + (n_e - n_h)^2 \tau_{dis}}{(n_e + n_h)(\tau_0 + \tau_{dis})} \tag{E.4}$$

$$= \tau_{dis} \frac{\left[4n_e n_h + (n_e - n_h)^2\right] \tau_0 + (n_e - n_h)^2 \tau_{dis}}{(n_e + n_h)(\tau_0 + \tau_{dis})} \tag{E.5}$$

$$= \tau_{dis} \frac{\left[4n_e n_h + n_e^2 - 2n_e n_h + n_h^2\right] \tau_0 + (n_e - n_h)^2 \tau_{dis}}{(n_e + n_h)(\tau_0 + \tau_{dis})} \tag{E.6}$$

$$= \tau_{dis} \frac{\left[n_e^2 + 2n_e n_h + n_h^2\right] \tau_0 + (n_e - n_h)^2 \tau_{dis}}{(n_e + n_h)(\tau_0 + \tau_{dis})} \tag{E.7}$$

$$= \tau_{dis} \frac{(n_e + n_h)^2 \tau_0 + (n_e - n_h)^2 \tau_{dis}}{(n_e + n_h)(\tau_0 + \tau_{dis})} \tag{E.8}$$

$$= \frac{(n_e + n_h)^2 \tau_0 + (n_e - n_h)^2 \tau_{dis}}{(n_e + n_h)\left(1 + \dfrac{\tau_0}{\tau_{dis}}\right)}. \tag{E.9}$$

At this point, the authors took the zeroth-order Taylor expansion in $\frac{\tau_0}{\tau_{dis}}$. If we interpret this as strictly $\tau_0 = 0$, then we get

$$\tilde{\sigma} \approx \frac{(n_e - n_h)^2}{n_e + n_h} \tau_{dis}. \tag{E.10}$$

Of course, this only captures the dissipative part of Eq. E.1, and not the electron-hole interacting part. To get the next order contribution then, we must take a higher-order Taylor expansion.

Now, let us take the first-order Taylor expansion in $\frac{\tau_0}{\tau_{dis}}$ of the denominator in Eq. E.9; we will not yet expand the numerator because we cannot guarantee that $(n_e + n_h)^2 \tau_0 \ll (n_e - n_h)^2 \tau_{dis}$, because we would like the formula to work arbitrarily close to charge

neutrality:

$$\tilde{\sigma} \approx \frac{(n_e + n_h)^2 \tau_0 + (n_e - n_h)^2 \tau_{dis}}{n_e + n_h} \left[1 - \frac{\tau_0}{\tau_{dis}}\right]. \tag{E.11}$$

Re-arranging some terms, we get

$$\tilde{\sigma} \approx \frac{(n_e - n_h)^2}{n_e + n_h}\tau_{dis} + \left[\frac{(n_e + n_h)^2}{n_e + n_h} - \frac{(n_e - n_h)^2}{n_e + n_h}\right]\tau_0 - (n_e + n_h)\frac{\tau_0^2}{\tau_{dis}} \tag{E.12}$$

$$\approx \frac{(n_e - n_h)^2}{n_e + n_h}\tau_{dis} + \frac{4n_e n_h}{n_e + n_h}\tau_0 - \frac{(n_e + n_h)^2}{(n_e + n_h)}\frac{\tau_0^2}{\tau_{dis}}. \tag{E.13}$$

At this point, the authors of Ref. 3 discarded the last term in Eq. E.13 under the premise that it is small. To discard the last term, we must have $(n_e - n_h)^2 \tau_{dis} \ll (n_e + n_h)^2 \frac{\tau_0^2}{\tau_{dis}}$. For any given values of τ_0, τ_{dis}, we can choose a point arbitrarily close to charge neutrality where this condition fails, and we cannot discard the last term. We thus conclude that equation E.1 from Ref. 3 only holds for a certain distance away from charge neutrality, likely related to the disorder-enabled hydrodynamics discussed in Ref. 82.

In fact, through a careful mathematical trick, we can write an exact version of Eq. E.1, by adding just a single scattering rate term. We will use the easy-to-prove identity

$$\frac{A}{1+x} = A - \frac{Ax}{1+x}. \tag{E.14}$$

We begin with rearranging Eq. E.9:

$$\tilde{\sigma} = \frac{(n_e + n_h)^2 \tau_0 + (n_e - n_h)^2 \tau_{dis}}{(n_e + n_h)\left(1 + \frac{\tau_0}{\tau_{dis}}\right)} \tag{E.15}$$

$$= \frac{(n_e + n_h)^2 \tau_0}{(n_e + n_h)\left(1 + \frac{\tau_0}{\tau_{dis}}\right)} + \frac{(n_e - n_h)^2 \tau_{dis}}{(n_e + n_h)\left(1 + \frac{\tau_0}{\tau_{dis}}\right)}. \tag{E.16}$$

We apply the identity in E.14 to the second term in Eq. E.16, setting $x = \frac{\tau_0}{\tau_{dis}}$ and $A = \frac{(n_e - n_h)^2 \tau_{dis}}{(n_e + n_h)}$. We thus obtain

$$\tilde{\sigma} = \frac{(n_e + n_h)^2 \tau_0}{(n_e + n_h)\left(1 + \frac{\tau_0}{\tau_{dis}}\right)} + \frac{(n_e - n_h)^2 \tau_{dis}}{(n_e + n_h)} - \frac{\frac{(n_e - n_h)^2 \tau_{dis}}{(n_e + n_h)} \frac{\tau_0}{\tau_{dis}}}{1 + \frac{\tau_0}{\tau_{dis}}} \tag{E.17}$$

$$= \frac{(n_e - n_h)^2}{(n_e + n_h)} \tau_{dis} + \frac{\left[(n_e + n_h)^2 - (n_e - n_h)^2\right] \tau_0}{(n_e + n_h)\left(1 + \frac{\tau_0}{\tau_{dis}}\right)} \tag{E.18}$$

$$= \frac{(n_e - n_h)^2}{(n_e + n_h)} \tau_{dis} + \frac{(4 n_e n_h) \tau_0}{(n_e + n_h)\left(1 + \frac{\tau_0}{\tau_{dis}}\right)} \tag{E.19}$$

$$\boxed{\tilde{\sigma} = \frac{(n_e - n_h)^2}{(n_e + n_h)} \tau_{dis} + \frac{4 n_e n_h}{n_e + n_h} \left(\frac{1}{\tau_0} + \frac{1}{\tau_{dis}}\right)^{-1}}. \tag{E.20}$$

We see that Eq. E.20 is nothing but Eq. 1 from Ref. 3, but now with a disorder scattering rate added via Matthiesen's to the relative electron-hole motion term. Intuitively, this makes sense: At exactly charge neutrality an electric current is equally shared by electrons and holes with no net momentum (no center-of-mass motion); however, disorder scattering can still randomize the momentum of an individual electron or hole

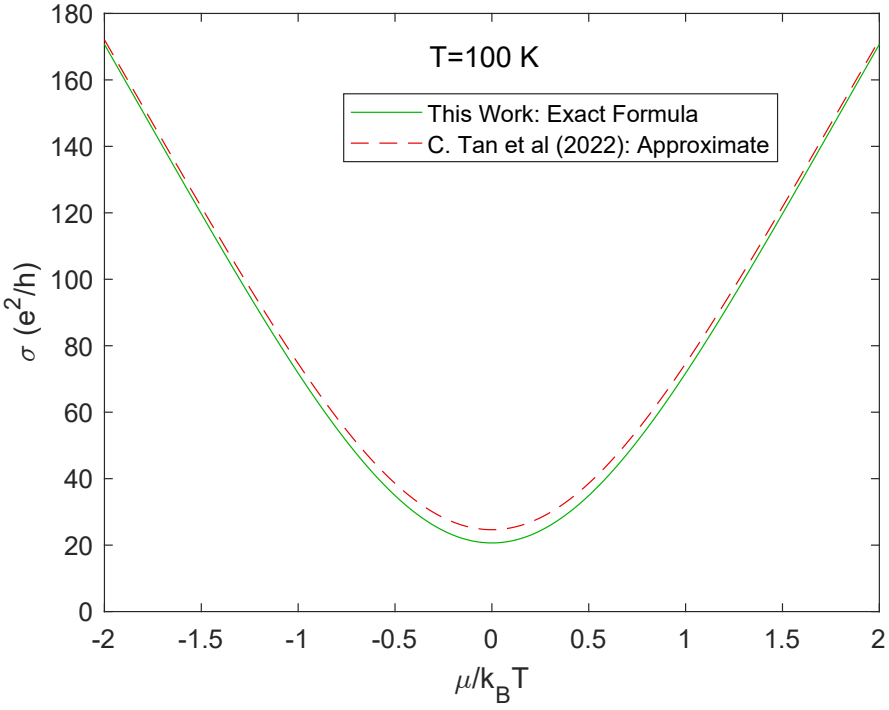

Figure E.1: Red: Conductivity formula from Ref. 3, Eq. 1. Green: Exact formula from this work, Eq. E.20.

in a collision, thus relaxing the electrical current. Put another way, the electron and hole components of the current, which have their own nonzero net momenta, are still individually relaxed by disorder scattering; the presence of the other does not protect one from impurity-scattering momentum relaxation.

We plot our exact Eq. E.20 and Eq. 1 from Ref. 3 in Fig. E.1, showing the difference between the two. We use the parameters for $T = 100$ K from Ref. 3. At high density, the two formulas agree, as we expected, but near charge neutrality, they disagree. At charge neutrality, the exact formula gives a conductivity of $\sigma_0 = 20.7\ e^2/h$, which is 16% lower than the approximate formula of Ref. 3, which would give $\sigma_0 = 24.6\ e^2/h$.

In the limit of zero phonon and disorder scattering, the two formulas would agree; however, this may not be experimentally possible because even in a disorder-free sample,

there will still be phonon scattering.

The true logic of this world is in the calculus of probabilities.

James Clerk Maxwell

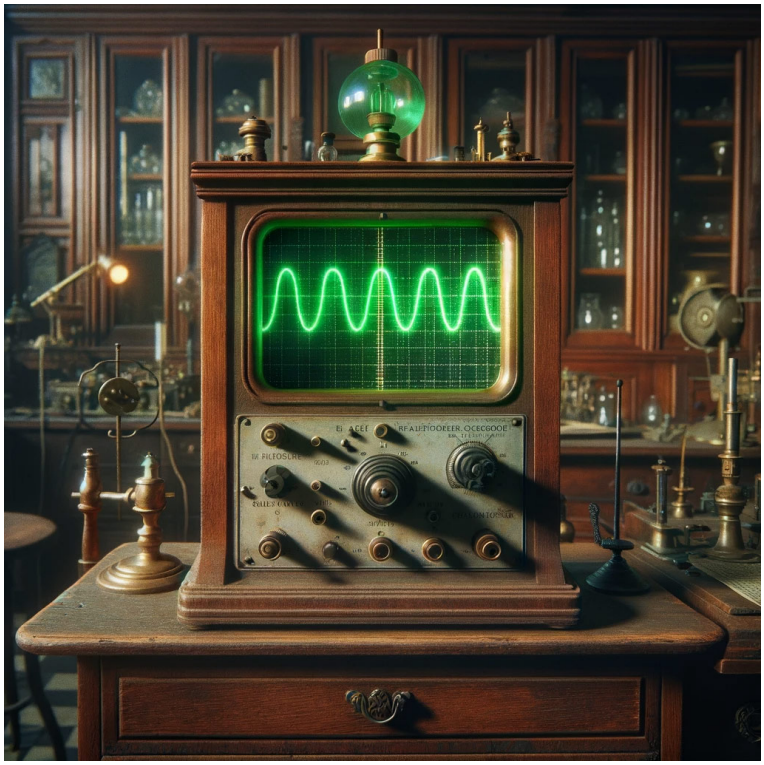

F

Standard Error of Lock-In Amplifier Measurements

Very often in the laboratory, we will use a digital lock-in amplifier to measure a very small signal that is AC-modulated to help improve the signal-to-noise ratio. In

measuring any quantity precisely by taking an average of many datapoints, we often want a confidence interval on our average to quantify our measurement precision. While this is a rather trivial task for discrete, uncorrelated measurement datapoints, the case is not so straightforward for the measurement of a signal on a lock-in amplifier, which is a time-varying continuous signal with some correlation time onto itself. In this Appendix, we present a method for estimating the uncertainty or precision of such a measurement.

For measuring the AC noise modulation, we use a lock-in amplifier, typically a Stanford Research Systems SR830, locked in to a frequency of approximately $2f \sim 26$ Hz. To perform a measurement, we will typically set the lock-in to a time constant of $\tau = 300$ ms, and then take several readings that are $\Delta \sim 300$ ms apart to compute an average. The number of readings N is typically 20-200, depending on what level of precision we would like. Finally, we would like to quantify the uncertainty in our measurement.

Statistically, the uncertainty in a measurement that is a mean of a large number of normally distributed points is the standard error s, typically approximated by

$$s \sim \sigma/\sqrt{N}, \tag{F.1}$$

where σ is the standard deviation of the points in the measurement, and N is the number of (statistically independent) data points. In a continuous lock-in measurement, the data points we take at a time interval of Δ are not statistically independent and have a certain correlation with each other that falls off with time; this is the result of the low-pass filter in the lock-in circuit after the mixer.

If over a measurement time t_m we collect N such correlated data points, we can consider that we have an effective number $\tilde{N}$ of independent datapoints, with $\tilde{N} < N$. We have observed that that the effective number of independent datapoints is related

to the effective noise bandwidth (ENBW) via

$$\tilde{N} = t_m \cdot \mathrm{ENBW}. \tag{F.2}$$

The ENBW is given on page 3-21 of the SR830 manual[138]; in particular for a low-pass filter slope of 24 dB/oct, the ENBW is $5/(64\tau)$ where τ is the lock-in time constant. This means that the lock-in gives an effectively independent datapoint every $\frac{64}{5}\tau$ seconds, which is 3.84 s for $\tau = 300$ ms. It doesn't matter what Δ actually is; as long it's somewhat lower than $\frac{64}{5}\tau$, the datapoints will be correlated enough that shortening Δ and acquiring more points in the same amount of time t_m won't change the average or the standard error.

The ENBW characterizes the spectral width of the low-pass filter, and therefore is also characteristic of the response and thus auto-correlation time of the filter. A formal proof that these are equivalent or related is outside the scope of this experimental thesis. However, we can provide some empirical evidence supporting our observation by looking at the auto-correlation of measured lock-in data points.

It was shown[251] that for an auto-correlated time series, an unbiased estimate for the standard error of the mean is given by scaling the calculated standard error by a factor f defined via

$$f \approx \sqrt{\frac{1+\rho}{1-\rho}}, \tag{F.3}$$

where ρ is the estimate of the auto-correlation coefficient for all sample-point r_i pairs,

defined via

$$\rho = \frac{\sum_{i=2}^{n} \hat{r}_i \hat{r}_{i-1}}{\sum_{i=2}^{n} \hat{r}_i^2}. \tag{F.4}$$

There are many variants of this estimate that vary with the inclusion or exclusion of endpoints in the denominator.

The exact sample correlation ρ will depend on the lock-in parameters and exact timing of the measurements, so here we use a specific example from an experimental run. We performed 500 measurements of the noise voltage modulation on a lock-in with 83 averaging points each ($t_m = 30\,\mathrm{s}$), with an average of 361 ms elapsed between measurement points, as shown in Fig. F.1(a).

The auto-correlation functions (ACF) of all 500 measurements are shown in Fig. F.1(b). The mean ACF at a lag value of 1 is 0.852, giving $f = 3.54$. Thus, the standard error of the mean of V should be

$$s_{\langle V \rangle} = f \frac{s}{\sqrt{N}} = 3.54 \frac{s}{\sqrt{83}}, \tag{F.5}$$

where s is the standard deviation of the measured 83 data points.

If we instead try to compute $\tilde{N}$ from the ENBW, we get a re-scaling factor for the number of data points of

$$f \sim \frac{\sqrt{N}}{\sqrt{\tilde{N}}} = \frac{\sqrt{83}}{\sqrt{7.8}} = 3.26. \tag{F.6}$$

The number we get from the ENBW of 3.26 is satisfyingly close to that computed from

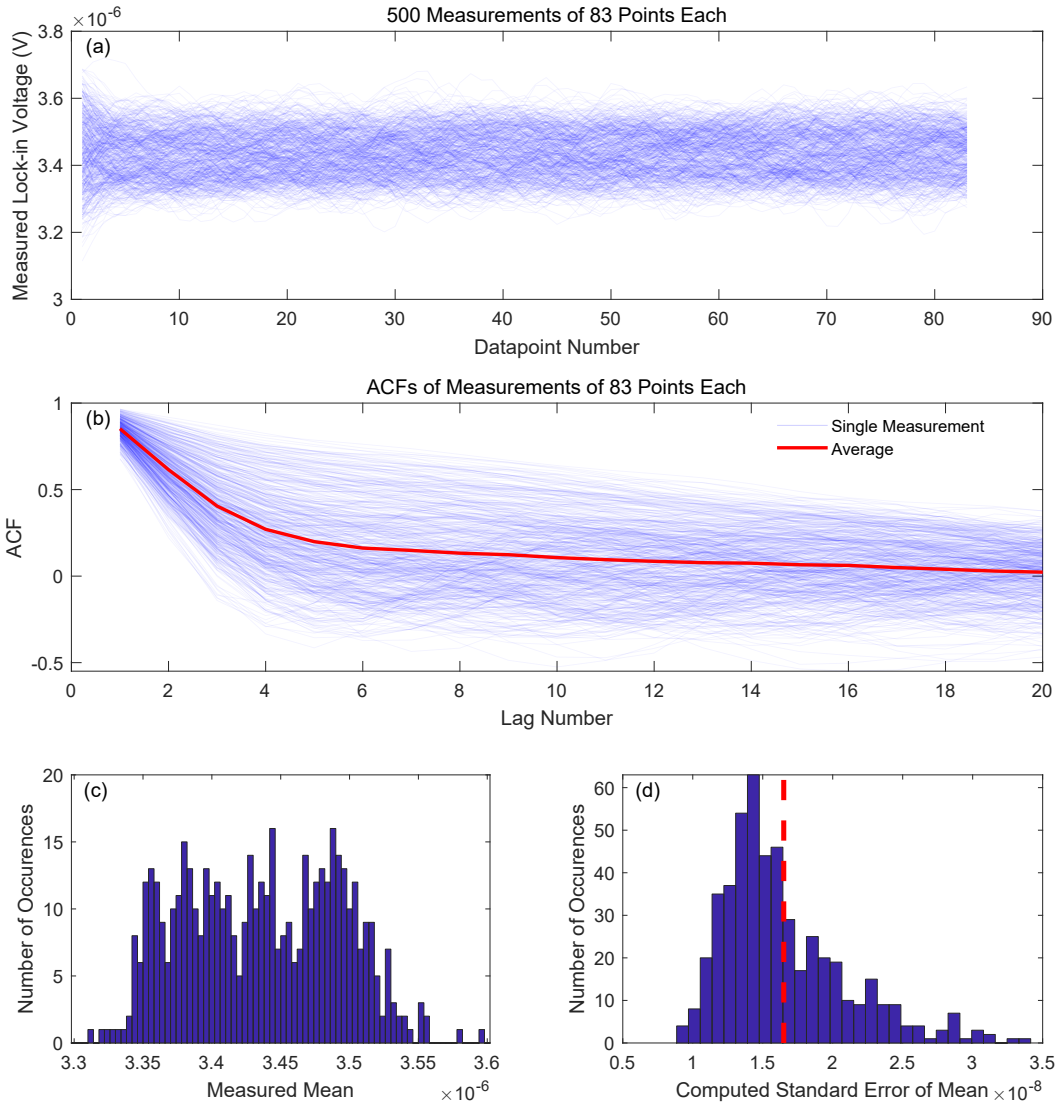

Figure F.1: **(a)** Time series density plot of measured lock-in X voltage; the datapoints are spaced by $\sim 361\,\mathrm{ms}$, and the entire 83 datapoint collection takes $30\,\mathrm{s}$. There are 500 traces on this plot, fluctuating around an average of $\sim 3.45\,\mu\mathrm{V}$. The self-correlation of any individual trace is seen as the wavy pattern. **(b)** Autocorrelation function (ACF) density plot, vs lag number up to 20, of the 500 traces from panel (a). Red curve indicates the average over the 500 traces. By approximately 7 lags or $7 \times 0.361\,\mathrm{s} \approx 2.5\,\mathrm{s}$, the correlation has mostly decayed to zero. **(c)** Distribution histogram of the measured mean of all 500 traces. The mean of each trace individually is computed by averaging the 83 datapoints in panel (a). The computed standard deviation of the means is $5.64/times10^{-8}\,\mathrm{V}$. **(d)** Distribution histogram of the individually computed standard errors of the mean, for all 500 measurement traces. The standard error of the mean, for each trace, is computed via Eq. F.6. The average of the computed standard errors is $1.65 \times 10^{-8}\,\mathrm{V}$, shown as the red dashed line.

the ACF of 3.54.

Because we did 500 measurements, we can actually measure the standard deviation of the mean and compare it to the computed standard errors via this method. The histogram of the means from 500 measurements is shown in Fig. F.1(c). The mean of the means is $\mu_{\langle V \rangle} = 3.4357 \times 10^{-6}$ V, and the standard deviation of the means is $\sigma_{\langle V \rangle} = 5.64 \times 10^{-8}$ V.

Fig. F.1(d) plots a histogram of the estimated standard errors of the mean from the 500 measurements via $s_{\langle V \rangle} = f\frac{s}{\sqrt{N}}$. The mean of the estimated standard errors of the mean is $\langle s_{\langle V \rangle} \rangle = 1.65 \times 10^{-8}$ (red dashed line), underestimating the measured standard deviation of the mean by a facor of 3.4; it is only coincidental that this number is close to f.

One mechanism to cause the measured standard deviation of the mean to be significantly larger than the estimated standard error is low-frequency DC-like drifts of the actual measurement value. This can be very difficult to measure, but we can motivate this explanation by looking at the auto-correlation of the 500 means. Fig. F.2(a) plots the auto-correlation of the 500 means for 1 to 499 lags in blue. We can see that the ACF at lag 1 is 0.24, significantly higher than the rest of the ACFs, indicating a not insignificant correlation due to drift. If there were no drift, the ACF at lag 1 should be marginally larger than zero, only due to small overlapping endpoint correlations between successive measurement runs. Additionally, we can plot the smoothed ACF for 1 to 499 lags (red); we see that it takes about 150–200 lags for for the ACF to reach zero within the noise fluctuations, indicating some DC drift when averaged over many runs.

As another way to see the drift, we plot the means of each of the 500 individual measurement runs in Fig. F.2(b) in blue, relative to the mean of the means in black. Within the noise of the individual means, there is no clearly visible drift. The red

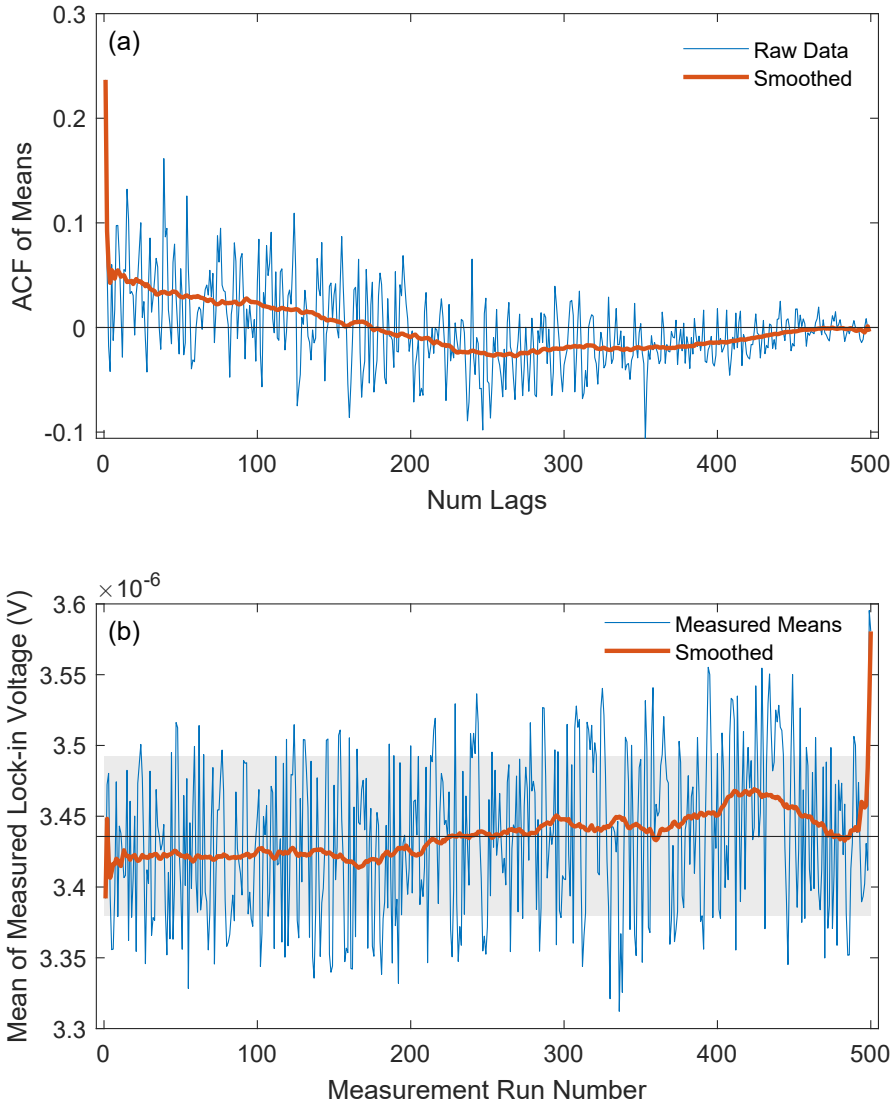

Figure F.2: **(a** Autocorrelation of the measured data means. Blue: autocorrelation, vs lag number, of the measured data means from the 500 measurement runs. Red: smoothed out autocorrelation to better see the trends. The increased value of the ACF at lag 1, as well as the slow decay over $\sim$ 200 lags, indicates a quickly-moving and a slowly-moving drift component of the measurement value over time, which can cause a larger spread of the data means in Fig. F.1(c). **(b)** Data drift over time, plotted vs measurement number. Blue: The measured means of each of 500 measurement runs, vs the run number. Red: the means, smoothed over a 65-point moving box average. The jumps at the beginning and end are due to the running average box being truncated. Black line: mean of all the means, to be used as a reference. Overall, there is a slow drift of means over time. The light gray box behind the data indicates the $\mu_{\langle V\rangle} \pm \sigma_{\langle V\rangle}$, which would contain 68% of the means if they were normally distributed.

curve shows the means smoothed out over 65 points, removing the local statistical noise and revealing the overall DC drift. The jumps at the beginning and end are due to the running average box being truncated in the smoothing algorithm. During the span of 500 measurements, the "true" value that we have attempted to measure drifted by approximately 5×10^{-8} V. If the "true" value did not drift, then we would expect the 65-point moving average to be centered, within its own noise, on the overall mean of the mean, which does not happen. This DC drift of the measurement value acts to smear out or widen the distribution shown in Fig. F.1(c), likely contributing to its more plateau-like shape instead of the expected Gaussian bell curve. This slow drift smoothed out over 65 points, however, is not large enough to explain the factor of 3.4 difference between $\sigma_{\langle V \rangle}$ and $s_{\langle V \rangle}$. We propose that a faster-timescale drift, that is responsible for the high ACFs at low lag numbers much smaller than 65, may contribute significantly to the spread of the means.

Finally, because we have only $\tilde{N} = 7.8$ effectively independent datapoint for each measurement run of 30 s, the calculated standard error may be significantly underestimated due to the small sample size. Additional statistical experiments are needed to better understand the mechanism and source of the uncertainty in our lock-in measurements.

The fundamental laws necessary for the mathematical treatment of a large part of physics and the whole of chemistry are thus completely known, and the difficulty lies only in the fact that application of these laws leads to equations that are too complex to be soluble.

Paul Dirac

G

Mathematical Details for Noise in Viscous Transport in Corbino under Magnetic Field

This Appendix describes the mathematical details of Johnson noise in a self-heating configuration for a viscous Corbino device under magnetic field, and it directly complements the experimental results presented in Chapter 6. This Appendix was written by our collaborator Aaron Hui as part of the project for Chapter 6, and we have reproduced it in this dissertation for completeness, with his kind permission.

Here, we derive the result for Johnson noise. This problem consists of two major steps - computing the temperature profile T, and converting the bulk noise generated by T into the current noise measured at the contacts. Because this procedure involves solving the Stokes equations in multiple times in slightly different forms, we begin by studying its general solution.

G.1 Stokes Equation: General Solution

We consider flow in an annular domain Ω with inner radius r_i and outer radius r_o under a uniform magnetic field $\mathbf{B} = B\hat{\mathbf{z}}$. The Stokes equations are

$$\nu\nabla^2\mathbf{v} + \frac{q}{m}\mathbf{v}\times\mathbf{B} - \frac{q}{m}\nabla\phi = -\mathbf{g} \tag{G.1}$$

$$\nabla\cdot\mathbf{v} = 0 \tag{G.2}$$

where ν is the kinematic viscosity, q the hydrodynamic charge, m the hydrodynamic mass, and $\mathbf{g}$ a generic forcing term ($\nabla^2\mathbf{v}$ is the *vector* Laplacian). As we will only be concerned with angular-averaged quantities $\overline{X} = \int \frac{d\theta}{2\pi}X$, we can simplify these equations

in orthonormal polar coordinates to

$$\int dr\Big(\mathfrak{L}[\overline{v}_r] + \omega_c \overline{v}_\theta\Big) + \frac{q}{m}\,\overline{\phi}\Big|_{r_i}^{r_o} = \int dr \overline{g}_r \tag{G.3}$$

$$\mathfrak{L}[\overline{v}_\theta] = \overline{g}_\theta + \omega_c \overline{v}_r \tag{G.4}$$

$$\overline{v}_r = \frac{I}{nq}\frac{1}{2\pi r} \tag{G.5}$$

where we define the linear "dissipation" or friction operator $\mathfrak{L}[v] \equiv \gamma v - \nu\left[\partial_r^2 v + \frac{1}{r}\partial_r v - \frac{v}{r^2}\right]$ and the constant I is the total radial current. Notice that incompressibility Eq. G.5 immediately gives us the solution for $\overline{v}_r$. This allows us to decouple Eq. G.4 and solve it independently. Furthermore, we evade solving for $\overline{\phi}$ by performing the $\int dr$ integral in Eq. G.3. In what follows, we will drop the overbars and implicitly understand that all quantities are angular-averaged. To finish solving the above equations, we must specify boundary conditions (BCs).

For Eq. G.4, we take no-slip $v_\theta|_{\partial\Omega} = 0$. With this BC, we abstractly denote the solution

$$v_\theta = \mathfrak{L}^{-1}[g_\theta + \omega_c v_r] = \mathfrak{L}^{-1}[g_\theta] + \omega_c \mathfrak{L}^{-1}[v_r] \tag{G.6}$$

where $\mathfrak{L}^{-1}$ is a linear operator. This notation can be motivated by the fact $\mathfrak{L} \circ \mathfrak{L}^{-1}[g] = g$.*

Finally, for Eq. G.3 we specify voltage-fixed BCs in two steps. First, we specify the external (measured) voltage difference $-\phi_c|_{r_i}^{r_o} = V$ from r_i to r_o. Then, there also exists a contact voltage drop $[\phi_c - \phi]_{r\in\partial\Omega} = \frac{2m\nu}{q}\,\frac{\mathbf{v}\cdot\hat{\mathbf{r}}}{r}\big|_{r\in\partial\Omega}$ on the boundary[58]. Therefore,

*In the theory of PDEs, there is a precise sense in which $\mathfrak{L}$ is an invertible linear operator with inverse given by $\mathfrak{L}^{-1}$. See e.g. 252 for details.

Eq. G.3 can be rewritten

$$IR = V + \int dr \left(g_r - \omega_c \mathfrak{L}^{-1}[g_\theta] \right) \tag{G.7}$$

$$R = \frac{m}{nq^2} \int dr (\mathfrak{L} + \omega_c^2 \mathfrak{L}^{-1}) \left[\frac{1}{2\pi r} \right] - \frac{m\nu}{nq^2} \frac{1}{\pi} \frac{1}{r^2} \Bigg|_{r_i}^{r_o} \tag{G.8}$$

where R is the two-terminal resistance. As an aside, this procedure easily generalizes to the Ohmic-Stokes case by simply altering the form of $\mathfrak{L}$; we utilize this fact in Sec. G.4. For convenience, we denote the Stokes equations with the above BCs, i.e. the Stokes problem, as $\mathbb{S}[\mathbf{v}; \mathbf{g}, V]$.

In particular, $\mathfrak{L}^{-1}[g]$ is given by

$$\mathfrak{L}^{-1}[g] = -\frac{r_o v_p(r_o) - r_i v_p(r_i)}{r_o^2 - r_i^2} r + \frac{r_i^2 r_o^2}{r_o^2 - r_i^2} \left(\frac{v_p(r_o)}{r_o} - \frac{v_p(r_i)}{r_i} \right) \frac{1}{r} + v_p(r) \tag{G.9}$$

$$v_p(r) \equiv -\frac{1}{\nu} \frac{1}{r} \int^r dr' r' \int^{r'} dr'' g(r'') \tag{G.10}$$

where v_p is a particular solution satisfying $\mathfrak{L}[v_p] = g$. Notice we have defined $v_p(r)$ using antiderivatives; to fix the integration constants, one can arbitrarily fix the lower integration bound.

G.2 Temperature Profile

Obtaining the temperature profile is done in two steps. First, we compute the velocity profile from the steady-state Stokes equations. Then, computing the resulting viscous heating from the velocity, we solve the heat equation. The Stokes equations here have

$\mathbf{g} = 0$ (i.e. $\mathbb{S}[\mathbf{v}; 0, V]$), so by circular symmetry we have

$$v_r = \frac{I}{nq}\frac{1}{2\pi r} \tag{G.11}$$

$$v_\theta = \omega_c \frac{I}{nq}\mathfrak{L}^{-1}\left[\frac{1}{2\pi r}\right] = \frac{I}{nq}\frac{\omega_c}{2\pi\nu}\left[c_1 r + c_2\frac{1}{r} - \frac{1}{2}r\ln r\right] \tag{G.12}$$

where $c_1 = \frac{1}{2}\frac{r_o^2 \ln r_o - r_i^2 \ln r_i}{r_o^2 - r_i^2}$ and $c_2 = -\frac{1}{2}\frac{r_i^2 r_o^2}{r_o^2 - r_i^2}\ln\frac{r_o}{r_i}$. Then, we solve the heat equation

$$-\kappa\nabla^2 T = \mathfrak{q} \equiv \frac{1}{2\eta}(\sigma'_{ij})^2 \tag{G.13}$$

where $\eta = mn\nu$ is the dynamic viscosity, $\mathfrak{q}$ is the viscous heating density, and $\sigma'_{ij} = \eta(\partial_i v_j + \partial_j v_i)$ the viscous (deviatoric) stress tensor for incompressible flow[253]. We take fixed $T = T_0$ BCs for the heat equation. With circular symmetry, the *scalar* Laplacian simplifies and one explicitly finds

$$\mathfrak{q}(r) = \frac{m\nu}{nq^2}\frac{I^2}{(2\pi)^2}\left[\frac{4}{r^4} + \left(\frac{\omega_c}{2\nu}\right)^2\left(1 + \frac{4c_2}{r^2}\right)^2\right] \tag{G.14}$$

$$\begin{aligned}\delta T(r) = \frac{m\nu}{nq^2\kappa}I^2\frac{1}{(2\pi)^2}\Bigg[&\left(\frac{1}{r_i^2} - \frac{1}{r^2} - \left(\frac{1}{r_i^2} - \frac{1}{r_o^2}\right)\frac{\ln\frac{r}{r_i}}{\ln\frac{r_o}{r_i}}\right)\\ &+ \frac{\omega_c^2}{4\nu^2}\left(\frac{1}{4}\left[-(r^2 - r_i^2) + (r_o^2 - r_i^2)\frac{\ln\frac{r}{r_i}}{\ln\frac{r_o}{r_i}}\right]\right.\\ &\left.-4c_2\ln\frac{r}{r_i}\ln\frac{r}{r_o} + 4c_2^2\left[\frac{1}{r_i^2} - \frac{1}{r^2} - \left(\frac{1}{r_i^2} - \frac{1}{r_o^2}\right)\frac{\ln\frac{r}{r_i}}{\ln\frac{r_o}{r_i}}\right]\right)\Bigg]\end{aligned} \tag{G.15}$$

where $\delta T \equiv T - T_0$.

G.3 Current Noise

The current noise is also computed in two steps. We wish to compute $\langle \delta I(\omega \to 0)\delta I(t = 0)\rangle \equiv \langle \delta I \delta I_0\rangle$ at fixed voltage $\delta V = \langle \delta V \delta I_0\rangle = 0$, where from now on we suppress the frequency argument. The current noise equations are given by the Stokes problem $\mathbb{S}[\langle \delta \mathbf{v} \delta I_0\rangle; 2\langle \delta \mathbf{v}_s \delta I_0\rangle, 0]$[176,254], where we assume thermal density fluctuations can be ignored to obtain incompressibility[†]. However, to solve the noise problem we must compute the noise input $\langle \delta \mathbf{v}_s \delta I_0\rangle$.

To obtain the noise input $\langle \delta \mathbf{v}_s \delta I_0\rangle$, we solve the so-called hydrodynamic Shockley-Ramo problem: how much total current δI_0 is induced by a velocity source $\delta \mathbf{v}_s$? This has previously been studied in the free space[255,256] and Ohmic[165,257–259] cases, where there is a simple result known as the (generalized) Shockley-Ramo theorem. The hydrodynamic Shockley-Ramo problem is given by $\mathbb{S}\left[\delta \mathbf{v}; \mathfrak{L}[\delta \mathbf{v}_s], -\frac{2m\nu}{q}\ \frac{\delta v_{s,r}}{r}\Big|_{r_i}^{r_o}\right]$, which has solution

$$\delta I_0 R = -\frac{2m\nu}{q}\ \frac{\delta v_{s,r}}{r}\Big|_{r_i}^{r_o} + \frac{m}{q}\int dr\Big[\left(\mathfrak{L} + \omega_c^2 \mathfrak{L}^{-1}\right)[\delta v_{s,r}] - \omega_c\left(\mathfrak{L}^{-1}\mathfrak{L} - 1\right)[\delta v_{s,\theta}]\Big] \tag{G.16}$$

Physically, we can understand the hydrodynamic Shockley-Ramo problem as follows. The injected carriers $\delta \mathbf{v}_s$ induce a flow of internal carriers $\delta \mathbf{v} - \delta \mathbf{v}_s$. These internal carriers obey the Stokes equations and enforce incompressibility and BC constraints on the total current $\delta \mathbf{v}$ (see also Ref. 165). In particular, a velocity source "on the boundary" induces a contact voltage drop which drives total flow, as seen in the first

[†]Thermal density fluctuations are suppressed by the thermal Mach number $\sqrt{k_B T/(mc^2)}$, where c is the speed of sound[254]. A rough estimate with $m = m_e$ the electron mass at $T = 300K$ and $c \sim v_F \sim 10^6 m/s$ gives $\mathrm{Ma}_{\mathrm{th}} \sim .07$, so we expect thermal density fluctuations to be a subleading effect.

term of Eq. G.16.

With this result in hand, we can obtain the current noise from the noise problem $\mathbb{S}[\langle\delta\mathbf{v}\delta I_0\rangle; 2\langle\delta\mathbf{v}_s\delta I_0\rangle, 0]$. Substituting Eq. G.16 into $\langle\delta\mathbf{v}_s\delta I_0\rangle$ and simplifying, this is

$$T_{JN} \equiv \frac{R}{2k_B}\langle\delta I\delta I_0\rangle \tag{G.17}$$

$$= T_0 + \frac{m}{nq^2}\frac{1}{R}\int dr\left(\mathfrak{L} + \omega_c^2\mathfrak{L}^{-1}\right)\left[\frac{\delta T(r)}{2\pi r}\right] \tag{G.18}$$

where $\delta T \equiv T - T_0$ and we have used $\langle\delta v_{s,i}(\mathbf{r})\delta v_{s,j}(\mathbf{r}')\rangle = \frac{k_B T(r)}{mn}\delta(\mathbf{r}-\mathbf{r}')\delta_{ij}$ and $(\mathfrak{L}_r^{-1}\mathfrak{L}_r - 1)[\delta(\mathbf{r}-\mathbf{r}')] = 0$ since $\delta(\mathbf{r}-\mathbf{r}')$ vanishes on $\partial\Omega$ [‡]. Thus, Eq. G.18 relates the Johnson noise temperature to a complicated weighted average of the local temperature $T(r)$. Furthermore, we see that there are three effects of the magnetic field. One is to modify the velocity profile, changing the heating structure and therefore the overall temperature distribution. The second is to modify the temperature-averaging procedure as seen in Eq. G.18. Finally, the third is to modify the resistance R in the denominator.

It is useful to compare Eq. G.18 to the universal result in the Ohmic limit $\delta T_{JN}^{\text{ohm}} = \frac{PR}{12LT_0} = \frac{PR_{\text{th}}}{12}$, where R_{th} is the thermal resistance and L is the Wiedemann-Franz value of the Lorenz ratio[162,164]. Using the R_{th} form of this equation to define $\delta T_{JN}^{\text{ohm}}$ in the hydrodynamic regime, we find

$$f \equiv \frac{\delta T_{JN}}{\delta T_{JN}^{\text{ohm}}} \tag{G.19}$$

$$= \frac{12}{\ln s}\frac{a_0 + \left(\frac{\omega_c r_i^2}{\nu}\right)^2 a_2 + \left(\frac{\omega_c r_i^2}{\nu}\right)^4 a_4}{\left(R_0 + \left(\frac{\omega_c r_i^2}{\nu}\right)^2 R_2\right)^2} \tag{G.20}$$

[‡]The term $(\mathfrak{L}_r^{-1}\mathfrak{L}_r - 1)[\delta(\mathbf{r}-\mathbf{r}')]$ corresponds to a boundary-value problem of $\mathfrak{L}[v] = 0$, with boundary values determined by $\delta(\mathbf{r}-\mathbf{r}')$. Since we assume $\mathbf{r}$ can only take values in the interior of Ω, the delta function must vanish on Ω.

with coefficients

$$a_0 = \frac{-(s^2-1)^2 + 2(s^4-1)\ln s}{4\pi^2 s^4 \ln s} \tag{G.21}$$

$$a_2 = \frac{3(s^2-1)^3 - 4s^2(s^2-1)\ln^2 s - 8s^2(s^2+1)\ln^3 s}{64\pi^2 s^2(s^2-1)\ln s} \tag{G.22}$$

$$a_4 = \frac{-3+3s^4+76s^2\ln s}{2048\pi^2} - \frac{(s^2-1)^2}{512\pi^2 \ln s} - \frac{5s^2(s^2+1)\ln^2 s}{256\pi^2(s^2-1)} + \frac{s^4 \ln^3 s(-3+\ln^2 s)}{96\pi^2(s^2-1)^2} - \frac{s^4(s^2+1)\ln^4 s}{32\pi^2(s^2-1)^3} \tag{G.23}$$

$$R_0 = \frac{1}{\pi}\left(1 - \frac{1}{s^2}\right) \tag{G.24}$$

$$R_2 = \frac{1}{16\pi}\left(s^2 - 1 - \frac{4s^2\ln^2 s}{s^2-1}\right), \tag{G.25}$$

where $s = \frac{r_o}{r_i}$ is the aspect ratio and we write the resistance $R = \frac{m\nu}{nq^2 r_i^2}\left(R_0 + \left(\frac{\omega_c r_i^2}{\nu}\right)^2 R_2\right)$. In particular, the B-field dependence of the numerator of f is determined by the temperature profile and the temperature-averaging, while the denominator is completely determined by the resistance.

We plot the the ratio $f(B)$ as a function of magnetic field in Figs. G.1 and G.2. It is important to note that each curve is scaled differently, i.e. $B_0 = (m/q)(\gamma + \nu/r_i^2)$ is different for each curve. We see in the Ohmic-dominant regime where λ is small, $f(B)/f(0)$ increases above its limiting $f = 1$ Ohmic value. This occurs because there is an additional viscous heating channel at finite λ, increasing the Johnson noise. As λ increases, viscous flow corrections eventually dominate, pushing the heating (at constant power) towards the contacts. This reduces the effectiveness of heating, thus reducing the Johnson noise temperature.

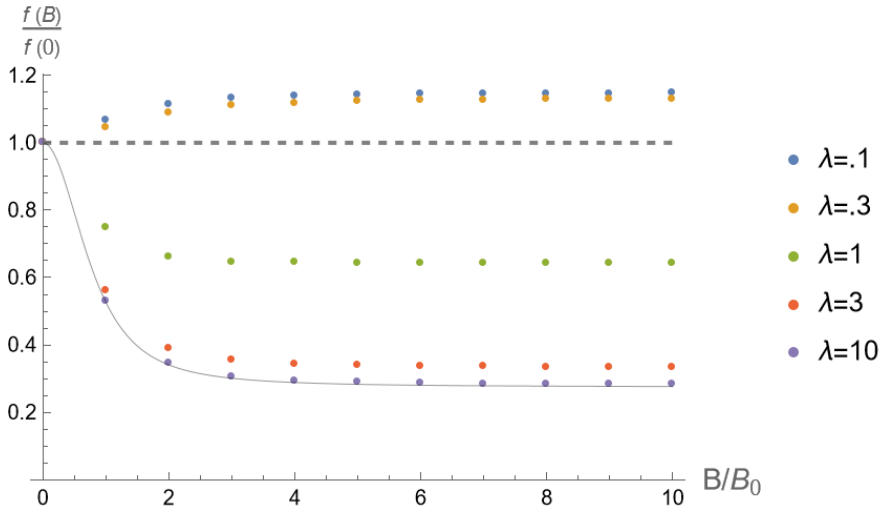

Figure G.1: The normalized $f(B)/f(0)$ for $r_o/r_i = 5$. The dashed line corresponds to the Ohmic $\lambda = 0$ value, while the solid thin line corresponds to the viscous $\lambda \to \infty$ value. These curves are plotted against B/B_0, where the scale $B_0 = (m/q)(\gamma + \nu/r_i^2)$ is different for each curve.

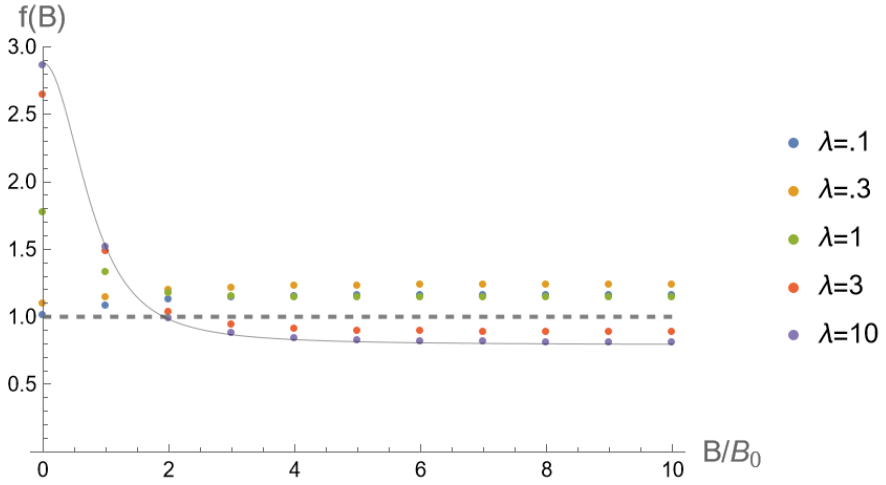

Figure G.2: The true $f(B)$ value for $r_o/r_i = 5$, from Fig. G.1.

G.4 Ohmic Limit

Here, we perform the analogous calculation for the Ohmic case. In the Ohmic limit $\nu \to 0$, we simply replace the operator $\mathfrak{L} \equiv \gamma v$ and rerun the calculation. First, we have

$$\mathfrak{L}^{-1}[g] = \frac{g}{\gamma} \tag{G.26}$$

In this limit, we've removed a leading-order derivative, thus the boundary conditions become superfluous. Thus, under voltage bias (the Ohmic version of $\mathbb{S}[\mathbf{v}; 0, V]$), we find

$$v_r = \frac{I}{nq}\frac{1}{2\pi r} \tag{G.27}$$

$$v_\theta = \omega_c \tau \frac{I}{nq}\frac{1}{2\pi r} \tag{G.28}$$

$$R = (1+\omega_c^2\tau^2)\frac{m\gamma}{nq^2}\frac{\ln\frac{r_o}{r_i}}{2\pi} \tag{G.29}$$

where $\tau \equiv \gamma^{-1}$ and R is the two-terminal resistance. Computing the Ohmic heating $\mathfrak{q} = mn\gamma v^2$ and temperature profile, we get

$$\mathfrak{q}(r) = (1+\omega_c^2\tau^2)\frac{I^2}{(nq)^2}\frac{1}{4\pi^2 r^2} = \frac{P}{2\pi \ln\frac{r_o}{r_i}}\frac{1}{r^2} \tag{G.30}$$

$$\delta T(r) = -\frac{P}{\kappa}\frac{1}{4\pi \ln\frac{r_o}{r_i}} \ln\frac{r}{r_i}\ln\frac{r}{r_o} \tag{G.31}$$

where $P \equiv I^2 R$ is the total dissipated power. Finally, using Eq. G.18 we find that

$$T_{JN} = \int dr \frac{T(r)}{r \ln\frac{r_o}{r_i}} = \frac{P R_{\text{th}}}{12} \tag{G.32}$$

Thus, we recover $f = 1$ in agreement with previous works[162,164].

The experiment left no doubt that, as far as accuracy of measurement went, the resistance disappeared.

Heike Kamerlingh Onnes

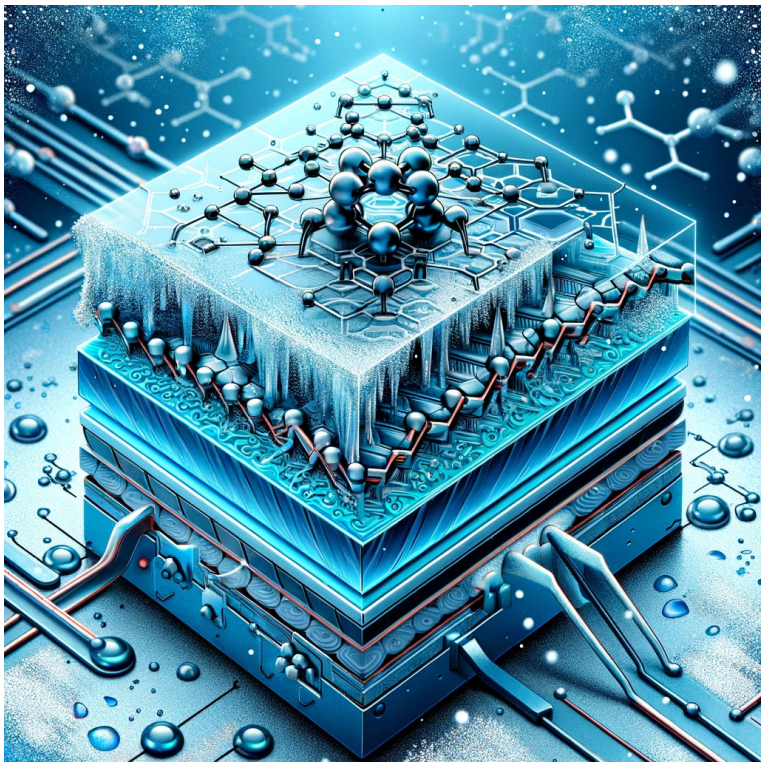

H

Cryostats and Cryogenic Hardware

In this Appendix, we describe the two cryostats used extensively for sample measurements in this thesis, and we describe some of the custom modifications we made to them in order to facilitate our noise measurements.

H.1 Sumitomo

This cryostat was sold under the Janis brand name, but it is really a closed-cycle Sumitomo Gifford-McMahon (GM) cryocooler with a few additional parts from Janis. Janis supplied the instrumentation collar, which allows electrical feedthroughs into the vacuum space, as well as the vacuum can, radiation shield, sample mounting hardware, and thermometry lines. The cryostat is shown mounted on a home-made aluminum plate inside of an enclosed rack, with the vacuum can installed, in Fig. H.1. Additional metal panels and doors for EMI shielding can be installed onto the rack enclosure. Visible immediately next to the cryostat are the two RF amplifier circuits and four amplifier power supplies. The cryostat has six RF lines, 40 DC lines using Fischer connectors at room temperature, and a sample temperature range of 3–300 K. The cryostat can reach base temperature from room temperature in about 70 minutes, but it is recommended to ramp down the temperature slowly to avoid thermal shock to the cryogenic LNAs mounted inside.

The inside of the cryostat is shown in Fig. H.2 from two different views, to see all the components. We have entirely re-fabricated the sample mount in order to allow us to mount 2 cryogenic LNAs at the base temperature of the cold plate, as well as allow the sample to be nearly independently warmed up relative to this cold plate, facilitating measurements of a warmer sample while keeping the LNAs at a constant low temperature to take advantage of their lower noise at low temperature. The sample package is weakly thermally anchored to the cold plate via a hollow aluminum rod. We have installed a separate heater and thermometer for both the LNA stage and the sample stage to independently control their temperatures via proportional-integral-derivative (PID) feedback. The thermometer for the cold plate is mounted on the backside of

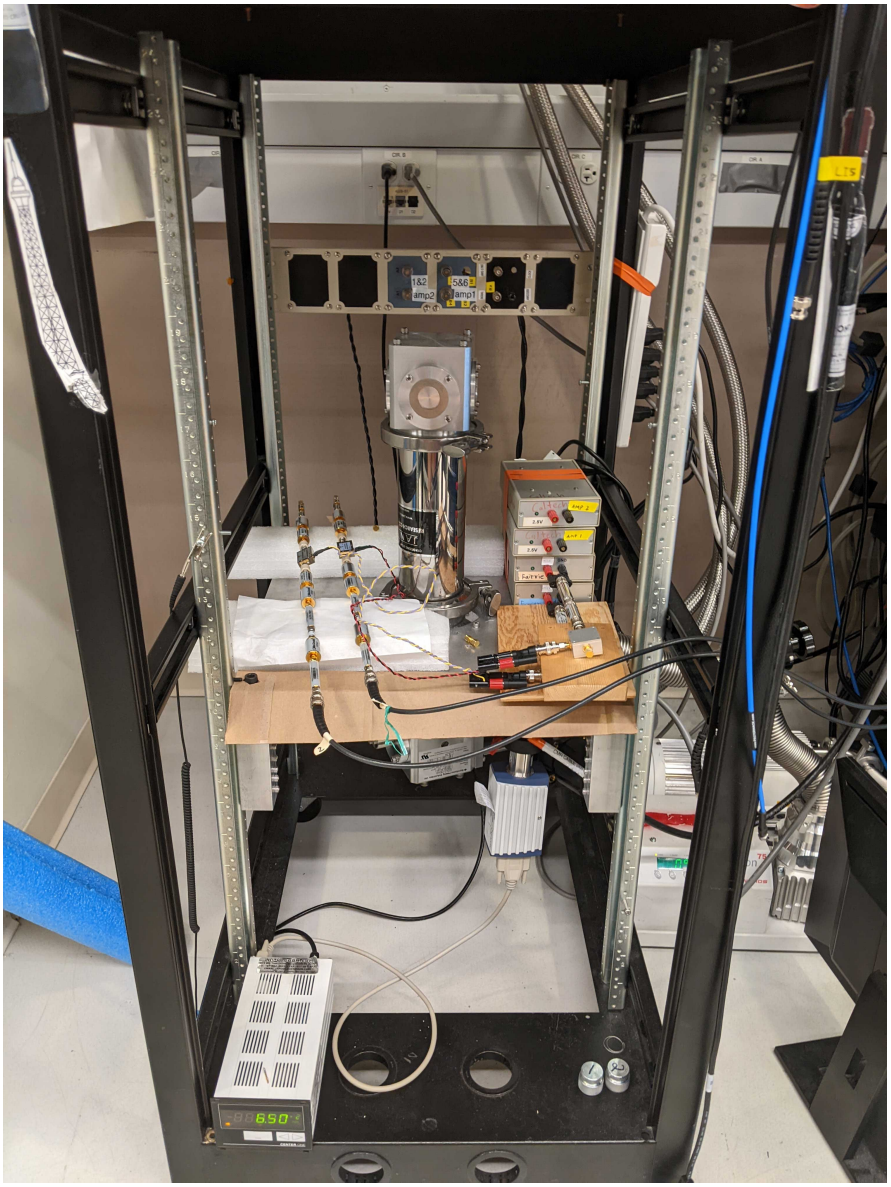

Figure H.1: Image of the Sumitomo cryostat mounted in its rack, with the vacuum can installed.

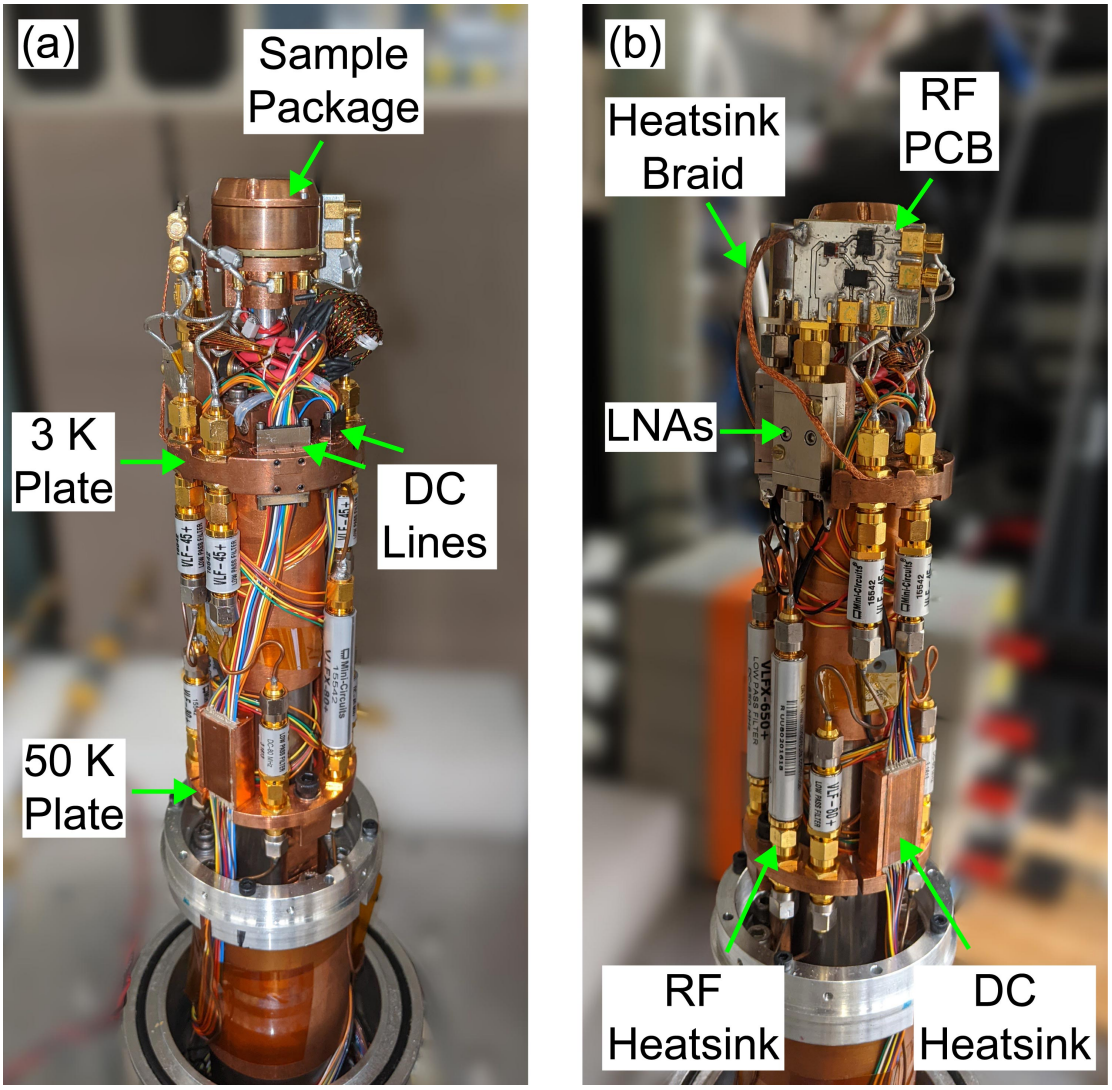

Figure H.2: **(a,b)** Images of the Sumitomo cryostat cold head, with labeled accessories, from two different views.

the LNA holder stand, allowing a more precise temperature control of the LNAs. The heater for the cold plate is in the same copper block as the hollow aluminum rod. As the sample is warmed up and more heat flows through the rod to the cold plate due to the temperature difference, the cold plate heater produces less heat. In this way, the temperature profile across the cold plate is kept as constant as possible while the sample temperature is varied, allowing more accurate temperature control of the LNAs.

We have installed two RF PCBs, each with two diplexers and a hybrid to realize the differential noise measurement scheme, directly onto the input port of the LNAs. We have heat-sunk these PCBs to the cold plate using copper braid (see Section 4.8). We have also mounted several RF lines that are heat-sunk at the first ($\sim 50\,\mathrm{K}$) cryogenic stage. There is a set of 25 and a set of 15 DC copper lines, with nano-D connectors, used for gates, thermometry, heating, and amplifier power supplies, that are also heat-sunk to the 50 K plate and the 3 K plate. The heat-sinking to the 50 K plate was done with silver epoxy into a copper block holder, and the heat-sinking to the 3K plate was done through the nano-D connector and a tight fitting holder. Some of these DC lines are left unused and may be repurposed for DC bias lines in the future.

Finally, we have also designed a new radiation shield, shown in Fig. H.3, optimized to maximize the space inside with wall thicknesses of nominally 0.068". This shield allows the top to be removed to visually examine the components inside to verify they are not contacting the radiation shield. The top cap threads into the main portion of shield with very fine threads (36 threads per inch on a 3" diameter), and different metals were chosen for these two parts to prevent galling. The cap should be very carefully threaded in and only gently hand-tightened; it has two wrench flats for emergency removal only, if it cannot be removed by hand.

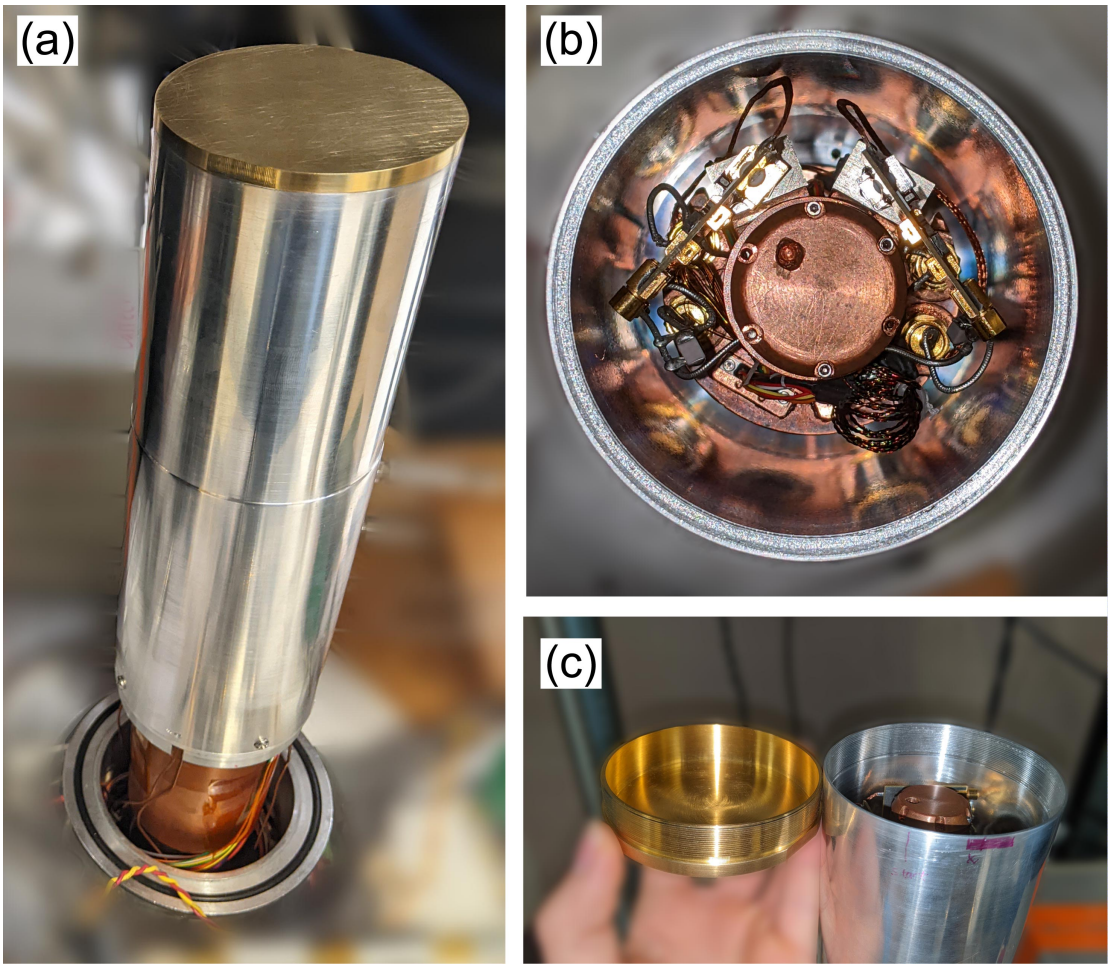

Figure H.3: **(a)** Custom-made radiation shield to maximize internal working space. The main body is from aluminum and the top cap is from brass. The top cap threads into the main body with a very fine-pitch thread. **(b)** View inside the radiation shield with the top cap removed, in order to verify the cold components are not contacting the radiation shield. **(b)** View of the top cap removed next to the radiation shield, showing the fine threads. Care must be taken when re-installing the top cap to avoid cross-threading it.

H.2 Janis

The other cryostat that we have used is a variable-temperature insert (VTI) cryostat, manufactured by Janis. This cryostat uses liquid helium and can achieve a sample temperature range of 1.6–300 K, although operation near room temperature boils off helium rapidly. The sample is cooled by a low-pressure vapor of helium, with the sample space continuously pumped to generate cooling from the vaporizer. Colder temperature can be achieved temporarily via single shot operation, by filling the sample space with liquid helium, and closing the needle valve while continuing to pump. Stronger pumping speed will generally allow a lower base temperature.

This cryostat contains a liquid-immersed superconducting magnet capable of producing a magnetic field up to 9 T, and thus we prefer to keep our LNAs further away from the magnet to avoid affecting their gain and noise properties with magnetic field sweeps. We place the LNAs, as well as the diplexers and hybrid, into a separate dewar that we fill with liquid nitrogen. The entire setup, with both the main cryostat and the side dewar containing the LNA electronics at 77 K, is shown in Fig. H.4. Importantly, very low-loss 1/4" braided coaxial cables carry the non-amplified Johnson noise from the probe output on the main cryostat, through room temperature, down into the liquid nitrogen dewar to the LNA electronics. The accessibility of these coaxial lines from room temperature allows the noise temperature matching technique described in Section 4.9.4, which is impossible in the Sumitomo cryostat.

The home-made probe for this VTI was originally made by Jesse Crossno[175], modified by Jonah Waissman, and then modified again by the present author. It is shown suspended in Fig. H.5. The probe holds the sample at the end and inserts it into the bore of the magnet. Ultimately, the most recent design include four 141 semi-rigid

Figure H.4: Images of the Janis setup, with the main cryostat on the left, and the liquid nitrogen dewar with LNA electronics on the right.

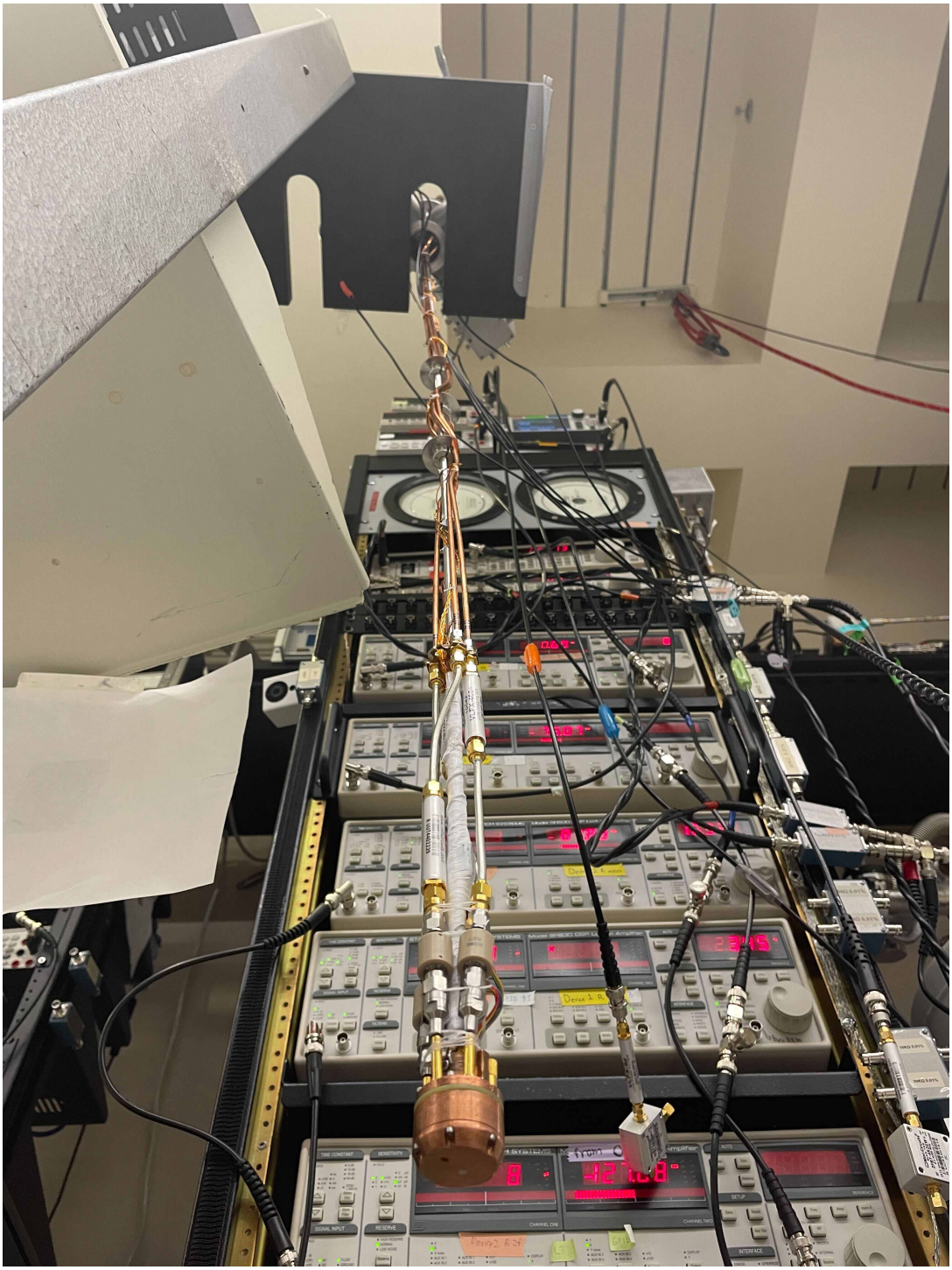

Figure H.5: The home-made RF probe for the VTI, in front of the Janis instrument rack.

coaxial cables for low loss running down the main length of the probe. After these 141 cables, there is a set of cold low-pass filters, a short run of thinner braided flexible coaxial cables, and then finally outer DC blocks before reaching the sample to improve thermal isolation. The thermal isolation was described in Section 4.8. Up to four outer DC blocks can be fit, with careful selection of RF connectors and the flexibility of the shorter coaxial cables.

The copper sample enclosure at the end of the probe is the same one used in the Sumitomo cryostat, and thus sample PCBs are entirely interchangeable between these two cryostats. The probe also has DC gate lines and thermometry/heater lines running down its length. As we saw in Section 4.10, electronic noise can couple very easily between these lines, and thus each one must be meticulously filtered.

On the probe, strategically placed waxed dental floss holds all the components tight in towards the center, preventing them from contacting the primary bore of the VTI and causing a thermal short. This is especially important close to the sample enclosure, to allow the sample to be heated significantly above the temperature of the vapor. The plastic jacket on the DC outer blocks is a good thermal insulator and is allowed to contact the inner walls of the primary VTI bore, thus centering the sample enclosure and probe within the bore.

The probe was originally designed for the Oxford VTI cryostat, but it was made to fit into the Janis cryostat as well by use of a KF to Tri-Clamp adapter. The Janis VTI uses the Tri-Clamp flange to hermetically seal the probe to the main body of the cryostat.

We can only see a short distance ahead, but we can see plenty there that needs to be done.

Alan Turing

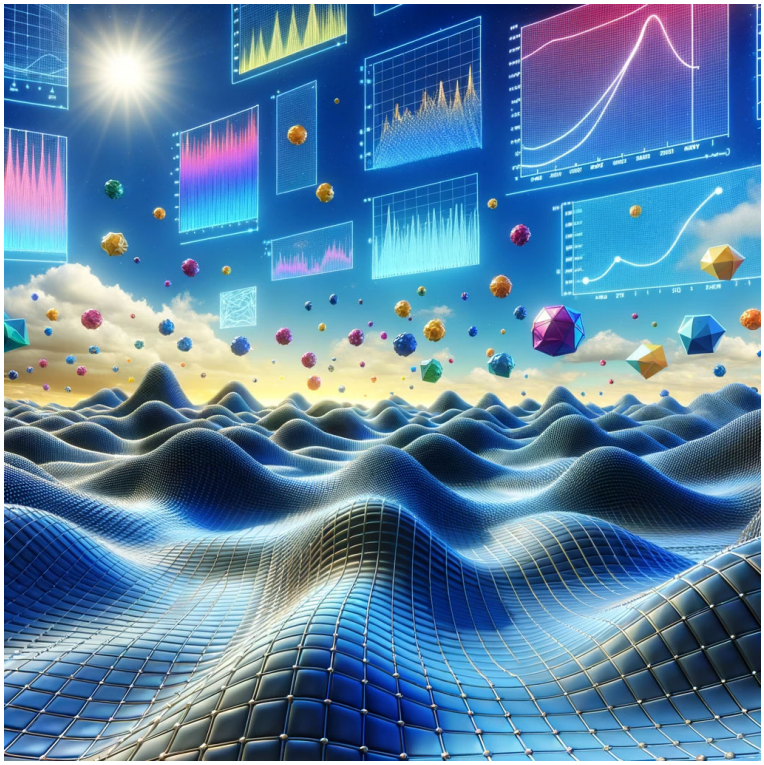

I

Matlab Codes

In writing this dissertation, I have used MATLAB to generate the data plots. MATLAB is a very powerful tool capable of generating very nice publication-quality vector graphics figures; however, a complete guide on using MATLAB to make plots is outside the scope of this thesis. Here, I will present some tips and tricks via code snippets that

I have used in producing the figures in this dissertation. It is assumed that the reader is already familiar with basic and intermediate level MATLAB plotting capabilities.

I.1 Legends

The default MATLAB legend shows the symbols next to black text labels for the data. Here, I demonstrate how to remove these symbols and make the color of the text match the data color, as well as give the legend a title:

```
figure;

% Plot the first dataset
h=plot(my_x_data,my_y_data1,'o-','color',my_color1);
hold on;

% Turn off the legend entry
set( get( get( h, 'Annotation'), 'LegendInformation' ), '
    IconDisplayStyle', 'off' );

% Generate a colored string, and plot it as a dummy invisible plot
my_display_name1=colorText('your data label here',my_color1);
line(NaN, NaN, 'Linestyle', 'none', 'Marker', 'none', 'Color', 'none'
    ,'DisplayName',my_display_name1);

% Repeat with second dataset
h=plot(my_x_data,my_y_data2,'o-','color',my_color2);
set( get( get( h, 'Annotation'), 'LegendInformation' ), '
    IconDisplayStyle', 'off' );
my_display_name2=colorText('your other data label here',my_color2);
line(NaN, NaN, 'Linestyle', 'none', 'Marker', 'none', 'Color', 'none'
    ,'DisplayName',my_display_name2);

% Generate the legend, set the title, and turn off the box
legend_title='           Your Legend Title'; %(use ~11 spaces)
lg=legend;
lg.Title.String=legend_title;
lg.Box='off';
```

I.2 Colormaps

Colormaps are often a serious topic of debate between scientists, as each often has their own unique preferences. I have developed a few home-made colormaps that shall satisfy most, with good contrast on a white background, that I have used in this thesis. They can be built with any number of colors. The colormaps can be defined and the color extracted via this example:

```
number_of_colors=11;
my_colormap=sequential_colormap(number_of_colors);
my_color=my_colormap(color_index,:);
```

The first colormap is a thermal colormap, useful for plotting data of different temperatures:

```
function my_map = thermal_colormap(num_colors)
    % Define a custom color list for the thermal colormap
    colorList=[0 0 .2; 0 0 1; .7 0 .7; 1 0 0; 1 .5 0];

    % Set the corresponding normalization values for the defined
       colors
    colorListNormalization=[0 .2 .5 .8 1];

    % Interpolate colors linearly across the specified range to
       create the colormap
    my_map=interp1(colorListNormalization, colorList, linspace(0,1,
       num_colors));
end
```

The second colormap is a sequential colormap, based on a modified version[260] of CBrewer's spectral colormap[261,262], that I further modified to make the central colors darker. It is useful for plotting data symmetric about zero, such as electron/hole density in graphene:

```
function map = sequential_colormap(n)
```

```
    % Define the base colors
    baseColors = [94, 79, 162;
        43, 144, 203;
        58, 189, 185;
        126.7, 178, 71.2;
        172, 163.2, 0;
        207.8, 173.1, 13.2;
        247, 146, 16;
        221, 68, 58;
        158, 1, 66];

    % Normalize to range [0, 1]
    baseColors = baseColors / 255;

    % Create the colormap
    m = size(baseColors, 1);
    x = linspace(0, 1, m);
    xi = linspace(0, 1, n);
    r = interp1(x, baseColors(:, 1), xi);
    g = interp1(x, baseColors(:, 2), xi);
    b = interp1(x, baseColors(:, 3), xi);
    map = [r(:), g(:), b(:)];
end
```

These colormaps are demonstrated in Fig. I.1.

I.3 Exporting Figures

Vector graphics are superior to raster graphics, as they can be infinitely zoomed or scaled and have a smaller file size. Vector figures are most reliably exported as .pdf files; the reader may also experiment with .svg and .eps files. Surface plots have been infamously difficult in older MATLAB versions to export as vector graphics, being rasterized instead. The method shown here will generally export them as vector graphics. This is the code to export figures as vector graphics:

```
addr='C:\your-filepath\your-filename.pdf';
exportgraphics(gcf, addr, 'ContentType', 'vector');
```

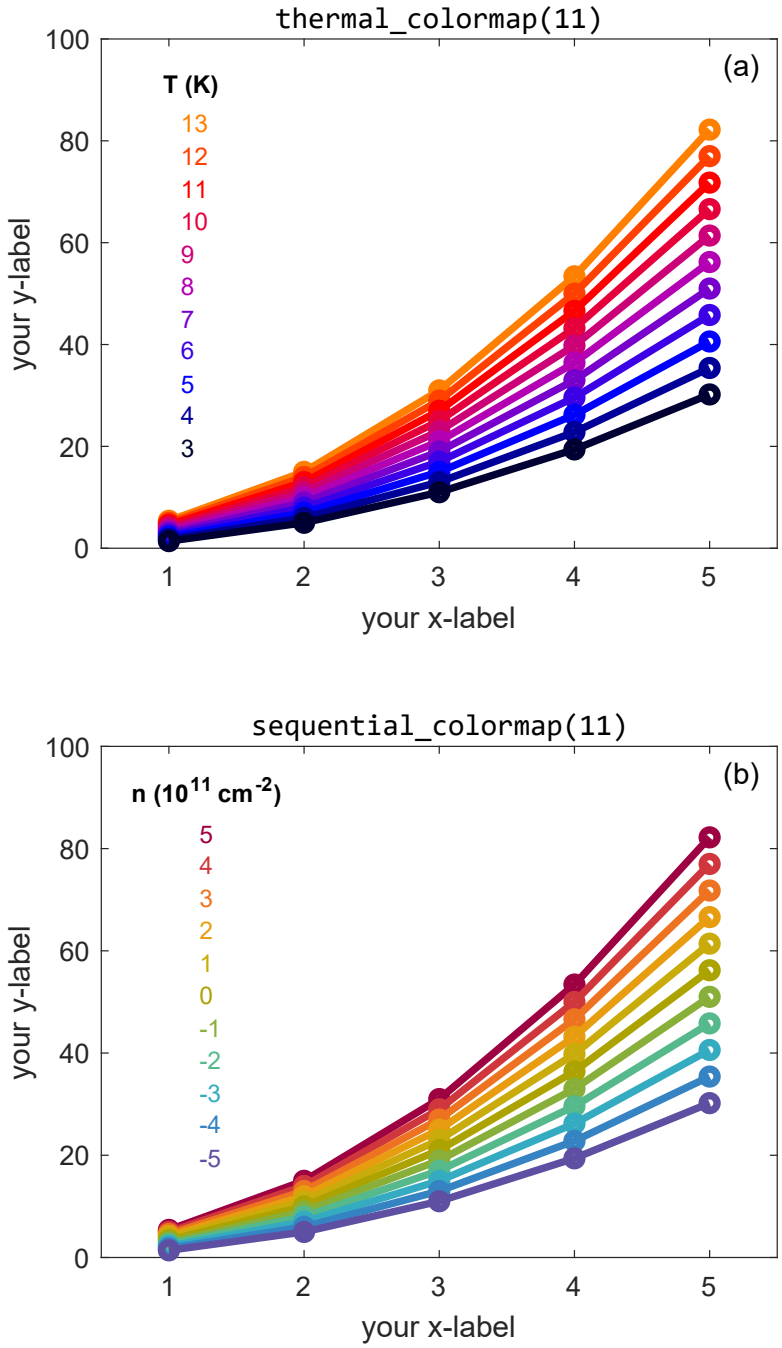

Figure I.1: **(a)** The thermal colormap, for 11 colors. **(b)** The sequential colormap, for 11 balanced colors.

If the colors come out looking weird on a vector graphics image, such as darker than expected, this problem can usually be solved by opening the .pdf file in Adobe Illustrator and then saving it again from Illustrator as a .pdf file.

Sometimes, the vector graphics may still rasterize, or the file size may be too large for complicated plots. In that case, the figure can be exported as .jpg file with a high resolution (e.g. 1200):

```
addr='C:\your-filepath\your-filename.jpg';
exportgraphics(gcf, addr, 'Resolution', '1200');
```

If I have seen further it is by standing on the shoulders of Giants.

Sir Isaac Newton

References

[1] J. Crossno, J. K. Shi, K. Wang, X. Liu, A. Harzheim, A. Lucas, S. Sachdev, P. Kim, T. Taniguchi, K. Watanabe, T. A. Ohki, and K. C. Fong, "Observation of the dirac fluid and the breakdown of the wiedemann-franz law in graphene," *Science*, vol. 351, no. 6277, pp. 1058–1061, Feb. 2016. [Online]. Available: https://doi.org/10.1126/science.aad0343

[2] A. Lucas, J. Crossno, K. C. Fong, P. Kim, and S. Sachdev, "Transport in inhomogeneous quantum critical fluids and in the dirac fluid in graphene," *Physical Review B*, vol. 93, no. 7, Feb. 2016. [Online]. Available: https://doi.org/10.1103/physrevb.93.075426

[3] C. Tan, D. Y. H. Ho, L. Wang, J. I. A. Li, I. Yudhistira, D. A. Rhodes, T. Taniguchi, K. Watanabe, K. Shepard, P. L. McEuen, C. R. Dean, S. Adam, and J. Hone, "Dissipation-enabled hydrodynamic conductivity in a tunable bandgap semiconductor," *Science Advances*, vol. 8, no. 15, Apr. 2022. [Online]. Available: https://doi.org/10.1126/sciadv.abi8481

[4] K. S. Novoselov, A. K. Geim, S. V. Morozov, D. Jiang, Y. Zhang, S. V. Dubonos, I. V. Grigorieva, and A. A. Firsov, "Electric field effect in atomically thin carbon films," *Science*, vol. 306, no. 5696, pp. 666–669, Oct. 2004. [Online]. Available: https://doi.org/10.1126/science.1102896

[5] A. K. Geim and I. V. Grigorieva, "Van der waals heterostructures," *Nature*, vol. 499, no. 7459, pp. 419–425, Jul. 2013. [Online]. Available: https://doi.org/10.1038/nature12385

[6] A. H. C. Neto, F. Guinea, N. M. R. Peres, K. S. Novoselov, and A. K. Geim, "The electronic properties of graphene," *Reviews of Modern Physics*, vol. 81, no. 1, pp. 109–162, Jan. 2009. [Online]. Available: https://doi.org/10.1103/revmodphys.81.109

[7] A. K. Geim, "Graphene: Status and prospects," *Science*, vol. 324, no. 5934, pp. 1530–1534, Jun. 2009. [Online]. Available: https://doi.org/10.1126/science.1158877

[8] M. Chhowalla, H. S. Shin, G. Eda, L.-J. Li, K. P. Loh, and H. Zhang, "The chemistry of two-dimensional layered transition metal dichalcogenide nanosheets," *Nature Chemistry*, vol. 5, no. 4, pp. 263–275, Mar. 2013. [Online]. Available: https://doi.org/10.1038/nchem.1589

[9] S. Manzeli, D. Ovchinnikov, D. Pasquier, O. V. Yazyev, and A. Kis, "2d transition metal dichalcogenides," *Nature Reviews Materials*, vol. 2, no. 8, Jun. 2017. [Online]. Available: https://doi.org/10.1038/natrevmats.2017.33

[10] M. Z. Hasan and C. L. Kane, "icolloquium/i: Topological insulators," *Reviews of Modern Physics*, vol. 82, no. 4, pp. 3045–3067, Nov. 2010. [Online]. Available: https://doi.org/10.1103/revmodphys.82.3045

[11] G. Fiori, F. Bonaccorso, G. Iannaccone, T. Palacios, D. Neumaier, A. Seabaugh, S. K. Banerjee, and L. Colombo, "Electronics based on two-dimensional materials," *Nature Nanotechnology*, vol. 9, no. 10, pp. 768–779, Oct. 2014. [Online]. Available: https://doi.org/10.1038/nnano.2014.207

[12] D. Jariwala, V. K. Sangwan, L. J. Lauhon, T. J. Marks, and M. C. Hersam, "Emerging device applications for semiconducting two-dimensional transition metal dichalcogenides," *ACS Nano*, vol. 8, no. 2, pp. 1102–1120, Jan. 2014. [Online]. Available: https://doi.org/10.1021/nn500064s

[13] AlexanderAlUS. (2010, August) The ideal crystalline structure of graphene is a hexagonal grid. Licensed under the Creative Commons Attribution-Share Alike 3.0 Unported license. [Online]. Available: https://commons.wikimedia.org/wiki/File:Graphen.jpg

[14] C. R. Dean, A. F. Young, I. Meric, C. Lee, L. Wang, S. Sorgenfrei, K. Watanabe, T. Taniguchi, P. Kim, K. L. Shepard, and J. Hone, "Boron nitride substrates for high-quality graphene electronics," *Nature Nanotechnology*, vol. 5, no. 10, pp. 722–726, Aug. 2010. [Online]. Available: https://doi.org/10.1038/nnano.2010.172

[15] L. Wang, I. Meric, P. Y. Huang, Q. Gao, Y. Gao, H. Tran, T. Taniguchi, K. Watanabe, L. M. Campos, D. A. Muller, J. Guo, P. Kim, J. Hone, K. L. Shepard, and C. R. Dean, "One-dimensional electrical contact to a two-dimensional material," *Science*, vol. 342, no. 6158, pp. 614–617, Nov. 2013. [Online]. Available: https://doi.org/10.1126/science.1244358

[16] M. Yankowitz, J. Xue, and B. J. LeRoy, "Graphene on hexagonal boron nitride," *Journal of Physics: Condensed Matter*, vol. 26, no. 30, p. 303201, Jul. 2014. [Online]. Available: https://doi.org/10.1088/0953-8984/26/30/303201

[17] J. Xue, J. Sanchez-Yamagishi, D. Bulmash, P. Jacquod, A. Deshpande, K. Watanabe, T. Taniguchi, P. Jarillo-Herrero, and B. J. LeRoy, "Scanning tunnelling microscopy and spectroscopy of ultra-flat graphene on hexagonal boron nitride," *Nature Materials*, vol. 10, no. 4, pp. 282–285, Feb. 2011. [Online]. Available: https://doi.org/10.1038/nmat2968

[18] A. A. Zibrov, C. Kometter, H. Zhou, E. M. Spanton, T. Taniguchi, K. Watanabe, M. P. Zaletel, and A. F. Young, "Tunable interacting composite fermion phases in a half-filled bilayer-graphene landau level," *Nature*, vol. 549, no. 7672, pp. 360–364, Sep. 2017. [Online]. Available: https://doi.org/10.1038/nature23893

[19] S. Wu, L. Wang, Y. Lai, W.-Y. Shan, G. Aivazian, X. Zhang, T. Taniguchi, K. Watanabe, D. Xiao, C. Dean, J. Hone, Z. Li, and X. Xu, "Multiple hot-carrier collection in photo-excited graphene moiré superlattices," *Science Advances*, vol. 2, no. 5, May 2016. [Online]. Available: https://doi.org/10.1126/sciadv.1600002

[20] Y. Kim, P. Herlinger, P. Moon, M. Koshino, T. Taniguchi, K. Watanabe, and J. H. Smet, "Charge inversion and topological phase transition at a twist angle induced van hove singularity of bilayer graphene," *Nano Letters*, vol. 16, no. 8, pp. 5053–5059, Jul. 2016. [Online]. Available: https://doi.org/10.1021/acs.nanolett.6b01906

[21] X. Liu, Z. Hao, K. Watanabe, T. Taniguchi, B. I. Halperin, and P. Kim, "Interlayer fractional quantum hall effect in a coupled graphene double layer," *Nature Physics*, vol. 15, no. 9, pp. 893–897, Jun. 2019. [Online]. Available: https://doi.org/10.1038/s41567-019-0546-0

[22] J. Son, J. Kwon, S. Kim, Y. Lv, J. Yu, J.-Y. Lee, H. Ryu, K. Watanabe, T. Taniguchi, R. Garrido-Menacho, N. Mason, E. Ertekin, P. Y. Huang, G.-H. Lee, and A. M. van der Zande, "Atomically precise graphene etch stops for three dimensional integrated systems from two dimensional material heterostructures," *Nature Communications*, vol. 9, no. 1, Sep. 2018. [Online]. Available: https://doi.org/10.1038/s41467-018-06524-3

[23] K. Bolotin, K. Sikes, Z. Jiang, M. Klima, G. Fudenberg, J. Hone, P. Kim, and H. Stormer, "Ultrahigh electron mobility in suspended graphene," *Solid State Communications*, vol. 146, no. 9-10, pp. 351–355, Jun. 2008. [Online]. Available: https://doi.org/10.1016/j.ssc.2008.02.024

[24] A. S. Mayorov, R. V. Gorbachev, S. V. Morozov, L. Britnell, R. Jalil, L. A. Ponomarenko, P. Blake, K. S. Novoselov, K. Watanabe, T. Taniguchi, and A. K. Geim, "Micrometer-scale ballistic transport in encapsulated graphene at room

temperature," *Nano Letters*, vol. 11, no. 6, pp. 2396–2399, May 2011. [Online]. Available: https://doi.org/10.1021/nl200758b

[25] L. Banszerus, T. Sohier, A. Epping, F. Winkler, F. Libisch, F. Haupt, K. Watanabe, T. Taniguchi, K. Müller-Caspary, N. Marzari, F. Mauri, B. Beschoten, and C. Stampfer, "Extraordinary high room-temperature carrier mobility in graphene-wse$_2$ heterostructures," 2019. [Online]. Available: https://arxiv.org/abs/1909.09523

[26] X. Du, I. Skachko, A. Barker, and E. Y. Andrei, "Approaching ballistic transport in suspended graphene," *Nature Nanotechnology*, vol. 3, no. 8, pp. 491–495, Jul. 2008. [Online]. Available: https://doi.org/10.1038/nnano.2008.199

[27] K. I. Bolotin, K. J. Sikes, J. Hone, H. L. Stormer, and P. Kim, "Temperature-dependent transport in suspended graphene," *Physical Review Letters*, vol. 101, no. 9, Aug. 2008. [Online]. Available: https://doi.org/10.1103/physrevlett.101.096802

[28] Y. Zhang, T.-T. Tang, C. Girit, Z. Hao, M. C. Martin, A. Zettl, M. F. Crommie, Y. R. Shen, and F. Wang, "Direct observation of a widely tunable bandgap in bilayer graphene," *Nature*, vol. 459, no. 7248, pp. 820–823, Jun. 2009. [Online]. Available: https://doi.org/10.1038/nature08105

[29] E. McCann and M. Koshino, "The electronic properties of bilayer graphene," *Reports on Progress in Physics*, vol. 76, no. 5, p. 056503, Apr. 2013. [Online]. Available: https://doi.org/10.1088/0034-4885/76/5/056503

[30] K. F. Mak, C. H. Lui, J. Shan, and T. F. Heinz, "Observation of an electric-field-induced band gap in bilayer graphene by infrared spectroscopy," *Physical Review Letters*, vol. 102, no. 25, Jun. 2009. [Online]. Available: https://doi.org/10.1103/physrevlett.102.256405

[31] F. Xia, D. B. Farmer, Y. ming Lin, and P. Avouris, "Graphene field-effect transistors with high on/off current ratio and large transport band gap at room temperature," *Nano Letters*, vol. 10, no. 2, pp. 715–718, Jan. 2010. [Online]. Available: https://doi.org/10.1021/nl9039636

[32] F. Schwierz, "Graphene transistors," *Nature Nanotechnology*, vol. 5, no. 7, pp. 487–496, May 2010. [Online]. Available: https://doi.org/10.1038/nnano.2010.89

[33] I. Colmiais, V. Silva, J. Borme, P. Alpuim, and P. M. Mendes, "Towards RF graphene devices: A review," *FlatChem*, vol. 35, p. 100409, Sep. 2022. [Online]. Available: https://doi.org/10.1016/j.flatc.2022.100409

[34] Y. Wu, K. A. Jenkins, A. Valdes-Garcia, D. B. Farmer, Y. Zhu, A. A. Bol, C. Dimitrakopoulos, W. Zhu, F. Xia, P. Avouris, and Y.-M. Lin, "State-of-the-art graphene high-frequency electronics," *Nano Letters*, vol. 12, no. 6, pp. 3062–3067, May 2012. [Online]. Available: https://doi.org/10.1021/nl300904k

[35] M. Jin, Z. Wei, Y. Meng, H. Shu, Y. Tao, B. Bai, and X. Wang, "Silicon-based graphene electro-optical modulators," *Photonics*, vol. 9, no. 2, p. 82, Jan. 2022. [Online]. Available: https://doi.org/10.3390/photonics9020082

[36] Y. Gao, R.-J. Shiue, X. Gan, L. Li, C. Peng, I. Meric, L. Wang, A. Szep, D. Walker, J. Hone, and D. Englund, "High-speed electro-optic modulator integrated with graphene-boron nitride heterostructure and photonic crystal nanocavity," *Nano Letters*, vol. 15, no. 3, pp. 2001–2005, Mar. 2015. [Online]. Available: https://doi.org/10.1021/nl504860z

[37] C. T. Phare, Y.-H. D. Lee, J. Cardenas, and M. Lipson, "Graphene electro-optic modulator with 30 GHz bandwidth," *Nature Photonics*, vol. 9, no. 8, pp. 511–514, Jul. 2015. [Online]. Available: https://doi.org/10.1038/nphoton.2015.122

[38] Q. Ma, T. I. Andersen, N. L. Nair, N. M. Gabor, M. Massicotte, C. H. Lui, A. F. Young, W. Fang, K. Watanabe, T. Taniguchi, J. Kong, N. Gedik, F. H. L. Koppens, and P. Jarillo-Herrero, "Tuning ultrafast electron thermalization pathways in a van der waals heterostructure," *Nature Physics*, vol. 12, no. 5, pp. 455–459, Jan. 2016. [Online]. Available: https://doi.org/10.1038/nphys3620

[39] L. M. Gächter, R. Garreis, J. D. Gerber, M. J. Ruckriegel, C. Tong, B. Kratochwil, F. K. de Vries, A. Kurzmann, K. Watanabe, T. Taniguchi, T. Ihn, K. Ensslin, and W. W. Huang, "Single-shot spin readout in graphene quantum dots," *PRX Quantum*, vol. 3, no. 2, May 2022. [Online]. Available: https://doi.org/10.1103/prxquantum.3.020343

[40] L. Banszerus, K. Hecker, S. Möller, E. Icking, K. Watanabe, T. Taniguchi, C. Volk, and C. Stampfer, "Spin relaxation in a single-electron graphene quantum dot," *Nature Communications*, vol. 13, no. 1, Jun. 2022. [Online]. Available: https://doi.org/10.1038/s41467-022-31231-5

[41] L. Banszerus, S. Möller, C. Steiner, E. Icking, S. Trellenkamp, F. Lentz, K. Watanabe, T. Taniguchi, C. Volk, and C. Stampfer, "Spin-valley coupling in single-electron bilayer graphene quantum dots," *Nature Communications*, vol. 12, no. 1, Sep. 2021. [Online]. Available: https://doi.org/10.1038/s41467-021-25498-3

[42] A. Kurzmann, H. Overweg, M. Eich, A. Pally, P. Rickhaus, R. Pisoni, Y. Lee, K. Watanabe, T. Taniguchi, T. Ihn, and K. Ensslin, "Charge

detection in gate-defined bilayer graphene quantum dots," *Nano Letters*, vol. 19, no. 8, pp. 5216–5221, Jul. 2019. [Online]. Available: https://doi.org/10.1021/acs.nanolett.9b01617

[43] C. Tong, R. Garreis, A. Knothe, M. Eich, A. Sacchi, K. Watanabe, T. Taniguchi, V. Fal'ko, T. Ihn, K. Ensslin, and A. Kurzmann, "Tunable valley splitting and bipolar operation in graphene quantum dots," *Nano Letters*, vol. 21, no. 2, pp. 1068–1073, Jan. 2021. [Online]. Available: https://doi.org/10.1021/acs.nanolett.0c04343

[44] C. Tong, A. Kurzmann, R. Garreis, W. W. Huang, S. Jele, M. Eich, L. Ginzburg, C. Mittag, K. Watanabe, T. Taniguchi, K. Ensslin, and T. Ihn, "Pauli blockade of tunable two-electron spin and valley states in graphene quantum dots," *Physical Review Letters*, vol. 128, no. 6, Feb. 2022. [Online]. Available: https://doi.org/10.1103/physrevlett.128.067702

[45] A. S. T. Pires, "Ads/cft correspondence in condensed matter," 2010. [Online]. Available: https://arxiv.org/abs/1006.5838

[46] S. Sachdev, *Condensed Matter and AdS/CFT*. Berlin, Heidelberg: Springer Berlin Heidelberg, 2011, pp. 273–311. [Online]. Available: https://doi.org/10.1007/978-3-642-04864-7_9

[47] Y. Seo, G. Song, P. Kim, S. Sachdev, and S.-J. Sin, "Holography of the dirac fluid in graphene with two currents," *Physical Review Letters*, vol. 118, no. 3, Jan. 2017. [Online]. Available: https://doi.org/10.1103/physrevlett.118.036601

[48] G. Song, Y. Seo, and S.-J. Sin, "Determination of dynamical exponents of graphene at quantum critical point by holography," *Physical Review D*, vol. 102, no. 12, Dec. 2020. [Online]. Available: https://doi.org/10.1103/physrevd.102.126023

[49] Y. Seo, G. Song, C. Park, and S.-J. Sin, "Small fermi surfaces and strong correlation effects in dirac materials with holography," *Journal of High Energy Physics*, vol. 2017, no. 10, Oct. 2017. [Online]. Available: https://doi.org/10.1007/jhep10(2017)204

[50] M. Rogatko and K. I. Wysokinski, "Two interacting current model of holographic dirac fluid in graphene," *Physical Review D*, vol. 97, no. 2, Jan. 2018. [Online]. Available: https://doi.org/10.1103/physrevd.97.024053

[51] M. Müller, L. Fritz, S. Sachdev, and J. Schmalian, *Graphene: Relativistic Transport in a Nearly Perfect Quantum Liquid*, pp. 602–607. [Online]. Available: https://www.worldscientific.com/doi/abs/10.1142/9789814304634_0055

[52] L. D. Landau, "The theory of a fermi liquid," *Soviet Physics JETP*, vol. 3, no. 6, p. 920, 1957.

[53] A. Lucas and K. C. Fong, "Hydrodynamics of electrons in graphene," *Journal of Physics: Condensed Matter*, vol. 30, no. 5, p. 053001, Jan. 2018. [Online]. Available: https://doi.org/10.1088/1361-648x/aaa274

[54] N. W. Ashcroft and N. D. Mermin, *Solid State Physics*. Holt, Rinehart and Winston, 1976.

[55] C. Kittel, *Quantum Theory of Solids*. Hoboken, NJ: Wiley, 1963.

[56] ——, *Elementary Statistical Physics*. New York: John Wiley & Sons, 1958.

[57] L. Fritz and T. Scaffidi, "Hydrodynamic electronic transport," 2023. [Online]. Available: https://arxiv.org/abs/2303.14205

[58] M. Shavit, A. Shytov, and G. Falkovich, "Freely flowing currents and electric field expulsion in viscous electronics," *Physical Review Letters*, vol. 123, no. 2, Jul. 2019. [Online]. Available: https://doi.org/10.1103/physrevlett.123.026801

[59] A. Hui, personal communication.

[60] M. Polini and A. K. Geim, "Viscous electron fluids," *Physics Today*, vol. 73, no. 6, pp. 28–34, Jun. 2020. [Online]. Available: https://doi.org/10.1063/pt.3.4497

[61] D. A. Bandurin, I. Torre, R. K. Kumar, M. B. Shalom, A. Tomadin, A. Principi, G. H. Auton, E. Khestanova, K. S. Novoselov, I. V. Grigorieva, L. A. Ponomarenko, A. K. Geim, and M. Polini, "Negative local resistance caused by viscous electron backflow in graphene," *Science*, vol. 351, no. 6277, pp. 1055–1058, Mar. 2016. [Online]. Available: https://doi.org/10.1126/science.aad0201

[62] R. K. Kumar, D. A. Bandurin, F. M. D. Pellegrino, Y. Cao, A. Principi, H. Guo, G. H. Auton, M. B. Shalom, L. A. Ponomarenko, G. Falkovich, K. Watanabe, T. Taniguchi, I. V. Grigorieva, L. S. Levitov, M. Polini, and A. K. Geim, "Superballistic flow of viscous electron fluid through graphene constrictions," *Nature Physics*, vol. 13, no. 12, pp. 1182–1185, Aug. 2017. [Online]. Available: https://doi.org/10.1038/nphys4240

[63] P. Alekseev, "Negative magnetoresistance in viscous flow of two-dimensional electrons," *Physical Review Letters*, vol. 117, no. 16, Oct. 2016. [Online]. Available: https://doi.org/10.1103/physrevlett.117.166601

[64] R. Gurzhi, "Minimum of resistance in impurity-free conductors," *J. Exptl. Theoret. Phys*, vol. 44, pp. 771–772, Feb. 1963. [Online]. Available: http://jetp.ras.ru/cgi-bin/dn/e_017_02_0521.pdf

[65] I. Torre, A. Tomadin, A. K. Geim, and M. Polini, "Nonlocal transport and the hydrodynamic shear viscosity in graphene," *Physical Review B*, vol. 92, no. 16, Oct. 2015. [Online]. Available: https://doi.org/10.1103/physrevb.92.165433

[66] P. S. Alekseev, A. P. Dmitriev, I. V. Gornyi, V. Y. Kachorovskii, B. N. Narozhny, and M. Titov, "Nonmonotonic magnetoresistance of a two-dimensional viscous electron-hole fluid in a confined geometry," *Physical Review B*, vol. 97, no. 8, Feb. 2018. [Online]. Available: https://doi.org/10.1103/physrevb.97.085109

[67] ——, "Counterflows in viscous electron-hole fluid," *Physical Review B*, vol. 98, no. 12, Sep. 2018. [Online]. Available: https://doi.org/10.1103/physrevb.98.125111

[68] D. K. Efetov and P. Kim, "Controlling electron-phonon interactions in graphene at ultrahigh carrier densities," *Physical Review Letters*, vol. 105, no. 25, Dec. 2010. [Online]. Available: https://doi.org/10.1103/physrevlett.105.256805

[69] D. Y. H. Ho, I. Yudhistira, N. Chakraborty, and S. Adam, "Theoretical determination of hydrodynamic window in monolayer and bilayer graphene from scattering rates," *Physical Review B*, vol. 97, no. 12, Mar. 2018. [Online]. Available: https://doi.org/10.1103/physrevb.97.121404

[70] T. Sohier, M. Calandra, C.-H. Park, N. Bonini, N. Marzari, and F. Mauri, "Phonon-limited resistivity of graphene by first-principles calculations: Electron-phonon interactions, strain-induced gauge field, and boltzmann equation," *Physical Review B*, vol. 90, no. 12, Sep. 2014. [Online]. Available: https://doi.org/10.1103/physrevb.90.125414

[71] D. A. Bandurin, A. V. Shytov, L. S. Levitov, R. K. Kumar, A. I. Berdyugin, M. B. Shalom, I. V. Grigorieva, A. K. Geim, and G. Falkovich, "Fluidity onset in graphene," *Nature Communications*, vol. 9, no. 1, Oct. 2018. [Online]. Available: https://doi.org/10.1038/s41467-018-07004-4

[72] A. I. Berdyugin, S. G. Xu, F. M. D. Pellegrino, R. K. Kumar, A. Principi, I. Torre, M. B. Shalom, T. Taniguchi, K. Watanabe, I. V. Grigorieva, M. Polini, A. K. Geim, and D. A. Bandurin, "Measuring hall viscosity of graphene's electron fluid," *Science*, vol. 364, no. 6436, pp. 162–165, Apr. 2019. [Online]. Available: https://doi.org/10.1126/science.aau0685

[73] M. J. H. Ku, T. X. Zhou, Q. Li, Y. J. Shin, J. K. Shi, C. Burch, L. E. Anderson, A. T. Pierce, Y. Xie, A. Hamo, U. Vool, H. Zhang, F. Casola, T. Taniguchi, K. Watanabe, M. M. Fogler, P. Kim, A. Yacoby, and R. L. Walsworth, "Imaging viscous flow of the dirac fluid in graphene,"

Nature, vol. 583, no. 7817, pp. 537–541, Jul. 2020. [Online]. Available: https://doi.org/10.1038/s41586-020-2507-2

[74] J. A. Sulpizio, L. Ella, A. Rozen, J. Birkbeck, D. J. Perello, D. Dutta, M. Ben-Shalom, T. Taniguchi, K. Watanabe, T. Holder, R. Queiroz, A. Principi, A. Stern, T. Scaffidi, A. K. Geim, and S. Ilani, "Visualizing poiseuille flow of hydrodynamic electrons," *Nature*, vol. 576, no. 7785, pp. 75–79, Dec. 2019. [Online]. Available: https://doi.org/10.1038/s41586-019-1788-9

[75] Y. Nam, D.-K. Ki, D. Soler-Delgado, and A. F. Morpurgo, "Electron–hole collision limited transport in charge-neutral bilayer graphene," *Nature Physics*, vol. 13, no. 12, pp. 1207–1214, Aug. 2017. [Online]. Available: https://doi.org/10.1038/nphys4218

[76] G. Wagner, D. X. Nguyen, and S. H. Simon, "Transport in bilayer graphene near charge neutrality: Which scattering mechanisms are important?" *Physical Review Letters*, vol. 124, no. 2, Jan. 2020. [Online]. Available: https://doi.org/10.1103/physrevlett.124.026601

[77] M. Zarenia, S. Adam, and G. Vignale, "Temperature collapse of the electric conductivity in bilayer graphene," *Physical Review Research*, vol. 2, no. 2, Jun. 2020. [Online]. Available: https://doi.org/10.1103/physrevresearch.2.023391

[78] O. Corbino, "Das experimentelle studium des hallphänomens und die elektronentheorie der metalle," *Physikalische Zeitschrift*, vol. XII, pp. 842–845, Aug. 1911.

[79] M. J. M. de Jong, "Transition from sharvin to drude resistance in high-mobility wires," *Physical Review B*, vol. 49, no. 11, pp. 7778–7781, Mar. 1994. [Online]. Available: https://doi.org/10.1103/physrevb.49.7778

[80] A. Stern, T. Scaffidi, O. Reuven, C. Kumar, J. Birkbeck, and S. Ilani, "How electron hydrodynamics can eliminate the landauer-sharvin resistance," *Physical Review Letters*, vol. 129, no. 15, Oct. 2022. [Online]. Available: https://doi.org/10.1103/physrevlett.129.157701

[81] C. Kumar, J. Birkbeck, J. A. Sulpizio, D. Perello, T. Taniguchi, K. Watanabe, O. Reuven, T. Scaffidi, A. Stern, A. K. Geim, and S. Ilani, "Imaging hydrodynamic electrons flowing without landauer–sharvin resistance," *Nature*, vol. 609, no. 7926, pp. 276–281, Sep. 2022. [Online]. Available: https://doi.org/10.1038/s41586-022-05002-7

[82] M. Zarenia, T. B. Smith, A. Principi, and G. Vignale, "Breakdown of the wiedemann-franz law in ab-stacked bilayer graphene," *Physical Review*

B, vol. 99, no. 16, Apr. 2019. [Online]. Available: https://doi.org/10.1103/physrevb.99.161407

[83] M. Zarenia, A. Principi, and G. Vignale, "Disorder-enabled hydrodynamics of charge and heat transport in monolayer graphene," *2D Materials*, vol. 6, no. 3, p. 035024, May 2019. [Online]. Available: https://doi.org/10.1088/2053-1583/ab1ad9

[84] R. Franz and G. Wiedemann, "Ueber die wärme-leitungsfähigkeit der metalle," *Annalen der Physik und Chemie*, vol. 165, no. 8, pp. 497–531, 1853. [Online]. Available: https://doi.org/10.1002/andp.18531650802

[85] A. Sommerfeld, "Zur elektronentheorie der metalle auf grund der fermischen statistik," *Zeitschrift f r Physik*, vol. 47, no. 1-2, pp. 1–32, Jan. 1928. [Online]. Available: https://doi.org/10.1007/bf01391052

[86] A. Lavasani, D. Bulmash, and S. D. Sarma, "Wiedemann-franz law and fermi liquids," *Physical Review B*, vol. 99, no. 8, Feb. 2019. [Online]. Available: https://doi.org/10.1103/physrevb.99.085104

[87] Y.-T. Tu and S. D. Sarma, "Wiedemann-franz law in graphene," *Physical Review B*, vol. 107, no. 8, Feb. 2023. [Online]. Available: https://doi.org/10.1103/physrevb.107.085401

[88] D. X. Nguyen, G. Wagner, and S. H. Simon, "Quantum boltzmann equation for bilayer graphene," *Physical Review B*, vol. 101, no. 3, Jan. 2020. [Online]. Available: https://doi.org/10.1103/physrevb.101.035117

[89] A. Lucas and S. D. Sarma, "Electronic hydrodynamics and the breakdown of the wiedemann-franz and mott laws in interacting metals," *Physical Review B*, vol. 97, no. 24, Jun. 2018. [Online]. Available: https://doi.org/10.1103/physrevb.97.245128

[90] S. Ahn and S. Das Sarma, "Hydrodynamics, viscous electron fluid, and wiedeman-franz law in two-dimensional semiconductors," *Phys. Rev. B*, vol. 106, p. L081303, Aug 2022. [Online]. Available: https://link.aps.org/doi/10.1103/PhysRevB.106.L081303

[91] S. Li, A. Levchenko, and A. V. Andreev, "Hydrodynamic thermoelectric transport in corbino geometry," *Physical Review B*, vol. 105, no. 12, Mar. 2022. [Online]. Available: https://doi.org/10.1103/physrevb.105.125302

[92] H.-Y. Xie and M. S. Foster, "Transport coefficients of graphene: Interplay of impurity scattering, coulomb interaction, and optical phonons," *Physical Review*

B, vol. 93, no. 19, May 2016. [Online]. Available: https://doi.org/10.1103/physrevb.93.195103

[93] A. Principi and G. Vignale, "Violation of the wiedemann-franz law in hydrodynamic electron liquids," *Physical Review Letters*, vol. 115, no. 5, Jul. 2015. [Online]. Available: https://doi.org/10.1103/physrevlett.115.056603

[94] K. C. Fong and K. C. Schwab, "Ultrasensitive and wide-bandwidth thermal measurements of graphene at low temperatures," *Physical Review X*, vol. 2, no. 3, Jul. 2012. [Online]. Available: https://doi.org/10.1103/physrevx.2.031006

[95] K. C. Fong, E. E. Wollman, H. Ravi, W. Chen, A. A. Clerk, M. D. Shaw, H. G. Leduc, and K. C. Schwab, "Measurement of the electronic thermal conductance channels and heat capacity of graphene at low temperature," *Physical Review X*, vol. 3, no. 4, Oct. 2013. [Online]. Available: https://doi.org/10.1103/physrevx.3.041008

[96] J. Crossno, X. Liu, T. A. Ohki, P. Kim, and K. C. Fong, "Development of high frequency and wide bandwidth johnson noise thermometry," *Applied Physics Letters*, vol. 106, no. 2, p. 023121, Jan. 2015. [Online]. Available: https://doi.org/10.1063/1.4905926

[97] S. Yiğen and A. R. Champagne, "Wiedemann–franz relation and thermal-transistor effect in suspended graphene," *Nano Letters*, vol. 14, no. 1, pp. 289–293, Dec. 2013. [Online]. Available: https://doi.org/10.1021/nl403967z

[98] S. Yiğen, V. Tayari, J. O. Island, J. M. Porter, and A. R. Champagne, "Electronic thermal conductivity measurements in intrinsic graphene," *Physical Review B*, vol. 87, no. 24, Jun. 2013. [Online]. Available: https://doi.org/10.1103/physrevb.87.241411

[99] M. M. Sadeghi, Y. Huang, C. Lian, F. Giustino, E. Tutuc, A. H. MacDonald, T. Taniguchi, K. Watanabe, and L. Shi, "Tunable electron–flexural phonon interaction in graphene heterostructures," *Nature*, vol. 617, no. 7960, pp. 282–286, Apr. 2023. [Online]. Available: https://doi.org/10.1038/s41586-023-05879-y

[100] K. Rupp, M. Horowitz, F. Labonte, O. Shacham, K. Olukotun, L. Hammond, and C. Batten. (2021) Microprocessor trend data. GitHub repository. [Online]. Available: https://github.com/karlrupp/microprocessor-trend-data

[101] E. Pop, "Energy dissipation and transport in nanoscale devices," *Nano Research*, vol. 3, no. 3, pp. 147–169, Mar. 2010. [Online]. Available: https://doi.org/10.1007/s12274-010-1019-z

[102] H. Li, C. Xu, N. Srivastava, and K. Banerjee, "Carbon nanomaterials for next-generation interconnects and passives: Physics, status, and prospects," *IEEE Transactions on Electron Devices*, vol. 56, no. 9, pp. 1799–1821, Sep. 2009. [Online]. Available: https://doi.org/10.1109/ted.2009.2026524

[103] H. Li, C. Xu, and K. Banerjee, "Carbon nanomaterials: The ideal interconnect technology for next-generation ICs," *IEEE Design &amp Test of Computers*, vol. 27, no. 4, pp. 20–31, Jul. 2010. [Online]. Available: https://doi.org/10.1109/mdt.2010.55

[104] W.-S. Zhao, Z.-H. Cheng, J. Wang, K. Fu, D.-W. Wang, P. Zhao, G. Wang, and L. Dong, "Vertical graphene nanoribbon interconnects at the end of the roadmap," *IEEE Transactions on Electron Devices*, vol. 65, no. 6, pp. 2632–2637, Jun. 2018. [Online]. Available: https://doi.org/10.1109/ted.2018.2822664

[105] M. Liebau, A. P. Graham, G. S. Duesberg, E. Unger, R. Seidel, and F. Kreupl, "Nanoelectronics based on carbon nanotubes: Technological challenges and recent developments," *Fullerenes, Nanotubes and Carbon Nanostructures*, vol. 13, no. sup1, pp. 255–258, Apr. 2005. [Online]. Available: https://doi.org/10.1081/fst-200039292

[106] S. Z. Bisri, C. Piliego, J. Gao, and M. A. Loi, "Outlook and emerging semiconducting materials for ambipolar transistors," *Advanced Materials*, vol. 26, no. 8, pp. 1176–1199, Oct. 2013. [Online]. Available: https://doi.org/10.1002/adma.201304280

[107] D. G. Cahill, W. K. Ford, K. E. Goodson, G. D. Mahan, A. Majumdar, H. J. Maris, R. Merlin, and S. R. Phillpot, "Nanoscale thermal transport," *Journal of Applied Physics*, vol. 93, no. 2, pp. 793–818, Dec. 2002. [Online]. Available: https://doi.org/10.1063/1.1524305

[108] D. G. Cahill, P. V. Braun, G. Chen, D. R. Clarke, S. Fan, K. E. Goodson, P. Keblinski, W. P. King, G. D. Mahan, A. Majumdar, H. J. Maris, S. R. Phillpot, E. Pop, and L. Shi, "Nanoscale thermal transport. II. 2003–2012," *Applied Physics Reviews*, vol. 1, no. 1, p. 011305, Mar. 2014. [Online]. Available: https://doi.org/10.1063/1.4832615

[109] D. Pozar, *Microwave engineering*. Hoboken, NJ: Wiley, 2012.

[110] S. Ramo, J. R. Whinnery, and T. Van Duzer, *Fields and Waves in Communication Electronics*, 3rd ed. Wiley, 1994.

[111] S. J. Orfanidis, *Electromagnetic Waves and Antennas*. Rutgers University, 2016, vol. 1. [Online]. Available: http://www.ece.rutgers.edu/~orfanidi/ewa

[112] ——, *Electromagnetic Waves and Antennas*. Rutgers University, 2016, vol. 2. [Online]. Available: http://www.ece.rutgers.edu/~orfanidi/ewa

[113] J. F. Qu, S. P. Benz, H. Rogalla, W. L. Tew, D. R. White, and K. L. Zhou, "Johnson noise thermometry," *Measurement Science and Technology*, vol. 30, no. 11, p. 112001, Sep. 2019. [Online]. Available: https://doi.org/10.1088/1361-6501/ab3526

[114] H. Brixy, "Temperature measurement in nuclear reactors by noise thermometry," *Nuclear Instruments and Methods*, vol. 97, no. 1, pp. 75–80, Nov. 1971. [Online]. Available: https://doi.org/10.1016/0029-554x(71)90514-3

[115] J. Pearce, A. Greenen, P. Bramley, and D. Cruickshank, "Towards a practical johnson noise thermometer for long-term measurements in harsh environments," in *2015 4th International Conference on Advancements in Nuclear Instrumentation Measurement Methods and their Applications (ANIMMA)*. IEEE, Apr. 2015. [Online]. Available: https://doi.org/10.1109/animma.2015.7465506

[116] R. Kisner, C. Britton, U. Jagadish, J. Wilgen, M. Roberts, T. Blalock, D. Holcomb, M. Bobrek, and M. Ericson, "Johnson noise thermometry for harsh environments," in *2004 IEEE Aerospace Conference Proceedings (IEEE Cat. No.04TH8720)*. IEEE, Mar. 2004. [Online]. Available: https://doi.org/10.1109/aero.2004.1368053

[117] P. Bramley, D. Cruickshank, and J. Pearce, "The development of a practical, drift-free, johnson-noise thermometer for industrial applications," *International Journal of Thermophysics*, vol. 38, no. 2, Dec. 2016. [Online]. Available: https://doi.org/10.1007/s10765-016-2156-8

[118] P. Bramley, D. Cruickshank, and J. Aubrey, "Developments towards an industrial johnson noise thermometer," *Measurement Science and Technology*, vol. 31, no. 5, p. 054003, Feb. 2020. [Online]. Available: https://doi.org/10.1088/1361-6501/ab58a6

[119] E. Pop, S. Sinha, and K. Goodson, "Heat generation and transport in nanometer-scale transistors," *Proceedings of the IEEE*, vol. 94, no. 8, pp. 1587–1601, Aug. 2006. [Online]. Available: https://doi.org/10.1109/jproc.2006.879794

[120] Y. Shabany, *Heat transfer: Thermal management of electronics*. Boca Raton: CRC Press, Dec. 2009.

[121] N. Jarosik, C. L. Bennett, M. Halpern, G. Hinshaw, A. Kogut, M. Limon, S. S. Meyer, L. Page, M. Pospieszalski, D. N. Spergel, G. S. Tucker, D. T. Wilkinson, E. Wollack, E. L. Wright, and Z. Zhang, "Design, implementation,

and testing of the microwave anisotropy probe radiometers," *The Astrophysical Journal Supplement Series*, vol. 145, no. 2, pp. 413–436, Apr. 2003. [Online]. Available: https://doi.org/10.1086/346080

[122] G. F. Smoot, C. L. Bennett, A. Kogut, E. L. Wright, J. Aymon, N. W. Boggess, E. S. Cheng, G. de Amici, S. Gulkis, M. G. Hauser, G. Hinshaw, P. D. Jackson, M. Janssen, E. Kaita, T. Kelsall, P. Keegstra, C. Lineweaver, K. Loewenstein, P. Lubin, J. Mather, S. S. Meyer, S. H. Moseley, T. Murdock, L. Rokke, R. F. Silverberg, L. Tenorio, R. Weiss, and D. T. Wilkinson, "Structure in the COBE differential microwave radiometer first-year maps," *The Astrophysical Journal*, vol. 396, p. L1, Sep. 1992. [Online]. Available: https://doi.org/10.1086/186504

[123] M. Bersanelli, N. Mandolesi, and J. Marti-Canales, "Multi-band radiometer for measuring the cosmic microwave background," in *32nd European Microwave Conference, 2002.* IEEE, Oct. 2002. [Online]. Available: https://doi.org/10.1109/euma.2002.339344

[124] A. Kogut, D. J. Fixsen, S. Levin, M. Limon, P. M. Lubin, P. Mirel, M. Seiffert, and E. Wollack, "An instrument to measure the temperature of the cosmic microwave background radiation at centimeter wavelengths," *The Astrophysical Journal Supplement Series*, vol. 154, no. 2, pp. 493–499, Oct. 2004. [Online]. Available: https://doi.org/10.1086/422517

[125] N. E. Flowers-Jacobs, A. Pollarolo, K. J. Coakley, A. E. Fox, H. Rogalla, W. L. Tew, and S. P. Benz, "A boltzmann constant determination based on johnson noise thermometry," *Metrologia*, vol. 54, no. 5, pp. 730–737, Aug. 2017. [Online]. Available: https://doi.org/10.1088/1681-7575/aa7b3f

[126] J. Qu, S. P. Benz, K. Coakley, H. Rogalla, W. L. Tew, R. White, K. Zhou, and Z. Zhou, "An improved electronic determination of the boltzmann constant by johnson noise thermometry," *Metrologia*, vol. 54, no. 4, pp. 549–558, Jul. 2017. [Online]. Available: https://doi.org/10.1088/1681-7575/aa781e

[127] R. J. Soulen, W. E. Fogle, and J. H. Colwell, "Measurements of absolute temperature below 0.75 k using a josephson-junction noise thermometer," *Journal of Low Temperature Physics*, vol. 94, no. 5-6, pp. 385–487, Mar. 1994. [Online]. Available: https://doi.org/10.1007/bf00753823

[128] G. Schuster, "Thermodynamic consistency of the new ultra-low temperature scale PLTS-2000," in *AIP Conference Proceedings.* AIP, 2003. [Online]. Available: https://doi.org/10.1063/1.1627105

[129] B. Fellmuth, "PTB-96: The ultra-low temperature scale of PTB," in *AIP Conference Proceedings*. AIP, 2003. [Online]. Available: https://doi.org/10.1063/1.1627103

[130] D. R. White, R. Galleano, A. Actis, H. Brixy, M. D. Groot, J. Dubbeldam, A. L. Reesink, F. Edler, H. Sakurai, R. L. Shepard, and J. C. Gallop, "The status of johnson noise thermometry," *Metrologia*, vol. 33, no. 4, pp. 325–335, Aug. 1996. [Online]. Available: https://doi.org/10.1088/0026-1394/33/4/6

[131] J. Stefan, "Uber die beziehung zwischen der warmestrahlung und der temperatur, sitzungsberichte der mathematisch-naturwissenschaftlichen classe der kaiserlichen," *Akademie der Wissenschaften*, vol. 79, pp. S–391, 1879.

[132] L. Boltzmann, "Derivation of stefan's law, concerning the dependence of thermal radiation on temperature from the electromagnetic theory of light," *Annalen der Physik*, vol. 258, pp. 291–294, 1884.

[133] M. Planck, "Zur theorie des gesetzes der energieverteilung im normalspektrum," *VhDPG*, vol. 2, p. 238, 1900.

[134] ——, "Über das gesetz der energieverteilung im normalspektrum," *Annalen der Physik*, vol. 309, no. 4, pp. 553–563, 1901.

[135] J. B. Johnson, "Thermal agitation of electricity in conductors," *Physical Review*, vol. 32, no. 1, pp. 97–109, Jul. 1928. [Online]. Available: https://doi.org/10.1103/physrev.32.97

[136] H. Nyquist, "Thermal agitation of electric charge in conductors," *Physical Review*, vol. 32, no. 1, pp. 110–113, Jul. 1928. [Online]. Available: https://doi.org/10.1103/physrev.32.110

[137] Sbyrnes321, "JohnsonNoiseEquivalentCircuits," Wikipedia, 2013. [Online]. Available: https://commons.wikimedia.org/wiki/File:JohnsonNoiseEquivalentCircuits.svg

[138] S. R. Systems, *MODEL SR830 DSP Lock-In Amplifier*, 2nd ed., Stanford Research Systems, Sunnyvale, CA, October 2011, available at https://www.thinksrs.com/downloads/pdfs/manuals/SR830m.pdf.

[139] C. J. Borkowski and T. V. Blalock, "A new method of johnson noise thermometry," *Review of Scientific Instruments*, vol. 45, no. 2, pp. 151–162, Feb. 1974. [Online]. Available: https://doi.org/10.1063/1.1686578

[140] M. G. Pepper and J. B. Brown, "Absolute high-temperature johnson noise thermometry," *Journal of Physics E: Scientific Instruments*, vol. 12, no. 1, pp. 31–34, Jan. 1979. [Online]. Available: https://doi.org/10.1088/0022-3735/12/1/010

[141] R. H. Dicke, "The measurement of thermal radiation at microwave frequencies," *Review of Scientific Instruments*, vol. 17, no. 7, pp. 268–275, Jul. 1946. [Online]. Available: https://doi.org/10.1063/1.1770483

[142] D. F. Wait, "The sensitivity of the dicke radiometer," *Journal of Research of the National Bureau of Standards, Section C: Engineering and Instrumentation*, vol. 71C, no. 2, p. 127, Apr. 1967. [Online]. Available: https://doi.org/10.6028/jres.071c.015

[143] M. Banerjee, M. Heiblum, V. Umansky, D. E. Feldman, Y. Oreg, and A. Stern, "Observation of half-integer thermal hall conductance," *Nature*, vol. 559, no. 7713, pp. 205–210, Jun. 2018. [Online]. Available: https://doi.org/10.1038/s41586-018-0184-1

[144] H. Inoue, A. Grivnin, Y. Ronen, M. Heiblum, V. Umansky, and D. Mahalu, "Proliferation of neutral modes in fractional quantum hall states," *Nature Communications*, vol. 5, no. 1, Jun. 2014. [Online]. Available: https://doi.org/10.1038/ncomms5067

[145] Y. Ronen, Y. Cohen, J.-H. Kang, A. Haim, M.-T. Rieder, M. Heiblum, D. Mahalu, and H. Shtrikman, "Charge of a quasiparticle in a superconductor," *Proceedings of the National Academy of Sciences*, vol. 113, no. 7, pp. 1743–1748, Feb. 2016. [Online]. Available: https://doi.org/10.1073/pnas.1515173113

[146] P. Zhou, L. Chen, Y. Liu, I. Sochnikov, A. T. Bollinger, M.-G. Han, Y. Zhu, X. He, I. Božović, and D. Natelson, "Electron pairing in the pseudogap state revealed by shot noise in copper oxide junctions," *Nature*, vol. 572, no. 7770, pp. 493–496, Aug. 2019. [Online]. Available: https://doi.org/10.1038/s41586-019-1486-7

[147] L. Chen, D. T. Lowder, E. Bakali, A. M. Andrews, W. Schrenk, M. Waas, R. Svagera, G. Eguchi, L. Prochaska, Y. Wang, C. Setty, S. Sur, Q. Si, S. Paschen, and D. Natelson, "Shot noise indicates the lack of quasiparticles in a strange metal," 2022. [Online]. Available: https://arxiv.org/abs/2206.00673

[148] J. K. Viljas and T. T. Heikkilä, "Electron-phonon heat transfer in monolayer and bilayer graphene," *Physical Review B*, vol. 81, no. 24, Jun. 2010. [Online]. Available: https://doi.org/10.1103/physrevb.81.245404

[149] G. D. Mahan, *Many-Particle Physics*, 3rd ed. Kluwer Academic/Plenum Publishers, 2000.

[150] F. C. Wellstood, C. Urbina, and J. Clarke, "Hot-electron effects in metals," *Physical Review B*, vol. 49, no. 9, pp. 5942–5955, Mar. 1994. [Online]. Available: https://doi.org/10.1103/physrevb.49.5942

[151] A. C. Betz, F. Vialla, D. Brunel, C. Voisin, M. Picher, A. Cavanna, A. Madouri, G. Fève, J.-M. Berroir, B. Plaçais, and E. Pallecchi, "Hot electron cooling by acoustic phonons in graphene," *Physical Review Letters*, vol. 109, no. 5, Aug. 2012. [Online]. Available: https://doi.org/10.1103/physrevlett.109.056805

[152] C. B. McKitterick, D. E. Prober, and M. J. Rooks, "Electron-phonon cooling in large monolayer graphene devices," *Physical Review B*, vol. 93, no. 7, Feb. 2016. [Online]. Available: https://doi.org/10.1103/physrevb.93.075410

[153] A. Laitinen, M. Kumar, M. Oksanen, B. Plaçais, P. Virtanen, and P. Hakonen, "Coupling between electrons and optical phonons in suspended bilayer graphene," *Physical Review B*, vol. 91, no. 12, Mar. 2015. [Online]. Available: https://doi.org/10.1103/physrevb.91.121414

[154] A. Fay, R. Danneau, J. K. Viljas, F. Wu, M. Y. Tomi, J. Wengler, M. Wiesner, and P. J. Hakonen, "Shot noise and conductivity at high bias in bilayer graphene: Signatures of electron-optical phonon coupling," *Physical Review B*, vol. 84, no. 24, Dec. 2011. [Online]. Available: https://doi.org/10.1103/physrevb.84.245427

[155] E. A. A. Pogna, X. Jia, A. Principi, A. Block, L. Banszerus, J. Zhang, X. Liu, T. Sohier, S. Forti, K. Soundarapandian, B. Terrés, J. D. Mehew, C. Trovatello, C. Coletti, F. H. L. Koppens, M. Bonn, H. I. Wang, N. van Hulst, M. J. Verstraete, H. Peng, Z. Liu, C. Stampfer, G. Cerullo, and K.-J. Tielrooij, "Hot-carrier cooling in high-quality graphene is intrinsically limited by optical phonons," *ACS Nano*, vol. 15, no. 7, pp. 11 285–11 295, Jun. 2021. [Online]. Available: https://doi.org/10.1021/acsnano.0c10864

[156] D. Brunel, S. Berthou, R. Parret, F. Vialla, P. Morfin, Q. Wilmart, G. Fève, J.-M. Berroir, P. Roussignol, C. Voisin, and B. Plaçais, "Onset of optical-phonon cooling in multilayer graphene revealed by RF noise and black-body radiation thermometries," *Journal of Physics: Condensed Matter*, vol. 27, no. 16, p. 164208, Apr. 2015. [Online]. Available: https://doi.org/10.1088/0953-8984/27/16/164208

[157] A. Laitinen, M. Oksanen, A. Fay, D. Cox, M. Tomi, P. Virtanen, and P. J. Hakonen, "Electron–phonon coupling in suspended graphene: Supercollisions by ripples," *Nano Letters*, vol. 14, no. 6, pp. 3009–3013, May 2014. [Online]. Available: https://doi.org/10.1021/nl404258a

[158] A. C. Betz, S. H. Jhang, E. Pallecchi, R. Ferreira, G. Fève, J.-M. Berroir, and B. Plaçais, "Supercollision cooling in undoped graphene," *Nature Physics*, vol. 9, no. 2, pp. 109–112, Dec. 2012. [Online]. Available: https://doi.org/10.1038/nphys2494

[159] A. V. Talanov, J. Waissman, T. Taniguchi, K. Watanabe, and P. Kim, "High-bandwidth, variable-resistance differential noise thermometry," *Review of Scientific Instruments*, vol. 92, no. 1, p. 014904, Jan. 2021. [Online]. Available: https://doi.org/10.1063/5.0026488

[160] D. E. Prober, "Superconducting terahertz mixer using a transition-edge microbolometer," *Applied Physics Letters*, vol. 62, no. 17, pp. 2119–2121, Apr. 1993. [Online]. Available: https://doi.org/10.1063/1.109445

[161] F. Völklein, H. Reith, T. W. Cornelius, M. Rauber, and R. Neumann, "The experimental investigation of thermal conductivity and the wiedemann–franz law for single metallic nanowires," *Nanotechnology*, vol. 20, no. 32, p. 325706, Jul. 2009. [Online]. Available: https://doi.org/10.1088/0957-4484/20/32/325706

[162] C. Pozderac and B. Skinner, "Relation between johnson noise and heating power in a two-terminal conductor," *Physical Review B*, vol. 104, no. 16, Oct. 2021. [Online]. Available: https://doi.org/10.1103/physrevb.104.l161403

[163] E. V. Sukhorukov and D. Loss, "Universality of shot noise in multiterminal diffusive conductors," *Physical Review Letters*, vol. 80, no. 22, pp. 4959–4962, Jun. 1998. [Online]. Available: https://doi.org/10.1103/physrevlett.80.4959

[164] ——, "Noise in multiterminal diffusive conductors: Universality, nonlocality, and exchange effects," *Physical Review B*, vol. 59, no. 20, pp. 13 054–13 066, May 1999. [Online]. Available: https://doi.org/10.1103/physrevb.59.13054

[165] J. C. W. Song and L. S. Levitov, "Shockley-ramo theorem and long-range photocurrent response in gapless materials," *Physical Review B*, vol. 90, no. 7, Aug. 2014. [Online]. Available: https://doi.org/10.1103/physrevb.90.075415

[166] Y.-T. Tu and S. D. Sarma, "Wiedemann-franz law in graphene in the presence of a weak magnetic field," 2023. [Online]. Available: https://arxiv.org/abs/2307.05477

[167] V. I. Kozub and A. M. Rudin, "Shot noise in mesoscopic diffusive conductors in the limit of strong electron-electron scattering," *Physical Review B*, vol. 52, no. 11, pp. 7853–7856, Sep. 1995. [Online]. Available: https://doi.org/10.1103/physrevb.52.7853

[168] M. de Jong, "Shot noise and electrical conduction in mesoscopic systems," Ph.D. dissertation, Leiden University, June 1995.

[169] K. C. Fong, "Impact of contact resistance in lorenz number measurements," 2017. [Online]. Available: https://arxiv.org/abs/1711.04005

[170] A. H. Steinbach, J. M. Martinis, and M. H. Devoret, "Observation of hot-electron shot noise in a metallic resistor," *Physical Review Letters*, vol. 76, no. 20, pp. 3806–3809, May 1996. [Online]. Available: https://doi.org/10.1103/physrevlett.76.3806

[171] R. J. Schoelkopf, P. J. Burke, A. A. Kozhevnikov, D. E. Prober, and M. J. Rooks, "Frequency dependence of shot noise in a diffusive mesoscopic conductor," *Physical Review Letters*, vol. 78, no. 17, pp. 3370–3373, Apr. 1997. [Online]. Available: https://doi.org/10.1103/physrevlett.78.3370

[172] K. C. Fong, personal communication.

[173] A. Gahoi, S. Kataria, F. Driussi, S. Venica, H. Pandey, D. Esseni, L. Selmi, and M. C. Lemme, "Dependable contact related parameter extraction in graphene–metal junctions," *Advanced Electronic Materials*, vol. 6, no. 10, p. 2000386, Sep. 2020. [Online]. Available: https://doi.org/10.1002/aelm.202000386

[174] J. Waissman, L. E. Anderson, A. V. Talanov, Z. Yan, Y. J. Shin, D. H. Najafabadi, M. Rezaee, X. Feng, D. G. Nocera, T. Taniguchi, K. Watanabe, B. Skinner, K. A. Matveev, and P. Kim, "Electronic thermal transport measurement in low-dimensional materials with graphene non-local noise thermometry," *Nature Nanotechnology*, vol. 17, no. 2, pp. 166–173, Nov. 2021. [Online]. Available: https://doi.org/10.1038/s41565-021-01015-x

[175] J. Crossno, "Electronic thermal conductance of graphene via electrical noise," Ph.D. dissertation, Harvard University, 2017.

[176] A. Hui and B. Skinner, "Current noise of hydrodynamic electrons," *Physical Review Letters*, vol. 130, no. 25, Jun. 2023. [Online]. Available: https://doi.org/10.1103/physrevlett.130.256301

[177] J. L. M. Poiseuille, "Recherches sur la motion circulaire des fluides dans les tubes capillaires," *Comptes Rendus de l'Académie des Sciences*, vol. 15, pp. 1041–1048, 1842.

[178] L. Landau and E. Lifshitz, *Fluid Mechanics: Landau and Lifshitz: Course of Theoretical Physics, Volume 6*. Elsevier Science, 2013, vol. 6.

[179] S. Li, M. Khodas, and A. Levchenko, "Conformal maps of viscous electron flow in the gurzhi crossover," *Physical Review B*, vol. 104, no. 15, Oct. 2021. [Online]. Available: https://doi.org/10.1103/physrevb.104.155305

[180] H. Yoshino and K. Murata, "Significant enhancement of electronic thermal conductivity of two-dimensional zero-gap systems by bipolar-diffusion effect,"

Journal of the Physical Society of Japan, vol. 84, no. 2, p. 024601, Feb. 2015. [Online]. Available: https://doi.org/10.7566/jpsj.84.024601

[181] X. Liu, K. Watanabe, T. Taniguchi, B. I. Halperin, and P. Kim, "Quantum hall drag of exciton condensate in graphene," *Nature Physics*, vol. 13, no. 8, pp. 746–750, May 2017. [Online]. Available: https://doi.org/10.1038/nphys4116

[182] V. V. Talanov, N. M. L. Jr, V. Borzenets, N. Gagliolo, A. B. Cawthorne, and A. Orozco, "A scanning SQUID microscope with 200 MHz bandwidth," *Superconductor Science and Technology*, vol. 27, no. 4, p. 044032, Mar. 2014. [Online]. Available: https://doi.org/10.1088/0953-2048/27/4/044032

[183] L. Spietz, K. W. Lehnert, I. Siddiqi, and R. J. Schoelkopf, "Primary electronic thermometry using the shot noise of a tunnel junction," *Science*, vol. 300, no. 5627, pp. 1929–1932, Jun. 2003. [Online]. Available: https://doi.org/10.1126/science.1084647

[184] D. Rogovin and D. Scalapino, "Fluctuation phenomena in tunnel junctions," *Annals of Physics*, vol. 86, no. 1, pp. 1–90, Jul. 1974. [Online]. Available: https://doi.org/10.1016/0003-4916(74)90430-8

[185] U. Fano, "Ionization yield of radiations. II. the fluctuations of the number of ions," *Physical Review*, vol. 72, no. 1, pp. 26–29, Jul. 1947. [Online]. Available: https://doi.org/10.1103/physrev.72.26

[186] L. DiCarlo, J. R. Williams, Y. Zhang, D. T. McClure, and C. M. Marcus, "Shot noise in graphene," *Physical Review Letters*, vol. 100, no. 15, Apr. 2008. [Online]. Available: https://doi.org/10.1103/physrevlett.100.156801

[187] V. A. Khlus, "Current and voltage fluctuations in microjunctions between normal metals and superconductors," *Soviet physics, Journal of Experimental and Theoretical Physics*, vol. 93, no. 6, pp. 3806–3809, Dec. 1987. [Online]. Available: http://jetp.ras.ru/cgi-bin/dn/e_066_06_1243.pdf

[188] K. J. Tielrooij, J. C. W. Song, S. A. Jensen, A. Centeno, A. Pesquera, A. Z. Elorza, M. Bonn, L. S. Levitov, and F. H. L. Koppens, "Photoexcitation cascade and multiple hot-carrier generation in graphene," *Nature Physics*, vol. 9, no. 4, pp. 248–252, Feb. 2013. [Online]. Available: https://doi.org/10.1038/nphys2564

[189] D. Brida, A. Tomadin, C. Manzoni, Y. J. Kim, A. Lombardo, S. Milana, R. R. Nair, K. S. Novoselov, A. C. Ferrari, G. Cerullo, and M. Polini, "Ultrafast collinear scattering and carrier multiplication in graphene," *Nature Communications*, vol. 4, no. 1, Jun. 2013. [Online]. Available: https://doi.org/10.1038/ncomms2987

[190] K. J. Tielrooij, L. Piatkowski, M. Massicotte, A. Woessner, Q. Ma, Y. Lee, K. S. Myhro, C. N. Lau, P. Jarillo-Herrero, N. F. van Hulst, and F. H. L. Koppens, "Generation of photovoltage in graphene on a femtosecond timescale through efficient carrier heating," *Nature Nanotechnology*, vol. 10, no. 5, pp. 437–443, Apr. 2015. [Online]. Available: https://doi.org/10.1038/nnano.2015.54

[191] L. Shi, D. Li, C. Yu, W. Jang, D. Kim, Z. Yao, P. Kim, and A. Majumdar, "Measuring thermal and thermoelectric properties of one-dimensional nanostructures using a microfabricated device," *Journal of Heat Transfer*, vol. 125, no. 5, pp. 881–888, Sep. 2003. [Online]. Available: https://doi.org/10.1115/1.1597619

[192] C. Dames and G. Chen, "1ω ,2ω, and 3ω methods for measurements of thermal properties," *Review of Scientific Instruments*, vol. 76, no. 12, Dec. 2005. [Online]. Available: https://doi.org/10.1063/1.2130718

[193] E. V. Castro, K. S. Novoselov, S. V. Morozov, N. M. R. Peres, J. M. B. L. dos Santos, J. Nilsson, F. Guinea, A. K. Geim, and A. H. C. Neto, "Biased bilayer graphene: Semiconductor with a gap tunable by the electric field effect," *Physical Review Letters*, vol. 99, no. 21, Nov. 2007. [Online]. Available: https://doi.org/10.1103/physrevlett.99.216802

[194] J. B. Oostinga, H. B. Heersche, X. Liu, A. F. Morpurgo, and L. M. K. Vandersypen, "Gate-induced insulating state in bilayer graphene devices," *Nature Materials*, vol. 7, no. 2, pp. 151–157, Dec. 2007. [Online]. Available: https://doi.org/10.1038/nmat2082

[195] H. Min, B. Sahu, S. K. Banerjee, and A. H. MacDonald, "Ab initiotheory of gate induced gaps in graphene bilayers," *Physical Review B*, vol. 75, no. 15, Apr. 2007. [Online]. Available: https://doi.org/10.1103/physrevb.75.155115

[196] E. McCann, "Asymmetry gap in the electronic band structure of bilayer graphene," *Physical Review B*, vol. 74, no. 16, Oct. 2006. [Online]. Available: https://doi.org/10.1103/physrevb.74.161403

[197] T. Ohta, A. Bostwick, T. Seyller, K. Horn, and E. Rotenberg, "Controlling the electronic structure of bilayer graphene," *Science*, vol. 313, no. 5789, pp. 951–954, Aug. 2006. [Online]. Available: https://doi.org/10.1126/science.1130681

[198] S. Weinreb, J. Bardin, H. Mani, and G. Jones, "Matched wideband low-noise amplifiers for radio astronomy," *Review of Scientific Instruments*, vol. 80, no. 4, p. 044702, Apr. 2009. [Online]. Available: https://doi.org/10.1063/1.3103939

[199] D. R. Schmidt, R. J. Schoelkopf, and A. N. Cleland, "Photon-mediated thermal relaxation of electrons in nanostructures," *Physical Review Letters*, vol. 93, no. 4, Jul. 2004. [Online]. Available: https://doi.org/10.1103/physrevlett.93.045901

[200] D. White, "The noise bandwidth of sampled data systems," *IEEE Transactions on Instrumentation and Measurement*, vol. 38, no. 6, pp. 1036–1043, Dec. 1989. [Online]. Available: https://doi.org/10.1109/19.46397

[201] M. J. Roberts and T. V. Blalock, "Effect of filter frequency response on the uncertainty in measuring statistical estimators of input noise," *Review of Scientific Instruments*, vol. 56, no. 2, pp. 326–328, Feb. 1985. [Online]. Available: https://doi.org/10.1063/1.1138352

[202] P. Kittel, "Comment on the equivalent noise bandwidth approximation," *Review of Scientific Instruments*, vol. 48, no. 9, pp. 1214–1215, Sep. 1977. [Online]. Available: https://doi.org/10.1063/1.1135225

[203] M. Gupta, "Thermal noise in nonlinear resistive devices and its circuit representation," *Proceedings of the IEEE*, vol. 70, no. 8, pp. 788–804, 1982. [Online]. Available: https://doi.org/10.1109/proc.1982.12405

[204] H. Wang and M. Sen, "Analysis of the 3-omega method for thermal conductivity measurement," *International Journal of Heat and Mass Transfer*, vol. 52, no. 7-8, pp. 2102–2109, Mar. 2009. [Online]. Available: https://doi.org/10.1016/j.ijheatmasstransfer.2008.10.020

[205] L. Lu, W. Yi, and D. L. Zhang, "3 method for specific heat and thermal conductivity measurements," *Review of Scientific Instruments*, vol. 72, no. 7, pp. 2996–3003, Jul. 2001. [Online]. Available: https://doi.org/10.1063/1.1378340

[206] O. Bourgeois, T. Fournier, and J. Chaussy, "Measurement of the thermal conductance of silicon nanowires at low temperature," *Journal of Applied Physics*, vol. 101, no. 1, Jan. 2007. [Online]. Available: https://doi.org/10.1063/1.2400093

[207] L. R. Holland and R. C. Smith, "Analysis of temperature fluctuations in ac heated filaments," *Journal of Applied Physics*, vol. 37, no. 12, pp. 4528–4536, Nov. 1966. [Online]. Available: https://doi.org/10.1063/1.1708075

[208] J. Hou, X. Wang, P. Vellelacheruvu, J. Guo, C. Liu, and H.-M. Cheng, "Thermal characterization of single-wall carbon nanotube bundles using the self-heating 3 technique," *Journal of Applied Physics*, vol. 100, no. 12, Dec. 2006. [Online]. Available: https://doi.org/10.1063/1.2402973

[209] X. J. Hu, A. A. Padilla, J. Xu, T. S. Fisher, and K. E. Goodson, "3-omega measurements of vertically oriented carbon nanotubes on silicon," *Journal of Heat Transfer*, vol. 128, no. 11, pp. 1109–1113, Nov. 2005. [Online]. Available: https://doi.org/10.1115/1.2352778

[210] T.-Y. Choi, D. Poulikakos, J. Tharian, and U. Sennhauser, "Measurement of the thermal conductivity of individual carbon nanotubes by the four-point three-method," *Nano Letters*, vol. 6, no. 8, pp. 1589–1593, Jul. 2006. [Online]. Available: https://doi.org/10.1021/nl060331v

[211] A. S. Sedra and K. C. Smith, *Microelectronic Circuits*, 7th ed., ser. Oxford Series in Electrical and Computer Engineering (Hardco. Cary, NC: Oxford University Press, Nov. 2014.

[212] S. R. Systems, *Model DS360 Ultra Low Distortion Function Generator*, 2nd ed., Stanford Research Systems, Sunnyvale, CA, September 2021, available at https://www.thinksrs.com/downloads/pdfs/manuals/DS360m.pdf.

[213] B. Kent. (1999) Secrets of amplification. [Online]. Available: https://the-shed.nz/2018-6-27-secrets-of-amplification/

[214] N. Klimovich, P. Day, S. Shu, B. H. Eom, H. Leduc, and A. Beyer, "Demonstration of a quantum noise limited traveling-wave parametric amplifier," 2023. [Online]. Available: https://arxiv.org/abs/2306.11028

[215] T. C. White, J. Y. Mutus, I.-C. Hoi, R. Barends, B. Campbell, Y. Chen, Z. Chen, B. Chiaro, A. Dunsworth, E. Jeffrey, J. Kelly, A. Megrant, C. Neill, P. J. J. O'Malley, P. Roushan, D. Sank, A. Vainsencher, J. Wenner, S. Chaudhuri, J. Gao, and J. M. Martinis, "Traveling wave parametric amplifier with josephson junctions using minimal resonator phase matching," *Applied Physics Letters*, vol. 106, no. 24, Jun. 2015. [Online]. Available: https://doi.org/10.1063/1.4922348

[216] C. Macklin, K. O'Brien, D. Hover, M. E. Schwartz, V. Bolkhovsky, X. Zhang, W. D. Oliver, and I. Siddiqi, "A near–quantum-limited josephson traveling-wave parametric amplifier," *Science*, vol. 350, no. 6258, pp. 307–310, Oct. 2015. [Online]. Available: https://doi.org/10.1126/science.aaa8525

[217] S. Simbierowicz, V. Vesterinen, J. Milem, A. Lintunen, M. Oksanen, L. Roschier, L. Grönberg, J. Hassel, D. Gunnarsson, and R. E. Lake, "Characterizing cryogenic amplifiers with a matched temperature-variable noise source," *Review of Scientific Instruments*, vol. 92, no. 3, Mar. 2021. [Online]. Available: https://doi.org/10.1063/5.0028951

[218] L. Ranzani, G. Ribeill, B. Hassick, and K. C. Fong, "Wideband josephson parametric amplifier with integrated transmission line transformer," in *2022 IEEE International Conference on Quantum Computing and Engineering (QCE)*. IEEE, Sep. 2022. [Online]. Available: https://doi.org/10.1109/qce53715.2022.00052

[219] P. S. Alekseev and A. P. Dmitriev, "Viscosity of two-dimensional electrons," *Physical Review B*, vol. 102, no. 24, Dec. 2020. [Online]. Available: https://doi.org/10.1103/physrevb.102.241409

[220] A. Levchenko and J. Schmalian, "Transport properties of strongly coupled electron–phonon liquids," *Annals of Physics*, vol. 419, p. 168218, Aug. 2020. [Online]. Available: https://doi.org/10.1016/j.aop.2020.168218

[221] N. J. Couto, D. Costanzo, S. Engels, D.-K. Ki, K. Watanabe, T. Taniguchi, C. Stampfer, F. Guinea, and A. F. Morpurgo, "Random strain fluctuations as dominant disorder source for high-quality on-substrate graphene devices," *Physical Review X*, vol. 4, no. 4, Oct. 2014. [Online]. Available: https://doi.org/10.1103/physrevx.4.041019

[222] J. Martin, N. Akerman, G. Ulbricht, T. Lohmann, J. H. Smet, K. von Klitzing, and A. Yacoby, "Observation of electron–hole puddles in graphene using a scanning single-electron transistor," *Nature Physics*, vol. 4, no. 2, pp. 144–148, Nov. 2007. [Online]. Available: https://doi.org/10.1038/nphys781

[223] Y. Zhang, V. W. Brar, C. Girit, A. Zettl, and M. F. Crommie, "Origin of spatial charge inhomogeneity in graphene," *Nature Physics*, vol. 5, no. 10, pp. 722–726, Aug. 2009. [Online]. Available: https://doi.org/10.1038/nphys1365

[224] S. Samaddar, I. Yudhistira, S. Adam, H. Courtois, and C. Winkelmann, "Charge puddles in graphene near the dirac point," *Physical Review Letters*, vol. 116, no. 12, Mar. 2016. [Online]. Available: https://doi.org/10.1103/physrevlett.116.126804

[225] S. Li, A. Levchenko, and A. V. Andreev, "Hydrodynamic electron transport near charge neutrality," *Physical Review B*, vol. 102, no. 7, Aug. 2020. [Online]. Available: https://doi.org/10.1103/physrevb.102.075305

[226] E. Watanabe, A. Conwill, D. Tsuya, and Y. Koide, "Low contact resistance metals for graphene based devices," *Diamond and Related Materials*, vol. 24, pp. 171–174, Apr. 2012. [Online]. Available: https://doi.org/10.1016/j.diamond.2012.01.019

[227] M. Kamada, V. Gall, J. Sarkar, M. Kumar, A. Laitinen, I. Gornyi, and P. Hakonen, "Strong magnetoresistance in a graphene corbino disk at low

magnetic fields," *Physical Review B*, vol. 104, no. 11, Sep. 2021. [Online]. Available: https://doi.org/10.1103/physrevb.104.115432

[228] A. Levchenko, S. Li, and A. V. Andreev, "Hydrodynamic magnetoresistance in graphene corbino devices," *Physical Review B*, vol. 106, no. 20, Nov. 2022. [Online]. Available: https://doi.org/10.1103/physrevb.106.l201306

[229] M. M. Elahi, Y. Zeng, C. R. Dean, and A. W. Ghosh, "Direct evidence of klein-antiklein tunneling of graphitic electrons in a corbino geometry," 2022. [Online]. Available: https://arxiv.org/abs/2210.10429

[230] P. Gallagher, C.-S. Yang, T. Lyu, F. Tian, R. Kou, H. Zhang, K. Watanabe, T. Taniguchi, and F. Wang, "Quantum-critical conductivity of the dirac fluid in graphene," *Science*, vol. 364, no. 6436, pp. 158–162, Apr. 2019. [Online]. Available: https://doi.org/10.1126/science.aat8687

[231] L. Landau, "Diamagnetismus der metalle," *Zeitschrift für Physik*, vol. 64, no. 9-10, pp. 629–637, Sep. 1930. [Online]. Available: https://doi.org/10.1007/bf01397213

[232] B. I. Halperin, "Quantized hall conductance, current-carrying edge states, and the existence of extended states in a two-dimensional disordered potential," *Physical Review B*, vol. 25, no. 4, pp. 2185–2190, Feb. 1982. [Online]. Available: https://doi.org/10.1103/physrevb.25.2185

[233] M. O. Goerbig, "Electronic properties of graphene in a strong magnetic field," *Reviews of Modern Physics*, vol. 83, no. 4, pp. 1193–1243, Nov. 2011. [Online]. Available: https://doi.org/10.1103/revmodphys.83.1193

[234] K. I. Bolotin, F. Ghahari, M. D. Shulman, H. L. Stormer, and P. Kim, "Observation of the fractional quantum hall effect in graphene," *Nature*, vol. 462, no. 7270, pp. 196–199, Nov. 2009. [Online]. Available: https://doi.org/10.1038/nature08582

[235] B. I. Halperin and J. K. Jain, *Fractional quantum hall effects: New developments*, B. I. Halperin and J. K. Jain, Eds. Singapore, Singapore: World Scientific Publishing, Jun. 2020.

[236] M. Banerjee, M. Heiblum, A. Rosenblatt, Y. Oreg, D. E. Feldman, A. Stern, and V. Umansky, "Observed quantization of anyonic heat flow," *Nature*, vol. 545, no. 7652, pp. 75–79, Apr. 2017. [Online]. Available: https://doi.org/10.1038/nature22052

[237] R. A. Melcer, S. Konyzheva, M. Heiblum, and V. Umansky, "Direct determination of the topological thermal conductance via local power measurement," *Nature Physics*, vol. 19, no. 3, pp. 327–332, Jan. 2023. [Online]. Available: https://doi.org/10.1038/s41567-022-01885-5

[238] D. F. Mross, Y. Oreg, A. Stern, G. Margalit, and M. Heiblum, "Theory of disorder-induced half-integer thermal hall conductance," *Physical Review Letters*, vol. 121, no. 2, Jul. 2018. [Online]. Available: https://doi.org/10.1103/physrevlett.121.026801

[239] B. Dutta, V. Umansky, M. Banerjee, and M. Heiblum, "Isolated ballistic non-abelian interface channel," *Science*, vol. 377, no. 6611, pp. 1198–1201, Sep. 2022. [Online]. Available: https://doi.org/10.1126/science.abm6571

[240] R. A. Melcer, A. Gil, A.-K. Paul, P. Tiwary, V. Umansky, M. Heiblum, Y. Oreg, A. Stern, and E. Berg, "Heat conductance of the quantum hall bulk," 2023. [Online]. Available: https://arxiv.org/abs/2306.14977

[241] Y. Cao, V. Fatemi, A. Demir, S. Fang, S. L. Tomarken, J. Y. Luo, J. D. Sanchez-Yamagishi, K. Watanabe, T. Taniguchi, E. Kaxiras, R. C. Ashoori, and P. Jarillo-Herrero, "Correlated insulator behaviour at half-filling in magic-angle graphene superlattices," *Nature*, vol. 556, no. 7699, pp. 80–84, Mar. 2018. [Online]. Available: https://doi.org/10.1038/nature26154

[242] Y. Cao, V. Fatemi, S. Fang, K. Watanabe, T. Taniguchi, E. Kaxiras, and P. Jarillo-Herrero, "Unconventional superconductivity in magic-angle graphene superlattices," *Nature*, vol. 556, no. 7699, pp. 43–50, Mar. 2018. [Online]. Available: https://doi.org/10.1038/nature26160

[243] E. Y. Andrei and A. H. MacDonald, "Graphene bilayers with a twist," *Nature Materials*, vol. 19, no. 12, pp. 1265–1275, Nov. 2020. [Online]. Available: https://doi.org/10.1038/s41563-020-00840-0

[244] E. Y. Andrei, D. K. Efetov, P. Jarillo-Herrero, A. H. MacDonald, K. F. Mak, T. Senthil, E. Tutuc, A. Yazdani, and A. F. Young, "The marvels of moiré materials," *Nature Reviews Materials*, vol. 6, no. 3, pp. 201–206, Mar. 2021. [Online]. Available: https://doi.org/10.1038/s41578-021-00284-1

[245] H. Yang, L. Liu, H. Yang, Y. Zhang, X. Wu, Y. Huang, H.-J. Gao, and Y. Wang, "Advance in two-dimensional twisted moiré materials: Fabrication, properties, and applications," *Nano Research*, vol. 16, no. 2, pp. 2579–2596, Nov. 2022. [Online]. Available: https://doi.org/10.1007/s12274-022-5025-8

[246] G. Abbas, Y. Li, H. Wang, W.-X. Zhang, C. Wang, and H. Zhang, "Recent advances in twisted structures of flatland materials and crafting moiré superlattices," *Advanced Functional Materials*, vol. 30, no. 36, Jul. 2020. [Online]. Available: https://doi.org/10.1002/adfm.202000878

[247] Y. Liu, C. Zeng, J. Yu, J. Zhong, B. Li, Z. Zhang, Z. Liu, Z. M. Wang, A. Pan, and X. Duan, "Moiré superlattices and related moiré excitons in twisted van der waals heterostructures," *Chemical Society Reviews*, vol. 50, no. 11, pp. 6401–6422, 2021. [Online]. Available: https://doi.org/10.1039/d0cs01002b

[248] X. Liu, Z. Hao, E. Khalaf, J. Y. Lee, Y. Ronen, H. Yoo, D. H. Najafabadi, K. Watanabe, T. Taniguchi, A. Vishwanath, and P. Kim, "Tunable spin-polarized correlated states in twisted double bilayer graphene," *Nature*, vol. 583, no. 7815, pp. 221–225, Jul. 2020. [Online]. Available: https://doi.org/10.1038/s41586-020-2458-7

[249] X. Liu, C.-L. Chiu, J. Y. Lee, G. Farahi, K. Watanabe, T. Taniguchi, A. Vishwanath, and A. Yazdani, "Spectroscopy of a tunable moiré system with a correlated and topological flat band," *Nature Communications*, vol. 12, no. 1, May 2021. [Online]. Available: https://doi.org/10.1038/s41467-021-23031-0

[250] K. S. Novoselov, D. Jiang, F. Schedin, T. J. Booth, V. V. Khotkevich, S. V. Morozov, and A. K. Geim, "Two-dimensional atomic crystals," *Proceedings of the National Academy of Sciences*, vol. 102, no. 30, pp. 10 451–10 453, Jul. 2005. [Online]. Available: https://doi.org/10.1073/pnas.0502848102

[251] J. R. Bence, "Analysis of short time series: Correcting for autocorrelation," *Ecology*, vol. 76, no. 2, pp. 628–639, Mar. 1995. [Online]. Available: https://doi.org/10.2307/1941218

[252] L. Evans, *Partial Differential Equations*, ser. Graduate studies in mathematics. American Mathematical Society, 2010. [Online]. Available: https://books.google.com/books?id=Xnu0o_EJrCQC

[253] L. Landau and E. Lifshitz, *Fluid Mechanics: Landau and Lifshitz: Course of Theoretical Physics, Volume 6*. Elsevier Science, 2013, no. v. 6. [Online]. Available: https://books.google.com/books?id=eOBbAwAAQBAJ

[254] L. Landau, E. Lifshitz, and L. Pitaevskii, *Course of Theoretical Physics: Statistical Physics, Part 2 : by E.M. Lifshitz and L.P. Pitaevskii*, 1980, no. v. 9. [Online]. Available: https://books.google.com/books?id=QAcenQAACAAJ

[255] W. Shockley, "Currents to Conductors Induced by a Moving Point Charge," *Journal of Applied Physics*, vol. 9, no. 10, pp. 635–636, 10 1938. [Online]. Available: https://doi.org/10.1063/1.1710367

[256] S. Ramo, "Currents induced by electron motion," *Proceedings of the IRE*, vol. 27, no. 9, pp. 584–585, 1939.

[257] P. D. Yoder, K. Gärtner, and W. Fichtner, "A generalized Ramo–Shockley theorem for classical to quantum transport at arbitrary frequencies," *Journal of Applied Physics*, vol. 79, no. 4, pp. 1951–1954, 02 1996. [Online]. Available: https://doi.org/10.1063/1.361074

[258] G. Cavalleri, E. Gatti, G. Fabri, and V. Svelto, "Extension of ramo's theorem as applied to induced charge in semiconductor detectors," *Nuclear Instruments and Methods*, vol. 92, no. 1, p. 137–140, Mar. 1971. [Online]. Available: http://dx.doi.org/10.1016/0029-554X(71)90235-7

[259] Z. He, "Review of the shockley–ramo theorem and its application in semiconductor gamma-ray detectors," *Nuclear Instruments and Methods in Physics Research Section A: Accelerators, Spectrometers, Detectors and Associated Equipment*, vol. 463, no. 1–2, p. 250–267, May 2001. [Online]. Available: http://dx.doi.org/10.1016/S0168-9002(01)00223-6

[260] K. Hughes, "Default colormaps: Are parula and viridis really an improvement over jet?" https://brushingupscience.com/2019/10/01/default-colormaps-are-parula-and-viridis-really-an-improvement-over-jet/, 2019.

[261] MathWorks, "cbrewer2 - MATLAB Central File Exchange," https://www.mathworks.com/matlabcentral/fileexchange/58350-cbrewer2, Accessed in 2023.

[262] "Colorbrewer 2.0," https://colorbrewer2.org/, Accessed in 2023.

This thesis was typeset using LaTeX, originally developed by Leslie Lamport and based on Donald Knuth's TeX. The body text is set in 11 point Latin Modern Roman, which is most definitely not a revival of Claude Garamont's humanist typeface. The above illustration, "Whispers of Discovery", was created by ChatGPT 4 and DALL · E 3 and has not been released under any license; it remains in ownership of the author of this dissertation. A template that can be used to format a PhD thesis with this look and feel has been released under the permissive MIT (X11) license, and can be found online at github.com/suchow/Dissertate or from its author, Jordan Suchow, at suchow@post.harvard.edu.